Springer Series in Biomaterials Science and Engineering 7

Zhifei Dai *Editor*

Advances in Nanotheranostics II

Cancer Theranostic Nanomedicine

Springer

Springer Series in Biomaterials Science and Engineering

Volume 7

Series editor
Prof. Min Wang
Department of Mechanical Engineering
The University of Hong Kong
Pokfulam Road, Hong Kong
e-mail: memwang@hku.hk

Aims and scope

The Springer Series in Biomaterials Science and Engineering addresses the manufacture, structure and properties, and applications of materials that are in contact with biological systems, temporarily or permanently. It deals with many aspects of modern biomaterials, from basic science to clinical applications, as well as host responses. It covers the whole spectrum of biomaterials – polymers, metals, glasses and ceramics, and composites/hybrids – and includes both biological materials (collagen, polysaccharides, biological apatites, etc.) and synthetic materials. The materials can be in different forms: single crystals, polycrystalline materials, particles, fibers/wires, coatings, non-porous materials, porous scaffolds, etc. New and developing areas of biomaterials, such as nano-biomaterials and diagnostic and therapeutic nanodevices, are also focuses in this series. Advanced analytical techniques that are applicable in R & D and theoretical methods and analyses for biomaterials are also important topics. Frontiers in nanomedicine, regenerative medicine and other rapidly advancing areas calling for great explorations are highly relevant.

The Springer Series in Biomaterials Science and Engineering aims to provide critical reviews of important subjects in the field, publish new discoveries and significant progresses that have been made in both biomaterials development and the advancement of principles, theories and designs, and report cutting-edge research and relevant technologies. The individual volumes in the series are thematic. The goal of each volume is to give readers a comprehensive overview of an area where new knowledge has been gained and insights made. Significant topics in the area are dealt with in good depth and future directions are predicted on the basis of current developments. As a collection, the series provides authoritative works to a wide audience in academia, the research community, and industry.

More information about this series at http://www.springer.com/series/10955

Zhifei Dai
Editor

Advances in Nanotheranostics II

Cancer Theranostic Nanomedicine

Springer

Editor
Zhifei Dai
Department of Biomedical Engineering
College of Engineering
Peking University
Beijing, China

ISSN 2195-0644 ISSN 2195-0652 (electronic)
Springer Series in Biomaterials Science and Engineering
ISBN 978-981-10-0061-4 ISBN 978-981-10-0063-8 (eBook)
DOI 10.1007/978-981-10-0063-8

Library of Congress Control Number: 2015957361

Springer Singapore Heidelberg New York Dordrecht London

Printed on acid-free paper

Springer Science+Business Media Singapore Pte Ltd. is part of Springer Science+Business Media (www.springer.com)

Preface

Recent advances in nanotechnology have produced a variety of functional nanoparticles such as magnetic nanoparticles, quantum dots, metallic nanoparticles, silica nanoparticles, liposomes, polymersomes and dendrimers, etc. A key feature of these nanoparticles is that they are easier to accumulate in the tumor than in healthy tissues. It has been found that the small size of nanoparticles can have a profound impact on their mode of endocytosis, cellular trafficking, and processing. Due to the unique attributes such as electronic, magnetic, optical, and structural properties, nanoparticles have been shown to be capable of functioning either as carriers for chemotherapeutic drugs to improve their therapeutic efficacy or as therapeutic agents in photodynamic, gene, thermal, and photothermal therapy or as molecular imaging agents to detect and monitor cancer progression.

The successful integration of diagnosis and therapy on a single agent using multifunctional nanoparticles has led to the birth of a new, highly interdisciplinary research field named "nanotheranostics," which has given hope in developing innovative strategies to enable "personalized medicine" to diagnose, treat, and follow up patients with cancer.

Nanotheranostic agents may offer us a powerful tool for the in vivo assessment of drug biodistribution and accumulation at the target site, for the minimally invasive in vivo visualization of the drug release from a provided nanovehicle, and for the prediction and real-time monitoring of therapeutic outcome. Thus, constructing compact nanoformulations with highly integrated modalities is of the essence in nanotheranostics. Yet, it has been proven to be a big challenge to fuse multiple components on a single nanoscale particle for combined diagnostics and therapy.

Although efficient cancer therapy is still problematic, currently nanotheranostics is developing very fast with significant achievements, fostering a new avenue for cancer therapy and diagnosis. To translate these applications into clinical use, the nanotheranostic agents must be optimized by starting with small-animal models and scaling up to nonhuman primate models. This should lay a solid foundation for the long-term development of nanotheranostics into clinical medical practice.

A survey of the recent advances and basic principles of nanotheranostics with a particular emphasis on the design and fabrication of various multifunctional

nanoparticles for cancer imaging (diagnosis) and therapy is summarized in two volumes of books entitled *Advances in Nanotheranostics I: Design and Fabrication of Theranostic Nanoparticles* and *Advances in Nanotheranostics II: Cancer Theranostic Nanomedicine.*

The volume, *Advances in Nanotheranostics I: Design and Fabrication of Theranostic Nanoparticles,* has three parts: Part I, "Gold Nanostructure-Based Theranostics"; Part II, "Theranostic Luminescent Nanoparticles"; and Part III. "Dendrimers and Liposomes for Theranostics." Part I includes three chapters, summarizing synthesis, surface modification and functionalization of gold nanostructures, and their use as therapeutic components, imaging contrast agents and theranostic platforms for imaging-guided therapy. Part II contains four chapters, each focusing on one of the following: fabrication of lanthanide-doped upconversion nanoparticles, quantum dots and organic dye-loaded nanoparticles, as well as their applications for multimodal imaging, imaging-guided drug delivery, and therapy. Part III consists of three chapters, reviewing dendrimers and liposome-based nanodevices, nanoscale imaging agents, drug delivery systems, and theranostic nanosystems for cancer treatment, respectively.

The volume *Advances in Nanotheranostics II: Cancer Theranostic Nanomedicine* has the following structure: Part I, "Magnetic Nanoparticles for MRI-based Theranostics"; Part II, "Ultrasonic Theranostic Agents"; and Part III, "Nanoparticles for Cancer Theranostics." Part I contains three chapters, describing controlled synthesis and surface modification of magnetic nanoparticles, molecular imaging of tumor angiogenesis, and MRI-based theranostics with magnetic nanoparticles. Part II consists of three chapters, summarizing ultrasound contrast agent-based multimodal imaging, drug delivery and therapy, and hollow mesoporous silica nanoparticles for magnetic resonance/ultrasound imaging-guided tumor therapy. Part III includes four chapters, demonstrating multifunctional nanoprobes for multimodality imaging and therapy of gastric cancer, nanoparticles for molecular imaging-guided gene delivery and therapy, and silica nanoparticles and micelles for cancer nanotheranostics, respectively.

It is hoped that these books will be of great interest for readers who want to follow up the exciting new development in theranostic nanomedicine. Each chapter was written by well-recognized experts in the related field. I would like to thank the authors most sincerely for their excellent contributions and congratulate them for the brilliant efforts that have resulted in these superb volumes. I also want to express my thanks to Professor Min Wang at the Department of Mechanical Engineering, University of Hong Kong, who is the Series Editor of Springer Series in Biomaterials Science and Engineering, and Springer Beijing office for providing me such a wonderful opportunity to edit these books, especially Ms. June Tang and Ms. Heather Feng for their support in publishing these volumes.

Beijing, China Zhifei Dai

Contents

Contributors

Mian Chen Paul C. Lauterbur Research Center for Biomedical Imaging, Institute of Biomedical and Health Engineering, Shenzhen Institutes of Advanced Technology, Chinese Academy of Sciences, Shenzhen, China

Yu Chen Shanghai Institute of Ceramics, Chinese Academy of Sciences, Shanghai, China

Hangrong Chen Shanghai Institute of Ceramics, Chinese Academy of Sciences, Shanghai, China

Huabing Chen Jiangsu Key Laboratory of Translational Research and Therapy for Neuro-Psycho-Diseases, and College of Pharmaceutical Sciences, Soochow University, Suzhou, China

Xin Chu Department of Materials Science and Engineering, College of Engineering, Peking University, Beijing, China

Daxiang Cui Institute of Nano Biomedicine and Engineering, Department of Instrument Science and Engineering, National Center for Translational Medicine, Collaborative Innovational Center for System Biology, Shanghai Jiao Tong University, Shanghai, People's Republic of China

Zhifei Dai Department of Biomedical Engineering, College of Engineering, Peking University, Beijing, China

Chuang Gao Department of Biomedical Engineering, College of Engineering, Peking University, Beijing, China

Ning Gu State Key Laboratory of Bioelectronics, Jiangsu Key Laboratory for Biomaterials and Devices, School of Biological Science & Medical Engineering, Southeast University, Nanjing, People's Republic of China

Yanglong Hou Department of Materials Science and Engineering, College of Engineering, Peking University, Beijing, China

Hengte Ke Jiangsu Key Laboratory of Translational Research and Therapy for Neuro-Psycho-Diseases, and College of Pharmaceutical Sciences, Soochow University, Suzhou, China

Linlin Li Beijing Institute of Nanoenergy and Nanosystems, Chinese Academy of Sciences, Beijing, People's Republic of China

Pan Li Second Affiliated Hospital and Institute of Ultrasound Imaging of Chongqing Medical University, Chogqing, China

Gang Liu State Key Laboratory of Molecular Vaccinology and Molecular Diagnostics & Center for Molecular Imaging and Translational Medicine, School of Public Health, Xiamen University, Xiamen, China

Huiyu Liu College of Life Science and Technology, Beijing University of Chemical Technology, Beijing, People's Republic of China

Ming Ma Shanghai Institute of Ceramics, Chinese Academy of Sciences, Shanghai, China

Tianxin Miao Bioengineering Program, College of Engineering and Mathematical Sciences, College of Medicine, University of Vermont, Burlington, VT, USA

Jianlin Shi Shanghai Institute of Ceramics, Chinese Academy of Sciences, Shanghai, China

Rui Tian State Key Laboratory of Molecular Vaccinology and Molecular Diagnostics & Center for Molecular Imaging and Translational Medicine, School of Public Health, Xiamen University, Xiamen, China

Shunhao Wang College of Life Science and Technology, Beijing University of Chemical Technology, Beijing, People's Republic of China

Jun Xie State Key Laboratory of Bioelectronics, Jiangsu Key Laboratory for Biomaterials and Devices, School of Biological Science and Medical Engineering, Southeast University, Nanjing, People's Republic of China

Fei Yan Paul C. Lauterbur Research Center for Biomedical Imaging, Institute of Biomedical and Health Engineering, Shenzhen Institutes of Advanced Technology, Chinese Academy of Sciences, Shenzhen, China

Qi Yang Xuanwu Hospital, Capital Medical University, Beijing, China

Jing Yu Department of Materials Science and Engineering, College of Engineering, Peking University, Beijing, China

Research Center of Magnetic and Electronic Materials, College of Materials Science and Engineering, Zhejing University of Technology, Hangzhou, China

Yun Zeng State Key Laboratory of Molecular Vaccinology and Molecular Diagnostics & Center for Molecular Imaging and Translational Medicine, School of Public Health, Xiamen University, Xiamen, China

Department of Pharmacology, West China School of Preclinical and Forensic Medicine, Sichuan University, Chengdu, China

Chunfu Zhang State Key Laboratory of Oncogenes and Related Genes, Shanghai Cancer Institute, School of Biomedical Engineering, Shanghai Jiao Tong University, Shanghai, People's Republic of China

Yu Zhang Electrical Engineering Program, College of Engineering and Mathematical Sciences, University of Vermont, Burlington, VT, USA

Yu Zhang State Key Laboratory of Bioelectronics, Jiangsu Key Laboratory for Biomaterials and Devices, School of Biological Science and Medical Engineering, Southeast University, Nanjing, People's Republic of China

Hairong Zheng Paul C. Lauterbur Research Center for Biomedical Imaging, Institute of Biomedical and Health Engineering, Shenzhen Institutes of Advanced Technology, Chinese Academy of Sciences, Shenzhen, China

Yuanyi Zheng Second Affiliated Hospital and Institute of Ultrasound Imaging of Chongqing Medical University, Chogqing, China

The original version of the List of Contributors was revised. The name and affiliation of Yu Zhang from Chapter 8 has been corrected and Included. An erratum can be found at http://dx.doi.org/10.1007/978-981-10-0063-8_11

Part I
Magnetic Nanoparticles for MRI-Based Theranostics

Chapter 1
Design of Magnetic Nanoparticles for MRI-Based Theranostics

Yanglong Hou, Jing Yu, and Xin Chu

1.1 Introduction

Magnetic resonance imaging is one of the most important noninvasive diagnosis tools in medical science. Paramagnetic and superparamagnetic nanoparticles (NPs) can enhance MRI as contrast agents. By integrating functionalities such as drug carriers, hyperthermia agents, or optical probes as nanoscale MRI contrast agents, multifunctional NPs can be prepared, which are helpful to diagnosis and treatment of cancer and other diseases.

MRI has been the preferred tool for imaging the brain and the central nervous system and for assessing cardiac function and detecting tumors. It is expected to become a very important tool for molecular and cellular imaging due to its good ability of soft tissue imaging with high resolution [1]. It is also useful for the early detection of lesions. To make a diagnosis based on the MRI more accurate, we need MRI contrast agents which can help to sharp images and enhance the details. The most widely available MRI contrast agents are gadolinium chelates, within which Gd-DTPA is the best well-known one and has been used in clinical application for years. Superparamagnetic iron oxide (SPIO) is another kind of MRI contrast agents which was the first nano-sized one. The mechanisms for these two kinds of contrast agents are different.

Y. Hou (✉) • X. Chu
Department of Materials Science and Engineering, College of Engineering, Peking University, Beijing 100871, China
e-mail: hou@pku.edu.cn

J. Yu
Department of Materials Science and Engineering, College of Engineering, Peking University, Beijing 100871, China

Research Center of Magnetic and Electronic Materials, College of Materials Science and Engineering, Zhejing University of Technology, Hangzhou 310014, China

Z. Dai (ed.), *Advances in Nanotheranostics II*, Springer Series in Biomaterials Science and Engineering 7, DOI 10.1007/978-981-10-0063-8_1

As an important part of nanomaterials, magnetic nanoparticles (MNPs) have enormous potential for disease diagnosis and therapy. Due to their superior magnetic properties and high specific surface, MNPs are perceived as promising materials for MRI contrast agents, biomedical drug carriers, magnetic hyperthermia, etc. Based on the interaction between protons and surrounding molecules of tissues, MRI is a promising tool for medical imaging diagnosis of cancer and is considered as one of the most efficient imaging techniques in biomedicine. With strong magnetization, colloidal stable MNPs now attract much attention for their great potential in MRI. In particular, they can be used as contrast agents in MRI by inducing hypointensities on T_1- and T_2-weighted MRI maps. Drug loading and delivery is another biomedical application of MNPs. Magnetic drug delivery is a method to target drugs to the diseased area in the body. When drug is attached to a MNP and injected into blood flow, it is captured in the diseased area by locating a magnet close to the target location. In the action of magnetic field, the MNPs move irregularly in the target area which accelerates the release of drugs. Apart from pharmaceutical therapy, MNPs are also widely used in magnetic hyperthermia therapy. On account of excellent magnetic properties, MNPs, especially ferromagnetic NPs, could induce strong attractive forces between the dipoles of neighboring NPs and aggregate under a static magnetic field.

1.1.1 The Principle of MRI

MRI is mainly based on nuclear magnetic resonance (NMR) effect. In short, when the nuclei of protons are exposed to an external magnetic field, their spins align either parallel or antiparallel to the magnetic field which called Larmor precession (Fig. 1.1a). During their alignment, the spins process under a specified frequency, known as the Larmor frequency (ω). The Larmor precession can be described in Larmor equation (γ, gyromagnetic ratio; B_0, magnetic field):

$$\omega = \gamma B_0$$

When a "resonance" frequency in the radio-frequency (RF) range is introduced to the nuclei, the protons absorb energy and are excited to the antiparallel state. After the disappearance of the RF pulse, the excited nuclei relax to their initial, lower-energy state (Fig. 1.1b). There are two different relaxation pathways. The first, called longitudinal or T1 relaxation, involves the decreased net magnetization (Mz) recovering to the initial state (Fig. 1.1c). The second, called transverse or T2 relaxation, involves the induced magnetization on the perpendicular plane (Mxy) disappearing by the dephasing of the spins (Fig. 1.1d). Based on their relaxation processes, the contrast agents are classified as T1 and T2 contrast agents, and T1* and T2* are, respectively, described as their relaxation time. Commercially available T1 contrast agents are usually paramagnetic complexes, while T2 contrast agents are based on iron oxide NPs, which are the most representative NP agents. Because the values of T1* or T2* of normal tissue and lesions are not obviously different, the T1 or T2 contrast agents are able to be used in MRI.

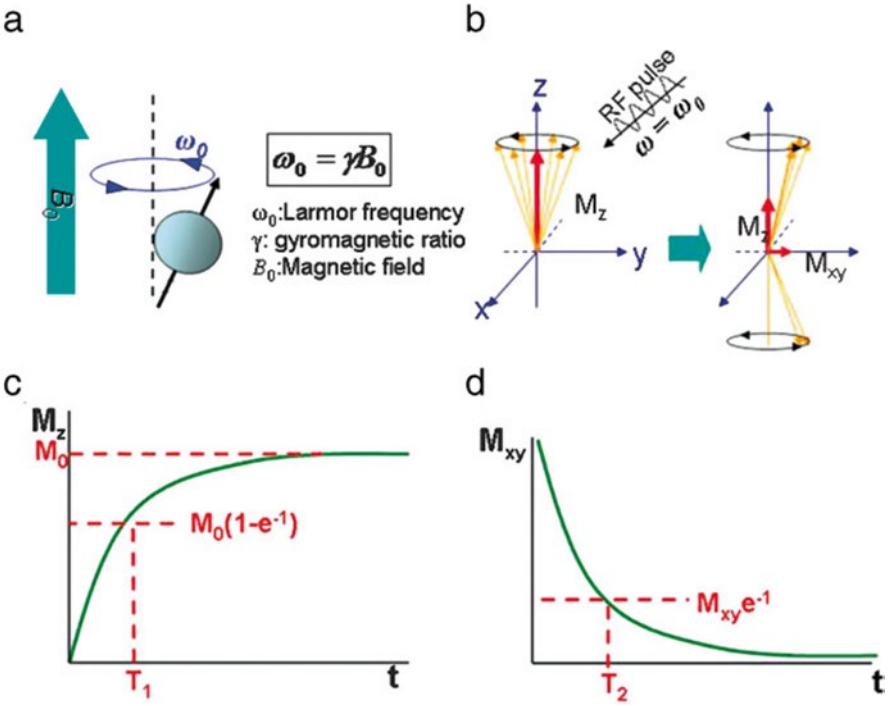

Fig. 1.1 Principle of magnetic resonance imaging. (**a**) Larmor precession, (**b**) magnetization of spins changes after induction of RF pulse, (**c**) T_1 relaxation process, (**d**) T_2 relaxation process (Reproduced with permission from Ref. [1]. Copyright 2009 WILEY-VCH Verlag GmbH & Co. KGaA, Weinheim)

1.1.2 The MRI Contrast Agents

To improve the MRI contrast, researchers expect to receive higher MR signal. The MRI contrast agents are designed to meet this demand by shortening the relaxation time. According to the patterns of MRI needed, MRI contrast agents can be divided into two groups: T_1 and T_2 contrast agents.

T_1 contrast agents are also known as paramagnetic contrast agents. There are several conditions which influence the MRI performance. The value of relaxation effectiveness increases with the coordination number of water molecules. Because a lot of paramagnetic metal ions are toxic, metal ions should be in a chelate form. According to theoretical analysis, several factors can affect the relaxation results, such as the exchange rate of coordination water, the distance of the coordination water and the paramagnetic center, and the magnetic moment of paramagnetic center. Accordingly, to achieve better relaxation effectiveness, T_1 contrast agents are

commonly designed to meet the demand of higher exchange rate, shorter distance between coordination water and paramagnetic center, and greater paramagnetic moment. Usually, the contrast agents of water molecules and the distance between water and paramagnetic center keep the exchange rate at a certain value. The controlling of relaxation usually relies on the paramagnetic center. Because of unpaired electrons in the ion is the source of the magnetic moment of ions, Mn^{2+}, Fe^{3+} which contains five unpaired electrons and Gd^{3+} which contains seven unpaired electrons, are regarded as the optimal candidates for MRI.

Take gadolinium ion for example, it has big spin magnetic moment and symmetrical field, and its coordination number can reach 8 or 9, which can obtain higher relaxation effectiveness and is expected to be used for imaging contrast agents. However, free gadolinium ion and its most complexes are not compatible with venous blood and easily to precipitate out. At the same time, gadolinium has a large renal toxicity, which makes it hard to be used directly. Therefore, it is required to develop the good stability and biocompatibility of gadolinium contrast agent.

In addition to gadolinium ion, bivalent manganese ion also has important applications in fabricating the paramagnetic contrast agents. Mn^{2+} contains five unpaired d electrons. Its net magnetic moment is $5.9\mu_B$, and the electron spin relaxation time is 10^{-8}–10^{-9} s, which is an appropriate electronic relaxation time [2]. The proton relaxation enhancement can influence the surrounding water proton relaxation process and shorten the relaxation time. Although manganese ion is an essential element which the human body contains about 10–20 mg, hydrated manganese ion cannot be directly used for imaging due to its unacceptable cardiac toxicity.

Different from the T_1 contrast agent, T_2 contrast agents mainly affect the proton transverse relaxation (spin-spin relaxation) processes [3]. Usually, they are known as superparamagnetic NPs. Generally speaking, the total magnetic moment is 657 times more than that of the proton magnetic moment paired electrons, and superparamagnetic particles tend to contain a large number of unpaired electrons. Under the action of applied magnetic field, the contrast agent NPs will be arranged according to the magnetic field direction, producing a larger net magnetic moment and significantly affecting the uniformity of local magnetic susceptibility. After removal of the external magnetic field, thermal disturbance makes the grain direction of the magnetic moment of contrast agent randomly arranged. The protons near contrast agent particles will soon step into the relaxation process of phases, which causes organization imaging relaxation time significantly shortened and showing a strong negative reinforcement effect [4–6]. According to the abovementioned mechanism, MNPs with high magnetic properties are required for the T_2 MRI contrast agents.

Superparamagnetic iron oxide (SPIO) is the most widely used superparamagnetic contrast agent. It has many remarkable advantages, such as good biocompatibility and degradability [7]. In addition to the essential trace element iron in the nanometer iron oxide, it does not contain other metal ions. Many biological toxicity tests show that nanometer iron oxide does not significantly affect the growth of cells. And the nanometer iron oxide can be metabolized by red blood cell lysosomes without harmful side effects to the human body. For the better application of MNPs in MRI, high magnetism MNPs, especially SPIO, are designed to be synthesized.

1.2 Chemical Preparation of MNPs for MRI Contrast Agents

Based on the excellent magnetic performance and good biocompatibility, MNP contrast agents have a wide range of applications in MRI. To obtain MNPs with better magnetic properties, the trend and degree of the influence on chemical growth of MNPs have been studied extensively. According to La Mer theory, when the monomer concentration is over the critical concentration, the explosive nucleation process will occur in the process of crystal growth. At that moment, a large number of precursors are participating in reaction and exhausted. Therefore, the key factor to prepare high-quality monodisperse MNPs is to control the nucleation and growth process properly. On account of the very high specific surface area, MNPs tend to conglomerate to reduce the surface energy. Using appropriate surface ligands can also reduce surface energy and prevent the conglomeration of MNPs which is a tool for controllable growth [8].

Currently, various protocols are developed to synthesize MNPs. The typical methods are coprecipitation method, polyol process, ultrasonic chemical method, soft template synthesis method, and thermal decomposition method. This section is an exhaustive introduction of these methods.

1.2.1 Coprecipitation Method

Coprecipitation method is a simple and convenient method for preparation of magnetic nanoparticles. By mixing the ferric iron salt solution with the ferrous iron salt solution under a certain proportion, a certain pH value, appropriate reaction temperature, and the existence of the precursor and stabilizer, researchers can get iron oxide nanoparticles within a range of particle size and morphology. Coprecipitation method only needs simple, mild conditions and the cost is low. The product has good dispersion in water, easy for further modification. But the iron oxide NPs prepared by this method always have irregular shape and wide size distribution. The particle size is so big as to produce aggregation easily. At the same time due to the low reaction temperature, the NPs are easy to be oxidized, which limits its application prospect in the field of contrast agents [9].

1.2.2 Polyol Process

Polyol process is a kind of preparation methods of iron oxide NPs. By using high boiling point polyhydric alcohol such as polyethylene glycol (PEG) as the solvent and using simple inorganic salt such as ferric chloride or metal organic compound like acetylacetone iron as precursor, this method can synthesize NPs with a

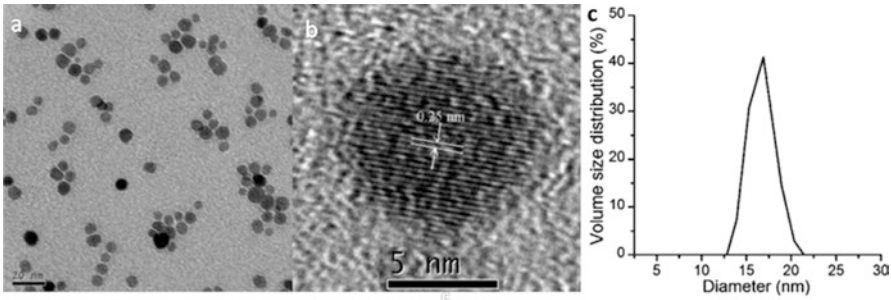

Fig. 1.2 Magnetite nanoparticles prepared by polyol process. (**a**) TEM image, (**b**) HRTEM image, (**c**) dynamic light scattering (DLS) of the aqueous dispersion of the magnetite nanoparticles (Reproduced with permission from Ref. [10]. Copyright 2007 Royal Society of Chemistry)

relatively narrow size distribution under a series of chemical reactions at high temperatures (Fig. 1.2). Polyol-prepared NPs tend to have very good water solubility, stability, and biocompatibility. Thus, these NPs have a wide range of applications in the field of nano contrast agents. Despite the reaction temperature of polyol method can reach 200 °C, it is not high enough for producing inorganic oxide crystallization process. Therefore, the products are often not well crystallized, and their magnetic performance is not equal to that of block magnetic materials [10].

1.2.3 Ultrasonic Chemical Method

Ultrasonic cavitation can generate instantaneous local high-temperature and high-pressure environment in solution and can be rapidly cooling. Such extreme conditions have a unique role for chemical reaction promotion. Ultrasonic chemical method is also a kind of preparation method of nanometer particles. For example, using $Fe(CO)_5$ as precursor and polyvinylpyrrolidone or oleic acid as stabilizer, iron oxide NPs are obtained through ultrasonic processing [11]. This method has also been extended to other NP synthesis. The reaction process of ultrasonic chemical method, however, is difficult to monitor and control. The morphology, homogeneity, and crystallinity of produced NPs are poor, so this method is rarely used in the field of nano contrast agent [12].

1.2.4 Soft Template Synthesis Method

Magnetic nano contrast agents can also be synthesized through the use of microemulsion or reverse micelles and other soft templates. By mixing incompatible two-phase system like water oil with surfactant under certain condition, a thermodynamically stable, uniform dispersion system can be formed, and the

micro-/nanoscale orderly assemblies can be obtained, such as microemulsion or reverse micelles. The orderly structure can provide a chemical reaction with limited reaction space, thereby restrict the growth and reunion of nanomaterials and lead to the generation of NPs of high solubility. In addition, because of the different structures and concentrations of the surfactants used, the micelle is not limited to the spherical shape. It can also be a rod or in other shapes, which lays a foundation for obtaining specific morphology of NPs. Both metal materials such as copper, cobalt, and silver and compound materials such as cadmium sulfide and iron oxide can be synthesized through this method conveniently. However, for reactions at low temperature, NPs prepared by this method have lower degree of crystallinity which restricts their use in the field of nano contrast agents [13].

1.2.5 Thermal Decomposition Method

High-temperature thermal decomposition method is a kind of controllable preparation of NPs with high quality. In the presence of high boiling point solvent ligand and metal precursors on the surface, NPs can decompose controllably at high temperature and very uniform size, and controllable morphology can be obtained [14]. In the high-temperature thermal decomposition method, there are two kinds of reaction precursor feeding modes: rapid injection and direct heating method [15]. When adopting the first way of feeding, reaction solution containing surface ligands must be heated to a certain temperature in advance. The metal precursor (usually have lower decomposition temperature) or the solution can be syringed to join the reaction system and realize the rapid and explosive NP nucleation. Then by controlling the further reaction temperature and time, researchers can control the growth process of NPs. Because most of the precursor in the process of injection has been exhausted, it is difficult for the rest of the precursor to nucleate. So this method is mainly used to implement the growth process of nanoparticles. In this system, all NPs have similar growth curve and monodisperse feature.

The other way of feeding just needs to mix ligands, metal precursors, and reaction solution at a certain proportion. By controlling the heating process, the reaction temperature, and the reaction time, the synthesized NPs can get controllable morphology and size. In the reaction system, long-chain surface ligands such as oleic acid, amine, and three octyl phosphonic and octyl oxygen phosphonic acids often play a very important role. Because of its strong ability of coordination and good thermal stability, the intermediate forms in this process are difficult to decompose. Under certain reaction temperature, the slow decomposition of intermediates can also get control of the size and shape of NPs. For example, by mixing organic metal compounds acetylacetone iron, oleic acid, oil amine, and 1, 2-dodecane in dibenzyl ether glycol at 300 °C, monodisperse NPs can be obtained. The particle size is adjustable from 4 to 8 nm. This method also can be used in the synthesis of ferromanganese oxygen, cobalt ferrite, and ferrite nanoparticles (Fig. 1.3) [16]. Recently, researchers found that using the acetylacetone iron, dibenzyl ether, and oil amine

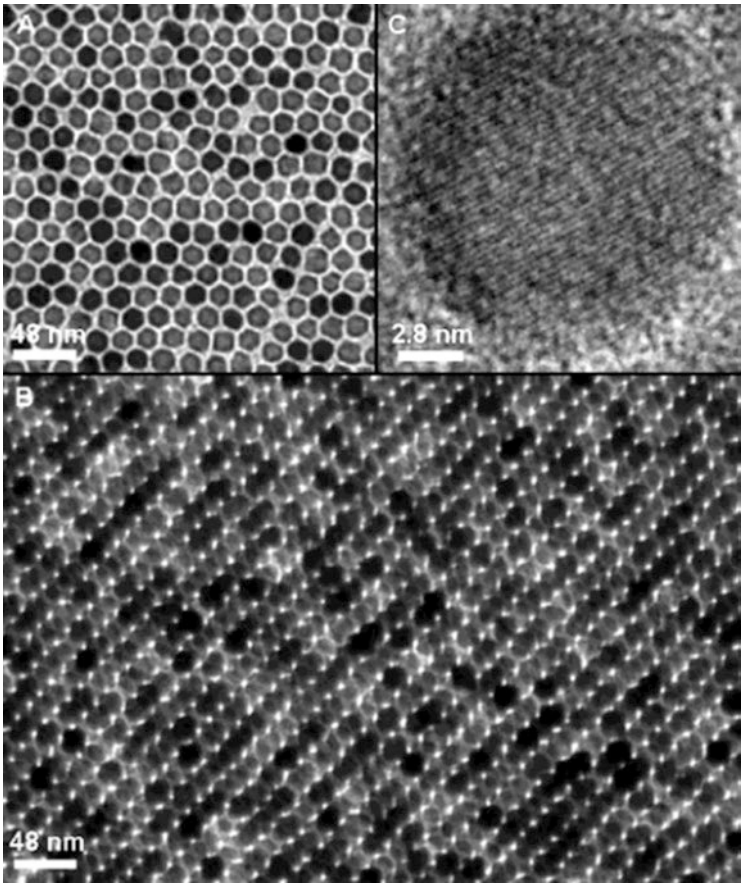

Fig. 1.3 TEM images of 16 nm Fe_3O_4 nanoparticles prepared by thermal decomposition method. (**a**) A monolayer assembly, (**b**) a multilayer assembly, (**c**) HRTEM image of a single Fe_3O_4 nanoparticle (Reproduced with permission from Ref. [16]. Copyright 2002 American Chemical Society)

can also get good reaction products, and the particle size is adjustable [17]. By adjusting the proportion of oleic acid and oil amine, the nanoparticle can be 14–100 nm in size with octahedral or truncated octahedral structures [18]. The ferrous oxide nanoparticles can be further transformed into magnetite Fe_3O_4, magnetic hematite gamma Fe_2O_3, hematite alpha Fe_2O_3, or iron, and Fe_3O_4 complex components for controllable synthesis of iron oxide, which provides a new train of thought. When using oleic acid as the reaction precursor iron, a large number of monodisperse spherical iron oxide nanoparticles can be synthesized. In introducing different cations (sodium, potassium, tetramethylammonium) to oleates as surface ligands, the cubic or double pyramidal iron oxide NPs can be synthesized [19]. In the use of certain amount of oil amine ligand as surface ligand, and the reaction

temperature is increased to 380 °C at the same time, the octahedral iron oxide NPs can be synthesized [20].

1.2.6 Solvothermal Method

Solvothermal method is a kind of reaction with precursor and appropriate stabilizer dissolved in a solvent in the airtight system in order to prepare NPs by high pressure. The product has good crystallinity, and sometimes researchers get metastable phase product. In a closed system, the solvent can't boil. When the reaction is heated to a temperature higher than the boiling point of the solvent under atmospheric pressure, it can produce a higher pressure. The higher the reaction temperature is, the larger the pressure is. The high reaction temperature and the large pressure are the characteristics of solvothermal method. Under such conditions, some thermodynamic allowable but slow kinetic-responsive reactions are likely to accelerate. Trivalent iron, for example, tends to be hydrolyzed spontaneously and forms a relatively stable iron hydroxide. The iron hydroxide can form Fe_2O_3 in further dehydration process. But under normal conditions, the two-step reaction is very slow. When using the hydrothermal method, better iron oxide materials can be synthesized. In the presence of vitamin C as the stabilizer and reducing agent in the water thermal processing, iron hydroxide oxygen can form smaller and more soluble Fe_3O_4 nanoparticles which have good magnetic resonance (NMR) relaxation effectiveness. Under another condition, the reaction temperature tends to be less than 200°, but it can still provide several atmospheric pressure or even higher pressure in hot water/solvent thermal reaction. This offers the synthesized nanomaterials with better crystallinity. After the introduction of nonaqueous solvents such as ethanol, a wider range of precursors and stabilizers can be used with better control of size and shape [21].

Besides, there are other synthesis methods such as sol–gel method and microemulsion method which are not typical. As a matter of fact, all these methods realize the uniform growth of MNPs by regulating or establishing the proper reaction conditions. Hence, with the continuous development of synthesis methods, the morphology MNPs are designed to become more regular and controllable.

1.3 Nano Contrast Agents for MRI

Based on the interaction between protons and surrounding molecules of tissues, MRI is becoming a promising tool for medical imaging diagnosis of cancer and is considered as one of the most efficient imaging techniques in biomedicine. Due to the superior magnetic properties and high specific surface, MNPs are perceived as ideal MRI contrast agents.

1.3.1 T_1 Nano Contrast Agents

The interaction of paramagnetic ions and water molecules at the center is the key factor of paramagnetic contrast agents to realize imaging function. Therefore, chelate is not the only form of paramagnetic contrast agents. Some recent researches showed paramagnetic NPs, such as gadolinium oxide, gadolinium phosphate, gadolinium fluoride and gadolinium NPs are good candidates for MRI contrast agents. This type of nano contrast agents for T_1-weighted images has very good signal enhancement effect. Through the modification of biocompatible materials, such as chitosan, PEG, or silica, gadolinium oxide NPs, which usually have a small-scale (<5 nm) crystal nucleus, are the typical ones [22].

There is also a research report about water-soluble fluoride gadolinium NPs or gadolinium-doped lanthanum fluoride NPs. According to the different surface charge, the researchers choose 2-ethyl amine phosphate and citric acid as coated molecules and got good imaging effect [23]. In general, nanometer materials have low horizontal/vertical relaxation effectiveness, indicating that it is more suitable for positive contrast agents.

Colloidal manganese sulfide is one of the first reported manganese-based magnetic nano contrast agents. Chilton group discussed the influence on lattice relaxation time for rat liver, lungs, and spin after intravenous injection of the colloid NPs and noted that the colloidal manganese sulfide NPs had certain effect of MRI [24]. By sodium sulfide precipitation with manganese acetate, pink sulfide colloid particles can be synthesized. Scanning electron microscopy shows that the particle size is ranging from 0.1 to 10 μm.

Hyeon group in South Korea reported that the manganese oxide NPs can get enhancement effect of T_1 image (Fig. 1.4). Using the manganese oxide NPs, good results achieved for the brain, liver, and kidney imaging. It is worth mentioning that by using manganese oxide NPs, researchers can obtain fine anatomical structure of brain tissue which is good for basic research in neuroscience and disease diagnosis [25]. They controlled the size of the particle which was prepared by thermal decomposition of manganese oxide nanoparticles. By regulating the manganese oxide NP morphology and size, they can control the relaxation properties. Hyeon group also reported the preparation of Mn_3O_4 nanoplates using hydroquinone ligand. The material showed better performance of relaxation. In addition, Chang group reports the fabrication of D-glucuronic acid-modified super-small manganese oxide NPs. The r_1 and r_2 values were 7.02 and 47.97 mM^{-1} s^{-1}, respectively [26].

Lee group reported the preparation of hollow manganese oxide NPs by first synthesizing 20 nm manganese oxide NPs and then selectively etching the cores. Compared to the same size solid NPs ($r_1 = 0.21$ $mM^{-1}s^{-1}$, $r_2 = 1.42$ $mM^{-1}s^{-1}$), hollow NPs showed better relaxation effectiveness ($r_1 = 1.49$ $mM-^{1}s^{-1}$, $r_2 = 7.74$ $mM^{-1}s^{-1}$) and drug delivery performance. The work shows that due to the large specific surface area of hollow NPs, it is more conducive to water molecules in contact with the surface of NPs, resulting in better relaxation effectiveness. Similarly, with the introduction of dopamine as a connecting molecule, Park group made hollow manganese

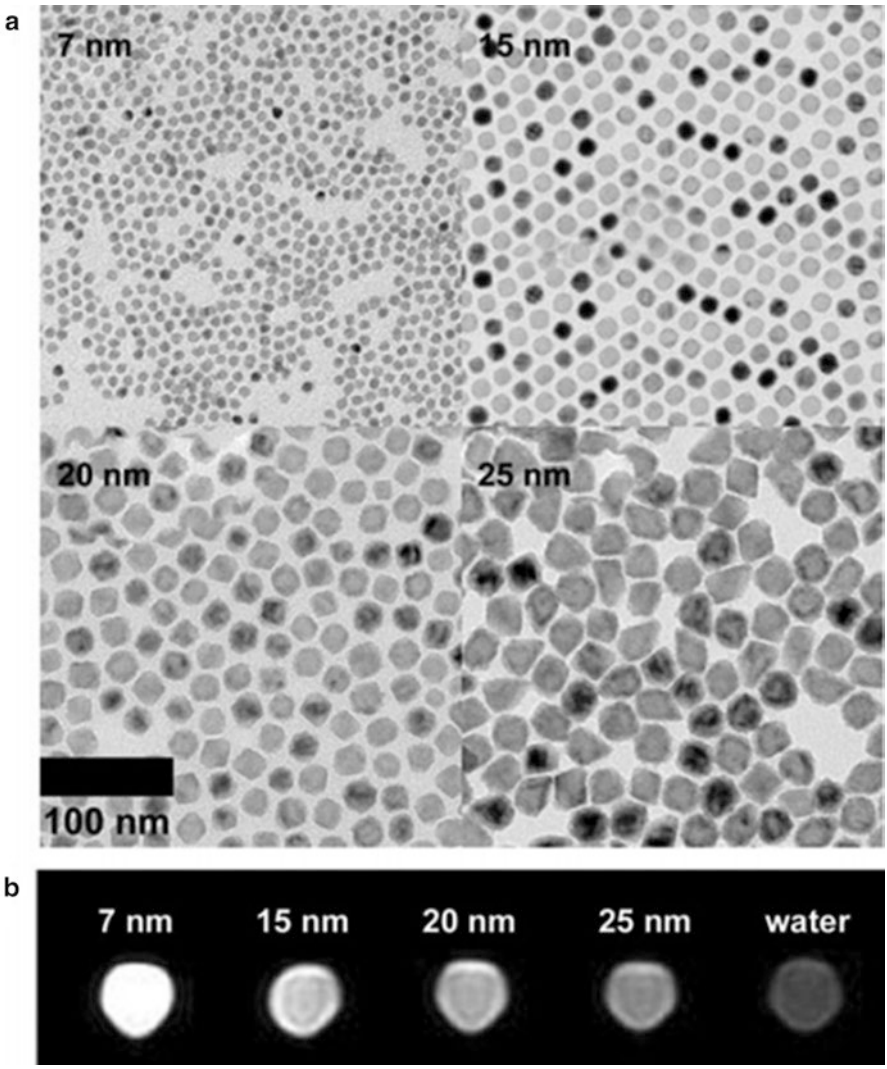

Fig. 1.4 (**a**) TEM images of water-dispersible MnO nanoparticles with particle sizes of 7, 15, 20, and 25 nm. (**b**) T1-weighted MR image of MnO nanoparticles from a 3.0 T clinical MRI system (Reproduced with permission from Ref. [25]. Copyright 2007 WILEY-VCH Verlag GmbH & Co. KGaA, Weinheim)

oxide NPs coupling with siRNA and the targeting reagent Herceptin. Experiments proved that the targeted NPs have a very good effect of imaging for breast cancer cells and can be a very good siRNA delivery carrier for targeted treatment of cancer cells [27]. Hyeon group also reported the mesoporous silica-coated hollow manganese oxide (HMnO@mSiO_2) nanomaterials as T_1 imaging agents. They proved the mesoporous silica can help the better access of the water molecules and manganese

oxide can get higher r_1 relaxation effectiveness. By using electroporation method, these NPs can be imported into tagged mesenchymal stem cells which can realize in vitro and in vivo detection. This work shows unique role of the hollow manganese oxide NPs in the field of cell markers [28].

1.3.2 T_2 Nano Contrast Agents

Based on the theory put forward by Koenig and Keller, proton transverse relaxation effectiveness is related to saturation magnetization intensity of NPs. The formula is shown as following [29]:

$$R_2 = \frac{1}{T_2} = \frac{a}{d_{\mathrm{NP}} D} \gamma^2 \mu^2 C_{\mathrm{NP}} J(\omega, \tau_D)$$

where a is constant, d_{NP} is the NP's size, μ is the magnetic moment, γ is the gyromagnetic ratio of water, C_{NP} is the concentration of the NPs, and $J(\omega,\tau_D)$ is the spectrum density function. We can see that the relaxation value R_2 increases with a reduction in MNPs' diameter d_{NP}. Because of the body's immune function, particles in the range from 30 nm to 50 μm in the blood are considered as foreign bodies [30]. Both of the above theories show that the size distribution contrast agent particle has great influence on the in vivo behavior. Therefore, the nanometer iron oxide contrast agents, superparamagnetic iron oxide (SPIO, 50–150 nm) and super-small superparamagnetic iron oxide (USPIO,<30 nm), have great value in developing MRI contrast agents on account of their small particle diameter (Table 1.1) [3].

SPIO distribution in the body has significant specificity, which is mainly used in reticular endothelial tissue imaging. After being injected into the human body, SPIO tends to combine with plasma protein in the blood, recognized by endothelial network through macrophages. So SPIO will be enriched in endothelial reticular cell tissues and organs such as the liver, spleen, lymph nodes, bone marrow, and other parts. The T_2 signal of SPIO-enriched organization will show obviously negative

Table 1.1 Examples and properties of commercial SPIO agents [3]

Agent	Class	Trade and common names	Status	Mean particle size
AMI-121	Oral SPIO	Lumirem, Gastromark, Ferumoxsil	Approved	>300 nm
OMP	Oral SPIO	Abdoscan	Approved	3.5 μm
AMI-227	USPIO	Sinerem, Combidex, Ferumoxtran	Phase III	20–40 nm
NC100150	USPIO	Clariscan	Completed phase II (discontinued)	20 nm
CODE 7228	USPIO	(Advanced magnetics)	Phase II	18–20 nm

enhancement. Because cancer organization does not contain the macrophages, it will not produce a similar phenomenon, so as to differentiate from the normal tissues. However, SPIO in clinical applications has some limitations. Though it can produce strong contrast effect, the negative signals could cover up the organization structure and are hard to be distinguished from false signals [31].

USPIO is dextran-coated magnetic iron oxide NPs. Its particle size is usually less than 30 nm. After intravenous injection, due to its small size, USPIO will not be recognized by endothelial network. So it can stay longer in the blood and possibly permeate through capillary wall into deeper tissue. In addition, it can also be targeted by linking reagent for target imaging [32]. USPIO has certain negative effect, but unlike SPIO, USPIO at the same time can increase the efficiency of the organization of the longitudinal relaxation. The space distribution also has influence on the imaging effect, because the distribution of the cluster USPIO negative effect is greater than the effect of the uniform distribution. USPIO has very broad application prospects in display and identification of the tumor of the lymph node and differential vascular imaging [33].

Though SPIO and USPIO have good MRI performance, there are a number of new designs of biological probes with multiple functions. For example, Fe_5C_2 nanoparticle is one of the most promising multifunctional probes among the new T_2 nano contrast agents [34]. Fe_5C_2 has a magnetic moment of about 140 emu/g, a value that is comparable to that of Co (about 160 emu/g) and two times higher than that of Fe_3O_4. The high magnetic moment leads to a respectable performance in T_2-weighted MRI, and the r2 value is 312 $mM^{-1}s^{-1}$ at 3 T which is much higher than that of Resovist. In consequence of a thin carbon shell coating, the Fe_5C_2 nanoparticles get high absorption in near-infrared (NIR) light for photothermal therapy (PTT). Besides, the Fe_5C_2 nanoparticles are facile to synthesis in one-pot method, compared with other NPs reported for both MRI and PTT like $Fe_3O_4@Cu_{2-X}S$ core–shell NPs which need intricate and multistep synthetic processes.

1.4 Multifunctionalization and Application of MNPs as MRI Contrast Agents

While the effort in developing new engineered MNPs and constructs with new chemistry and synthesis approaches continues growing, the importance of specific functionalization designs has been increasingly recognized. Because the surface of MNPs is the interface between nanomaterials and biological bodies, surface biocompatibility of nanomaterials is prerequisite to the biomedical application of nanomaterials [35]. As a facile and quick approach to adjust the properties of MNPs, surface modifications become a vital component of all biomedical applications of MNPs due to the addition of nonmagnetic surfactants.

In the field of nanomedicine, it requires new designs of biological probes with multiple functions. In addition to enhancing the MRI signal of MNPs, researchers

now devote to designing new type of multifunctional MNPs which show great application potential in both cancer diagnosis and therapy. As mentioned above, surface of these MRI-based probes is critical to their functionalities; some important multifunctionalization methods are highlighted.

1.4.1 Multifunctionalization Methods

The surface modifications mainly proceed via two approaches, ligand exchange and ligand adsorption. Ligand exchange is to change the hydrophobic ligand into a hydrophilic one. Generally, these ligands consist of hydrophilic groups and linking groups. The linking groups can combine with the surface of the MNPs, and the hydrophilic groups are exposed to the surrounding environment to make the MNPs disperse in the aqueous solution. The key point of a successful ligand exchange is to select the linking groups which have the strongest combination with the surface of MNPs. Ligand adsorption mainly means to adsorb molecules. These molecules are amphiphilic molecules which have both hydrophilic portion in one side and hydrophobic one in the other side. By means of hydrophobic forces, the hydrophobic portion can combine firmly with the hydrophobic surfactant of MNPs, and the hydrophilic portion is exposed so that the MNPs disperse in aqueous phase. Besides, chemical reaction is another approach for the surface modifications. Upon these three strategies, organic molecules, macromolecules, and inorganic materials can be usually used for this purpose. In this part, we will summarize the progress on surface modification of MNPs depending on the type of surface materials.

The important properties of cell phagocytosis of MNPs have expanded the applications of contrast-enhanced MRI beyond the vascular and tissue morphology imaging, enabling many novel applications of MNPs for MRI diagnosis of liver diseases, cancer metastasis to lymph nodes, and in vivo tracking of implanted cell and grafts with MRI [36]. The magnitude of contrast effects also needs to be improved for high sensitivity to the minimal changes in the disease and for biomarker-specific detection. Therefore, the surface modifications of MNPs are developed to meet the increasing interests for noninvasive in vivo imaging of molecular and cellular activities that target a disease. Surface modifications cannot only prevent MNPs from reacting and agglomerating in aqueous phase which is not only the precondition for biomedical applications but also endows MNPs with multifunctional properties such as fluorescent mark, cell targeting, drugs loading, and so on [37–39]. Furthermore, surface modifications are able to influence the magnetic performance of MNPs due to the addition of nonmagnetic surfactants.

1.4.1.1 Ligand Exchange or Adsorption of Organic Molecules

Ligand exchange is the most common way for surface modification of MNPs. In ligand exchange, monodentate ligand is the simplest ligand. With easy preparation, simple structure, and other advantages, monodentate ligands are widely used in

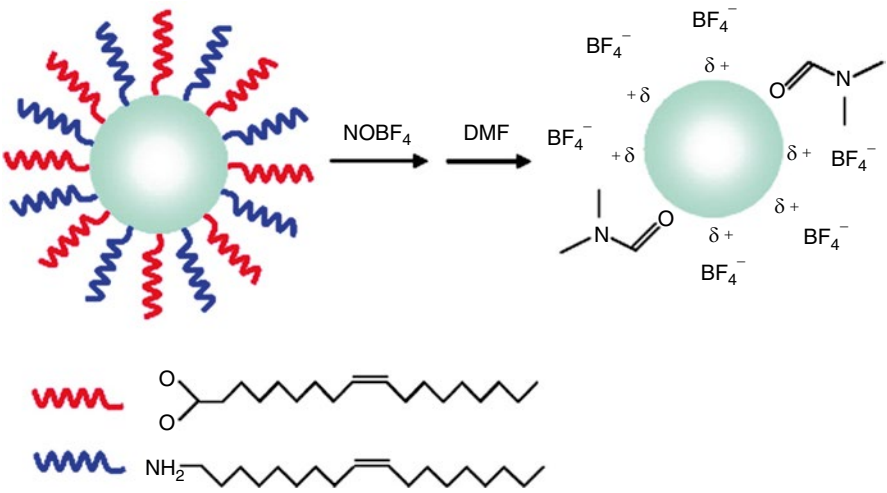

Fig. 1.5 Schematic illustration of surface modification of MNPs via the ligand exchange process with $NOBF_4$ (Reproduced with permission from Ref. [47]. Copyright 2011 American Chemical Society)

ligand exchanges. Since there is only one ligand, the binding force between monodentate ligands and MNPs is weak, and the combination process is reversible. To deal with this problem, researchers need to screen the ligands with strong coordination ability. Carboxyl [40, 41], sulfhydryl [42], silane [43], and some inorganic ions[44–46] are most common used in monodentate ligand exchange. Murray et al. used nitrosonium tetrafluoroborate ($NOBF_4$) to replace the organic ligands attached to the nanocrystal (NC) surface (Fig. 1.5) [47]. The replacement by inorganic BF_4^- anions enabled NCs to be fully dispersible in polar, hydrophilic solvents without changing the particle size and shape. After surface modification, the NCs were readily further functionalized by various capping molecules which greatly enrich the surface function of NCs.

Although monodentate ligands have simple structure and react fast with MNP surface, these MNPs are not stable in aqueous phase as a result of the reversible coordination process. This problem is preferably solved by the application of polydentate ligands. Polydentate ligands have a plurality of coordinating groups which significantly enhance the binding force with MNPs. Therefore, these surface-modified MNPs have high stability constant and exhibit favorable aqueous solubility. The polydentate ligands are diphenols [48–50], polyacids [51], polyols, and their derivatives [21, 52, 53]. For all of those, catechol and its derivatives are most commonly used. With electron donor of benzene ring structure, catechol and its derivatives can be intensively coupled with metal ions [49]. Hou et al. invented a rapid ligand exchange method to make hydrophobic Fe_3O_4 NPs into water-soluble NPs using dihydroxybenzoic acid as a ligand [54]. Another common polydentate ligand is dimercaptosuccinic acid (DMSA). As a small molecule, DMSA has notable superiority in hydrophily, biocompatibility, and coordination ability due to its double sulfhydryl and double carboxyl structure [55–57].

Some organic molecules are amphipathic. Their structures have both hydrophilic portion and hydrophobic portion which are liable to attach to the surface of MNPs. The hydrophilic portion is usually long-chain hydrocarbons, but the hydrophobic portion has different structures. In addition to enhance the dispersibility of MNPs in aqueous solution, optical dyes, targeting agents, and therapeutic agents are allowed to be used in the ligand adsorption process which help with the multifunction of MNPs [58]. By combination of organic dyes, MNPs perform dual-mode imaging property which contributes to disease diagnosis [59–61]. Among the organic dyes, near-infrared fluorescent (NIRF) dyes may be the best choice due to its low interference and excellent penetration distance of issues [62]. Likewise, surface modification with targeting agents and therapeutic agents is conducive to strengthen the diagnostic capacity of MNPs [22]. J. Manuel et al. synthesized biocompatible, multimodal, and theranostic functional iron oxide NPs which exerted excellent properties for targeted cancer therapy and optical and magnetic resonance imaging [63]. Using a novel water-based method, they finished the encapsulation of both near-infrared dyes and anticancer drugs and realized the theranostics [64]. In recent research, a novel method to synthesize Gd-NPs was reported wherein a Gd-based MR contrast agent self-assembled into gadolinium NPs under the action of furin proteins. These NPs can be used to locate the right position for treatment.

1.4.1.2 Polymer Coating

Polymers with multiple functional groups could be expediently combined with MNPs. Based on the influence of chelate effect and chemisorption, polymer coating usually needs the help of active terminal groups. Various monomeric species, such as bisphosphonates, DMSA, and alkoxysilanes, have been evaluated to facilitate attachment of polymer coatings on MNPs [50, 66]. In polymer coatings, polymers form a barrier among MNPs to avoid agglomeration and provide varieties of surface properties. As the most biocompatible MNPs developed for in vivo applications need to be stabilized and functionalized with coating materials, the coating moieties can affect the relaxation of water molecules in various forms, such as diffusion, hydration, and hydrogen binding [36]. In the research, these coatings also play the role to link MNPs with biomolecules or change the surface charge or chemical environment. Moreover, polymer coatings improve the colloidal stability of NPs as well [67]. For the complex structures of polymers, there are many aspects to affect the surface performance of MNPs, such as the molecular weight, the property of terminal groups, and the conformation of polymers.

Plenty of natural and synthetic polymers have been demonstrated in polymer coating [53, 68–70]. The glycan such as dextran or chitosan is widely used in polymer coatings [31, 71]. Chitosan, a biodegradable natural polymer, is derived by the deacetylation of chitin obtained from the shells of crustaceans. It has many biological applications because of its biological activities, biocompatibility, high charge

density, low toxicity toward mammalian cells, and ability to improve dissolution. Weissleder and his group did a great deal of research in dextran-coated iron oxide nanoparticles and derivative magnetic nanoparticles. Their work of monocrystalline iron oxide NPs (MION) [72] and cross-linked iron oxide (CLIO) NPs [73] presented that dextran-coated superparamagnetic iron oxide NPs were a well-established platform for the synthesis of multifunctional imaging agents [74]. Hyeon et al. developed chitosan oligosaccharide-stabilized ferrimagnetic iron oxide nanocubes (Chito-FIONs) as an effective heat nanomediator for cancer hyperthermia [75]. The Chito-FIONs exhibited superior magnetic heating ability compared to commercial superparamagnetic iron oxide NPs, leading to successful eradication of cancer cells through caspase-mediated apoptosis.

Another frequently used polymer is polyethylene glycol (PEG) [30, 76, 77]. PEG is a flexible and water-soluble polymer. The high hydrophilicity of PEG chains can render the MNP core soluble and stabilized in the aqueous media. PEG has been demonstrated to distinctly reduce the uptake by macrophages [60] so as to increase the blood circulation time in vivo. By changing the molecular weight of PEG, MNPs can be coated with controlled size [30, 78]. PEG-derivative modified MNPs were prepared by post-synthesis coating. With the increasing of the molecular weight, the number of branched chains and functionalities, higher stability, and better dispersion could be attained. Sun et al. using 3-(3,4-dihydroxyphenyl)propanoic acid and PEG as reactants synthesized heterobifunctional PEG ligand (Fig. 1.6) [79]. They successfully modified porous hollow NPs (PHNPs) of Fe_3O_4 via this ligand and achieved targeted delivery and controlled release of the cancer chemotherapeutic drug cisplatin. However, PEG is not favorable for most cells to uptake MNPs with PEG shell protection. To solve this problem, these MNPs can be modified by hyaluronic acid (HA), a targeting moiety, for stem cell uptake [80]. Recent study reported that different terminal groups partly affected the MRI images of MNPs [81].

Other polymers such as cellulose, poly(ethylene oxide) (PEO), poly(vinyl alcohol) (PVA), poly(acrylic acid) (PAA), and poly(lactide-co-glycolide) (PLGA) are also used in polymer coatings. PLGA and cellulose are Food and Drug Administration (FDA) approved for a variety of usage in humans and commonly employed for drug delivery and oral formulations. Xu et al. used a single emulsion method to make

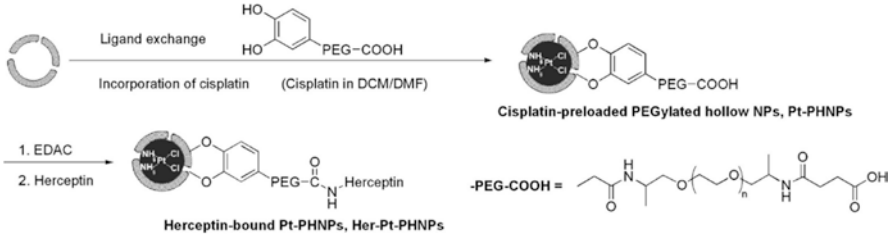

Fig. 1.6 Schematic illustration of surface modification of hollow NPs with heterobifunctional PEG ligand (Reproduced with permission from Ref. [79]. Copyright 2009 American Chemical Society)

oleic acid stabilized iron oxide NPs (10 nm core size) to be encapsulated in PLGA [82]. As a result of PLGA coating, the NPs had a much higher r_2 relaxivity than normal SPIO nanoparticles. Hong et al. synthesized a novel polymeric NPs (YCC-DOX) composed of poly(ethylene oxide)-trimellitic anhydride chloride-folate (PEO-TMA-FA), doxorubicin (DOX), and superparamagnetic iron oxide [83]. These NPs showed higher MRI sensitivity comparable to a conventional MRI contrast agent, even in its lower iron content. Lin et al. reported PAA-modified $GdVO_4$ NPs by filling PAA hydrogel into $GdVO_4$ hollow spheres. The PAA@ $GdVO_4$ NPs can act as a dual-mode agent for MR and up-conversion imaging and be applied for pH-dependent drug release due to its hollow structure [84].

Besides, other applications in polymer coatings are also beneficial. To simplify the coating procedures, researchers developed a series of copolymers to accomplish in situ coating of MNPs termed as one-pot method [85]. Nevertheless, the growth of nanocrystals can be influenced as a result of the existence of polymers which leads to abnormal structure and surface of MNPs [86]. Polymers or macromolecules such as peptide or PEG have the conformation to form monolayer by self-assembly [87], and in consequence, polymer coatings can be formed by self-assembling process on the surface of MNPs similarly [86, 88–91]. The effect on NPs' magnetic properties by polymer coatings is also a research field [71, 92, 93]. Gao et al. reported novel multifunctional polymeric micelles composed of a chemotherapeutic agent doxorubicin (DOXO) and a cRGD ligand [92]. They demonstrated that each micelle loaded a cluster of superparamagnetic iron oxide (SPIO) NPs inside which resulted in ultrasensitive MRI detection of the MNPs (Fig. 1.7).

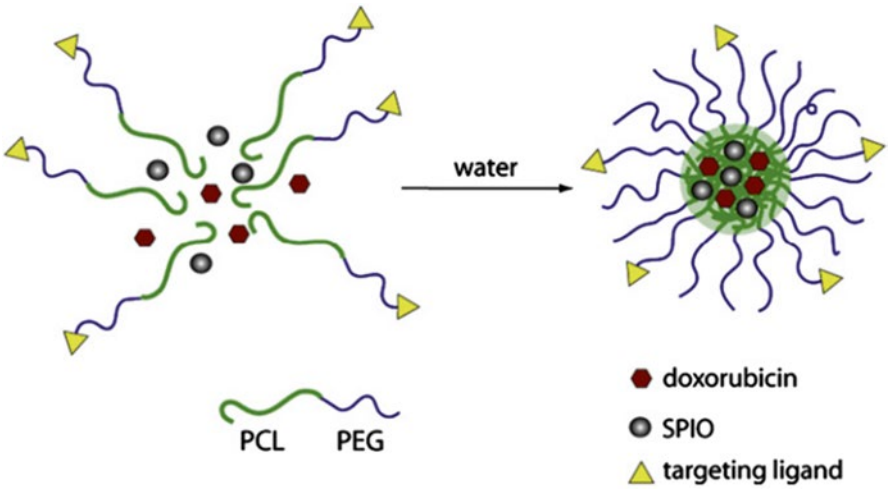

Fig. 1.7 Schematic illustration of the encapsulating process for DOX-SPIO (Reproduced with permission from Ref. [92]. Copyright 2008 Elsevier Ltd)

1.4.1.3 Silica Coating

For inorganic agents, the MNPs are generally coated by chemical reaction. Silica coating is the most widely used method for surface modification in inorganic coatings. Silica-coated MNPs always formed core–shell structures. Compared with organic coatings, silica coating has many particular advantages. Silica-coated NPs are robust, water soluble, colloidally stable, and photostable [94, 95]. Serving as protective coatings, silica shells are easy to synthesize and have controlled size. The general method to produce silica coating can be divided into two types: classical Stober method [96–98] (in aqueous phase) and sol–gel method [53, 99, 100] (in both aqueous and oleic phase).

The functionalization of silica shells is similar with the ligand adsorption. This inevitably causes too large diameter of the modified MNPs which affect biocompatibility, fluidity, stability, and magnetic performance of MNPs. To control the thickness of silica shell, researchers utilize tetraethoxysilane (TEOS) as the source of silica, and under a controlled reaction condition, silica coating MNPs with different diameters from 10 nm to 1 μm are finally obtained [53, 101, 102]. Zhang et al. studied the regulations of the controlled synthesis of Fe_3O_4@SiO_2 core–shell NPs via the reverse microemulsion method and found that the size of coated silica shell increased with the size of aqueous domain [103]. This result can guide us to avoid the formation of core-free silica particles (Fig. 1.8).

With controlled size, silica shells are appropriate for encapsulation of NPs and organic molecules like dyes or drugs. Salgueirino-Maceira et al. encapsulated Fe_3O_4 NPs and CdTe quantum dots within composite silica spheres [104]. These silica spheres can serve as both luminescent and magnetic nanomaterial. Zhu et al. accomplished the same function by embedding dye molecule inside the outer silica shell [105]. Researchers also focus on the synthesis of various core–shell structures. Deng et al. synthesized superparamagnetic microspheres with an Fe_3O_4@SiO_2 core

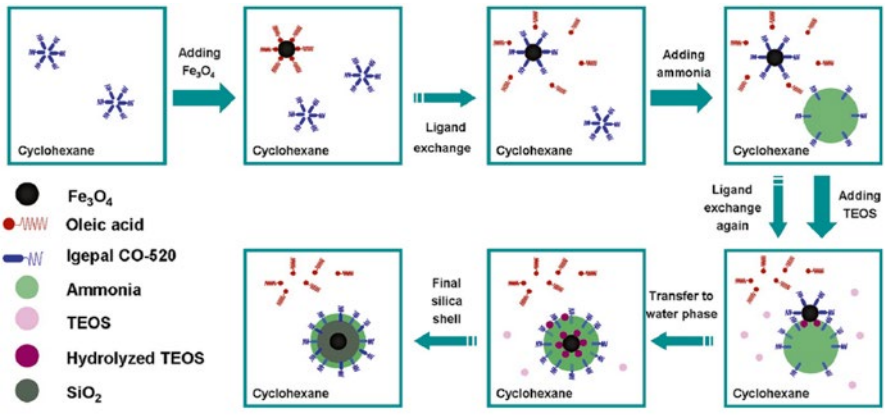

Fig. 1.8 The coating mechanism of SiO_2 on the surface of Fe_3O_4 NPs (Reproduced with permission from Ref. [103]. Copyright 2012 American Chemical Society)

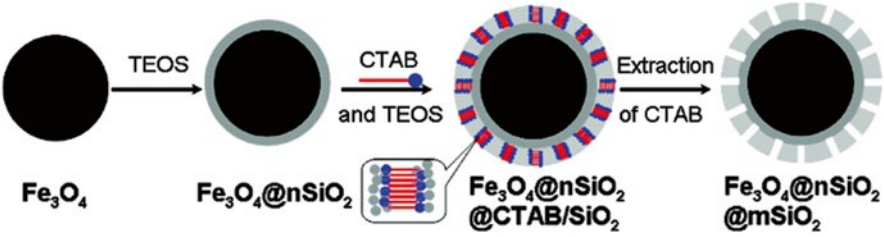

Fig. 1.9 The synthetic route of Fe_3O_4@nSiO_2@mSiO_2 (Reproduced with permission from Ref. [106]. Copyright 2008 American Chemical Society)

and perpendicularly aligned mesoporous SiO_2 shell (Fig. 1.9) [106]. The microspheres possessed very high magnetization, high surface area, large pore volume, and uniform accessible mesopores. Wu et al. reported a silica nanoshuttle as a drug delivery system with a nanoscale PEGylated-phospholipid coating and a 13-(chlorodimethylsilylmethyl)heptacosane-derived mesoporous silica NP [107]. The therapeutic and imaging agents were trapped, and ligand-assisted targeted delivery was achieved through surface functionalization of the phospholipids. Lately, silica shells with foamed or porous structures receive more attention for the ability to load and release drugs [108, 109].

As a robust core–shell structure, silica-coated MNPs can be functionalized with various biomolecules. In spite of the silica shell itself with adsorption of molecules, the silane coupling agents significantly influence this process [110, 111]. These agents always consist of siloxy (linking with silica shells) at one side and biocompatible groups like amino, sulfhydryl, and so on (linking with biomolecules) or even biomolecules themselves that are already incorporation of a silane group at another side. Using alkoxysilanes with active groups, such as aminopropylsilane (APS) or mercaptopropylsilane (MPS), biomolecules can be easily added to the outer shells [112–115].

1.4.1.4 Liposome and Micelle Encapsulation

As one of the earliest developed tools for drug delivery in nanomedicine, liposome has been developed all the time. Liposome is similar to the biological membrane structure of the microcapsule of bilayer structure, so it is usually biocompatible. With bilayer structure, amphipathic liposomes can encapsulate MNPs with range from 100 nm to 5 μm. Thus, another advantage of liposome encapsulation is to gather an amount of MNPs to the target. For these reasons, liposome complexes are an ideal platform for use as contrast agents of MRI [116, 117].

Polymeric micelles offer the advantage of multifunctional carriers which can serve as delivery vehicles carrying nanoparticles, hydrophobic chemotherapeutics, and other functional materials and molecules. Stimuli-responsive polymers are especially attractive since their properties can be modulated in a controlled manner.

Due to its large encapsulation range, molecules, proteins, DNA, and MNPs all can be encapsulated by liposome within one particle [118].

1.4.2 Theranostic Applications of MRI-Based MNPs

Except for the applications in enhancing MRI contrast, the MRI-based MNPs, with the ability of responding to magnetic field, can be further applied in magnetic targeting for targeted drug and gene delivery, magnetically triggered drug/gene delivery, magnetic hyperthermia, and magnetic controlled cell fate. Compared with other theranostic method, these applications are based on magnetic field, which is not significantly absorbed by tissue, permitting the remote management without physical or chemical contact.

1.4.2.1 Magnetic Targeting Therapy

When using NPs in theranostic, the potential toxicity of NPs should be the primary consideration for the production of ROS [119]. One way to reduce the potential toxicity is to reduce the dose of NPs which requires NPs of high targeting property. Because of the ability to respond to the external magnetic field, MNPs, different from common NPs relied on passive or positive targeting technique, are endowed with the characteristic targeting ability denoted as magnetic targeting. When exposed to an external magnetic field, MNPs can be magnetized, move under magnetic driving, and concentrate at a specific site [120]. Thus, MNPs can be located at the corresponding designated site due to the internalization by the endothelial cells at the targeted tissue. Moreover, by means of conjugating with drugs or gene on MNPs, this unique remotely and noninvasively targeting process can be applied in actuation for drug delivery and gene translation (Fig. 1.10) [120, 121].

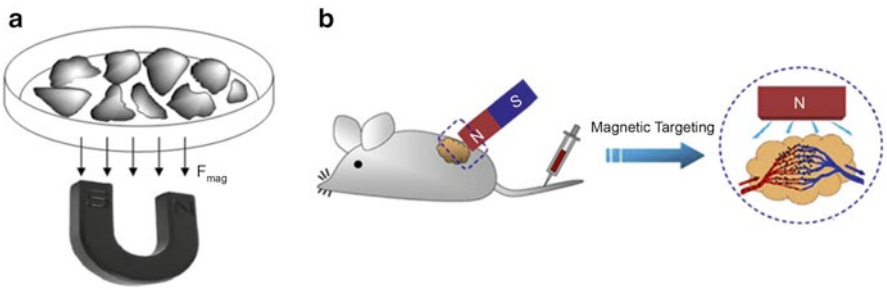

Fig. 1.10 A schematic illustration shows the concept of magnetically targeting (**a**) in vitro and (**b**) in vivo. ((**a**) Reproduced with permission from Ref. [120]. Copyright 2006 Nature Publication Group. (**b**) Reproduced with permission from Ref. [121]. Copyright 2012 Elsevier)

To date, drug delivery based on magnetic targeting has been applied in targeting various cancer cells, such as lung, prostate, brain, breast, and liver cells. Benefiting from the magnetic force, which can lead to either the enhancement of transfection efficiency or the targeting to the specific site, both DNA and RNA have been transfected by MNPs (noted as magnetofection) [120]. The magnetofection is significantly better than the commercially available transfection agent in some aspects owing to remarkable enhancement of the transfect efficiency in cell cultures and improvement of the tolerance and the controlling of scenario in vivo [122, 123].

1.4.2.2 Magnetic Controlling Drug Delivery

After appropriate surface modifications, MNPs can gain bioactive surface which enables them to load different kinds of drugs. Nevertheless, to fabricate a drug carrier, only to realize drug loading is far from enough and the achievement of drug delivery is more important in comparison. Drug delivery is a process of cell targeting. Various kinds of nanomaterials have been developed for drug delivery, including inorganic NPs, micelles, and polymers. In order to be effective at the target area, the drugs have to cross a variety of biological barriers such as organs, cells, and intracellular compartments because of the complexity of living body. However, the major problems of drug delivery come essentially from the lack of specificity with high cytotoxicity, which results in high side effects. To improve drug localization, magnetic force with an implanted or externally applied permanent magnet has been exploited as magnetically targeted drug delivery. Magnetic drug delivery is a method to target drugs to a diseased area in the body. The drug is attached to a magnetic nanoparticle and injected into blood flow. A magnetic field located close to the target location is used to capture the magnetic particles in the target area. In the action of magnetic field, the magnetic nanoparticles move irregularly in the target area which accelerates the release of drugs. In addition, MNPs modified with suitable affinity proteins can realize cell targeting as well.

MNP-based drug delivery not only transports the drugs to a specific site but also remotely controls drug release. Drugs can be attached to MNPs by conjugating a heat-sensitive linker [124] or through π–π interaction [125] and, in some situation, by co-embedding within thermal-sensitive polymers [126, 127]. Under an alternating magnetic field (AMF), MNPs can generate heat, which can improve the drug release due to the cracking of the linker or polymer (Fig. 1.11a) [128]. Moreover, drugs can also be loaded into porous materials with MNPs as valves. The magnetic heat generation can build up pressure inside the porous NPs, removing the molecular valves and triggering the drug release (Fig. 1.11b) [129, 130]. Interestingly, compared to normal heating at the same temperature, drug release prompted by magnetic hyperthermia is much improved, due to the synergistic effect of magnetic heating, magnetic disruption, and recrystallization [128]. Similarly, the overall efficiency of magnetofection can be further enhanced up to tenfold under oscillating magnetic

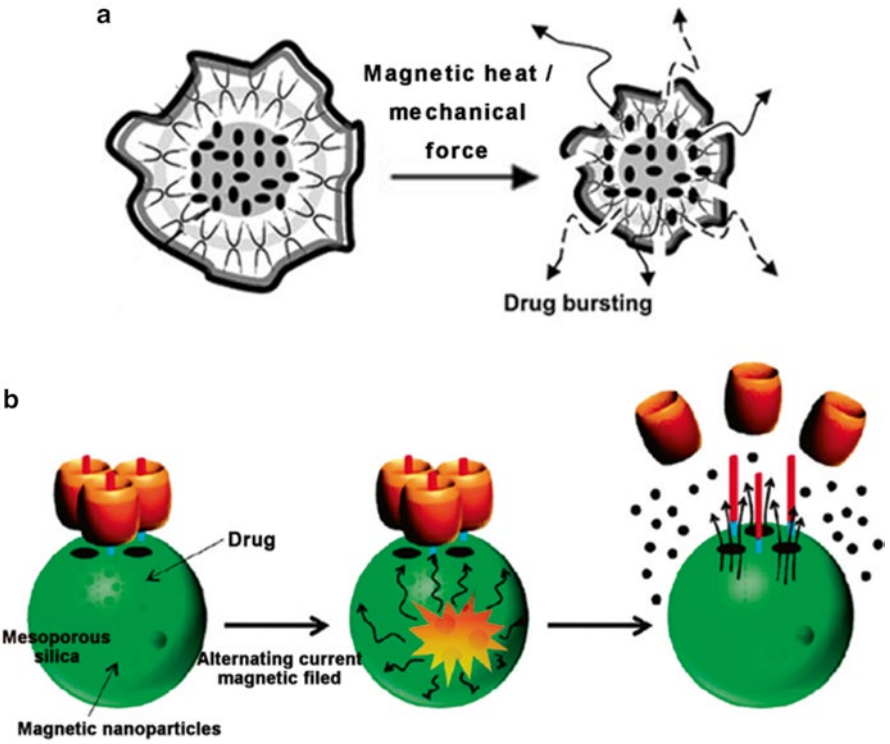

Fig. 1.11 (**a**) Shrinkage or deformation of polymers and (**b**) molecular valves. ((**a**) Reproduced with permission from Ref. [128]. Copyright 2009 WILEY-VCH Verlag GmbH & Co. KGaA, Weinheim. (**b**) Reproduced with permission from Ref. [130]. Copyright 2011, American Chemical Society)

arrays compared with magnetofection under static magnetic fields. Dobson et al. attributed it to the association of magnetic vectors with membranes and the transmission of mechanical forces from the lateral movement of the magnetic field to cellular membranes [131, 132].

1.4.2.3 Magnetic Hyperthermia

Apart from pharmaceutical therapy, MNPs are widely used in magnetic hyperthermia. Cancer can be overcome by initiating cell death or prompting the immune system directly with the action of the thermal energy generated by MNPs. Apoptosis, a programmed cell death way, generally can be induced by hyperthermia when stimulated by an "initiator" cysteinyl aspartate-specific protease (caspase). The result of cell death also can be inferred by morphological changes including

formation of membrane blebbing, cell rounding, and detach of actin [133, 134]. Under the action of magnetically modulated cancer hyperthermia, both caspase 3 and 7 and even TNF-α gene expression can be induced by MNPs which showed an excellent antitumor efficacy without severe toxicity [75, 135]. The immune system is quite sensitive to magnetic hyperthermia. By a heat shock, the immune response is activated which can bring down both primary tumor and metastatic lesions [136]. It is reported that owing to the activation of natural killer cell in the presence of heat-shock proteins at 42 °C, even though only one tumor was subjected to magnetic hyperthermia, both tumors at each femur in T-9 rat disappeared after the treatment [137]. This hyperthermia-triggering immunotherapy shows a great promise for rejecting tumors, especially metastasis tumor, which is now a challenge to cure.

Moreover, compared with hot water, this method is more efficient in inducing apoptosis although the mechanisms are still unknown [138]. So using magnetic hyperthermia is another way to realize cell necrosis which is a cell death process triggered by directly destroying the cellular structure, including loss of membrane structure and shrink of the cells [139]. After being engulfed into the endosome and exposed to AMF, MNPs can disrupt the endosomal membrane by heat, and the released endosomal content can destroy the cell membrane [140]. Some MNPs which are not engulfed into the cells and just dropped on the membrane surface can still be motivated by generating heat to disturb the membrane structure directly to induce cell necrosis [141].

In order to gain higher temperature by adding less MNPs, factors influencing the heating power are significant and are studied a lot. These factors mainly include the applied AMF and the structures, morphology, and the size of MNPs [75, 141, 142]. Briefly, the heating power is proportional to the amplitude and frequency of AMF, as well as magnetization of MNPs, and inversely proportional to the size distribution of MNPs [143, 144]. Properly modifying MNPs can also increase the heating power. Pawar et al. found that after functionalization with chitosan/glutaraldehyde, the hyperthermia effect of Fe_3O_4 NPs can be enhanced dramatically due to the improved water solubility [144]. Based on this phenomenon, we developed an aqueous solution of Fe_3O_4 NPs with a ferrofluidic behavior through the ligand exchange protocol with protocatechuic acid. This solution is highly stable in water and can be heated from 36 °C to 46 °C within 5 min with the concentration of only 1 mg/mL (Fig. 1.12) [145].

1.4.2.4 Cell Fate Controlling by Magnetic Field

Under exposure to external magnetic fields, some cell signaling pathways such as F-actin arrangement, cell alignment, intracellular ion fluctuations, and mitochondria activation may be changed [146, 147]. But these activations only need the force in the order of 10^{-15}–10^{-12} N (fN-pN), while some other activations, including antibody–antigen interaction, require a stronger force in the 10^{-9} N order (nN) and cannot be excited by magnetic field only [148, 149]. By introducing MNPs, the

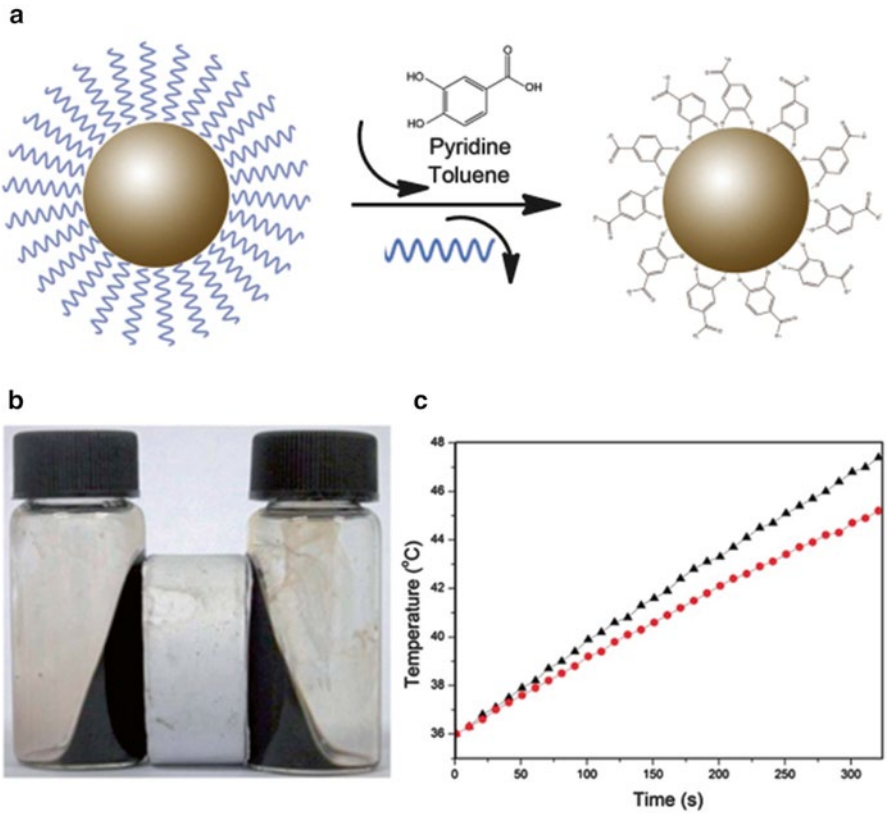

Fig. 1.12 (**a**) Schematic illustration of the rapid ligand exchange process of Fe_3O_4 NPs, (**b**) photographs of the ferrofluidic behavior of as synthesized Fe_3O_4 NPs in hexane (*left*) and in water after modification (*right*), (**c**) temperature profile during the hyperthermia experiment of 12 nm Fe_3O_4 NPs (*red*) and 25 nm Fe_3O_4 NPs (*black*) (Reproduced with permission from Ref. [139]. Copyright 2013 Royal Society of Chemistry)

influence of magnetic field to cells will be enlarged dramatically due to their specific response to the magnetic field. After conjugating with antibody or some ligands on MNPs, receptors of interest can be controlled precisely by generating mechanical stimulations of magnetic drug, rotation or twisting through the interaction of MNPs and cells, and finally influencing cell growth, differentiation, or even death [150, 151]. Cheon et al. induced strong attractive forces between neighboring NPs by static magnetic field with Zn^{2+}-doped ferrite MNPs, which prompted the clustering of specific protein after interacting with certain receptor, triggering cell apoptosis signaling pathways without damaging the cell membranes (Fig. 1.13) [152, 153]. AMF can also activate MNPs except for the magnetic hyperthermia. Gao et al. designed a magnetolytic therapy by using MNPs with their magnetic and nonmagnetic part separately. Due to the asymmetry in spatial distribution of magnetic component, NPs can rotate under a spinning magnetic field after attaching on cells,

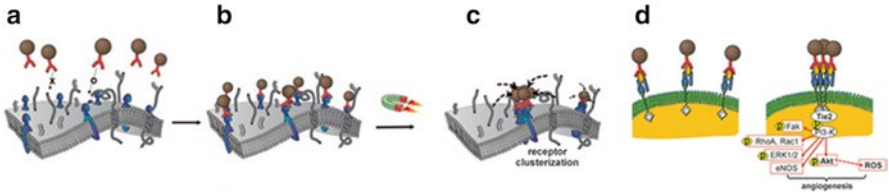

Fig. 1.13 Targeting and magnetic manipulation of Ab-Zn-MNPs. (**a**, **b**) Ab-Zn-MNPs selectively bind to the specific cell-surface Tie2 receptors; (**c**) In the presence of an external magnetic field, the Ab-Zn-MNPs are magnetized to form nanoparticle aggregates and induce the clustering of receptors to trigger intracellular signaling; (**d**) Tie2 receptor-bound NPs before and after application of the magnetic field (Reproduced with permission from Ref. [152]. Copyright 2010 WILEY-VCH Verlag GmbH & Co. KGaA, Weinheim)

killing the tumor cells owing to the compromised integrity of the cell membrane and then promoting cell apoptosis [154].

1.5 Conclusions and Outlook

Tremendous efforts have been made during the past few decades to design MNPs as MRI-based theranostics by deeply understanding the basic principle of MRI and developing novel synthetic and modification methods. By further surface modification with optical dyes, targeting agents, therapeutic drugs, or other functional molecules, these MNPs can be fabricated as multifunctional probes for diagnostics and therapy for diseases.

Now in a context of rapid development of MNPs in cancer therapy, researchers expect to gain MNPs with preferable integrative performance. It seems that the functionality is the priority of all demands on MNPs. However, we must think of comprehensive properties of MNPs like stability, safety, economy, and efficiency in research study rather than only multifunction so that the MNPs are able to apply in biomedicine. Accordingly, biocompatibility, toxicity, in vivo and in vitro targeting efficiency, and long-term stability of the functionalized MNPs are supposed to receive more attention. Meanwhile, there is an immense requirement of facile, efficient, biocompatible, and stabilized materials for surface modification. In the future, the development of MNPs is expected to realize diagnosis and therapy in nanoscale and with ongoing technique of surface engineering; the research of multifunctional MNPs is expected to be a frontier of biomedical science.

Acknowledgment This work was partially supported by National Natural Science Foundation of China (NSFC) (nos. 51125001, 81421004 and 51172005), the Research Fellowship for International Young Scientists of the National Natural Science Foundation of China (grant no. 51450110437), the Doctoral Program (no. 20090001120010), the Natural Science Foundation of Beijing (2122022), and PKU COE-Health Science Center Seed Fund.

References

1. Na HB, Song IC, Hyeon T (2009) Inorganic nanoparticles for MRI contrast agents. Adv Mater 21(21):2133–2148. doi:10.1002/adma.200802366
2. Pan DPJ, Schmieder AH, Wickline SA, Lanza GM (2011) Manganese-based MRI contrast agents: past, present, and future. Tetrahedron 67(44):8431–8444. doi:10.1016/j.tet.2011.07.076
3. Thorek DLJ, Chen A, Czupryna J, Tsourkas A (2006) Superparamagnetic iron oxide nanoparticle probes for molecular imaging. Ann Biomed Eng 34(1):23–38. doi:10.1007/s10439-005-9002-7
4. Bulte JWM, Kraitchman DL (2004) Iron oxide MR contrast agents for molecular and cellular imaging. NMR Biomed 17(7):484–499. doi:10.1002/nbm.924
5. Mornet S, Vasseur S, Grasset F, Duguet E (2004) Magnetic nanoparticle design for medical diagnosis and therapy. J Mater Chem 14(14):2161–2175. doi:10.1039/b402025a
6. Laurent S, Forge D, Port M, Roch A, Robic C, Elst LV, Muller RN (2008) Magnetic iron oxide nanoparticles: synthesis, stabilization, vectorization, physicochemical characterizations, and biological applications. Chem Rev 108(6):2064–2110. doi:10.1021/cr068445e
7. Wei XC, Wei ZW, Zhang LP, Liu YQ, He DY (2011) Highly water-soluble nanocrystal powders of magnetite and maghemite coated with gluconic acid: preparation, structure characterization, and surface coordination. J Colloid Interface Sci 354(1):76–81. doi:10.1016/j.jcis.2010.10.049
8. Kwon SG, Hyeon T (2008) Colloidal chemical synthesis and formation kinetics of uniformly sized nanocrystals of metals, oxides, and chalcogenides. Acc Chem Res 41(12):1696–1709. doi:10.1021/ar8000537
9. Racuciu M, Creanga DE, Airinei A (2006) Citric-acid-coated magnetite nanoparticles for biological applications. Eur Phys J E 21(2):117–121. doi:10.1140/epje/i2006-10051-y
10. Wan J, Cai W, Meng X, Liu E (2007) Monodisperse water-soluble magnetite nanoparticles prepared by polyol process for high-performance magnetic resonance imaging. Chem Commun 47:5004–5006. doi:10.1039/b712795b
11. Bang JH, Suslick KS (2007) Sonochemical synthesis of nanosized hollow hematite. J Am Chem Soc 129(8):2242. doi:10.1021/ja0676657
12. Suslick KS, Price GJ (1999) Applications of ultrasound to materials chemistry. Annu Rev Mater Sci 29:295–326. doi:10.1146/annurev.matsci.29.1.295
13. Bellusci M, La Barbera A, Seralessandri L, Padella F, Piozzi A, Varsano F (2009) Preparation of albumin-ferrite superparamagnetic nanoparticles using reverse micelles. Polym Int 58(10):1142–1147. doi:10.1002/pi.2642
14. Park J, An KJ, Hwang YS, Park JG, Noh HJ, Kim JY, Park JH, Hwang NM, Hyeon T (2004) Ultra-large-scale syntheses of monodisperse nanocrystals. Nat Mater 3(12):891–895. doi:10.1038/nmat1251
15. Park J, Joo J, Kwon SG, Jang Y, Hyeon T (2007) Synthesis of monodisperse spherical nanocrystals. Angew Chem-Int Ed 46(25):4630–4660. doi:10.1002/anie.200603148
16. Sun SH, Zeng H (2002) Size-controlled synthesis of magnetite nanoparticles. J Am Chem Soc 124(28):8204–8205. doi:10.1021/ja026501x
17. Xu ZC, Shen CM, Hou YL, Gao HJ, Sun SS (2009) Oleylamine as both reducing agent and stabilizer in a facile synthesis of magnetite nanoparticles. Chem Mater 21(9):1778–1780. doi:10.1021/cm802978z
18. Hou YL, Xu ZC, Sun SH (2007) Controlled synthesis and chemical conversions of FeO nanoparticles. Angew Chem-Int Ed 46(33):6329–6332. doi:10.1002/anie.200701694
19. Kovalenko MV, Bodnarchuk MI, Lechner RT, Hesser G, Schaffler F, Heiss W (2007) Fatty acid salts as stabilizers in size- and shape-controlled nanocrystal synthesis: the case of inverse spinel iron oxide. J Am Chem Soc 129(20):6352. doi:10.1021/ja0692478
20. Zhang LH, Wu JJ, Liao HB, Hou YL, Gao S (2009) Octahedral Fe_3O_4 nanoparticles and their assembled structures. Chem Commun 29:4378–4380. doi:10.1039/b906636e

21. Xiao L, Li J, Brougham DF, Fox EK, Feliu N, Bushmelev A, Schmidt A, Mertens N, Kiessling F, Valldor M, Fadeel B, Mathur S (2011) Water-soluble superparamagnetic magnetite nanoparticles with biocompatible coating for enhanced magnetic resonance imaging. ACS Nano 5(8):6315–6324. doi:10.1021/nn201348s
22. Veiseh O, Gunn JW, Zhang MQ (2010) Design and fabrication of magnetic nanoparticles for targeted drug delivery and imaging. Adv Drug Deliv Rev 62(3):284–304. doi:10.1016/j.addr.2009.11.002
23. Evanics F, Diamente PR, van Veggel F, Stanisz GJ, Prosser RS (2006) Water-soluble GdF3 and GdF3/LaF3 nanoparticles-physical characterization and NMR relaxation properties. Chem Mater 18(10):2499–2505. doi:10.1021/cm052299w
24. Chilton HM, Jackels SC, Hinson WH, Ekstrand KE (1984) Use of a paramagnetic substance, colloidal manganese sulfide, as an nmr contrast material in rats. J Nucl Med 25(5):604–607
25. Na HB, Lee JH, An KJ, Park YI, Park M, Lee IS, Nam DH, Kim ST, Kim SH, Kim SW, Lim KH, Kim KS, Kim SO, Hyeon T (2007) Development of a T-1 contrast agent for magnetic resonance imaging using MnO nanoparticles. Angew Chem Int Ed 46(28):5397–5401. doi:10.1002/anie.200604775
26. Baek MJ, Park JY, Xu WL, Kattel K, Kim HG, Lee EJ, Patel AK, Lee JJ, Chang YM, Kim TJ, Bae JE, Chae KS, Lee GH (2010) Water-soluble MnO nanocolloid for a molecular T-1 MR imaging: a facile one-pot synthesis, in vivo T-1 MR images, and account for relaxivities. ACS Appl Mater Interfaces 2(10):2949–2955. doi:10.1021/am100641z
27. Bae KH, Lee K, Kim C, Park TG (2011) Surface functionalized hollow manganese oxide nanoparticles for cancer targeted siRNA delivery and magnetic resonance imaging. Biomaterials 32(1):176–184. doi:10.1016/j.biomaterials.2010.09.039
28. Kim T, Momin E, Choi J, Yuan K, Zaidi H, Kim J, Park M, Lee N, McMahon MT, Quinones-Hinojosa A, Bulte JWM, Hyeon T, Gilad AA (2011) Mesoporous silica-coated hollow manganese oxide nanoparticles as positive T-1 contrast agents for labeling and MRI tracking of adipose-derived mesenchymal stem cells. J Am Chem Soc 133(9):2955–2961. doi:10.1021/ja1084095
29. Kellar KE, Fujii DK, Gunther WHH, Briley-Saebo K, Spiller M, Koenig SH (1999) 'NC100150' a preparation of iron oxide nanoparticles ideal for positive-contrast MR angiography. MAGMA 8(3):207–213
30. Xie J, Xu C, Kohler N, Hou Y, Sun S (2007) Controlled PEGylation of monodisperse Fe_3O_4 nanoparticles for reduced non-specific uptake by macrophage cells. Adv Mater 19(20):3163. doi:10.1002/adma.200701975
31. Corot C, Robert P, Idee JM, Port M (2006) Recent advances in iron oxide nanocrystal technology for medical imaging. Adv Drug Deliv Rev 58(14):1471–1504. doi:10.1016/j.addr.2006.09.013
32. Kresse M, Wagner S, Pfefferer D, Lawaczeck R, Elste V, Semmler W (1998) Targeting of ultrasmall superparamagnetic iron oxide (USPIO) particles to tumor cells in vivo by using transferrin receptor pathways. Magn Reson Med 40(2):236–242. doi:10.1002/mrm.1910400209
33. Chambon C, Clement O, Leblanche A, Schoumanclaeys E, Frija G (1993) Superparamagnetic iron-oxides as positive mr contrast agents – in vitro and in vivo evidence. Magn Reson Imaging 11(4):509–519. doi:10.1016/0730-725x(93)90470-x
34. Yu J, Yang C, Li JDS, Ding YC, Zhang L, Yousaf MZ, Lin J, Pang R, Wei LB, Xu LL, Sheng FG, Li CH, Li GJ, Zhao LY, Hou YL (2014) Multifunctional Fe_5C_2 nanoparticles: a targeted theranostic platform for magnetic resonance imaging and photoacoustic tomography-guided photothermal therapy. Adv Mater 26(24):4114–4120. doi:10.1002/adma.201305811
35. Jun YW, Seo JW, Cheon A (2008) Nanoscaling laws of magnetic nanoparticles and their applicabilities in biomedical sciences. Acc Chem Res 41(2):179–189. doi:10.1021/ar700121f
36. Huang J, Zhong XD, Wang LY, Yang LL, Mao H (2012) Improving the magnetic resonance imaging contrast and detection methods with engineered magnetic nanoparticles. Theranostics 2(1):86–102. doi:10.7150/thno.4006

37. Pankhurst QA, Thanh NTK, Jones SK, Dobson J (2009) Progress in applications of magnetic nanoparticles in biomedicine. J Phys D-Appl Phys 42(22). doi:10.1088/0022-3727/42/22/224001
38. Koo OM, Rubinstein I, Onyuksel H (2005) Role of nanotechnology in targeted drug delivery and imaging: a concise review. Nanomed Nanotechnol Biol Med 1(3):193–212. doi:10.1016/j.nano.2005.06.004
39. Veiseh O, Sun C, Gunn J, Kohler N, Gabikian P, Lee D, Bhattarai N, Ellenbogen R, Sze R, Hallahan A, Olson J, Zhang MQ (2005) Optical and MRI multifunctional nanoprobe for targeting gliomas. Nano Lett 5(6):1003–1008. doi:10.1021/nl0502569
40. Song HT, Choi JS, Huh YM, Kim S, Jun YW, Suh JS, Cheon J (2005) Surface modulation of magnetic nanocrystals in the development of highly efficient magnetic resonance probes for intracellular labeling. J Am Chem Soc 127(28):9992–9993. doi:10.1021/ja051833y
41. Ghosh R, Pradhan L, Devi YP, Meena SS, Tewari R, Kumar A, Sharma S, Gajbhiye NS, Vatsa RK, Pandey BN, Ningthoujam RS (2011) Induction heating studies of Fe_3O_4 magnetic nanoparticles capped with oleic acid and polyethylene glycol for hyperthermia. J Mater Chem 21(35):13388–13398. doi:10.1039/c1jm10092k
42. Fauconnier N, Pons JN, Roger J, Bee A (1997) Thiolation of maghemite nanoparticles by dimercaptosuccinic acid. J Colloid Interface Sci 194(2):427–433. doi:10.1006/jcis.1997.5125
43. Cao HN, He J, Deng L, Gao XQ (2009) Fabrication of cyclodextrin-functionalized superparamagnetic Fe_3O_4/amino-silane core-shell nanoparticles via layer-by-layer method. Appl Surf Sci 255(18):7974–7980. doi:10.1016/j.apsusc.2009.04.199
44. Yang HH, Masse S, Zhang H, Helary C, Li LF, Coradin T (2014) Surface reactivity of hydroxyapatite nanocoatings deposited on iron oxide magnetic spheres toward toxic metals. J Colloid Interface Sci 417:1–8. doi:10.1016/j.jcis.2013.11.031
45. Xiong MH, Bao Y, Yang XZ, Wang YC, Sun BL, Wang J (2012) Lipase-sensitive polymeric triple-layered nanogel for "On-Demand" drug delivery. J Am Chem Soc 134(9):4355–4362. doi:10.1021/ja211279u
46. Ahn J, Moon DS, Lee JK (2013) Arsenic acid as a robust anchor group for the surface modification of Fe_3O_4. Langmuir 29(48):14912–14918. doi:10.1021/la402939r
47. Dong AG, Ye XC, Chen J, Kang YJ, Gordon T, Kikkawa JM, Murray CB (2011) A generalized ligand-exchange strategy enabling sequential surface functionalization of colloidal nanocrystals. J Am Chem Soc 133(4):998–1006. doi:10.1021/ja108948z
48. Yuen AKL, Hutton GA, Masters AF, Maschmeyer T (2012) The interplay of catechol ligands with nanoparticulate iron oxides. Dalton Trans 41(9):2545–2559. doi:10.1039/c2dt11864e
49. Amstad E, Gehring AU, Fischer H, Nagaiyanallur VV, Hahner G, Textor M, Reimhult E (2011) Influence of electronegative substituents on the binding affinity of catechol-derived anchors to Fe_3O_4 nanoparticles. J Phys Chem C 115(3):683–691. doi:10.1021/jp1109306
50. Amstad E, Gillich T, Bilecka I, Textor M, Reimhult E (2009) Ultrastable iron oxide nanoparticle colloidal suspensions using dispersants with catechol-derived anchor groups. Nano Lett 9(12):4042–4048. doi:10.1021/nl902212q
51. Hussein-Al-Ali SH, El Zowalaty ME, Hussein MZ, Ismail M, Dorniani D, Webster TJ (2014) Novel kojic acid-polymer-based magnetic nanocomposites for medical applications. Int J Nanomedicine 9:351–362. doi:10.2147/ijn.s53847
52. Cai HD, Li KG, Shen MW, Wen SH, Luo Y, Peng C, Zhang GX, Shi XY (2012) Facile assembly of Fe_3O_4@Au nanocomposite particles for dual mode magnetic resonance and computed tomography imaging applications. J Mater Chem 22(30):15110–15120. doi:10.1039/c2jm16851k
53. Tie SL, Lee HC, Bae YS, Kim MB, Lee K, Lee CH (2007) Monodisperse Fe_3O_4/Fe@SiO_2 core/shell nanoparticles with enhanced magnetic property. Colloids Surf A Physicochem Eng Asp 293(1–3):278–285. doi:10.1016/j.colsurfa.2006.07.044
54. Hao R, Yu J, Ge ZG, Zhao LY, Sheng FG, Xu LL, Li GJ, Hou YL (2013) Developing Fe_3O_4 nanoparticles into an efficient multimodality imaging and therapeutic probe. Nanoscale 5(23):11954–11963. doi:10.1039/c3nr04157c

55. Chen ZP, Zhang Y, Zhang S, Xia JG, Liu JW, Xu K, Gu N (2008) Preparation and characterization of water-soluble monodisperse magnetic iron oxide nanoparticles via surface double-exchange with DMSA. Colloids Surf A Physicochem Eng Asp 316(1–3):210–216. doi:10.1016/j.colsurfa.2007.09.017
56. Liu YX, Chen ZP, Gu N, Wang JK (2011) Effects of DMSA-coated Fe_3O_4 magnetic nanoparticles on global gene expression of mouse macrophage RAW264.7 cells. Toxicol Lett 205(2):130–139. doi:10.1016/j.toxlet.2011.05.1031
57. Yantasee W, Hongsirikarn K, Warner CL, Choi D, Sangvanich T, Toloczko MB, Warner MG, Fryxell GE, Addleman RS, Timchalk C (2008) Direct detection of Pb in urine and Cd, Pb, Cu, and Ag in natural waters using electrochemical sensors immobilized with DMSA functionalized magnetic nanoparticles. Analyst 133(3):348–355. doi:10.1039/b711199a
58. Xie J, Chen K, Huang J, Lee S, Wang JH, Gao J, Li XG, Chen XY (2010) PET/NIRF/MRI triple functional iron oxide nanoparticles. Biomaterials 31(11):3016–3022. doi:10.1016/j.biomaterials.2010.01.010
59. Bertorelle F, Wilhelm C, Roger J, Gazeau F, Menager C, Cabuil V (2006) Fluorescence-modified superparamagnetic nanoparticles: intracellular uptake and use in cellular imaging. Langmuir 22(12):5385–5391. doi:10.1021/la052710u
60. Zhang Y, Kohler N, Zhang MQ (2002) Surface modification of superparamagnetic magnetite nanoparticles and their intracellular uptake. Biomaterials 23(7):1553–1561. doi:10.1016/s0142-9612(01)00267-8
61. Chekina N, Horak D, Jendelova P, Trchova M, Benes MJ, Hruby M, Herynek V, Turnovcova K, Sykova E (2011) Fluorescent magnetic nanoparticles for biomedical applications. J Mater Chem 21(21):7630–7639. doi:10.1039/c1jm10621j
62. Hilderbrand SA, Weissleder R (2010) Near-infrared fluorescence: application to in vivo molecular imaging. Curr Opin Chem Biol 14(1):71–79. doi:10.1016/j.cbpa.2009.09.029
63. Santra S, Kaittanis C, Grimm J, Perez JM (2009) Drug/dye-loaded, multifunctional iron oxide nanoparticles for combined targeted cancer therapy and dual optical/magnetic resonance imaging. Small 5(16):1862–1868. doi:10.1002/smll.200900389
64. Xie J, Lee S, Chen XY (2010) Nanoparticle-based theranostic agents. Adv Drug Deliv Rev 62(11):1064–1079. doi:10.1016/j.addr.2010.07.009
65. Cao C-Y, Shen Y-Y, Wang J-D, Li L, Liang G-L (2013) Controlled intracellular self-assembly of gadolinium nanoparticles as smart molecular MR contrast agents. Scientific reports 3. doi:10.1038/srep01024
66. Zhang C, Wangler B, Morgenstern B, Zentgraf H, Eisenhut M, Untenecker H, Kruger R, Huss R, Seliger C, Semmler W, Kiessling F (2007) Silica- and alkoxysilane-coated ultrasmall superparamagnetic iron oxide particles: a promising tool to label cells for magnetic resonance imaging. Langmuir 23(3):1427–1434. doi:10.1021/la061879k
67. Pierrat S, Zins I, Breivogel A, Sonnichsen C (2007) Self-assembly of small gold colloids with functionalized gold nanorods. Nano Lett 7(2):259–263. doi:10.1021/nl062131p
68. Gupta AK, Naregalkar RR, Vaidya VD, Gupta M (2007) Recent advances on surface engineering of magnetic iron oxide nanoparticles and their biomedical applications. Nanomedicine 2(1):23–39. doi:10.2217/17435889.2.1.23
69. Gupta AK, Gupta M (2005) Synthesis and surface engineering of iron oxide nanoparticles for biomedical applications. Biomaterials 26(18):3995–4021. doi:10.1016/j.biomaterials.2004.10.012
70. Cassidy MC, Chan HR, Ross BD, Bhattacharya PK, Marcus CM (2013) In vivo magnetic resonance imaging of hyperpolarized silicon particles. Nat Nanotechnol 8(5):363–368. doi:10.1038/nnano.2013.65
71. Mikhaylova M, Kim DK, Bobrysheva N, Osmolowsky M, Semenov V, Tsakalakos T, Muhammed M (2004) Superparamagnetism of magnetite nanoparticles: dependence on surface modification. Langmuir 20(6):2472–2477. doi:10.1021/la035648e

72. Josephson L, Tung CH, Moore A, Weissleder R (1999) High-efficiency intracellular magnetic labeling with novel superparamagnetic-tat peptide conjugates. Bioconjug Chem 10(2):186–191. doi:10.1021/bc980125h
73. Wunderbaldinger P, Josephson L, Weissleder R (2002) Crosslinked iron oxides (CLIO): a new platform for the development of targeted MR contrast agents. Acad Radiol 9:S304–S306. doi:10.1016/s1076-6332(03)80210-6
74. Tassa C, Shaw SY, Weissleder R (2011) Dextran-coated iron oxide nanoparticles: a versatile platform for targeted molecular imaging, molecular diagnostics, and therapy. Acc Chem Res 44(10):842–852. doi:10.1021/ar200084x
75. Bae KH, Park M, Do MJ, Lee N, Ryu JH, Kim GW, Kim C, Park TG, Hyeon T (2012) Chitosan oligosaccharide-stabilized ferrimagnetic iron oxide nanocubes for magnetically modulated cancer hyperthermia. ACS Nano 6(6):5266–5273. doi:10.1021/nn301046w
76. Amstad E, Zurcher S, Mashaghi A, Wong JY, Textor M, Reimhult E (2009) Surface functionalization of single superparamagnetic iron oxide nanoparticles for targeted magnetic resonance imaging. Small 5(11):1334–1342. doi:10.1002/smll.200801328
77. Li XH, Sun ZG (1995) Synthesis of magnetic polymer microspheres and application for immobilization of proteinase of balillus-sublitis. J Appl Polym Sci 58(11):1991–1997. doi:10.1002/app.1995.070581109
78. Sandiford L, Phinikaridou A, Protti A, Meszaros LK, Cui X, Yan Y, Frodsham G, Williamson PA, Gaddum N, Botnar RM, Blower PJ, Green MA, de Rosales RTM (2013) Bisphosphonate-anchored PEGylation and radiolabeling of superparamagnetic iron oxide: long-circulating nanoparticles for in vivo multimodal (T1 MRI-SPECT) imaging. ACS Nano 7(1):500–512. doi:10.1021/nn3046055
79. Cheng K, Peng S, Xu C, Sun S (2009) Porous hollow Fe_3O_4 nanoparticles for targeted delivery and controlled release of cisplatin. J Am Chem Soc 131(30):10637–10644. doi:10.1021/ja903300f
80. Li L, Jiang W, Luo K, Song H, Lan F, Wu Y, Gu Z (2013) Superparamagnetic iron oxide nanoparticles as MRI contrast agents for non-invasive stem cell labeling and tracking. Theranostics 3(8):595–615. doi:10.7150/thno.5366
81. Yan M, Sheng T, Gang B, Chuang G, Zhifei D (2013) Indocyanine green loaded SPIO nanoparticles with phospholipid-PEG coating for dual-modal imaging and photothermal therapy. Biomaterials 34(31):7706–7714. doi:10.1016/j.biomaterials.2013.07.007
82. Xu CJ, Miranda-Nieves D, Ankrum JA, Matthiesen ME, Phillips JA, Roes I, Wojtkiewicz GR, Juneja V, Kultima JR, Zhao WA, Vemula PK, Lin CP, Nahrendorf M, Karp JM (2012) Tracking mesenchymal stem cells with iron oxide nanoparticle loaded poly(lactide-co-glycolide) microparticles. Nano Lett 12(8):4131–4139. doi:10.1021/nl301658q
83. Maeng JH, Lee DH, Jung KH, Bae YH, Park IS, Jeong S, Jeon YS, Shim CK, Kim W, Kim J, Lee J, Lee YM, Kim JH, Kim WH, Hong SS (2010) Multifunctional doxorubicin loaded superparamagnetic iron oxide nanoparticles for chemotherapy and magnetic resonance imaging in liver cancer. Biomaterials 31(18):4995–5006. doi:10.1016/j.biomaterials.2010.02.068
84. Kang X, Yang D, Dai Y, Shang M, Cheng Z, Zhang X, Lian H, Ma P, Lin J (2013) Poly(acrylic acid) modified lanthanide-doped GdVO4 hollow spheres for up-conversion cell imaging, MRI and pH-dependent drug release. Nanoscale 5(1):253–261. doi:10.1039/c2nr33130f
85. Cao SW, Zhu YJ (2008) Surfactant-free preparation and drug release property of magnetic hollow core/shell hierarchical nanostructures. J Phys Chem C 112(32):12149–12156. doi:10.1021/jp803131u
86. Yang XQ, Chen YH, Yuan RX, Chen GH, Blanco E, Gao JM, Shuai XT (2008) Folate-encoded and Fe_3O_4-loaded polymeric micelles for dual targeting of cancer cells. Polymer 49(16):3477–3485. doi:10.1016/j.polymer.2008.06.005
87. Peppas NA, Hilt JZ, Khademhosseini A, Langer R (2006) Hydrogels in biology and medicine: from molecular principles to bionanotechnology. Adv Mater 18(11):1345–1360. doi:10.1002/adma.200501612

88. Kohler N, Fryxell GE, Zhang MQ (2004) A bifunctional poly(ethylene glycol) silane immobilized on metallic oxide-based nanoparticles for conjugation with cell targeting agents. J Am Chem Soc 126(23):7206–7211. doi:10.1021/ja049195r
89. Fu L, Dravid VP, Johnson DL (2001) Self-assembled (SA) bilayer molecular coating on magnetic nanoparticles. Appl Surf Sci 181(1–2):173–178. doi:10.1016/s0169-4332(01)00388-9
90. Nakanishi T, Masuda Y, Koumoto K (2004) Site-selective deposition of magnetite particulate thin films on patterned self-assembled monolayers. Chem Mater 16(18):3484–3488. doi:10.1021/cm049423g
91. Bull SR, Guler MO, Bras RE, Meade TJ, Stupp SI (2005) Self-assembled peptide amphiphile nanofibers conjugated to MRI contrast agents. Nano Lett 5(1):1–4. doi:10.1021/nl0484898
92. Nasongkla N, Bey E, Ren JM, Ai H, Khemtong C, Guthi JS, Chin SF, Sherry AD, Boothman DA, Gao JM (2006) Multifunctional polymeric micelles as cancer-targeted, MRI-ultrasensitive drug delivery systems. Nano Lett 6(11):2427–2430. doi:10.1021/nl061412u
93. Zhu H, Tao J, Wang W, Zhou Y, Li P, Li Z, Yan K, Wu S, Yeung KWK, Xu Z, Xu H, Chu PK (2013) Magnetic, fluorescent, and thermo-responsive Fe_3O_4/rare earth incorporated poly(St-NIPAM) core-shell colloidal nanoparticles in multimodal optical/magnetic resonance imaging probes. Biomaterials 34(9):2296–2306. doi:10.1016/j.biomaterials.2012.11.056
94. Erathodiyil N, Ying JY (2011) Functionalization of inorganic nanoparticles for bioimaging applications. Acc Chem Res 44(10):925–935. doi:10.1021/ar2000327
95. Yu C, Qi Y, Xiufeng J, Shengjian Z, Hangrong C, Yuanyi Z, Yang S, Haiyun Q, Zheng W, Yaping L, Xia W, Kun Z, Linlin Z, Jianlin S (2012) Manganese oxide-based multifunctionalized mesoporous silica nanoparticles for pH-responsive MRI, ultrasonography and circumvention of MDR in cancer cells. Biomaterials 33(29):7126–7137. doi:10.1016/j.biomaterials.2012.06.059
96. Liz-Marzan LM, Giersig M, Mulvaney P (1996) Synthesis of nanosized gold-silica core-shell particles. Langmuir 12(18):4329–4335. doi:10.1021/la9601871
97. Graf C, Vossen DLJ, Imhof A, van Blaaderen A (2003) A general method to coat colloidal particles with silica. Langmuir 19(17):6693–6700. doi:10.1021/la0347859
98. Lu ZY, Dai J, Song XN, Wang G, Yang WS (2008) Facile synthesis of Fe_3O_4/SiO_2 composite nanoparticles from primary silica particles. Colloids Surf A Physicochem Eng Asp 317(1–3):450–456. doi:10.1016/j.colsurfa.2007.11.020
99. Salgueirino-Maceira V, Correa-Duarte MA, Farle M, Lopez-Quintela A, Sieradzki K, Diaz R (2006) Bifunctional gold-coated magnetic silica spheres. Chem Mater 18(11):2701–2706. doi:10.1021/cm0603001
100. Zhou ZH, Xue JM, Wang J, Chan HSO, Yu T, Shen ZX (2002) $NiFe_2O_4$ nanoparticles formed in situ in silica matrix by mechanical activation. J Appl Phys 91(9):6015–6020. doi:10.1063/1.1462853
101. Xu ZZ, Wang CC, Yang WL, Fu SK (2005) Synthesis of superparamagnetic Fe_3O_4/SiO_2 composite particles via sol–gel process based on inverse miniemulsion. J Mater Sci 40(17):4667–4669. doi:10.1007/s10853-005-3924-1
102. Ma DL, Guan JW, Normandin F, Denommee S, Enright G, Veres T, Simard B (2006) Multifunctional nano-architecture for biomedical applications. Chem Mater 18(7):1920–1927. doi:10.1021/cm052067x
103. Ding HL, Zhang YX, Wang S, Xu JM, Xu SC, Li GH (2012) $Fe_3O_4@SiO_2$ core/shell nanoparticles: the silica coating regulations with a single core for different core sizes and shell thicknesses. Chem Mater 24(23):4572–4580. doi:10.1021/cm302828d
104. Salgueirino-Maceira V, Correa-Duarte MA, Spasova M, Liz-Marzan LM, Farle M (2006) Composite silica spheres with magnetic and luminescent functionalities. Adv Funct Mater 16(4):509–514. doi:10.1002/adfm.200500565
105. Chang Q, Zhu LH, Yu C, Tang HQ (2008) Synthesis and properties of magnetic and luminescent Fe_3O_4/SiO_2/Dye/SiO_2 nanoparticles. J Lumin 128(12):1890–1895. doi:10.1016/j.jlumin.2008.05.014

106. Deng Y, Qi D, Deng C, Zhang X, Zhao D (2008) Superparamagnetic high-magnetization microspheres with an Fe_3O_4@SiO_2 core and perpendicularly aligned mesoporous SiO_2 shell for removal of microcystins. J Am Chem Soc 130(1):28. doi:10.1021/ja0777584
107. Wang LS, Wu LC, Lu SY, Chang LL, Teng IT, Yang CM, Ho JAA (2010) Biofunctionalized phospholipid-capped mesoporous silica nanoshuttles for targeted drug delivery: improved water suspensibility and decreased nonspecific protein binding. ACS Nano 4(8):4371–4379. doi:10.1021/nn901376h
108. Son SJ, Reichel J, He B, Schuchman M, Lee SB (2005) Magnetic nanotubes for magnetic-field-assisted bioseparation, biointeraction, and drug delivery. J Am Chem Soc 127(20):7316–7317. doi:10.1021/ja0517365
109. Zhang SL, Chu ZQ, Yin C, Zhang CY, Lin G, Li Q (2013) Controllable drug release and simultaneously carrier decomposition of SiO_2-drug composite nanoparticles. J Am Chem Soc 135(15):5709–5716. doi:10.1021/ja3123015
110. Li GP, Shen B, He NY, Ma C, Elingarami S, Li ZY (2011) Synthesis and characterization of Fe_3O_4@SiO_2 core-shell magnetic microspheres for extraction of genomic DNA from human whole blood. J Nanosci Nanotechnol 11(12):10295–10301. doi:10.1166/jnn.2011.5200
111. Selvan ST, Tan TTY, Yi DK, Jana NR (2010) Functional and multifunctional nanoparticles for bioimaging and biosensing. Langmuir 26(14):11631–11641. doi:10.1021/la903512m
112. Gu JH, Zhang W, Yang XL (2013) Preparation of a superparamagnetic MRI contrast agent with a tumor targeting function. Mater Lett 94:8–10. doi:10.1016/j.matlet.2012.12.030
113. Huang WW, Yang X, Zhao S, Zhang M, Hu XL, Wang J, Zhao HT (2013) Fast and selective recognizes polysaccharide by surface molecularly imprinted film coated onto aldehyde-modified magnetic nanoparticles. Analyst 138(21):6653–6661. doi:10.1039/c3an01149f
114. Mahdavi M, Bin Ahmad M, Haron MJ, Gharayebi Y, Shameli K, Nadi B (2013) Fabrication and characterization of SiO_2/(3-aminopropyl)triethoxysilane-coated magnetite nanoparticles for lead(II) removal from aqueous solution. J Inorg Organomet Polym Mater 23(3):599–607. doi:10.1007/s10904-013-9820-2
115. Pan MR, Sun YF, Zheng J, Yang WL (2013) Boronic acid-functionalized core-shell-shell magnetic composite microspheres for the selective enrichment of glycoprotein. ACS Appl Mater Interfaces 5(17):8351–8358. doi:10.1021/am401285x
116. Kim MJ, Jang DH, Lee YI, Jung HS, Lee HJ, Choa YH (2011) Preparation, characterization, cytotoxicity and drug release behavior of liposome-enveloped paclitaxel/Fe_3O_4 nanoparticles. J Nanosci Nanotechnol 11(1):889–893. doi:10.1166/jnn.2011.3267
117. Mulder WJM, Strijkers GJ, van Tilborg GAF, Griffioen AW, Nicolay K (2006) Lipid-based nanoparticles for contrast-enhanced MRI and molecular imaging. NMR Biomed 19(1):142–164. doi:10.1002/nbm.1011
118. Kim D-H, Vitol EA, Liu J, Balasubramanian S, Gosztola DJ, Cohen EE, Novosad V, Rozhkova EA (2013) Stimuli-responsive magnetic nanomicelles as multifunctional heat and cargo delivery vehicles. Langmuir 29(24):7425–7432. doi:10.1021/la3044158
119. Sharifi S, Behzadi S, Laurent S, Laird Forrest M, Stroeve P, Mahmoudi M (2012) Toxicity of nanomaterials. Chem Soc Rev 41(6):2323–2343. doi:10.1039/c1cs15188f
120. Dobson J (2006) Gene therapy progress and prospects: magnetic nanoparticle-based gene delivery. Gene Ther 13(4):283–287. doi:10.1038/sj.gt.3302720
121. Cheng L, Yang K, Li Y, Zeng X, Shao M, Lee S-T, Liu Z (2012) Multifunctional nanoparticles for upconversion luminescence/MR multimodal imaging and magnetically targeted photothermal therapy. Biomaterials 33(7):2215–2222. doi:10.1016/j.biomaterials.2011.11.069
122. Zhou Y, Tang Z, Shi C, Shi S, Qian Z, Zhou S (2012) Polyethylenimine functionalized magnetic nanoparticles as a potential non-viral vector for gene delivery. J Mater Sci Mater Med 23(11):2697–2708. doi:10.1007/s10856-012-4720-5
123. Huettinger C, Hirschberger J, Jahnke A, Koestlin R, Brill T, Plank C, Kuechenhoff H, Krieger S, Schillinger U (2008) Neoadjuvant gene delivery of feline granulocyte-macrophage colony-stimulating factor using magnetofection for the treatment of feline fibrosarcomas: a phase I trial. J Gene Med 10(6):655–667. doi:10.1002/jgm.1185

124. N'Guyen TTT, Duong HTT, Basuki J, Montembault V, Pascual S, Guibert C, Fresnais J, Boyer C, Whittaker MR, Davis TP, Fontaine L (2013) Functional iron oxide magnetic nanoparticles with hyperthermia-induced drug release ability by using a combination of orthogonal click reactions. Angew Chem Int Ed 52(52):14152–14156. doi:10.1002/anie.201306724
125. Li R, Wu R, Zhao L, Wu M, Yang L, Zou H (2010) P-glycoprotein antibody functionalized carbon nanotube overcomes the multidrug resistance of human leukemia cells. ACS Nano 4(3):1399–1408. doi:10.1021/nn9011225
126. Hu S-H, Chen Y-Y, Liu T-C, Tung T-H, Liu D-M, Chen S-Y (2011) Remotely nano-rupturable yolk/shell capsules for magnetically-triggered drug release. Chem Commun 47(6):1776–1778
127. Kim Y-J, Ebara M, Aoyagi T (2013) A smart hyperthermia nanofiber with switchable drug release for inducing cancer apoptosis. Adv Funct Mater 23(46):5753–5761. doi:10.1002/adfm.201300746
128. Liu T-Y, Liu K-H, Liu D-M, Chen S-Y, Chen IW (2009) Temperature-sensitive nanocapsules for controlled drug release caused by magnetically triggered structural disruption. Adv Funct Mater 19(4):616–623. doi:10.1002/adfm.200801304
129. Thomas CR, Ferris DP, Lee J-H, Choi E, Cho MH, Kim ES, Stoddart JF, Shin J-S, Cheon J, Zink JI (2010) Noninvasive remote-controlled release of drug molecules in vitro using magnetic actuation of mechanized nanoparticles. J Am Chem Soc 132(31):10623–10625. doi:10.1021/ja1022267
130. Yoo D, Lee J-H, Shin T-H, Cheon J (2011) Theranostic magnetic nanoparticles. Acc Chem Res 44(10):863–874. doi:10.1021/ar200085c
131. Lim J, Dobson J (2012) Improved transfection of HUVEC and MEF cells using DNA complexes with magnetic nanoparticles in an oscillating field. J Genet 91(2):223–227. doi:10.1007/s12041-012-0164-4
132. Plank C, Zelphati O, Mykhaylyk O (2011) Magnetically enhanced nucleic acid delivery. Ten years of magnetofection – progress and prospects. Adv Drug Deliv Rev 63(14–15):1300–1331. doi:10.1016/j.addr.2011.08.002
133. Nedelcu G (2008) Magnetic nanoparticles impact on tumoral cells in the treatment by magnetic fluid hyperthermia. Dig J Nanomater Biostruct 3(3):103–107
134. Prasad NK, Rathinasamy K, Panda D, Bahadur D (2007) Mechanism of cell death induced by magnetic hyperthermia with nanoparticles of [gamma]-$MnxFe_{2-x}O_3$ synthesized by a single step process. J Mater Chem 17(48):5042–5051
135. Ito A, Shinkai M, Honda H, Kobayashi T (2001) Heat-inducible TNF-alpha gene therapy combined with hyperthermia using magnetic nanoparticles as a novel tumor-targeted therapy. Cancer Gene Ther 8(9):649–654. doi:10.1038/sj.cgt.7700357
136. Colombo M, Carregal-Romero S, Casula MF, Gutierrez L, Morales MP, Boehm IB, Heverhagen JT, Prosperi D, Parak WJ (2012) Biological applications of magnetic nanoparticles. Chem Soc Rev 41(11):4306–4334. doi:10.1039/c2cs15337h
137. Ito A, Shinkai M, Honda H, Wakabayashi T, Yoshida J, Kobayashi T (2001) Augmentation of MHC class I antigen presentation via heat shock protein expression by hyperthermia. Cancer Immunol Immunother 50(10):515–522. doi:10.1007/s00262-001-0233-7
138. Rodriguez-Luccioni HL, Latorre-Esteves M, Mendez-Vega J, Soto O, Rodriguez AR, Rinaldi C, Torres-Lugo M (2011) Enhanced reduction in cell viability by hyperthermia induced by magnetic nanoparticles. Int J Nanomed 6:373–380. doi:10.2147/ijn.s14613
139. Marcos-Campos I, Asín L, Torres TE, Marquina C, Tres A, Ibarra MR, Goya GF (2011) Cell death induced by the application of alternating magnetic fields to nanoparticle-loaded dendritic cells. Nanotechnology 22(20):205101
140. Asín L, Ibarra M, Tres A, Goya G (2012) Controlled cell death by magnetic hyperthermia: effects of exposure time, field amplitude, and nanoparticle concentration. Pharm Res 29(5):1319–1327. doi:10.1007/s11095-012-0710-z

141. Guardia P, Di Corato R, Lartigue L, Wilhelm C, Espinosa A, Garcia-Hernandez M, Gazeau F, Manna L, Pellegrino T (2012) Water-soluble iron oxide nanocubes with high values of specific absorption rate for cancer cell hyperthermia treatment. ACS Nano 6(4):3080–3091. doi:10.1021/nn2048137
142. Jang J-T, Nah H, Lee J-H, Moon SH, Kim MG, Cheon J (2009) Critical enhancements of MRI contrast and hyperthermic effects by dopant-controlled magnetic nanoparticles. Angew Chem Int Ed 48(7):1234–1238. doi:10.1002/anie.200805149
143. Rosensweig RE (2002) Heating magnetic fluid with alternating magnetic field. J Magn Magn Mater 252(1–3):370–374. doi:10.1016/s0304-8853(02)00706-0
144. Kita E, Oda T, Kayano T, Sato S, Minagawa M, Yanagihara H, Kishimoto M, Mitsumata C, Hashimoto S, Yamada K, Ohkohchi N (2010) Ferromagnetic nanoparticles for magnetic hyperthermia and thermoablation therapy. J Phys D Appl Phys 43(47):474011
145. Patil RM, Shete PB, Thorat ND, Otari SV, Barick KC, Prasad A, Ningthoujam RS, Tiwale BM, Pawar SH (2014) Superparamagnetic iron oxide/chitosan core/shells for hyperthermia application: improved colloidal stability and biocompatibility. J Magn Magn Mater 355(0):22–30. doi:http://dx.doi.org/10.1016/j.jmmm.2013.11.033
146. Shin J, Yoo C-H, Lee J, Cha M (2012) Cell response induced by internalized bacterial magnetic nanoparticles under an external static magnetic field. Biomaterials 33(22):5650–5657. doi:10.1016/j.biomaterials.2012.04.033
147. Smith C-AM, Fuente J, Pelaz B, Furlani EP, Mullin M, Berry CC (2010) The effect of static magnetic fields and tat peptides on cellular and nuclear uptake of magnetic nanoparticles. Biomaterials 31(15):4392–4400. doi:10.1016/j.biomaterials.2010.01.096
148. Hinterdorfer P, Baumgartner W, Gruber HJ, Schilcher K, Schindler H (1996) Detection and localization of individual antibody-antigen recognition events by atomic force microscopy. Proc Natl Acad Sci USA 93(8):3477–3481
149. Smith SB, Cui Y, Bustamante C (1996) Overstretching B-DNA: the elastic response of individual double-stranded and single-stranded DNA molecules. Science 271(5250):795–799. doi:10.1126/science.271.5250.795
150. Lee SI, Park KH, Kim SJ, Kang YG, Lee YM, Kim EC (2012) Mechanical stress-activated immune response genes via Sirtuin 1 expression in human periodontal ligament cells. Clin Exp Immunol 168(1):113–124. doi:10.1111/j.1365-2249.2011.04549.x
151. Wang N, Butler J, Ingber D (1993) Mechanotransduction across the cell surface and through the cytoskeleton. Science 260(5111):1124–1127. doi:10.1126/science.7684161
152. Lee J-H, Kim ES, Cho MH, Son M, Yeon S-I, Shin J-S, Cheon J (2010) Artificial control of cell signaling and growth by magnetic nanoparticles. Angew Chem Int Ed 49(33):5698–5702. doi:10.1002/anie.201001149
153. Cho MH, Lee EJ, Son M, Lee J-H, Yoo D, Kim J-W, Park SW, Shin J-S, Cheon J (2012) A magnetic switch for the control of cell death signalling in in vitro and in vivo systems. Nat Mater 11(12):1038–1043. doi:10.1038/nmat3430
154. Hu S-H, Gao X (2010) Nanocomposites with spatially separated functionalities for combined imaging and magnetolytic therapy. J Am Chem Soc 132(21):7234–7237. doi:10.1021/ja102489q

Chapter 2
Controlled Synthesis and Surface Modification of Magnetic Nanoparticles with High Performance for Cancer Theranostics Combining Targeted MR Imaging and Hyperthermia

Jun Xie, Ning Gu, and Yu Zhang

Multifunctional inorganic nanoparticle (NP)-based theranostic agents are emerging as promising paradigm toward personalized nanocarrier or nanomedicine for the disease diagnosis and specific treatment [1–6]. Among these NPs, magnetic nanoparticles (MNPs) are very prominent since they have already been introduced into the clinical practice because of their unique physicochemical properties, such as high magnetic performance, excellent magnetically induced heating ability, and biocompatibility [7–11]. As conventional contrast imaging agents, MNP-based magnetic resonance (MR) imaging with substantial signal enhancement can help to locate active tumors and determine tumor stages, which is used for cancer early detection and diagnosis [7, 8, 10]. As a promising cancer therapy, MNP-induced targeted hyperthermia is mainly based on the heat generation by magnetic materials exposed to an alternating current magnetic field (ACMF), which provides the minimal damnification to deliver a therapeutic dose of heat specifically to cancerous regions [7, 8, 11]. To ensure an optimal strategy for cancer treatment in vivo, the integration of theranostics combining simultaneously magnetic resonance imaging (MRI) and efficient heat induction into a single nano-formulation has gained increased interest for researchers.

Developing the functional MNPs with high performance has become an important goal for efficient cancer theranostics. The high performance of MNPs, including superior magnetism, high magnetically induced heating effects, favorable biocompatibility, accurate targeting ability, and long circulation, is optimized by the controlled synthesis and surface functionalization. This is a rather challenging issue. In this regard, we will begin our review with the goal of describing controlled synthesis and surface modification of the MNPs with high performance, giving a

J. Xie • N. Gu • Y. Zhang (✉)
State Key Laboratory of Bioelectronics, Jiangsu Key Laboratory for Biomaterials and Devices, School of Biological Science and Medical Engineering, Southeast University, Nanjing 210096, People's Republic of China
e-mail: zhangyu@seu.edu.cn

Z. Dai (ed.), *Advances in Nanotheranostics II*, Springer Series in Biomaterials Science and Engineering 7, DOI 10.1007/978-981-10-0063-8_2

background on the advantages of these high-quality MNPs and the advanced synthetic methods currently under investigation. We will then conclude with a discussion of current clinical applications of the MNPs, especially in cancer targeted MR imaging and hyperthermia in vivo, and get a perspective of MNP-mediated cancer theranostics strategy.

2.1 Controlled Synthesis and Surface Modification of MNPs with High Performance

In the last decades, much research has been dedicated to the synthesis of MNPs because the synthesis directly determines the physical properties of MNPs, including the composition, magnetism, size distribution, and morphology [12–15], which are fundamental for further biomedical applications. Generally, the synthesized bare MNPs are rapidly cleared from the blood circulation when passing through the biological defense system and vascular barriers. So introducing a surface modification, such as amphiphilic molecules, bifunctional polymeric ligands, or biomolecules, can provide a stabilizing layer that prevents MNP agglomeration and enhances colloidal stability, which is crucial requirement for almost any biomedical application of MNPs [16–19]. In the practical clinical application, the development of new types of MNPs with high performance, such as advanced MR contrast molecular imaging and magnetic heat generation ability, and prominent magnetic attractive forces for the transportation and movement of biological objects is particularly important. It will bring potential advantages and opportunities afforded by MNPs as platform materials for theranostics.

2.1.1 Conventional Synthesis of MNPs

Developing functional MNPs with high performance has become an important goal for chemists due to the chemical processes involved in the controlled synthesis and surface functionalization. During the last decades, many publications have described efficient synthetic routes to MNPs with different compositions and phases, including iron oxide pure metals (e.g., Fe_3O_4 and $\gamma-Fe_2O_3$) [20–23], magnetic dopant ferrite metals (e.g., $MnFe_2O_4$, $CoFe_2O_4$, and $ZnFe_2O_4$) [24–27], and metal alloy (e.g., FeCo and FePt) [28–31]. In conventional methods, such as coprecipitation, thermal decomposition, and/or reduction, microemulsion synthesis and hydrothermal synthesis techniques can all be directed at the synthesis of size-/shape-controlled, high-crystallinity, and monodisperse MNPs, which have been well documented and still described in progress [32–43].

The comparison of advantages and disadvantages of the abovementioned synthetic methods are briefly summarized in Table 2.1. As a whole, in terms of simplic-

Table 2.1 Summary comparison of conventional synthetic methods of MNPs

Synthetic method	Synthetic progress	Solvent, reaction temperature, and period	Size distribution	Shape control
Coprecipitation	MNPs are commonly made by hydrolysis/condensation of M^{2+} and Fe^{3+} ions by a base, usually NaOH, or $NH_3 \cdot H_2O$, in an aqueous solution or in reverse micelles [32–35]	Water, 20 ~ 80 °C, a few minutes	Relatively narrow	Not good
Thermal decomposition	MNPs can be made by reductive thermal decomposition of metal acetylacetonates or carboxylates in an organic phase in high-boiling organic solvents containing stabilizing surfactants [36–38]	Organic compound, 250 ~ 320 °C, a few hours	Very narrow	Very good
Microemulsion	A microemulsion is a thermodynamically stable isotropic dispersion of two immiscible liquids, where the microdomain of either or both liquids is stabilized by an interfacial film of surfactant molecules, which can be used as a nanoreactor for the formation of MNPs [39]	Organic compound, 20 ~ 50 °C, a few hours	Relatively narrow	Good
Hydrothermal synthesis	A process occurs spontaneously across the interface of metal linoleate and the water–ethanol solutions in a closed and high-pressure/high-temperature system. The MNPs generated at the interface are coated with a layer of linoleic acid, resulting in a spontaneous phase-separation process and the formation of hydrophobic MNPs [40–42]	Water–ethanol compound, 220 °C, a few hours	Very narrow	Very good

ity of the synthesis, coprecipitation is the preferred route and is suitable for mass production of MNPs, but it is difficult to control the synthesis of MNPs with uniform size distributions and various morphologies. Microemulsion methods can be used to synthesize the monodisperse MNPs; however, this method requires a complicated condition within a large amount of solvent, and the yield is very low. As an alternative, hydrothermal synthesis by a liquid–solid–solution reaction is a relatively suitable and little explored method to synthesize size- and shape-tunable

MNPs with high quality, but the reaction is in a closed and high-pressure system, hence lacking the ability for large-scale and practical application. In terms of size and morphology control of the MNPs, thermal decomposition seems the best method to obtain the high-performance MNPs (e.g., monodispersity, improved crystallinity, and larger magnetization) developed to date. In this regard, we will focus on the recent advance and advantage in the thermal decomposition synthesis of monodisperse MNPs with controlled size, shape, composition, and structure, and we will also try to present typical and representative examples for the discussion of this synthetic pathway and the corresponding formation mechanism.

2.1.2 Advantage of Synthesis of High-Quality MNPs by Thermal Decomposition

2.1.2.1 Formation Mechanism of Monodisperse MNPs by Thermal Decomposition

Recently, significant advances in preparing monodisperse MNPs have been made by the use of the thermal decomposition of organometallic precursors in high-boiling organic solvents in the presence of some stabilizing surfactants [36–38, 44–50]. The precursors usually include metal acetylacetonates [44, 45], metal cupferronates [46], or carboxylates [47]. Fatty acids [48], oleic acid [49], oleylamine [45], and hexadecylamine [50] are often used as typical capping surfactants. In MNP synthesis, a classical crystallization mode based on the supersaturation of solution is usually used to explain the crystal nucleation/growth kinetics, which plays a fundamental role in tailoring the MNPs with controllable sizes and shapes [44, 51]. The crystal process evaluated by variation of the monomer concentration can be described by using a La Mer model. With the supply of the precursor and surfactants, the monomer concentration was gradually increased and reached the minimum nucleation concentration. The reaction of molecular or atomic species rapidly takes the concentration of the precipitating species to above critical supersaturation. A large number of critical nuclei should be formed in a short interval of time, and the ensuing spontaneous nucleation that reduces the monomer concentration was rapidly decreased to below the nucleation threshold, at which stage the existing nuclei grow simultaneously at the same rate without production of fresh nuclei. When no new monomers were supplied in the reaction solution, the monomer was continuously consumed for subsequent particle growth, finally leading to the formation of monodisperse nanoparticles [44, 51].

2.1.2.2 Size Effects

One important parameter for high performance of MNPs is their appropriate size. As the MNP size decreases, their surface effect becomes more pronounced due to the increased volume fraction of surface atoms within the whole nanoparticle, which

is reflected in reduced symmetry for the chemical surroundings of magnetic metal cations at the surface by the incomplete coordination [52–54]. Consequently, the surface magnetic structure is greatly different from that in the body of MNPs, and the magnetic interactions in the surface layer could have a notable effect on the magnetic properties of the MNPs [52, 55–57]. Generally, naturally ferromagnetic MNPs undergo a transition from multi- to single-domain magnetic structure as their size is reduced to below 80 ~ 90 nm. Further size reduction to less than 20 nm, the individual MNPs behave as a single magnetic domain and exhibit negligible remanence and coercivity, leading to their predominant superparamagnetism, which plays a critical role in practical applications [58]. In addition, the appropriate size of MNCs is highly related to their capabilities for effectively overcoming the biological defense system and vascular barriers in vivo. For example, MNPs with a large hydrodynamic diameter (e.g., >100 nm) are readily taken up by the mononuclear phagocyte system (MPS) and occur primarily in the liver and spleen [52, 59], while very smaller particles (e.g., <10 nm) may "leak" from the larger pores of fenestrated vascular networks or first-pass elimination by the kidney [35]. Hence, the MNPs with sizes of 10 ~ 100 nm can escape from phagocytes and travel through blood vessels with a reasonably high blood half-life (>1 h) [52, 60]. These relatively small-sized MNPs can have enhanced permeability and retention (EPR) effects at the target tissues because they can easily pass through the larger fenestrations of the blood vessels in the vicinity of cancerous tissues in vivo [61, 62].

Monodisperse ferrite MNPs with desired size distribution were usually made by varying reaction conditions or by seed-mediated growth in a high-temperature decomposition synthesis [63–65]. For instance, it was found that separation of nucleation and growth in time is required for the formation of monodisperse MNPs. By varying synthetic parameters including precursors, solvents, amount of surfactants, and heating rate of the solution, the MNP size from 2 to 9 nm could be controlled with 1 nm accuracy [63], as shown in Fig. 2.1a. Additionally, a practical and relatively simple approach for the synthesis of crystalline MNP controllable size is seed-mediated crystal growth, which is proved to be a reproducible method and is of great fundamental and technological interest for researchers [64]. The process firstly involves high-temperature (usually up to 300 °C) reaction of metal acetylacetonate with 1,2-hexadecanediol and surfactants (such as oleic acid (OA) and oleylamine (OAm)), in making monodisperse smaller-sized MNPs. With the smaller MNPs as seeds, the larger MNPs can be successfully synthesized by seed-mediated growth (Fig. 2.1b). The process can result in MNPs with desired size distribution and is readily suitable for mass production.

2.1.2.3 Shape Effects: From 0-D Nanocrystals to 3-D Nanoclusters

Recently, keen interests have been expanded into controlling the shape of nanostructure and also into understanding the correlations between the material properties, function, and its shape [65–74]. These shape–function relationships are particularly interesting for magnetic nanostructure, because the physical and chemical properties of the nanostructure are highly dependent on the material

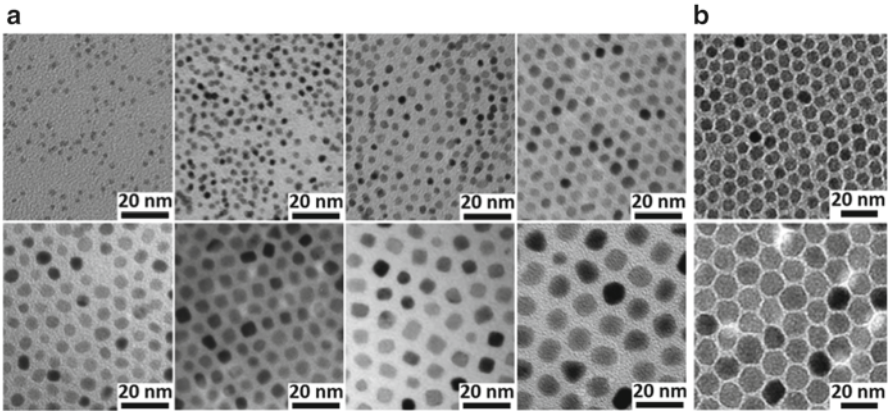

Fig. 2.1 (**a**) TEM images of synthesized MNPs of size from 2 to 9 nm by varying synthetic parameters (Reprinted with permission from Ref. [63]. Copyright 2007, American Chemical Society). (**b**) TEM bright field images of synthesized MNPs used by seed-mediated growth (Reprinted with permission from Ref. [64]. Copyright 2004, American Chemical Society)

morphology, which can enhance the prospects for promising application in a wide range of scientific and technological fields, including magnetism, electronics, catalysis, biochemistry, and medicine [44, 45, 65–74]. The shape of magnetic nanostructure can be simply classified by their dimensionality. Generally, 0-D magnetic nanostructures (e.g., spheres, cubes, and polyhedrons) are the most basic motifs among shaped nanocrystals.

The improved understanding and investigation of the shape-controllable synthetic mechanism is reviewed here. Generally, the essence of shape controlling of nanostructures is tuning the growth rate in specific directions, which is governed by the intrinsic surface energy and the monomer concentration in the crystal growth process. For magnetic ferrite nanocrystals, the typical spinel structure is based on a face-centered cubic model with three low-energy facets, {100}, {110}, and {111} (Fig. 2.2a) [44, 45, 65]. The {100} planes show the lowest surface energy, while the {111} planes have the highest [65]. In this regard, the choice of appropriate surfactant remains an important challenge in the shape controlling of nanocrystals, because the surfactant can selectively bind to specific crystal facets with lower energy, and tunes their growing rate. The OA as a typical capping surfactant is used to stabilize the formation of magnetic nanocrystals in a decomposition reaction of metal precursors. For example, by adjusting OA/OAm ratios, the synthesized spherical, cubical, and starlike nanocrystals were systematically investigated (Fig. 2.2b) [65]. The OA with its carboxylic group bound strongly onto certain crystal facets of initial nuclei, forming a stabilizing layer. Whereas, the OAm with an amine group as a crucial reducing agent here has relatively weak binding onto the crystal surface. It was evident that the various crystal planes are well capped and stabilized and the differential growth of crystal facets is negligible when OA was sufficient, thus leading to uniform spherical shape. Contrastively, when insufficient

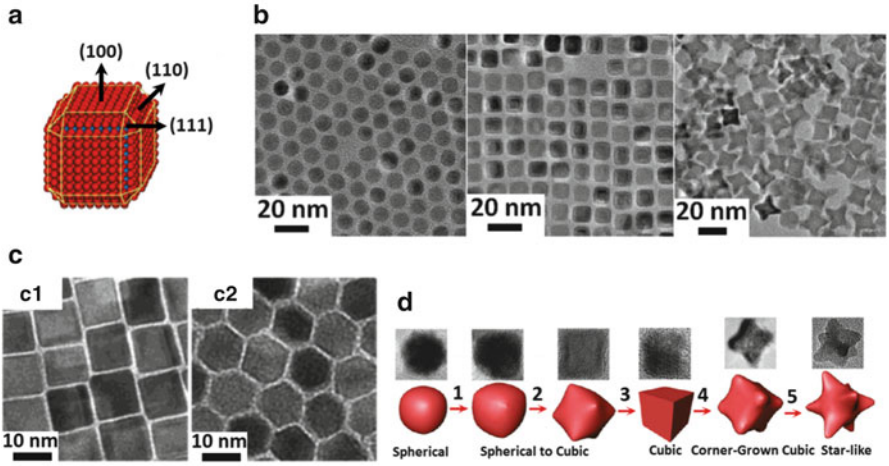

Fig. 2.2 (**a**) The face-centered cubic (*fcc*) models of typical spinel structure with three low-energy facets (Reprinted with permission from Ref. [44]. Copyright 2011, American Chemical Society). (**b**) TEM images of synthesized spherical, cubical, and starlike MNPs (Reprinted with permission from Ref. [65]. Copyright 2013, American Chemical Society). (**c**) TEM images of the synthesized cubelike and polyhedron-shaped MNPs (Reprinted with permission from Ref. [66]. Copyright 2004, American Chemical Society). (**d**) Schematic illustration of the shape evolution mechanism of MNPs (Reprinted with permission from Ref. [67]. Copyright 2009, American Chemical Society)

amounts of OA were used, it induced the preferential stabilization on the {100} crystal facets with lower energy, and grew along the [75] or [76] direction, resulting in the formation of cubical and starlike nanocrystals with the terminated {100} facets [65]. Another study had also described that the shape of magnetic nanocrystals was tuned by varying the amount of stabilizers to metal precursors [66]. When the surfactant/precursor ratio was smaller than 3:1, the nanocrystals were nearly spherical with no well-defined facets, and increasing the ratio to 3:1 yields cubelike particles. If the nanocrystals were further prepared using seed-mediated growth, the polyhedron-shaped particles were obtained (Fig. 2.2c) [66].

Besides the surface energy-mediated surfactant effects, the monomer concentration synchronously tailors the morphology of magnetic nanocrystals [67]. A few initial "crystal units" might appear at the stage from the decomposition of precursor, in which the monomer concentration was continually increased, gradually leading to the formation of spherical nanocrystals. Generally, most of spherical nanocrystals might keep growing to form the cubic shape until the excess monomers in the solution were nearly exhausted and their concentration reduced to the equilibrium concentration. The definite formation of nanocrystals was dependent on the reaction temperature, heating rate, and aging time. As the continuous consumption of the monomer, a limited number of nuclei could grow to form large nanocubes. The concentration of defects and surface energy in individual crystallites decreased in going from the corners, to the edges, to the crystal faces of nanocubes. Thus, the growth preferences for different sections of nanocubes are the corners, the edges,

and the faces, respectively [67]. The shape evolution with increasing aging time from spherical to the intermediate spherical-to-cubic, to cubic, and eventually to corner-grown nanocube morphology was shown in Fig. 2.2d [67].

In addition, successes in similar monodisperse magnetic nanostructures with corner-grown shape synthesized by thermal decomposition of iron oleates had been reported by Gao and co-workers [68]. They reported that introducing the chloride anions as the capping agent had an important role in the formation of the nanostructures with specific morphology. The size-controllable octapod magnetic nanostructures consisting of uniform four-armed starlike iron oxide particles with high yield were prepared in the presence of NaCl (Fig. 2.3a) [68]. One possible forming mechanism was that the chloride ions were selectively bound to iron ions exposed on the high-index facets (probably [311]) during the nanostructure growth [68].

Except for 0-D magnetic nanocrystals, 1-D nanostructures could also be interesting for studying structural anisotropy, magnetic properties, and their corresponding biomedical applications [69–71]. For example, dextran-encapsulated 1-D chains of iron oxide nanoworms showed enhanced retention effects at the tumor sites and increased blood circulation time [69]. Furthermore, anisotropic 1-D nanostructures can interact and penetrate cellular membranes more efficiently, which makes them to be good candidates as drug carriers [70]. Herein, Bao et al. reported a simple colloidal synthesis method for preparing the single-crystalline 1-D magnetic nanorods by the iron oleate precursor thermal decomposition, where the aspect ratios of the iron oxide nanorods could be tuned by changing reaction temperatures (Fig. 2.3b) [71]. They found that the oleic ligand on the iron oleate complex was proposed to have played an important role in directing the elongated nanostructure formation at

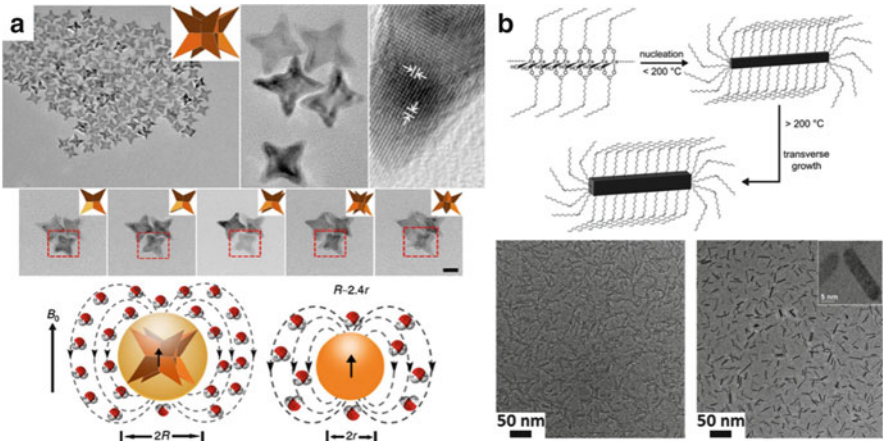

Fig. 2.3 (**a**) TEM, higher magnification, and tilted TEM images of octapod MNPs (inset: geometric model). Scale bar, 100 nm, and schematic cartoon of ball models of octapod and spherical MNPs with the same geometric volume. Scale bar, 20 nm (Reprinted with permission from Ref. [68]. Copyright 2013, Macmillan Publishers Ltd). (**b**) Proposed growth mechanism and TEM images of iron oxide nanorods (Reproduced from Ref. [71] by permission of The Royal Society of Chemistry)

the nucleation stage below 200 °C [71]. When further raising the reaction temperature, the structure directing oleate group may start to desorb and decompose. The transverse growth of the nanorods would then outgrow the longitudinal one, which also served to decrease the surface energy and structure anisotropy [71].

Unlike 0-D or 1-D nanostructures, recent synthetic studies of 3-D magnetic nanostructure have mostly focused on the "clusters" or "assemblies." Their peculiar structures of 3-D nanoclusters based on crystal aggregation have been shown theoretically and experimentally to be able to influence their magnetic properties, which are used as efficient mediators for MRI and hyperthermia in cancer treatment [72]. Furthermore, the clusters of magnetic nanoparticles with multiple crystal facets tend to have a larger surface area than individual nanocrystals [73], which may play a dominant role in catalytic research and application. In nanocrystal synthesis, a classical crystallization mode based on the supersaturation of solution is usually used to explain the crystal nucleation/growth process of nanocrystals with controllable sizes and shapes [74]. In contrast, another significant mechanism named nonclassical "oriented attachment" is recently proposed, where nanoparticles with common crystal orientations directly combine together to form larger ones [77]. The aggregation-based crystal growth theory shows its specific characteristics and roles in the formation of larger and irregular nanoclusters.

The strategy of forming magnetic nanoclusters by oriented attachment of individual nanocrystals has the advantage of controllably increasing the magnetization while retaining the superparamagnetic characteristics. Recently, Gupta's group reported novel superparamagnetic 3-D "nanoflowers," which composed of self-assembled spherical and rodlike colloidal nanocrystals (Fig. 2.4a) [73]. The formation of such nanoclusters was likely because of the burst boiling accompanied by a temperature drop when injecting a small amount of hexane during the heating and aging steps. The effects might slow down the growth of the nuclei and promote their assembly to form clusters by the particle coalescence (from interaction between the nuclei) or oriented attachment to decrease the surface energy [73]. Similarly, Zhang's group had synthesized highly ordered, self-assembled 3-D nanoclusters with sharp and obtuse edges, which were fabricated by controlling the nucleation/growth dynamics [65]. They found that shortening nucleation duration might bring a deficient nucleation and induce a rapid increase in monomer concentration, which accelerated subsequent growth process of nanocrystals, leading to the formation of the starlike nanocrystals with larger size. They are further oriented to assemble reciprocally, gradually forming initial "branched" nanoclusters to minimize the magnetostatic energy, owing to their size-dependent magnetic dipolar interaction [65]. Furthermore, the surface-defect-induced secondary growth of the "branched" nanoclusters might considerably improve their uniformity, resulting in the final "multibranched" nanoclusters with formation of sharp or obtuse edges [65]. They revealed the transformation of 0-D nanocrystals to 3-D nanoclusters as well as the shape evolution, which provide a synthetic strategy for shape-controlled nanostructure, as shown in Fig. 2.4b.

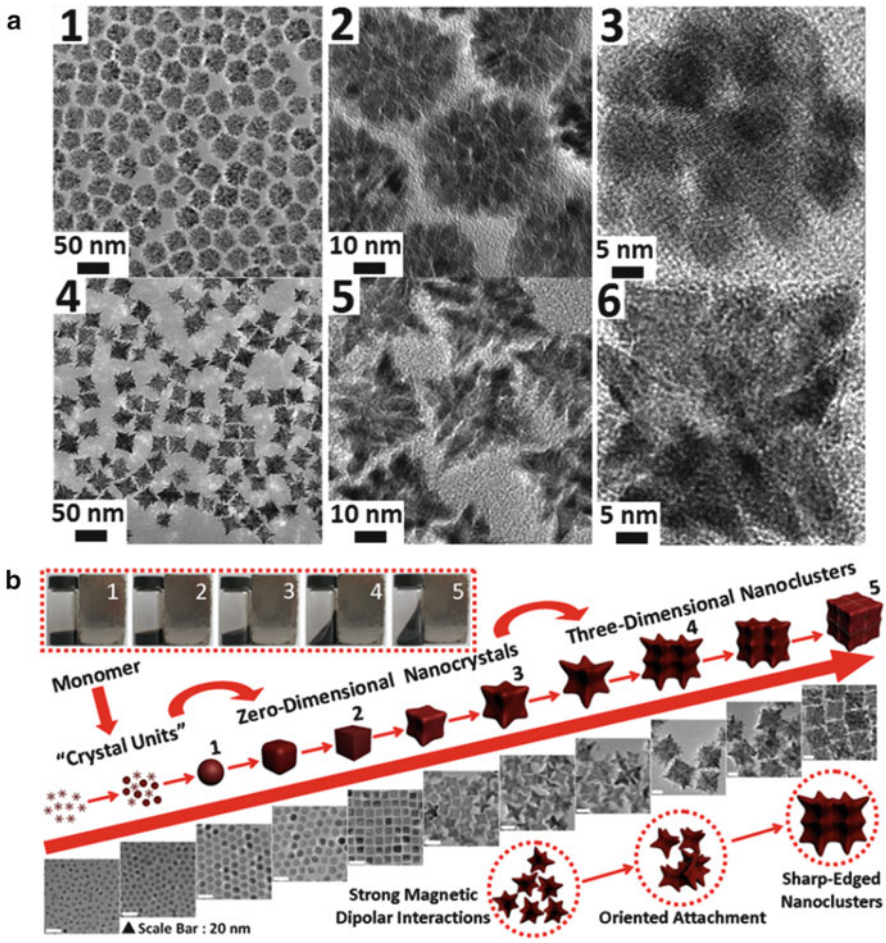

Fig. 2.4 (**a**) TEM images of 3-D self-supported (1–3) spherical and (4–6) cubic magnetic nanoclusters composed of intergrown spherical and rodlike MNPs, respectively (Reprinted with permission from Ref. [73]. Copyright 2009, American Chemical Society). (**b**) Schematic illustration of the transformation of 0-D magnetic nanocrystals to 3-D nanoclusters (Reprinted with permission from Ref. [65]. Copyright 2013, American Chemical Society)

2.1.2.4 Magnetic Metal-Dopant Effects

The magnetism of magnetic nanostructures can be greatly influenced by doping with magnetically susceptible elements. This strategy is demonstrated for the synthesis of binary ferrite MFe_2O_4 (M = Mn, Co, Ni, etc.) nanostructure with controllable sizes and shapes in which Fe^{2+} ions are replaced by other transition-metal M^{2+} dopants [24–26, 64–67, 78–80]. For inverse spinel Fe_3O_4 nanostructure, it has a crystal structure constructed of face-centered cubic packed lattice of oxygen atoms with the tetrahedral sites (T_d) occupied by Fe^{3+} ions and octahedral sites (O_h)

occupied by Fe^{3+} and Fe^{2+} ions [52]. Fe^{3+} has a d^5 configuration, and Fe^{2+} has a d^6 configuration with a high-spin state; the calculated total magnetic moment per unit Fe_3O_4 is 4 μ_B [52]. For metal-dopant substitution of ferrite MFe_2O_4, such as $MnFe_2O_4$, $CoFe_2O_4$, and $NiFe_2O_4$ nanostructure, the magnetic moments per unit can be estimated as 5 μ_B, 3 μ_B, and 2 μ_B under their electron spin configurations, respectively (Fig. 2.5a) [10]. It is worthwhile to note that the mass magnetization (M_s) value is highest for $MnFe_2O_4$ nanostructure (110 emu $\cdot$ g^{-1} MnFe) and decreases for Fe_3O_4 nanostructure (101 emu $\cdot$ g^{-1} Fe), which is proportionate to the magnetic moment values [10]. This doped $MnFe_2O_4$ nanostructure can also induce significant *T2*-weighted MR contrast-enhancement effects with the coefficient *r2* of 358 $mM^{-1}s^{-1}$, which is more than two times higher than the values of conventional iron oxide-related MR contrast agents [10]. Significantly, a recent report of the successful Zn^{2+} doping leads to an extremely high magnetization value (175 emu $\cdot$ g^{-1}) tuning and provides the larger MRI contrast effects ($r2 = 860$ $mM^{-1}s^{-1}$) (Fig. 2.5b) [78]. This increased MR contrast-enhancement capability of magnetic metal-doped nanostructures is advantageous, for example, for imaging-guided tumor diagnosis in vivo (See Sect. 2.2).

The high magnetization values of the metal-dopant nanostructure can also be used to achieve magnetically induced heat generation under an alternating current magnetic field (ACMF), which is evaluated by specific loss power (SLP) or specific absorption rate (SAR) values, the standard criterion for hyperthermia effects (defined as the thermal power dissipation divided by the mass of the magnetic material and the heat capacity of solution) [78, 81, 82]. For instance, the SLP value of 15 nm $(Zn_{0.4}Mn_{0.6})Fe_2O_4$ nanoparticles is 432 W g^{-1}, which is four times larger than that of Feridex (115 W g^{-1}) when measured under the identical conditions [78]. The high performance of Mn/Zn-doped ferrite nanoparticles plays a significant role in the thermal treatment of cancer and other diseases (See Sect. 2.3).

Except for the total magnetic moment increase, the metal-dopant substitution-induced novel core–shell structure may constitute an important strategy for achieving excellent magnetic properties drastically different from those of regular doped ferrite nanoparticles [79–81, 83]. Zhong's group recently reported a core–shell-structured ternary nanocube consisting of Fe_3O_4 core and Mn–Zn shells synthesized by controlling the reaction temperature in the absence of conventionally used reducing agents, as shown in Fig. 2.5c. The core–shell-structured nanocubes displayed unique magnetic properties, such as increased coercivity and field-cooled/zero-field-cooled characteristics by a combination of the core–shell composition, which was useful for magnetic and catalytic applications [79]. In addition, Cheon's group had designed some versatile core and shell combinations including $CoFe_2O_4$@$MnFe_2O_4$, $CoFe_2O_4$@Fe_3O_4, Fe_3O_4@$CoFe_2O_4$, and $Zn_{0.4}Co_{0.6}Fe_2O_4$@$Zn_{0.4}Mn_{0.6}Fe_2O_4$ with mutual coupling of magnetically hard and soft components (Fig. 2.5d) [80]. They took the advantage of the exchange coupling between a magnetically hard core and magnetically soft shell to tune the magnetic properties of the nanostructure and maximized the heat induction, which was a gauge of the conversion efficiency [80]. The coupled system could allow optimal tuning of magnetocrystalline anisotropy (K) values in particular, as well as M values, to achieve high SLP values while

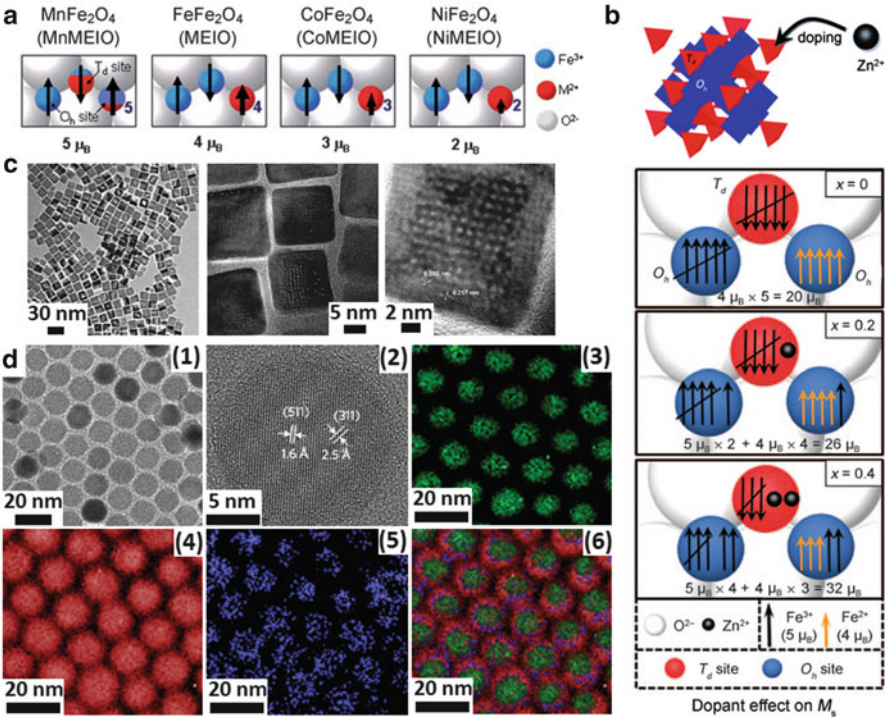

Fig. 2.5 (**a**) Magnetic spin structures of metal-doped MFe_2O_4 (M = Mn, Fe, Co, Ni) NPs (Reprinted with permission from Ref. [10]. Copyright 2007, Nature). (**b**) Zn^{2+}-doped magnetic spin alignment diagrams in spinel-structured $(Zn_xFe_{1-x})Fe_2O_4$ NPs (Reprinted with permission from Ref. [78]. Copyright 2009, John Wiley & Sons Ltd). (**c**) TEM images of morphologies of Mn–Zn ferrite core–shell nanocubes (Reprinted with permission from Ref. [79]. Copyright 2010, American Chemical Society). (**d**) TEM image (*1*), high-resolution TEM image (*2*) of core–shell $CoFe_2O_4$@$MnFe_2O_4$ NPs, and (*3–6*) the corresponding electron energy loss spectrum (EELS) mapped images: (*3*) Co-mapped image, (*4*) Fe-mapped image (*5*), Mn-mapped image, (*6*) and overlay image of (*3–6*) (Reprinted with permission from Ref. [80]. Copyright 2011, Macmillan Publishers Ltd)

maintaining the superparamagnetism (e.g., $CoFe_2O_4$@$MnFe_2O_4$, 2,280 W g^{-1}; $CoFe_2O_4$@Fe_3O_4, 1,120 W g^{-1}; $MnFe_2O_4$@$CoFe_2O_4$, 3,034 W g^{-1}; Fe_3O_4@$CoFe_2O_4$, 2,795 W g^{-1}; $Zn_{0.4}Co_{0.6}Fe_2O_4$@$Zn_{0.4}Mn_{0.6}Fe_2O_4$, 3,886 W g^{-1}) [80]. These optimized core–shell nanostructure with adequate biocompatibility could be a highly effective new nanoscale tool useful for magnetic hyperthermia therapy and other advanced nanobiotechnology applications, such as drug release, and thermal activation induced anticancer drug release carriers.

2.1.2.5 Metal Alloy

The magnetic metal alloy nanostructure (e.g., FeCo or FePt) fabricated by thermal decomposition synthesis is another example of magnetic nanostructures with high performance [28, 52, 63]. In these nanostructures, all the magnetic spins align

parallel to the external magnetic field, so they typically have higher magnetic moments, leading to larger magnetocrystalline anisotropy and magnetization [52]. Take 7 nm-sized FeCo nanostructures for example; their magnetic moment was approximately 2.4 μ_B per magnetic atom, while that of Fe_3O_4 nanostructures was 1.3 μ_B per magnetic atom [28, 52]. These monodisperse FeCo nanostructures had an exceptionally high magnetization value of 215 emu $\cdot$ g^{-1} metal, and the coefficient *r2* value was determined to be 644 $mM^{-1}s^{-1}$, which was much larger than that of conventional Feridex contrast agents [28]. These advantages successfully endowed them with efficient *T1*-weighted MR imaging ability in vitro or in vivo.

2.1.3 Surface Modification of MNPs

2.1.3.1 Ligand Conjugation

Surface modification of MNPs discussed here is critical to improving their stability, biocompatibility, and functionality, which has widely received enormous attention in biomedical applications in vivo. Recently, a variety of ligand conjugation strategies for MNPs have been developed to give high colloidal stability in aqueous biofluids and to avoid aggregation which can occur under physiological conditions using different synthetic routes (Fig. 2.6) [20, 52, 84–96]. One commonly used method for surface coating is the physical adsorption of material onto the surface of

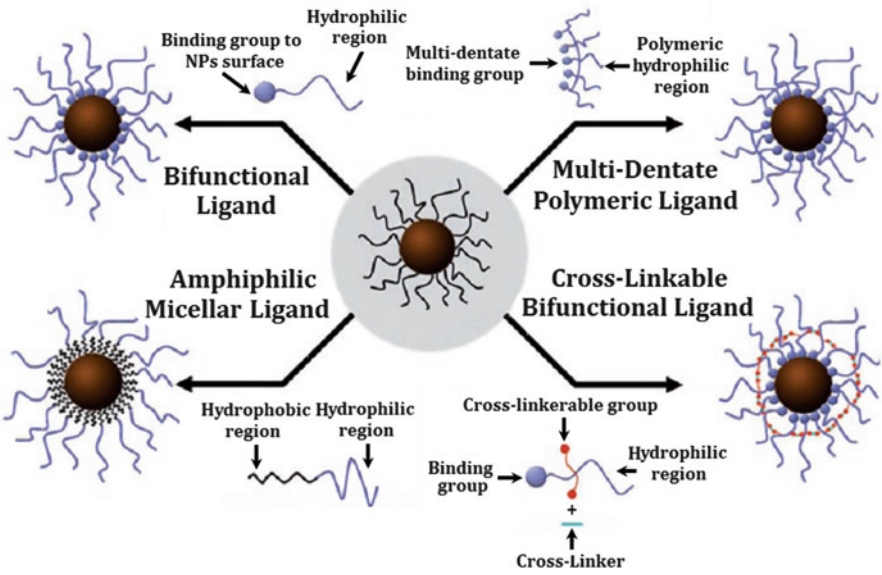

Fig. 2.6 Surface modification strategies for designing MNPs with high colloidal stability (Reprinted with permission from Ref. [52]. Copyright 2008, John Wiley & Sons Ltd)

the particle. Another such method to coat MNP surfaces also involves covalently or ionically bonding a polymer to the particle surface [84].

In general, as a conventional ligand, the biologically inert polymer chains have been used to modify MNPs for controlling the particle shape, size, and functionality that permits multiple applications. Polyethylene glycol (PEG) is one such polymer being explored for use in biological particle systems because of its solubility in water, low immunogenicity, biocompatibility, and fast clearance ability. The surface modification of MNPs with PEG, known as PEGylation, has been proposed for the improved stealth properties covered extensively in the literature [85, 86]; they include: (1) shielding the surface charge, increasing the hydrophilicity, and decreasing the interfacial free tension of the MNPs, which leads to reduced interaction and identification by opsonin proteins; (2) generating repulsive forces through the compression of flexible PEG chains on the surface of MNPs, which results in preventing specific binding to proteins; (3) and inhibiting phagocytosis by the reticuloendothelial system (RES), prolonging half-life in blood circulation, and promoting the EPR effect in vivo. To achieve the necessary stealth properties, the most suitable molecular weight of the PEG chain has been reported between 1,500 and 5,000 Da [86]. It is worthwhile to note that the direct one-step PEGylation of MNPs has the additional advantages of providing small and uniform MNPs [87–89]. As reported, PEGylated MNPs as small as from 4 to 9.8 nm had been prepared directly from monocarboxyl-terminated PEG through the covalent binding to the surface hydroxy groups by thermal decomposition of $[Fe(acac)_3]$ in pyrrolidone and PEG [87]. The further MRI experiments performed on living rats demonstrated that the PEG-modified MNPs had long circulation time and very good biocompatibility and could potentially be used as MRI contrast agents. Many multifunctional PEG *ligands* have been commercially available for modifying MNPs. For instance, the MNPs were frequently coated with the combination of bifunctional PEG-silane [90–92]. The PEGylated MNPs had been synthesized by coating the MNPs first with a silane group using either amino propyl trimethoxy silane (APTMS) or amino propyl triethoxy silane (APTES) and then functionalized the amine terminal group with a carboxy-terminated PEG for attaching to targeting groups [90].

In addition, a challenge in developing therapeutic PEGylated MNPs conjugated with polypeptide or antibodies has recently shown a promising application. In order to increase the probability of the long-circulating PEGylated MNPs to the desired target, the MNP surface should be labeled with polypeptide or antibodies that specifically bind to surface epitopes or receptors on the target sites. These ligands have to be not macrophage recognizable and coupled to the surface of stealth carriers [84, 93]. In this regard, Chen's group had firstly modified iron oxide NP surface with PEG copolymer, making them water soluble and function extendable. These MNPs were then covalently conjugated with a near-infrared fluorescent (NIRF) dye (IRDye800) and a cyclic arginine–glycine–aspartic acid (RGD)-containing peptide c(RGDyK) for integrin $\alpha_v\beta_3$ targeting, which possessed excellent tumor integrin targeting efficiency and specificity as well as limited RES uptake for molecular MRI diagnostics [93]. It is to be observed that the antibody coupling has at least two drawbacks: the overall dimensions of the antibodies (ca. 20 nm) may cause MNPs

to poorly diffuse through biological barriers in vivo, and their immunogenicity may evoke an immune response within an organism [84]. So the coupling of small non-immunogenic ligands to polymeric carriers should be noticed and investigated.

Besides PEG, other block copolymers, such as polyaniline or polystyrene, can also be used to coat MNPs by the oxidative polymerization in the presence of the oxidant ammonium peroxydisulfate [94–96]. For example, Asher et al. reported that single Fe_3O_4 MNPs (ca.10 nm) can be embedded in polystyrene spheres through emulsion polymerization to give stable superparamagnetic photonic crystals [95]. Zhang et al. had used this method for coating $MnFe_2O_4$ MNPs with polystyrene, yielding core–shell nanoparticles with sizes below 15 nm [96].

The use of cross-linkable small molecules as bifunctional ligands can also be advantageous since the cross-linking endows MNPs with the high structural stability with only a marginal increase in their hydrodynamic diameter [52, 97]. For example, 2,3-dimercaptosuccinic acids (DMSAs) could stabilize 12 nm-sized Fe_3O_4 NPs through chelate bonding of the carboxylate group to the MNPs and structural stabilization by disulfide cross-linkages between the ligands, and the remaining free thiol group of the ligand could be used for further bioconjugation [97]. These results indicated that these DMSA-coated MNPs were fairly stable in the phosphate-buffered saline (PBS) which were sufficiently suitable for in vivo utilization.

The other ligands, including the oligonucleotides, polysaccharides, acids, and amines, are also widely used in the surface modification of MNPs. Take folic acid (FA) for example; Hayashi et al. had designed the MNP nanoclusters modified with FA and PEG to promote their accumulation in tumors [98]. The surface modification was attained simultaneously as follows: (1) several allyl-MNPs became enclosed by PEG via the thiol–ene click reaction with thiol-functionalized PEG (SH-PEG), resulting in forming SH-PEG-MNP nanoclusters, and (2) FA-PEG-MNP nanoclusters were then produced when using thiol- and FA-heterobifunctionalized PEG (SH-PEG-FA) instead of SH-PEG [98]. The clustered FA-PEG-MNPs with high relaxivity and the SAR value were potentially used for the cancer targeted hyperthermia (See Sect. 2.3).

As a whole, the utilization of ligand conjugation can markedly improve colloidal stability of MNPs in aqueous solutions. But the thin ligand coating is not a good enough barrier to prevent oxidation of the highly reactive metal particles, and the ligand-coated MNPs indicate relatively low intrinsic stability in solution at higher temperature and other pH [20]. So the development of other surface modification methods for protecting MNPs against deterioration is of great importance.

2.1.3.2 Hydrophobic Interaction

An alternative approach for noncovalent binding to the MNP surface relies on the hydrophobic interaction. In this method, lipid-based colloidal aggregates, such as liposomes, microemulsions, and micelles, can carry hydrophilic cargo in the aqueous lumen and hydrophobic cargo in the lipid membrane interior [99]. They have been used extensively in recent decades as MNP surface coating and drug carriers

to improve pharmacokinetic properties or the bioavailability of the drug, to increase the target-to-background ratio of the drug or MNPs [19, 99–107]. In one method of lipid functionalization of the MNP surface, MNPs and lipids are first coprecipitated and then redispersed in water [19, 100]. In another method, the MNPs and lipids are incorporated together through an emulsion formed by an organic solvent and water, and the excess coating material is removed by magnetic separation [101]. For instance, Anderson's group developed a simple method to coat MNPs with a cationic lipid-like material. Herein, the monodisperse MNPs were first dispersed along with oleic acid and lipids in chloroform. Instead of completely drying the forming emulsions, the solvent *N*-methyl-*2*-pyrrolidone (NMP) was then added to induce adhesion between the MNP surface and lipids and sonicated under nitrogen protection. Finally, the chloroform was thoroughly evaporated away, which prevented phase separation when particles were transferred to the aqueous phase (Fig. 2.7a) [19]. The lipid-coated magnetic aggregates as delivery platform here were capable of delivering DNA and siRNA to cells, which could offer the potential for magnetically guided targeting, as well as an opportunity to combine gene therapy with MRI and magnetic hyperthermia (See Sects. 2.2 and 2.3).

Another ideal magnetic nanoscale drug delivery lipid vehicle was designed and achieved by stealth liposomes comprising self-assembled superparamagnetic iron oxide NPs individually stabilized with palmityl-nitroDOPA incorporated in the lipid membrane, as was shown in Fig. 2.7b. The ACMF was used to control the timing and dose of repeatedly released thermally sensitive cargo from such lipid vesicles by locally heating the membrane and changing its permeability. This novel delivery system thus created the possibility to assemble and track versatile and efficient drug delivery vehicles and nanoreactors [102].

The PEG–phospholipid has also been used to improve the stability and pharmacokinetics of MNPs in the physiological environment [105–107]. On the one hand, the lipid coating on the MNP surface can provide remarkable biocompatibility and biodegradability, and on the other the PEG polymers located at outmost layers are used extensively for improving blood circulation in vivo. Bao's group developed a new solvent-exchange method, in which PEG–lipid copolymer (DSPE-mPEG) and MNPs assembled in a solvent system with ascending solvent polarity [105]. They found that the assembly of amphiphilic molecules on hydrophobic surface of 14 nm-sized MNPs can be induced controllably by increasing the polarity of solvent systems with miscible solvents. Similarly, Zhang's group synthesized a well-established Mn–Zn ferrite MNPs coated with DSPE-PEG2000 through hydrophobic interaction between lipid and oleic acid/oleylamine (Fig. 2.7c). The monodisperse PEGylated MNPs with core–shell structure (15 nm) exhibited excellent performance, such as high magnetism of 98 emu $\cdot$ g^{-1} Fe, *r2* of 338 mM^{-1}s^{-1}, and SAR value of 324 W g^{-1} Fe [106]. These advantages endowed them with efficient passive targeting ability in vivo for prominent tumor MRI and magnetically induced heating when exposed to ACMF, based on EPR effects (See Sect. 2.3).

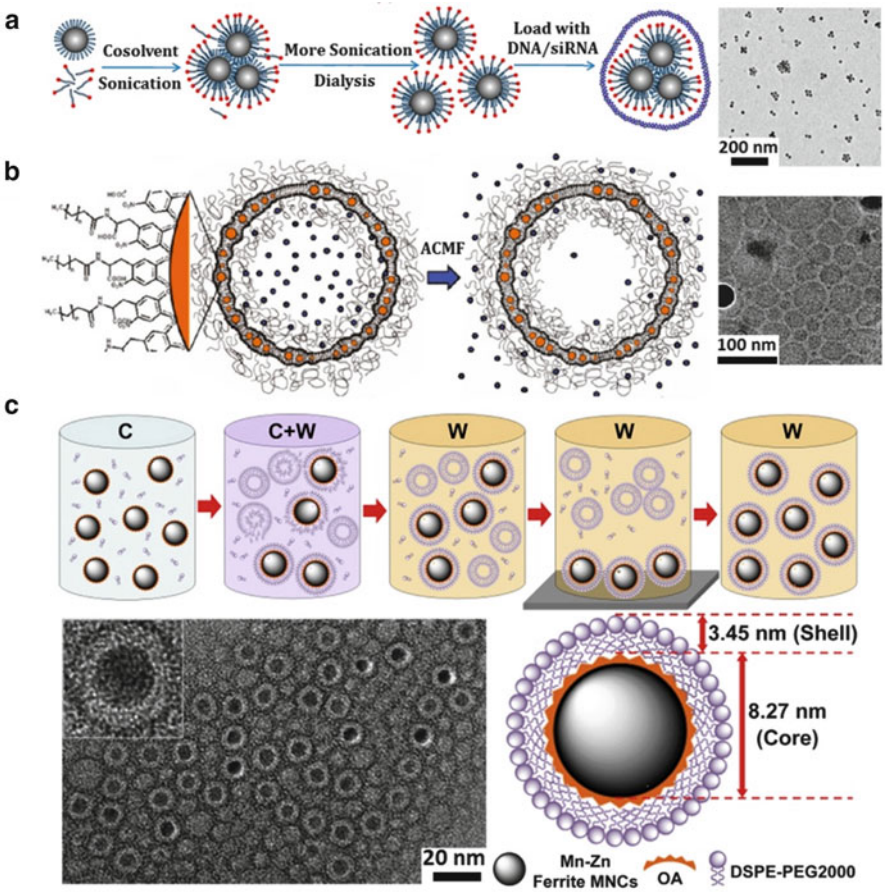

Fig. 2.7 (**a**) Schematic plot of the procedure of lipid-coating iron oxide nanoclusters and corresponding TEM image (Reprinted with permission from Ref. [19]. Copyright 2013, American Chemical Society). (**b**) Schematic of drug-loaded liposomes containing iron oxide NPs in their bilayer and the triggered release under the ACMF (Reprinted with permission from Ref. [102]. Copyright 2011, American Chemical Society). (**c**) A schematic diagram of PEGylated lipid-coated Mn–Zn ferrite MNP synthesis (C, chloroform; W, water) and TEM images/schematic diagram of PEGylated lipid-coated MNPs (Reprinted with permission from Ref. [106]. Copyright 2014, Elsevier)

2.1.3.3 Precious Metal and Inorganic Material Coating

Some precious metals and inorganic materials can be deposited on magnetic nanoparticles through reactions in the chemical conjugation, microemulsion, redox transmetalation, iterative hydroxylamine seeding, or other methods, to protect the cores against oxidation and to improve their functionality [75, 76, 108–113]. In a precious metal coating, the bifunctional composite nanostructure containing Au/Ag and MNPs is traditionally obtained by physical deposition of a thin Au/Ag film onto

a spherical MNP, by adsorption of $HAuCl_4$ on the MNP surface followed by the reduction, or via electroplating through the nanoscale templates [75, 76, 108, 109]. For instance, Sun's group reported the dumbbell-like Au–Fe_3O_4 NPs, as illustrated in Fig. 2.8a. They firstly synthesized Au NPs by injecting $HAuCl_4$ solution into the reaction mixture and then in situ decomposing the $Fe(CO)_5$ precursors on the surface of the Au NPs followed by oxidation in 1-octadecene solvent in the presence of oleic acid and oleylamine and heating the mixture to reflux (300 °C), leading to dumbbell-like Au–Fe_3O_4 NPs [108]. Additionally, they also presented a facile synthesis of Au- and Ag-coated Fe_3O_4 NPs with core–shell structure [109]. The synthesis started with room temperature coating of Au on the surface of Fe_3O_4 NPs by reducing $HAuCl_4$ in a chloroform/oleylamine solution. The Au-coated Fe_3O_4 NPs were then transferred into water by mixing them with sodium citrate and cetyltrimethylammonium bromide (CTAB) (Fig. 2.8b). The water-soluble Fe_3O_4/Au NPs served as seeds for the formation of Fe_3O_4/Au NPs with thicker Au coating by simply adding more $HAuCl_4$ in the reducing condition or for the preparation of Fe_3O_4/Au/Ag NPs by adding $AgNO_3$ to the reaction mixture [109]. Wang et al. also developed the monodispersed core–shell Fe_3O_4@Au NPs by chemical deposition (Fig. 2.8c) [76, 110]. Following the formation of Fe_3O_4 NPs as seeds with the desired sizes, Au was deposited onto the surface of Fe_3O_4 NPs by the reduction of $Au(acac)_3$ in the presence of capping and reducing agents at elevated temperature (180 ~ 190 °C) [110]. In this process, the careful manipulation of the reaction temperature was the key factor, which could control the thermally activated deposition of Au on the exposed Fe_3O_4 NP surface and subsequent re-encapsulation of the Au shell surface by the capping agent [76].

The gold coating on the surface of MNPs functionalized with thiol (–SH) or amino ($–NH_2$) groups as another surface modification method is especially interesting recently, since the gold surface can be easily functionalized with these groups [111, 112]. This treatment allows further linkage of functional ligands which may make the MNPs@Au suitable for catalytic and other optical applications. For instance, Goon et al. reported a facile method of synthesizing 50 ~ 150 nm MNPs@

Fig. 2.8 (**a**) Schematic diagram of dumbbell-like Au–Fe_3O_4 NP synthesis and corresponding TEM images (Reprinted with permission from Ref. [108]. Copyright 2005, American Chemical Society). (**b**) Schematic illustration of hydrophilic Fe_3O_4/Au NP synthesis and corresponding TEM images (Reprinted with permission from Ref. [109]. Copyright 2007, American Chemical Society). (**c**) The formation of Fe_3O_4@Au NPs in the presence of capping agents which involves capping-shell desorption, deposition of Au on the exposed Fe_3O_4 surface, and re-encapsulation, TEM images, and size distributions of the Fe_3O_4@Au NPs (Reprinted with permission from Ref. [110]. Copyright 2005, American Chemical Society). (**d**) Schematic representation of the synthesis of Fe_3O_4@Au NPs, based on the PEI self-assembled onto negatively charged Fe_3O_4 NPs and corresponding TEM image (Reprinted with permission from Ref. [111]. Copyright 2009, American Chemical Society). (**e**) Schematic illustration of bifunctional Au–Fe_3O_4 NP synthesis by chemical bond (such as Au–S) interaction and corresponding TEM images (Reprinted with permission from Ref. [112]. Copyright 2007, American Chemical Society)

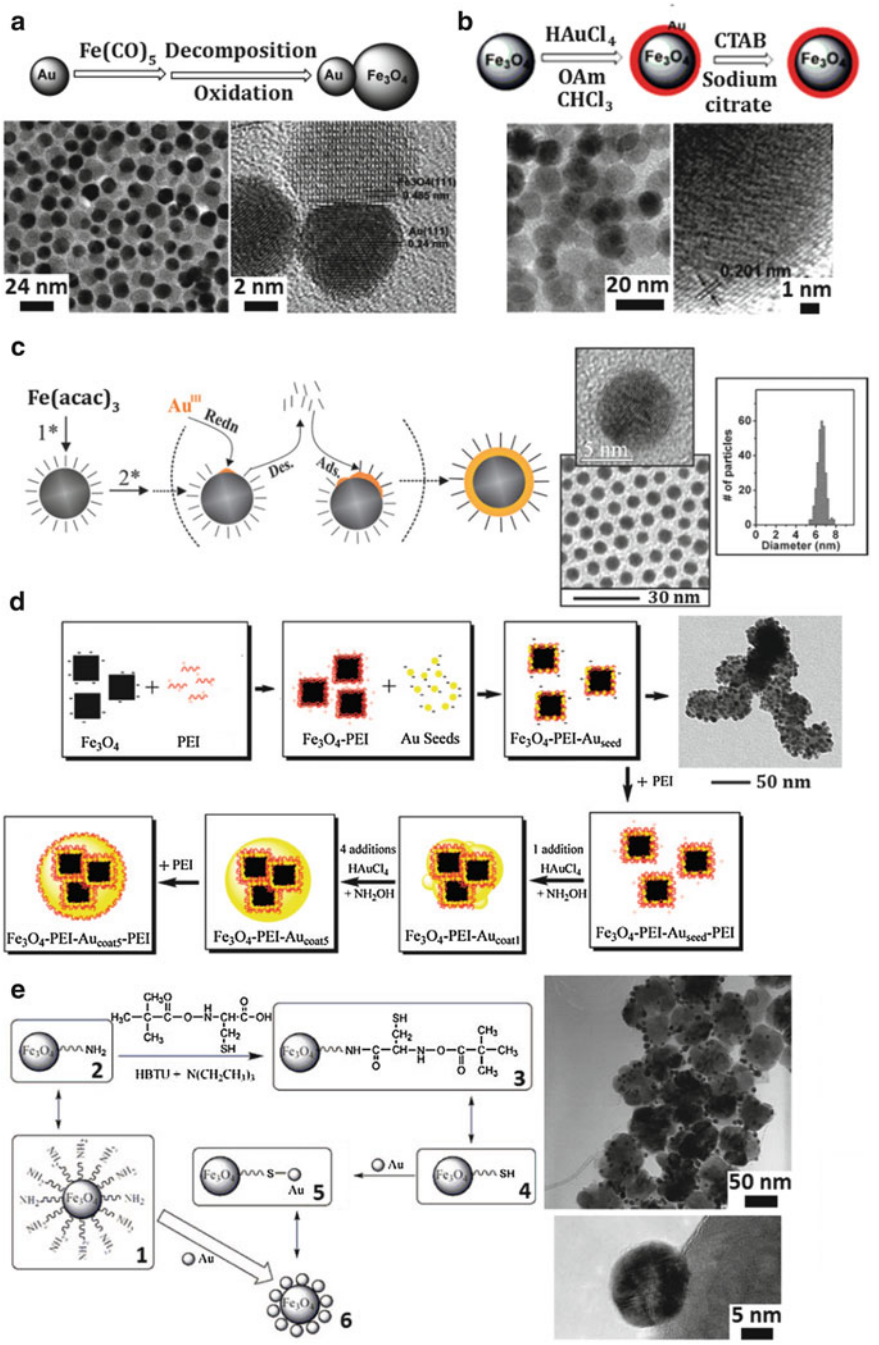
a
Fe(CO)5 Decomposition
Oxidation
Au
Fe3O4
24 nm
2 nm
b
HAuCl4
OAm
CHCl3
CTAB
Sodium citrate
20 nm
1 nm
c
Fe(acac)3
1*
2*
AuIII
Redn
Des.
Ads.
5 nm
30 nm
# of particles
Diameter (nm)
d
Fe3O4
PEI
Fe3O4-PEI
Au Seeds
Fe3O4-PEI-Auseed
+ PEI
50 nm
Fe3O4-PEI-Auseed-PEI
1 addition
HAuCl4
+ NH2OH
Fe3O4-PEI-Aucoat1
4 additions
HAuCl4
+ NH2OH
Fe3O4-PEI-Aucoat5
+ PEI
Fe3O4-PEI-Aucoat5-PEI
e
HBTU + N(CH2CH3)3
1
2
3
4
5
6
Au
50 nm
5 nm

Au composites via the use of a biocompatible polyethyleneimine (PEI) for the dual function of attaching gold seeds and preventing the formation of large aggregates [111]. They showed that successful Au coating of MNPs requires the self-assembly of a layer of PEI onto MNP cores by Au–N chemical bond interaction and subsequent saturation of the surface with 2 nm gold seeds. In order to form a protective layer of gold shell, the additional PEI could be used to increase MNPs@Au stability against aggregation, which was important for further application (Fig. 2.8d) [111]. Bao et al. had reported their recent success in the synthesis of bifunctional Au–Fe_3O_4 NPs that are formed by simply linking two separately prepared nanomaterials by chemical bond (such as Au–S) interaction, rather than using chemical deposition processes (Fig. 2.8e) [112]. Due to the introduction of Au nanoparticles, the resulting bifunctional Au–Fe_3O_4 NPs could be easily modified with other functional molecules to realize various technological separations and detections simply under a magnet [112].

Except for the precious metal coating, of some inorganic materials, such as silica, carbon coatings also have the advantages arising from the higher chemical and thermal stability as well as biocompatibility and easy surface modification [20, 113–118]. A silica shell does not only protect the magnetic cores but also prevent the direct contact of the magnetic core with additional agents linked to the silica surface, thus avoiding unwanted interactions [20]. Xia et al. had shown that the commercially available MNPs can be directly coated with silica shells by the hydrolysis of tetraethoxysilane (TEOS) [113]. The MNPs here were diluted with deionized water and 2-propanol, and then ammonia solution and various amounts of TEOS were added to the reaction mixture under stirring at room temperature for about 3 h. The coating thickness could be controlled by changing the amount of TEOS [113]. Johnson et al. had described a simple method to prepare carbon-coated magnetic Fe and Fe_3C NPs by direct thermal decomposition of the iron stearate at 900 °C under an argon atmosphere [117]. Lu et al. had synthesized highly stable 11 nm-sized carbon-coated cobalt MNPs. They indicated that the cobalt NPs could be coated with furfuryl alcohol which was converted first into poly(furfuryl alcohol) and then carbonized in the presence of CTAB used as the carbon source during the pyrolysis, resulting in a stable protection layer against air oxidation [118].

2.2 MNPs with High Performance for MR Imaging Diagnostics

Recently, biomedical imaging techniques including representative positron-emission tomography (PET), magnetic resonance imaging (MRI), and X-ray computed tomography (CT) are vital in the diagnosis of various diseases due to their analytic ability at molecular or cellular levels [7, 8, 10, 52, 119–123]. In this regard, a new discipline, known as “molecular imaging,” which combines molecular biology and in vivo imaging, has emerged. MRI as one of the most powerful diagnosis

techniques has been the preferred tool for the brain and the central nervous system imaging and for the tumor detection, since it can give noninvasive, highly sensitive, and target-specific detection of diseases by the help of MRI contrast agents. In general, the MRI contrast agents should possess as high as possible relaxivity and as small as possible size. In the past years, a variety of MNPs, such as superparamagnetic iron oxide nanoparticles, are important and representative MRI contrast agents, and it has received great attention for clinical liver imaging [124, 125]. These MNP-based MRI contrast agents are composed of three parts: (1) the magnetic core, which can generate distinct MR signal enhancement; (2) the surface water-dispersible layers of MNPs, which endow their compatibility and stability in the biological environment; and (3) the bioactive materials on the terminal of MNPs for their active targeting purpose [124].

Under an applied magnetic field (B_0), the designed MNPs are magnetized with additional magnetic moment and generate an induced magnetic field, perturbing the nuclear spin relaxation processes of the water protons. Based on their relaxation processes, some conventional MRI contrast agents are mostly effective in a single imaging mode of either longitudinal (*T1*) relaxation mode (bright signals) or transverse (*T2*) relaxation mode (dark signals) (Fig. 2.9a) [8]. The commercially available *T1* contrast agents are usually paramagnetic complexes, while *T2* contrast agents are based on iron oxide nanoparticles. Take the typical *T2*-MR contrast effect for example; the magnetic relaxation processes of the water protons in the presence of MNPs are perturbed, and the spin–spin relaxation time is shortened. The perturbation leads to the MR signal contrast enhancement, which appears as a darkening of the corresponding MR image [52] (Fig. 2.9b). The degree of the *T2* contrast effect is represented by the spin–spin relaxivity *R2* ($R2 = 1/T2$), and the relaxivity

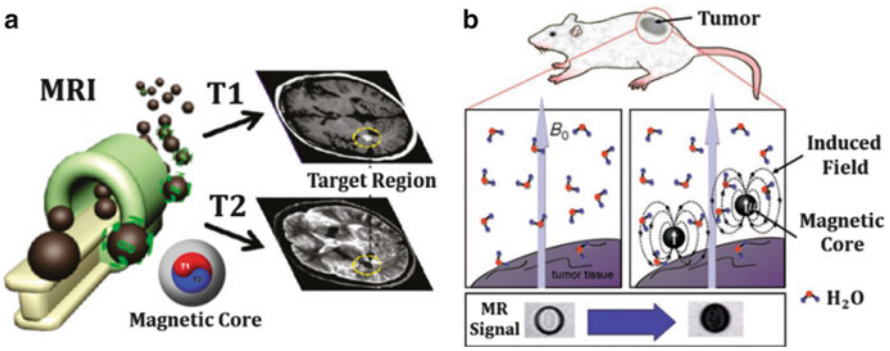

Fig. 2.9 (**a**) Responsive MR signals for a bright image in the T1 mode and a dark image in the T2 mode (Reprinted with permission from Ref. [8]. Copyright 2011, American Chemical Society). (**b**) MR contrast effects of MNPs. Under an external field (B_0), the MNPs are magnetized with a magnetic moment and generate an induced magnetic field which perturbs the nuclear spin relaxation processes of the water protons. This perturbation leads to MR contrast enhancement which appears as darkening of the corresponding section of the MR image (Reprinted with permission from Ref. [52]. Copyright 2008, John Wiley & Sons Ltd)

coefficient (*r2*), which is obtained as the gradient of the plot of *R2* versus the molarity of magnetic atoms, is a standardized contrast-enhancement indicator [52].

The MR contrast-enhancement effect in vivo of MNPs can be greatly influenced by their size, shape, magnetism, surface chemistry, and biocompatibility, which are the most important considerations in clinical cancer early detection and diagnosis. Therefore, the development of the MNPs with high performance is particularly important. In recent years, some relevant research groups have developed a variety of MNPs with excellent magnetic properties, high sensitivity, low toxicity, long blood circulation, and specific target function served as contrast-enhancing MRI probes. We can attempt from the following cases [105, 126–128]. For instance, Tong et al. have described a method for coating magnetic iron oxide nanoparticles with phospholipid PEG1000 through the hydrophobic interaction between lipid and oleic acid/oleylamine on MNP surface. They further demonstrate that, by fine-tuning the core size and PEG coating of MNPs, the *r2* relaxivity per particle can be increased by >200-fold. With 14 nm core and PEG1000 coating, the MNPs have *r2* relaxivity of 385 $mM^{-1}s^{-1}$, which is among the highest per-Fe atom relaxivities. In addition, intravenous injection of the MNPs resulted in the significant enhancement in *T2*-MRI contrast of tumor tissue, which demonstrated the potential of the MNPs for clinical applications (Fig. 2.10a) [105]. In addition, Lee et al. have developed a new $MnFe_2O_4$–Herceptin probe with high performance to make the ultrasensitive in vitro detection of cancer cells possible since the probe interacts with all HER2/neu-positive cancer cells. Significantly, improved *T2*-MR imaging of cancers is possible utilizing this probe which has a large *r2* of 358 $mM^{-1}s^{-1}$. When the MNP probe is tail intravenously injected into a mouse, very small tumors can be specifically detected with a high MR contrast effect. In particular, these MNPs with high performance have little toxicity for potential in vivo ultrasensitive cancer imaging applications. These features make them appealing candidates for early detection and diagnosis of cancer and many other diseases (Fig. 2.10b) [10, 52, 121].

2.3 MNPs with High Performance for Cancer Targeted Hyperthermia

Magnetically induced heat generation from NPs can be used for various purposes including cancer therapy known as hyperthermia [7, 8, 129–138]. Once the MNPs are in the desired location in vivo (where they are concentrated) upon exposure to an ACMF with appropriate field and frequency, the MNPs continuously emit heat via Néel and Brownian pathways (Fig. 2.11a), generating heat and increasing the temperature of the surrounding diseased tissue. Ideally, the cancer tissue is heated to approximately 42 ~ 55 °C, which reduces the viability of the cancer cells. Comparing with the conventional radio frequency-, microwave-, and laser wavelength-induced thermotherapy, the magnetic hyperthermia is more superior and predominant. It can focus on the MNPs' exact location of both transplantable

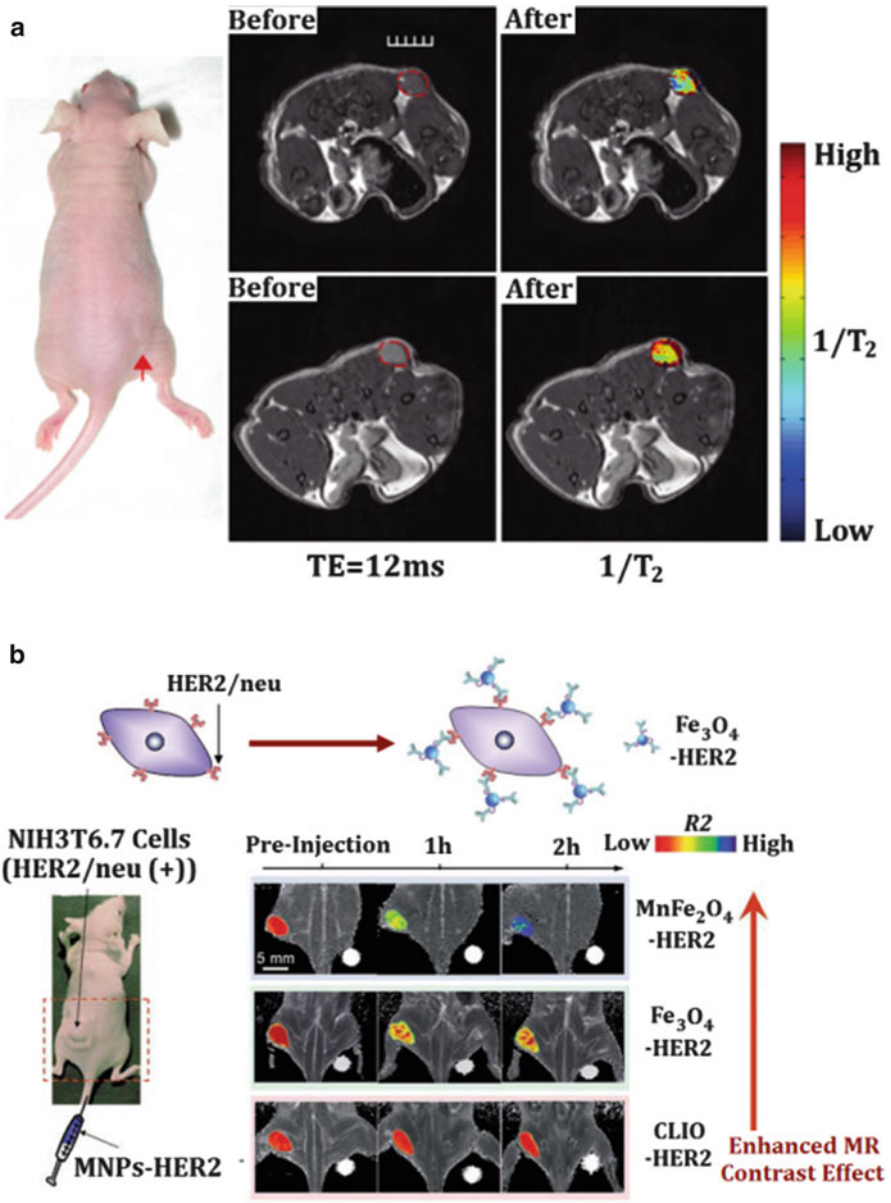

Fig. 2.10 (**a**) In vivo tumor MR imaging. *Arrow* shows the location of the subcutaneous tumor and MR images of tumor before probe injection. MR images collected after 1 h following the injection of 14 nm MNPs conjugated with antibodies against mouse VEGFR-1 (Reprinted with permission from Ref. [105]. Copyright 2010, American Chemical Society). (**b**) Intravenous tail vein injection of the MNP–Herceptin probes into a mouse with a small HER2/neu-positive cancer in the proximal femur region. In comparison, MNP–Herceptin probes and CLIO–Herceptin probes were also tested. Color-mapped MR images of the mouse at different times following injection (Reprinted with permission from Ref. [10]. Copyright 2007, Macmillan Publishers Ltd, Ref. [52]. Copyright 2008, John Wiley & Sons Ltd, and Ref. [121]. Copyright 2005, American Chemical Society)

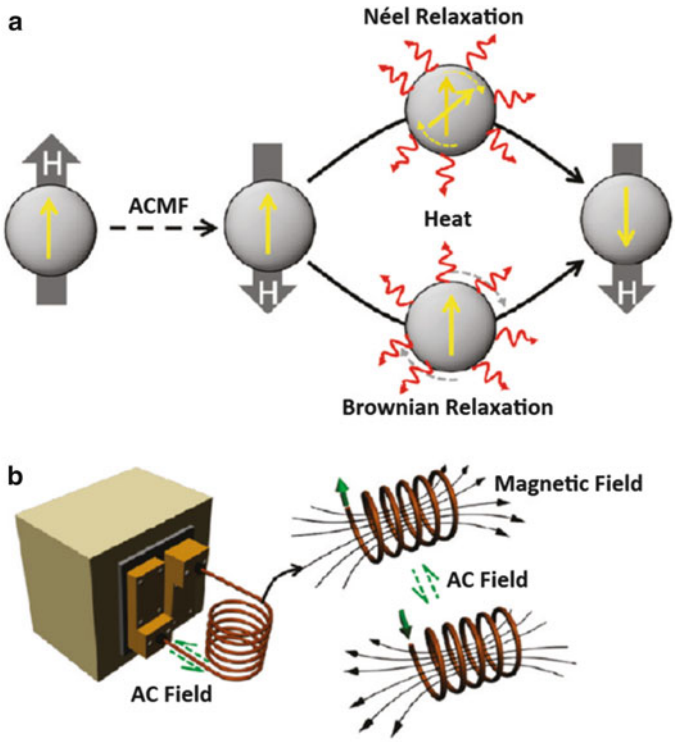

Fig. 2.11 The MNPs for magnetic hyperthermia under an ACMF: (**a**) Néel and Brownian relaxation processes and (**b**) experimental apparatus (Reprinted with permission from Ref. [8]. Copyright 2011, American Chemical Society)

and in situ carcinoma in vivo and provides a noninvasive way to efficiently raise the tumor temperatures to therapeutic levels [8, 133], which is considered a promising cancer therapy in further clinical application.

The magnetic hyperthermia device consists of the radio link control (RLC) circuit, including the resistor, inductor, and capacitor, causing the induction of an ACMF. The water-jacketed coil is usually used to cool down the coil temperature (Fig. 2.11b) [8]. Unfortunately, most of the studies on magnetic hyperthermia used harmful ACMF with high amplitude and frequency for patients in clinical application. Some experiments have shown that the designed low- or mid-frequency ACMF (100 ~ 400 kHz) has been demonstrated to be safe and beneficial for potential application [7, 8, 134, 135], and data on the therapeutic effect of the hyperthermia assessed under ACMF with the product of the amplitude and frequency of $<5\times10^9$ $Am^{-1}s^{-1}$ is required [136–138], but to date, none of the FDA-approved MNPs have been exploited for hyperthermia purposes. The first instance of selective inductive heating of lymph nodes using MNPs under an ACMF was probably in 1957 [139], since then the MNP-mediated hyperthermia in vivo has progressed much. But the clinical trial of MNPs designed by Jordan et al. for hyperthermia had

been at Berlin's Charité Hospital in 14 patients with a severe type of brain cancer using local injection of 15 nm-sized iron oxide NPs in a water suspension. The field amplitudes here between 3.8 and 13.5 kA m^{-1} at 100 kHz were employed [140]. Johannsen et al. also had used an ACMF with a frequency of 100 kHz and variable field strength of 0 ~ 18 kA m^{-1} in clinical use. To measure heating rate in situ, fiber-optic thermocouples were surgically positioned into the prostate, urethra, rectum, perineum, scrotum, and left ear and monitored with software to keep field strength constant or be adjusted to the desired temperatures [141]. In addition, the favorable recent results of "nanothermotherapy" study in clinical phase II led by German company MagForce Nanotechnologies [130–132] demonstrated the magnetic hyperthermia potential.

In the majority of cases, the MNP-mediated cancer hyperthermia therapy strategies are applied in two ways: (1) the high temperature for short-time periods (>50 °C for 10 ~ 30 min) in tumor tissue, commonly referred to as thermal ablation, and (2) the lower temperatures for long-time periods (42 ~ 45 °C for at least 30 min) in tumor tissue often called mild hyperthermia [142]. Generally, the threshold thermal exposure for mild hyperthermia treatment can induce distinct apoptosis effect. Simultaneously, it can result in the tumor vascular damage and the reduction in tumor blood flow in the vasculature, thereby impairing oxygen and nutrient supply, inducing the anti-angiogenesis effect [106]. Whereas thermal ablation can alter the tumor microenvironment in terms of hypoxia, perfusion in tumors and immunological function kill the tumor cells directly with heat treatment and finally lead to tumor tissue necrosis and coagulation [7]. The heat ablation induction can also raise the metabolism and transition (meaning the structural transformation from an ordered to a disordered state) of cellular structures, such as DNA and proteins [7, 142–144]. Accordingly, protein aggregation, insolubilization, increased fluidity of cellular membranes, disruption in ion permeability through cellular membranes, inhibition of amino acid transport, morphological changes as a consequence of damaged cytoskeletal system, and inhibition of DNA repair are typical effects at the cellular level [7, 142]. For instance, in an experiment conducted by Hilger et al., the tumor-bearing mice received an intratumoral injection of iron oxide NPs at 4–18 mg per 100 mg tumor tissue and were then exposed to an ACMF (amplitude, 6.5 kA m^{-1}; frequency, 400 kHz) for 50 min. During hyperthermia treatment, the temperature of tumor tissue changes varied from 12 °C to 73 °C, and the histological examination of the tumor tissue revealed the presence of the early stages of coagulation and necrosis [145]. Huang et al. had described the use of the MNPs that, with a well-tolerated intravenous dose, achieved a tumor concentration of 1.9 mg [Fe]/g tumor in a subcutaneous carcinoma mouse model. With an ACMF of 38 kA m^{-1} at 980 kHz, tumor tissue could be heated to 60 °C in 2 min, durably ablating them with millimeter precision, leaving the surrounding tissue intact [146]. More recent studies have also focused on increasing the efficiency of this thermal ablation treatment [147–149]. Although thermal ablation can effectively destroy tumor tissue, a major limitation with this type of therapy in its overall effectiveness is due to the difficulties of heating large tumors. In this regard, designing an effective magnetic hyperthermia strategy, such as the MNP injection method and dose, and the appropriate

size of ACMF helical coil device, to make sure the whole tumor tissue region reaches a sufficient temperature, is challenging for researchers.

Direct intratumoral injection of MNPs is a conventional method for magnetic hyperthermia, which is demonstrated to be safe and beneficial in clinical application [146, 147]. It has the advantages of achieving high concentrations of MNPs in the tumor regions and inducing tumor thermal ablation under the exposure to ACMF, rapidly controlling tumor growth. But it severely suffers from not covering tumors adequately, being invasive, and typically leaving undertreated regions, leading to the cancer regrowth [146]. In contrast, intravenous administration of MNPs covers irregular tumor shapes more precisely, loads many tumors simultaneously, and is minimally invasive, which has a practical advantage in cancer targeted magnetic hyperthermia (TMH) [106]. Previous attempts to implement intravenous injection of MNPs followed by ACMF heating showed some efficacy but were not able to fully ablate tumors, as required concentration was not reached in the tumors [150, 151]. Additional barrier to this approach was the toxicity of the MNPs at a level that achieves the required tumor loading after injection.

To achieve adequate concentrations of MNPs in the tumor, the excellent performances of MNPs, such as the higher magnetic characteristic, biocompatibility, and increased tumor-targeting ability, are crucial for their successful cancer TMH. As previously mentioned, one way of characterizing the heating ability of MNPs under an ACMF is calculating their SAR values. Firstly, there is a great challenge for optimizing the size, shape, and structure of MNPs to achieve higher heating power. In detail, it was shown that the spherical MNPs with a mean size of ~20 nm are suitable for clinical hyperthermia as the previous depiction [152], and cubic-shaped iron oxide NPs or flower-shaped NPs had recently shown considerably improved hyperthermia properties, compared to optimized 20 nm spherical iron oxide NPs [72, 137]. The current progress in the synthesis of MNPs now allowed for their variable and controlled core–shell structures [80]. A very important antitumor effect induced by hyperthermia had been thus noticed with core–shell MNPs consisting of a core displaying a high magnetic anisotropy surrounded by a shell with a small magnetic anisotropy [80]. In an attempt to develop new ferrite NPs with higher thermal energy transfer capability, a metal-dopant (e.g., Mn^{2+} or Zn^{2+}) substitution strategy had also been pursued in recent studies [52, 78]. For instance, it was proved that this strategy for enhancing SAR value (432 W g^{-1}) of doped $(Zn_{0.4}Mn_{0.6})Fe_2O_4$ NPs, achieving higher nanomagnetism, was very important. The high SAR could bring better efficacy with lower dosage levels, leading to a fourfold enhancement in hyperthermic effects in vitro compared to conventional Feridex measured under an ACMF at 500 kHz and 37 kA m^{-1} [78]. In the study of Zhang et al., doping Mn–Zn ferrite MNPs (8 nm) were proved to exhibit extremely high magnetization value with 98 emu g^{-1} Fe and a magnetically induced temperature elevation (~30 °C in aqueous solution for 15 min by application of an ACMF with 390 kHz and 12 A) [106]. The outstanding performances made the MNPs promising as an excellent material for early diagnosis and therapy in vivo.

Secondly, the improved MNP-mediated tumor-targeting efficiency as another strategy plays a vital role in practical TMH in vivo. As an essential challenge, the

MNPs should be conjugated to the surface coating or targeting molecule to achieve efficient accumulation in tumor tissues with MNP-mediated intravenous injections. Generally, the leaky vasculature of tumors may promote MNP accumulation as the blood flows through the tumor, but the MNPs without surface modification are rapidly cleared from the blood circulation when passing through the biological defense system and vascular barriers in vivo [129]. When the immune system does not recognize the MNPs, the MNPs may have a longer blood circulation time, promoting their passive targeting ability and increasing their accumulation in the tumor tissue because of the aforementioned EPR effect. The previously mentioned coatings (e.g., specifically PEG and liposomes) are the mostly responsible for passive targeting effect and increased blood circulation time of the MNPs. It was proved that the lipid DSPE-PEG2000-coated Mn–Zn ferrite MNPs with a core–shell structure in an average diameter of 48.6 nm can drastically minimize the recognition and phagocytosis of macrophages and simultaneously improve their biocompatibility, which endowed them with efficient passive targeting ability in vivo for prominent magnetically induced heating when exposed to ACMF, based on the EPR effects (Fig. 2.12a) [80, 106]. To ensure sufficient accumulation, the use of MNPs with a well-tolerated intravenous single dose of 18 mg Fe kg^{-1} mouse body weight was described. With an ACMF of 12 A at 390 kHz, the tumor surface sites could be heated to approximately 43 °C in 30 min based on MNC-mediated intravenous injections [106]. The MNP-mediated passive targeting can successfully accumulate at tumors, but there is also concurrent accumulation in some other tissues, most notably the liver and spleen. It makes the restricted use of passive targeting for tumor hyperthermia purpose.

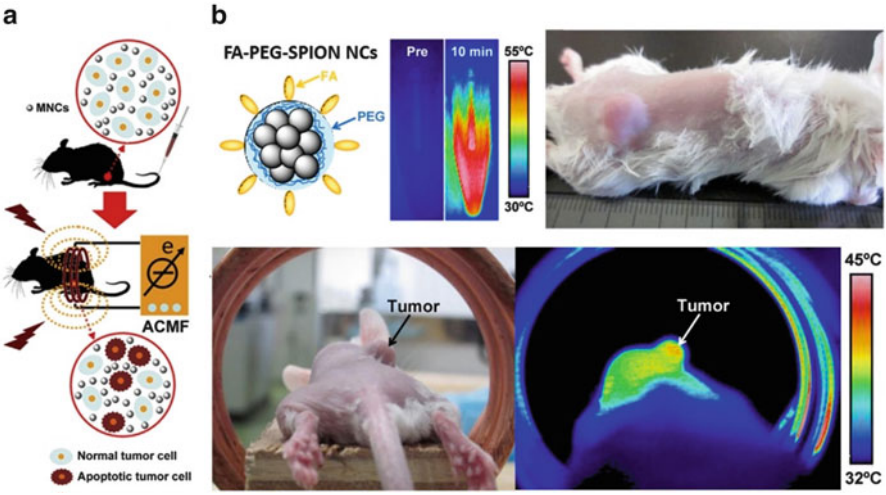

Fig. 2.12 (**a**) A schematic diagram of MNPs for the magnetically induced mice cancer theranostics (Reprinted with permission from Ref. [106]. Copyright 2014, Elsevier). (**b**) The FA-PEG-SPION NPs with intravenous administration for mice cancer TMH (Reprinted with permission from Ref. [98]. Copyright 2013, Theranostics)

Approaches of MNP-mediated active targeting in relation to TMH are proposed with the aim of improving the MNP accumulation beyond passive targeting. It has the advantage that MNPs can be selectively deposited in the tumor region after the intravenous application without needing to puncture the tumor tissue with intratumoral injection methods. The active targeting ligands, such as antibodies, tat peptides, RGD peptides, FA, and chlorotoxin, are often modified on the initial surface of MNPs [129]. The targeting ligands can increase the cellular uptake of MNPs in targeted cell either by endocytosis or binding to targeted cell surface. A promising active targeted hyperthermia method for treating prostate cancer was developed by Cui et al., in which they synthesized fluorescent MNPs conjugated with single-chain Fv antibody against an overexpressed γ-seminoprotein [153]. Through studies of targeted MNPs intravenously administered into mice, they showed a steady increase of MNP concentration in the tumor after 2, 6, 9, 12, and 24 h injection. Mice receiving treatment with a magnetic field had a longer life expectancy (7 weeks) than mice not receiving treatment with a magnetic field (4 weeks) [129, 153]. Hayashi et al. had also modified the magnetic nanoclusters with FA, to promote sufficient accumulation in tumors [98]. Twenty-four hours after intravenous injection of FA-modified nanoclusters, they accumulated locally in the cancer tissues. The tumors of the mice then underwent local heating by application of an ACMF (8 kA m^{-1} and 230 kHz) for 20 min. The temperature of the tumor was higher than the surrounding tissues by ~6 °C (Fig. 2.12b) [98].

Thirdly, for clinically available TMH, the optimization of ACMF with adequate frequency, field, and helical coil device is also challenging, which can provide the base for theranostics strategies. It was used in the MNP-mediated hyperthermia clinical trial treating prostate cancer using a 100 kHz machine designed for human patients and later in human glioma trials which demonstrated to be safe and have some benefits [140, 141]. In the experiments of mice modes, the highest amplitude and frequency of an ACMF were set to 38 kA m^{-1} and 980 kHz, in which the mice were observed to have no obvious clinical signs of toxicity (no weight loss or abnormal behavior) [146]. Xie et al. designed a magnetic induction coil device with 3 cm in diameter and 1.5 cm in length in ACMF. The designed ACMF system just made the tumor region of a mouse placed in the center of magnetic induction, focusing the heat into very small tumor regions, and promoted higher thermal energy production, which was used for making TMH a more effective approach to cancer therapy with decreased risk of heating surrounding healthy tissues (e.g., liver and spleen) [106].

The TMH has recently emerged as a promising therapeutic approach for cancer treatment due to intravenous administration of MNPs with high performance to deliver a therapeutic dose of heat specifically to cancerous regions under ACMF. However, it is proved that the single injection of MNPs was difficult in achieving necessary concentration in tumor because of the metabolism and clearance by correlative organs. So the extraordinary strategies of high-quality MNP-mediated TMH attained in further study may be attributed to a combination of the following factors: (1) the dosages of MNCs used here which are considerably larger than that used in previous MR imaging, (2) designing the TMH strategy of repetitious MNP-administered intravenous injections (3 ~ 6 time) and the long-lasting

hyperthermia, and (3) the TMH which can combine with other thermotherapies or chemotherapies, triggering the cancer synergetic therapy.

References

1. Li YP, Lin TY, Luo Y et al (2014) A smart and versatile theranostic nanomedicine platform based on nanoporphyrin. Nat Commun 5(4712):1–15
2. Lee DE, Koo H, Sun IC et al (2012) Multifunctional nanoparticles for multimodal imaging and theragnosis. Chem Soc Rev 41:2656–2672
3. Xie J, Lee S, Che XY (2010) Nanoparticle-based theranostic agents. Adv Drug Deliv Rev 62:1064–1079
4. Choi KY, Liu G, Lee S et al (2012) Theranostic nanoplatforms for simultaneous cancer imaging and therapy: current approaches and future perspectives. Nanoscale 4:330–342
5. Luk BT, Fang RH, Zhang LF (2012) Lipid and polymer-based nanostructures for cancer theranostics. Theranostics 2:1117–1126
6. Pan D (2013) Theranostic nanomedicine with functional nanoarchitecture. Mol Pharm 10:781–782
7. Hilger I, Kaiser WA (2012) Iron oxide-based nanostructures for MRI and magnetic hyperthermia. Nanomedicine 7:1443–1459
8. Yoo D, Lee JH, Shin TH et al (2011) Theranostic magnetic nanoparticles. Acc Chem Res 44:863–874
9. Pankhurst QA, Connolly J, Jones SK et al (2003) Applications of magnetic nanoparticles in biomedicine. J Phys D Appl Phys 36:167–181
10. Lee JH, Huh YM, Jun YW et al (2007) Artificially engineered magnetic nanoparticles for ultra-sensitive molecular imaging. Nat Med 13:95–99
11. Rosensweig RE (2002) Heating magnetic fluid with alternating magnetic field. J Magn Magn Mater 252:370–374
12. Gupta AK, Gupta M (2005) Synthesis and surface engineering of iron oxide nanoparticles for biomedical applications. Biomaterials 26:3995–4021
13. Mornet S, Vasseur S, Grasset F et al (2006) Magnetic nanoparticle design for medical applications. Prog Solid State Chem 34:237–247
14. Berkowit AE, Schuele WJ, Flanders PJ (1968) Influence of crystallite size on the magnetic properties of acicular γ-Fe_2O_3 particles. J Appl Phys 38:1261–1263
15. Leslie-Pelecky DL (1996) Magnetic properties of nanostructured materials. Chem Mater 8:1770–1783
16. Xu C, Xu K, Gu H et al (2004) Dopamine as a robust anchor to immobilize functional molecules on the iron oxide shell of magnetic nanoparticles. J Am Chem Soc 126:9938–9939
17. Basiruddin SK, Arindam S, Jana NR et al (2010) Advances in coating chemistry in deriving soluble functional nanoparticle. J Phys Chem C 114:11009–11017
18. Liu SJ, Han YC, Gao MY et al (2010) Investigations on the interactions between plasma proteins and magnetic iron oxide nanoparticles with different surface modifications. J Phys Chem C 114:21270–21276
19. Jiang S, Eltoukhy AA, Love KT et al (2013) Lipidoid-coated iron oxide nanoparticles for efficient DNA and siRNA delivery. Nano Lett 13:1059–1064
20. Lu AH, Salabas EL, Schuth F (2007) Magnetic nanoparticles: synthesis, protection, functionalization, and application. Angew Chem Int Ed 46:1222–1244
21. Neveu S, Bee A, Robineau M et al (2002) Size-selective chemical synthesis of tartrate stabilized. J Colloid Interf Sci 255:293–298
22. Grasset F, Labhsetwar N, Li D (2002) Synthesis and magnetic characterization of zinc ferrite nanoparticles with different environments: powder, colloidal solution, and zinc ferrite-silica core-shell nanoparticles. Langmuir 18:8209–8216

23. Sun SH, Zeng H (2002) Size-controlled synthesis of magnetite nanoparticles. J Am Chem Soc 124:8204–8205
24. Liang HF, Wang ZC (2010) Adsorption of bovine serum albumin on functionalized silica-coated magnetic $MnFe_2O_4$ nanoparticles. Mater Chem Phys 124:964–969
25. Kim DH, Nikles DE, Brazel CS (2010) Synthesis and characterization of multifunctional chitosan-$MnFe_2O_4$ nanoparticles for magnetic hyperthermia and drug delivery. Materials 3:4051–4065
26. Beji Z, Hanini A, Smiri LS et al (2010) Magnetic properties of Zn-substituted $MnFe_2O_4$ nanoparticles synthesized in polyol as potential heating agents for hyperthermia. Evaluation of their toxicity on endothelial cells. Chem Mater 22:5420–5429
27. Robinson DB, Persson HHJ, Zeng H et al (2005) DNA-functionalized MFe_2O_4 (M = Fe, Co, or Mn) nanoparticles and their hybridization to DNA-functionalized surfaces. Langmuir 21:3096–3103
28. Seo WS, Lee JH, Sun XM et al (2006) FeCo/graphitic-shell nanocrystals as advanced magnetic-resonance-imaging and near-infrared agents. Nat Mater 5:971–976
29. Shevchenko EV, Talapin DV, Rogach AL (2002) Colloidal synthesis and self-assembly of $CoPt_3$ nanocrystals. J Am Chem Soc 124:11480–11485
30. Sun SH (2006) Recent advances in chemical synthesis, self-assembly, and applications of FePt nanoparticles. Adv Mater 18:393–403
31. Park J II, Cheon J (2001) Synthesis of "solid solution" and "core-shell" type cobalt-platinum magnetic nanoparticles via transmetalation reactions. J Am Chem Soc 123:5743–5746
32. Kang YS, Risbud S, Rabolt JF et al (1996) Synthesis and characterization of nanometer-size Fe_3O_4 and γ-Fe_2O_3 particles. Chem Mater 8:2209–2211
33. Hong CY, Jang IJ, Horng HE et al (1997) Ordered structures in Fe_3O_4 kerosene-based ferrofluids. J Appl Phys 81:4275–4277
34. Fried T, Shemer G, Markovich G et al (2001) Ordered two-dimensional arrays of Ferrite nanoparticles. Adv Mater 13:1158–1161
35. Zhang ZJ, Wang ZL, Chakoumakos BC (1998) Temperature dependence of cation distribution and oxidation state in magnetic Mn-Fe Ferrite nanocrystals. J Am Chem Soc 120:800–1804
36. Park J, An K, Hwang Y et al (2004) Ultra-large-scale syntheses of monodisperse nanocrystals. Nat Mater 3:891–895
37. Sun SH, Zeng H, Robinson DB (2003) Monodisperse MFe_2O_4 (M = Fe, Co, Mn) nanoparticles. J Am Chem Soc 126:273–279
38. Redl FX, Black CT, Papaefthymiou GC (2004) Magnetic, electronic, and structural characterization of nonstoichiometric iron oxides at the nanoscale. J Am Chem Soc 126:14583–14599
39. Langevin D (1992) Micelles and microemulsions. Annu Rev Phys Chem 43:341–346
40. Wang X, Zhuang J, Peng Q (2005) A general strategy for nanocrystal synthesis. Nature 437:121–124
41. Deng H, Li XL, Peng Q et al (2005) Monodisperse magnetic single-crystal Ferrite microspheres. Angew Chem Int Ed 117:2842–2845
42. Deng H, Li XL, Peng Q et al (2005) Monodisperse magnetic single-crystal Ferrite microspheres. Angew Chem Int Ed 44:2782–2785
43. Cheon J, Kang NJ, Lee SM et al (2004) Shape evolution of single-crystalline iron oxide nanocrystals. J Am Chem Soc 126:1950–1951
44. Ho CH, Tsai CP, Chung CC et al (2011) Shape-controlled growth and shape-dependent cation site occupancy of monodisperse Fe_3O_4 nanoparticles. Chem Mater 23:1753–1760
45. Gao GH, Liu XH, Shi RR (2010) Shape-controlled synthesis and magnetic properties of monodisperse Fe_3O_4 nanocubes. Cryst Growth Des 10:2888–2894
46. Rockenberger J, Scher EC, Alivisatos AP (1999) A new nonhydrolytic single-precursor approach to surfactant-capped nanocrystals of transition metal oxides. J Am Chem Soc 121:11595–11596

47. Farrell D, Majetich SA, Wilcoxon JP (2003) Preparation and characterization of monodisperse Fe nanoparticles. J Phys Chem B 107:11022–11030
48. Jana NR, Chen YF, Peng XG (2004) Size- and shape-controlled magnetic (Cr, Mn, Fe, Co, Ni) oxide nanocrystals via a simple and general approach. Chem Mater 16:3931–3935
49. Samia ACS, Hyzer K, Schlueter JA et al (2005) Ligand effect on the growth and the digestion of Co nanocrystals. J Am Chem Soc 127:4126–4127
50. Li Y, Afzaal M, O'Brien P (2006) The synthesis of amine-capped magnetic (Fe, Mn, Co, Ni) oxide nanocrystals and their surface modification for aqueous dispersibility. J Mater Chem 16:2175–2180
51. Murray CB, Kagan CR (2000) Synthesis and characterization of monodisperse nanocrystals and close-packed nanocrystal assemblies. Ann Rev Mater Sci 30:545–610
52. Jun YW, Lee JH, Cheon J (2008) Chemical design of nanoparticle probes for high-performance magnetic resonance imaging. Angew Chem Int Ed 47:122–5135
53. Vestal CR, Zhang ZJ (2003) Effects of surface coordination chemistry on the magnetic properties of $MnFe_2O_4$ spinel Ferrite nanoparticles. J Am Chem Soc 125:9828–9833
54. Gradmann UJ (1991) Surface magnetism. Magn Magn Mater 100:481–496
55. Kodama RH, Berkowitz AE, McNiff EJ Jr et al (1997) Surface spin disorder in ferrite nanoparticles. J Appl Phys 81:5552–5557
56. Spada FE, Parker FT, Nakakura CY et al (1993) Studies of anisotropy mechanisms in polyphosphate-treated magnetic iron oxide particles. J Magn Magn Mater 120:129–135
57. Tronc E, Ezzir A, Cherkaoui R et al (2000) Surface-related properties of γ-Fe_2O_3 nanoparticles. J Magn Magn Mater 221:63–79
58. Kolen'ko YV, Bañobre-López M, Rodríguez-Abreu C et al (2014) Large-scale synthesis of colloidal Fe_3O_4 nanoparticles exhibiting high heating efficiency in magnetic hyperthermia. J Phys Chem C 118:8691–8701
59. Tanimoto A, Kuribayashi S (2006) Application of superparamagnetic iron oxide to imaging of hepatocellular carcinoma. Eur J Radiol 58:200–216
60. Gupta AK, Wells S (2004) Surface-modified superparamagnetic nanoparticles for drug delivery: preparation, characterization, and cytotoxicity studies. IEEE Trans Nanobiosci 3:66–73
61. Firth JA (2002) Endothelial barriers: from hypothetical pores to membrane proteins. J Anat 200:541–548
62. Hirano A, Matsui T, Pathol H (1975) Vascular structures in brain tumors. Hum Pathol 6:611–621
63. Nandwana V, Elkins KE, Poudyal N (2007) Size and shape control of monodisperse FePt nanoparticles. J Phys Chem C 111:4185–4189
64. Sun SH, Zeng H, Robinson DB et al (2004) Monodisperse MFe_2O_4 (M = Fe, Co, Mn) nanoparticles. J Am Chem Soc 126:273–279
65. Xie J, Yan CZ, Zhang Y et al (2013) Shape evolution of "multibranched" Mn–Zn Ferrite nanostructures with high performance: a transformation of nanocrystals into nanoclusters. Chem Mater 25:3702–3709
66. Zeng H, Rice PM, Wang SX (2004) Shape-controlled synthesis and shape-induced texture of $MnFe_2O_4$ nanoparticles. J Am Chem Soc 126:11458–11459
67. Bao NZ, Shen LM, An W et al (2009) Formation mechanism and shape control of monodisperse magnetic $CoFe_2O_4$ nanocrystals. Chem Mater 21:3458–3468
68. Zhao ZH, Zhou ZJ, Bao JF et al (2013) Octapod iron oxide nanoparticles as high-performance T_2 contrast agents for magnetic resonance imaging. Nat Commun 4(2266):1–7
69. Agrawal A, Min DH, Singh N et al (2009) Functional delivery of siRNA in mice using dendriworms. ACS Nano 3:495–504
70. Pantarotto D, Singh R, McCarthy D et al (2004) Functionalized carbon nanotubes for plasmid DNA gene delivery. Angew Chem Int Ed 43:5242–5246
71. Bao L, Low WL, Jiang J et al (2012) Colloidal synthesis of magnetic nanorods with tunable aspect ratios. J Mater Chem 22:7117–7120

72. Hugounenq P, Levy M, Alloyeau D et al (2012) Iron oxide monocrystalline nanoflowers for highly efficient magnetic hyperthermia. J Phys Chem C 116:15702–15712
73. Bao NZ, Shen LM, Wang YH et al (2009) Controlled growth of monodisperse self-supported superparamagnetic nanostructures of spherical and rod-like $CoFe_2O_4$ nanocrystals. J Am Chem Soc 131:12900–12901
74. Hu M, Jiang JS (2010) Non-classical crystallization controlled by centrifugation. CrystEngComm 12:3391–3393
75. Wei YH, Klajn R, Pinchuk AO (2008) Synthesis, shape control, and optical properties of hybrid Au/Fe_3O_4 "nanoflowers". Small 4:1635–1639
76. Wang LY, Park HY, Lim SII et al (2008) Core@shell nanomaterials: gold-coated magnetic oxide nanoparticles. J Mater Chem 18:2629–2635
77. Zhang J, Huang F, Lin Z (2009) Progress of nanocrystalline growth kinetics based on oriented attachment. Nanoscale 2:18–34
78. Jang JT, Nah H, Lee JH et al (2009) Critical enhancements of MRI contrast and hyperthermic effects by dopant-controlled magnetic nanoparticles. Angew Chem Int Ed 48:1234–1238
79. Wang LY, Wang X, Luo J et al (2010) Core-shell-structured magnetic ternary nanocubes. J Am Chem Soc 132:17686–17689
80. Lee JH, Jang JT, Choi JS et al (2011) Exchange-coupled magnetic nanoparticles for efficient heat induction. Nat Nanotechnol 6:418–422
81. Habib AH, Ondeck CL, Chaudhary P et al (2008) Evaluation of iron-cobalt/ferrite core shell nanoparticles for cancer thermotherapy. J Appl Phys 103:07A307
82. Fortin JP, Wilhelm C, Servais J et al (2007) Size-sorted anionic iron oxide nanomagnets as colloidal mediators for magnetic hyperthermia. J Am Chem Soc 129:2628–2635
83. Zeng H, Li J, Liu J et al (2002) Exchange-coupled nanocomposite magnets by nanoparticle self-assembly. Nature 420:395–398
84. Mornet S, Vasseur S, Grasset F et al (2004) Magnetic nanoparticle design for medical diagnosis and therapy. J Mater Chem 14:2161–2175
85. Karakoti AS, Das S, Thevuthasan S et al (2011) PEGylated inorganic nanoparticles. Angew Chem Int Ed 50:1980–1994
86. Howard MD, Jay M, Dziublal TD et al (2008) PEGylation of nanocarrier drug delivery systems: state of the art. Nanotechnology 4:133–148
87. Li Z, Wei L, Gao MY et al (2005) One-pot reaction to synthesize biocompatible magnetite nanoparticles. Adv Mater 17:1001–1005
88. Amstad E, Zurcher S, Mashaghi A et al (2009) Surface functionalization of single superparamagnetic iron oxide nanoparticles for targeted magnetic resonance imaging. Small 5:1334–1342
89. Gu L, Shen Z, Feng C et al (2008) Synthesis of PPEGMEA-g-PMAA densely grafted double hydrophilic copolymer and its use as a template for the preparation of size-controlled superparamagnetic Fe_3O_4/polymer nano-composites. J Mater Chem 18:4333–4340
90. Larsen EKU, Nielsen T, Wittenborn T et al (2009) Size-dependent accumulation of PEGylated silane-coated magnetic iron oxide nanoparticles in murine tumors. ACS Nano 3:1947–1951
91. Solin N, Kjellgren J, Szabo KJ et al (2004) Pincer complex-catalyzed allylation of aldehyde and imine substrates via nucleophilic η^1-allyl palladium intermediates. J Am Chem Soc 126:7026–7033
92. Sun C, Sze R, Zhang MQ et al (2006) Folic acid-PEG conjugated superparamagnetic nanoparticles for targeted cellular uptake and detection by MRI. J Biomed Mater Res Part A 78A:550–557
93. Chen K, Xie J, Xu HY et al (2009) Triblock copolymer coated iron oxide nanoparticle conjugate for tumor integrin targeting. Biomaterials 30:6912–6919
94. Deng JG, Ding XB, Zhang WH et al (2002) Magnetic and conducting Fe_3O_4-cross-linked polyaniline nanoparticles with core-shell structure. Polymer 43:2179–2184
95. Xu XL, Friedman G, Humfeld KD et al (2001) Superparamagnetic photonic crystals. Adv Mater 13:1681–1684

96. Vestal CR, Zhang ZJ (2002) Atom transfer radical polymerization synthesis and magnetic characterization of $MnFe_2O_4$/polystyrene core/shell nanoparticles. J Am Chem Soc 124:14312–14313
97. Huh YM, Jun YW, Song HT et al (2005) In vivo magnetic resonance detection of cancer by using multifunctional magnetic nanocrystals. J Am Chem Soc 127:12387–12391
98. Hayashi K, Nakamura M, Sakamoto W et al (2013) Superparamagnetic nanoparticle clusters for cancer theranostics combining magnetic resonance imaging and hyperthermia treatment. Theranostics 3:366–376
99. Mulder WJM, Strijkers GJ, van Tilborg GAF et al (2006) Lipid-based nanoparticles for contrast-enhanced MRI and molecular imaging. NMR Biomed 19:142–164
100. Gonzales M, Krishnan KM (2005) Synthesis of magnetoliposomes with monodisperse iron oxide nanocrystal cores for hyperthermia. J Magn Magn Mater 293:265–270
101. Namiki Y, Namiki T, Yoshida H et al (2009) A novel magnetic crystal-lipid nanostructure for magnetically guided in vivo gene delivery. Nat Nanotechnol 4:598–606
102. Amstad E, Kohlbrecher J, Muller E et al (2011) Triggered release from liposomes through magnetic actuation of iron oxide nanoparticle containing membranes. Nano Lett 11:1664–1670
103. Katagiri K, Nakamura M, Koumoto K et al (2010) Magnetoresponsive smart capsules formed with polyelectrolytes, lipid bilayers and magnetic nanoparticles. ACS Appl Mater Inter 2:768–773
104. Namiki Y, Fuchigami T, Tada N et al (2011) Nanomedicine for cancer: lipid-based nanostructures for drug delivery and monitoring. Acc Chem Res 44:1080–1093
105. Tong S, Hou SJ, Zheng ZK et al (2010) Coating optimization of superparamagnetic iron oxide nanoparticles for high T_2 relaxivity. Nano Lett 10:4607–4613
106. Xie J, Zhang Y, Yan CY et al (2014) High-performance PEGylated MneZn ferrite nanocrystals as a passive-targeted agent for magnetically induced cancer theranostics. Biomaterials 35:9126–9136
107. Gu L, Fang RH, Sailor MJ et al (2012) In vivo clearance and toxicity of monodisperse iron oxide nanocrystals. ACS Nano 6:4947–4954
108. Yu H, Chen M, Rice PM et al (2005) Dumbbell-like bifunctional Au-Fe_3O_4 nanoparticles. Nano Lett 5:379–382
109. Xu ZC, Hou YL, Sun SH (2007) Magnetic Core/Shell Fe_3O_4/Au and Fe_3O_4/Au/Ag nanoparticles with tunable plasmonic properties. J Am Chem Soc 129:8698–8699
110. Wang LY, Luo G, Fan Q et al (2005) Monodispersed core-shell Fe_3O_4@Au nanoparticles. J Phys Chem B 109:21593–21601
111. Goon IY, Lai LMH, Lim M et al (2009) Fabrication and dispersion of gold-shell-protected magnetite nanoparticles: systematic control using polyethyleneimine. Chem Mater 21:673–681
112. Bao J, Chen W, Liu TT et al (2007) Bifunctional Au-Fe_3O_4 nanoparticles for protein separation. ACS Nano 1:293–298
113. Lu Y, Yin Y, Mayers BT et al (2002) Modifying the surface properties of superparamagnetic iron oxide nanoparticles through a sol–gel approach. Nano Lett 2:183–186
114. Santra S, Tapec R, Theodoropoulou N et al (2001) Synthesis and characterization of silica-coated iron oxide nanoparticles in microemulsion: the effect of nonionic surfactants. Langmuir 17:2900–2906
115. Yi DK, Lee SS, Papaefthymiou GC et al (2006) Nanoparticle architectures templated by SiO_2/Fe_2O_3 nanocomposites. Chem Mater 18:614–619
116. Ung T, Liz-MarzXn LM, Mulvaney P (1998) Controlled method for silica coating of silver colloids. Influence of coating on the rate of chemical reactions. Langmuir 14:3740–3748
117. Geng J, Jefferson DA, Johnson BFG et al (2004) Direct conversion of iron stearate into magnetic Fe and Fe_3C nanocrystals encapsulated in polyhedral graphite cages. Chem Commun 2442–2443

118. Lu AH, Li W, Matoussevitch N et al (2005) Highly stable carbon-protected cobalt nanoparticles and graphite shells. Chem Commun 98–100
119. Taboada E, Rodríguez E, Roig A et al (2007) Relaxometric and magnetic characterization of ultrasmall iron oxide nanoparticles with high magnetization evaluation as potential *T1* magnetic resonance imaging contrast agents for molecular imaging. Langmuir 23:4583–4588
120. Cheon J, Lee JH (2008) Synergistically integrated nanoparticles as multimodal probes for nanobiotechnology. Acc Chem Res 41:1630–1640
121. Jun YW, Huh YM, Choi JS et al (2005) Nanoscale size effect of magnetic nanocrystals and their utilization for cancer diagnosis *via* magnetic resonance imaging. J Am Chem Soc 127:5732–5733
122. Weissleder R, Moore A, Mahmood U et al (2000) In vivo magnetic resonance imaging of transgene expression. Nat Med 6:351–354
123. Artemov D, Bhujwalla ZM, Bulte JW (2004) Magnetic resonance imaging of cell surface receptors using targeted contrast agents. Curr Pharm Biotechnol 2:165–172
124. Na HB, Song IC, Hyeon T (2009) Inorganic nanoparticles for MRI contrast agents. Adv Mater 21:2133–2148
125. Kim T, Murakami T, Hori M et al (2009) Effect of superparamagnetic iron oxide on tumor-to-liver contrast at *T2**-weighted gradient-echo MRI: comparison between 3.0T and 1.5T MR systems. J Magn Reson Imaging 29:595–600
126. Liu DF, Wu W, Ling JJ et al (2011) Effective PEGylation of iron oxide nanoparticles for high performance in vivo cancer ima*ging*. Adv Funct Mater 21:1498–1504
127. Lee N, Choi Y, Lee Y et al (2012) Water-dispersible ferrimagnetic iron oxide nanocubes with extremely high *r2* relaxivity for highly sensitive in vivo MRI of tumors. Nano Lett 12:3127–3131
128. Hu FQ, Wei L, Zhou Z et al (2006) Preparation of biocompatible magnetite nanocrystals for in vivo magnetic resonance detection of cancer. Adv Mater 18:2553–2556
129. Stone R, Willi T, Rosen Y et al (2011) Targeted magnetic hyperthermia. Ther Deliv 2:815–838
130. Walter A, Billotey C, Garofalo A et al (2014) Mastering the shape and composition of dendronized iron oxide nanoparticles to tailor magnetic resonance imaging and hyperthermia. Chem Mater 26:5252–5264
131. Maier-Hauff K, Rothe R, Scholz R et al (2007) Intracranial thermotherapy using magnetic nanoparticles combined with external beam radiotherapy: results of a feasibility study on patients with glioblastoma multiforme. Neuro Oncol 81:53–60
132. Maier-Hauff K, Ulrich F, Nestler D et al (2011) Efficacy and safety of intratumoral thermotherapy using magnetic iron-oxide nanoparticles combined with external beam radiotherapy on patients with recurrent glioblastoma multiforme. J Neuro Oncol 103:317–324
133. Trana N, Webster TJ (2010) Magnetic nanoparticles: biomedical applications and challenges. J Mater Chem 20:8760–8767
134. Jordan A, Scholz R, Wust P et al (1997) Effects of magnetic fluid hyperthermia (MFH) on C_3H mammary carcinoma in vivo. Int J Hyperthermia 13:587–605
135. Hilger I, Rapp A, Greulich KO et al (2005) Assessment of DNA damage in target tumor cells after thermoablation in mice. Radiology 237:500–506
136. Laurent S, Dutz S, Hafeli UO et al (2011) Magnetic fluid hyperthermia: focus on superparamagnetic iron oxide nanoparticles. Adv Colloid Interface Sci 166:8–23
137. Guardia P, Riccardo DC, Lartigue L et al (2012) Water-soluble iron oxide nanocubes with high values of specific absorption rate for cancer cell hyperthermia treatment. ACS Nano 6:3080–3091
138. Hergt R, Dutz S (2007) Magnetic particle hyperthermia-biophysical limitations of a visionary tumour therapy. J Magn Magn Mater 311:187–192
139. Gilchrist RK, Medal R, Shorey WD et al (1957) Selective inductive heating of lymph nodes. Ann Surg 146:596–606

140. Jordan A, Wust P, Faehling H et al (2009) Inductive heating of ferrimagnetic particles and magnetic fluids: physical evaluation of their potential for hyperthermia. Int J Hyperthermia 25:499–511
141. Johannsen M, Gneveckow U, Eckelt L et al (2005) Clinical hyperthermia of prostate cancer using magnetic nanoparticles: presentation of a new interstitial technique. Int J Hyperthermia 21:637–647
142. Lepock JR (2003) Cellular effects of hyperthermia: relevance to the minimum dose for thermal damage. Int J Hyperthermia 19:252–266
143. Thrall DE, Larue SM, Pruitt AF et al (2006) Changes in tumour oxygenation during fractionated hyperthermia and radiation therapy in spontaneous canine sarcomas. Int J Hyperthermia 22:365–373
144. Song CW, Park H, Griffin RJ et al (2001) Improvement of tumor oxygenation by mild hyperthermia. Radiat Res 155:515–528
145. Ingrid H, Robert H, Rudolf H et al (2002) Thermal ablation of tumors using magnetic nanoparticles: An in vivo feasibility study. Invest Radiol 37:580–586
146. Huang HS, Hainfeld JF (2013) Intravenous magnetic nanoparticle cancer hyperthermia. Int J Nanomed 8:2521–2532
147. Ren YY, Zhang HJ, Chen BA et al (2012) Multifunctional magnetic Fe_3O_4 nanoparticles combined with chemotherapy and hyperthermia to overcome multidrug resistance. Int J Nanomed 7:2261–2269
148. Bruners P, Hodenius M, Baumann M et al (2008) Magnetic thermal ablation using ferrofluids: influence of administration mode on biological effect in different porcine tissues. Cardiovasc Intervent Radiol 31:1193–1199
149. Elsherbini AA, Saber M, Aggag M et al (2011) Magnetic nanoparticle–induced hyperthermia treatment under magnetic resonance imaging. Imaging 29:272–280
150. Balivada S, Rachakatla RS, Wang H et al (2010) A/C magnetic hyperthermia of melanoma mediated by iron(0)/iron oxide core/shell magnetic nanoparticles: a mouse study. BMC Cancer 10:119–1–9
151. DeNardo SJ, DeNardo GL, Natarajan A et al (2007) Thermal dosimetry predictive of efficacy of 111 In-ChL6 nanoparticle AMF–induced thermoablative therapy for human breast cancer in mice. J Nucl Med 48:437–444
152. Gazeau F, Lévy M, Wilhelm C et al (2008) Optimizing magnetic nanoparticle design for nanothermotherapy. Nanomed 3:831–844
153. Daxiang Cui YH, Zhiming L, Song H et al (2009) Fluorescent magnetic nanoprobes for in vivo targeted imaging and hyperthermia therapy of prostate cancer. Nano Biomed Eng 1:61–74

Chapter 3
Molecular Imaging of Tumor Angiogenesis with Magnetic Nanoprobes

Chunfu Zhang

Abbreviations

aFGF	Acidic fibroblast growth factor
Anx	Anginex
APTMS	3-Aminopropyltrimethoxysilane
bFGF	Basic fibroblast growth factor
CT	Computerized tomography
DOTA	1,4,7,10-Tetraazacyclododecane-1,4,7,10-tetraacetic acid
DSPC	Disaturated-phosphatidylcholine
DSPE	Distearoylphosphatidylethanolamine
DTPA	Diethylenetriamine pentaacetic acid
DWI	Diffusion-weighted images
ECM	Extracellular matrix
HDL	High-density lipoprotein
HIF	Hypoxia-inducible factor
HUVECs	Human umbilical vein endothelial cells
ICP-MS	Inductively coupled plasma mass spectrometry
MMPs	Matrix metalloproteinases
MNCs	Magnetite nanoclusters
MRI	Magnetic resonance imaging
OI	Optical imaging
ORS	Off-resonance saturation
PDGF	Platelet-derived growth factor
PEG	Poly(ethylene glycol)
PEG-PLA	Poly(ethylene glycol)-block-poly(D,L-lactide)

C. Zhang (✉)
State Key Laboratory of Oncogenes and Related Genes, Shanghai Cancer Institute, School of Biomedical Engineering, Shanghai Jiao Tong University, Shanghai 200030, China
e-mail: cfzhang@sjtu.edu.cn

Z. Dai (ed.), *Advances in Nanotheranostics II*, Springer Series in Biomaterials Science and Engineering 7, DOI 10.1007/978-981-10-0063-8_3

PET	Positron emission tomography
PFC	Perfluorocarbon
RAD	Arginine-alanine-aspartic acid
RGD	Arginine-glycine-aspartic acid
rHDL	Reconstituted high-density lipoprotein
SPECT	Single-photon emission computed tomography
SPIO	Superparamagnetic iron oxide nanoparticles
SPPM	Superparamagnetic polymeric micelles
TEM	Transmission electron microscope
TGF-β	Transforming growth factor-beta
US	Ultrasound
VEGF	Vascular endothelial growth factor

3.1 Brief Introduction to Tumor Angiogenesis

Angiogenesis is the process in which new blood vessels arise from the existing ones. This is present physiologically in the adult during wound healing, in the development of the ovarian follicle and corpus luteum, and in the proliferating endometrium [1]. Pathological angiogenesis is also a component of much diverse pathologies ranging from diabetes and atherosclerosis to cancer, a disease that cannot progress without the formation of new blood vessels [2]. Tumors in particular rely on angiogenesis for their continued growth [3, 4]. Solid tumors will not grow larger than 2–3 mm in diameter in the absence of new blood vessels [5]. When tumors grow beyond such size, the increased interstitial pressure within the tumor inhibits the diffusion of metabolites and nutrients necessary for tumor growth. A state of cellular hypoxia begins. Hypoxia increases cellular hypoxia-inducible factor (HIF) transcription. Binding of the hypoxia-inducible factor to the hypoxia response element turns on the expression of VEGF. VEGF is a family of vascular endothelial growth factors, including VEGF-A, VEGF-B, VEGF-C, and VEGF-D. VEGF-A is one key player in the angiogenic process, induces vasodilatation of preexisting capillaries, and increases vascular permeability. The increase in permeability allows extravasation of plasma protein laying down a provisional matrix for endothelial cell migration and tube formation. For endothelial cell migration, the cells need to loosen contacts from each other and from the basement membrane and the extracellular matrix surrounding the vessels [6]. Therefore, degradation of extracellular matrix is requisite, which is catalyzed by plasmin-related enzymes, matrix metalloproteinases (MMPs), chymase, and tryptase through the proteolytic process.

After this degradation, endothelial cells, mediated by cell adhesion receptors, like the integrin αvβ3, proliferate and migrate until they form unstable microvessels. In a further step, mesenchymal cells release angiopoietin-1, which interacts with Tie-2 receptor tyrosine kinase, mediating capillary organization and stabilization [7]. The newly built endothelial cells form tight junctions with each other, leading to new tubes which are connected with the microcirculation. Blood flow can then be

established [8]. In addition to angiogenic factors, a variety of other factors (e.g., TGF-β, PDGF, bFGF, aFGF, IL-8, and uPA) are involved in this process, which are locally secreted by numerous cells like stromal, endothelial, and cancer cells but can also derive from blood and the extracellular matrix [9, 10]. The detailed mechanisms of angiogenesis can refer to previous reports [1, 11].

Various classes of adhesion molecules are involved in tumor angiogenesis. Members of the integrin, cadherin, selectin, and immunoglobulin families contribute to each step of tumor vascularization, not only by mediating cell-cell and cell-matrix interactions but also by participating in those signaling events that regulate the extension and the maturation of neoforming vessels [12, 13]. These molecules have been exploited as targets for molecular imaging and quantification of tumor angiogenesis [14]. Among these molecules, integrins have been extensively studied [15]. Integrins are heterodimeric transmembrane glycoproteins, which consist of two noncovalently bound transmembrane subunits with large extracellular segments that bind to create heterodimers with distinct adhesive capabilities [16]. Up to now, 18 α and 8 β subunits have been described, which assemble into 24 different integrins (receptors). Among all 24 integrins discovered to date, integrin αvβ3 is the most extensively studied [17–19], which is significantly upregulated on activated endothelial cells during angiogenesis but not on quiescent endothelial cells [20]. Clinical studies showed that the expression of integrin αvβ3 correlated with tumor grade [21, 22] and thus suggested integrin αvβ3 as a marker of malignancy. Therefore, the ability to noninvasively detect αvβ3 expression in living subjects would allow a better characterization of tumors and help to identify tumor regions with higher aggressiveness. In this context, in the past few years, a vast array of sensitive molecular imaging agents associated with angiogenesis-specific targets have been developed for molecular imaging of integrin αvβ3 expression for early detection of cancers using different modalities [19, 23, 24].

3.2 Modalities Used for Tumor Angiogenesis Imaging

The modalities that have been proposed for imaging tumor angiogenesis include positron emission tomography (PET), single-photon emission computed tomography (SPECT), optical imaging (OI), ultrasound (US), computerized tomography (CT), and magnetic resonance imaging (MRI) [15, 25]. These systems provide a wealth of information that is highly complementary.

Both PET and SPECT use radioactive material as imaging agent. SPECT utilizes gamma radiation tracer. SPECT imaging is performed by using a gamma camera to acquire multiple 2-D images (also called projections), from multiple angles. A computer is then used to apply a tomographic reconstruction algorithm to the multiple projections, yielding a 3-D dataset. This dataset may then be manipulated to show thin slices along any chosen axis of the body. PET takes advantage of the unique properties of radioactive isotopes that decay via positron emission. The emitted positrons annihilate with electrons up to a few millimeters away, causing two gamma photons to be emitted in opposite directions. The gamma photons are detected when they reach a scintillator in the scanning device, creating a burst of

light which is detected by photomultiplier tubes or silicon avalanche photodiodes. The technique depends on simultaneous or coincident detection of the pair of photons moving in approximately opposite directions. The raw data collected by a PET scanner are a list of "coincidence events" representing near-simultaneous detection of annihilation photons by a pair of detectors. Coincidence events can be grouped into projection images, called sinograms, that are sorted by the angle of each view. The sinograms are ultimately reconstructed into tomographic images following dead time correction, detector normalization, subtraction of random coincidences, attenuation correction, and scatter correction [26].

PET and SPECT are very sensitive (10^{-11}–10^{-12} M for PET, 10^{-10}–10^{-11} M for SPECT) and highly quantitative and have no limitation of penetration depth. However, both PET and SPECT involve the use of ionizing radiation, which is impractical for frequent imaging due to potential damage to the living subjects from the cumulative irradiation dose. Another limitation of PET and SPECT is low spatial resolution, namely, the lack of an anatomical reference frame. This shortcoming has recently been addressed by combining these instruments with either CT or MRI, producing a single scanner capable of accurately identifying molecular events with precise correlation to anatomical findings [27]. Compared to PET, SPECT is less expensive and more widely available. But SPECT is generally less sensitive and has a lower spatial resolution (8–10 mm for SPECT, 5–7 mm for PET) [28].

The basic principle for in vivo fluorescence imaging is similar to that used in fluorescence microscopy techniques, such as conventional fluorescence microscopy, confocal microscopy, multiphoton microscopy, and optical coherence tomography. When an incident light illuminates fluorophores in living subject, the fluorophores are excited and low-energy photons are emitted, which are captured by the detector, a charge-coupled device (CCD) camera. Fluorescence imaging usually makes use of photons emitted in the near-infrared and far-red range. However, when whole animals are interrogated, the desired information is typically associated with biochemical events occurring deeply within the tissue. This implies that photons being part of detected signal have undergone multiple scattering events in the process of irradiance of the excitation light into the body and radiance of the emission out of the body. Therefore, the depth of penetration is limited to only a few centimeters, which makes it virtually impossible to study deep tissues in large animals or human subjects, unless one uses endoscopes or their equivalent to get closer to the tissue(s) of interest [29, 30]. Moreover, the spatial resolution of fluorescence imaging is low. The strengths of fluorescence imaging are high sensitive and relatively safe.

Ultrasound imaging (ultrasonography) is based on reflection of acoustic waves with frequency higher than 20 kHz, generally ~ 1–20 MHz. Acoustic waves are generated by a transducer and enter the body. Some sound waves are reflected back to the transducer where they are detected and converted into electrical signals. These signals are then processed by a computer and displayed as an image. Ultrasound imaging is inexpensive, widely available, and completely noninvasive; therefore, it is a promising technique for evaluation of tumor angiogenesis. However, the limitations of US are the dependence on the skill of the operator and limited depth

penetration. Moreover, not all regions of the body are accessible with US (lung, bone, and brain in adults), and adequate documentation for comparison of examinations at different time points is still problematic in a clinical setting [31].

CT is a technique that relies on differential levels of X-ray attenuation by tissues within the body to produce images reflecting anatomy. Tissues that strongly absorb X-rays (e.g., bone) appear white while others that absorb poorly (e.g., air) appear black. CT employs tomography and can produce a three-dimensional anatomic image of the subject being scanned. The advantages of CT include its fast acquisition time, high spatial resolution (preclinical, 0.05–0.2 mm; clinical, 0.5–1.0 mm), cost effectiveness, availability, relative simplicity, and no limitations in penetration depth. The main limitations are low soft tissue contrast and high exposure to radiation [32].

3.3 Principle of MRI

Atoms are in constant motion and spin about their axes, which gives rise to angular momentum. Along with angular momentum, nuclei with unequal protons and neutrons can produce a small magnetic field. This magnetic field is termed magnetic moment and, like angular momentum, is a vector quantity. The ratio of angular momentum to magnetic moment is known as the gyromagnetic ratio and is unique for each magnetically active nucleus [33].

Magnetic resonance imaging generates tissue images by measuring the interaction between an external magnetic field and the magnetic moment of water protons. The orientations of the magnetic moments are random in the absence of an external magnetic field [34]. When a patient is placed in a MRI scanner, the proton magnetic moments align either along (low energy) or against (high energy) the static magnetic field (B0) of the scanner and create a net magnetization pointing in the direction of the main magnetic field of the scanner.

Nuclear magnetic resonance (NMR) measures the change of the magnetization by applying radiofrequency (RF) pulses. When an RF pulse is applied to create an oscillating electromagnetic field (B1) perpendicular to the main field, the protons absorb the energy and are temporarily excited to a higher energy state. The net magnetization rotates away from its equilibrium orientation due to the absorption of RF energy. After the radio frequency pulse is switched off, relaxation occurs in which the protons release the absorbed energy to the surroundings and return to their original configuration by two simultaneous events: the recovery of the net magnetization toward the equilibrium orientation and the dephasing of the transverse magnetization. The first case is termed as the spin-lattice or longitudinal (T_1) relaxation, and the latter is spin-spin or transverse (T_2) relaxation [35].

The T_1 relaxation time is defined as the time taken for the longitudinal magnetization to recover approximately 63 % of its initial value after being flipped into the magnetic transverse plane by a 90° radiofrequency pulse. This recovery of

magnetization follows an exponential growth process, with T_1 being the time constant describing the rate of growth:

$$M(t) = M_0\left(1 - e^{(-t/T1)}\right) \tag{3.1}$$

where t is the time following the RF pulse.

The T_2 relaxation time is defined as time taken for the magnetic resonance signal to irreversibly decay to 37 % of its initial value after its generation by tipping the longitudinal magnetization toward the magnetic transverse plane. The decay of the transverse magnetization follows an exponential process with the time constant of T_2:

$$\mathbf{M}_{\mathbf{X-Y}}(t) = \mathbf{M}_0\, \mathrm{e}^{(-t/T2)} \tag{3.2}$$

where t is the amount of time following a radio frequency pulse and T_2 is the transverse relaxation time. Since the main magnetic field of MRI scanners is not perfectly homogenous, the inhomogeneity of the magnetic field also causes dephasing of individual magnetizations of protons, resulting in more rapid loss of transverse magnetization. The process is called T_2* relaxation.

T_2 relaxation generally proceeds more rapidly than T_1 recovery. Different tissues have different T_2 and T_1 relaxation times, which is the base for MRI.

MRI measures the magnetic relaxation properties of protons, but this requires excitation by radiofrequency. Radiofrequency waves have wavelengths on the order of one centimeter and can penetrate deep into the body. Therefore, MRI has no limitation for tissue penetration [36]. Moreover, compared to PET and SPECT, MRI does not use ionizing radiation and offers higher resolution and soft tissue contrast. In addition, MRI allows for multiparametric imaging in which T_1–, T_2–, and diffusion-weighted images (DWI) are obtained in one session, each reflecting a different tissue signal [37]. Clinically, multiparametric imaging combining DWI with anatomical T_1-weighted imaging dramatically increased specificity and accuracy of bone metastases detection in patients with lung cancer compared to DWI alone [38]. Similarly, the combination of DWI/T_2-weighted imaging dramatically improved the sensitivity and specificity of DWI in the detection of abdominal malignancies including prostate cancer [37, 39]. Recent advances in whole-body diffusion-weighted imaging show promise for diagnosing lesions throughout the entire human body as well as for assessing lymph node metastases, with superior spatial resolution and sensitivity and specificity [37]. Furthermore, MR spectroscopy can be used to assess tumor pH and metabolic activity [40]. When combined with MRI, the functional and molecular information can be coregistered with anatomical information within a single imaging method, which would improve the diagnostic specificity of malignant cancers. These advantages make MRI highly desirable for molecular imaging. However, the sensitivity for detection of targeting agents is relatively low. Therefore, high sensitivity and specificity of the imaging probes for the targets are often necessary for successful detection of tumor angiogenesis. The comparison of different noninvasive imaging modalities is shown in Table 3.1 [42].

Table 3.1 Characteristics of noninvasive imaging modalities [15, 41]

Imaging technique	Positron emission tomography (PET)	Single-photon emission computed tomography (SPECT)	Magnetic resonance imaging (MRI)	Ultrasound (US)	Optical imaging (OI)	Computerized tomography (CT)
Detection	High-energy γ-rays	Lower-energy γ-rays	Radio waves	High-frequency sound	Visible light and infrared	X-ray
Resolution	1–2 mm	1–2 mm	10–100 μm	50 μm	2–5 mm	50–200 μm
Depth	No limit	No limit	No limit	mm–cm	1–2 cm	No limit
Time	Minutes to hours	Minutes to hours	Minutes to hours	Seconds to minutes	Seconds to minutes	Seconds to minutes
Sensitivity	10^{-11}–10^{-12} M	10^{-10}–10^{-11} M	10^{-3}–10^{-5} M	Not well characterized	10^{-9}–10^{-12} M	10^{-3}–10^{-5} M
Imaging agents	^{18}F-, ^{64}Cu-, ^{11}C-labeled compounds	^{99m}Tc- or ^{111}In-labeled compounds	Paramagnetic chelates, magnetic particles	Microbubbles	Fluorophores	Heavy atom containing contrast agents, for example, iodine, barium, and gadolinium salts
Target	Physiological, molecular	Physiological, molecular	Anatomical, physiological, molecular	Anatomical, physiological	Physiological, molecular	Anatomical, physiological, molecular
Quantitative	Yes	Yes	No	Yes	Yes	Yes

3.4 MRI Contrast Agents

MRI is widely used for clinical examination, and currently, about 40 % examinations are performed using contrast agents. MRI contrast agents can generally be classified into two categories: T_1 contrast agent (shortening T_1 relaxation time) and T_2 contrast agent (shortening T_2 relaxation time). Gadolinium (III) ion-based contrast agents are typically T_1 contrast agent and most widely used clinically so far. The Gd(III) ion has seven unpaired electrons and favorable electronic spin relaxation properties that make for very efficient catalysis of water proton relaxation. To reduce cytotoxicity, Gd(III) ion is often chelated to a low-molecular weight complex, such as DOTA and DTPA [43]. Such gadolinium complexes are injected intravenously, and most will distribute rapidly into all accessible extracellular spaces and are eliminated from the body through the kidneys with a typical elimination half-life of about 1.6 h. Therefore, small molecular gadolinium chelates are often used as extracellular contrast agent with short imaging window. To elongate the circulation time, gadolinium complexes are usually conjugated to naturally or synthesized high molecular weight polymers, which are often used as blood pool contrast agents for MRI angiography. The gadolinium-based contrast agents typically are used in combination with T_1-weighted MRI acquisitions and produce a hyperintense (bright) signal in tissue regions in which the agent accumulates.

The contrast agent to enhance the relaxation rates of surrounding water protons is linearly correlated to its concentration:

$$\frac{1}{T_{1,2}} = \frac{1}{T_0} + \mathrm{r}_{1,2}\mathrm{C} \tag{3.3}$$

where $1/T_{1,2}$ is the relaxation rate of water protons with contrast agents; $1/T_0$ is the relaxation rate of water protons; $r_{1,2}$ is the relaxivity of contrast agents, i.e., longitudinal r_1 or transverse r_2; and C is the concentration of contrast agents. The term $r_{1,2}$ is expressed as per second per millimole liter and is characteristic of the contrast agent efficacy.

Superparamagnetic iron oxide (SPIO) nanoparticles are commonly used as T_2 contrast agent. Typically, SPIO contrast agents consist of SPIO core and hydrophilic coating layer. For commercially available SPIO contrast agents, SPIO cores are composed of magnetite (Fe_3O_4) and/or maghemite (Fe_2O_3) and the coating layers are dextran or its derivatives [44]. Due to its high magnetic susceptibility, SPIO can dephase neighboring protons in a region equivalent to many times the size of the particle itself [45]. Compared with gadolinium contrast agents, SPIO has excellent relaxivity. However, unlike the gadolinium contrast agents, which have similar transverse and longitudinal relaxivities at clinically relevant magnetic fields, SPIO has significantly greater transverse relaxivity compared with longitudinal relaxivity. Thus, SPIO tends to find greater application on magnetic susceptibility-based acquisitions in T_2-weighted or T_2*-weighted MRI, in which they produce a hypointense (dark) signal [46].

SPIO contrast agents are more biocompatible than gadolinium contrast agents because the human blood is rich in iron species, which are mostly stored as ferritin in the body [47, 48]. SPIO can also produce positive contrast when the particles are relatively small. Very small superparamagnetic iron oxide nanoparticles (VSOP) about 4 nm in size coated with citric acid have been developed for angiography (VSOP-C184, 0.47 T: $r_1 = 18.7$ and $r_2 = 30$ $s^{-1}mM^{-1}$) [49, 50]. Kim et al. synthesized extremely small iron oxide nanoparticles (ESIONs, around 3 nm), which exhibited a high r_1 relaxivity (4.78 $s^{-1}mM^{-1}$) and low r_2/r_1 ratio (6.12) at 3 T. They demonstrated that the ESIONs were an efficient T_1 contrast agent both in vitro and in vivo [51]. Borase et al. prepared galactose-coated SPIO about 8.3 nm in size. The SPIO had an r_1 relaxivity of 16 $s^{-1}mM^{-1}$ and an r_2 relaxivity of 62 $s^{-1}mM^{-1}$ at the typical clinical frequency of 61 MHz (1.5 T) [52]. We recently developed zwitterionic-polymer-modified SPIO with a core size of around 6 nm. The particles had an r_1 relaxivity of 8.98 $s^{-1}mM^{-1}$ at 1.41 T (60 MHz) and demonstrated superior blood pool contrast [53]. Small-sized SPIO are potential MRI T_1 contrast agents.

3.5 MR Molecular Imaging of Tumor Angiogenesis by Targeting Integrin αvβ3

3.5.1 Imaging with Gd(III)-Containing Contrast Agents

By far, the most widely used MRI contrast agents are those based on the paramagnetic gadolinium [Gd(III)] ion. The Gd(III) ion is chelated to low-molecular weight ligands, such as diethylenetriamine pentaacetic acid (DTPA) and 1,4,7,10-tetraazacyclododecane-1,4,7,10-tetraacetic acid (DOTA), to reduce toxicity [43]. Although binding of few gadolinium complexes to angiogenic targets does usually not provide sufficiently high signal-to-noise ratio, efforts to targeted MR imaging of tumor angiogenesis with RGD peptide directly conjugated Gd complexes (i.e., Gd-DOTA, Gd-DTPA) were successful [54, 55].

Deberbh et al. evaluated the efficiency of P1227 (Guerbet Research, Paris, France), RGD peptide-coupled gadolinium-tetraazacyclododecane tetraacetic acid (Gd-DOTA), for specific MR imaging of tumor associate angiogenesis [55]. After being introduced into mice bearing HT29 human colorectal tumors intravenously, MR signal intensity in tumor rim was significantly enhanced compared with mice injected with Gd-DOTA (Fig. 3.1). However, the enhancement was able to be suppressed by cilengitide, αvβ3 inhibitor. In addition, when using P1227, a significant correlation was observed between normalized enhancement of the tumor rim and immunohistochemical αvβ3 integrin expression. Although RGD peptide directly coupled Gd complex could address tumor angiogenic vessels, the main limitation of the contrast agent is low MRI sensitivity, which may prohibit early detection of cancers.

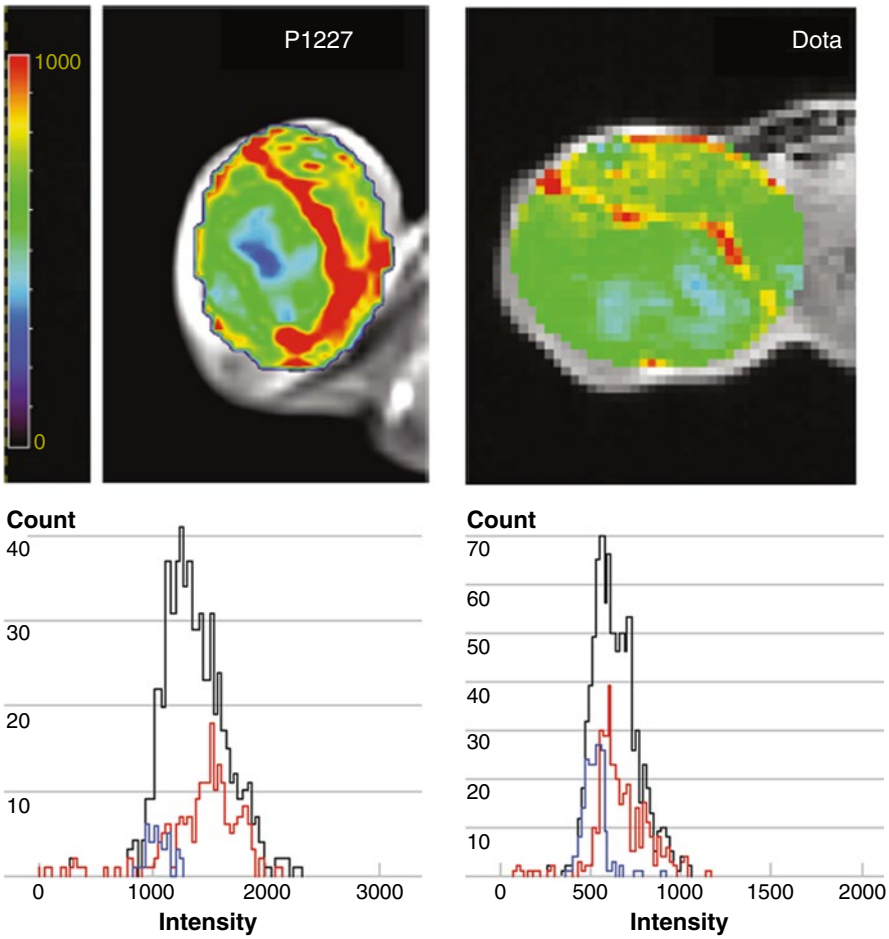

Fig. 3.1 Enhancement pattern observed following administration of P1227 (*upper left*) or gadolinium-tetraazacyclododecane tetraacetic acid (*upper right*). The histograms (*lower row*) show frequency of signal intensities in the entire tumor (*black*), central (core) region (*blue*), and tumor rim (*red*) (Reprinted with permission from Ref. [55], with kind permission from Springer Science + Business Media)

In order to enhance the detection sensitivity, gadolinium complexes are very often loaded onto nanocarriers. By this way, initial efforts to specifically visualize angiogenic targets were successful. The first MRI approach for imaging αvβ3 expression on tumor angiogenesis was demonstrated by Sipkins et al. [56]. In this seminal study, cross-linked liposomes with high payload of gadolinium (containing 30 % of Gd(III) chelate-labeled lipid) and mean size of 300–350 nm were conjugated with anti-integrin αvβ3 antibody (LM609). After administration into rabbits with squamous cell carcinoma (Vx2) intravenously, the "hot spots" of tumor angio-

genesis were able to be detected by MRI. Moreover, MR signal intensity enhancement correlated well with integrin αvβ3 expression levels.

Lanza et al. have developed a highly MRI-sensitive nanosystem that has a perfluorocarbon core covered with a monolayer of lipids [57]. Paramagnetic lipids (e.g., gadolinium-diethylenetriamine pentaacetic acid-*bis*-oleate) were incorporated into the lipid monolayer for detection with MR imaging. After conjugation with peptidomimetic αvβ3 antagonist, the paramagnetic perfluorocarbon nanoparticles were tried for tumor angiogenesis detection with a clinical 1.5 T MRI scanner [58]. Dynamic imaging indicated that MR signal enhancement continued to build over at least 2 h after the probe injection, while the background blood pool effects were nondetectable. Despite the relatively large diameter of approximate 270 nm, the probes penetrated into the leaky tumor neovasculature but did not migrate into the interstitium substantially. In a following study, the same group extended these results and demonstrated that nude mice with human melanoma tumor xenograft (C-32) with size about 30 mm^3 could also be detected with a clinical 1.5 T MRI scanner using the same integrin αvβ3-targeted paramagnetic nanoparticles [59], which may enable characterizing and staging of early melanoma in a clinical setting (Fig. 3.2) [60].

Other endeavors for improving MR sensitivity for tumor angiogenesis imaging include developing of gadolinium containing micelles, liposomes (a spherical vesicle composed of a bilayer of naturally occurring phospholipids), or high-density lipoprotein like nanoparticles [61]. These nanoconstructs can enable detection in the picomolar range (particle concentration) and, therefore, enable visualization with MR imaging of sparse binding sites [62]. Strijkers et al. have introduced a paramagnetic liposome, which consisted of DSPE, PEG2000-DSPE, maleimide-PEG2000-DSPE, cholesterol, and 25 mol % Gd-DTPA-di(stearylamide) [63]. The presence of this high payload of Gd-containing lipids ensures a high particulate relaxivity. In addition, the paramagnetic liposome was also encoded with 0.1 mol % rhodamine fluorescent lipids. The final size of the liposome was 150 nm. After conjugated with cyclic RGD peptides, the liposomal contrast agent (RGD-liposomes) was used to identify the angiogenic endothelium in tumor-bearing mice. MRI indicated that the RGD-liposomes localized to a large extent in the tumor rim after injected intravenously. Nonspecific liposomes, liposomes coupled with scramble RAD peptides (RAD liposomes), also targeted the tumor, but showed a diffuse distribution pattern (Fig. 3.3). The different mechanisms of accumulation were established with fluorescence microscopy, which revealed that RGD-liposomes were exclusively associated with tumor blood vessels, whereas RAD liposomes were mainly localized in the extravascular compartment (Fig. 3.4) [63].

The above integrin αvβ3-specific RGD-liposomes were also applied for noninvasive evaluation of the angiostatic therapy efficacy of anginex or endostatin for tumor by MRI [64]. The percentage of enhanced pixels in the tumor on T1-weighted MRI after injection with RGD-liposomes served as a noninvasive in vivo readout of angiogenic activity. It was found closely reflecting the treatment effects as deduced from the ex vivo analyses.

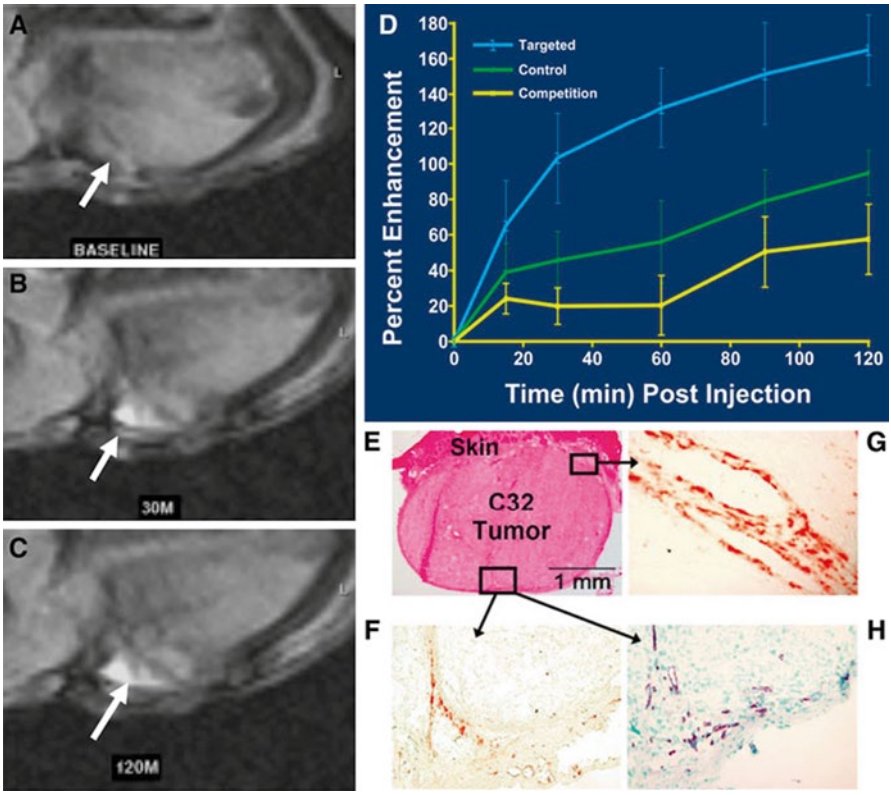

Fig. 3.2 T_1-weighted MR image (axial view, 1.5 T) of an athymic nude mouse before injection of αvβ3-targeted paramagnetic nanoparticles. (**a)** Baseline image of a C32 tumor that is difficult to detect. (**b**) 30-min postinjection. (**c**) 120-min postinjection. *White arrows* point to tumor in panels **a**, **b**, and **c**. Tumor diameter 2.5 mm. (**d**) Time course of MRI signal enhancement in tumor-bearing mice treated with αvβ3-targeted paramagnetic nanoparticles (*blue*), nontargeted contrast agent (*green*), or a competition procedure (*yellow*). T_1-weighted signal enhancement in the targeted group was nearly twice that in the control animals given the untargeted agent ($P < 0.05$). Competitive blockage of αvβ3-integrin sites greatly diminished contrast ($P < 0.05$). (**e**–**h**) Immunohistochemistry revealing endothelial cell location and angiogenic vessel αvβ3-integrin expression along the periphery of C32 tumors and associated with infiltrating connective tissue. (**e**) H&E (×4). (**f**) β3-integrin (×20). (**g**) β3-integrin (×60). (**h**) PECAM-1 (×20, nuclear counterstained) (Reprinted with permission from Ref.[60])

High-density lipoprotein (HDL), an endogenous nanoparticle, is compatible with the immune system and can escape removal by the reticuloendothelial system. HDL nanoparticles have been used as carriers for delivery of drugs to tumors and have also been rerouted for tumor imaging [65]. Chen et al. have reconstituted HDL (rHDL) with amphiphilic Gd-DTPA and fluorescent dye [66]. After modification with RGD peptides (rHDL-RGD), rHDL-RGD was applied for targeting integrin αvβ3 for depicting tumor angiogenesis. The hydrodynamic size of rHDL-RGD was 12.1 ± 2.1 nm, and the T_1 relaxivity was 8.7 ± 0.2 $mM^{-1}s^{-1}$, much higher than that of

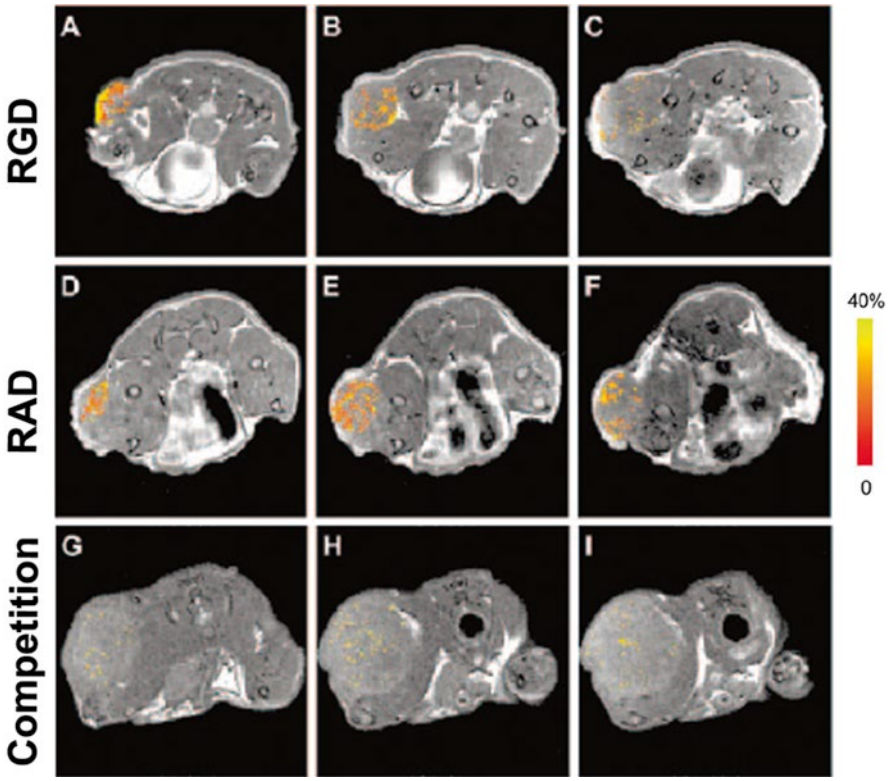

Fig. 3.3 In vivo visualization of tumor angiogenesis by application of αvβ3-targeted paramagnetic and fluorescent liposomes. (**a, b** and **c**) MR images of three slices through a mouse with a xenograft human LS174T colon carcinoma in a subcutaneous location on the right flank. The images were taken 35 min after injection of RGD-conjugated liposomes, which target the αvβ3 integrins expressed on the angiogenic tumor endothelium. Pixels in the tumor that were significantly enhanced by the presence of the paramagnetic liposomes were highlighted and color-coded according to the scale on the right. Enhancement was mainly found at the rim of the tumor in correspondence with the spatial distribution of angiogenic blood vessels. The percentage of enhanced pixels serves as a noninvasive readout of angiogenic activity. (**d, e** and **f**) MR images of a mouse 35 min after injection with nonspecific RAD-conjugated liposomes. Nonspecific liposomes distributed more evenly throughout the whole tumor. (**g, h** and **i**) MR images of a mouse 35 min after pretreatment with nonparamagnetic RGD-conjugated liposomes to block the αvβ3 integrin followed by injection with paramagnetic RGD-conjugated liposomes. Only a small number of pixels showed signal enhancement proving specificity of the αvβ3 targeting concept (Reprinted from Ref. [63], with kind permission from Springer Science + Business Media)

Gd-DTPA (Magnevist, ~3 $mM^{-1}s^{-1}$). The specificity of rHDL-RGD for integrin αvβ3 was demonstrated by incubating proliferating human umbilical vein endothelial cells (HUVECs, integrin αvβ3 positive) with rHDL-RGD or control (scramble peptide RAD encoded rHDL (rHDL-RAD) and plain rHDL). Both fluorescence imaging and MRI indicated that cell uptake of rHDL-RGD was more pronounced than those of rHDL-RAD and rHDL in short term (less than 2 h). Moreover, the

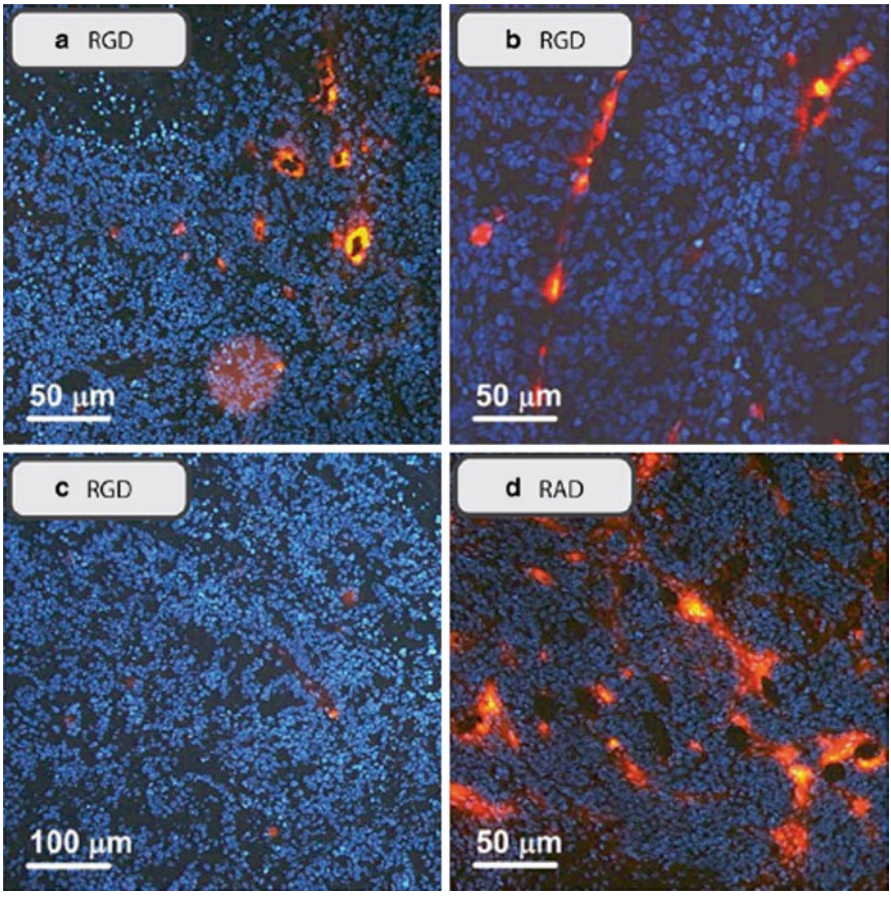

Fig. 3.4 Fluorescence microscopy of dissected tumors of mice, which were injected with paramagnetic, fluorescent, RGD- or RAD-conjugated liposomes. (**a, b**) In the rim of the tumors, the *red* rhodamine fluorescence originating from the RGD-conjugated liposomes revealed circular and longitudinal distribution patterns associated with blood vessels. Cell nuclei were stained with DAPI (*blue fluorescence*). (**c**) A slice through the middle of the tumor revealed no fluorescence from RGD-conjugated liposomes, in agreement with a lack of angiogenic blood vessels in this location. (**d**) A diffuse pattern of fluorescence was observed in tumors of mice injected with nonspecific RAD-conjugated liposomes, indicative for nonspecific distribution beyond the blood vessels throughout the whole tumor (Reprinted from Ref. [63], with kind permission from Springer Science + Business Media)

uptake could be inhibited upon competition with free RGD peptides. Introduced into mice bearing human EW7 Ewing's sarcoma intravenously, rHDL-RGD rapidly accumulated in tumors. Confocal microscopy revealed rHDL-RGD to be associated with tumor endothelial cells, while rHDL and rHDL-RAD were mainly found in the interstitial space. This study demonstrates HDL is a potent platform for preparing high-sensitivity molecular imaging probes for imaging of tumor-associated processes.

Monitoring progression of tumor neovasculature during tumor growth is essential for pretreatment stratification or to assess therapeutic response of antiangiogenesis therapy. In this regard, MRI has distinct advantages over other imaging modalities, such as PET, SPECT, and CT, due to its high-spatial-resolution imaging without ionizing radiation. In this context, vascular-constrained αvβ3-targeted perfluorocarbon (PFC) nanoparticles incorporating a lipid-modified gadolinium-diethylenetriamine pentaacetic acid (Gd-DTPA) bis-oleate (BOA) chelate (Gd-DTPA-BOA) or Gd-DOTA phosphatidylethanolamine (PE) chelate (Gd-DOTA-PE) has been prepared to assess the dependence of neovascular molecular magnetic resonance imaging on relaxivity (r_1) of αvβ3-targeted paramagnetic PFC nanoparticles and delineated the temporal-spatial evolution of angiogenesis for individual animals [67]. Using a Vx2 rabbit tumor model, it was found that MR signal intensity enhancement of the neovascular activation was better with the higher-relaxivity Gd-DOTA-PE nanoparticles (ionic $r_1 = 13.3$ mM^{-1} s^{-1}; particulate $r_1 = 1\ 260\ 000$ mM^{-1} s^{-1}) than with Gd-DTPA-BOA nanoparticles (ionic $r_1 = 10.3$ mM^{-1} s^{-1}; particulate $r_1 = 927\ 000$ mM^{-1} s^{-1}). A neovascular index of the tumor, calculated as the percentage of contrast-enhanced surface volume relative to the total surface volume and used as a metric of neovascularity, showed progression of MR imaging-detectable neovasculature of 1.0 % ± 0.3, 4.5 % ± 0.9, and 9.3 % ± 1.4 on post-implant days 8, 14, and 16, respectively; in comparison, the neovascular index for the nontargeted control was less than 1.5 % throughout the study (Fig. 3.5). This study indicated that high-spatial-resolution molecular MR imaging with improved relaxivity αvβ3-targeted Gd-DOTA-PE nanoparticles could provide quantitative, temporal, and spatially resolved assessments of tumor neovasculature, which has the potential to enable better detection of angiogenic regions in heterogeneous tumors and to improve the monitoring and individualization of anti-angiogenic treatments [68].

Besides the abovementioned paramagnetic formulations, various other Gd(III)-containing small or macromolecules have been developed for T1-weighted imaging of tumor angiogenesis [35].

3.5.2 Imaging with Superparamagnetic Iron Oxide (SPIO) Nanoparticles

SPIO is the most widely used T_2 (or T_2*) contrast agent in MRI [69]. A number of SPIO-based MRI contrast agents have already been used in the clinical setting [70]. We first reported MR imaging of tumor angiogenesis by RGD peptide-encoded SPIO (RGD-SPIO) with a clinical 1.5 T MRI scanner [71]. The SPIO was prepared by coprecipitation of Fe^{+2} and Fe^{+3} in the basic condition, modified with organic silane ((3-aminopropyl)trimethoxysilane) and c(RGDyE). The mean size of the particles as determined by TEM was 10 ± 3 nm. Surface charge of the particles was positive with isoelectric point at pH 9.6. T_2 relaxivity was 134 s^{-1} mM^{-1}. Compared

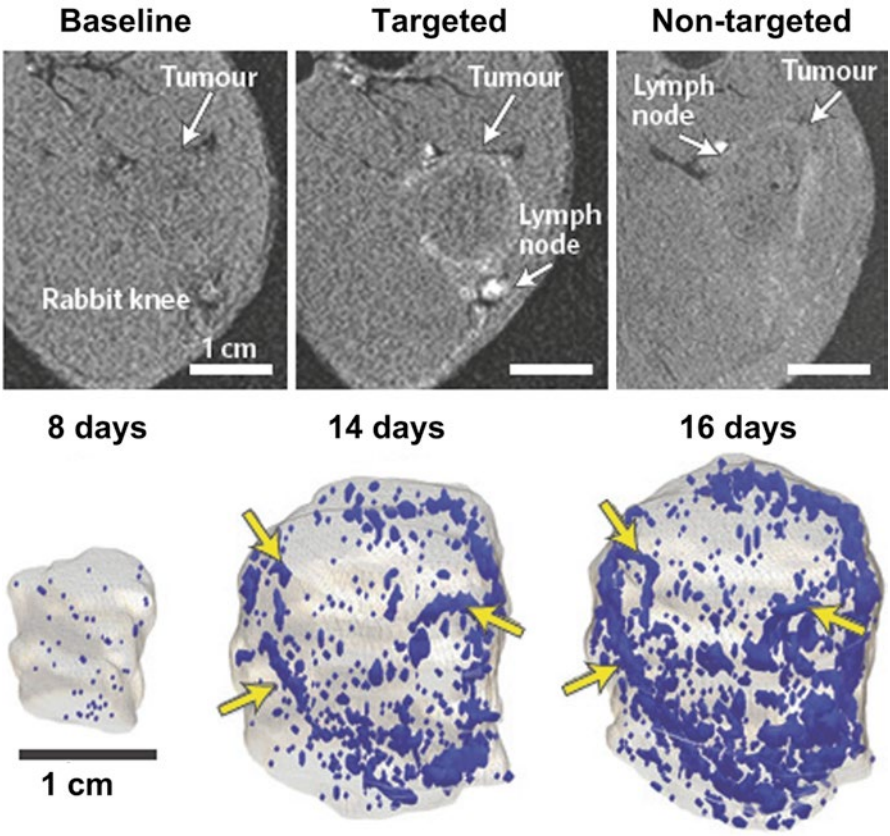

Fig. 3.5 In vivo T_1-weighted magnetic resonance images of angiogenic activity in VX2 tumors injected with αvβ3-targeted, paramagnetic perfluorocarbon nanoparticles in a rabbit model. *Top*: The outline of the tumor periphery is clearly seen with a targeted imaging agent, but not with non-targeted nanoparticles. *Bottom*: Neovascular maps show contrast-enhanced voxels over time. Angiogenic blood vessels markedly increased between days 8 and 14, with continued progression noted on day 16. Contrast-enhanced pixels are shown in *blue*. *Arrows* indicate examples of consistent enhancement patterns over time (Reprinted by permission from Macmillan Publishers Ltd: Ref. [67] Copyright 2014)

with plain SPIO, human umbilical vein endothelial cells (HUVECs, integrin αvβ3 positive) had a higher uptake of RGD-SPIO for both internalization through the cell membrane and accumulation within endosomes. Moreover, the uptake was reduced after inhibiting the cells with free RGD peptides, which verified the specificity of RGD-SPIO for integrin αvβ3. In line with the in vitro observations, after intravenous injection of RGD-SPIO into mice bearing squamous carcinoma (HaCaT-ras-A-5RT3 or A341), T_2*-weighted MR imaging identified the heterogeneous distribution of αvβ3-positive tumor vessels by an irregular signal intensity decrease in HaCaT-ras-A-5RT3 xenografts, whereas the signal intensity decreased more

homogeneously in the control tumors (A431) with predominantly small and uniformly distributed vessels (Fig. 3.6). This study indicated that integrin αvβ3-targeted SPIO was able to noninvasively differentiate tumors with high and lower area fractions of αvβ3-positive tumor vessels.

In an extended study, the same RGD-SPIO was applied for detection of tumor angiogenesis with different αvβ3 expression profiles by a 3 T MRI scanner [72]. R_2* pseudo-color images revealed that A549 tumor, a lung tumor with αvβ3 expression on both tumor cells and tumor angiogenic vessels, had homogenous signal intensity decrease throughout the whole tumor area, whereas MR signal intensity decrease in 3LL tumors, a lung tumor with αvβ3 expression only on tumor angiogenic vessels, was only distributed on the tumor periphery. The authors concluded that in addition to targeting tumor angiogenic vessels, RGD-SPIO could also extravasate from the vessels, addressing αvβ3-positive tumor cells.

For preparation of water-soluble SPIO, the coprecipitation method often leads to SPIO with poorly defined nanocrystalline size, stoichiochemistry, and magnetism, which in turn influence the quality of MR signals [73]. Alternatively, high-quality, near-monodisperse SPIO can be prepared by thermal decomposition of iron organic precursors, such as $Fe(acac)_3$, $Fe(CO)_3$, and $Fe(oleic\ acid)_3$, at high temperature in the presence of surfactants (oleic acid and oleylamine) [74, 75]. However, these SPIO cannot be biofunctionalized as they are coated with hydrophobic surfactants and are water insoluble and do not have suitable functional groups for bioconjugation. In this context, Xu et al. have developed a general strategy to fabricate an MR molecular imaging probe in one step by replacing hydrophobic surfactants with small peptides terminated with cysteine, such as RGD-Cys and RGD-PEG-Cys [76]. The hydrodynamic sizes of RGD-Cys- and RGD-PEG-Cys-SPIO were 11 and 13 nm, respectively. The in vitro studies indicated that RGD-Cys-SPIO and RGD-PEG-Cys-SPIO specifically targeted αvβ3-positive cells (A549), with RGD-Cys-SPIO achieving this more efficiently. Administered into mice bearing A549 non-small cell lung tumor intravenously, both RGD functionalized SPIOs were able to reach and label the αvβ3-expressing tumors, much more efficiently than nonpeptide functionalized particles (Cys-SPIO). Histological studies of tumor tissues showed that the probes not only targeted the tumor neovasculatures but also extravasated from vessels, addressing the tumor cells. The efficacy of the ligand exchange method for preparation of small peptide modified SPIO probes was also corroborated by other study [77]. This one-step procedure for preparation of the probe was shown in Fig. 3.7.

Sensitive molecular imaging and detection of tumors or their supporting neovascularity require high-avidity, target-specific probes that produce robust signal amplification. Clustering individual SPIO into SPIO clusters can dramatically enhance the MR sensitivity of SPIO contrast agent [78–80], which makes it possible for detection of tumor angiogenesis at very early stage [81]. In this context, Nasongkla et al. [82] developed multifunctional, SPIO-containing polymeric micelles by assembly of hydrophobic SPIO with amphiphilic copolymers and further modified the micelles with RGD peptides (c(RGDfK)) for detection of integrin αvβ3. The mean size of the micelles was 46 nm. Clustering of individual SPIO

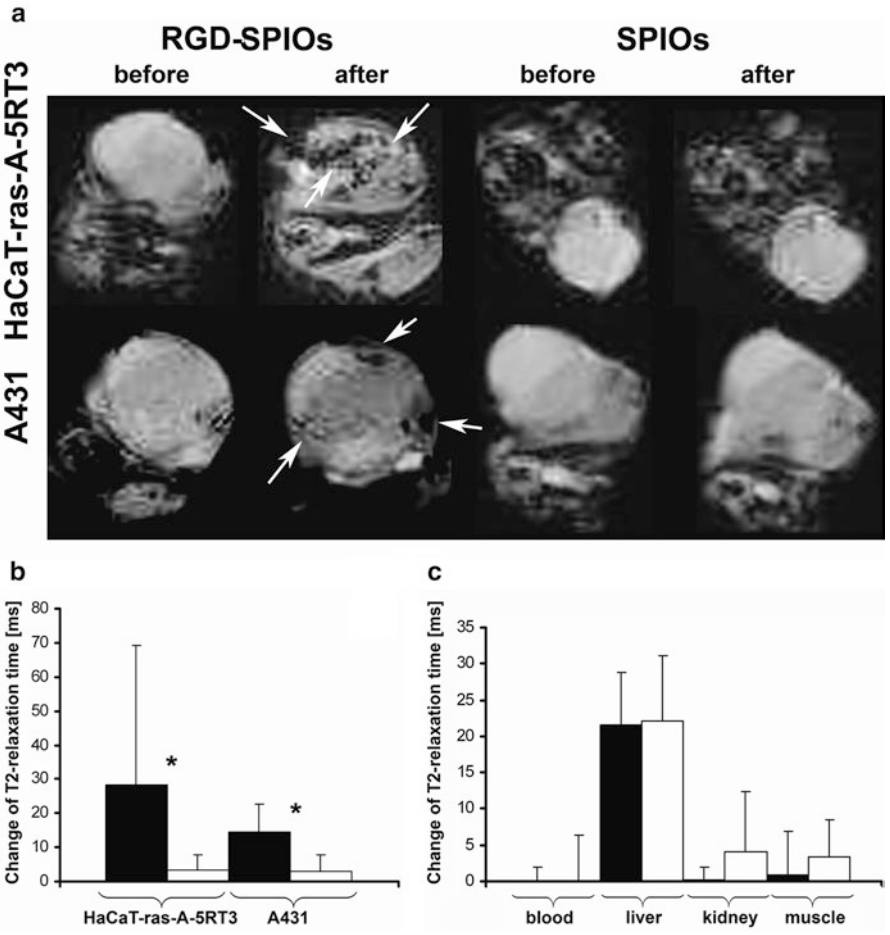

Fig. 3.6 MR imaging of tumors with different αvβ3 expression profiles. (**a**) T_2*-weighted MR images of nude mice bearing s.c. HaCaT-ras-A-5RT3 (*top row*) and A431 tumors (*bottom row*) before and 6 h after i.v. injection of RGD-SPIOs and SPIOs, respectively. In HaCaT-ras-A-5RT3 tumors, focal areas with strong and heterogeneous signal intensity (SI) decrease are observed in the tumor center and periphery after injection of RGD-SPIOs (*arrows*). Only few spots with high susceptibility are found at the margin of the control tumor after injection of SPIOs. SI changes in the A431 tumor are much less pronounced and more homogeneous and focal areas with strong SI decrease are only found at the tumor margins (*arrows*). No signal changes are observed in control tumors by visual inspection. (**b**) Change of T_2 relaxation times in HaCaT-ras-A-5RT3 ($n=8$) and A431 ($n=6$) tumors after injection of RGD-SPIOs and SPIOs, respectively. Absolute T_2 relaxation times before/after injection with RGD-SPIOs were $124.44 \pm 55.09/94.09 \pm 17.12$ ms in HaCaT-ras-A-5RT3 and $105.66 \pm 10.67/90.16 \pm 7.84$ ms in A431 tumors. The values for injection with SPIOs were $95.97 \pm 16.97/93.74 \pm 15.86$ ms (HaCaT-ras-A-5RT3) and $106.47 \pm 13.16/101.46 \pm 13.28$ ms (A431 tumors), respectively. *, $P<0.05$. (**c**) Change of T_2 relaxation times in the blood, liver, kidney, and muscle of A431 tumor-bearing mice after injection of RGD-SPIOs ($n=6$) and SPIOs ($n=6$), respectively. Absolute T_2 relaxation times (FSD) before/after injection of RGD-SPIOs were $101.8 \pm 17.58/101.76 \pm 17.77$ ms in the blood, $53.06 \pm 3.81/31.56 \pm 5.54$ ms in the liver, $90.53 \pm 10.05/90.4 \pm 8.60$ ms in the kidney, and $51.33 \pm 8.88/50.40 \pm 5.11$ ms in the muscle. For SPIOs, the values were $77.26 \pm 15.73/79.28 \pm 10.90$ ms in the blood, $56.66 \pm 7.90/37.33 \pm 4.43$ ms in the liver, $82.26 \pm 17.37/70.90 \pm 17.36$ ms in the kidney, and $50.40 \pm 5.68/46.04 \pm 3.78$ ms in the muscle. Columns, mean; bars, SD (Reprinted with permission from Ref. [71] Copyright 2007, American Association for Cancer Research)

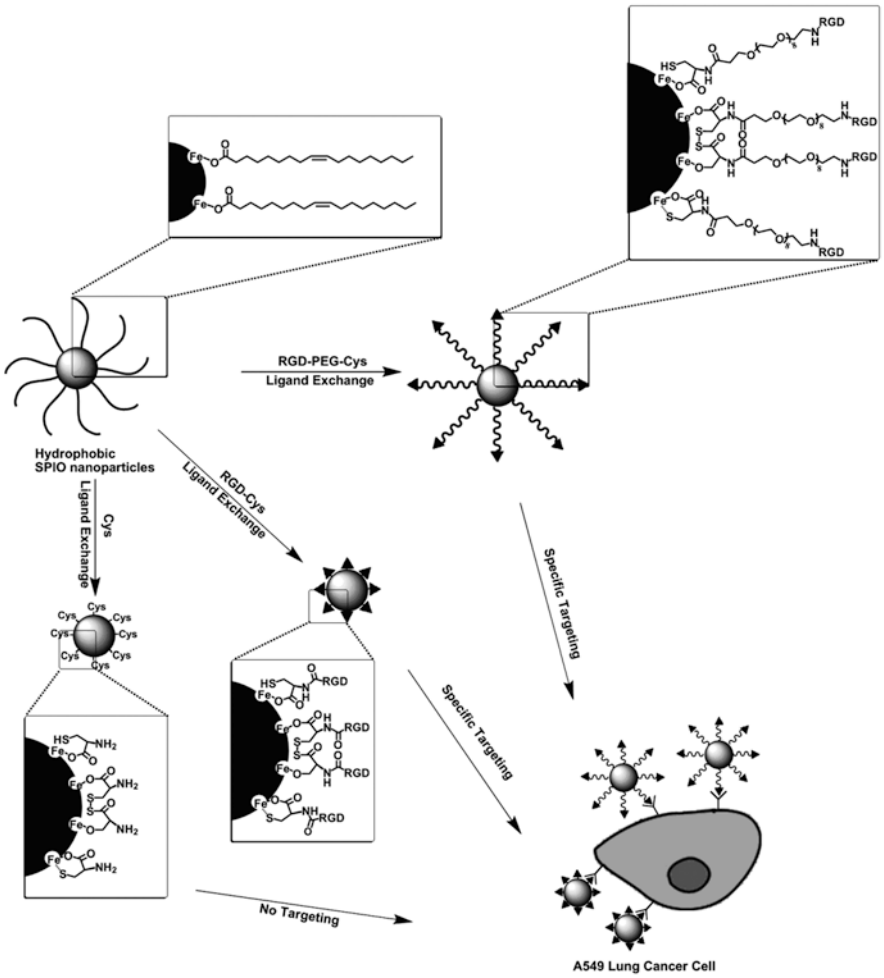

Fig. 3.7 Scheme for one-step ligand exchange method for preparation of αvβ3-targeted probes (Reproduced from Ref. [77] by permission of The Royal Society of Chemistry)

inside micelle cores has demonstrated the dramatic increase in T_2 relaxivity (per Fe). As a result, in a phantom study, picogram concentrations of the micelles were detected [83]. In a following study, the same group has fabricated SPIO micelles with even higher SPIO payload (33 wt %) using amphiphilic poly(ethylene glycol)-block-poly(D,L-lactide) copolymer (PEG-PLA, molecular weights for PEG and PLA blocks are 5 kDa) and hydrophobic SPIO (9.9 ± 0.4 nm in diameter). The size of the micelles was 75 ± 11 nm determined by transmission electron microscope (TEM). After encoded with cyclic(RGDfC) peptides (denoted as cRGD-encoded SPPM), the micelles were administered into mice bearing A549 non-small cell lung tumors. The neovasculatures of the tumors were clearly manifested by a 4.7 T ani-

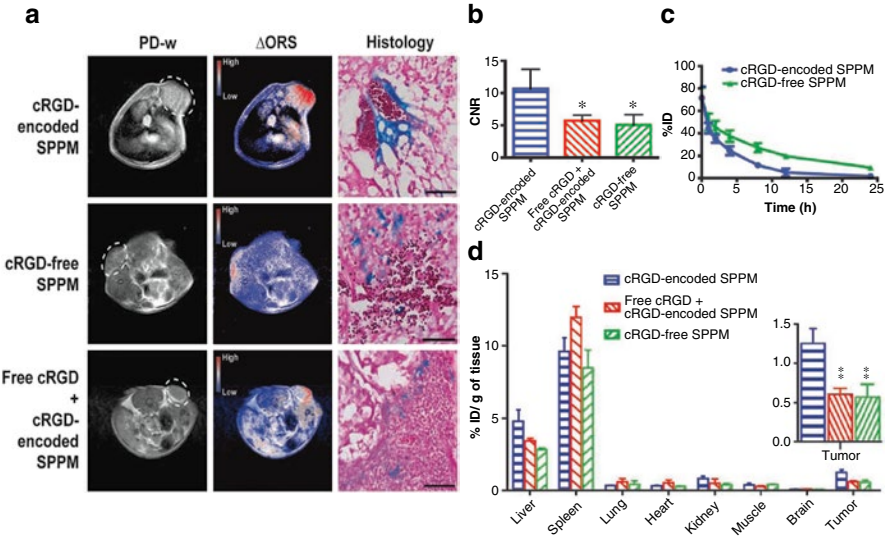

Fig. 3.8 (**a**) In vivo ORS imaging of cRGD-encoded SPPM, cRGD-free SPPM, and a mixture of cRGD-encoded SPPM with free cRGD peptide injected i.v. in mice bearing A549 tumor xenografts (6 mg Fe/kg). The ΔORS images showed more accumulation of cRGD-encoded SPPM in A549 tumor xenograft than cRGD-free SPPM and cRGD-encoded SPPM co-injected with free cRGD peptide (18 molar excess). The same phase LUT scale was used in all three ΔORS images for direct contrast comparison. The proton density-weighted (PD-w) images were acquired by a SE sequence (TR = 2 s, TE = 9 ms). Histological sections by *Prussian blue staining* showed Fe presence from SPPM samples in tumor tissues. The scale bars are 50 μm in all three images. (**b**) Comparisons of contrast-to-noise ratio (CNRs) of ΔORS images of A549 tumor xenograft ($n = 4$) injected with cRGD-encoded SPPM, cRGD-free SPPM, and a mixture of cRGD-encoded SPPM with free cRGD peptide (18 molar excess), respectively. (**c**) Plasma concentration versus time relationships ($n = 4$ for each SPPM group) for cRGD-encoded SPPM and cRGD-free SPPM. (**d**) Biodistribution profiles ($n = 3$) of different SPPM formulations (cRGD-encoded SPPM, cRGD-free SPPM, and cRGD-encoded SPPM co-injected with free cRGD) 1 h after i.v. administration. The asterisks (* in B and ** in D, inset) indicate statistical significance ($P \leq 0.05$) between the SPPM group of interest and cRGD-encoded SPPM based on the Student's *t* test (Reprinted with permission from Ref. [84] Copyright 2009, American Association for Cancer Research)

mal MRI scanner, and the imaging efficacy was further enhanced by an off-resonance saturation (ORS) technique (Fig. 3.8) [84]. Tumor accumulation of cRGD-encoded SPPM was corroborated by biodistribution study, which indicated that tumor uptake of cRGD-encoded SPPM (1.3 ± 0.3 % ID/g) was significantly higher than that of cRGD-free SPPM (0.6 ± 0.3 % ID/g). However, most of the micelles were sequestered by the spleen (~10 % ID/g) and liver (~4 % ID/g). Plasma clearance of the micelles showed a two-phase behavior over 24 h. The plasma half-lives for the initial phase were 0.34 ± 0.09 h for cRGD-encoded SPPM and 0.40 ± 0.34 h for cRGD-free SPPM. Those for the slow clearance phase were 3.9 ± 0.8 h and 9.2 ± 0.8 h for the cRGD-encoded and cRGD-free SPPM, respectively (Fig. 3.8).

Recently, we fabricated high MR-sensitive SPIO cluster probes specific for tumor angiogenesis with the similar approach: assembling hydrophobic SPIO with

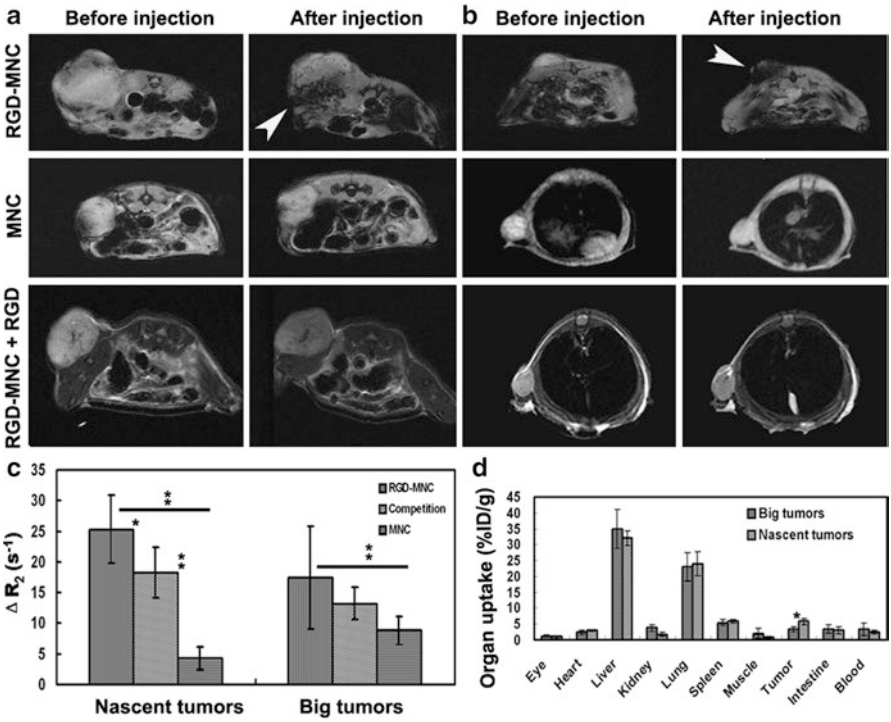

Fig. 3.9 MR detection of tumors with RGD-MNC and its biodistribution. (**a**, **b**) T_2-weighted MR images of big tumors (**a**) and nascent tumors (**b**) before and after intravenous injection of RGD-MNC, MNC, or RGD-MNC plus free RGD peptide at the dose of 200 μmol Fe/kg. For competition study, free RGD peptide (100 μL, 0.15 mM) was injected 1 h before RGD-MNC administration. (**c**) The corresponding T_2 relaxation rate changes of tumors after and before probe injection, $*p<0.05$, $**p<0.01$. (**d**) Biodistribution of iodine-125 labeled RGD-MNC in nascent and big tumor groups 12 h post injection (Reprinted from Ref. [81] Copyright 2012, with permission from Elsevier)

amphiphilic PEG-PLA copolymers into clusters and subsequently conjugating c(RGDyC) peptide onto the clusters (RGD-MNCs) for detection of nascent tumors [81]. As-synthesized RGD-MNCs were pretty monodispersed with size about 62 nm, highly sensitive ($r_2=464.94\ s^{-1}mM^{-1}$), and specific for αvβ3 positive cells. After introduced into mice bearing H1299 lung tumors at different growth stages intravenously, both nascent ($35\pm6.6\ mm^3$) and big tumors ($256\pm22.3\ mm^3$) were registered by RGD-MNCs and detected by a clinical MRI (3 T) scanner, with the nascent tumors demonstrating more pronounced MR contrast (Fig. 3.9). Consistent with MRI findings, biodistribution studies indicated that accumulation of RGD-MNCs by nascent tumors was more significant than that by large ones (5.83 ± 1.01 %ID/g vs 3.42 ± 0.93 %ID/g, $P<0.05$). However, the uptake by the liver (32.05 ± 2.31%ID/g for nascent tumors, 35.21 ± 6.10 %ID/g for large tumors) and uptake by the lung (24.66 ± 3.78 %ID/g for nascent tumors, 23.01 ± 4.51 %ID/g for

large tumors) were dominant for both tumor groups. Immunohistochemical studies revealed that MR signal decrease was closely correlated with the histological characteristics of tumors (i.e., microvessel densities and αvβ3 expression levels) at different growth stages. This study demonstrated that MR molecular imaging with highly sensitive RGD-MNC probes presented a significant opportunity for early detection of tumors and possible characterization of tumor angiogenesis at different tumor growth stages.

More significantly, due to the high avidity of RGD-MNC probes for αvβ3 integrin, the probes were internalized by endothelial cells in tumor angiogenic vasculature after accumulating in tumor, which enhanced X-ray absorption contrast of tumor angiogenic vessels significantly. As a result, angiogenic hot spots in tumors and even the individual angiogenic vessels can be observed by a high-resolution preclinical CT (Fig. 3.10) [85].

SPIO is conventional T_2 contrast agent. However, when the particles are relatively small, SPIO can also produce positive contrast and be used as T_1 contrast agent. We recently developed ultrasmall superparamagnetic iron oxide nanoparticles, about 3.5 nm in size with good T_1 ($r_1 = 8.2\ s^{-1}\ Mm^{-1}$) and reasonable T_2 contrast effects ($r_2 = 20.1\ s^{-1}\ mM^{-1}$) by the polyol method. The particles were functionalized using c(RGDyC) peptides and labeled with 99mTc (Tc-USPION-RGD) to prepare molecular imaging probes for detecting tumor angiogenesis [86], which could specifically target αvβ3-positive cells, inducing more cell ingestion, unlike that in the case of the control probes [functionalized with scrambled c(RADyC) peptides,

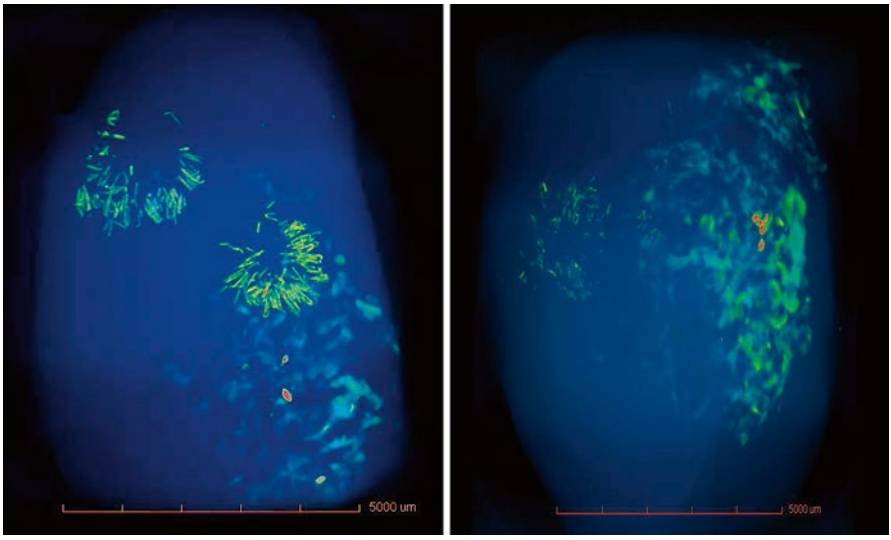

Fig. 3.10 Ex vivo micro-CT 3-D reconstruction of tumors. (**a**) Angiogenic hot spots in tumor were clearly manifested after injection with RGD-MNCs at the dose of 400 μmol Fe/kg (injection volume: 300 μL). (**b**) Mice injected with RAD-MNCs at the same dose. The tumor tissues were removed 48 h after the probe injection and fixed by formalin (our unpublished data)

Tc-USPION-RAD]. After the probes were injected into the mice bearing H1299 lung tumors, T_1/T_2-weighted magnetic resonance imaging and single-photon emission computed tomography revealed that they addressed tumor angiogenic vessels, which were distributed mainly in the peripheral region of tumors. Biodistribution studies indicated that tumor accumulation of the probes was significant [13.8 ± 9.6 %ID/g ($p < 0.01$), which is more than that of the control probes, 4.5 ± 1.9 %ID/g], and could be inhibited by free RGD peptides (6.0 ± 2.8 %ID/g, $p < 0.01$). This study demonstrated that the dual-contrast (T_1/T_2) magnetic resonance and dual-modal imaging probe based on ultrasmall superparamagnetic iron oxide nanoparticle are very promising for the molecular imaging of tumor angiogenesis.

3.5.3 *Imaging with Dual-Targeting Probes*

In order to further improve the specificity of MR molecular imaging probes for tumor angiogenesis, dual-targeting approach has been proposed [87]. Cyclic RGD peptide (RGD) and anginex (Anx), targeting integrin αvβ3 and Galectin-1, respectively, were simultaneously conjugated to paramagnetic liposomes (Anx/RGD-L). The size of the dual-targeting liposomes was about 200 nm. Compared with single-peptide-coupled liposomes, Anx-L or RGD-L, the specificity of Anx/RGD-L for activated endothelial cells was significantly improved both in vitro and in vivo due to the synergistic targeting effects of the two kinds of specific ligands [88]. However, because of its relatively short circulation time (half-life, less than 0.5 h for RGD/Anx-L and 11.2 ± 2.5 h for RGD-L), the targeting efficiency of RGD/Anx-L was 16 % less than that of RGD-L 24 h post injection. Inductively coupled plasma mass spectrometry (ICP-MS) measurements of the organ-associated Gd(III) 24 h post injection revealed significant differences in the contrast agent biodistribution. Anx/RGD-L or Anx-L had similar tumor Gd levels of 2.5 ± 0.7 μg/g tissue, significantly lower than that found in tumors of mice that received RGD-L (18 ± 11 μg/g). However, the accumulation of both types of Anx-containing liposomes in the spleen was approximately 40 % higher compared to RGD-L, whereas the liver uptake was similar in all the cases.

3.5.4 *Biological Effects of RGD Peptide-Conjugated Probes on Tumor Cells*

The biological effects of integrin-specific probes on αvβ3-positive tumor cells or endothelial cells were less studied. Kiessling et al. have prepared 3-aminopropyltrimethoxysilane (APTMS)-coated SPIO. The particles were 10 ± 3 nm and positively charged. After functionalized with cyclic (RGDyK) peptides (RGD-SPIO), they found RGD-SPIO had differential effects on human

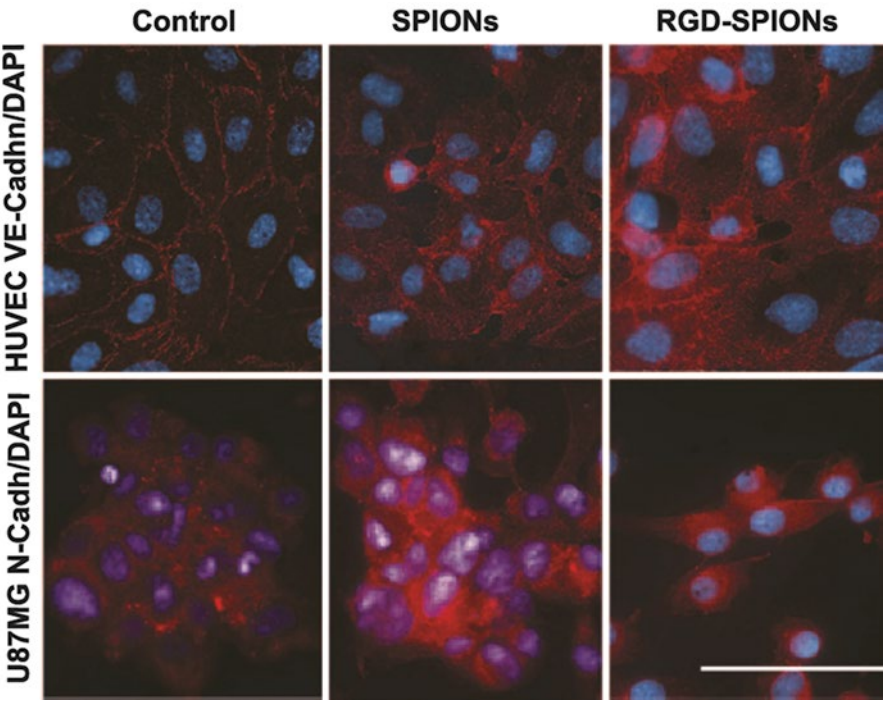

Fig. 3.11 Immunofluorescence microscopy of HUVECs and U87MG cells. Staining (*red*) was performed against VE-cadherin (*VE-Cadh)* (HUVEC) and N-cadherin *(N-Cadh.)* (U87MG) cells. Cell nuclei were stained with 4,6-diamidino-2-phenylindole *(DAPI)* (*blue*). In HUVECs incubated with regular growth medium containing SPIOs or not, VE-cadherin was located along the lateral cell membrane, which results in a netlike pattern of the cell monolayer at fluorescence microscopy. After RGD-SPIO incubation, this pattern is still present. However, an enhanced perinuclear staining also occurs. In U87MG cells incubated with regular growth medium in presence of SPIOs or not, intercellular contacts are more punctual. While N-cadherin is most strongly expressed at intercellular contact zones, it can be located in other parts of the plasma membrane and perinuclearly. After incubation with RGD-SPIOs, however, cells lose most of their intercellular contacts, round up, and separate from each other. Bar = 20 μm (Reprinted with permission from Ref. [89])

umbilical vein endothelial cells (HUVECs), ovarian carcinoma (MLS) cells, and glioblastoma (U87MG) cells [89]. RGD-SPIO induced U87MG cells turning round and loosing contacts from each other, which led to cell uptake of RGD-SPIO less than that of plain SPIO. However, RGD-SPIO had no such effects on HUVECs and MLS, and both kinds of cells internalized more RGD-SPIO than plain SPIO (Fig. 3.11). T_2*-weighted MR imaging indicated that tumors accumulated RGD-SPIO significantly more than plain SPIO. However, histological studies of tumor tissues identified RGD-SPIO mainly constrained on the tumor angiogenic vessels, not addressing tumor cells (U87MG). The authors ascribed this to the differential effects of RGD-SPIO on tumor cells and endothelial cells.

Kluza et al. have observed that liposomes functionalized with anti-αvβ3 integrin cyclic RGD peptide (RGD-L), anti-Galectin-1 anginex peptide (Anx-L), or both of them simultaneously (Anx/RGD-L) affected the proliferation of HUVECs and decreased the cell number both in S phase and G2/M phase, with Anx/RGD-L more significantly [87]. Based on these findings, they suggested that Anx/RGD-L could be used for therapeutic purpose. These studies demonstrate that if molecular imaging is performed for detection of tumor angiogenesis with αvβ3-targeted probes, biologic effects of the probes must be considered, which can be highly divergent between different cells and may lead to different targeting sites of the probes.

3.6 Summary and Future Perspectives

In this chapter, we summarized the advance in MR molecular imaging of tumor angiogenesis by targeting integrin αvβ3 with RGD peptide modified magnetic probes. For detection of the sparse angiogenic marker, the imaging probes evolved from paramagnetic nanoparticles to high sensitive SPIO, further to ultrahigh sensitive SPIO clusters. With SPIO cluster probes, nascent tumors could be detected, and MR signal changes were closely correlated with histological characteristics of tumors (i.e., microvessel densities and αvβ3 expression levels) at different growth stages. In order to further improve the detection specificity, dual-targeting approach, targeting two different angiogenic markers simultaneously, was also proposed. However, the pharmacokinetics of the probes must be carefully evaluated before application. In addition, more attentions should be paid on the biological effects of angiogenesis targeting probes on tumor cells, which may affect their ultimate targeting sites. Taking these results together, MR molecular imaging of angiogenesis for early detection of tumors is very promising. However, there is still a need for improvement of pharmacokinetics, specific binding, and signaling of the probes.

One disadvantage of MRI is its inherently low sensitivity to contrast agent [90]. Most efforts for improving the detection sensitivity are to enhance the sensitivity and specificity of imaging probes, and, as summarized above, tremendous progresses have been achieved in this direction. However, currently radionuclide-based imaging (i.e., SPECT and PET) is still the most sensitive and highly quantitative method [91]. Nevertheless, MRI can provide high-resolution anatomic information. Therefore, dual-modal imaging probes combining both MRI and radionuclide-based imaging properties in one unit should be of particular interest for tumor angiogenesis imaging. Especially, with the development of PET/MRI integrated system [92, 93] and its progression to clinical application [94], simultaneous acquisition of PET and MRI data is possible, which would create enormous possibilities and provide completely new opportunities to study pathology and biochemical processes in vivo. Therefore, PET/MRI contrast agents deserve much more research effort in this field in the near future.

Acknowledgments This work was supported by the National Natural Science Foundation of China (81230030, 81571729) and the Grants from the State Key Laboratory of Oncogenes and Related Genes (90-15-03).

References

1. Carmeliet P (2000) Mechanisms of angiogenesis and arteriogenesis. Nat Med 6:389–395
2. Folkman J (1972) Anti angiogenesis: new concept for therapy of solid tumours. Ann Surg 175:409–416
3. Weidner N, Semple JP, Welch WR, Folkman J (1991) Tumor angiogenesis and metastasis-correlation in invasive breast carcinoma. N Engl J Med 324:1–8
4. Chiang ACMJ (2008) Molecular basis of metastasis. N Engl J Med 359:2814–2823
5. Folkman J (1971) Tumor angiogenesis: therapeutic implications. N Engl J Med 285:1182–1186
6. Rundhaug JE (2005) Matrix metalloproteinases and angiogenesis. J Cell Mol Med 9:267–285
7. Yancopoulos GD, Davis S, Gale NW, Rudge JS, Wiegand SJ, Holash J (2000) Vascular-specific growth factors and blood vessel formation. Nature 407:242–248
8. Nussenbaum F, Herman IM (2010) Tumor angiogenesis: insights and innovations. J Oncol 2010:132641
9. Hagedorn M, Bikfalvi A (2000) Target molecules for antiangiogenic therapy: from basic research to clinical trials. Crit Rev Oncol Hematol 34:89–110
10. Folkman J, Klagsbrun M (2001) Angiogenic factors. Science 235:442–447
11. Auguste P, Lemiere S, Larrieu-Lahargue F (2005) Molecular mechanisms of tumor vascularization. Crit Rev Oncol Hematol 54(1):53–61
12. Ramjaun AR, Hodivala-Dilke K (2009) The role of cell adhesion pathways in angiogenesis. Int J Biochem Cell Biol 41:521–530
13. Francavilla C, Maddaluno L, Cavallaro U (2009) The functional role of cell adhesion molecules in tumor angiogenesis. Semin Cancer Biol 19:298–309
14. Snoeks TJA, Löwik CWGM, Kaijzel EL (2010) 'In vivo' optical approaches to angiogenesis imaging. Angiogenesis 13:135–147
15. Mahmoudi M, Serpooshan V, Laurent S (2011) Engineered nanoparticles for biomolecular imaging. Nanoscale 3:3007–3026
16. Ruoslahti E (1996) RGD and other recognition sequences for integrins. Annu Rev Cell Dev Biol 12:697–715
17. Cai W, Gambhir SS, Chen X (2005) Multimodality tumor imaging targeting integrin αvβ3. Biotechniques 39:S6–S17
18. Liu S (2009) Radiolabeled cyclic RGD peptides as integrin αvβ3-targeted radiotracers: maximizing binding affinity via bivalency. Bioconjug Chem 20(12):2199–2213
19. Danhier F, Breton AL, Préat V (2012) RGD-based strategies to target alpha(v) beta(3) integrin in cancer therapy and diagnosis. Mol Pharm 9:2961–2973
20. Hood JD, Cheresh DA (2002) Role of integrins in cell invasion and migration. Nat Rev Cancer 2:91–100
21. Brooks PC, Clark RAF, Cheresh DA (1994) Requirement of vascular integrin αvβ3 for angiogenesis. Science 264:569–571
22. Gladson CL (1996) Expression of integrin avb3 in small blood vessels of glioblastoma tumors. J Neuropathol Exp Neurol 55:1143–1149
23. Liu Z, Peng R (2010) Inorganic nanomaterials for tumor angiogenesis imaging. Eur J Nucl Med Mol Imaging 37(Suppl 1):S147–S163

24. Zhang Y, Yang Y, Cai W (2011) Multimodality imaging of integrin αvβ3 expression. Theranosttiics 1:135–148
25. Beer AJ, Schwaiger M (2008) Imaging of integrin αvβ3 expression. Cancer Metastasis Rev 27:631–644
26. Wernick MN, Aarsvold JN (2004) Emission tomography: the fundamentals of PET and SPECT. Academic, Orlando
27. Pichler BJ, Judenhofer MS, Pfannenberg C (2008) Multimodal imaging approaches: PET/CT and PET/MRI. Handb Exp Pharmacol 185:109–132
28. Blake P, Johnson B, VanMeter JW (2003) Positron emission tomography (PET) and single photon emission computed tomography (SPECT): clinical applications. J Neuroophthalmol 23:34–41
29. Contag CH (2007) In vivo pathology: seeing with molecular specificity and cellular resolution in the living body. Annu Rev Pathol 2:277–305
30. Kim HL (2009) Optical imaging in oncology. Urol Oncol 27:298–300
31. Deshpande N, Pysz MA, Willmann JK (2010) Molecular ultrasound assessment of tumor angiogenesis. Angiogenesis 13:175–188
32. James ML, Gambhir SS (2012) A molecular imaging primer: modalities, imaging agents, and applications. Physiol Rev 92:897–965
33. Levitt MH (2008) Spin dynamics: basics of nuclear magnetic resonance. Wiley, New York
34. Brown MA, Semelka RC (2003) MRI basic principles and applications, 3rd edn. Wiley, Hoboken
35. Tan M, Lu Z-R (2011) Integrin targeted MR imaging. Theranostics 1:83–101
36. Kobayashi H, Longmire MR, Ogawa M, Choyke PL (2011) Rational chemical design of the next generation of molecular imaging probes based on physics and biology: mixing modalities, colors and signals. Chem Soc Rev 40:4626–4648
37. Kwee TC, Takahara T, Ochiai R, Katahira K, Van Cauteren M, Imai Y, Nievelstein RA, Luijten PR (2009) Whole body diffusion-weighted magnetic resonance imaging. Eur J Radiol 70:409–417
38. Takenaka D, Ohno Y, Matsumoto K, Aoyama N, Onishi Y, Koyama H, Nogami M, Yoshikawa T, Matsumoto S, Sugimura K (2009) Detection of bone metastases in non-small cell lung cancer patients: comparison of whole-body diffusion-weighted imaging (DWI), whole-body MR imaging without and with DWI, whole-body FDG-PET/CT, and bone scintigraphy. J Magn Reson Imaging 30:298–308
39. Tsushima Y, Takano A, Taketomi-Takahashi A, Endo K (2007) Body diffusion-weighted MR imaging using high b-value for malignant tumor screening: usefulness and necessity of referring to T2-weighted images and creating fusion images. Acad Radiol 14:643–650
40. He Q, Xu RZ, Shkarin P, Pizzorno G, Lee-French CH, Rothman DL, Shungu DC, Shim H (2004) Magnetic resonance spectroscopic imaging of tumor metabolic markers for cancer diagnosis, metabolic phenotyping, and characterization of tumor microenvironment. Dis Markers 19(2–3):69–94
41. Weissleder R, Pittet MJ (2008) Imaging in the era of molecular oncology. Nature 452:580–589
42. Dobrucki LW, de Muinck ED, Lindner JR, Sinusas AJ (2010) Approaches to multimodality imaging of angiogenesis. J Nucl Med 51:66S–79S
43. Caravan P, Ellison JJ, McMurry TJ, Lauffer RB (1999) Gadolinium(III) chelates as MRI contrast agents: structure, dynamics, and applications. Chem Rev 99(9):2293–2352
44. Kiessling F, Mertens ME, Grimm J, Lammers T (2014) Nanoparticles for imaging: top or flop? Radiology 273(1):10–28
45. Kim BYS, Rutka JT, Chan WCW (2010) Nanomedicine. N Engl J Med 363:2434–2443
46. Weinstein JS, Varallyay CG, Dosa E, Gahramanov S, Hamilton B, Rooney WD, Muldoon LL, Neuwelt EA (2010) Superparamagnetic iron oxide nanoparticles: diagnostic magnetic resonance imaging and potential therapeutic applications in neurooncology and central nervous system inflammatory pathologies, a review. J Cereb Blood Flow Metab 30:15–35

47. Byrne SL, Krishnamurthy D, Wessling-Resnick M (2013) Pharmacology of iron transport. Annu Rev Pharmacol Toxicol 53:2.1–2.20
48. Reddy LH, Arias JL, Nicolas J, Couvreur P (2012) Magnetic nanoparticles: design and characterization, toxicity and biocompatibility, pharmaceutical and biomedical applications. Chem Rev 112:5818–5878
49. Schnorr J, Wagner S, Abramjuk C, Wojner I, Schink T, Kroencke TJ, Schellenberger E, Hamm B, Pilgrimm H, Taupitz M (2004) Comparison of the Iron oxide-based blood-pool contrast medium VSOP-C184 with gadopentetate dimeglumine for first-pass magnetic resonance angiography of the aorta and renal arteries in pigs. Invest Radiol 39:546–553
50. Matthias T, Susanne W, Jörg S, Irina K, Herbert P, Henrike B-F, Bernd H (2004) Phase I clinical evaluation of citrate-coated monocrystalline very small superparamagnetic iron oxide particles as a new contrast medium for magnetic resonance imaging. Invest Radiol 39(7):394–405
51. Kim BH, Lee N, Kim H, An K, Park YI, Choi Y, Shin K, Lee Y, Kwon SG, Na HB, Park J-G, Ahn T-Y, Kim Y-W, Moon WK, Choi SH, Hyeon T (2011) Large-scale synthesis of uniform and extremely small-sized iron oxide nanoparticles for high-resolution T1 magnetic resonance imaging contrast agents. J Am Chem Soc 133:12624–12631
52. Borase T, Ninjbadgar T, Kapetanakis A, Roche S, O'Connor R, Kerskens C, Heise A, Brougham DF (2013) Stable aqueous dispersions of glycopeptide-grafted selectably functionalized magnetic nanoparticles. Angew Chem Int Ed 52:3164–3167
53. Xiao W, Lin J, Li M, Ma Y, Chen Y, Zhang C, Li D, Gu H (2012) Prolonged in vivo circulation time by zwitterionic modification of magnetite nanoparticles for blood pool contrast agents. Contrast Media Mol Imaging 7:320–327
54. Park J-A, Lee J-J, Jung J-C, Yu D-Y, Oh C, Ha S, Kim T-J, Chang Y (2008) Gd-DOTA conjugate of RGD as a potential tumor-targeting MRI contrast agent. ChemBioChem 9:2811–2813
55. Debergh I, Damme NV, Naeyer DD, Smeets P, Demetter P, Robert P, Carme S, Pattyn P, Ceelen W (2014) Molecular imaging of tumor-associated angiogenesis using a novel magnetic resonance imaging contrast agent targeting αvβ3 integrin. Ann Surg Oncol 21:2097–2104
56. Sipkins DA, Cheresh DA, Kazemi MR, Nevin LM, Bednarski MD, Li KCP (1998) Detection of tumor angiogenesis in vivo by αvβ3-targeted magnetic resonance imaging. Nat Med 4:623–626
57. Lanza GM, Winter PM, Caruthers SD, Hughes MS, Cyrus T, Marsh JN, Neubauer AM, Partlow KC, Wickline SA (2006) Nanomedicine opportunities for cardiovascular disease with perfluorocarbon nanoparticles. Nanomedicine (Lond) 1(3):321–329
58. Winter PM, Caruthers SD, Kassner A, Harris TD, Chinen LK, Allen JS, Lacy EK, Zhang H, Robertson JD, Wickline SA, Lanza GM (2003) Molecular imaging of angiogenesis in nascent Vx-2 rabbit tumors using a novel αvβ3-targeted nanoparticle and 1.5 tesla magnetic resonance imaging. Cancer Res 63:5838–5843
59. Schmieder AH, Winter PM, Caruthers SD, Harris TD, Williams TA, Allen JS, Lacy EK, Zhang H, Scott MJ, Hu G, Robertson JD, Wickline SA, Lanza GM (2005) Molecular MR imaging of melanoma angiogenesis with αvβ3-targeted paramagnetic nanoparticles. Magn Reson Med 53:621–627
60. Lanza GM, Caruthers SD, Winter PM, Hughes MS, Schmieder AH, Hu G, Wickline SA (2010) Angiogenesis imaging with vascular-constrained particles: the why and how. Eur J Nucl Med Mol Imaging 37(Suppl 1):S114–S126
61. Mulder WJM, Strijkers GJ, van Tilborg GAF, Griffioen AW, Nicolay K (2006) Lipid-based nanoparticles for contrast-enhanced MRI and molecular imaging. NMR Biomed 19:142–164
62. Morawski AM, Winter PM, Crowder KC, Caruthers SD, Fuhrhop RW, Scott MJ, Robertson JD, Abendschein DR, Lanza GM, Wickline SA (2004) Targeted nanoparticles for quantitative imaging of sparse molecular epitopes with MRI. Magn Reson Med 51(3):480–486
63. Strijkers GJ, Kluza E, Van Tilborg GAF, van der Schaft DWJ, Griffioen AW, Mulder WJM, Nicolay K (2010) Paramagnetic and fluorescent liposomes for target-specific imaging and therapy of tumor angiogenesis. Angiogenesis 13:161–173

64. Mulder WJ, van der Schaft DW, Hautvast PA, Strijkers GJ, Koning GA, Storm G, Mayo KH, Griffioen AW, Nicolay K (2007) Early in vivo assessment of angiostatic therapy efficacy by molecular MRI. FASEB J 21:378–383
65. Gianella A, Read JC, Cormode DP, Fayad ZA, Mulder WJM (2012) Multifunctional nanoparticles for target-specific imaging and therapy. In: Svenson S, Prud'homme RK (eds) Multifunctional nanoparticles for drug delivery applications. Springer, New York, pp 155–171
66. Chen W, Jarzyna PA, van Tilborg GAF, Nguyen VA, Cormode DP, Klink A, Griffioen AW, Randolph GJ, Fisher EA, Mulder WJM, Fayad ZA (2010) RGD peptide functionalized and reconstituted high-density lipoprotein nanoparticles as a versatile and multimodal tumor targeting molecular imaging probe. FASEB J 24:1689–1699
67. Li C (2014) A targeted approach to cancer imaging and therapy. Nat Mater 13:110–115
68. Kiessling F (2013) Science to practice: will contrast agents for molecular imaging of angiogenesis help overcome the limitations of functional vascular imaging? Radiology 268(2):309–311
69. Tassa C, Shaw SY, Weissleder R (2011) Dextran-coated iron oxide nanoparticles: a versatile platform for targeted molecular imaging, molecular diagnostics, and therapy. Acc Chem Res 44(10):842–852
70. Aeinstein JS, Varallyay CG, Dosa E, Gahramanov S, Hamilton B, Rooney WD, Muldoon LL, Neuwelt EA (2010) Superparamagnetic iron oxide nanoparticles: diagnostic magnetic resonance imaging and potential therapeutic applications in neurooncology and central nervous system inflammatory pathologies, a review. J Cereb Blood Flow Metab 30:15–35
71. Zhang C, Jugold M, Woenne EC, Lammers T, Morgenstern B, Mueller MM, Zentgraf H, Bock M, Eisenhut M, Semmler W, Kiessling F (2007) Specific targeting of tumor angiogenesis by RGD-conjugated ultrasmall superparamagnetic iron oxide particles using a clinical 1.5-T magnetic resonance scanner. Cancer Res 67(4):1555–1562
72. Jiang T, Zhang C, Zheng X, Xu X, Xie X, Liu H, Liu S (2009) Noninvasively characterizing the different αvβ3 expression patterns in lung cancers with RGD-USPIO using a clinical 3.0T MR scanner. Int J Nanomed 4:241–249
73. Sjögren CE, Johansson C, Naevestad A, Sontum PC, Briley-Saebø K, Fahlvik AK (1997) Crystal size and properties of superparamagnetic iron oxide (SPIO) particles. Magn Reson Imaging 15:55–67
74. Ho D, Sun X, Sun S (2011) Monodisperse magnetic nanoparticles for theranostic applications. Acc Chem Res 44(10):875–882
75. Jeong U, Teng X, Wang Y, Yang H, Xia Y (2007) Superparamagnetic colloids: controlled synthesis and niche application. Adv Mater 19:33–60
76. Xu F, Lei D, Du X, Zhang C, Xie X, Yin D (2011) Modification of MR molecular imaging probes with cysteine-terminated peptides and their potential for in vivo tumour detection. Contrast Media Mol Imaging 6:46–54
77. Huang G, Zhang C, Li S, Khemtong C, Yang SG, Tian R, Minna JD, Brown KC, Gao J (2009) A novel strategy for surface modification of superparamagnetic iron oxide nanoparticles for lung cancer imaging. J Mater Chem 19:6367–6372
78. Xie X, Zhang C (2010) Controllable assembly of hydrophobic superparamagnetic iron oxide nanoparticle with mPEG-PLA copolymer and its effect on MR transverse relaxation rate. J Nanomater 2011:Article ID 152524
79. Xu F, Cheng C, Xu F, Zhang C, Xu H, Xie X, Yin D, Gu H (2009) Superparamagnetic magnetite nanocrystal clusters: a sensitive tool for MR cellular imaging. Nanotechnology 20(40):405102
80. Wang Y, Xu F, Zhang C, Lei D, Tang Y, Xu H, Zhang Z, Lu H, Du X, Yang G-Y (2011) High MR sensitive fluorescent magnetite nanocluster for stem cell tracking in ischemic mouse brain. Nanomed Nanotechnol Biol Med 7:1009–1019
81. Zhang C, Xie X, Liang S, Li M, Liu Y, Gu H (2012) Mono-dispersed high MR sensitive magnetite nano cluster probe for detection of nascent tumor by MR molecular imaging. Nanomed Nanotechnol Biol Med 8:996–1006

82. Nasongkla N, Bey E, Ren J, Ai H, Khemtong C, Guthi JS, Chin S-F, Sherry AD, Boothman DA, Gao J (2006) Multifunctional polymeric micelles as cancer-targeted, MRI-ultrasensitive drug delivery systems. Nano Lett 6(11):2427–2430
83. Ai H, Flask C, Weinberg B, Shuai X-T, Pagel MD, Farrell D, Duerk J, Gao J (2005) Magnetite-loaded polymeric micelles as ultrasensitive magnetic-resonance probes. Adv Mater 17:1949–1952
84. Khemtong C, Kessinger CW, Ren J, Bey EA, Yang SG, Guthi JS, Boothman DA, Sherry AD, Gao J (2009) In vivo off-resonance saturation magnetic resonance imaging of AvB3-targeted superparamagnetic nanoparticles. Cancer Res 69(4):1651–1658
85. Liu P, Li J, Zhang C, Xu LX (2013) Micro-CT molecular imaging of tumor angiogenesis using a magnetite nano-cluster probe. J Biomed Nanotechnol 9(6):1041–1049
86. Xue S, Zhang C, Yang Y, Zhang L, Cheng D, Zhang J, Shi H, Zhang Y (2015) 99mTc-labeled iron oxide nanoparticles for dual-contrast (T1/T2) magnetic resonance and dual-modality imaging of tumor angiogenesis. J Biomed Nanotechnol 11:1027–1037
87. Kluza E, Schaft DWJ, Hautvast PAI, Mulder WJM, Mayo KH, Griffioen AW, Strijkers GJ, Nicolay K (2010) Synergistic targeting of αvβ3 integrin and galectin-1 with heteromultivalent paramagnetic liposomes for combined MR imaging and treatment of angiogenesis. Nano Lett 10:52–58
88. Kluza E, Jacobs I, Hectors SJCG, Mayo KH, Griffioen AW, Strijkers GJ, Nicolay K (2012) Dual-targeting of αvβ3 and galectin-1 improves the specificity of paramagnetic/fluorescent liposomes to tumor endothelium in vivo. J Control Release 158(2):207–214
89. Kiessling F, Huppert J, Zhang C, Jayapaul J, Zwick S, Woenne EC, Mueller MM, Zentgraf H, Eisenhut M, Addadi Y, Neeman M, Semmler W (2009) RGD-labeled USPIO inhibits adhesion and endocytotic activity of αvβ3-integrin-expressing glioma cells and only accumulates in the vascular tumor compartment. Radiology 253:462–469
90. Kircher MF, Willmann JK (2012) Molecular body imaging: MR imaging, CT, and US part I principles. Radiology 263(3):633–643
91. Kircher MF, Willmann JK (2012) Molecular body imaging: MR imaging, CT, and US part II applications. Radiology 264(2):349–368
92. Judenhofer MS, Wehrl HF, Newport DF, Catana C, Siegel SB, Becker M, Thielscher A, Kneilling M, Lichy MP, Eichner M, Klingel K, Reischl G, Widmaier S, Röcken M, Nutt RE, Machulla H-J, Uludag K, Cherry SR, Claussen CD, Pichler BJ (2008) Simultaneous PET-MRI: a new approach for functional and morphological imaging. Nat Med 14(4):459–465
93. Wehrl HF, Sauter AW, Judenhofer MS, Pichler BJ (2010) Combined PET/MR imaging – technology and applications. Technol Cancer Res Treat 9(1):5–20
94. Drzezga A, Souvatzoglou M, Eiber M, Beer AJ, Fürst S, Martinez-Möller A, Nekolla SG, Ziegler S, Ganter C, Rummeny EJ, Schwaiger M (2012) First clinical experience with integrated whole-body PET/MR: comparison to PET/CT in patients with oncologic diagnoses. J Nucl Med 53:845–855

Part II
Ultrasonic Theranostic Agents

Chapter 4
Multifunctional Ultrasound Contrast Agents Integrating Targeted Imaging and Therapy

Chuang Gao and Zhifei Dai

4.1 Introduction

Among all the diagnostic imaging techniques, ultrasound (US) imaging represents the safest, fastest, and least expensive method of scanning for many types of medical diagnosis [1–4]. However, its image quality is often inferior compared to the other imaging modality such as magnetic resonance imaging. Therefore, methods for improving image contrast are highly desirable. Ultrasound contrast agents (UCAs) have been widely employed to enhance ultrasonic signals. The most routinely used UCAs are prepared as aqueous dispersions of gas (e.g., perfluorocarbon) microbubbles (MBs) coated with a thin shell made of protein [5], polymer [6, 7], lipid [8, 9], or surfactant [10, 11]. Numerous large-scale, multicenter clinical studies have proven that the advantages and the diagnostic potential of microbubble-based contrast agents in combination with modern ultrasonographic techniques such as harmonic imaging for better management of patients [12, 13]. Actually, contrast-enhanced ultrasound imaging gives better tumor characterization in various visceral organs and makes the study of heart kinetics and vessel patency better [14]. Tremendous reports have demonstrated the effectiveness of microbubble-based agents in many fields of clinical imaging. It is now fully sympathized in routine clinical practice that microbubble-based agents earn an essential place in the US field.

The microbubble-based agents approved for clinical applications were firmly established for safety and efficacy essentially as drugs [15]. The diagnostic ultrasound with microbubble-based agents allows one to solve many diagnostic problems directly in the US unit. In a variety of clinical situations, it seems to be a promising replacement for common diagnostic examinations which are more costly

C. Gao • Z. Dai (✉)
Department of Biomedical Engineering, College of Engineering,
Peking University, Beijing 100871, China
e-mail: zhifei.dai@pku.edu.cn

Z. Dai (ed.), *Advances in Nanotheranostics II*, Springer Series
in Biomaterials Science and Engineering 7, DOI 10.1007/978-981-10-0063-8_4

and have well-known risks involving, for example, the employment of radioisotopes for single photon emission computed tomography (SPECT) and the use of more toxic contrast agents for magnetic resonance imaging [16]. Microbubble-based agents are principally employed in the areas of the large vessels, the heart, and the parenchymal organs for the assessment of vessel patency, evaluation of heart chamber kinetics, and identification and characterization of tumors. Nevertheless, numerous other interesting applications have been developed, such as the quantification of organ perfusion and gene therapy using microbubble-based contrast agents.

The reliable generation of bioeffects by diagnostic ultrasound with UCAs provides opportunities for therapeutic applications. Diagnostic ultrasound with UCAs has been explored for drug delivery from the blood pool to the interstitium using the microvascular leakage effect. By using diagnostic imaging with a noncommercial UCA, Vancraeynest et al. succeeded in delivering nanoparticles to the heart [17]. When the parameters were elevated for therapeutic efficacy, the severe microscale injury of the heart was achieved. Moreover, the phenomenon of sonoporation may be utilized to induce gene transfection into cells which survive the membrane injury, showing a potential application to gene therapy for diagnostic ultrasound [18].

One of the most unique features of UCAs for their use in biomedicine is the capability to load multiple functional components, such as several therapeutic species and/or medical nanoparticles (drug, gene, quantum dots (QDs), gold, Fe_3O_4, etc.), into the shell of ultrasound-responsive MBs to enable multiple applications, e.g., diagnosis and therapy or multimodal imaging (Fig. 4.1). Multifunctional ultrasound contrast agent may serve as a bridge to greatly expand the diagnostic and therapeutic potential of US. The ultrasound-based multifunctional imaging agents take advantage of other imaging modalities to make up for the shortcomings of insufficient resolution of diagnostic US imaging. In addition, theranostic MBs can

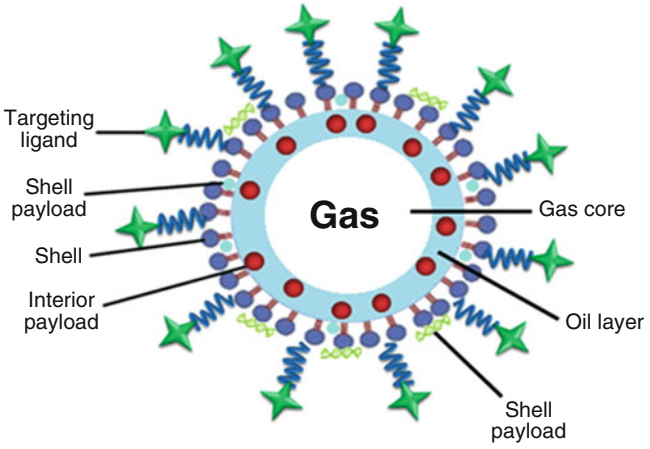

Fig. 4.1 Multifunctional ultrasound contrast agent constructed by loading multiple functional components into the shell and core domain of MBs (Reprinted with permission from Ref. [19]. Copyright 2014 American Chemical Society)

be used for imaging-guided therapy, real-time monitoring of therapy process, and the evaluation after the treatment. Integrating multiple functionalities into the same UCA can avoid the additional stress on the body's blood clearance mechanisms accompanying administration of multiple doses of agents. Therefore, multifunctional microbubble-based UCA possesses the congenital superiority as theranostic nanomedicine to accomplish the simultaneous imaging and therapy. The current review will focus on the state-of-the-art UCA platforms for multimodal imaging and theranostics.

4.2 General Design of Ultrasound Contrast Agents

4.2.1 Requirements of an Ideal Ultrasound Contrast Agent

An ideal ultrasound contrast agent is generally required to have the following characteristics [20]:

1. Absolute safety and no toxicity to the patient at the commonly injected contrast dose
2. Complete biodegradability and biotolerability
3. Good stability and robustness in vivo (the imaging time is long enough to fulfill the procedure of diagnosis)
4. Easy detectability by ultrasound imaging systems
5. The established relationship between the concentration of ultrasound contrast agent and the intensity of ultrasound signals
6. Low UCA dose (preferably at a milliliter) injected to the patient
7. Simple administration procedure (preferably via a short intravenous injection)
8. Minor treatment and preparation before administration
9. Good storage stability (a shelf life of a couple of years is preferred)
10. Low production costs

Nevertheless, the ideal ultrasound contrast agents often own a series of contradictory characteristics, so we have to reach a compromise in some cases.

4.2.2 General Design of the Microbubble-Based Ultrasound Contrast Agents

A thick impermeable shell can enhance the microbubble stability, reduce the gas diffusion rate from the microbubbles, and increase the resistance to hydrostatic pressure [21]. In addition, the shells with higher thickness may be applied to load a variety of drugs for ultrasound-mediated drug delivery [22]. Yet, the microbubble shell of ultrasound contrast agent may have a slight limitation to the microbubble

vibration in the field of diagnostic ultrasound. The microbubbles with the so thick shell are not able to scatter ultrasound efficiently to provide a feasible contrast upon ultrasound irradiation [23]. Therefore, we have to reach a compromise between the reasonably high echogenicity and the sufficient stability by optimizing microbubble shell thickness. It was also found that the mechanical properties of the shell affect the microbubble's resonance frequency and acoustic spectrum. For example, the changes in the shell stiffness can have effect on the acoustic response of microbubbles. Especially, the echogenic response of microbubbles may decrease at a certain resonance frequency.

The materials applied to fabricate the shell of microbubbles must be absolutely biocompatible with no immune response, such as the lipids used for the construction of the shells of Sonazoid and Sonovue and polymeric cyanoacrylate in Sonovist. The general designs of the UCA materials commonly include three options. The first design is a perfluorocarbon liquid emulsion, which may produce gas microbubbles on demand. The liquid nanoemulsion droplets of perfluoropentane can be stabilized by a fluorinated surfactant (Echogen) or surfactants carrying a net negative charge (Sonogen). The second design type of ultrasound contrast agents is based on the dry powder in the vial filled with perfluorocarbon. Prior to injection, the dry powder is reconstituted using aqueous solution to form the shell-covered microbubble aqueous dispersion. Sonazoid is designed as a dry powder which is prepared from lipid-stabilized microbubble encapsulating decafluorobutane and can be quickly dissolved after addition of water [24]. This kind of agent is likely produced by high-shear mixing/sonication of the lipid/surfactant aqueous dispersion containing decafluorobutane gas with a high molecular weight, followed by spray-drying or freeze-drying. After complete removal of water, vials are filled with decafluorobutane gas. The third design of ultrasound contrast agents (e.g., Optison) involves high-shear mixing octafluoropropane gas in the medium which can immediately self-assemble the shell on the interface between the aqueous phase and the gas phase. The agent is stored as an aqueous dispersion with no need of lyophilization or freezing. No extra production steps such as reconstituting microbubble materials are needed before injection.

The Definity agent (Dupont Pharma) is fabricated by employing an intermediate strategy between a second design type and a third design type from an aqueous dispersion of submicron liposomes in an octafluoropropane-filled vial [25]. Liposomes can be constructed reproducibly on a large scale. Such aqueous dispersion of liposomes may be sterile-filtered and packaged by filling the vials with aqueous liposome dispersion and octafluoropropane and sealing the vial with stoppers. Before injection into the patient, the sealed vial is rapidly mixed for a short time with a mechanical shaker.

Recently, Dai et al. developed stabilized microbubbles by using ultrasonification of a mixture of PEG stearate and Span 60 [26]. A monolayer of Span 60 is formed on the interface between the aqueous phase and the gas phase. Several molar percent of PEG stearate molecules are introduced into the bubble shell by inserting stearic acid tail into the monolayer of Span 60. The monolayer on the microbubble surface keeps the solid state during the refrigerated storage due to the ~52 °C melt-

ing point of PEG stearate, which inhibits the fusion of microbubbles. PEG chains protrude out of the bubble shell into the surrounding aqueous phase, forming a dense PEG brush, which acts as an extra repulsion barrier to inhibit the fusion of microbubbles. Similar to stealth liposomes, the PEG brush on the shell surface of microbubbles can operate as an extra steric protection of the microbubble-based ultrasound contrast agent, resulting in reduced nonspecific binding and prolonged circulation time in vivo. Therefore, it provides a possibility to construct microbubbles with the long-term storage in the aqueous phase.

4.2.3 Ultrasound Contrast Agent Based Drug Delivery

The ultrasound wave may deeply penetrate into the living tissue and easily focus in a confined beam so it can be employed for the ultrasound-mediated drug delivery and selective release in combination with microbubble agents. Drugs were coadministered with the microbubbles, followed by activation by ultrasound and microbubbles, resulting in the great improvement of thrombolysis efficacy using a plasminogen activator enzyme [27]. Breaking up the thrombus structure with ultrasound action aids the thrombolytic enzyme influx into the site and elimination of the degradation products. It has been demonstrated that the circulating microparticles or red blood cells outside of the capillaries were successfully delivered into the circumjacent tissues by employing ultrasound in combination with Optison microbubbles [28].

The transfection of DNA plasmid into the tissues and cells was enhanced by using a similar approach [29]. Microbubbles carrying a net positive charge were fabricated to bind plasmid DNA. In order to ensure selective attachment to the cells of interest, targeting ligands are often used to modify the DNA/microbubble complexes. Such DNA/microbubble complexes may be triggered using ultrasound irradiation to impel DNA into the circumjacent cells and tissue for transfection. Moreover, some smaller molecular weight species, such as antisense oligonucleotides [30], paclitaxel [22], and dexamethasone [22], are able to be transferred via ultrasound-mediated microbubble destruction by introducing the drugs to the microbubble membrane. Upon irradiation of ultrasound, the microbubble collapses and the gas core loses, and the drug contained microbubble shell fragments can be delivered from the microbubble into the circumjacent tissue. Generally, the "sonoporation effect" is applied to describe the above applications.

4.2.4 Tissue-Specific Ultrasound Contrast Agents

The ultrasound contrast agents modified with the targeting ligand are expected to accumulate in the target sites of high receptor density, resulting in significant contrast enhancement ultrasound imaging of that targeting area. A surfactant-stabilized

nanoemulsion of fluorocarbon liquid was coupled with antibody by using biotin–avidin interaction or covalent attachment for the use as an MRI and ultrasound contrast agent [31]. This nanoemulsion showed weak echo signal in the blood vessels, but its long circulation time allowed for the targeting nanoemulsion to selectively accumulate at the target area. Some ultrasound contrast response was generated when the target surface was fully covered with the nanoemulsion particles [32], but it was usually demonstrated at higher frequencies. In addition, the dose of the nanoemulsion particles needed for obvious contrast was rather high. Nonetheless, the employment of fluorocarbon-filled microbubble formulations remains to be a valid strategy for the design of targeting ultrasound contrast agents.

Microbubble shell can be modified with targeting ligands via an avidin–biotin coupling strategy, or via a hydrophobic interaction in the monolayer shell of microbubbles, or a combination of both. Due to the simplicity of an avidin–biotin sandwich technique, many targeting ligands (e.g., antibodies) can be conveniently biotinylated to modify the microbubble. But, the patients should avoid systemic administration of avidin or streptavidin. We can conjugate targeting ligands to the microbubble directly or via a flexible polyethylene glycol spacer arm. Employment of the polyethylene glycol spacer arm permits tighter binding in some cases [33]. It was reported in an animal model that the microbubbles, which were modified with anti-P-selectin antibodies via an avidin–biotin coupling strategy, exhibited obvious accumulation in the inflammation sites and ischemia/reperfusion injury [34].

The surface density of targeting ligands on the microbubbles functions with the size of ligands. Larger ligands (like antibodies) are only permitted to attach limited amount of ligand molecules per microbubble. On the contrary, the peptide-based ligands allow for coupling a ten times higher amount of ligand molecules per microbubble because of their smaller size. The higher ligand surface density provides the microbubble more retention opportunity on the target sites. As an example, small ligand of RGD-based peptide was attached to MRX-408 microbubbles containing decafluorobutane by using a PEG linkage [35]. It was demonstrated that these RGD-conjugated MRX-408 microbubbles could accumulate on the activated platelets by selectively targeting glycoprotein GPIIb/IIIa, which could enhance ultrasound imaging of thrombus and was also useful for accelerating thrombolysis. Phosphatidylserine is a biomarker molecule for Kupffer cells to endocytose aged red blood cells [36] or for neutrophils/macrophages to scavenge the fragments or apoptotic cells [37]. Therefore, the introduction of phosphatidylserine into the microbubble shells may lead to the preferential rapid uptake of the microbubble to, e.g., leukocytes in the inflammation sites [38], which may be applied to evaluate the inflammation areas via preferential accumulation of ultrasound contrast by echo imaging. Leukocytes or macrophages may completely endocytosed microbubbles. Thus, the entire cell can efficiently be a viscous extension of the microbubble shell [39], resulting in stabilization of the bubble against gas loss. It can be a good explanation why air-containing Levovist microbubbles may retain in the liver for about half hour upon systemic administration. Specific targeting of microbubble-based ultrasound contrast agents to the receptors on the endothelial lining

surface can be applied for the detection of actively growing tumors and to the evaluation of the therapeutic efficacy by visualizing areas of apoptosis and/or active angiogenesis [40].

4.2.5 The Effect of the Microbubble Size Distribution

Size distribution of microbubbles has great effect on the microbubble stability, behavior, and acoustic response in vivo. The microbubble response to pressure waves can be described using the Rayleigh–Plesset equation. The scattering intensity of ultrasound is found to be proportional to the sixth power of the microbubble diameter [41]. However, the microbubble must be less than 7 μm in diameter in order to cross pulmonary capillaries with the blood flow after systemic administration and go alone to the left ventricle. Large bubbles (e.g., 0.1 or 1 mm in diameter) cannot be injected into the bloodstream since such large bubble can be rapidly resided in the vasculature as emboli, seriously restricting the blood flow. The microbubbles with the diameter of several micrometers remain to have good echogenicity in the most used ultrasound frequency range of several MHz. Yet, the microbubbles smaller than 1 μm show less echogenicity [42]. The surface-to-volume ratio of smaller microbubbles is much higher and loses the core gas much more easily during blood circulation and during the ultrasound-mediated microbubble destruction.

4.3 Ultrasound Contrast Agent for Molecular Imaging

4.3.1 Basic Concept of Ultrasound Molecular Imaging

The contrast agent typically used for ultrasound is MBs with the diameter of 1–7 μm that are confined to the intravascular space with no significant retention in the diseased tissue unless selective molecular imaging is induced. By utilizing acoustically active microbubbles or nanobubbles which are targetedly bound to function-specific epitopes upon intravenous injection, ultrasound molecular imaging provides the capability of real-time and noninvasive imaging of molecular markers of diseases employing diagnostic ultrasound imaging systems. The surface modification of microbubbles with a receptor-specific ligand confers microbubbles attaching to a disease-specific tissues or cells. Since the microbubbles attach to the diseased sites, ultrasound imaging can show a persistent enhanced contrast effect, revealing the existence and location of the interesting molecules in real time.

By using custom-designed microbubble-based contrast agents retained in the regions of disease by changes in the structures of the shell or by the conjugation of specific targeting ligands to their outer surface, ultrasound molecular imaging combines the advantages of contrast-enhanced ultrasound with the ability to character-

ize pathologic markers at a molecular level. The ligands commonly used for targeting modification of microbubbles include peptides [43], antibodies[44, 45], and disintegrins [46]. But, peptidomimetics or other adhesion ligands that can be conjugated directly to the contrast agent shell are also included [47]. As MBs are pure intravascular tracers, their use as molecular imaging agents is therefore restricted to diseases which are mediated by pathophysiologic events present in the intravascular compartment, such as inflammation [48], thrombus formation [49, 50], and angiogenesis [51, 52].

Molecular imaging with US is becoming an exciting field since it offers a high sensitivity for contrast agents, excellent biocompatibility, and significant clinical translation potential by introducing a new dimension of diagnostic capability to this already ubiquitous modality. Ultrasound molecular imaging may open a way to detect pathology and observe the treatment effect before phenotypic changes occur with advancing understanding in molecular changes involved in disease progression. Nevertheless, ultrasonic molecular imaging still confronts several big challenges before rising to its full diagnostic potential. In order to determine whether and how much molecular targets present, the contrast agents are required to specifically adhere to sufficient molecular targets to overwhelm the signal contributions from nonspecific retention. Moreover, the ultrasound system should possess sufficient sensitivity to detect the targeted agents present at the pathology sites to assess the pathology in its entirety.

4.3.2 Ultrasound Molecular Imaging of Cancer

Angiogenesis is an important process in tumor growth, invasion, and metastasis. There is currently great need for imaging angiogenic markers in vivo both for diagnostic purposes and for assessing therapeutic effects. The $\alpha_v\beta_3$ targeting has been achieved with either monoclonal antibodies or peptides with the arginine-glycine-aspartic acid (RGD) motif. MBs targeted against vascular endothelial growth factor receptor 2 (VEGFR2), $\alpha_v\beta_3$ integrin, and endoglin were used to successfully image angiogenesis in various mouse models of cancer [53]. In vivo transverse ultrasound image was obtained on orthotopically implanted human breast adenocarcinoma xenograft (MDA-MB-231 cells) in nude mouse after intravenous administration of 5×107 VEGFR2-targeted contrast MBs (BR55). Strong imaging signal was observed in breast cancer compared to surrounding normal tissue due to increased angiogenesis and upregulation of VEGFR2 on angiogenic vascular endothelial cells in breast cancer. Moreover, multi-targeting MBs were demonstrated to be more effective than single-targeting MBs [54]. For example, for imaging tumor angiogenesis in ovarian cancer xenografts in mice, the dual-targeting MBs to the two angiogenesis markers (VEGFR2 and $\alpha_v\beta_3$ integrin) accumulate in tumors better than single-targeted MBs to either VEGFR2 or $\alpha_v\beta_3$ integrin alone [55]. Warram et al. [56] also developed triple-targeting MBs to $\alpha_v\beta_3$ integrin, P-selectin, and VEGFR2 and evaluated their imaging signals in human MDA-MB-231 breast cancer

tumor-bearing mice, suggesting that a 40 % increase in tumor image intensity after dosing with triple-targeting MBs compared with single- and dual-targeting MBs.

MBs are confined to the intravascular space due to the microscaled size. Although the vascular permeability in tumor is enlarged, only those particles with size smaller than 700 nm are allowed to extravasate. So some smaller, submicron-sized contrast agents that are able to enter the extravascular space of tumors are being widely investigated [57], such as liposomes, liquid perfluorocarbon nanodroplets, nanobubbles (NBs), and solid NPs. Except that a large amount of particles accumulate to the region of interest by disease-specific molecular target, these small contrast agents however show relative weak acoustic signal due to their smaller sizes. Yin et al. [58] synthesized small lipid-based NBs that were able to retain similar echogenicity compared to MBs in vitro since they were passively targeting the tumor site in nude rats. Rapoport et al. [59] demonstrated that perfluoropentane NBs were able to extravasate into tumor tissue in human breast cancer xenografts in nude mice and provide a long-lasting contrast agent. This feature makes liquid perfluorocarbon nanodroplet the mostly reported nanosized ultrasound contrast agents. Lanza et al. [60] used biotin-linked perfluorocarbon nanodroplets to target avidin-modified nitrocellulose film, and the signal intensity increased 66 dB. In vivo experiments showed that such biotin-bearing nanodroplets specifically enhanced the ultrasound imaging [61].

4.3.3 Ultrasound Molecular Imaging of Cardiovascular Disease

Molecular contrast echocardiography is vitally needed for the visualization of various pathologies, ranging from myocardial infarction-related ischemia/reperfusion injury to heart transplant rejection, to the adhesion molecules of the upregulated leukocyte throughout the course of microvascular inflammation, to the monitoring of atherosclerosis development, and to the imaging of vulnerable plaque in the arteries, as well as thrombi and angiogenesis. A biomarker of atherosclerosis involves the overexpression of adhesion molecules which may trigger leukocyte infiltration on the endothelium and may be visualized with diagnostic ultrasound in combination with targeted microbubbles [45]. The designation of leukocyte adhesion molecules of the endothelium could be used to tag “vulnerable patients” who may have the risk of atherosclerotic cardiovascular disease even prior to clinical events. Since the diseased sites of atherosclerosis are on the blood vessel wall, detecting adhesion molecules in larger peripheral vessels, such as the thoracic aorta and carotid arteries, can characterize patients with atherogenesis and thus offer a peripheral “window” to the risks of coronary atherosclerosis. After intravenous injection of lipid microbubbles bearing VCAM-1 antibodies, whose thoracic aortic adhesion was microscopically verified, lasting acoustic contrast enhancement of the thoracic aorta was observed by noninvasive vascular ultrasound imaging. In addition, it was found

that the magnitude of video signal change referred to the extent of plaque formation. This indicated that the microbubbles targeting VCAM-1 can be used to detect and quantify the inflammation in the early stage of atherosclerosis.

The MBs bearing sialyl LewisX (tetrasaccharide, a P-selectin ligand) were reported by Villanueva et al. to show persistent and contrast-enhanced ultrasound signal in the ischemic region previously occurred [62]. It indicates that transthoracic echo imaging employing MBs binding to a microvascular endothelial biomarker of previous ischemia can be helpful for the etiologic diagnosis of patients with acute or recent chest pain and the delineation of the extent of myocardium at risk [63]. Ultrasound molecular imaging has also been applied for the diagnosis of deep venous thrombosis of the legs and intracardiac thrombi. Microbubbles modified with short peptide sequences of RGD have successfully been targeted to the activated glycoprotein IIb/IIIa receptor of platelets, and attachment of these microbubbles to clots in vitro and in vivo has been shown by ultrasound vascular imaging [64]. Abciximab, an antibody against this activated platelet receptor, could also be used for bubble clot targeting [50]. It suggested that targeted ultrasound imaging can serve as an efficient tool to delineate the thrombi.

4.4 Ultrasound Contrast Agents for Multimodal Imaging

The imaging enhanced by contrast agent allows noninvasive diagnosis of the disease and real-time monitoring of the particle localization, such as ultrasound imaging, computed tomography (CT), and magnetic resonance imaging (MRI). So far no imaging modality is perfect. Each imaging technique shows its own advantages and limitations. It is often a conundrum to select diagnostic imaging modality in clinic. The imaging modalities with the highest sensitivity have relatively poor spatial resolution, while those with high spatial resolution have relatively poor sensitivity.

Recently, the idea to integrate multiple modalities has gained broad interests. The first fused PET/CT instrument came to market in 2001. Moreover, the emerging of the fused PET/MRI instrument expands imaging frontiers. The excitement over these multimodal imaging instruments boosts the design and development of multimodal contrast agent to raise the clinical benefits of hybrid instrument technology [65]. Compared to the other imaging modality, US imaging is advantageous due to its features of real-time results, low cost, high safety, and availability of portable devices. Besides, the microbubble-based UCAs can serve as a carrier to load conveniently the other modality contrast agents to enhance multimodal imaging.

4.4.1 US/MR Dual-Modal Imaging Contrast Agents

Ultrasound imaging takes advantages of real-time results, low cost, and availability of portable devices, but the major problem is its relative low sensitivity. On the contrary, MRI is a particularly attractive imaging modality due to the excellent

anatomical detail and relatively high sensitivity. As well known, in the practical diagnosis process, US is firstly used for tumor localization, when the results are not sure, MRI will be done for confirmation. Furthermore, US could real-time monitor the surgical resection. Due to the great repercussions on the clinical diagnosis and on surgical protocol, the development of multimodal contrast agents for in vivo imaging is increasingly pursued. Contrast agents combining ultrasound and magnetic resonance imaging received much attention because they ally the real-time monitoring of ultrasound imaging to MR imaging with high spatial resolution and high sensitivity. Moreover, this technique enables to improve the comfort of the patient because it is noninvasive and rapid and avoids the use of radiochemicals.

Among the different contrast materials, the perfluorocarbons have the unique feature for the enhancement of both US and MRI all by itself [66]. However, the clinical applications of the contrast agent have been limited due to the relatively low strength of the organic shells, large micrometer size, and polydispersed size distribution. Recently, the two typical dual contrast agents for both magnetic resonance and ultrasound imaging have been constructed by incorporating T_1-weighted Gd-DTPA complex [67] and the T_2-weighted superparamagnetic iron oxide (SPIO) nanoparticles [68, 69] into hollow silica nanospheres (HSNSs) and microbubbles generated from polylactic acid (PLA) and polyvinyl alcohol (PVA), respectively (Fig. 4.2). The integration of US and MRI contrast agent can provide signals from blood pool to surrounding tissue simultaneously for the different tracer distribution. Attachment of Gd-DTPA and cyclo-arginine-glycine-aspartic acid c(RGD) peptide on the surface of HSNSs nanoparticles resulted in a significant US and MRI positive contrast enhancement effect on cancer cells. The resulted HSNSs@(Gd-DTPA)-RGD were then used as a targeted contrast agent for dual-modality imaging of

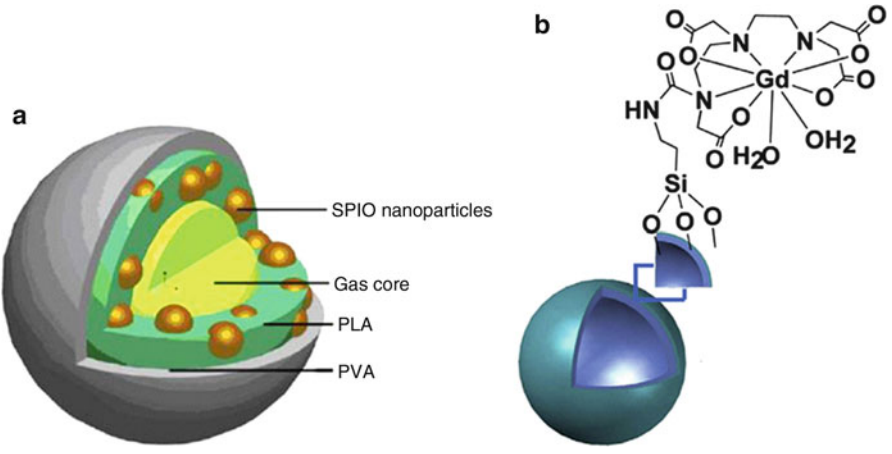

Fig. 4.2 The schematic diagram of (**a**) the SPIO NPs encapsulated MBs; (**b**) DTPA-Gd conjugated HSNSs. ((**a**) Reprinted from Ref. [68], Copyright 2009, with permission from Elsevier. (**b**) Reprinted from Ref. [67], Copyright 2014, with permission from Elsevier)

tumor-bearing mice. Targeted dual-modality of US and MRI data clearly revealed that the HSNSs@(Gd-DTPA)-RGD specifically targeted cancer cells overexpressing $\alpha_v\beta_3$ integrins on the cell surface through a receptor-mediated delivery pathway.

4.4.2 US/Optical Dual-Modal Imaging Contrast Agents

Optical imaging has high sensitivity and multicolor imaging capability which is very important for in vitro and in small animal experiments. However, the low spatial resolution due to the strong scattering in the tissue limits its clinic applications. On the contrary, US have become a prominent technique in diagnostic clinical medicine owing to the unique features. Thus, the optical imaging is often used in in vitro and ex vivo experiments to verify the US diagnostic. Besides, the fluorescence imaging has been used for imaging-guided resection of tumors to increase the overall survival [70–72]. And then, the combination of optical imaging and US imaging would provide great benefit for the real-time monitoring of the therapy process. As earlier as 2000, optical imaging was used as an effective adjunct to ultrasound in differentiating benign from malignant breast lesions [73], improving the ultrasound specificity and reducing unnecessary biopsies. Therefore, the dual functional contrast agent for fluorescence and US imaging received much attention because they can integrate the high sensitivity of fluorescence imaging and the good spatial resolution of US imaging. Recently, a US/fluorescent dual-modal imaging agent was developed by Ke et al. via layer-by-layer deposition of poly(allylamine hydrochloride) and CdTe quantum dots (QDs) onto ST68 MBs generated from Span 60 and Tween 80 [74]. In vivo experiments found that CdTe QD-modified MBs showed both significant ultrasound contrast enhancement in rabbit kidney and hypodermic fluorescent imaging in the tumor-bearing nude mice (Fig. 4.3). Besides, such contrast agent shows the potential for delivering the QDs to disease site for enhanced fluorescent imaging by ultrasound-targeted microbubble destruction (UTMD) technique [75].

To date, both nanobubbles and microbubbles show poor in vivo tumor selectivity over nontargeted organs. Mai et al. [76] reported a biocompatible chitosan–vitamin C lipid-based nanobubble conjugating cyanine 5.5 as a dual-modal contrast agent for tumor-selective imaging in a mouse tumor model. Single bubble spheres and clusters of bubble spheres are included in cyanine 5.5-nanobubble suspension with the size ranging between 400 and 800 nm. In vitro cell experiments showed that cyanine 5.5 dye was able to accumulate in cancer cells because of the unique conjugated nanobubble structure. After intravenous injection of cyanine 5.5-nanobubbles, ultrasound signals were found to be enhanced greatly and persist over 2 h at tumor site. In vivo fluorescence imaging showed that cyanine 5.5-nanobubbles were mainly located at tumor site and in the bladder of mice. The fluorescence emission was persistently observed over 24 h at tumor site. Subsequent analysis confirmed that cyanine 5.5-nanobubbles only selectively accumulated at the intact subcutane-

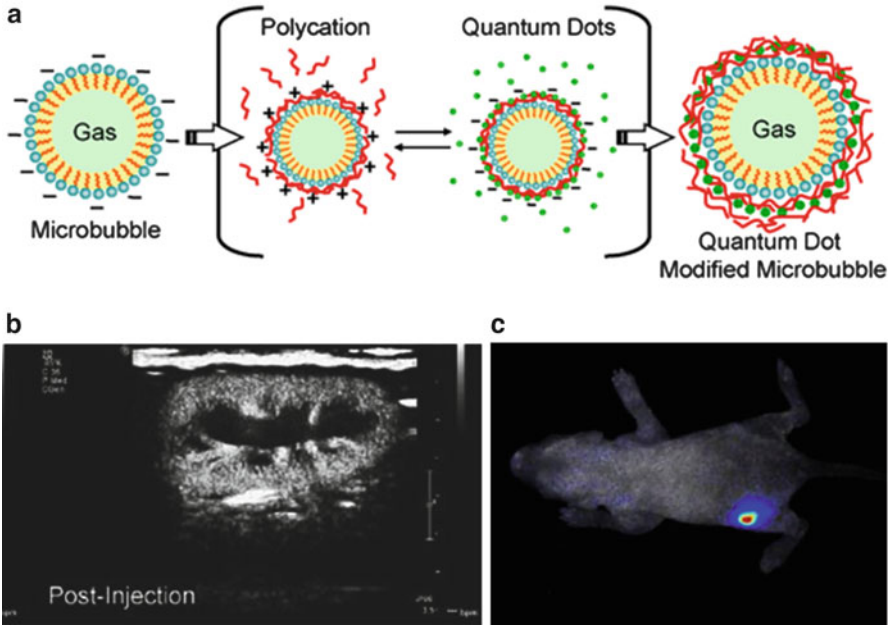

Fig. 4.3 (**a**) Schematic QD-modified MBs: fabrication process and capability to serve as a dual-modal contrast agent, (**b**) pulse inversion harmonic images of the rabbit right kidney, and (**c**) optical image postinjection of QD-modified MBs (Reprinted with permission from Ref. [74], © IOP Publishing)

ous tumor site and in isolated tumor tissue and no accumulation was seen in liver tissue post-intravenous injection. All these results suggested that cyanine 5.5-nanobubbles have achieved tumor-selective imaging in vivo due to the unique cross-link structure with a negative-charged surface.

4.4.3 US/Photoacoustic Dual-Modal Imaging Contrast Agents

Despite the high sensitivity, optical imaging suffers from either shallow penetration depth or poor spatial resolution due to strong light scattering. Photoacoustic (PA) imaging has emerged as a combined technology which integrates the high molecular sensitivity of optical imaging and the good spatial resolution of US imaging. PA imaging employs near-infrared light to introduce US waves via optical absorption and photothermal expansion. Thus, PA imaging can be used as a complementary imaging modality to ultrasound imaging. The PA can be conveniently integrated with US due to the ability to share components responsible for detecting the ultrasound wave. In addition, the combination can provide high spatial resolution images at a greater depth, which is beneficial to clinical applications.

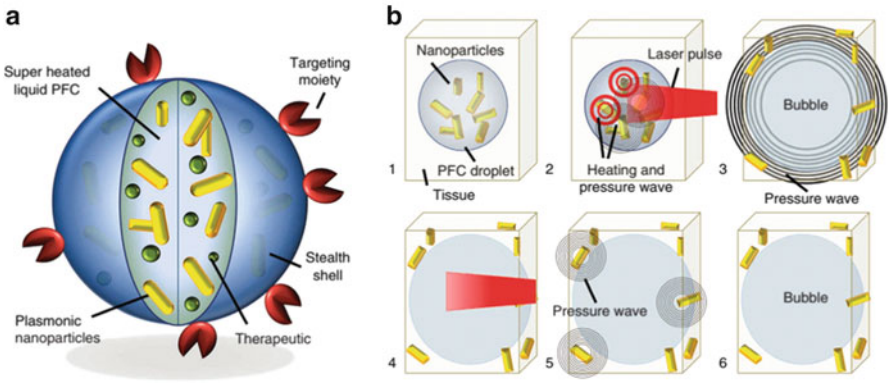

Fig. 4.4 (**a**) Diagram depicting the dual-contrast agent concept: photoacoustic droplet consisting of plasmonic nanoparticles suspended in encapsulated PFC (a superheated liquid at body temperature) and capped with a BSA shell. PAnDs may further contain therapeutic cargo and be surface functionalized for molecular targeting and cell–particle interactions. (**b**) Step-by-step diagram of remote activation of PAnDs, providing photoacoustic signal via two mechanisms: vaporization of PAnDs (steps 2–3) and thermal expansion caused by plasmonic nanoparticles (steps 4–5). The resulting gas microbubble of PFC (step 6) provides us contrast due to acoustic impedance mismatch between gas and the surround environment (Reprinted with permission from Macmillan Publishers Ltd: Ref. [80], Copyright 2012)

Dai et al. reported a versatile oil-in-water emulsion method to construct water-dispersible polypyrrole micro-/nanocapsules using a soluble polypyrrole complex. Owing to the encapsulated perfluorooctylbromide and strong near-infrared absorption of polypyrrole shell, the resulted polypyrrole capsules can serve as a dual-modal contrast agent to enhance both ultrasound and photoacoustic imaging [77, 78]. Zheng et al. fabricated porsche microbubbles porphyrin–lipid shell as a dual-modality US/PA contrast agent [79]. The inclusion of porphyrin–lipid in the MB shells results in unexpected physical properties, such as the increased yield, the increased shell stiffness, the improved serum stability over MBs without porphyrin–lipid, and the narrow volumetric size distribution with a peak size of 2.7 ± 0.2 μm. Using an acoustic model, the porsche stiffness was calculated to be three to five times greater than that of commercial lipid MBs. Especially, the unique narrow volumetric size distribution of porsche MBs is advantageous for molecularly targeted imaging. Porsche MBs were found to be intrinsically suitable for both ultrasound and photoacoustic imaging with a clinical and higher resonance frequency of 9–10 MHz. The distinctive properties of porsche MBs make them potentially advantageous as combined US/PA imaging agents and for emerging MB applications such as drug or gene delivery.

Recently, Hannah et al. reported a dual contrast agent based on photoacoustic nanodroplets (PAnDs) consisting of a perfluorocarbon core, surfactant shell, and encapsulated plasmonic nanoparticles (Fig. 4.4) [80]. Under pulsed laser irradiation (780 nm wavelength, 5–7 ns pulse duration, 10 Hz pulse repetition rate, 5.0 mJ cm^{-2}), the liquid perfluorocarbon undergoes a liquid-to-gas phase transition generating giant photoacoustic transients from these dwarf nanoparticles. By utilizing

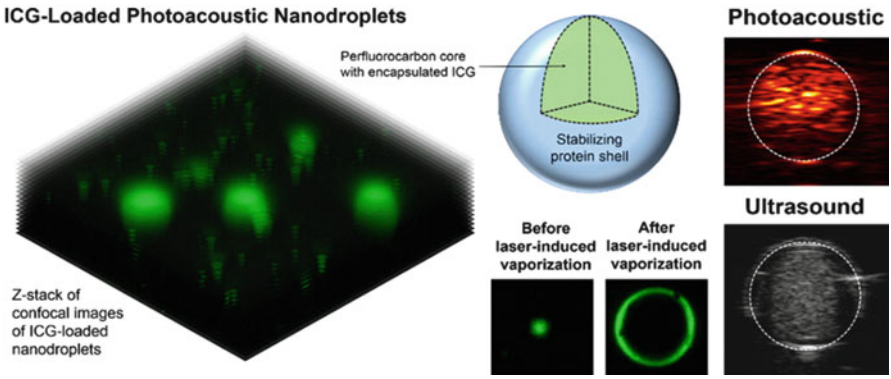

Fig. 4.5 Great enhancement of photoacoustic and ultrasound images was achieved by using a dual contrast agent of ICG-loaded photoacoustic nanodroplets (Reprinted with permission from Ref. [82]. Copyright 2014 American Chemical Society)

vaporization for photoacoustic signal generation, this exogenous contrast agent provides significantly higher signal amplitude than that from the traditionally used mechanism, thermal expansion. In addition, the triggered gaseous phase conduces to significant ultrasound contrast enhancement. Both phantom and animal studies prove that such nanodroplets can operate as dual contrast agents to enhance both photoacoustic and ultrasound imaging through optically triggered vaporization. In another work, the same group synthesizes nanodroplets encapsulating gold nanorods with a peak absorption near 1064 nm, which are optimal for extended photoacoustic imaging depth and contrast, safety, and system cost [81]. The remarkable contrast enhancement in a biological environment shows that these 1064 nm triggerable photoacoustic nanodroplets are a robust biomedical tool to enhance image contrast at clinically relevant depths. To expedite clinical translation, indocyanine green (ICG) was used as an efficient optical absorber to replace gold nanostructures (Fig. 4.5) [82]. Analysis of contrast and contrast-to-noise ratio showed that the resulting ICG-loaded perfluorocarbon nanodroplets achieved great enhancement of photoacoustic and ultrasound images. Since ICG-loaded perfluorocarbon nanodroplet is biocompatible, nontoxic, and biologically safe, it may become a valuable tool for various imaging modalities and have promising therapeutic applications.

4.4.4 Trimodal Imaging Contrast Agents

Porsche MBs were further demonstrated by Huynh et al. to be an intrinsically trimodal agent for ultrasound, photoacoustic, and fluorescence imaging (Fig. 4.6) [83]. Compared to the US/PA dual-modal porsche MBs, the porphyrin content was increased by threefold from 15 to 50 molar % in the trimodal porsche MBs. The authors observed a distinct shift in the Q-band absorbance from that of the

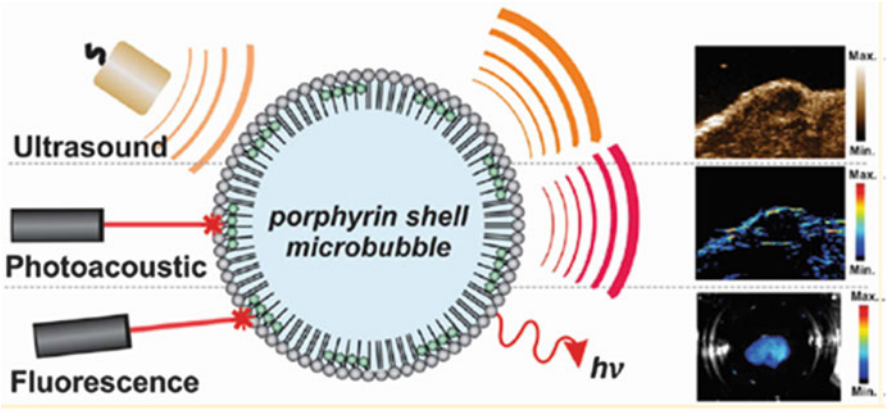

Fig. 4.6 In vivo imaging of MBs in a KB tumor xenograft at 10–30 s post-intravenous injection of 280 μL of MB–PBS solution at a concentration of 2×10^9 MBs/mL. The US contrast mode image (*right top*) and the photoacoustic image (*right middle*) show the infusion of MBs by an increase in signal. The ex vivo fluorescence imaging verifies the distribution (*right bottom*) (Reprinted with permission from Ref. [83]. Copyright 2014 American Chemical Society)

monomeric porphyrin, a characteristic of ordered aggregation. The ordered aggregation resulted in the high optical absorption and fluorescence generation. Therefore, porsche MBs generate an intrinsically trimodal agent for ultrasound, photoacoustic, and fluorescence imaging based on a single-component porphyrin–lipid structure. Particularly, this multimodal capability is reached with no additional complexity and potential errors of combining multiple separate imaging components.

The same group further upgraded the trimodal contrast agent by replacing the porphyrin liquid with bacteriochlorophyll–lipid (BChl–lipid) which has more favorable optical properties in the near-infrared window. In addition, the low-frequency ultrasound could trigger the conversion of microbubbles to nanoparticles which processed the same optical properties as the original microbubble (Fig. 4.7) [84]. The encapsulated gas provides ultrasound imaging contrast and the porphyrins in the shell confer photoacoustic and fluorescent properties. Furthermore, the micro-to-nano conversion of porphyrin microbubbles can potentially be used to bypass the enhanced permeability and retention effect when delivering drugs to tumors. Ultrasound imaging is used to monitor the influx of porphyrin microbubbles into the tumor, while photoacoustic imaging can be used to validate the micro-to-nano conversion and retention of porphyrins in the tumor. In addition, fluorescence imaging of whole blood can be employed for investigating the cause of the decrease in photoacoustic signal to further verify the results. Therefore, porphyrin microbubbles introduce a variety of new imaging and therapeutic applications for microbubbles, harnessing the advantages of ultrasound-based methods.

Aiming to accomplish real-time, high-resolution, and high-sensitivity images simultaneously, another trimodal imaging contrast agent was developed by loading SPIO nanoparticles into the core of poly(lactic acid) microbubble, followed by adsorbing CdTe QDs onto the microbubble surface for US, MR, and fluorescence imaging [85]. The strong fluorescence of the obtained MBs confirmed that CdTe

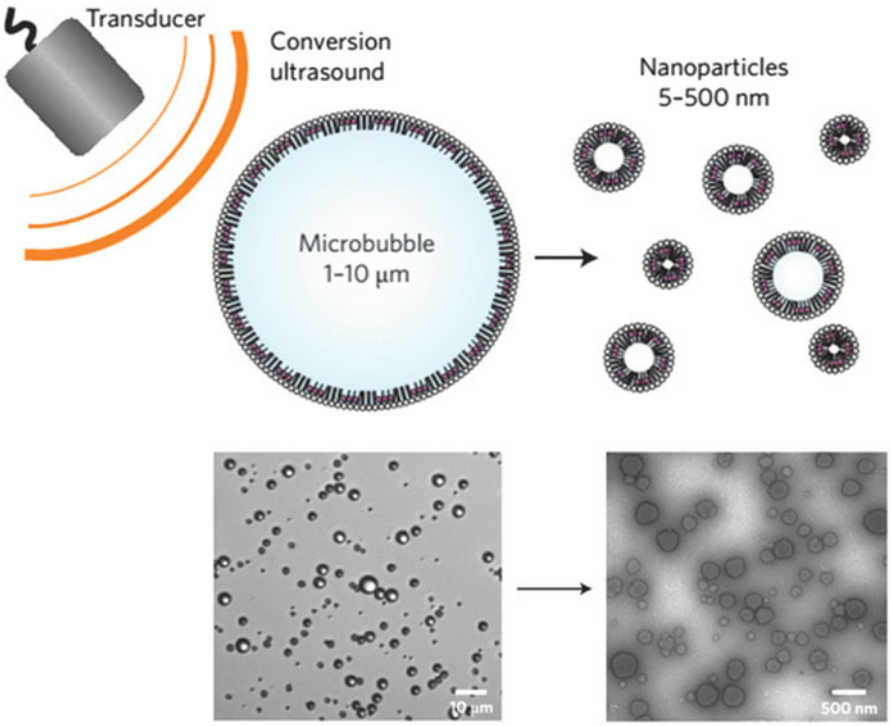

Fig. 4.7 Schematics of porphyrin microbubbles and their micro-to-nano conversion (Reprinted with permission from Macmillan Publishers Ltd: Ref. [84], Copyright 2015).

QDs were successfully deposited onto the surface. The loading SPIO nanoparticles confer MBs' capability to enhance T_2-weighted MR imaging. Furthermore, the in vitro and in vivo ultrasonography indicated that MBs still maintained excellent ultrasound contrast property after loading CdTe QDs and SPIO nanoparticles. The above three imaging methodologies are complementary in modern diagnostic practice due to the combination of real-time, cost-effective US-based imaging with high spatial resolution and excellent soft-tissue contrast of MRI and highly sensitive fluorescent imaging. In addition, the versatility of this strategy provides further feasibility to load other suitable nanoparticles, target molecules or drugs for multimodal imaging, and enhanced targeting and local drug delivery, boosting the development of a new multifunctional diagnostic tool.

4.5 Multifunctional Ultrasound Contrast Agents for Imaging-Guided HIF Therapy

High-intensity focused ultrasound (HIFU) has attracted extensive attention among biological and medical researchers due to its essential therapeutic applications, such as the thermal ablation of pathological lesions, the temporary disruption of the skin

and the blood–brain barrier, the minimally invasive ultrasound-mediated drug delivery through the transient formation of pores on cell membranes, the ultrasound-induced breakdown of blood clots, and the targeted release of drugs using ultrasound- and temperature-sensitive drug carriers. Theoretically, HIFU destroys the malignant lesions by depositing and converting the acoustic energy into heat in the local volume to rapidly increase the tissue temperature and induce the thermal coagulative necrosis. However, the current HIFU therapy is still not satisfactory clinically owing to its relatively low therapeutic resolution and efficacy. To destroy malignant lesions efficiently without or with little side effect, HIFU enhancement agents have been strongly recommended to enhance the final therapeutic efficacy by lowering the pressure threshold and enlarging the lesion site.

Chen et al. developed a nanoscaled inorganic HIFU enhancement agent consisting of mesoporous silica nanocapsules (MSNCs) as the carriers and an encapsulated temperature-sensitive biocompatible perfluorohexane (PFH) compound as a bubble generator [86]. It was found that the resulted enhancement agent of MSNC-PFH had a pronounced coagulative necrosis effect on bovine liver tissues at the low power of 70 W, and the ablated volume was much enlarged at 120 W compared to mesoporous silica nanocapsules. Upon injection of MSNC-PFH, the tumor could be ablated in just 2 s at as low as 120 W, while no detectable necrosis was observed in cancerous tissues even at 400 W for 2 s when only PBS control was injected. Because of its high stability, efficient PFH loading and release, enhanced tumor ablation capability, and easy uptake by target tissues, such enhancement agent of MSNC-PFH can be a promising theranostic agent for effective HIFU imaging and therapy.

As a successive study, the same group [87] designed a novel multifunctional nanotheranostic agent for combined redox-responsive ultrasound imaging and ultrasound imaging-guided HIFU therapy by further loading a redox-responsive copolymer of polyethylene glycol-disulfide (S-S) hyaluronic acid with the HIFU enhancement agent of MSNC–PFH. The grafted PEG and HA layers endow the nanotheranostic agent of MPH_{SS}–PFH excellent dispersity and targeting capability. After intravenous administration, MPH_{SS}–PFH agent accumulated in the tumor of HepG2 hepatic carcinoma cancer-bearing nude mice due to EPR effect and active targeting of HA to CD44, and then ultrasound contrast enhancement of nanotheranostic MPH SS–PFH could be achieved by the structure transition from the cross-linking to retro cross-linking state of PEG–HA_{SS} complex because of the reducing environment in tumors. In just 30 min of postinjection and blood circulation, the tumor boundary becomes considerably more brightened with an average grayscale value of 47, and the signals are still obvious even in 10 h postinjection with a high grayscale value of 52. Because of the efficient accumulation, PFH bubble cavitations, and thermal effects of nanotheranostic MPH_{SS}–PFH in target tumor environment under redox-responsive MPH_{SS}–PFH-intensified ultrasound imaging guidance, the tailored ultrasound-guided efficient HIFU ablation therapy in vivo has been successfully conducted on human cervical carcinoma HeLa tumor-bearing nude mice in 30 min post-intravenous injection of MPH_{SS}–PFH.

Zhou et al. reported a promising contrast agent based on folate-targeted PFH nanoemulsion (TNEs) for improved ultrasound imaging and enhanced HIFU abla-

tion of tumor via a two-step emulsification process [88]. The targeted temperature-responsive organic nanoemulsion (TNEs) was composed of PFH as liquid core and hydrophilic shells which is consisted of phosphatidylcholine, DSPE-PEG(2000)-folate, glycerol phospholipids, cholesterol, and pulronic poloxame. By employing the "small to big" temperature-responsive phase-transformation strategy, the typical dilemma was successfully resolved on the low imaging and therapeutic efficiencies of small nanoparticles and the difficulties of microsized bubbles to penetrate into the tumor tissues. After the intravenous administration, the permeability of the nanoemulsions into the tumor tissues was enhanced due to their nanosized particle size, and the targeting molecular modification promoted more particles accumulated in the tumor. After enough nanoemulsions accumulated in the tumor tissue, the PFH core (boiling point $\approx$ 56 °C) could act as a phase-change agent under the irradiation of HIFU. When the temperature is increased to 56 °C due to the thermal effect of HIFU, the liquid core of TNEs can be converted sufficiently into microbubbles via the acoustic droplet vaporization (ADV) mechanism. It is very favorable to enhance the capabilities of ultrasound imaging and therapy. The generated bubbles could also be used for US enhanced imaging to monitor the ADV process. Moreover, the HIFU-induced microbubbles could enhance the cavitation effect, thus enhancing ultrasound energy deposition in the targeted region, conducing to the significantly enlarged necrotic volume within single exposure to HIFU irradiation, hence shorter duration, lower power requirement, and less repetition of HIFU ablation of a large lesion. This stimuli-responsive ultrasound imaging and HIFU therapy offer an alternative way to improve the precisions of ultrasonography and efficiency of ultrasound therapy.

Sun et al. developed Fe_3O_4-containing PLGA microcapsules with a mean diameter of 885 nm for enhanced US/MR dual-modal imaging and HIFU therapy [89]. Both in vitro and in vivo studies demonstrated excellent contrast-enhanced capability for US and MR imaging by using Fe_3O_4-containing PLGA microcapsules. In vivo HIFU ablation experiments were performed on breast cancer-bearing rabbit. The HIFU therapeutic process is guided by ultrasound imaging after percutaneous injection of Fe_3O_4-containing PLGA microcapsules at an acoustic power of 150 W and exposure time of 5 s. The results showed the administration of the agent induced the obvious signal enhancement compared with saline and pure PLGA microcapsules as the control. In addition, such agent can be used as the synergistic agent for the noninvasive HIFU breast cancer surgery to improve the HIFU therapeutic efficiency. The pathological examination further verified the structure changes of the targeted tissues.

Since HIFU ablation has its intrinsic limitations for curing residual tumor and preventing tumor, Zhang et al. fabricated methotrexate-loaded PLGA nanobubbles conjugating active tumor-targeting monoclonal anti-HLA-G antibodies (mAbHLA-G) for combination of US imaging, HIFU synergistic agent, and drug loading in a single nanoconstruct (Fig. 4.8) [90]. The obtained mAbHLA-G/MTX/PLGA NBs could enhance the ultrasound imaging both in vitro and in vivo and can specifically target to the HLA-G overexpressing JEG-3 cells both in vitro and in vivo. Their blood circulation time in vivo was much longer than nontargeted MTX/PLGA NBs.

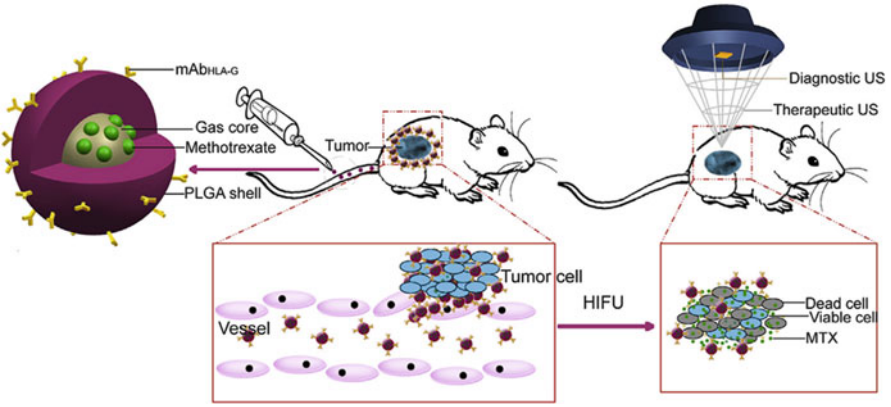

Fig. 4.8 Schematic illustration of the structure of mAbHLA-G/MTX/PLGA NBs and how mAbHLA-G/MTX/PLGA NBs as a synergistic agent improve the treatment efficacy of HIFU ablation for tumor and residual tumor cells (Reprinted from Ref. [90], Copyright 2014, with permission from Elsevier)

The targeted NBs can significantly improve the efficiency of HIFU ablation by changing the acoustic environment. Except for the unique features for contrast-enhanced US imaging and synergistic agents for HIFU, the focused ultrasound can promote the on-demand MTX release from the mAbHLA-G/MTX/PLGA NBs both in vitro and in vivo, which could be used for killing the residual cancer cells after HIFU ablation to maximize the therapeutic effect. Both in vivo histopathology test and immunohistochemical analysis revealed that the combination of mAbHLA-G/MTX/PLGA NBs and HIFU induces the most serious coagulative necrosis, the lowest proliferation index, and the highest apoptotic index. Therefore, the targeted mAbHLA-G/MTX/PLGA NBs can serve as a nanotheranostic agent for the highly efficient, imaging-guided, and noninvasive HIFU synergistic therapy of cancer with the supplementary functions of killing residual tumor cells and preventing tumor recurrence/metastasis.

4.6 Ultrasound Contrast Agents Enhanced Imaging-Guided Photothermal Therapy

4.6.1 Hybrid Ultrasound Contrast Agents for Imaging-Guided Photothermal Therapy

Photothermal therapy for cancer has been widely investigated as a minimally invasive alternative to conventional surgical treatment due to its precisely energy delivery to target tissue and the sensitivity of tumor tissue to temperature increase. Near-infrared light in combination with appropriate light-absorbing agents is

particularly attractive for selective photothermal interaction because of the low absorbance of human tissues in this region. With the development of nanotechnology, a variety of nanomaterials, such as gold nanomaterials (gold nanorod, gold nanocage, and gold nanoshell) [91–93], carbon nanomaterials (carbon nanotubes, grapheme, nanohorns) [94–96], CuS nanoparticles [97], Prussian blue nanoparticles [98], polypyrrole nanoparticles [99], etc., have been explored as NIR-absorbing agents for photothermal therapy of cancers. Before photothermal therapy, the location and size of cancers should be identified; during therapy, the treatment procedure should be monitored in real time; and after therapy, the effectiveness has to be evaluated. All these tasks can be carried out by contrast-enhanced imaging. By guiding laser irradiation with contrast-enhanced imaging, the tumor can be ablated by site-specific photothermal treatment with no damage to the normal tissue.

The utilization of ultrasound contrast agents can improve greatly the resolution and sensitivity of clinical ultrasound imaging. Ultrasound imaging offers a valuable opportunity to administer cancer photothermal therapy with real-time guidance to ensure proper targeting. Due to its readily availability for portable devices, low cost, and lack of radiation exposure [100], percutaneous ultrasound has become a favorite tool to target cancer. In addition, endoscopic ultrasound-guided therapy has emerged as a promising and rapidly developing field that endows another dimension to ultrasound-guided therapy [101]. Uniquely, endoscopic ultrasound can direct therapy toward intra-abdominal cancers that are not easy to access by percutaneous routes. Moreover, it has been demonstrated as a powerful methodology to estimate the temperature change during photothermal therapy by measuring thermally induced differential motion of speckle [102].

Poly(lactic acid) (PLA) microcapsules show good ultrasound contrast-enhanced capabilities [103]. The plasmon resonance and the resulting optical absorption of gold nanoshells can be tuned to the region of near infrared by controlling the thickness of the gold shell and the diameter of the core [104]. The strong optical absorption of nanoshells can rapidly increase the local temperature under the NIR irradiation [105]. Therefore, the NIR-absorbed gold nanoshells can be used as photoabsorbers for remote NIR photothermal ablation therapy. To realize ultrasound imaging-guided photothermal therapy, Dai et al. fabricated for the first time a nanotheranostic agent based on gold nanoshelled microcapsules (GNS-MCs) by electrostatic adsorption of gold nanoparticles as seeds onto the PLA microcapsule surfaces, followed by the formation of gold nanoshells by using a surface seeding method [106] (Fig. 4.9). In vivo enhanced ultrasound imaging experiment was carried out on the New Zealand white rabbits. After bolus intravenous injection of GNS-MCs, excellent enhancements of rabbit kidney were clearly seen within 30 s and lasted more than 5 min. HeLa cells were completely killed after incubation with GNS-MCs followed by an 808 nm laser for 10 min. On the contrary, cancer cells treated with either GNS-MCs or a high-intensity NIR laser alone were not killed at all. The results revealed the potential of GNS-MCs for US imaging-guided photothermal therapy for cancer. However, the GNS-MCs still encountered two main obstacles: (1) the diameter of GNS-MCs (2.32 ± 1.07 μm) is too large to pass through the vessels feeding the tumor; (2) the spatial and anatomical resolution of US imaging is

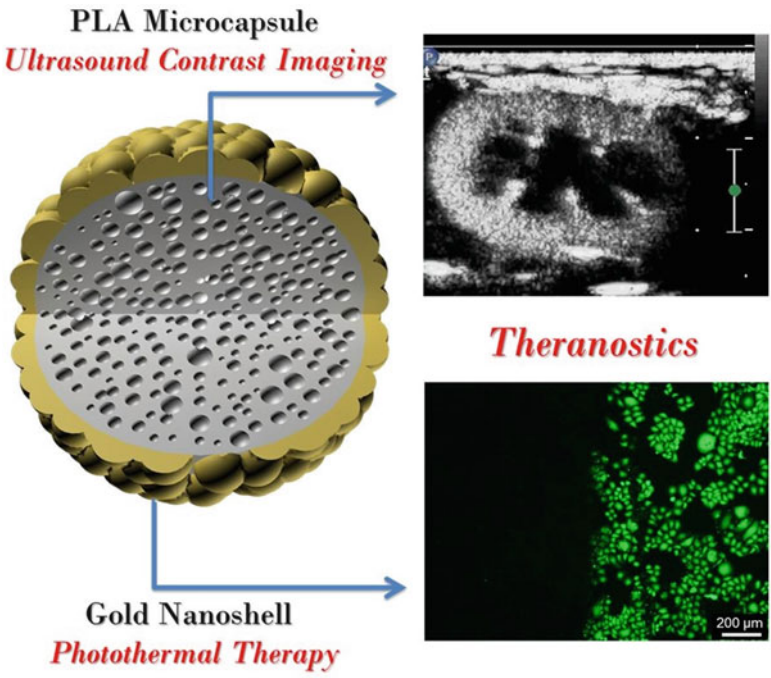

Fig. 4.9 Gold nanoshelled microcapsules operate as a novel theranostic agent for both contrast-enhanced ultrasonic imaging and photohyperthermia (Modified from Ref. [106])

relatively poor. The disadvantages of US might be overcome by the integration of MRI. Therefore, the combination of US and MRI integrated with photothermal therapy could achieve a multifunctional theranostic platform for bimodal imaging-guided and monitored photothermal tumor ablation.

In order to accomplish more efficient photothermal tumor ablation, Dai et al. further upgraded gold nanoshelled microcapsules to nanoscaled theranostic agents for bimodal US/MRI contrast imaging-guided photothermal tumor ablation by incorporating two extra components of SPIOs and PFOB into the PLA nanocapsules (NCs) with additional PEGylation [107]. The SPIOs-embedded PFOB nanocapsules with PEGylated gold shells (PGS-SP NCs) were synthesized via an adapted oil-in-water (O/W) emulsion solvent evaporation process [21], followed by the formation of gold nanoshells using a surface seeding method [30] and surface PEGylation using methoxy-poly(ethylene glycol)-thiol) (Fig. 4.10). Sufficient agent accumulation in diseased areas was achieved by replacing microcapsules with nanoscale capsules as well as PEGylation to help nanocapsules escape the rapid clearance from the bloodstream to increase the circulation time and reinforce the enhanced permeability and retention effect. The in vivo experiments showed that the echo intensity was greatly enhanced within several seconds after the bolus intravenous injection of the agent PGS-SP NCs. Besides, after the intravenous administration of the PGS-SP NCs, the average T2-weighed MR signal intensity in the tumor area decreased rapidly by

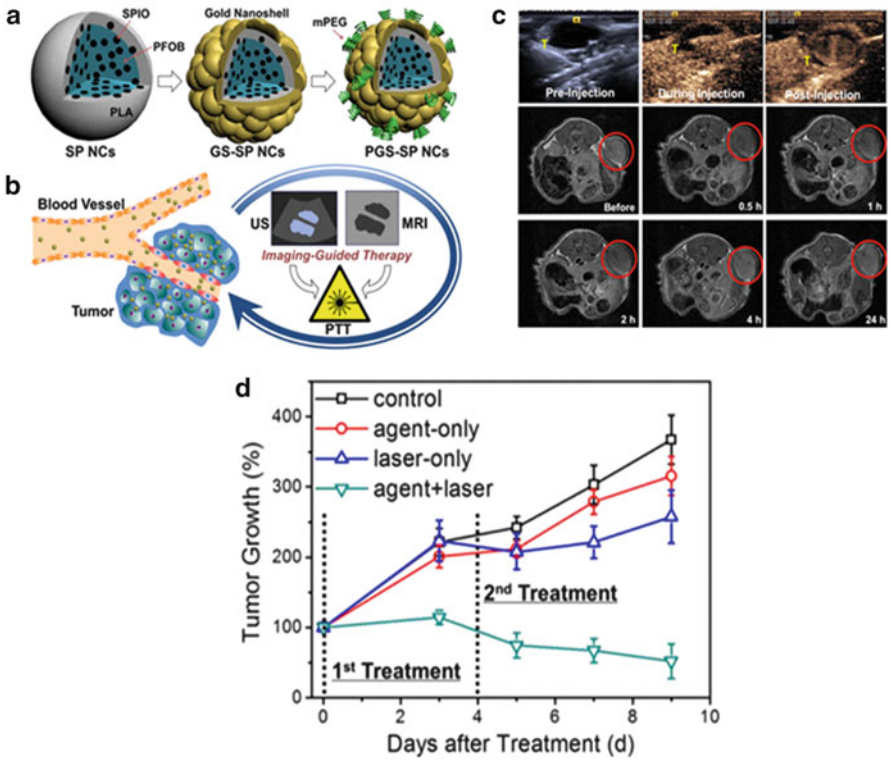

Fig. 4.10 (**a**) Schematic illustration of the fabrication procedure of PGS-SP NCs. (**b**) The biomodal US/MRI-guided tumor PTT process using the nanotheranostic agent. (**c**) Contrast-enhanced ultrasonograms before, during, and after the intratumoral injection of the agent (0.2 mL, 2 mg mL^{-1}) into the mice for visualization of the agent distribution to guide the following therapy (tumors highlighted by T); T2-weighted MR images of the tumors at different time points after intravenous injection of the agent (0.15 mL, 2 mg mL^{-1}) for visualization of tumor areas to guide the following photothermal ablation (tumors are highlighted in the *red circles*). (**d**) Therapeutic effectiveness expressed as tumor growth rate in each group after one-time treatment in nude mouse xenograft models (data expressed as mean ± s.d., n = 8) (Reproduced from Ref. [107] by permission of Theranostics)

31.6 % from 76.7 ± 11.6 to 52.4 ± 8.9. It indicated that introduction of SPIOs into nanocapsules resulted in more accurate diagnostic information from contrast-enhanced MRI images. The phototherapy was carried out on the HT-1080 tumor-bearing nude mice. It was shown that tumors in the agent-laser group decreased significantly (34 % smaller in tumor size); however the other groups grew rapidly. Such a single nanotheranostic agent with the combination of US and MR imaging would be of great value to offer more comprehensive diagnostic information and the dynamics of disease progression for more accurate location of the therapeutic focusing spot in the targeted tumor tissue for more effective tumor ablation.

With large atomic number (z = 79), high X-ray absorption coefficient (5.16 cm^2 g^{-1} at 100 keV), and especially the great biocompatibility and nontoxicity [108],

gold nanostructures could be the ideal candidates for contrast-enhanced CT imaging, providing about 2.7 times greater contrast enhancement per unit weight than iodine, the clinical applied CT contrast agents [109]. This enables the gold nanoshell potential dual functional nanomaterials for combined CT diagnosis and photothermal therapy. The clinical application of ACUSON S3000 ultrasound system combining real-time US and 3-D CT has triggered great interest in designing multifunctional contrast agents for US/CT bimodal imaging or theranostic agents for US/CT bimodal imaging-guided therapy. Dai et al. explored the capability of PFOB nanocapsules coated with PEGylated gold nanoshell for combined systemic US/CT imaging diagnosis and NIR light laser-induced photohyperthermia. The resulting nanocapsule agent not only provided excellent contrast enhancement for both ultrasound and CT imaging in vitro and in vivo but also served as efficient photothermal agent for tumor ablation on xenografted nude mouse modal. CT imaging can provide additional anatomic information while US imaging could achieve real-time imaging.

Recently, the group developed gold nanoparticles containing PLA microcapsules followed by depositing graphene oxide (GO) onto the microcapsule surface via electrostatic layer-by-layer self-assembly technique for US/CT bimodal imaging-guided photothermal tumor destruction. Au NPs act as a contrast agent to enhance CT imaging and GO is used as a strong NIR light-absorbing agent for photothermal ablation of cancer [110]. In vivo CT and US imaging experiments showed that the obtained microcapsules could serve as a contrast agent to simultaneously enhance X-ray CT imaging and US imaging greatly. In addition, the near-infrared light ablated the tumor completely within 9 days in the presence of the microcapsules and the tumor growth inhibition was 83.8 %. The combination of real-time US with 3-D CT through a single microcapsule agent is very helpful for accurately interpreting the obtained images, identifying the size and location of the tumor, guiding and monitoring the photothermal therapy, as well as evaluating the effectiveness of photothermal therapy. Li et al. fabricated a multifunctional theranostic agent by loading iron oxide nanoparticles into PLA microcapsules followed by surface functionalization with graphene oxide. The resulting microcapsules could serve as a contrast agent to simultaneously enhance ultrasound, magnetic resonance, and photoacoustic imaging, as well as photothermal therapy of cancer [111].

Ultrasound-mediated drug delivery as well as image guidance may play a major role in improving the local deposition of a therapeutic agent and reducing the systemic side effects. However, the “hard” gold nanoshells are not easy to be disrupted, and most of them will not penetrate into the tumor due to the relative large size, which may lead to insufficient ablation of tumor cells. Unlike photothermal conducting gold shells, the much smaller CuS nanoparticles have more chance to reach their targets and be cleared from the body through the renal system [112]. In addition, the NIR absorption of CuS nanoparticles from *d–d* transition of Cu^{2+} ions is not affected by the solvent or the surrounding environment when CuS NPs are formulated or delivered in vivo [97]. Therefore, a novel microbubble system was developed for both ultrasound imaging and targeted CuS nanoparticle delivery through ultrasound-targeted microbubble destruction (UTMD) to kill tumor cells by photo-

thermal effect by Zha et al. [113] (Fig. 4.11a). The composite MBs were fabricated by depositing photothermal CuS NPs onto the outer surface of ST68 microbubbles filled with inert gas of perfluoropropane (CuS-ST68 MBs). Besides outstanding ultrasound imaging capability, the "soft" CuS-ST68 MBs could activate violently and then release the CuS nanoparticles, which could penetrate into the tumor interstitium to kill the tumor cells sufficiently with the aid of NIR light irradiation. The excellent US imaging enhanced capability is proved in in vitro and in vivo experiment. The samples were filtrated through 0.45 um filters after insonation to simulate leaky tumor vascular, and the result revealed more than 98 % CuS NPs were passed through the filters, verifying the capacity of ultrasound-mediated CuS delivery. In the cancer cell photothermal ablation experiment (Fig. 4.11b), only the HeLa cells

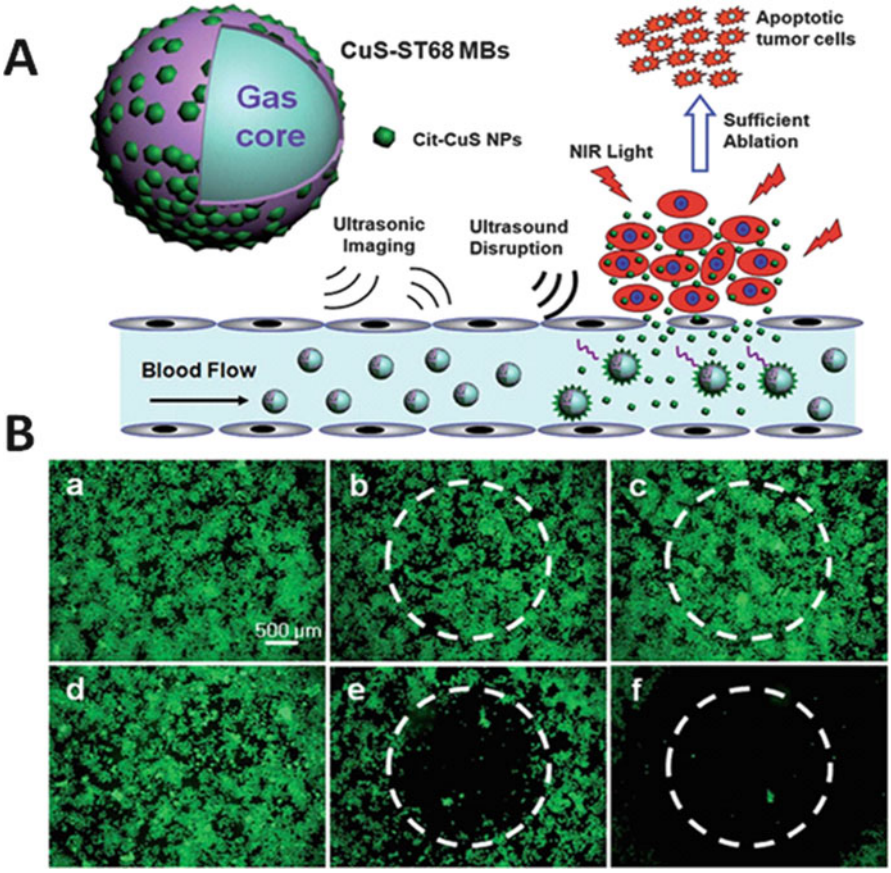

Fig. 4.11 (**a**) Schematic illustration of combined ultrasonic imaging and enhanced photothermal therapy with CuS-ST68 MBs through UTMD. (**b**) Photothermal therapeutic efficacies of the CuS-ST68 MBs: (*a*) no agent and no laser; (*b*) laser only; (*c*) ST68 MBs with 5 min laser irradiation; (*d*) CuS-ST68 MBs only, ST68-CuS MBs with (*e*) 5 min and (*f*) 10 min laser irradiation (Reproduced from Ref. [113] with permission from the Royal Society of Chemistry)

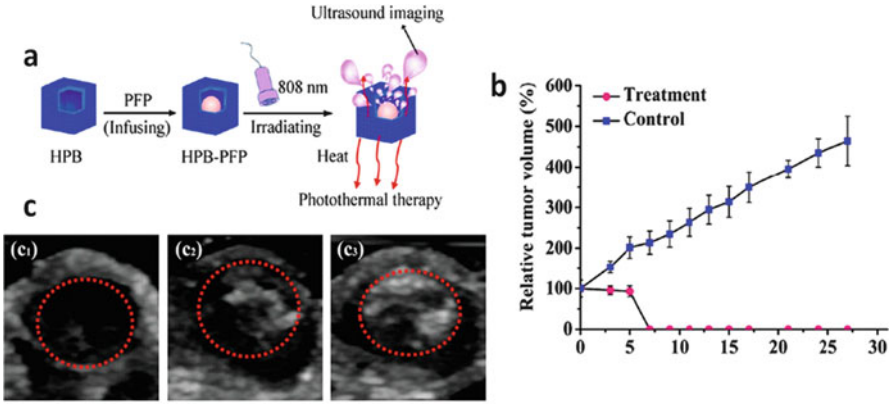

Fig. 4.12 (**a**) Schematic illustration of HPB–PFP formation and US-guided PTT upon laser irradiation, (**b**) relative tumor volume with time after PTT curve, (**c**) in vivo US images of tumor site (*red dotted circle*) (*c1*) before and (*c2*) after injection of HPB–PFP solution (30 μL, 200 ppm) and (*c3*) after being irradiated by 808 nm laser light at 2 W/cm^2 for 5 min (Reprinted with permission from Ref. [114]. Copyright 2015 American Chemical Society)

incubated with CuS-ST68 MBs followed by NIR laser irradiation experienced substantial cellular death, revealing that CuS-ST68 MBs had the potential of releasing CuS NPs under high ultrasound energy to penetrate into the tumor tissue for efficient photothermal ablation of cancer cells.

Jia et al. developed a n-perfluoropentane (PFP)-encapsulated hollow mesoporous Prussian blue (HPB) nanoparticles by vacuum infusion for combined ultrasound tumor imaging and photothermal therapy. When irradiated by NIR laser, the heat produced by HPB can not only cause the coagulation necrosis of tumors but also induce the liquid–gas phase transition, which results in the great enhancement of US signal intensity (Fig. 4.12) [114].

Both US and PA are noninvasive imaging tools, which share the components responsible for detecting the sound wave. Dual-modal contrast agents for US and PA have become a potential method that provides complementary information, US imaging for morphological details and PA imaging for functional information. Recently, Wang et al. proposed a US/PA dual-modality contrast agent composed of gold nanorods and human serum albumin-shelled MBs [115]. The gold nanorods were used as NIR light absorber to enhance the PA signals and generate photothermal effect.

Although the laser-induced photothermal therapy has attracted much attention as a noninvasive approach, it usually fails in cancer therapy by using photothermal therapy alone because of the inhomogeneous heat distribution with tumor tissue and thus leading the tumor recurrence and metastasis. The combination of NIR photothermal and chemotherapy can greatly enhance the sensitivity of chemotherapy, which in turn could further kill the residual tumor cells after the photothermal treatment. For this purpose, Cai et al. developed a multifunctional nanotheranostic platform composed of perfluoropentane (PFP) and doxorubicin (DOX) containing

mesoporous Prussian blue NPs (HMPBs) for in vivo synergistic chemothermal tumor therapy and synchronous diagnostic and monitoring by US and PA imaging [116]. The resulted HMPBs showed excellent photothermal effect attributed to its high molar extinction coefficient (~1.2×10^{11} $M^{-1}cm^{-1}$) and very high photothermal conversion efficiency (41.4 %). Besides, ultrahigh drug loading capacity was up to 1782 mg g^{-1} because of the special characteristics of hollow mesoporous structure, such as numerous mesopores and huge cavity in the outer shell, and the presence of electrostatic interaction between HMPBs (negative charged) and DOX (positive charged), as well as strong coordinative bonding between inherent Fe(III) in the structure of HMPBs and chemical groups of DOX at pH 7.4. The drug delivery is stimuli-responsive at reduced PH value and/or increased temperature, which is beneficial for targeted drug delivery to enhance the antitumor efficiency and reduce the side effects of chemotherapy. The in vivo cancer therapy is performed on HeLa tumor-bearing female nude mice. Compared to the control groups, the entire treatment group showed inhibited tumor growth. The DOX/PFP-loaded HMPBs without laser showed a higher tumor inhibitory effect than free DOX because the DOX/PFP-loaded HMPBs were more internalized by cancer cells. The group treated with the PFP-loaded HMPBs in combination with NIR laser irradiation showed much enhanced inhibitory rate because of the photothermal effect of HMPBs, but failed in complete removal of the tumor. The group treated with DOX/PFP-loaded HMPBs and laser irradiation showed remarkably enhanced inhibitory effect, and the tumor completely disappeared in 4 weeks posttreatment. It provided an evidence for the excellent synergistic effect in the chemothermal therapy for tumor, which is promising to overcome the inevitably tumor recurrence and metastasis that resulted from the inhomogeneous ablation of single thermal therapy. In addition, the therapy can be guided and monitored by using the PA/US dual-modal imaging.

4.6.2 Ultrasound Contrast Agents Based on Polypyrrole Microcapsules for Imaging-Guided Photothermal Therapy

Despite the significant advantages of ultrasound imaging for guiding photothermal therapy, only a few theranostic photothermal agents with capability to enhance ultrasound imaging were developed by physically grafting NIR-absorbing Au nanoshell, Au nanorods, or CuS nanoparticles to ready-made ultrasound contrast agents usually based on microbubbles. Yet, such type of hybrid theranostic agents are still facing numerous hindrances since the incorporating inorganic components would affect the microbubble acoustic response, i.e., a change in the shell stiffness results in the change of the acoustic spectrum and resonance frequency of microbubbles. Especially, microbubble echogenic response at a certain frequency can be reduced. In addition, the potential long-term toxicity of the loaded inorganic components would hinder their further in vivo applications [117]. The simple physical

combination of different diagnostic and therapeutic elements can give a relatively high onetime dose which can induce systemic toxicity and impose an additional stress for the patients to excrete the theranostic agents [118]. It is highly pursued to develop photothermal agents with excellent echogenic response merely from biocompatible organic components for attacking these problems head on.

Polypyrrole (PPy) materials are of great interest in biomedical application because of outstanding stability and good biocompatibility. Because of very low long-term cytotoxicity of PPy materials at low concentrations of PPy NPs (<200 μg mL^{-1}) [119], PPy NPs have been demonstrated as photothermal agent with high photothermal conversion efficiency for tumor ablation owing to the strong NIR absorption spectrum [99]. Due to the excellent echogenic responsiveness and effective scattering of microbubbles, it is highly desired to develop biocompatible NIR-absorbing PPy hollow microspheres (PPyHMs) with outstanding US-responsive capability for US imaging-guided photothermal therapy. Nevertheless, due to the insolubility of polypyrrole materials in common solvents [120], PPyHMs were usually fabricated from in situ polymerization of pyrrole monomer on sacrificial templates, such as polystyrene microspheres [121]. The complicated fabrication process and poor dispersity of PPyHMs limited their further biomedical applications. Zha et al. constructed a photothermal UCA based on microbubbles for the first time merely from polypyrrole via a facile oil-in-water (O/W) microemulsion method [122] (Fig. 4.13a). The PPyHMs showed a well-defined spherical shape, hollow structure, and the diameter with an average of about 0.876 μm using polyvinylpyrrolidone (PVP) as a stabilizer (Fig. 4.13b). On the contrary, no broken and collapsed PPy microspheres were obtained when polyvinyl alcohol (PVA) was used as a stabilizer (Fig. 4.13c). PPyHMs showed a broad absorption band extending from the visible to the NIR region in water, providing the potential application of PPyHMs for NIR light-induced photothermal therapy (Fig. 4.13d). Upon NIR laser irradiation, an obvious concentration-dependent temperature increase was observed for PPyHM solutions (Fig. 4.13e). The solution temperature was elevated from 19.5 °C to 50.6 °C when 100 μg mL^{-1} PPyHM solution was exposed to NIR laser for 10 min. In contrast, only 1.1 °C temperature elevation occurred in the absence of PPyHMs, confirming that PPyHMs could act as an efficient photothermal agent.

The in vivo US imaging-guided photothermal therapy was investigated using PPyHMs as the photothermal agent in a U87-MG tumor mouse model. The local temperature was examined by an infrared (IR) thermal camera (Fig. 4.14a). During the injection of the PPyHMs, tumor areas of the PPyHMs + laser groups were monitored in real time via US contrast imaging to ensure the evenly distribution of the agent and guide the following photothermal therapy (Fig. 4.14b). Then, the tumor-bearing mice of the laser-only groups and the PPyHMs + laser groups with continuous anesthesia were treated with the 808 nm laser irradiation at a low power density of 0.64 W cm^{-2}. The average temperature in the tumor areas of mice from PPyHMs + laser group could rapidly increase to ~60 °C within 5 min, which can kill tumor cells in vivo efficiently. The tumors were effectively ablated only in the presence of PPyHMs in combination with laser exposure, leaving black scars at their original sites without showing reoccurrence. Unlike the PPyHMs + laser group, tumors in

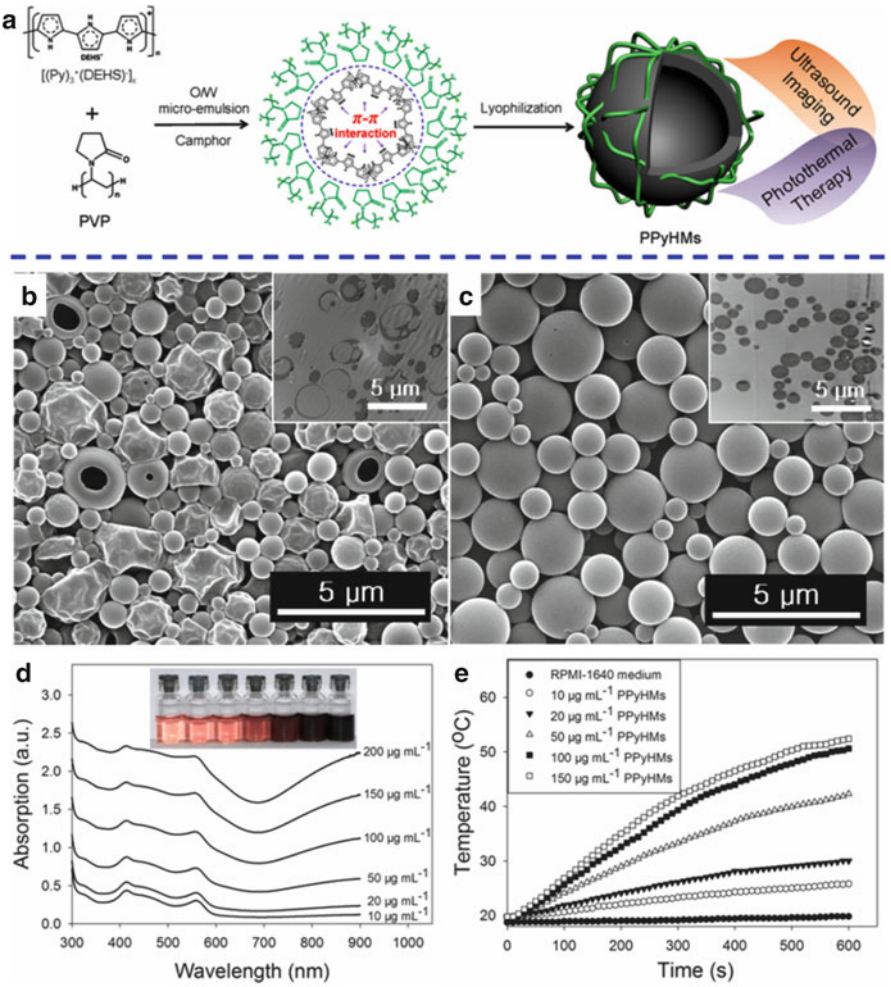

Fig. 4.13 (**a**) Schematic illustration of the formation of echogenic PPyHMs for combined US imaging and photothermal therapy via a facile O/W microemulsion method; SEM and ultrathin-section TEM images of obtained PPyHMs with (**b**) PVP and (**c**) PVA as stabilizers; (**d**) UV–vis–NIR spectra of various concentrations of PPyHMs dispersed in RPMI-1640 culture medium, and inset was the photograph for various concentrations of PPyHMs dispersed in RPMI-1640 culture medium, indicating good dispersibility; (**e**) heating curves of PPyHMs in RPMI-1640 culture medium at different concentrations under 808 nm laser irradiation (Reprinted with permission from Macmillan Publishers Ltd: Ref. [42], Copyright 2013)

other three control groups showed similar growth speed, suggesting that either laser irradiation or PPyHMs alone does not affect the tumor development (Fig. 4.14c, d). Hematoxylin and eosin (H&E) staining of tumor slices showed that significant cancer cell damage, such as karyorrhexis and karyolysis, was noticed only in the tumor with both PPyHM injection and laser irradiation but not in other three control

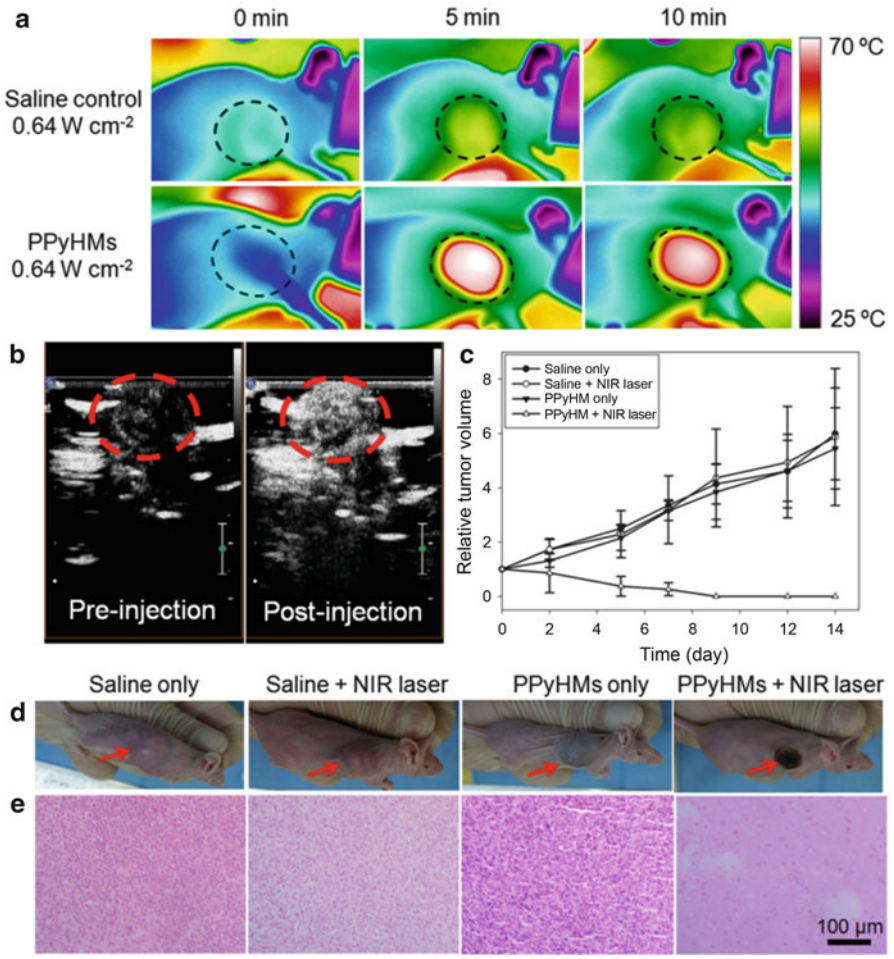

Fig. 4.14 In vivo US imaging-guided photothermal therapy. (**a**) IR thermal images of tumor-bearing mice with and without PPyHM injection exposed to the NIR laser at the power density of 0.64 W cm^{-2} recorded at different time intervals. (**b**) Contrast-enhanced ultrasonograms after the intratumoral injection of PPyHMs (0.2 mL, 2 mg mL^{-1}) into the mice from PPyHMs + laser group for visualization of the agent distribution to guide the following photothermal therapy (tumors are highlighted in the *red circles*). (**c**) The tumor growth curves of different groups of mice after PTT treatment. The tumor volumes were normalized to their initial sizes. (**d**) Representative photographs of mice bearing U87-MG tumors after various different treatments indicated. (**e**) H&E stained tumor slices collected from different groups of mice immediately after laser irradiation. The PPyHMs-injected tumor was severely damaged after laser irradiation (Reprinted with permission from Macmillan Publishers Ltd: Ref. [42], Copyright 2013)

groups, confirming again the excellent therapeutic effectiveness of PPyHMs under NIR laser irradiation (Fig. 4.14e). It should be pointed that we used a rather low laser power density (0.64 W cm^{-2}) to minimize the adverse effects. Combining US imaging and photothermal therapy through PPyHMs is especially attractive due to low dose, simplicity, and cost-effectiveness, no need to incorporate additional NIR-absorbing inorganic components into UCAs. As a successive work, Zha et al. constructed water-dispersible PPy nano- and microcapsules encapsulating perfluorooctylbromide [77]. Because of the favorable NIR-absorbing property of the PPy shell and the good echogenicity of the PFOB core, the resulting PFOB-loaded PPy nano- and microcapsules operated as an excellent multifunctional photothermal agent for a real-time US imaging-guided photothermal treatment of cancer. Therefore, PPy-based UCAs show great potential as a new generation of theranostic agents for clinical applications.

4.7 Ultrasound Contrast Agents for Imaging-Guided Drug Delivery

Despite the development of various new therapeutic innovations such as HIFU and photothermal therapy, chemotherapy remains currently the standard treatment for a wide variety of cancers. Both the pharmacological actions and toxicological effects of a chemotherapeutic drug are related to tissue concentration of the drug. Therefore, the objective of local delivery is to increase the local concentration of a chemotherapeutic agent at the site of disease while minimizing side effects to healthy cells and tissue. Imaging and image guidance of minimally invasiveness play a major role in the preclinical setting as well as in the clinical environment. Ultrasound-mediated drug delivery under imaging guidance may improve the local deposition of a chemotherapeutic agent and reduce the systemic side effects.

The blood–brain barrier (BBB) can be opened temporarily and locally by focused ultrasound (FUS) in combination with circulating microbubbles. Currently, contrast-enhanced magnetic resonance imaging is often applied for monitoring contrast agent leakage to verify BBB opening and infer drug deposition. Despite being administered concurrently, MBs, therapeutic agent, and contrast agent have distinct pharmacodynamic behaviors, thus complicating the quantification and optimization of BBB opening and drug delivery. In recent years, many groups have focused their attention on the development of multifunctional agents for ultrasound imaging-guided and ultrasound-triggered drug delivery.

In order to resolve the above problems, Fan et al. developed an SPIO-labeled phospholipid-based microbubbles incorporating therapeutic agent (doxorubicin, DOX) [123]. These DOX-SPIO-MBs were designed to not only induce BBB opening and therapeutic agent delivery upon FUS exposure but also serve as a US/MR dual imaging contrast agent for directly confirming drug quantification/deposition. In addition, SPIO particles would allow active guiding through magnetic targeting

to achieve enhanced drug delivery by applying an external magnet attached to the scalp in a rat glioma model. It was found that DOX-SPIO-MBs were stable and provided significant superparamagnetic/acoustic properties for imaging. Animals were monitored by T2-weighted MRI and susceptibility-weighted imaging, and the concentration of SPIO nanoparticles was determined by spin–spin relaxivity. After intravenous injection of DOX-SPIO-MBs followed by FUS treatment for 90 s, the mean echo intensity of regions of interest (ROI) in the cortex was enhanced 25.4 % at a maximized value and then remained 12.5 % mean echo intensity enhancement after 18 min of circulation. This long in vivo lifetime of DOX-SPIO-MBs would be beneficial to drug delivery. MRI signal loss was observed in the dorsal sagittal sinus (DSS) and parenchyma vessels (PV) over time due to DOX-SPIO-MBs injection, and the decrease was evaluated to be 40.2 % and 13.3 %, respectively, compared to the control ROI within cerebral cortex (CC). The reduced signals persisted for at least 20 min. BBB opening and drug delivery were achieved concurrently during the FUS exposure. Release of chemotherapeutic agent encapsulated within MBs can be controlled by FUS to reduce reticuloendothelial system (RES) uptake and cell proliferation. In contrast, the FUS treatment cannot enhance the delivery of free DOX. Moreover, the released SPIO nanoparticles were actively targeted to the tumor through magnetic targeting to further enhance and accelerate the local SPIO deposition. The local SPIO deposition in tumor regions increased to 22.4 % due to magnetic targeting. Therefore, DOX-SPIO-MBs combined with FUS can serve as an excellent theranostic tool for future image-guided drug delivery to brain tumors.

Wu et al. proposed a nanodevice based on cut short multiwalled carbon nanotubes (MWCNTs) grafted with polyethylenimine (PEI) for further covalent conjugation to fluorescein isothiocyanate (FITC) and prostate stem cell antigen (PSCA) monoclonal antibody (mAb) (Fig. 4.15) [124]. The in vitro and in vivo toxicity data demonstrated that the obtained nanoagent of CNT-PEI(FITC)-mAb has good biocompatibility. Combined flow cytometry and confocal luminescence imaging experiments confirm that the nanoagent of CNT-PEI(FITC)-mAb can specifically target the cancer cells which overexpress PSCA. In vivo imaging experiments were performed on PC-3 tumor-bearing node mice. After intravenous administration of the nanoagent of CNT-PEI(FITC)-mAb, the echo signal intensity increased quickly within 30 s and then maintains at a steady level, which is markedly higher than that for CNT-PEI(FITC) group and free mAbPSCA competition group. These positive results reveal that CNT-PEI(FITC)-mAb has great potential to be used as a targeted US contrast agent for real-time monitoring of a tumor. The in vivo anticancer efficacy was tested using PC-3 tumor-bearing mice as animal models. The experiment group mice were intravenously injected with 200 mL of CNT-PEI(FITC)-mAb/DOX every 3 days at a drug dose of 5 mg/kg per injection. In the experimental group, the mice tumor growth exhibited considerable slowdown (1.58-fold tumor growth), compared with the other control groups, such as CNT-PEI(FITC)/DOX-treated group (2.13-fold tumor growth) and free DOX group (2.7-fold tumor growth). It obviously demonstrates that CNT-PEI(FITC)-mAb can targetedly deliver drug to the tumors and suppress tumor growth. Therefore, the CNT-

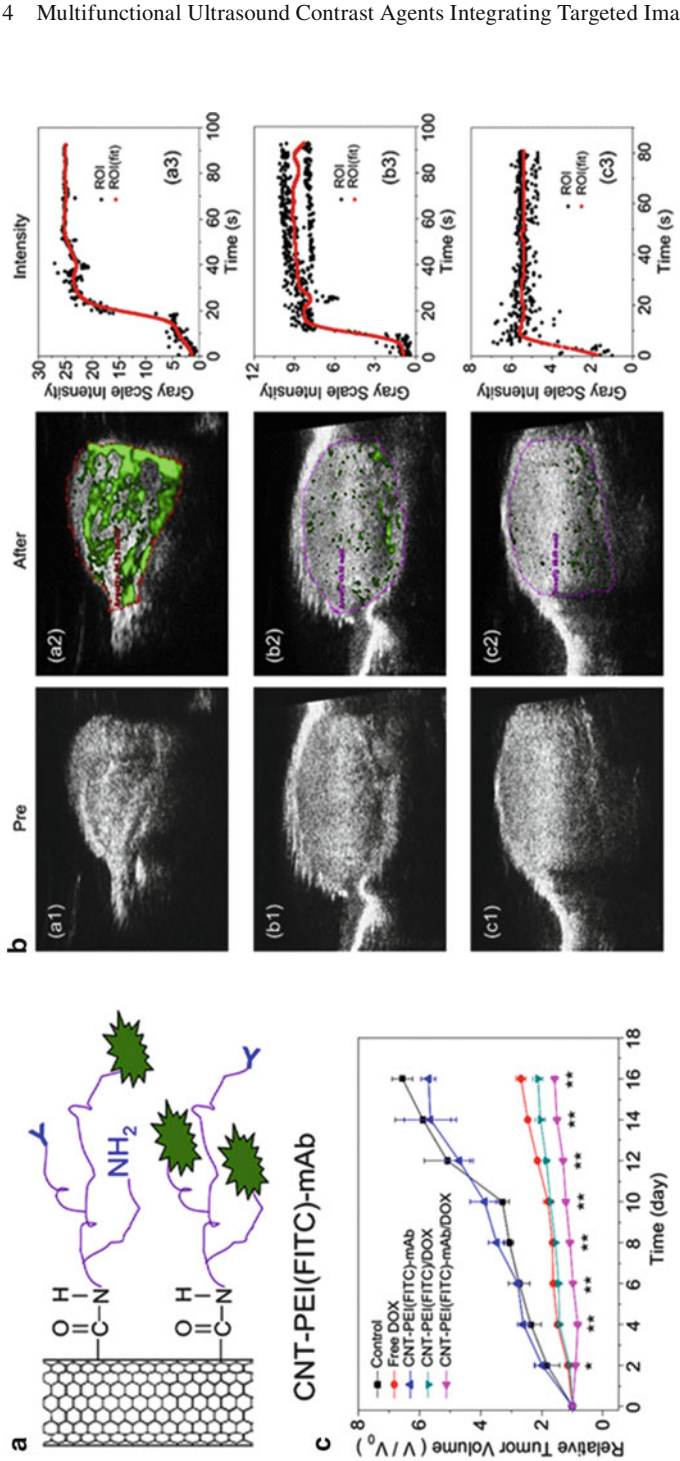

Fig. 4.15 (**a**) Schematic diagram of the synthesis process for CNT-PEI(FITC)-mAb; (**b**) in vivo US imaging data for PC-3 tumor-bearing mice before (*a1–b1*) and after (*a2–b2*) intravenous injection of CNT-PEI(FITC)-mAb (panel a) and CNT-PEI(FITC) (panel b), together with contrast-enhanced US images for the mice pretreated with free mAbPSCA before and after CNT-PEI(FITC)-mAb injection (panel c). (*a3–c3*) Typical grayscale intensity recording in corresponding region (marked in *a2–c2*). (**c**) Tumor growth curves for mice treated with free DOX, CNT-PEI(FITC)-mAb, CNT-PEI(FITC)/DOX, and CNT-PEI(FITC)-mAb/DOX, in comparison with the blank control. The tumor volumes were normalized to their initial sizes. $^{*}P<0.05$, $^{**}P<0.01$ (CNT-PEI(FITC)-mAb/DOX group versus CNT-PEI(FITC)/DOX group) (Reprinted from Ref. [44], Copyright 2014, with permission from Elsevier)

PEI(FITC)-mAb can be employed as a potential multifunctional platform for simultaneous US imaging and drug delivery applications.

Because of upregulated glycolysis to produce lactates and protons in an extracellular environment, the extracellular pH of tumor tissues (6.8–7.2) is lower than that of normal tissues (pH 7.4) [125]. Aiming to choose the lower pH of tumor tissues as a target for tumoral US imaging and simultaneous therapeutic strategies, Min et al. developed doxorubicin-loaded calcium carbonate ($CaCO_3$)-mineralized nanoparticles (DOX-$CaCO_3$-MNPs) with the capability to generate CO_2 bubbles and trigger the release of DOX at tumoral acidic pH through a block copolymer templated in situ mineralization approach (Fig. 4.16) [126]. In vivo studies were performed on cell carcinoma (SCC-7) tumor-bearing C3H/HeN nude mice. The nanoparticles exhibited strong echogenic signals at tumoral acid pH by producing carbon dioxide (CO_2) bubbles and showed excellent echo persistence. Enhancement in US images was observed within 30 min after an intratumoral injection of a DOX-$CaCO_3$-MNP dispersion and lasted up to 120 min, indicating that the DOX-$CaCO_3$-MNPs generated CO_2 bubbles at tumor tissues (PH = ~6.8) sufficient for echogenic reflectivity under a US field. DOX-$CaCO_3$-MNPs have potential to act as a US contrast agent

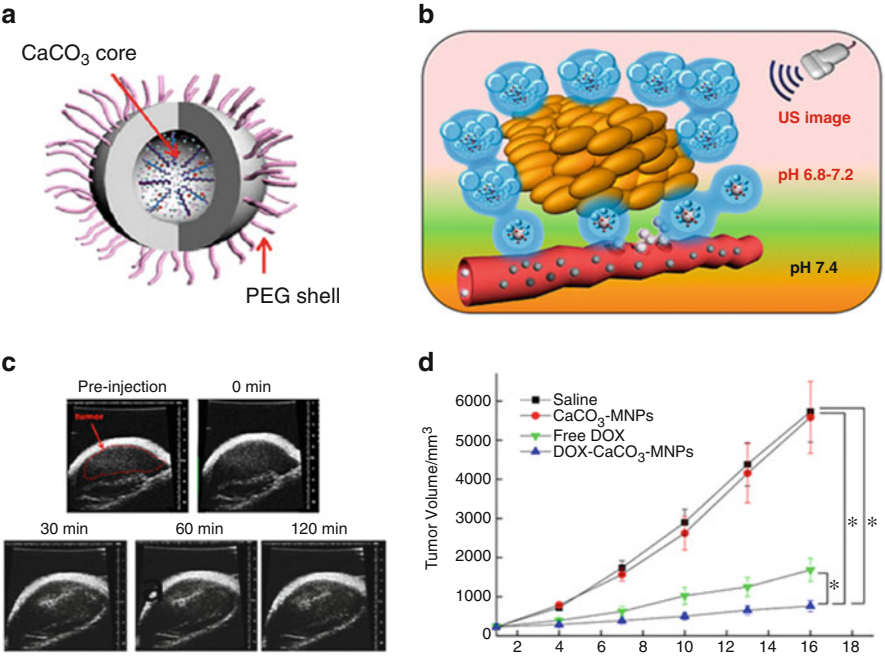

Fig. 4.16 (**a**) Schematic illustration DOX-$CaCO_3$-MNPs. (**b**) Bubble generation and drug release after accumulation of DOX-$CaCO_3$-MNPs at tumor tissues. (**c**) In vivo US imaging of the SCC-7 tumor by intratumoral injection of DOX-$CaCO_3$-MNPs. (**d**) Changes in tumor volumes after injection of saline, $CaCO_3$-MNPs, free DOX, and DOX-$CaCO_3$-MNPs (Reprinted with permission from Ref. [46]. Copyright 2015 American Chemical Society)

for visualization of the low PH environment in tumors. On the contrary, the DOX-$CaCO_3$-MNPs located in the liver (PH = ~7.3) or tumor-free subcutaneous area (PH = ~7.4) showed no enhancement for 120 min due to generating no bubbles of CO_2 necessary for US contrast. The DOX-$CaCO_3$-MNPs could also trigger the DOX release simultaneously with CO_2 bubble generation at the acidic tumoral environment. The therapeutic efficacy of ultrasound imaging-guided chemotherapy was evaluated on the same tumor model. Intratumoral administration of the DOX-CaCO3-MNPs led to a significant inhibition of tumor growth. At 16-day postinjection, the free DOX suppressed the tumor weight by 61 %, while the DOX-CaCO3-MNPs reduced the tumor weight by 85 % as compared with control saline solution. Therefore, the nanoagent of DOX-$CaCO_3$-MNPs exhibited excellent US imaging capability and effective antitumor therapeutic activity in tumor-bearing mice, which may serve as a useful guide for development of various theranostic nanoparticles for US imaging and therapy of various cancers. Although interesting, it has to be noted that the administration of DOX-CaCO3-MNPs was performed intratumorally, limiting the application to well accessible tumors.

The traditional UCAs based on microscaled bubbles have reluctant accumulation in target organs and insufficient stability, which may hinder the accurate response to the ultrasound and limit their further clinical application. In addition, after carrying out the diagnostic or therapeutic functions, elimination of drug carriers from the biologic system should be of concern to us [127]. The drug carriers with large sizes may avoid renal filtration, probably leading to increasing toxicity [128]. In order to overcome these problems, Yang et al. designed and developed a new type of triple-stimuli responsive (ultrasound/pH/glutathione) biodegradable nanocapsules, which was composed of perfluorohexane as a core, and the doxorubicin-loaded biodegradable poly(methacrylic acid) (PMAA) as the shell (Fig. 4.17) [129]. The ultrasound imaging potential of these nanocapsules was investigated on the pancreatic tumor-bearing nude mouse. The PMAA shell has high doxorubicin-loading content (36 wt%) and great drug encapsulation efficiency (93.5 %). These soft nanocapsules have uniform size of 300 nm. After intravenous administration, the DOX-loaded PMAA nanocapsules passively accumulated in the tumor due to EPR effect. Both B-mode and power Doppler ultrasound images showed that the filled PFH can effectively enhance US imaging signal through acoustic droplet vaporization (ADV), thus revealing their potential as an effective ultrasound contrast agents for diagnostic ultrasound imaging and guiding drug delivery. Additionally, due to the tumoral acidic pH and the glutathione reduction condition, a pH/GSH-responsive micellization/demicellization transition was expected, leading to a selective release of the entrapped drug. In vitro drug release studies confirmed the release of doxorubicin from PMAA nanocapsules was responsive to triple stimuli of ultrasound/pH/GSH. The disulfide-cross-linked PMAA shell is biodegradable and thus safe for normal organisms, enabling us to optimize the balance of diagnostic, therapeutic, and biodegradable functionalities in a multifunctional theranostic nanoplatform.

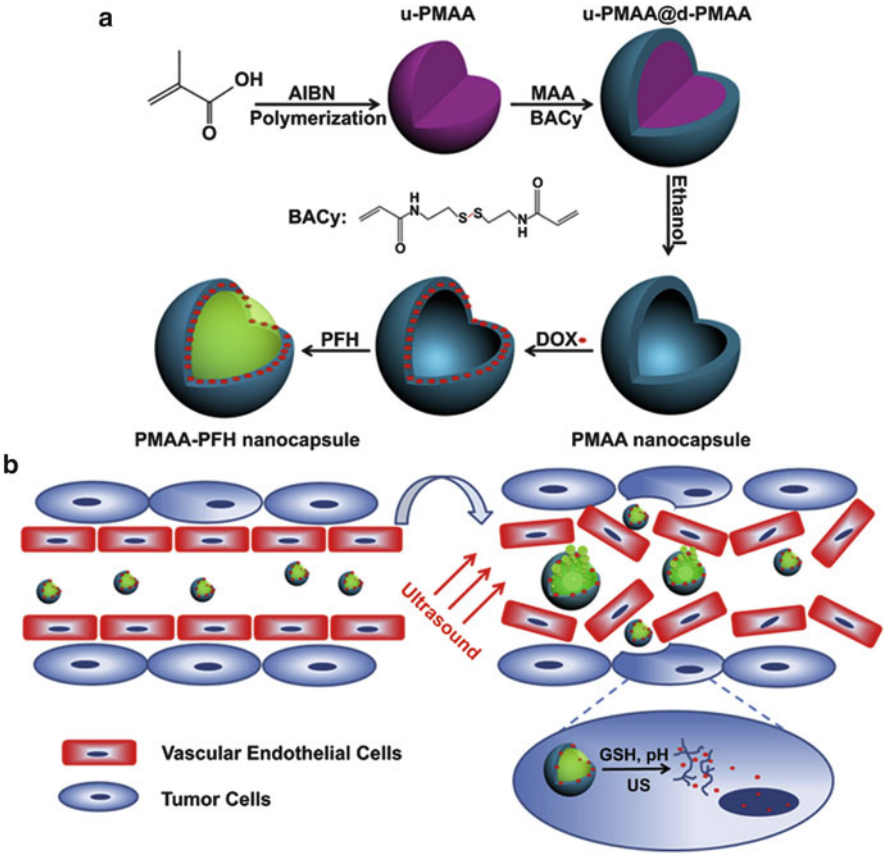

Fig. 4.17 (**a**) Schematic representation of the preparation of DOX-loaded PMAA–PFH nanocapsules. (**b**) Schematic procedure for imaging-guided ultrasound-triggered drug delivery to tumors using biodegradable PMAA-PFH nanocapsules (Reprinted from Ref. [129], Copyright 2014, with permission from Elsevier)

4.8 Photoacoustic Effect-Based Tumor Therapy

Traditional UCAs based on microbubbles have been widely applied in the field of diagnostic ultrasound over the last decades. However, there are still great limitations for in vivo application for microbubble-assisted tumor ultrasound imaging owing to gas diffusion, short circulation lifetime, and poor vascular permeability for the micrometer-scale diameter of microbubbles. Recently, phase-transition perfluorocarbon liquid nanodroplets have attracted intensive research interests due to efficient permeation out of the blood circulation into tumor tissues [130]. Although the perfluorocarbon liquid cores initially show poor ultrasound contrast, significantly enhanced ultrasound contrast can be achieved upon being triggered into gaseous phase [131]. Usually, ultrasound irradiation with a relatively high-pressure

amplitude is applied to trigger the perfluorocarbon liquid into gaseous phase, which is called as acoustic droplet vaporization (ADV). Yet, the pressures and frequencies of conventional diagnostic ultrasound are proved not sufficient to vaporize the surface-stabilizing agents of the droplets [132]. As an alternative way, optical droplet vaporization (ODV) has been recently reported to induce perfluorocarbon nanodroplets [133]. Laser irradiation instead of ultrasound exposure was used to trigger the liquid-to-gas transition of perfluorocarbon nanodroplets incorporating optical absorbing materials. Upon exposure to relatively low pulsed laser energy, conventional photoacoustic signals can be generated due to the transient thermoelastic expansion of the optical absorbers. Contrarily, when the laser energy is beyond a certain threshold, the energy absorbed by optical absorbers may conduce to a sufficiently high local temperature, triggering the liquid-to-gas transition (vaporization) of the droplet. Consequently, the generation of much stronger (nonlinear) temporary photoacoustic signals can be induced compared to those from thermoelastic expansion [80]. Moreover, the triggered gas phase can cause remarkable contrast enhancement to ultrasound imaging as well [134]. Up to now, a variety of optical absorbers have been explored for ODV materials to induce perfluorocarbon nanodroplets. For example, PbS nanoparticles, gold nanostructures [135], and ICG [82] have demonstrated great potential for ODV-based photoacoustic and ultrasound imaging applications.

Recently, Jian et al. fabricated an India ink incorporated optically triggerable phase-transition perfluorohexane nanodroplets (INDs) within a poly-lactic-co-glycolic acid (PLGA) shell by using a modified three-step emulsion process. The nanodroplets could provide not only three types of contrast mechanisms, conventional/thermoelastic photoacoustic, phase-transition/nonlinear photoacoustic, and ultrasound imaging contrasts, but also a new avenue for photoacoustic effect-mediated tumor therapy (Fig. 4.18) [136]. Perfluorohexane with a boiling point of 56 °C can be triggered to gaseous phase by the heat generated from ink based on photothermal conversion. The INDs underwent a liquid–gas phase transition both in vitro and in vivo upon pulsed laser illumination above a relatively low energy threshold (0.5 mJ/cm^2), offering excellent contrasts for photoacoustic and ultrasound dual-modality imaging.

It was found that both traditional and thermoelastic photoacoustic imaging could be enhanced greatly by using the INDs, and the photoacoustic amplitude increased linearly with increasing IND concentrations. When the laser energy is increased to 8 mJ/cm^2, the photoacoustic signal raised to 10 times larger than the conventional signals immediately and then declined to a lower steady state after nearly 30 s. In vivo ultrasound imaging experiment was performed on tumor-bearing nude mice. After the intratumoral injection of INDs followed by laser irradiation for 10 s (12 mJ/cm^2), the ultrasound signal was enhanced 20 times. It indicated that in vivo vaporization of INDs can be triggered with low laser energy within short irradiation time. The triggered gaseous bubbles can produce a significant acoustic impedance mismatch with the surrounding environment, providing excellent contrast for ultrasound imaging in vivo. Thus, the ultrasound imaging could be used to identify the liquid-to-gas process. Interestingly, the nanodroplets have been shown to be capable of destructing cancer cells in vivo with further increased laser energy to ~18 mJ/cm^2

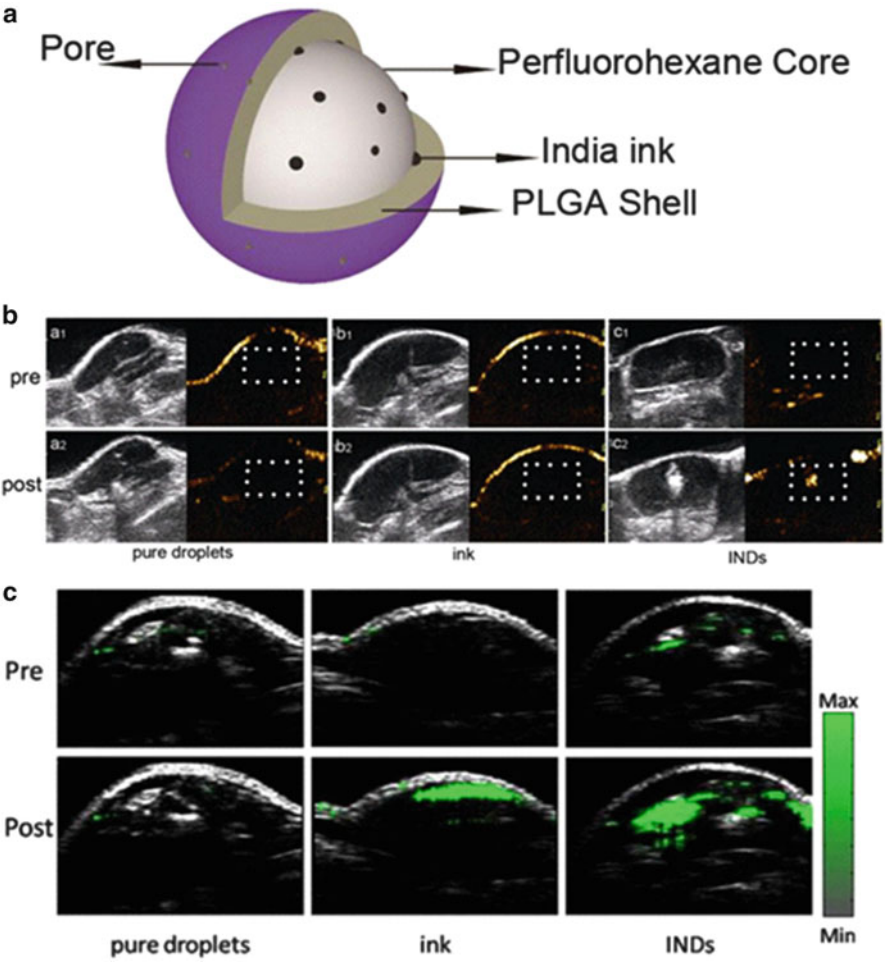

Fig. 4.18 (**a**) Schematic illustration of the architecture of IND NPs; (**b**) US images in routine (*gray scale*) and contrast (*color scale*) modes of the INDs, pure ink (same ink particle concentration as that incorporated in INDs), and pure droplet (without any ink incorporated; with the same PLGA concentration as in INDs) solutions before and after laser irradiation with a fluence of 5 mJ/cm^2 for 10 s (532 nm, Nd:YAG laser). (**c**) In vivo B-scan photoacoustic images of the tumor area before and after intratumoral injection of 40 mg/mL INDs, pure ink, and pure droplets (Reprinted with permission from Ref. [136], Copyright 2014, Theranostics publishing)

for 3 min. The obvious coagulative necrosis and massive cell injuries were observed presumably due to the photoacoustic effect induced shock-wave generation from the particles of the incorporated India ink. In another work, the same group reported the similar results by loading both DiI dye and gold nanoparticles into the perfluorohexane nanodroplets to replace India ink [137]. Therefore, the multifunctional phase-transition nanodroplets have potential to serve as a theranostic agent for photoacoustic/ultrasound dual-modality molecular imaging and targeted, localized cancer therapy.

4.9 Conclusion and Perspective

Multifunctional ultrasound contrast agents can be constructed by loading various functional components, such as doxorubicin, paclitaxel, ICG, quantum dots, gold, grapheme, and Fe_3O_4, into the shells and/or core domains of UCAs, followed by outfitting with ligands for targeting delivery to the tumor sites. Each component has a different function, such as molecular targeting, contrast-enhanced imaging (ultrasound, fluorescence, MRI, CT, photoacoustic imaging, etc.), and therapy (chemotherapy, photothermal therapy, photodynamic therapy, gene therapy, or combined therapy). Therefore, state-of-the-art UCAs can serve as a theranostic platform to be capable of noninvasive imaging diagnosis, real-time imaging guidance, and remote-controlled therapy.

Image-guided therapy based on multifunctional UCAs enables real-time feedback on the biodistribution and the target site accumulation of pharmacologically active agents, allowing for the optimization of drug delivery systems in general, as well as for predicting treatment responses. Furthermore, attempts can be made to correlate the in vitro characteristics of drug carriers to their in vivo capabilities by visualizing and validating some of the basic properties of drug delivery systems. Consequently, it is expected that even more efforts will be invested in developing multifunctional UCAs and that these systems and strategies will contribute substantially to realizing the potential of targeted therapeutic interventions. Nevertheless, many important problems still need to be solved, such as the limited payload of MBs and the short circulation time. Future work should focus on the development of highly stable, biocompatible, targeted multifunctional ultrasound imaging and therapeutic agents and accelerate their clinical translation. Thus, the continued collaboration between chemists, biologists, and clinicians is particularly essential to adapting often biologically incompatible UCAs with outstanding imaging properties for realistic uses.

Acknowledgments This work was financially supported by National Natural Science Foundation for Distinguished Young Scholars (Grant No. 81225011), State Key Program of National Natural Science of China (Grant No. 81230036), and National Natural Science Foundation of China (Grant No. 21273014 and No. 81201186).

References

1. Park JI, Jagadeesan D, Williams R et al (2010) Microbubbles loaded with nanoparticles: a route to multiple imaging modalities. ACS Nano 4:6579–6586
2. Stride E, Edirisinghe M (2008) Novel microbubble preparation technologies. Soft Matter 4:2350–2359
3. Zhang Y, Yang Y, Cai W (2011) Multimodality imaging of integrin αvβ3 expression. Theranostics 1:135
4. Kiessling F, Gaetjens J, Palmowski M (2011) Application of molecular ultrasound for imaging integrin expression. Theranostics 1:127

5. Feinstein SB, Ten Cate FJ, Zwehl W et al (1984) Two-dimensional contrast echocardiography. I In vitro development and quantitative analysis of echo contrast agents. J Am Coll Cardiol 3:14–20
6. El-Sherif DM, Wheatley MA (2003) Development of a novel method for synthesis of a polymeric ultrasound contrast agent. J Biomed Mater Res A 66:347–355
7. Straub JA, Chickering DE, Church CC et al (2005) Porous PLGA microparticles: AI-700, an intravenously administered ultrasound contrast agent for use in echocardiography. J Control Release 108:21–32
8. Leong-Poi H, Christiansen J, Heppner P et al (2005) Assessment of endogenous and therapeutic arteriogenesis by contrast ultrasound molecular imaging of integrin expression. Circulation 111:3248–3254
9. Rychak JJ, Lindner JR, Ley K et al (2006) Deformable gas-filled microbubbles targeted to P-selectin. J Control Release 114:288–299
10. Basude R, Duckworth JW, Wheatley MA (2000) Influence of environmental conditions on a new surfactant-based contrast agent: ST68. Ultrasound Med Biol 26:621–628
11. Takeuchi S, Sato T, Kawashima N (2002) Nonlinear response of microbubbles coated with surfactant membrane developed as ultrasound contrast agent – experimental study and numerical calculations. Colloid Surf B 24:207–216
12. Klibanov AL (2009) Preparation of targeted microbubbles: ultrasound contrast agents for molecular imaging. Med Biol Eng Comput 47:875–882
13. Bartolotta TV, Quaia E (2005) Contrast media in ultrasonography: basic principles and clinical applications. Springer Science & Business Media, Heidelberg
14. Miller DL, Li P, Dou C et al (2005) Influence of contrast agent dose and ultrasound exposure on cardiomyocyte injury induced by myocardial contrast echocardiography in rats 1. Radiology 237:137–143
15. Miller DL (2007) Overview of experimental studies of biological effects of medical ultrasound caused by gas body activation and inertial cavitation. Prog Biophys Mol Biol 93:314–330
16. Brinker J (2002) What every cardiologist should know about intravascular contrast. Rev Cardiovasc Med 4:S19–S27
17. Vancraeynest D, Havaux X, Pouleur AC et al (2006) Myocardial delivery of colloid nanoparticles using ultrasound-targeted microbubble destruction. Eur Heart J 27:237–245
18. Pislaru SV, Pislaru C, Kinnick RR et al (2003) Optimization of ultrasound-mediated gene transfer: comparison of contrast agents and ultrasound modalities. Eur Heart J 24:1690–1698
19. Guo C, Jin Y, Dai Z (2014) Multifunctional ultrasound contrast agents for imaging guided photothermal therapy. Bioconjug Chem 25:840–854
20. Klibanov AL (2002) Ultrasound contrast agents: development of the field and current status. In: Contrast agents II. Springer, Heidelberg
21. Perkins A, Frier M, Hindle A et al (1997) Human biodistribution of an ultrasound contrast agent (quantison) by radiolabelling and gamma scintigraphy. Br J Radiol 70:603–611
22. Unger EC, McCreery TP, Sweitzer RH et al (1998) Acoustically active lipospheres containing paclitaxel: a new therapeutic ultrasound contrast agent. Invest Radiol 33:886–892
23. Church CC (1995) The effects of an elastic solid surface layer on the radial pulsations of gas bubbles. J Acoust Soc Am 97:1510–1521
24. Hvattum E, Normann PT, Oulie I et al (2001) Determination of perfluorobutane in rat blood by automatic headspace capillary gas chromatography and selected ion monitoring mass spectrometry. J Pharm Biomed Anal 24:487–494
25. FRITZ TA, UNGER EC, SUTHERLAND G et al (1997) Phase I clinical trials of MRX-115: a new ultrasound contrast agent. Invest Radiol 32:735–740
26. Xing Z, Ke H, Wang J et al (2010) Novel ultrasound contrast agent based on microbubbles generated from surfactant mixtures of span 60 and polyoxyethylene 40 stearate. Acta Biomater 6:3542–3549

27. Tachibana K (1992) Enhancement of fibrinolysis with ultrasound energy. J Vasc Interv Radiol 3:299–303
28. Price RJ, Skyba DM, Kaul S et al (1998) Delivery of colloidal particles and red blood cells to tissue through microvessel ruptures created by targeted microbubble destruction with ultrasound. Circulation 98:1264–1267
29. Lawrie A, Brisken A, Francis S et al (2000) Microbubble-enhanced ultrasound for vascular gene delivery. Gene Ther 7:2023–2027
30. Porter TR, Iversen PL, Li S et al (1996) Interaction of diagnostic ultrasound with synthetic oligonucleotide-labeled perfluorocarbon-exposed sonicated dextrose albumin microbubbles. J Ultrasound Med 15:577–584
31. Lanza GM, Trousil RL, Wallace KD et al (1998) In vitro characterization of a novel, tissue-targeted ultrasonic contrast system with acoustic microscopy. J Acoust Soc Am 104:3665–3672
32. Hall CS, Marsh JN, Scott MJ et al (2000) Time evolution of enhanced ultrasonic reflection using a fibrin-targeted nanoparticulate contrast agent. J Acoust Soc Am 108:3049–3057
33. Kim DH, Klibanov AL, Needham D (2000) The influence of tiered layers of surface-grafted poly (ethylene glycol) on receptor-ligand-mediated adhesion between phospholipid monolayer-stabilized microbubbles and coated glass beads. Langmuir 16:2808–2817
34. Lindner JR, Song J, Christiansen J et al (2001) Ultrasound assessment of inflammation and renal tissue injury with microbubbles targeted to P-selectin. Circulation 104:2107–2112
35. Wu Y, Unger EC, McCREERY TP et al (1998) Binding and lysing of blood clots using MRX-408. Invest Radiol 33:880–885
36. Allen T, Williamson P, Schlegel RA (1988) Phosphatidylserine as a determinant of reticulo-endothelial recognition of liposome models of the erythrocyte surface. Proc Natl Acad Sci U S A 85:8067–8071
37. Fadok VA, Voelker DR, Campbell PA et al (1992) Exposure of phosphatidylserine on the surface of apoptotic lymphocytes triggers specific recognition and removal by macrophages. J Immunol 148:2207–2216
38. Lindner JR, Coggins MP, Kaul S et al (2000) Microbubble persistence in the microcirculation during ischemia/reperfusion and inflammation is caused by integrin-and complement-mediated adherence to activated leukocytes. Circulation 101:668–675
39. Lindner JR, Dayton PA, Coggins MP et al (2000) Noninvasive imaging of inflammation by ultrasound detection of phagocytosed microbubbles. Circulation 102:531–538
40. Ferrara KW, Merritt CR, Burns PN et al (2000) Evaluation of tumor angiogenesis with US: imaging, doppler, and contrast agents. Acad Radiol 7:824–839
41. Clay CS, Medwin H (1977) Acoustical oceanography: principles and applications. Wiley, New York
42. Soetanto K, Chan M (2000) Fundamental studies on contrast images from different-sized microbubbles: analytical and experimental studies. Ultrasound Med Biol 26:81–91
43. Tweedle MF (2009) Peptide-targeted diagnostics and radiotherapeutics. Acc Chem Res 42:958–968
44. Villanueva FS, Jankowski RJ, Klibanov S et al (1998) Microbubbles targeted to intercellular adhesion molecule-1 bind to activated coronary artery endothelial cells. Circulation 98:1–5
45. Weller GE, Lu E, Csikari MM et al (2003) Ultrasound imaging of acute cardiac transplant rejection with microbubbles targeted to intercellular adhesion molecule-1. Circulation 108:218–224
46. Stieger SM, Dayton PA, Borden MA et al (2008) Imaging of angiogenesis using cadence™ contrast pulse sequencing and targeted contrast agents. Contrast Media Mol Imaging 3:9–18
47. Lanza GM, Wickline SA (2003) Targeted ultrasonic contrast agents for molecular imaging and therapy. Curr Prob Cardiol 28:625–653
48. Kaufmann BA, Carr CL, Belcik JT et al (2010) Molecular imaging of the initial inflammatory response in atherosclerosis implications for early detection of disease. Arterioscler Thromb Vasc Biol 30:54–59

49. Unger EC, McCreery TP, Sweitzer RH et al (1998) In vitro studies of a new thrombus-specific ultrasound contrast agent. Am J Cardiol 81:58G–61G
50. Alonso A, Della Martina A, Stroick M et al (2007) Molecular imaging of human thrombus with novel Abciximab immunobubbles and ultrasound. Stroke 38:1508–1514
51. Pochon S, Tardy I, Bussat P et al (2010) BR55: a lipopeptide-based VEGFR2-targeted ultrasound contrast agent for molecular imaging of angiogenesis. Invest Radiol 45:89–95
52. Pysz MA, Foygel K, Rosenberg J et al (2010) Antiangiogenic cancer therapy: monitoring with molecular US and a clinically translatable contrast agent (BR55) 1. Radiology 256:519–527
53. Kaneko OF, Willmann JK (2012) Ultrasound for molecular imaging and therapy in cancer. Quant Imaging Med Surg 2:87
54. Ferrante E, Pickard J, Rychak J et al (2009) Dual targeting improves microbubble contrast agent adhesion to VCAM-1 and P-selectin under flow. J Control Release 140:100–107
55. Willmann JK, Lutz AM, Paulmurugan R et al (2008) Dual-targeted contrast agent for US assessment of tumor angiogenesis in vivo 1. Radiology 248:936–944
56. Warram JM, Sorace AG, Saini R et al (2011) A triple-targeted ultrasound contrast agent provides improved localization to tumor vasculature. J Ultrasound Med 30:921–931
57. Deshpande N, Needles A, Willmann JK (2010) Molecular ultrasound imaging: current status and future directions. Clin Radiol 65:567–581
58. Yin T, Wang P, Zheng R et al (2012) Nanobubbles for enhanced ultrasound imaging of tumors. Int J Nanomedicine 7:895
59. Rapoport N, Gao Z, Kennedy A (2007) Multifunctional nanoparticles for combining ultrasonic tumor imaging and targeted chemotherapy. J Natl Cancer Inst 99:1095–1106
60. Lanza GM, Wallace KD, Fischer SE et al (1997) High-frequency ultrasonic detection of thrombi with a targeted contrast system. Ultrasound Med Biol 23:863–870
61. Lanza GM, Wallace KD, Scott MJ et al (1996) A novel site-targeted ultrasonic contrast agent with broad biomedical application. Circulation 94:3334–3340
62. Villanueva FS, Lu E, Bowry S et al (2007) Myocardial ischemic memory imaging with molecular echocardiography. Circulation 115:345–352
63. Villanueva FS, Wagner WR (2008) Ultrasound molecular imaging of cardiovascular disease. Nat Clin Pract Cardiovasc Med 5:S26–S32
64. Schumann PA, Christiansen JP, Quigley RM et al (2002) Targeted-microbubble binding selectively to GPIIb IIIa receptors of platelet thrombi. Invest Radiol 37:587–593
65. Louie A (2010) Multimodality imaging probes: design and challenges. Chem Rev 110:3146–3195
66. Pisani E, Tsapis N, Galaz B et al (2008) Perfluorooctyl bromide polymeric capsules as dual contrast agents for ultrasonography and magnetic resonance imaging. Adv Funct Mater 18:2963–2971
67. An L, Hu H, Du J et al (2014) Paramagnetic hollow silica nanospheres for in vivo targeted ultrasound and magnetic resonance imaging. Biomaterials 35:5381–5392
68. Yang F, Li Y, Chen Z et al (2009) Superparamagnetic iron oxide nanoparticle-embedded encapsulated microbubbles as dual contrast agents of magnetic resonance and ultrasound imaging. Biomaterials 30:3882–3890
69. Liu Z, Lammers T, Ehling J et al (2011) Iron oxide nanoparticle-containing microbubble composites as contrast agents for MR and ultrasound dual-modality imaging. Biomaterials 32:6155–6163
70. Nguyen QT, Olson ES, Aguilera TA et al (2010) Surgery with molecular fluorescence imaging using activatable cell-penetrating peptides decreases residual cancer and improves survival. Proc Natl Acad Sci U S A 107:4317–4322
71. Gray DC, Kim EM, Cotero VE et al (2012) Dual-mode laparoscopic fluorescence image-guided surgery using a single camera. Biomed Opt Express 3:1880–1890
72. Tichauer KM, Samkoe KS, Sexton KJ et al (2012) Improved tumor contrast achieved by single time point dual-reporter fluorescence imaging. J Biomed Opt 17:0660011–06600110

73. Zhu Q, Conant E, Chance B (2000) Optical imaging as an adjunct to sonograph in differentiating benign from malignant breast lesions. J Biomed Opt 5:229–236
74. Ke H, Xing Z, Zhao B et al (2009) Quantum-dot-modified microbubbles with bi-mode imaging capabilities. Nanotechnology 20:425105
75. Hernot S, Klibanov AL (2008) Microbubbles in ultrasound-triggered drug and gene delivery. Adv Drug Deliv Rev 60:1153–1166
76. Mai L, Yao A, Li J et al (2013) Cyanine 5.5 conjugated nanobubbles as a tumor selective contrast agent for dual ultrasound-fluorescence imaging in a mouse model. Plos One 8, e61224
77. Zha Z, Wang J, Zhang S et al (2014) Engineering of perfluorooctylbromide polypyrrole nano-/microcapsules for simultaneous contrast enhanced ultrasound imaging and photothermal treatment of cancer. Biomaterials 35:287–293
78. Zha Z, Deng Z, Li Y et al (2013) Biocompatible polypyrrole nanoparticles as a novel organic photoacoustic contrast agent for deep tissue imaging. Nanoscale 5:4462–4467
79. Huynh E, Lovell JF, Helfield BL et al (2012) Porphyrin shell microbubbles with intrinsic ultrasound and photoacoustic properties. J Am Chem Soc 134:16464–16467
80. Wilson K, Homan K, Emelianov S (2012) Biomedical photoacoustics beyond thermal expansion using triggered nanodroplet vaporization for contrast-enhanced imaging. Nat Commun 3:618
81. Hannah AS, VanderLaan D, Chen YS et al (2014) Photoacoustic and ultrasound imaging using dual contrast perfluorocarbon nanodroplets triggered by laser pulses at 1064 nm. Biomed Opt Express 5:3042–3052
82. Hannah A, Luke G, Wilson K et al (2013) Indocyanine green-loaded photoacoustic nanodroplets: dual contrast nanoconstructs for enhanced photoacoustic and ultrasound imaging. ACS Nano 8:250–259
83. Huynh E, Jin CS, Wilson BC et al (2014) Aggregate enhanced trimodal porphyrin shell microbubbles for ultrasound, photoacoustic, and fluorescence imaging. Bioconjug Chem 25:796–801
84. Huynh E, Leung BYC, Helfield BL et al (2015) In situ conversion of porphyrin microbubbles to nanoparticles for multimodality imaging. Nat Nanotechnol 10:325–332
85. Miao ZH, Guo C, ZL L (2015) Fabrication of a multimodal microbubble platform for MR, US and fluorescence imaging application. J Nanosci Nanotechnol doi:10.1166/jnn.2015.10952
86. Wang X, Chen H, Chen Y et al (2012) Perfluorohexane-encapsulated mesoporous silica nanocapsules as enhancement agents for highly efficient High Intensity Focused Ultrasound (HIFU). Adv Mater 24:785–791
87. Wang X, Chen H, Zhang K et al (2014) An intelligent nanotheranostic agent for targeting, redox-responsive ultrasound imaging, and imaging-guided high-intensity focused ultrasound synergistic therapy. Small 10:1403–1411
88. Zhou Y, Wang Z, Chen Y et al (2013) Microbubbles from gas-generating perfluorohexane nanoemulsions for targeted temperature-sensitive ultrasonography and synergistic HIFU ablation of tumors. Adv Mater 25:4123–4130
89. Sun Y, Zheng Y, Ran H et al (2012) Superparamagnetic PLGA-iron oxide microcapsules for dual-modality US/MR imaging and high intensity focused US breast cancer ablation. Biomaterials 33:5854–5864
90. Zhang X, Zheng Y, Wang Z et al (2014) Methotrexate-loaded PLGA nanobubbles for ultrasound imaging and synergistic targeted therapy of residual tumor during HIFU ablation. Biomaterials 35:5148–5161
91. Chen J, Glaus C, Laforest R et al (2010) Gold nanocages as photothermal transducers for cancer treatment. Small 6:811–817
92. Jang B, Park JY, Tung CH et al (2011) Gold nanorod – photosensitizer complex for near-infrared fluorescence imaging and photodynamic/photothermal therapy in vivo. ACS Nano 5:1086–1094

93. Choi WI, Kim J-Y, Kang C et al (2011) Tumor regression in vivo by photothermal therapy based on gold-nanorod-loaded, functional nanocarriers. ACS Nano 5:1995–2003
94. Moon HK, Lee SH, Choi HC (2009) In vivo near-infrared mediated tumor destruction by photothermal effect of carbon nanotubes. ACS Nano 3:3707–3713
95. Zhou F, Xing D, Ou Z et al (2009) Cancer photothermal therapy in the near-infrared region by using single-walled carbon nanotubes. J Biomed Opt 14:021009
96. Yang K, Zhang S, Zhang G et al (2010) Graphene in mice: ultrahigh in vivo tumor uptake and efficient photothermal therapy. Nano Lett 10:3318–3323
97. Li Y, Lu W, Huang Q et al (2010) Copper sulfide nanoparticles for photothermal ablation of tumor cells. Nanomedicine 5:1161–1171
98. Fu G, Liu W, Feng S et al (2012) Prussian blue nanoparticles operate as a new generation of photothermal ablation agents for cancer therapy. Chem Commun 48:11567–11569
99. Zha Z, Yue X, Ren Q et al (2013) Uniform polypyrrole nanoparticles with high photothermal conversion efficiency for photothermal ablation of cancer cells. Adv Mater 25:777–782
100. Cosgrove D (2006) Ultrasound contrast agents: an overview. Eur J Radiol 60:324–330
101. Sandhu IS, Bhutani MS (2002) Gastrointestinal endoscopic ultrasonography. Med Clin North Am 86:1289–1317
102. Varghese T, Zagzebski J, Chen Q et al (2002) Ultrasound monitoring of temperature change during radiofrequency ablation: preliminary in-vivo results. Ultrasound Med Biol 28:321–329
103. El-Sherif DM, Lathia JD, Le NT et al (2004) Ultrasound degradation of novel polymer contrast agents. J Biomed Mater Res A 68:71–78
104. Hirsch LR, Stafford R, Bankson J et al (2003) Nanoshell-mediated near-infrared thermal therapy of tumors under magnetic resonance guidance. Proc Natl Acad Sci U S A 100:13549–13554
105. Yang J, Lee J, Kang J et al (2009) Smart drug-loaded polymer gold nanoshells for systemic and localized therapy of human epithelial cancer. Adv Mater 21:4339–4342
106. Ke HT, Wang JR, Dai ZF et al (2011) Gold-nanoshelled microcapsules: a theranostic agent for ultrasound contrast imaging and photothermal therapy. Angew Chem Int Ed Engl 50:3017–3021
107. Ke HT, Wang JR, Tong S et al (2014) Gold nanoshelled liquid perfluorocarbon magnetic nanocapsules: a nanotheranostic platform for bimodal ultrasound/magnetic resonance imaging guided photothermal tumor ablation. Theranostics 4:12–23
108. Bendayan M, Hayat M (1989) Colloidal gold: principles, methods, and applications. Academic Press, San Diego
109. Geso M (2007) Gold nanoparticles: a new X-ray contrast agent. Br J Radiol 80:64–65
110. Jin Y, Wang J, Ke H et al (2013) Graphene oxide modified PLA microcapsules containing gold nanoparticles for ultrasonic/CT bimodal imaging guided photothermal tumor therapy. Biomaterials 34:4794–4802
111. Li XD, Liang XL, Yue XL et al (2014) Imaging guided photothermal therapy using iron oxide loaded poly (lactic acid) microcapsules coated with graphene oxide. J Mater Chem B 2014(2):217–223
112. Zhang G, Yang Z, Lu W et al (2009) Influence of anchoring ligands and particle size on the colloidal stability and in vivo biodistribution of polyethylene glycol-coated gold nanoparticles in tumor-xenografted mice. Biomaterials 30:1928–1936
113. Zha Z, Wang S, Zhang S et al (2013) Targeted delivery of CuS nanoparticles through ultrasound image-guided microbubble destruction for efficient photothermal therapy. Nanoscale 5:3216–3219
114. Jia X, Cai X, Chen Y et al (2015) Perfluoropentane-encapsulated hollow mesoporous Prussian blue nanocubes for activated ultrasound imaging and photothermal therapy of cancer. ACS Appl Mater Interfaces 7:4579–4588
115. Wang Y, Liao A, Chen J et al (2012) Photoacoustic/ultrasound dual-modality contrast agent and its application to thermotherapy. J Biomed Opt 17:0450011–0450018

116. Cai X, Jia X, Gao W et al (2015) A versatile nanotheranostic agent for efficient dual-mode imaging guided synergistic chemo-thermal tumor therapy. Adv Funct Mater 25:2520–2529
117. Sharifi S, Behzadi S, Laurent S et al (2012) Toxicity of nanomaterials. Chem Soc Rev 41:2323–2343
118. Ma Y, Dai Z, Zha Z et al (2011) Selective antileukemia effect of stabilized nanohybrid vesicles based on cholesteryl succinyl silane. Biomaterials 32:9300–9307
119. Ramanaviciene A, Kausaite A, Tautkus S et al (2007) Biocompatibility of polypyrrole particles: an in-vivo study in mice. J Pharm Pharmacol 59:311–315
120. Jang KS, Ko HC, Moon B et al (2005) Observation of photoluminescence in polypyrrole micelles. Synth Met 150:127–131
121. Bai MY, Cheng YJ, Wickline SA et al (2009) Colloidal hollow spheres of conducting polymers with smooth surface and uniform, controllable sizes. Small 5:1747–1752
122. Zha ZB, Wang JR, Qu EZ et al (2013) Polypyrrole hollow microspheres as echogenic photothermal agent for ultrasound imaging guided tumor ablation. Sci Rep 3
123. Fan CH, Ting CY, Lin HJ et al (2013) SPIO-conjugated, doxorubicin-loaded microbubbles for concurrent MRI and focused-ultrasound enhanced brain-tumor drug delivery. Biomaterials 34:3706–3715
124. Wu H, Shi H, Zhang H et al (2014) Prostate stem cell antigen antibody-conjugated multiwalled carbon nanotubes for targeted ultrasound imaging and drug delivery. Biomaterials 35:5369–5380
125. Gerweck LE, Seetharaman K (1996) Cellular pH gradient in tumor versus normal tissue: potential exploitation for the treatment of cancer. Cancer Res 56:1194–1198
126. Min KH, Min HS, Lee HJ et al (2015) pH-controlled gas-generating mineralized nanoparticles: a theranostic agent for ultrasound imaging and therapy of cancers. ACS Nano 9:134–145
127. Park JH, Gu L, Von Maltzahn G et al (2009) Biodegradable luminescent porous silicon nanoparticles for in vivo applications. Nat Mater 8:331–336
128. Poland CA, Duffin R, Kinloch I et al (2008) Carbon nanotubes introduced into the abdominal cavity of mice show asbestos-like pathogenicity in a pilot study. Nat Nanotechnol 3:423–428
129. Yang P, Li D, Jin S et al (2014) Stimuli-responsive biodegradable poly (methacrylic acid) based nanocapsules for ultrasound traced and triggered drug delivery system. Biomaterials 3:2079–2088
130. Kripfgans OD, Fowlkes JB, Miller DL et al (2000) Acoustic droplet vaporization for therapeutic and diagnostic applications. Ultrasound Med Biol 26:1177–1189
131. Couture O, Bevan PD, Cherin E et al (2006) A model for reflectivity enhancement due to surface bound submicrometer particles. Ultrasound Med Biol 32:1247–1255
132. Singh R, Husseini GA, Pitt WG (2012) Phase transitions of nanoemulsions using ultrasound: experimental observations. Ultrason Sonochem 19:1120–1125
133. Strohm E, Rui M, Gorelikov I et al (2011) Vaporization of perfluorocarbon droplets using optical irradiation. Biomed Opt Express 2:1432–1442
134. Strohm E, Rui M, Gorelikov I et al (2011) Optical droplet vaporization of micron-sized perfluorocarbon droplets and their photoacoustic detection. SPIE BiOS. International Society for Optics and Photonics,78993H-78993H-7
135. Wei CW, Lombardo M, Larson-Smith K et al (2014) Nonlinear contrast enhancement in photoacoustic molecular imaging with gold nanosphere encapsulated nanoemulsions. Appl Phys Lett 104:033701
136. Jian J, Liu C, Gong Y et al (2014) India ink incorporated multifunctional phase-transition nanodroplets for photoacoustic/ultrasound dual-modality imaging and photoacoustic effect based tumor therapy. Theranostics 4:1026
137. Sun Y, Wang Y, Niu C et al (2014) Laser-activatible PLGA microparticles for image-guided cancer therapy in vivo. Adv Funct Mater 24:7674–7680

Chapter 5
Next-Generation Ultrasonic Theranostic Agents for Molecular Imaging and Therapy: Design, Preparation, and Biomedical Application

Hairong Zheng, Yuanyi Zheng, Fei Yan, Mian Chen, and Pan Li

5.1 Introduction

Since the first reported use of ultrasound contrast agents (UCAs) in 1968, the increased needs regarding clinical applications have triggered the rapid development of next-generation UCA. UCAs are highly echogenic microbubbles with many unique properties, which can basically improve the sensitivity of conventional ultrasound imaging to the microcirculation that can be exploited to improve both diagnoses and therapies.

UCAs rely on the different ways in which sound waves are reflected from interfaces between substances. This may be the surface of a small air bubble or a more complex structure. Commercially available contrast media are gas-filled microbubbles that are administered intravenously to the systemic circulation. Microbubbles have a high degree of echogenicity, which is the ability of an object to reflect the ultrasound waves. The echogenicity difference between the gas in the microbubbles and the soft tissue surroundings of the body is immense. Thus, ultrasonic imaging using microbubble contrast agents enhances the ultrasound backscatter, or reflection of the ultrasound waves, to produce a unique sonogram with increased contrast due to the high echogenicity difference.

UCA can be used to image blood perfusion in organs, measure blood flow rate in the heart and other organs, and has other applications as well. The resonance of microbubbles in response to an incident ultrasound pulse results in nonlinear har-

H. Zheng (✉) • F. Yan • M. Chen
Paul C. Lauterbur Research Center for Biomedical Imaging, Institute of Biomedical and Health Engineering, Shenzhen Institutes of Advanced Technology, Chinese Academy of Sciences, Shenzhen 518055, China
e-mail: hr.zheng@siat.ac.cn

Y. Zheng • P. Li
Second Affiliated Hospital and Institute of Ultrasound Imaging of Chongqing Medical University, Chogqing 400010, China

Z. Dai (ed.), *Advances in Nanotheranostics II*, Springer Series in Biomaterials Science and Engineering 7, DOI 10.1007/978-981-10-0063-8_5

monic emission that serves as the signature of microbubbles in microbubble-specific imaging. Various targeting ligands can be conjugated to the surface of microbubbles to attain ligand-directed and site-specific accumulation for targeted imaging. On the other hand, inertial cavitation and destruction of microbubbles can produce a strong mechanical stress enhancing the permeability of the surrounding tissues and can further increase the extravasation of drugs from the blood into the cytoplasm or interstitium. Stable cavitation by high-frequency ultrasound can also mildly increase tissue permeability without causing any damage even at a high acoustic pressure. Microbubbles can carry drugs, release them upon ultrasound-mediated microbubble destruction, and simultaneously enhance vascular permeability to increase drug deposition in tissues.

In addition to current developments in UCA technology, this review introduces the design, preparation, and biomedical application of next-generation ultrasonic theranostic agents in molecular imaging and therapy.

5.2 Design and Preparation

5.2.1 The Development Process and Classification of UCA

Agitated saline as the original UCA was injected into the heart, and then the cloud-like echoes were imaged from the aortic root [1]. Since then, many efforts have been made to develop effective UCA for clinical applications. Table 5.1 shows some commercially available UCA.

The first generation of UCA air bubbles was produced on the basis of the hand-cranked concussion of saline or hydrogen peroxide water. For example, Takada et al. [9] used carbon dioxide mixed with physiologic saline and injected through a catheter positioned into the hepatic artery for small hepatic carcinomas' ultrasound detection. This kind of bubbles has many shortages in its application, such as extremely unstable with short lifetime, nonuniform and too big in size, incapable of pulmonary capillary transport, easy to form air embolism, and so on [10].

Table 5.1 Some commercially developed UCA

Agent	Stabilization	Gas	Manufacturer	Reference
Albunex®	Albumin	Air	Mallinckrodt Medical, Inc.	[2]
Levovist®	Galactose	Air	Schering AG	[3]
SHU563A	Polymer	Air	Schering AG	[4]
Optison®	Albumin	Perfluoropropane	Molecular Biosystems Inc.	[5]
Aerosomes®	Lipid	Perfluoropropane	ImaRx Pharmaceutical	[6]
SonoVue™	Lipid	Sulfur hexafluoride	Bracco Corp.	[7]
Imagent US®	Surfactants	Perfluorohexane	Alliance Pharmaceutical	[8]

The second generation of UCA was air bubbles stabilized by a phospholipid or albumin shell. For instance, Feinstein et al. [11] first used sonication method to make repeatable and stable albumin-coated air microbubbles, which had a longer lifetime, uniform and smaller in size, and could pass pulmonary circulation for left ventricular echocardiography imaging. Albunex® (Mallinckrodt Medical, Inc. St. Louis, MO) and Levovist® (Schering AG, Berlin, Germany), as the representative products of the second generation of UCA, are presently in clinical application.

However, air-based agents are still not stable enough in vivo and can be rapidly destroyed after administration in the bloodstream [12]. The main reason is that air can diffuse through the shell and then dissolve in the surrounding medium within 1 min, leading gas loss from the microbubbles. To address this issue, low solubility and dispersion gas are used as alternative to air. For example, fluorocarbon, with low surface tension, high fluidity, and excellent spreading characteristics, was used as a gas-filled agent, providing minutes of contrast duration in vivo [13]. Optison® (Molecular Biosystems), Aerosomes® (ImaRx Pharmaceuticals), and Imagent US® (Alliance Pharmaceutical) are currently in commercial availability, which can also be recognized as the third generation of UCA.

In recent years, there has been growing development for the notion of the fourth generation of UCA, called targeted UCA. They are gas-filled microbubbles with targeting ligands attached to their shells [14]. They can circulate through the organism and accumulate at the target tissue for ultrasound molecular imaging. In addition, the fourth generation of UCA can also be used as carriers for drug- or gene-targeted delivery. All these will further promote the ability of ultrasound for early detection and therapeutic strategy of disease.

As the shell covering the surface of the bubbles is crucial for its stability and targeting ligand modification, the designing and selection of the shell become particularly important. In general, the shell can be divided as follows:

- Human albumin (such as Optison®). However, it is usually limited by its poor stability, temperature sensitivity, and immunogenicity.
- Lipid (such as SonoVue™), which is biocompatible, stable, and easy to be modified and functionalized for drug or gene delivery.
- Biodegradable polymer (such as SHU563A, AI-700), which also has a good property, but needs larger acoustic pressure to cause the nonlinear resonance than lipid microbubbles.
- Surfactant (such as Imagent US®). Span60, tween40, tween80, or other nonionic surfactants are usually used to fabricate microbubbles.

5.2.2 Microbubble Production Techniques

5.2.2.1 Traditional Methods

Traditional methods, such as sonication, mechanical agitation, or freeze-drying (lyophilization), are used to produce microbubbles [15, 16].

Sonication method is based on the generation of the positive and negative pressure under high-frequency vibration, and the negative pressure will result in the gas dissolution in the solution form tiny bubbles. Meanwhile, the organic molecules such as lipids, proteins, or other amphipathic polymers dissolved in the solution will quickly cover the surface of gas core and then stabilize the formed microbubbles. Although sonication can produce microbubbles efficiently, it still faces some challenges. For example, the process parameters, such as the power and position of the transducer in the liquid, are not easily controlled, which will cause poor reproducibility, and are not suitable for large-scale production. In addition, it is hard to keep aseptic in the production process and face the possibility of heavy metal pollution. Moreover, the hyperthermal effect of sonication will destroy the shell of microbubbles and lead to the inactivation of functional molecules (e.g., ligands, drugs, or genes) within microbubbles.

Mechanical agitation method is based on high-frequency mechanical oscillations, which will make different temporal phase between positive and negative pressure in each point of solution. The presence time and intensity of the negative pressure will influence the size of microbubbles. In general, the higher the frequency, the faster the conversion between positive and negative pressures, which leads to the shorter presence time of negative pressure and the smaller size of the microbubbles. On the other hand, the lower the amplitude, the smaller the intensity of the negative pressure, which also leads to the smaller size of microbubbles. This method can handle the shortage of sonication method mentioned above. However, it is difficult in size and shell thickness control, leading to the instability of acoustic characteristics.

Freeze-drying method is a common method for polymer- or phospholipid-coated microbubble preparation. In brief, microspheres with water core were prepared by double emulsion solvent evaporation, and then water congeals into ice. Subsequently, using vacuum freeze-drying made the ice core from the solid phase to the gas phase to form hollow microbubbles. In addition, the liposomes composed by phospholipid and lyoprotectant will also take shape of porous structure during freeze-drying process, and then the gas can be sealed in the cavities and form microbubbles after filling with saline and shaking. The advantage of this method is more convenient for transport, storage, and reconstruction.

5.2.2.2 Microfluidic Chip Methods

With the development of microelectromechanical systems (MEMS), T-junction and flow-focusing-based microfluidic chip methods have been established for microbubble production [17, 18]. Compared to the traditional methods above, these methods are more convenient for the size and distribution of microbubbles. The principle of T-junction is that the front of dispersed gas phase meets the continuous solution phase at the cross region of the T-shaped junction and then is pressed, forming microbubble in the downstream. Meanwhile, as shown in the Fig. 5.1, flow-focusing method could be divided into three stages: (1) the gas flow enters into the channel

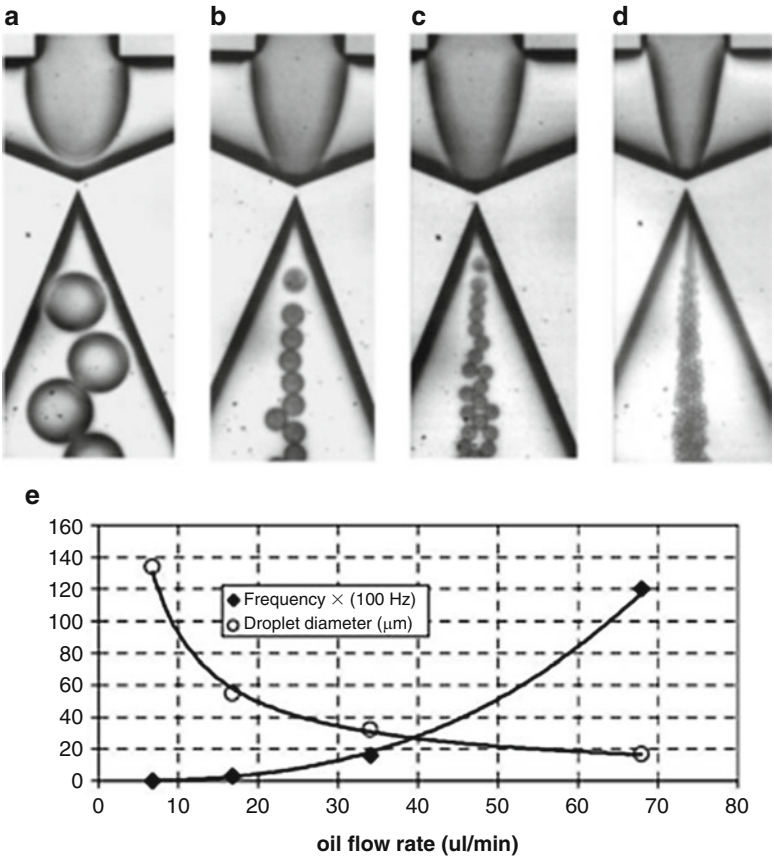

Fig. 5.1 (**a–d**) Formation of water-in-silicone oil droplets using a flow-focusing design with an embedded circular orifice. (**e**) Graph showing decreasing droplet size and increasing frequency of formation with increasing oil flow rate (Reprinted with permission from Ref. [18]. Copyright 2006, Royal Society of Chemistry)

and extends to the outlet, while the width of the gas flow is unchanged; (2) the gas flow constrains the liquid flow toward the outlet and increases the hydrostatic pressure of the upstream and outlet, leading the width of the gas flow to become thinner; and (3) with the Rayleigh–Plateau being unstable, the gas flow becomes fractured and the bubble is released, then the gas flow goes back to the upstream of the outlet for the next cycle. Talu et al. [19] used this method to produce stable monodisperse lipid microbubbles, which could last for several months. However, with different experimental parameters, such as capillary numbers, Weber number, and the shape and size of the cross-sectional channel, the microbubble formation mechanism will be different, and only part of the phenomenon has got a reasonable explanation. In addition, the production rate and efficiency are still very low, which is not suitable for large-scale production so far.

5.2.3 Preparation of Targeted Microbubbles

In addition to output-stabilized and size-designed microbubbles, how to construct these microbubbles with target ability is very significant for molecular imaging and therapy. The most common method is modification of the microbubble shell surface with targeted group, such as antibodies, peptides, glycoproteins, and other small molecules [20, 21]. As microbubbles are limited within the blood vessels after intravenous administration, the targeting sites mainly focus on the surface of the vascular endothelial cells, which exhibit many special adhesion molecules, such as the integrin family [22], selectin family [23], and immunoglobulin superfamily [24]. It was reported that $A_v\beta_3$ integrin, endoglin, and vascular endothelial growth factor receptor (VEGFR) were three of the best characterized molecular markers of tumor angiogenesis [25]. Thus, the evaluation of microbubbles targeted to these markers could be used for tumor detection. In general, there are three methods for the modification of the microbubbles with targeted agents:

- Non-covalent adsorption. By adjusting the solution pH, ionic strength, and temperature, microbubbles can be interacted with targeted agents by electrostatic, π-effects, van der Waals forces, or hydrophobic effects. This method is very simple, but the targeted ability of obtained particle is poor in vivo, which is easily influenced by the complex environment in blood.
- Covalent cross-linking reaction. One way is to prepare the shell of microbubbles with active groups first and then covalent binding these active groups with targeted agents through chemical reactions, such as the reaction of amine and carboxyl groups or click chemistry reaction. The other way is using a cross-linker, which has active groups at both ends of its chemical structure and then has a covalent cross-linking reaction with target agents and the shell of microbubbles, respectively. Unlike non-covalent adsorption, covalent cross-linking reaction is stable mechanically and thermally, so it is difficult to break once formed (Fig. 5.2a) [26].
- Biotin–avidin system. Biotin is a small molecule widely distributed in vivo and can be easily synthesized. It has an unusual structure composed of aureido (tetrahydroimidizalone) ring and valeric acid side chains, which can be covalently combined with an antigen, antibody, enzyme, or nucleic acid. This process is called biotinylation and will not change the activity of markers. Meanwhile, avidin is a tetrameric protein containing four identical subunits, each of which can bind to biotin with a high degree of affinity and specificity. Thus, biotinylated target agents will be very easily grafted onto the surface of avidin-modified microbubbles (Fig. 5.2b) [26].

In the preparation process, some issues need to be paid attention. First, it should consider the order of modification process, such as before or after the generation of bubbles, especially when some targeting agents are easily inactivated. Second, optimization of the ligand number and its distance from the shell is helpful for the success of microbubble targeting. Third, it is necessary to get rid of excess free targeting

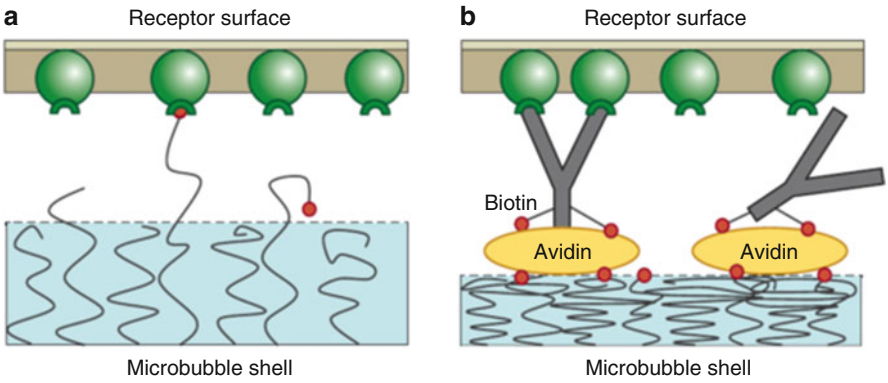

Fig. 5.2 Ligand architectures. Cartoons show different schemes for the presentation of various ligand types: (**a**) small hydrophilic ligands can be covalently attached to the distal end of the carrier lipopolymer. The diffusion of the ligand is dictated by the polymer chain dynamics; (**b**) large, protein ligands can be attached by biotin (*red*) and avidin (*yellow*) linkage. The large size (60 kDa) and multiple binding pockets in the avidin create a sort of scaffold that is supported by the polymeric brush (2–5 kDa) (Reprinted with permission from Ref. [26]. Copyright 2007, Annual Reviews)

agents from the microbubbles. If not, the free targeting agents will also bind to the targeted organs and reduce the recognition efficiency of microbubbles.

5.2.4 Drug-Loaded Microbubbles

Microbubbles is not only used as UCA but is also introduced as a promising drug delivery platform for drug delivery. Structurally, microbubbles consist of a gas core, surrounded by a monolayer or multilayer polymer shell. Based on this special structure, drug could be attached to the external surface by covalent or non-covalent bonds or incorporated the drugs into the polymer shell via an intercalation mechanism (Fig. 5.3) [27]. For example, lipid microbubbles with the positively charged groups of the shell are usually used for DNA loading through electrostatic interactions [28]. After loading, the structure and function of DNA are intact even after insonation. More interestingly, using microbubbles as DNA delivery vehicles can protect DNA from enzymatic degradation and enhance the transfection efficiency [29]. Compared with liposome drug delivery systems, microbubble-based drug delivery systems present more superiority. On the one hand, microbubble is a good UCA for ultrasound imaging, which is beneficial for real-time tracking drug distribution. On the other hand, at high ultrasound intensities, microbubbles begin to oscillate violently, resulting in the destruction of the microbubbles, which is known as inertial cavitation. This phenomenon is very useful for drug-controlled release that will increase drug concentration on the targeted location and reduce the side effects of drug to normal tissues.

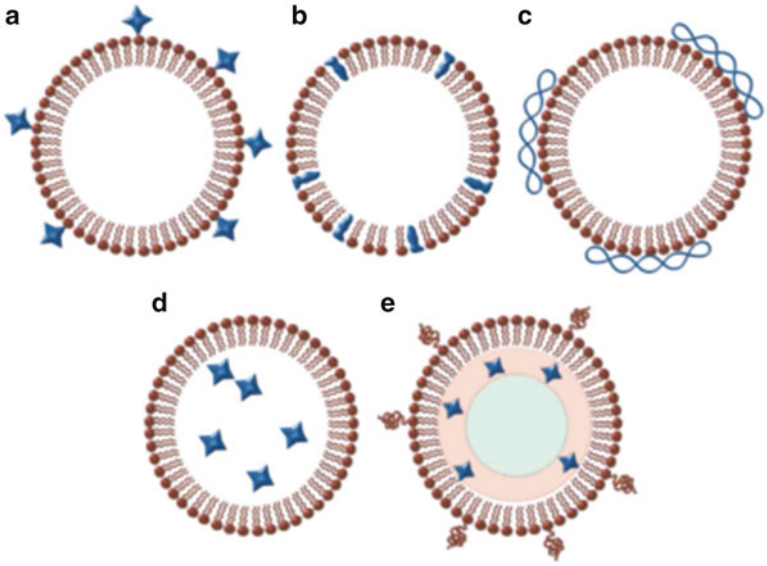

Fig. 5.3 Different strategies of microbubbles to load drugs. (**a**) Drugs may be attached to the membrane surrounding the microbubble. (**b**) Drugs may be imbedded within the membrane itself. (**c**) Materials, e.g., DNA, may be bound noncovalently to the surface of the microbubbles. (**d**) Microbubbles might also be formulated to load the interior with drug and gas, or hydrophobic drugs can be incorporated into a layer of oily material that forms a film around the microbubble, which is then surrounded by a stabilizing membrane. (**e**) In this example, a targeting ligand is incorporated on the membrane allowing targeted delivery of the drug. Note that although in these examples the stabilizing materials are shown as lipids, but it could also be polymeric materials (Reprinted with permission from Ref. [27]. Copyright 2002, Elsevier)

However, microbubble-based drug delivery systems also face some challenges. First, after injection into the systemic circulation, the half-life of microbubble in the blood is relatively short. Second, for the size reason, microbubbles are mainly limited within the blood vessels that are not conducive for drug penetration. Third, the amount of drug carried in microbubble is relatively limited, and it may not be able to prevent leakage of drugs from the bubble. Therefore, it is necessary to optimize the parameters of microbubble, such as size, charge, components, the thickness of the shell, or the surface modification situation.

5.2.5 Fluorocarbon-Based UCA

It has been reported that the contrast enhancement effect was mainly dependent on microbubble size. Large microbubbles (>4 um) strongly enhanced the ultrasound imaging with positive contrast, while small microbubbles (<2 um) showed little enhancement [30]. However, large size of microbubbles is a major limitation to delivering drugs to the outside of the blood vessels or the central nervous system. It

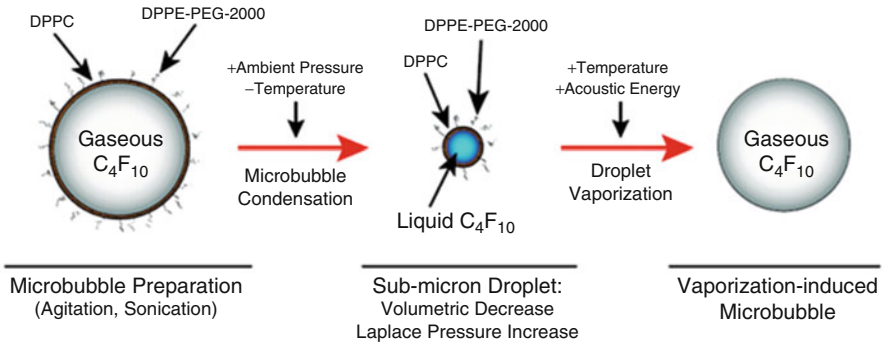

Fig. 5.4 The phase transition of perfluorocarbon was used for the construction of UCA (Reprinted with permission from Ref. [31]. Copyright 2011, American Chemical Society)

means that the requirements of microbubble-based ultrasound imaging and that of drug delivery system are different, which is not conducive for ultrasonic theranostic agent construction. To solve this problem, the phase transition of liquid perfluorocarbon can be used (Fig. 5.4) [31]. When the external pressure is reduced to vapor pressure or the temperature rises to above the boiling point, liquid–vapor phase transition will occur. Perfluorocarbon, compounded with only carbon and fluorine, has good properties, such as low surface tension, high fluidity, high inertness, and nontoxicity. Perfluoropentane is one of the most used perfluorocarbon for liquid–vapor phase transition, whose boiling point is about 29 °C at atmospheric pressure [32]. By the construction of nanoscale liquid perfluoropentane emulsion with targeted agents, it can be used as nanocarrier for drug delivery. Moreover, under certain condition, liquid perfluoropentane conversion into vapor phase results in the significant increase in particle size, which is beneficial for ultrasound imaging. For example, Rapoport et al. [33–35] have developed a series of drug-loaded perfluorocarbon nanoemulsions by the walls made of biodegradable block copolymers. Upon intravenous injections, these nanoemulsions could be observed with a long-lasting, strong, and selective ultrasound contrast in the tumor, indicating their coalescence into larger, highly echogenic microbubbles in the tumor tissue and the capability of combining ultrasonography and targeted chemotherapy.

5.2.6 Multimodality UCA

Each medical imaging modality has its unique strengths and limitations. In clinical practice, the use of multiple modalities may help complete the comprehensive assessment of patients, which means that multiple contrast agents will be given to the patients. The use of multiple agents might increase the economic burden of patients and increase the toxicity and might have interference with each other. Therefore, in recent years, the idea of developing composite contrast agent, which

is qualified to enhance the imaging of multiple imaging techniques, has gained popularity among researchers, and they have come to realize that the multimodality imaging agents can be used to exploit the merits of different imaging modalities to obtain beneficial information for diagnosis and the different imaging modalities could be harnessed with complementary abilities rather than any modality alone in tandem [36]. In order to meet the needs of multimodal imaging, people investigated the integration of two or more imaging modalities within a single device for simultaneous acquisition of anatomical, functional, and molecular information of biological tissue [37]. Ultrasound-based mono-modal imaging possesses many merits such as portability, nonionizing radiation, cost-effectiveness, and high temporal resolution. But there also exist insufficiencies including high operator dependence and being easy to be affected by bone or gas. The observation plane of ultrasound is too small to obtain comprehensive anatomical structure information. And the markedly increased resolution of ultrasound with higher frequencies is at the cost of limited depth of penetration. Thus, the fusion of ultrasound with other imaging modalities to produce multimodality imaging can make up these drawbacks and improve the diagnosis accuracy, which also extends the range of ultrasound molecular imaging [38].

A variety of modalities have been explored for multimodality imaging, including ultrasound (US), nuclear modalities such as positron emission tomography (PET) and single-photon emission computed tomography (SPECT), magnetic resonance imaging (MRI), optical imaging, photoacoustic imaging (PA), and more. Currently, there are three important areas of multimodality molecular imaging research: multimodality instrumentations for image collection, software tools for image construction/registration, and multimodality imaging agents for obtaining molecular information of diseases. The following introduces the ultrasound-based contrast agents for multimodality imaging.

5.2.6.1 US/PA

The combination of ultrasound and photoacoustic imaging supplies a nonionizing, noninvasive, real-time imaging technique capable of visualizing optical absorption properties of tissue at reasonable depth and high spatial resolution, which is a rapidly emerging biomedical and clinical imaging technique. The benefits of the combination are not at the expense of existing ultrasound or photoacoustic imaging functions. The photoacoustic imaging systems are inherently compatible with ultrasound imaging, thereby enabling multimodality imaging with complementary contrast. It has technical significance to develop the highly optical absorption and biocompatible optical contrast agents in the UCA since photoacoustic imaging is highly sensitive to optical absorption.

Indocyanine green (ICG) is one of the first optical contrast agents approved by the Food and Drug Administration (FDA) for clinical applications [39]. The fluorescence emission peak of ICG, with an excitation wavelength of 748–789 nm and emission wavelength of 814–851 nm, falls in the near-infrared wavelength range

with deep penetration of light [40]. The encapsulation of ICG in the ultrasound microbubbles (MBs) or nanobubbles (NBs) will prolong its circulation half-life and protect it from nonspecific molecular interactions [37]. Xu et al. [41] reported that the encapsulation of ICG in the poly(lactic-co-glycolic acid) (PLGA) MBs has yielded dual-mode contrasts for simultaneous US and fluorescence imaging of cancer and they observed more stabilized absorption and fluorescence emission characteristics for aqueous and plasma suspensions of ICG-encapsulated microbubbles. They also fabricated multiple tumor simulators by entrapping ICG MBs or NBs at various concentrations in gelatin phantoms for simultaneous US and PA imaging. And they conjugated the MBs and NBs with CC49 antibody to target TAG-72, a human glycoprotein complex expressed in many epithelial-derived cancers and found that the ICG MBs and NBs can be potentially used as a general contrast agent for multimodal intraoperative imaging of tumor boundaries and therapeutic margins [42].

Gold nanoparticles (GNP) are another optical contrast agent and have a wide application due to their unique physicochemical properties [43]. The GNPs may also be loaded in the MBs or NBs. Simultaneous photoacoustic and US imaging have been observed from GNP-loaded perfluorocarbons droplets, as shown in Fig. 5.5.

In addition to ICG and GNPs, other optical absorption agents, such as India ink, can also be encapsulated in MBs and NBs. Jeon et al. [44] reported generated micro-

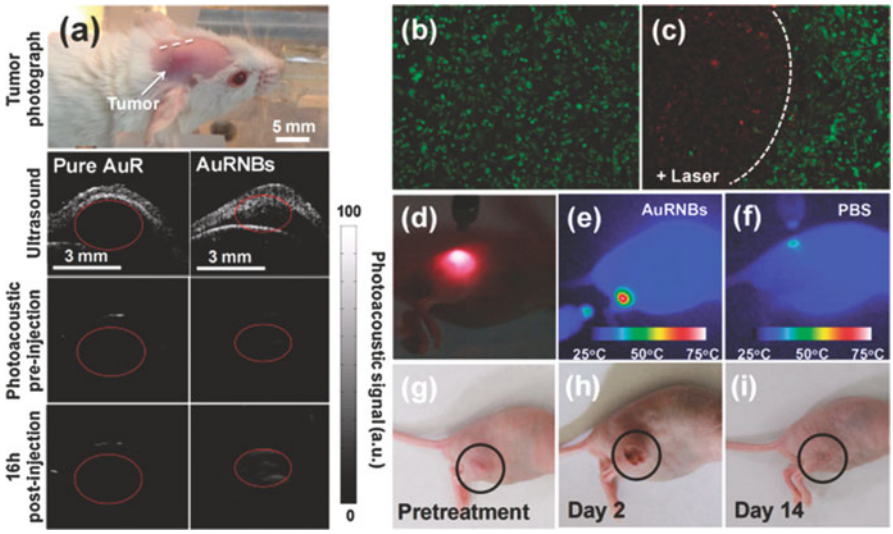

Fig. 5.5 Simultaneous photoacoustic and US imaging with GNP-loaded perfluorocarbons droplets. (**a**) Ultrasound and photoacoustic images of one vertical slice through the tumor. (**b**) Before irradiation and (**c**) after irradiation (808 nm for 2 min, in region *left* of the marker curve), essentially all cells were killed. (**d**–**f**) Converting light absorption into heat by the photothermal effect of AuRNBs and PBS. (**g**–**i**) The NIR laser for pretreatment and treatment after 2 days and 14 days (Reprinted with permission from Ref. [43]. Copyright 2013, Royal Society of Chemistry)

bubbles (a standard UCA) in a solution of methylene blue (a standard photoacoustic dye). India ink-loaded MBs and NBs have been fabricated by a modified double emulsion process [45].

5.2.6.2 US/MRI

MRI is an imaging modality widely used for disease diagnosis and for making therapeutic schedule. The major disadvantage of MRI is its low sensitivity, which results in quite long acquisition times. The fusion of MRI and ultrasound can simplify or settle a series of problems such as spatial and temporal registration, showing great potential for broad application in clinical practice.

Superparamagnetic iron oxide (SPIO) has been a hotspot in the field of multimodality imaging. Many reports showed that SPIO in combination with microbubble can be used for both ultrasound and MR imaging in order to achieve good spatial and temporal resolution. Wang et al. [46] developed the superparamagnetic poly(lactic-co-glycolic acid) (PLGA) microcapsules (Fe_3O_4/PLGA) for the application in ultrasound/magnetic resonance dual-modality biological imaging. Hydrophobic Fe_3O_4 nanoparticles were successfully integrated into PLGA microcapsules by a typical double emulsion evaporation process. Brismar et al. [47] developed an US/MRI dual-mode contrast agent by the introduction of iron oxide nanoparticles (SPIONs) in the shell or on the external surface of the poly(vinyl alcohol) MBs. The presence of SPIONs provided enough magnetic susceptibility to the MBs to accomplish good detectability both in vitro and in vivo. Liu et al. [48] reported the fabrication of iron oxide nanoparticle-embedded polymeric microbubbles as dual-mode contrast agents for hybrid MR/US imaging. These magnetic nano-in-micro imaging probes were prepared via a one-pot emulsion polymerization to form poly(butyl cyanoacrylate) microbubbles, along with the oil-in-water (O/W) encapsulation of iron oxide nanoparticles in the bubble shell. These hybrid imaging agents showed strong contrast in US and an increased transversal relaxation rate in MR.

Based on nanoparticle-based UCA for molecular ultrasound imaging using acoustic droplet vaporization (ADV) [49, 50] or optical droplet vaporization (ODV) [51, 52], Yuanyi Zheng and his group in Chongqing Medical University recently have fabricated the magnetic yolk–shell spheres via a surfactant-assembly sol–gel coating process and a following spontaneous self-transformation procedure. As shown in Fig. 5.6, the perfluorohexane (PFH) was infused into the yolk–shell spheres by capillary action. These nanoparticles could enhance the MRI imaging, and upon exposing to an alternating current (a.c.) magnetic field, the magnetic energy was efficiently transformed into thermal energy by the magnetic droplets, thus leading to the vaporization of the loaded PFH, and a large number of bubbles are released from the mesopores in the outer shells. The generated gas bubbles not only could increase echogenicity for ultrasound imaging but also enhanced the magnetic thermal tumor ablation through stimulating a series of cavitation-related bio-effects, such as mechanical oscillation, cell membrane opening, and free radical release.

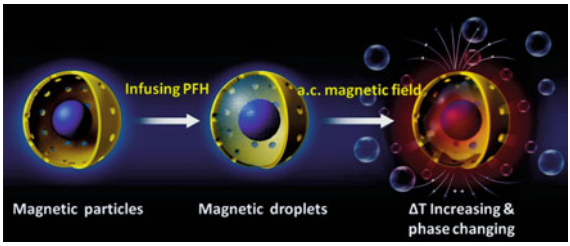

Fig. 5.6 Illustration of the fabrication process of the magnetic droplets and the mechanism of the magnetic droplets vaporization under an a.c. magnetic field

5.2.6.3 US/CT

Like MRI, CT has been widely used in the clinic as well. The major disadvantage of CT is its low sensitivity, which results in quite long acquisition times. Thus, the fusion of CT and ultrasound also can simplify or settle a series of problems such as spatial and temporal registration, showing great potential for broad application in clinical practice.

The earliest study on the US/CT dual-mode imaging employed liquid perfluorocarbon emulsion, the perfluorooctyl bromide (PFOB) nanoparticles. They have the native capability of being UCAs' and CT contrast agents [53, 54]. Liquid PFOB nanoparticles are stable against pressure, air, heat, and shear press. Due to their high boiling point (143 °C), nanosize diameter (60 ~ nm), and stability in vivo, PFOB nanoparticles have stronger tissue penetration ability and long circulation life [55]. Although their backscattering signal is weak because of their small size and liquid core, they come to strong echogenicity when accumulated in tissue, thereby obviously enhancing the signal while reducing the background noise. Also, the bromide atom creates hindrance for X-ray to penetrate, thus could be used to enhance CT imaging. As shown in Fig. 5.7, Dai et al. [56] developed an US/CT dual-mode imaging and theranostic microcapsules by introducing gold nanoparticles into poly(lactic acid) microcapsules via a double-microemulsion method, followed by depositing grapheme oxide onto the microcapsule surface through electrostatic layer-by-layer self-assembly technique. They proved that the microcapsules could serve as a contrast agent to simultaneously enhance US imaging and X-ray CT imaging in vitro and in vivo.

5.2.6.4 Other Imaging

In order to meet the needs of better location and visualization of tumor margins, triple-modality imaging strategies have also been explored. Kim et al. [57] used gold, iron oxide, and islet cells to synthesize capsule-in-capsules which provided immunoprotection for xenografted cells and were detectable by MRI, CT, and US

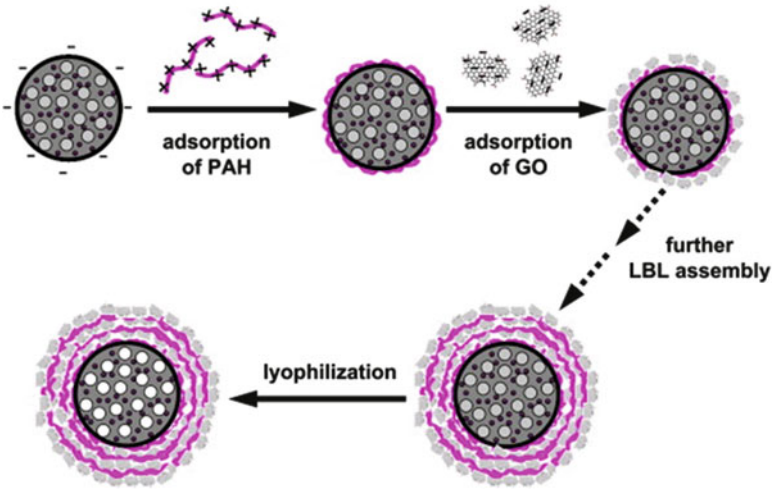

Fig. 5.7 Illustration of the fabrication process of microcapsule of Au@PLA-(PAH/GO) by layer-by-layer (LBL) technique (Reprinted with permission from Ref. [56]. Copyright 2013, Elsevier)

trimodal imaging. Application of these capsules provided a useful strategy to non-invasively detect the spatial and temporal kinetics of the quantity and location of xenografted islets. Barnett et al. [58] designed novel immunoprotective alginate microcapsule formulations containing perfluorocarbons (PFCs) that may increase cell function, provide immunoprotection for xenografted cells, and simultaneously enable multimodality imaging. The results showed that fluorinated capsule could be detected by micro-CT, ultrasonography, and MRI triple-modality imaging. As shown in Fig. 5.8, Kircher et al. [59] reported a triple-modality strategy, which is the first to allow combined MRI, photoacoustic imaging, and Raman imaging (MPR). They developed a gold–silica-based SERS nanoparticle coated with Gd^{3+} ions and found that after these MPR nanoparticles accumulated in the orthotopic mouse glioblastoma but not in healthy brain tissue due to the enhanced permeability and retention (EPR) effect. The duration time for the particles in the tumor is more than 1 week and could be detected with all three modalities in living mice with at least picomolar sensitivity. Qin et al. [60] reported a photoacoustic imaging (PAI), MRI, and PET triple-modality imaging strategy. They introduced the tyrosinase (TYR) gene into cells, and the expressed tyrosinase catalyzes the synthesis of melanin from tyrosine precursors. The melanin could be imaged by three modalities including photoacoustic imaging (PAI), MRI, and PET since melanin has a broad optical absorption spectrum which provides contrast for PAI and has the ability to chelate metal ions (e.g., Fe^{3+}) which provides contrast for MRI13. And, PET can be realized through introducing the melanin avid probes such as N-(2-(diethylamino)ethyl)-^{18}F-5-fluoropicolinamide (^{18}F-P3BZA) as a PET reporter probe.

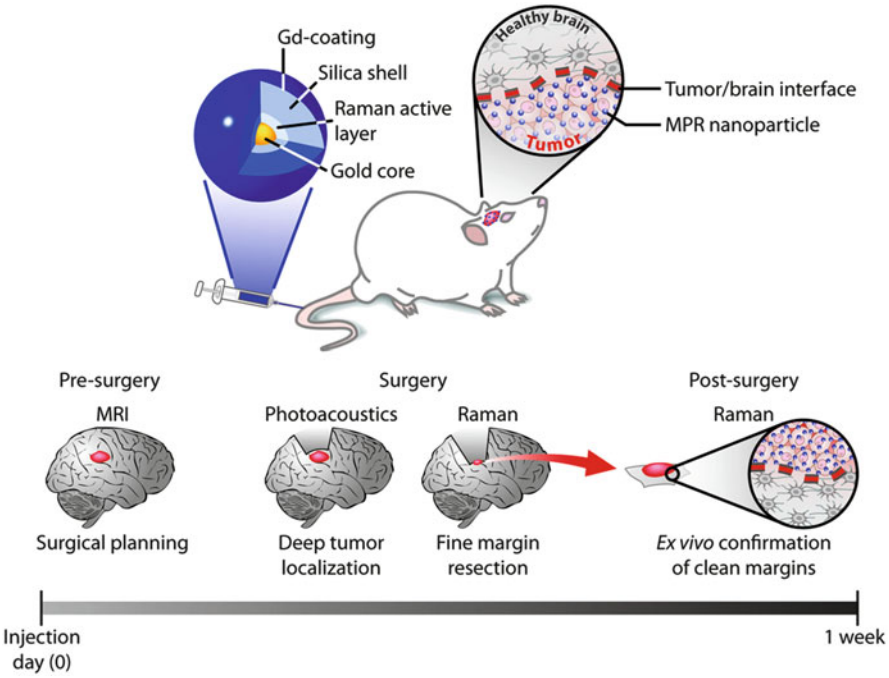

Fig. 5.8 Triple-modality MPR concept. Detectability of MPRs by MRI allows for preoperative detection and surgical planning. Photoacoustic imaging, with its relatively high resolution and deep tissue penetration, is then able to guide bulk tumor resection intraoperatively. Raman imaging, with its ultrahigh sensitivity and spatial resolution, can then be used to remove any residual microscopic tumor burden. The resected specimen can subsequently be examined using a Raman probe ex vivo to verify clear tumor margins (Reprinted with permission from Ref. [59]. Copyright 2012, Nature Publishing Group)

5.3 Biomedical Applications

5.3.1 Targeted UCA

UCAs have been widely used for enhanced diagnostic imaging in clinical practice. With the advent of targeted UCA, contrast-enhanced ultrasonography has emerged into molecular imaging for displaying pathophysiological processes at molecular and cellular level.

5.3.1.1 Imaging Angiogenesis

Angiogenesis is an important pathophysiological process involved in a broad spectrum of diseases such as cancer, rheumatoid arthritis, and atherosclerosis. Noninvasive imaging modality is very useful in the early detection of the tumors, the assessment

of atherosclerotic plaques, and for monitoring response to therapy. Targeted contrast ultrasonography with microbubbles provides a promising noninvasive molecular imaging approach to visualize and evaluate angiogenesis. Since specific endothelial receptors would be overexpressed during different phases of angiogenesis, various targeted microbubbles conjugating with ligands have been designed to imaging angiogenesis process. These microbubbles are mainly targeted to endothelial adhesion molecules which are involved in activation and remodeling, growth factor receptors, and specific markers for inflammatory cells in vascular remodeling [61–63]. A large number of studies have been focused on ultrasound molecular imaging of tumor with targeted microbubbles as angiogenesis plays a very important role during the process of tumor occurrence and progress. The ability to visualize and qualify angiogenesis of targeted microbubbles not only allows the early diagnosis of solid tumors or metastasis but also helps choose appropriate adjuvant anti-angiogenesis therapy based. Avβ3 integrin, endoglin, and vascular endothelial growth factor (VEGF) receptor (VEGFR2) are three of the best characterized molecular markers of tumor angiogenesis. The evaluation of microbubbles targeted to these markers has been extensively studied in various tumor models by many groups. Deshpande prepared microbubbles respectively targeted to these three markers and used the microbubbles to evaluate their temporal expression levels in three solid tumors. It is found that contrast-enhanced ultrasound imaging with these targeted microbubbles allows longitudinal assessment and monitoring of expression levels of $\alpha_v\beta_3$ integrin, endoglin, and VEGFR2 in breast, ovarian, and pancreatic cancer xenografts in mice. In addition, these targeted microbubbles can visualize the expression variety of different molecular markers among different tumors and the change at different tumor stage [64].

VEGFR2 is a primary angiogenic marker for angiogenesis and the development of pathological conditions such as cancer, diabetic retinopathy, and neovascular age-related macular degeneration [64–66]. This receptor is expressed mainly by endothelial cells and is upregulated in the tumor vasculature to promote angiogenesis.

Microbubbles targeted to VEGFR-2 have been used for in vivo noninvasive detection and quantification of VEGFR-2 expression in hepatocellular carcinoma, breast, thyroid, and prostate cancer in animal experiments and to differentiate benign from malignant lesions. Furthermore, this targeted contrast agent is likely useful in the prediction of response to anti-angiogenic therapy as it can monitor the tumor angiogenic activity [67–70]. The biotin–streptavidin linkage method is commonly used to prepare VEGFR-2 targeted microbubbles, but it cannot be used in clinic due to the immunogenic response in humans. Recently, Pochon et al. [71] developed a kind of clinically translatable microbubble (BR55) with a heterodimer peptide targeting the vascular endothelial growth factor receptor 2 (VEGFR-2). It has been widely used to detect, qualify, and monitor angiogenesis in vitro or in vivo study. Grouls et al. [72] reported that VEGFR-2-targeted microbubbles enable the distinction of early stages of liver dysplasia from normal liver in transgenic mouse model. Bzyl et al. [73] applied 3D molecular ultrasound using clinically translatable VEGFR-2-targeted microbubbles (BR55) to assess angiogenic activity in very small

breast lesions in nude mice and suggested that it is potential to detect and characterize these lesions.

5.3.1.2 Imaging Ischemia Disease

Ultrasound molecular imaging with microbubbles targeted to selectins and other biomarkers in vascular endothelium has been well described in ischemic disease model. Unique advantages including noninvasiveness, rapid and early detection, quantification, accurate localization, and guidance for therapeutic intervention have been validated in many studies. P- and E-selectin-targeted microbubbles have been used to detect myocardial and renal ischemic injury and show the potential application in humans [74, 75].

Clinical evaluation and management of the patients with chest pain which is suggestive of acute coronary syndromes (ACS) remains a common problem. The diagnosis of transient myocardial ischemia is challenging especially in patients without clear symptoms or electrocardiographic and/or biomarker features. For myocardial ischemia followed by reperfusion, the expression of molecular marker such as selectins in endothelial cells would change at very early stage which could be detected by ultrasound molecular imaging. Hyvelin et al. [76] used dual selectin-targeted microbubbles to detect and monitor the time course of expression of selectins after resolution of the ischemic event in rats. It is shown that targeted microbubbles produced high late-phase enhancement for ultrasound imaging within the ischemic myocardium area compared with remote myocardial tissue and persisted up to 24 h after the acute ischemic event, which validates the value of ultrasound molecular imaging for detecting transient myocardial ischemia. The diagnosis of ACS based on the detection of ischemic memory is a promising application for the imaging modality using targeted UCA because of noninvasiveness, convenience, low cost, and early detection. Leng et al. [77] developed a biodegradable polymer microbubble contrast agent targeted to human E-selectin via a short synthetic peptide and found that it enables echocardiographic detection of recent ischemia through ultrasound molecular imaging, providing a noninvasive method for myocardial ischemic memory imaging to identify acute coronary syndromes. As shown in Fig. 5.9, ultrasound molecular imaging with microbubbles targeted to endothelial ICAM-1 provides more reliable and earlier evidence of a recent myocardial ischemic event in the late phase of reperfusion compared with routine methods such as electrocardiography, echocardiography, and plasma troponin I levels [78].

5.3.1.3 Diagnosis of Inflammatory Disease

In clinic, there have been applications of nontargeted commercial microbubbles with contrast-enhanced ultrasound imaging (CEUS) for diagnosing and monitoring inflammatory disease. In patients with stricture of the bowel lumen and resultant incomplete mechanical bowel obstruction in the context of Crohn's disease, it is

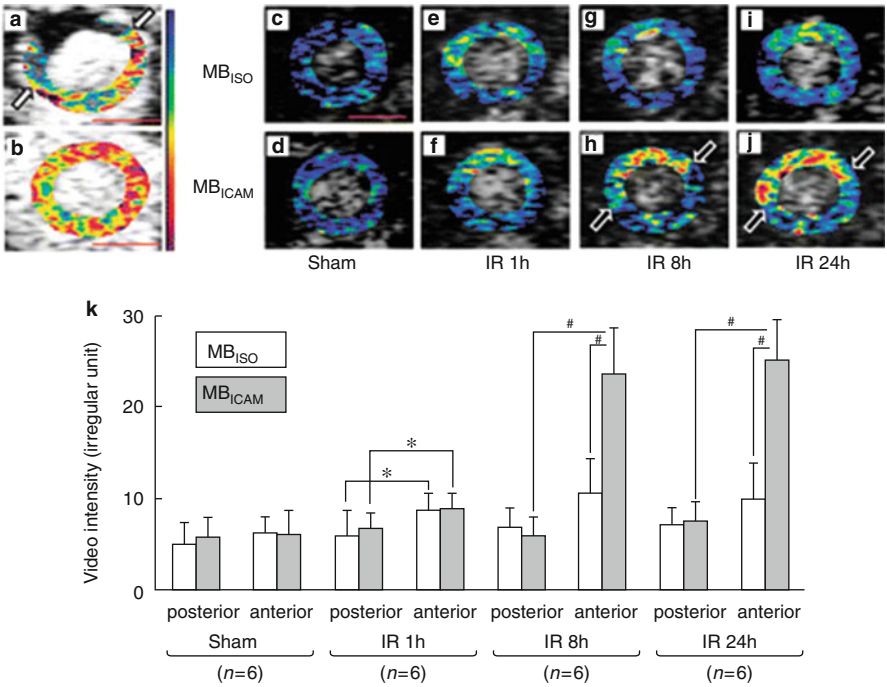

Fig. 5.9 Results of ultrasound molecular imaging. The risk area for ischemia during left anterior descending branch occlusion (**a**, marked by *arrows*) resolved after reperfusion (**b**). Examples of background-subtracted color-coded contrast-enhanced targeted ultrasound images over the time course (1, 8, and 24 h) of reperfusion with MBICAM and MBISO injection in three different mice and one sham mouse are shown in (**c–j**). The areas of enhancement produced by MBICAM in the late phase, marked by *arrows* (**h** and **j**), correspond to the risk area for ischemia (**a**). The VI of MBICAM and MBISO in both the ischemic anterior wall and nonischemic posterior wall of each group was quantified (**k**). $*P<0.05$; $\#P=0.000–0.004$. MBICAM, microbubbles with rat anti-mouse ICAM-1 monoclonal antibody; MBISO, microbubbles with nonspecific rat antibody. Data are given as mean ± SD. Scale bar = 3 mm (same scale bar in **c–j**) (Reprinted with permission from Ref. [78]. Copyright 2010, Oxford University Press)

important to determine if there is active inflammation at the site of stricture or if the strictured segment is fibrotic. The quantitative analysis of small bowel wall contrast enhancement after microbubble contrast agent injection may differentiate inflammatory from fibrotic ileal strictures [79]. CEUS can also help discern mass-forming pancreatitis from pancreatic neoplasm. The use of quantitatively evaluated transabdominal contrast-enhanced ultrasonography with microbubbles can help in the differentiation of patients with mass-forming pancreatitis from patients with pancreatic adenocarcinomas. The performances of this imaging modality are similar to those of CECT in the diagnosis focal pancreatitis [80, 81]. These studies help accumulate experience in the diagnosis of inflammatory disease with UCA.

The imaging of inflammation is an ideal application for targeted UCA, and they are increasingly used in preclinical studies to measure the expression of vascular

markers during inflammation process. The strategy for imaging inflammation with microbubbles has been targeted to endothelial cell adhesion molecules that are upregulated in response to proinflammatory stimuli and that participate in leukocyte recruitment. Ligands for adhesion molecules such as the intercellular adhesion molecule (ICAM) family, vascular cell adhesion molecule-1 (VCAM-1), and selectins are conjugated to the shell surface of microbubbles. The use of these targeted microbubbles has been examined in experimental models of several typical inflammatory diseases such as Crohn's disease (CD) and inflammatory bowel disease (IBD) [82, 83]. In these studies, targeted imaging with contrast ultrasound enabled accurate qualifying and monitoring of inflammation and correlated well with the spatial extent expression of inflammatory cell activity on immunohistochemistry.

As shown in Fig. 5.10, Bachmann et al. [84] carried out research on targeted ultrasound imaging of inflammatory disease for the first time. A microbubble contrast agent targeted to mucosal addressin cellular adhesion molecule-1 was developed and used to detect and quantify intestinal inflammation in experimental ileitis. This study firstly confirmed the potential value of ultrasound molecular imaging in diagnosing and monitoring inflammation activity in patients with IBD.

P-selectin glycoprotein ligand 1, expressed on the surface of leukocytes, is the natural ligand of both P- and E-selectins. A recombinant P-selectin glycoprotein ligand immunoglobulin G [rPSGL-Ig] is currently being evaluated as an anti-inflammatory drug in clinical trials. Microbubbles functionalized with a recombi-

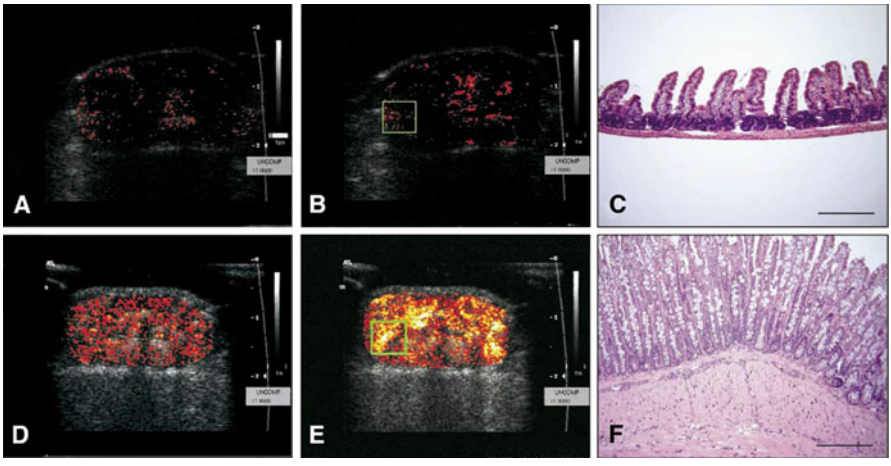

Fig. 5.10 MB_M-targeted, contrast-enhanced transabdominal US in SAMP mice. (**a**) Healthy AKR mice showed weak background signal following either MB_I or (**b**) MB_M infusion, whereas (**e**) accumulations of MB_M produced strong acoustic echoes that appear as bright regions in color-coded images. (**d**) Background-subtracted color-coded images of MBI in SAMP mice produced little baseline signal. (**c**) Histologic analysis of ileal tissues isolated from AKR control (panel B, *green box*) showed normal bowel architecture with no evidence of inflammation, whereas (**f**) ileal tissues obtained from bright regions of SAMP mice showed gross morphologic changes, including acute and chronic inflammation (scale bar =250 mm), indicative of severe disease (scale bar = 250 um) (Reprinted with permission from Ref. [84]. Copyright 2006, Elsevier)

nant P-selectin glycoprotein ligand-1 analogue rPSGL-Ig (MBrPSGL-Ig) displayed firm in vitro binding on the coating of both recombinant E- or P-selectin, with an efficiency similar to microbubbles comprising antibody specific for E-selectin (MBE) or P-selectin (MBP). The molecular imaging study demonstrates that MBrPSGL-Ig provides imaging signal higher than those measured with antibody or sialyl Lewis X containing microbubbles. Therefore, microbubble conjugated with rPSGL-Ig is a powerful agent to image the expression of both E- and P-selectins in the context of an inflammatory process [85]. Wang et al. [86] bond rPSGL-Ig to the microbubble shell to develop a clinically translatable dual-targeted (P- and E-selectin) contrast agent for the quantification of inflammation in murine acute colitis model with IBD. The dual-targeted microbubbles showed strong attachment to both human and mouse P- and E-selectins, and the combination with contrast-enhanced ultrasound specifically enables detection and quantification of inflammation. The US imaging with MB selectin correlates well with FDG uptake at PET/CT imaging which has been widely used clinically and can be used to evaluate the disease activity in patients with IBD. The study provides evidence for the further clinical application of targeted UCA in inflammatory disease.

5.3.1.4 Molecular Imaging of Intravascular Atherosclerosis and Thrombus

The use of ultrasound molecular imaging with targeted microbubbles includes the early and rapid detection of atherosclerosis [87–89] and identification of plaque vulnerability. There are many potential targets for molecular imaging in atherosclerosis that could be useful in diagnosing or managing atherosclerotic disease. A considerable amount of research in ultrasound-targeted imaging of atherosclerosis has been performed in vitro and animal experiments [90–92].

Differentiating stable from vulnerable atherosclerotic plaques is crucial for the interventional treatment to prevent acute atherothrombotic events. Assessing future risk of atherosclerosis plaque may rely on the detection of early inciting events such oxidative stress, lipid accumulation, or upregulation of endothelial cell adhesion molecules that participate in inflammatory activity. Favorably, inflammatory phenotype of atherosclerotic plaques could be demonstrated by targeted ultrasound imaging. It is capable of rapidly quantifying vascular inflammatory changes that occur in different stages of atherosclerosis [87].

In animal models of disease, ultrasound molecular imaging of ICAM-1, VCAM-1, and P-selectin has been shown to produce signal enhancement preferentially at sites of plaque formation and to reveal the degree of underlying plaque inflammatory activity. Other potential biomarkers in vessel endothelium have also been explored to develop targeted microbubbles for the demonstration of inflammatory changes.

Contrast-enhanced ultrasound imaging with microbubbles targeted toVCAM-1 and P-selectin is used to detect the earliest stages of atherosclerotic disease even prior to the development of fatty streaks, suggesting this technology may be useful

for the next generation of preventive therapies. Platelet–endothelial interactions have been linked to increased inflammatory activation and prothrombotic state in atherosclerosis. Contrast-enhanced ultrasound (CEU) imaging with microbubbles or cyclic RGD-modified microbubbles targeted to activated glycoprotein IIb/IIIa could achieve a noninvasive in vivo detection of inflammation-activated platelets and thrombosis in large arteries, thus providing a potential tool for identification of vulnerable atherosclerotic plaques before the advent of serious clinical events [93].

Short-term treatment with apocynin in atherosclerosis reduces endothelial cell adhesion molecule expression. This change in endothelial phenotype can also be detected by ultrasound molecular imaging before any measurable decrease in macrophage content and is not associated with a detectable change in oxidative burden [94].

Dysregulated endothelial vWF is suggested to be a marker for high-risk atherosclerotic disease. Molecular imaging using GPIbα as a targeting moiety can detect the presence of activated vWF on the vascular endothelium. This strategy may provide a means to noninvasively detect an advanced prothrombotic and inflammatory phenotype in atherosclerotic disease [95].

It is useful to image thrombus formation in large vessels or in the microcirculation for making treatment decisions in patients with acute atherothrombotic syndromes such as stroke and TIA or in patients at high risk for cerebral embolic disease. Targeted microbubbles were used to image thrombus formation or platelet–endothelial interactions more than a decade ago.

Wang et al. [96] conjugated lipid-shell-based gas-filled microbubbles to a single-chain antibody specific for activated glycoprotein IIb/IIIa and demonstrated that contrast-enhanced ultrasound with these microbubbles could selectively target activated platelets, thus allowing real-time molecular imaging of acute arterial thrombosis and monitoring of the success or failure of pharmacological thrombolysis in vivo. As shown in Fig. 5.11, Nakatsuka et al. [61] developed thrombin-sensitive contrast agent–aptamer cross-linking strand–aptamer cross-linked microbubbles that produce ultrasound harmonic signal only when exposed to elevated thrombin levels. The thrombin aptamer cross-linking strand (TACS) that responds to thrombin was incorporated into microbubble shell, and the binding of thrombin results in the complete displacement of the polymer–DNA strands. As the thrombin concentration increases, TACS strands are removed from the bubble shell, and full, unhindered oscillation can occur, producing very sharp harmonic peaks. These smart stimulus-responsive contrast agents have excellent potential for improving cardiovascular imaging techniques and the diagnostic power of an important imaging modality.

In ultrasound molecular imaging, the attachment performance of microbubble contrast agent varies depending on the fluid shear stress as well as on the microbubble and substrate molecular composition and site densities [62]. Shear forces from flow is the greatest challenge for adherent microbubbles in large vessels [63]. To improve contrast-enhanced visualization of targeted microbubbles in circulation, several strategies have been taken to increase their binding ability with molecular markers expressed on the vessel lumen. Ferrante et al. [62] applied dual targeting

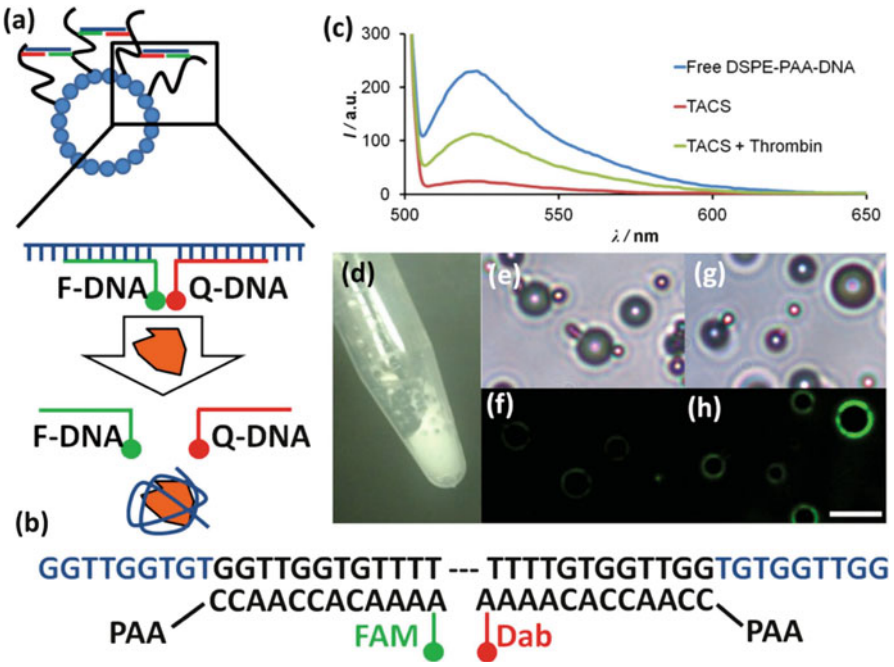

Fig. 5.11 Design of aptamer-activated microbubbles. (**a**) Schematic representation of fluorescence activation by thrombin binding. (**b**) Thrombin aptamer cross-linking strand (TACS). (**c**) Fluorescence emission spectra of DSPE-PAA-FAM and DSPE-PAA-Quencher (*blue*), after addition of TACS (*red*) and addition of thrombin (*green*) (λ ex = 465 nm). (**d**) Microbubble suspension after sonication. (**e–f**) Bright field and fluorescence images of cross-linked bubbles. (**g–h**) Bright field and fluorescence images of cross-linked bubbles after addition of thrombin. Fluorescence increases after TACS interacts with thrombin. Scale bar = 5 μm (Reprinted with permission from Ref. [61]. Copyright 2012, Wiley-VCH)

method to improve microbubble contrast agent adhesion to VCAM-1 and P-selectin under flow. The results suggest that dual-targeted contrast agents may be useful for atherosclerotic plaque detection at physiologically relevant shear stresses.

In addition, ultrasound at very low pressures and long pulse lengths can be used to force acoustically active agents along the axis of the ultrasound beam without disruption of the agent. Borden et al. [97] have demonstrated that this acoustic "radiation force" can be used to localize contrast agents along the wall of a vessel both in vitro and in vivo for an appropriately directed ultrasound beam. The radiation force may present a means to assist the adhesion or accumulation of targeted contrast agents by increasing the proximity of flowing agents to adhesion ligands, by reducing the velocity of flowing agents, and by causing free microbubbles to be attracted to already-adherent microbubbles [98]. Wu et al. [99] developed a microbubble contrast agent targeted to vascular cell adhesion molecule-1 (VCAM-1) (CD106) and coupled it with a magnetic guidance system, which could improve the efficacy of contrast-enhanced molecular ultrasonography of atherosclerosis in the

aorta. The magnetic targeted microbubble system results in greater attachment to endothelial VCAM-1 in atherosclerotic aortas in conditions of high shear stress and improved detection of early inflammatory changes of atherosclerosis.

5.3.2 Theranostic Applications

5.3.2.1 General Introduction

UCA have been used for diagnostic imaging since a few decades ago. In recent years, with the development of microbubbles and acoustic particles carrying drug, gene, or other therapeutic substances, their function has extended to therapeutic area, attracting increasing interest in targeted therapy, especially in the treatment of cancer and cardiovascular and inflammatory disease. And some UCAs are directly applied to image-guided therapy or synergistic treatment [100–104]. Ultrasound-mediated drug delivery using contrast agent is a safe and noninvasive approach for targeted drug delivery. Microbubbles based on a shell encapsulating a high-molecular weight gas with very low water solubility is the most widely used form for contrast-enhanced ultrasound imaging as well as drug or gene delivery. Perfluorocarbon gas-filled microbubbles are sufficiently stable for circulating in the vasculature as blood pool agents, they act as carriers of drug or gene until they reach the site of interest. Then diagnostic ultrasound can be applied to image the microbubbles, and simultaneously therapeutic ultrasound at low intensity can be used to burst these microbubbles at this site, causing localized release of the drug or gene [105, 106]. Furthermore, microbubble cavitation induced by therapeutic ultrasound facilitates the permeabilization of surrounding capillary and cell membranes, resulting in improved cell uptake or enhanced transfection efficiency [107]. In addition, microbubbles binding with therapeutic antibodies or peptides not only serve as probes for ultrasound molecular imaging but also generate targeted therapy after destruction by sonication [96, 108, 109]. Other types of UCA such as microbubble–liposome particle complex [110–112], acoustic liposome, and phase-shifted perfluorocarbon emulsion are also developed and used for image-guided drug or gene delivery [113–115].

Many strategies have been described to use microbubbles as drug or gene carriers, and ultrasound-targeted microbubble destruction (UTMD) technology has been demonstrated in a number of studies. Therapeutic substance can be encapsulated into the inner space or incorporated into the shell of microbubbles, and they can also be attached to the microbubble surface. In other studies, microbubbles and the therapeutic substance can be coadministered, taking advantage of increased cell and capillary permeability only after UTMD [116]. Incorporating and encapsulating unstable bioactive substance into microbubbles has additional advantages, including protection against degradation or disintegration and decrease of systematic side effects after intravenous administration [117, 118]. Various physicochemical concepts are demonstrated to produce UCA carrying therapeutics according to their

properties. Charged therapeutics (e.g., DNA, RNA) can be coupled electrostatically to the outer MB surface if cationic lipids or denatured proteins are used. Lipophilic molecules can be integrated into the monolayer of phospholipids microbubbles. Biodegradable polymer materials are used to prepare microbubbles or acoustic nanoparticles loaded with various therapeutic substances.

Various therapeutic substances have been delivered with UTMD system in animal experiments, including drugs, small molecules, and gene therapy vectors. Microbubbles served as delivery vehicles in most studies as they produce excellent enhanced ultrasound imaging as well as cavitation effect, which are both crucial to improve therapeutic efficacy. However, the UTMD system is faced with inherent difficulties. Microbubbles have a short circulation time in vivo (3–15 min half-life), and their drug loading capacity is seriously limited by both the thin shell (few nanometers) and gas core [119, 120].

Hence, using microbubbles as a gene therapy vector may have superiority as usually only one application may be required for gene therapy and a rather low payload can suffice for a therapeutic response. Moreover, gene therapy vectors mostly have to be locally administered.

To increase the drug payload, thick-shelled microbubbles are developed using polymeric materials or proteins, offering a much larger loading space. In addition, acoustically active lipospheres with a thick drug-carrying oil layer have much higher payload for hydrophobic drugs [121, 122]. The loading capacity of MBs for plasmid DNA can be increased by raising their positive surface charge [123]. For this purpose, cationic materials are added and incorporated into the shell during the process of MBs' preparation, and multiple layer technique can be used [28, 124].

As shown in Fig. 5.12, conjugating nanometer-sized particles (e.g., liposomes, lipoplexes) to microbubbles may take advantage of both the high loading capacity of particles and fine acoustic properties of microbubbles [110]. These hybrid vehicles can be used for both drug and gene delivery, and the performances in vitro and in animal models have been studied in several groups [111, 112]. Phase-shift per-

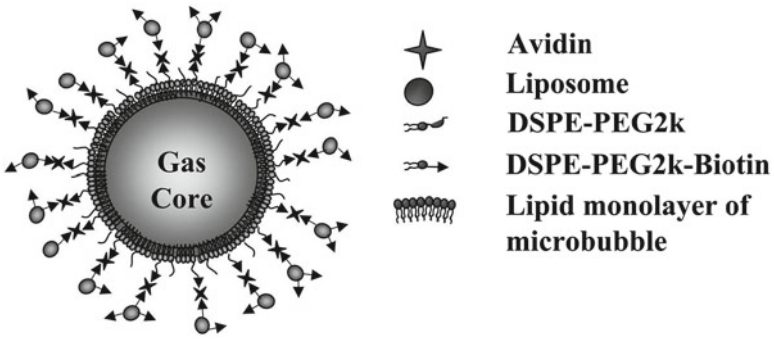

Fig. 5.12 Illustration of a microbubble carrying liposomes on its surface. Microbubbles coated with 5 % DSPE-PEG2k and 5 % DSPE-PEG2k-biotin were conjugated with liposomes carrying 5 % DSPE-PEG2k-biotin and 5 % NBD-cholesterol via avidin molecules (Reprinted with permission from Ref. [110]. Copyright 2007, Elsevier)

fluorocarbon nanoemulsions and nanodroplets as microbubble precursors are developed to overcome the limitations of microbubbles such as short circulation time and poor extravascular penetration. These stable, nanoscaled microbubble precursors could effectively accumulate in tumor tissue by passive or active targeting and then convert into microbubbles in situ under the condition of ultrasound exposure, heating, or laser irradiation. Ultrasound activates phase transition of drug-loaded emulsions via acoustic droplet vaporization (ADV) and locally releases the drug. This novel drug delivery system has shown excellent therapeutic potential in targeted cancer therapy [49, 114, 125].

5.3.2.2 Imaging, Drug and Gene Delivery, and Image-Guided Therapy

Chemotherapy is the most important nonsurgical method for treatment of cancer, but systemic toxicity becomes one of the biggest challenges. Various targeted drug delivery systems have been developed to resolve this major issue. The technique of ultrasound-targeted microbubble destruction (UTMD) for drug and gene delivery has shown an attractive application in disease treatment, especially in cancer therapy [105, 126, 127]. A variety of MBs loaded with antitumor drugs have been successfully developed and have produced promising therapeutic effect in combination with ultrasound in vitro and in vivo [113, 122, 128].

Antitumor drug-loaded MBs are injected to the circulation and fragmented when exposed to a certain intensity of ultrasound. The resultant fragments containing drug then begin to accumulate within the tumor and slowly release drug. Thus, a targeted and sustained antitumor effect is obtained. The tumor inhibition may be further enhanced through the enhanced permeability and retention (EPR) effect at the cellular and capillary levels in tumor tissue in the presence of microbubble [120, 129–131]. As demonstrated in a number of studies [132, 133], UTMD-mediated delivery system has been successfully used to increase the local drug concentration and to enhance the antitumor effect in animal models. In sonicated tumors, the doxorubicin concentration was significantly higher than that in contralateral tumors without ultrasound exposure, resulting in the improved therapeutic efficacy.

The first studies with drug-loaded MBs were made by Unger et al. Paclitaxel and doxorubicin are the most commonly used chemotherapeutics in ultrasound and microbubble-mediated drug delivery system. Fokong et al. [134] developed a type of poly(butyl cyanoacrylate) (PBCA)-based hard-shell MB and show that both hydrophilic and hydrophobic model drugs can be efficiently and stably entrapped within the ~50 nm shell of PBCA MB. They functionalized the surface of fluorophore-loaded MB with anti-VEGFR2 antibodies and found that it enables image-guided and targeted model drug delivery to tumor blood vessels. Their findings indicate that polymer-based MBs are highly suitable systems for image-guided, targeted, and triggered drug delivery to tumors and tumor blood vessels.

Generally, solid, ultrasound accessible, and well-perfused solid tumor would allow for the treatment of UTMD system. Nonetheless, some key issues such as accurate controlled release, quantitative analysis, and systemic side effects due to

nonspecific distribution of microbubbles remain to be investigated in future preclinical studies. In addition, the main challenge at present is that MBs suffer from a low drug loading content; therefore, they do not generally result in an efficient therapeutic delivery vehicle especially in cancer therapy [135–137]. In the preclinical studies, for gene delivery with plasmids attached to the microbubble shell, 10–100 times typical human dose of MBs is needed to obtain a therapeutic effect [110, 138]. This causes a big obstacle for clinical use in the future.

Indeed, many attempts have been made to increase payload of MBs in recent years. Though conjugating liposomes to microbubble and making an inner oil layer in the bubble shell can improve the loading capacity to some extent, the drug payload remains rather limited. Moreover, these methods based on the complex transformation of microbubble structure may lead to some new challenges, such as low yields, instability, and the loss of the capability to be imaged and controlled by ultrasound [113, 135, 137]. An alternative option to solve this problem may consist in decreasing the dosing by selecting the antitumor drug with a powerful activity, which would also reduce the dose of microbubble injection. Clearly, the smaller the dose of drug required for therapeutic efficacy, the smaller the number of MBs needed for the delivery system. Therefore, it is advantageous to develop the MBs that can carry antitumor drugs capable of powerful activity at a low dosage, in order that the low loading obstacle can be overcome. Li et al. [139] designed HCPT-loaded phospholipid MBs and showed that it is possible to overcome the low drug loading obstacle of microbubble as well as the disadvantages of 10-HCPT in clinical use. They successfully loaded phospholipid MBs with 10-HCPT at a high encapsulation efficiency and loading content. 3.12 ml HLMs formulation ($\sim 1.6 \times 10^{10}$) is expected to carry about 4 mg of 10-HCPT which is sufficient to obtain therapeutic efficacy in clinical application, and thus the required amount of MBs is greatly reduced to a reasonable dose for intravenous injection.

In recent years, phase-shift nanoemulsions and droplets have been developed and used as both UCA and drug carriers. These novel delivery vehicles have many more advantages such as better stability and stronger penetrability compared to conventional microbubble contrast agent, facilitating long circulation time and extravascular molecular imaging. Furthermore, they are favorable to be developed as contrast agent for multimodal imaging due to a well-established preparation technology. There has been a growing interest for the research on development and application of this novel delivery system for cancer therapy.

It has been a long history for UCA in the application of cardiovascular system. Microbubble contrast agent was firstly used as an agent for blood pool imaging. There have been a large number of studies for the application of UCA in cardiovascular disease including ischemia disease, atherosclerotic plaque, and venous thrombus. Thus, ultrasound-mediated drug or gene delivery system has been widely used in the treatment of cardiovascular diseases. Relatively, much more interest was concentrated on gene delivery with UCA. The superiority of UTMD delivery system for the targeted therapy of cardiovascular diseases has been demonstrated in numerous studies. Compared to conventional method, UTMD technology has unique advantages such as image-guided delivery and enhanced vascular and cellular

permeability. In particular, UTMD induces transient and reversible opening of blood–brain barrier (BBB), facilitating drug release from microbubbles and extravasation into brain tissue.

Inducing angiogenesis is an important strategy to treat ischemia diseases in the field of cardiovascular system. UTMD-induced angiogenesis by gene delivery has been applied to the treatment of myocardial infarction [140], injury after stroke [141], peripheral vascular disease [142], etc. Different forms of vascular endothelial growth factor (VEGF) plasmid DNA in combination with UTMD was used to induce angiogenesis in rat and mouse hearts [140, 143] or limbs [144]. Wang et al. [145] attached pcD2VEGF121 gene to microbubbles and used UTMD strategy to improve the transfection efficiency in rats with myocardial infarction. The effectiveness of UTMD-mediated gene delivery for the treatment of cardiovascular disease needs to be demonstrated in large animal models in future studies.

The imaging of inflammation is an ideal application for targeted UCA, since it involves the expression of adhesion molecules by the endothelial cells lining the vascular system. UTMD-mediated drug or gene delivery system has also been induced to treat inflammatory disease such as atherosclerosis and Crohn's disease (CD). Tlaxca et al. [82] developed and evaluated MBs bearing luciferase plasmid and functionalized them with antibodies to MAdCAM-1 (MB-M) or VCAM-1 (MB-V), biomarkers of gut endothelial cell inflammation. UTMD was then performed to deliver luciferase plasmid to the GI tract in inflamed mesenteric endothelium in the CD-like TNFΔARE mouse model, and targeted luciferase expression in the midgut was achieved. The study demonstrates that microbubble contrast agent in combination with UTMD has the potential to be a minimally invasive treatment strategy to ameliorate CD and other inflammatory conditions.

In addition, UCA enhances the role of ultrasound image guidance for tissue biopsy, radiofrequency, or thermal ablation of lesions [146–148]. Tardy et al. [70] use BR55, a new VEGFR2-specific UCA to image prostate tumors in an orthotopic model in the rat and compare the contrast enhancement with that of SonoVue. They found BR55 showed a high binding affinity to prostate tumors, resulting in a strong enhancement of the lesions as early as a few minutes after contrast injection, whereas only minimal nonspecific accumulation was found in the healthy part of the gland. BR55 can provide additional information by highlighting the sites of active angiogenesis, which would be particularly valuable for prostate cancer detection and for biopsy guidance.

Recently, a growing interest can be seen in therapeutic applications of ultrasound in sonothrombolysis [149]. Combined with thrombolytic drugs, the treatment of acute ischemic stroke can be further improved by ultrasound and microbubbles. The main mechanisms of microbubble-enhanced sonothrombolysis may involve acoustic cavitation and thermal effects. This potential therapeutic application of microbubble contrast agent is supported by a broad range of in vitro and in vivo study and compared to conventional drug treatment or ultrasound without microbubbles [150–153].

Another therapeutic function of UCA is to induce temporary opening of BBB, thus enabling therapeutic agent delivery into the brain leading to significant improvement of treatment efficacy for central nervous system (CNS) disease such

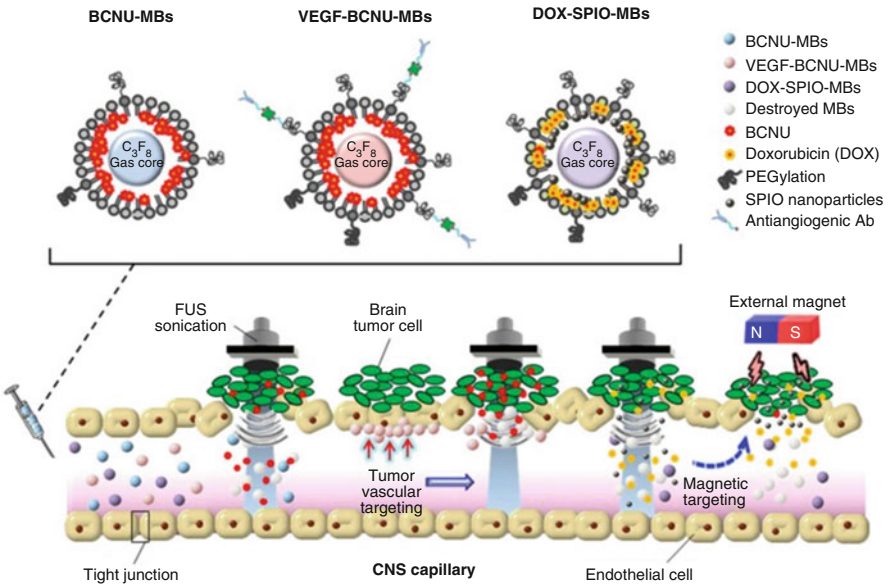

Fig. 5.13 Application of multifunction microbubbles for focused ultrasound-induced brain tumor drug delivery (Reprinted with permission from Ref. [154]. Copyright 2014, Ivyspring International Publisher)

as brain tumor. The presence of BBB is a significant impediment to the delivery of therapeutic agents to the brain for treatment of brain diseases. As shown in Fig. 5.13, UCA combined with focused ultrasound can be developed as a noninvasive method for transiently increasing the permeability of the BBB to promote drug delivery to targeted regions of the brain. The benefit of UCA such as microbubble-induced transient and local opening of BBB has been demonstrated in a number of studies [154–157].

5.4 Summary and Outlook

With the aforementioned microbubble technology, ultrasonic theranostic agents can serve as a multifunction platform that is useful not only in diagnoses but also in therapies, permitting simultaneous imaging and localization of the therapy.

5.4.1 Superiorities and Advantages

Ultrasonic theranostic agents have the significant superiorities regarding the noninvasion, feasibility, and effectiveness in clinical applications. Most importantly, ultrasonic theranostic agent-based imaging allows real-time evaluation of blood

flow, which is safer than molecular imaging modalities such as radionuclide imaging because it does not involve radiation. Feasible, targeting strategies for microbubbles are versatile and modular, and targeting a new area only entails conjugating a new ligand. In addition, since microbubbles can generate such strong signals, a lower intravenous dosage is needed, and micrograms of microbubbles are needed compared to milligrams for other molecular imaging modalities such as MRI contrast agents.

5.4.2 Challenges and Limitations

Although ultrasonic theranostic agents have the clear advantages in aspects of molecular imaging and therapy, they suffer from the following disadvantages. Obviously, microbubbles have low residence times in circulation because they either get taken up by immune system cells or get taken up by the liver or spleen even when they are coated with PEG. Besides, given that microbubbles burst at low ultrasound frequencies and at high mechanical indices (MI), which is the measure of the acoustic power output of the ultrasound imaging system, increasing MI increases image quality, but there are trade-offs with microbubble destruction, and their destruction could cause local microvasculature ruptures and hemolysis to some extent. Targeting ligands that bind to receptor characteristic of intravascular diseases can be conjugated to microbubbles, enabling the microbubble complex to accumulate selectively in areas of interest in preclinical experiments or clinical practices; however, they can be immunogenic since most current targeting ligands used are derived from animal culture, which will limit their application scopes. Furthermore, low targeted microbubble adhesion efficiency, which means a small fraction of injected microbubbles bind to the area of interest, is one of the main reasons that targeted contrast-enhanced ultrasound remains in the preclinical development stages.

The applications of ultrasonic theranostic agents in microbubble-specific imaging, ultrasound-aided drug delivery, and targeted imaging and therapy are promising but require further improvement for clinical use.

References

1. Gramiak R, Shah PM (1968) Echocardiography of the aortic root. Invest Radiol 3(5):356–366
2. Keller MW, Glasheen W, Kaul S (1989) Albunex: a safe and effective commercially produced agent for myocardial contrast echocardiography. J Am Soc Echocardiogr 2(1):48–52
3. Bhutani MS, Hoffman BJ, Van Velse A et al (1997) Contrast-enhanced endoscopic ultrasonography with galactose microparticles: SHU508 A (Levovist). Endoscopy 29(07):635–639
4. Bauer A, Mahler M, Urbank A et al (1997) Microvascular imaging-results from a phase I study of the novel polymeric ultrasound contrast agent SHU 563A. In: Advances in echo imaging using contrast enhancement. Springer, Nanda NC, Schlief R and Goldberg BB (Eds), pp 685–690

5. Podell S, Burrascano C, Gaal M et al (1999) Physical and biochemical stability of Optison®, an injectable ultrasound contrast agent. Biotechnol Appl Biochem 30(3):213–223
6. Unger EC, Lund P, Shen D et al (1991) Aerosomes as blood pool and cardiovascular contrast agents for US: in vivo studies. Radiology 181:225
7. Schneider M (1999) SonoVue, a new ultrasound contrast agent. Eur Radiol 9(3):347
8. Pelura TJ (1998) Clinical experience with AF0150 (Imagent US), a new ultrasound contrast agent. Acad Radiol 5:69–71
9. Takada T, Yasuda H, Uchiyama K et al (1990) Contrast-enhanced intraoperative ultrasonography of small hepatocellular carcinomas. Surgery 107(5):528–532
10. Ziskin MC, Bonakdarpour A, Weinstein DP et al (1972) Contrast agents for diagnostic ultrasound. Invest Radiol 7(6):500–505
11. Feinstein SB, Ten Cate FJ, Zwehl W et al (1984) Two-dimensional contrast echocardiography. I. In vitro development and quantitative analysis of echo contrast agents. J Am Coll Cardiol 3(1):14–20
12. Shapiro JR, Reisner SA, Amico AF et al (1990) Reproducibility of quantitative myocardial contrast echocardiography. J Am Coll Cardiol 15(3):602–609
13. Moran CM, Anderson T, Pye SD et al (2000) Quantification of microbubble destruction of three fluorocarbon-filled ultrasonic contrast agents. Ultrasound Med Biol 26(4):629–639
14. Klibanov AL (1999) Targeted delivery of gas-filled microspheres, contrast agents for ultrasound imaging. Adv Drug Del Rev 37(1):139–157
15. Xu Q, Nakajima M, Ichikawa S et al (2008) A comparative study of microbubble generation by mechanical agitation and sonication. Innovative Food Sci Emerg Technol 9(4):489–494
16. Bjerknes K, Sontum PC, Smistad G et al (1997) Preparation of polymeric microbubbles: formulation studies and product characterisation. Int J Pharm 158(2):129–136
17. Chen C, Zhu Y, Leech PW et al (2009) Production of monodispersed micron-sized bubbles at high rates in a microfluidic device. Appl Phys Lett 95(14):144101
18. Yobas L, Martens S, Ong WL et al (2006) High-performance flow-focusing geometry for spontaneous generation of monodispersed droplets. Lab Chip 6(8):1073–1079
19. Talu E, Lozano MM, Powell RL et al (2006) Long-term stability by lipid coating monodisperse microbubbles formed by a flow-focusing device. Langmuir 22(23):9487–9490
20. Dayton PA, Pearson D, Clark J et al (2004) Ultrasonic analysis of peptide-and antibody-targeted microbubble contrast agents for molecular imaging of αvβ3-expressing cells. Mol Imaging 3(2):125
21. Kaufmann BA, Lindner JR (2007) Molecular imaging with targeted contrast ultrasound. Curr Opin Biotechnol 18(1):11–16
22. Brooks PC, Clark RA, Cheresh DA (1994) Requirement of vascular integrin alpha v beta 3 for angiogenesis. Science 264(5158):569–571
23. Tedder TF, Steeber DA, Chen ANJUN et al (1995) The selectins: vascular adhesion molecules. FASEB J 9(10):866–873
24. Palmeri D, van Zante A, Huang CC et al (2000) Vascular endothelial junction-associated molecule, a novel member of the immunoglobulin superfamily, is localized to intercellular boundaries of endothelial cells. J Biol Chem 275(25):19139–19145
25. Ribatti D, Crivellato E, Russo F et al (2004) Vascular targeting: a new antitumor activity. Drug Des Rev-Online 1(2):119–122
26. Ferrara K, Pollard R, Borden M (2007) Ultrasound microbubble contrast agents: fundamentals and application to gene and drug delivery. Biomed Eng 9:415–447
27. Unger EC, Matsunaga TO, McCreery T et al (2002) Therapeutic applications of microbubbles. Eur J Radiol 42(2):160–168
28. Borden MA, Caskey CF, Little E et al (2007) DNA and polylysine adsorption and multilayer construction onto cationic lipid-coated microbubbles. Langmuir 23(18):9401–9408
29. Sirsi SR, Hernandez SL, Zielinski L et al (2012) Polyplex-microbubble hybrids for ultrasound-guided plasmid DNA delivery to solid tumors. J Control Release 157(2):224–234
30. Sirsi S, Feshitan J, Kwan J et al (2010) Effect of microbubble size on fundamental mode high frequency ultrasound imaging in mice. Ultrasound Med Biol 36(6):935–948

31. Sheeran PS, Luois S, Dayton PA et al (2011) Formulation and acoustic studies of a new phase-shift agent for diagnostic and therapeutic ultrasound. Langmuir 27(17):10412–10420
32. Kripfgans OD, Fowlkes JB, Miller DL et al (2000) Acoustic droplet vaporization for therapeutic and diagnostic applications. Ultrasound Med Biol 26(7):1177–1189
33. Gao Z, Kennedy AM, Christensen DA et al (2008) Drug-loaded nano/microbubbles for combining ultrasonography and targeted chemotherapy. Ultrasonics 48(4):260–270
34. Rapoport N, Christensen DA, Kennedy AM et al (2010) Cavitation properties of block copolymer stabilized phase-shift nanoemulsions used as drug carriers. Ultrasound Med Biol 36(3):419–429
35. Rapoport N, Gao Z, Kennedy A (2007) Multifunctional nanoparticles for combining ultrasonic tumor imaging and targeted chemotherapy. J Natl Cancer Inst 99(14):1095–1106
36. Jin YS, Ke HT, Dai ZF (2012) Multifunctional ultrasound contrast agent. Prog Chem 24(12):2424–2430
37. Xu RX (2011) Multifunctional microbubbles and nanobubbles for photoacoustic imaging. Contrast Media Mol Imaging 6(5):401–411
38. Cai W, Chen X (2008) Multimodality molecular imaging of tumor angiogenesis. J Nucl Med 49(2):113S–128S
39. Lin Y, Chen ZY, Yang F (2013) Ultrasound-based multimodal molecular imaging and functional ultrasound contrast agents. Curr Pharm Des 19(18):3342–3351
40. Ku G, Wang LV (2005) Deeply penetrating photoacoustic tomography in biological tissues enhanced with an optical contrast agent. Opt Lett 30(5):507–509
41. Xu RX, Huang J, Xu JS et al (2009) Fabrication of indocyanine green encapsulated biodegradable microbubbles for structural and functional imaging of cancer. J Biomed Opt 14(3):034020
42. Qin R, Xu J, Xu R et al (2010) Fabricating multifunctional microbubbles and nanobubbles for concurrent ultrasound and photoacoustic imaging. Proc SPIE 7567, Design and Performance Validation of Phantoms Used in Conjunction with Optical Measurement of Tissue II 7567(11):1–2
43. Chen PJ, Hu SH, Fan CT et al (2013) A novel multifunctional nano-platform with enhanced anti-cancer and photoacoustic imaging modalities using gold-nanorod-filled silica nanobeads. Chem Commun 49(9):892–894
44. Jeon M, Song W, Huynh E et al (2014) Methylene blue microbubbles as a model dual-modality contrast agent for ultrasound and activatable photoacoustic imaging. J Biomed Opt 19(1):16005
45. Jian J, Liu C, Gong Y et al (2014) India ink incorporated multifunctional phase-transition nanodroplets for photoacoustic/ultrasound dual-modality imaging and photoacoustic effect based tumor therapy. Theranostics 4(10):1026–1038
46. Sun Y, Zheng Y, Ran H et al (2012) Superparamagnetic PLGA-iron oxide microcapsules for dual-modality US/MR imaging and high intensity focused US breast cancer ablation. Biomaterials 33(24):5854–5864
47. Brismar TB, Grishenkov D, Gustafsson B et al (2012) Magnetite nanoparticles can be coupled to microbubbles to support multimodal imaging. Biomacromolecules 13(5):1390–1399
48. Liu Z, Lammers T, Ehling J et al (2011) Iron oxide nanoparticle-containing microbubble composites as contrast agents for MR and ultrasound dual-modality imaging. Biomaterials 32(26):6155–6163
49. Kang ST, Yeh CK (2011) Intracellular acoustic droplet vaporization in a single peritoneal macrophage for drug delivery applications. Langmuir 27(21):13183–13188
50. Kripfgans OD, Fowlkes JB, Miller DL et al (2000) Acoustic droplet vaporization for therapeutic and diagnostic applications. Ultrasound Med Biol 26(7):11771189
51. Strohm EM, Rui M, Kolios MC (2010) Optical Droplet Vaporization (ODV): photoacoustic characterization of perfluorocarbon droplets. In: Ultrasonics symposium (IUS), 2010 IEEE, IEEE, San Diego, CA, USA, pp 495–498
52. Strohm E, Rui M, Gorelikov I et al (2011) Vaporization of perfluorocarbon droplets using optical irradiation. Biomed Opt Express 2(6):1432–1442

53. Mattrey RF, Scheible FW, Gosink BB et al (1982) Perfluoroctylbromide: a liver/spleen-specific and tumor-imaging ultrasound contrast material. Radiology 145(3):759–762
54. Mattrey RF, Long DM, Multer F et al (1982) Perfluoroctylbromide: a reticuloendothelial-specific and tumor-imaging agent for computed tomography. Radiology 145(3):755–758
55. Mattrey RF, Leopold GR, vanSonnenberg E et al (1983) Perfluorochemicals as liver- and spleen-seeking ultrasound contrast agents. J Ultrasound Med 2(4):173–176
56. Jin Y, Wang J, Ke H et al (2013) Graphene oxide modified PLA microcapsules containing gold nanoparticles for ultrasonic/CT bimodal imaging guided photothermal tumor therapy. Biomaterials 34(20):4794–4802
57. Kim J, Arifin DR, Muja N et al (2011) Multifunctional capsule-in-capsules for immunoprotection and trimodal imaging. Angew Chem Int Ed 50(10):2317–2321
58. Barnett BP, Ruiz-Cabello J, Hota P et al (2011) Fluorocapsules for improved function, immunoprotection, and visualization of cellular therapeutics with MR, US, and CT imaging. Radiology 258(1):182–191
59. Kircher MF, de la Zerda A, Jokerst JV et al (2012) A brain tumor molecular imaging strategy using a new triple-modality MRI-photoacoustic-Raman nanoparticle. Nat Med 18(5):829–834
60. Qin C, Cheng K, Chen K et al (2013) Tyrosinase as a multifunctional reporter gene for Photoacoustic/MRI/PET triple modality molecular imaging. Sci Rep. doi:10.1038/srep01490
61. Nakatsuka MA, Mattrey RF, Esener SC et al (2012) Aptamer-crosslinked microbubbles: smart contrast agents for thrombin-activated ultrasound imaging. Adv Mater 24(45):6010–6016
62. Ferrante EA, Pickard JE, Rychak J et al (2009) Dual targeting improves microbubble contrast agent adhesion to VCAM-1 and P-selectin under flow. J Control Release 140(2):100–107
63. Wang S, Mauldin FW, Klibanov AL et al (2013) Shear forces from flow are responsible for a distinct statistical signature of adherent microbubbles in large vessels. Mol Imaging 12(6):396–408
64. Deshpande N, Ren Y, Foygel K et al (2011) Willmann, Tumor angiogenic marker expression levels during tumor growth: longitudinal assessment with molecularly targeted microbubbles and US imaging. Radiology 258(3):804–811
65. Inaba Y, Lindner JR (2012) Molecular imaging of disease with targeted contrast ultrasound imaging. Transl Res 159(3):140–148
66. Piedra M, Allroggen A, Lindner JR (2009) Molecular imaging with targeted contrast ultrasound. Cerebrovasc Dis 27:66–74
67. BaronToaldo M, Salvatore V, Marinelli S et al (2014) Use of VEGFR-2 targeted ultrasound contrast agent for the early evaluation of response to sorafenib in a mouse model of hepatocellular carcinoma. Mol Imaging Biol 1:9
68. Nunn A, Pochon S, Tardy I et al (2012) Microbubble-conjugated vascular endothelial growth factor receptor 2 binding peptide. In: Molecular Imaging and Contrast Agent Database National Center for Biotechnology Information (US)
69. Mancini M, Greco A, Salvatore G et al (2013) Imaging of thyroid tumor angiogenesis with microbubbles targeted to vascular endothelial growth factor receptor type 2 in mice. BMC Med Imaging 13:31
70. Tardy I, Pochon S, Theraulaz M et al (2010) Ultrasound molecular imaging of VEGFR2 in a rat prostate tumor model using BR55. Invest Radiol 45(10):573–578
71. Pochon S, Tardy I, Bussat P et al (2010) BR55: a lipopeptide-based VEGFR2-targeted ultrasound contrast agent for molecular imaging of angiogenesis. Invest Radiol 45(2):89–95
72. Grouls C, Hatting M, Rix A et al (2013) Liver dysplasia: US molecular imaging with targeted contrast agent enables early assessment. Radiology 267(2):487–495
73. Bzyl J, Palmowski M, Rix A et al (2013) The high angiogenic activity in very early breast cancer enables reliable imaging with VEGFR2-targeted microbubbles (BR55). Eur Radiol 23(2):468–475
74. Davidson BP, Kaufmann BA, Belcik JT et al (2012) Detection of antecedent myocardial ischemia with multiselectin molecular imaging. J Am Coll Cardiol 60(17):1690–1697

75. Andonian S, Coulthard T, Smith AD et al (2009) Real-time quantitation of renal ischemia using targeted microbubbles: in-vivo measurement of P-selectin expression. J Endourol 23(3):373–378
76. Hyvelin JM, Tardy I, Bettinger T et al (2014) Ultrasound molecular imaging of transient acute myocardial ischemia with a clinically translatable P- and E-selectin targeted contrast agent: correlation with the expression of selectins. Invest Radiol 49(4):224–235
77. Leng X, Wang J, Carson A et al (2014) Ultrasound detection of myocardial ischemic memory using an E-selectin targeting peptide amenable to human application. Mol Imaging 13(4):1–9
78. Yan Y, Liao Y, Yang L et al (2011) Late-phase detection of recent myocardial ischaemia using ultrasound molecular imaging targeted to intercellular adhesion molecule-1. Cardiovasc Res 89(1):175–183
79. Wilson SR, Burns PN (2010) Microbubble-enhanced US in body imaging: what role? Radiology 257(1):24–39
80. D'Onofrio M, Zamboni G, Tognolini A et al (2006) Mass-forming pancreatitis: value of contrast-enhanced ultrasonography. World J Gastroenterol 12(26):4181–4184
81. Fan Z, Li Y, Yan K et al (2013) Application of contrast-enhanced ultrasound in the diagnosis of solid pancreatic lesions – a comparison of conventional ultrasound and contrast-enhanced CT. Eur J Radiol 82(9):1385–1390
82. Tlaxca JL, Rychak JJ, Ernst PB et al (2013) Ultrasound-based molecular imaging and specific gene delivery to mesenteric vasculature by endothelial adhesion molecule targeted microbubbles in a mouse model of Crohn's disease. J Control Release 165(3):216–225
83. Forsberg F (2012) Science to practice: can contrast-enhanced US of targeted microbubbles be used to monitor and quantify inflammation in patients with inflammatory bowel disease? Radiology 262(1):1–2
84. Bachmann C, Klibanov AL, Olson TS et al (2006) Targeting mucosal addressin cellular adhesion molecule (MAdCAM)-1 to noninvasively image experimental Crohn's disease. Gastroenterology 130(1):8–16
85. Bettinger T, Bussat P, Tardy I et al (2012) Ultrasound molecular imaging contrast agent binding to both E- and P-selectin in different species. Invest Radiol 47(9):516–523
86. Wang H, Machtaler S, Bettinger T et al (2013) Molecular imaging of inflammation in inflammatory bowel disease with a clinically translatable dual-selectin-targeted US contrast agent: comparison with FDG PET/CT in a mouse model. Radiology 267(3):818–829
87. Kaufmann BA, Sanders JM, Davis C et al (2007) Molecular imaging of inflammation in atherosclerosis with targeted ultrasound detection of vascular cell adhesion molecule-1. Circulation 116(3):276–284
88. Okimoto H, Ishigaki Y, Koiwa Y et al (2008) A novel method for evaluating human carotid artery elasticity: possible detection of early stage atherosclerosis in subjects with type 2 diabetes. Atherosclerosis 196(1):391–397
89. Kaufmann BA, Carr CL, Belcik JT et al (2010) Molecular imaging of the initial inflammatory response in atherosclerosis: implications for early detection of disease. Arterioscler Thromb Vasc Biol 30(1):54–59
90. Yan F, Li X, Jin Q et al (2012) Ultrasonic imaging of endothelial CD81 expression using CD81-targeted contrast agents in in vitro and in vivo studies. Ultrasound Med Biol 38(4):670–680
91. Metzger K, Vogel S, Chatterjee M et al (2015) High-frequency ultrasound-guided disruption of glycoprotein VI-targeted microbubbles targets atheroprogressison in mice. Biomaterials 36:80–89
92. Leung K (2004) Magnetic microbubbles conjugated with anti-vascular cell adhesion molecule-1 monoclonal antibody 429. In: Molecular Imaging and Contrast Agent Database National Center for Biotechnology Information (US)
93. Wu W, Wang Y, Shen S et al (2013) In vivo ultrasound molecular imaging of inflammatory thrombosis in arteries with cyclic Arg-Gly-Asp-modified microbubbles targeted to glycoprotein IIb/IIIa. Invest Radiol 48(11):803–812

94. Khanicheh E, Qi Y, Xie A et al (2013) Molecular imaging reveals rapid reduction of endothelial activation in early atherosclerosis with apocynin independent of antioxidative properties. Arterioscler Thromb Vasc Biol 33(9):2187–2192
95. McCarty OJ, Conley RB, Shentu W et al (2010) Molecular imaging of activated von Willebrand factor to detect high-risk atherosclerotic phenotype. JACC Cardiovasc Imaging 3(9):947–955
96. Wang X, Hagemeyer CE, Hohmann JD et al (2012) Novel single-chain antibody-targeted microbubbles for molecular ultrasound imaging of thrombosis: validation of a unique noninvasive method for rapid and sensitive detection of thrombi and monitoring of success or failure of thrombolysis in mice. Circulation 125(25):3117–3126
97. Borden MA, Zhang H, Gillies RJ et al (2008) A stimulus-responsive contrast agent for ultrasound molecular imaging. Biomaterials 29(5):597–606
98. Wang S, Mauldin FW, Klibanov AL et al (2015) Ultrasound-based measurement of molecular marker concentration in large blood vessels: a feasibility study. Ultrasound Med Biol 41(1):222–234
99. Wu J, Leong-Poi H, Bin J et al (2011) Efficacy of contrast-enhanced US and magnetic microbubbles targeted to vascular cell adhesion molecule-1 for molecular imaging of atherosclerosis. Radiology 260(2):463–471
100. Meloni MF, Goldberg SN, Livraghi T et al (2001) Hepatocellular carcinoma treated with radiofrequency ablation: comparison of pulse inversion contrast-enhanced harmonic sonography, contrast-enhanced power Doppler sonography, and helical CT. AJR Am J Roentgenol 177(2):375–380
101. Kisaka Y, Hirooka M, Kumagi T et al (2006) Usefulness of contrast-enhanced ultrasonography with abdominal virtual ultrasonography in assessing therapeutic response in hepatocellular carcinoma treated with radiofrequency ablation. Liver Int 26(10):1241–1247
102. Xie F, Lof J, Matsunaga T et al (2009) Diagnostic ultrasound combined with glycoprotein IIb/IIIa-targeted microbubbles improves microvascular recovery after acute coronary thrombotic occlusions. Circulation 119(10):1378–1385
103. Zhou Y, Wang Z, Chen Y et al (2013) Microbubbles from gas-generating perfluorohexane nanoemulsions for targeted temperature-sensitive ultrasonography and synergistic HIFU ablation of tumors. Adv Mater 25(30):4123–4130
104. Hanajiri K, Maruyama T, Kaneko Y et al (2006) Microbubble-induced increase in ablation of liver tumors by high-intensity focused ultrasound. Hepatol Res 36(4):308–314
105. Mayer CR, Geis NA, Katus HA et al (2008) Ultrasound targeted microbubble destruction for drug and gene delivery. Expert Opin Drug Deliv 5(10):1121–1138
106. Unger EC, Porter T, Culp W et al (2004) Therapeutic applications of lipid-coated microbubbles. Adv Drug Deliv Rev 56(9):1291–1314
107. Fan Z, Kumon RE, Deng CX (2014) Mechanisms of microbubble-facilitated sonoporation for drug and gene delivery. Ther Deliv 5(4):467–486
108. Pysz MA, Foygel K, Rosenberg J et al (2010) Antiangiogenic cancer therapy: monitoring with molecular US and a clinically translatable contrast agent (BR55). Radiology 256(2):519–527
109. Yan P, Chen KJ, Wu J et al (2014) The use of MMP2 antibody-conjugated cationic microbubble to target the ischemic myocardium, enhance Timp3 gene transfection and improve cardiac function. Biomaterials 35(3):1063–1073
110. Kheirolomoom A, Dayton PA, Lum AF et al (2007) Acoustically-active microbubbles conjugated to liposomes: characterization of a proposed drug delivery vehicle. J Control Release 118(3):275–284
111. Yan F, Li U, Deng Z et al (2013) Paclitaxel-liposome-microbubble complexes as ultrasound-triggered therapeutic drug delivery carriers. J Control Release 166(3):246–255
112. Yoon YI, Kwon YS, Cho HS et al (2014) Ultrasound-mediated gene and drug delivery using a microbubble-liposome particle system. Theranostics 4(11):1133–1144
113. Ibsen S, Benchimol M, Simberg D et al (2011) A novel nested liposome drug delivery vehicle capable of ultrasound triggered release of its payload. J Control Release 155(3):358–366

114. Rapoport NY, Kennedy AM, Shea JE et al (2009) Controlled and targeted tumor chemotherapy by ultrasound-activated nanoemulsions/microbubbles. J Control Release 138(3):268–276
115. Yang P, Li D, Jin S et al (2014) Stimuli-responsive biodegradable poly(methacrylic acid) based nanocapsules for ultrasound traced and triggered drug delivery system. Biomaterials 35(6):2079–2088
116. Bekeredjian R, Grayburn PA, Shohet RV (2005) Use of ultrasound contrast agents for gene or drug delivery in cardiovascular medicine. J Am Coll Cardiol 45(3):329–335
117. Ibsen S, Schutt CE, Esener S (2013) Microbubble-mediated ultrasound therapy: a review of its potential in cancer treatment. Drug Des Devel Ther 7:375–388
118. Lentacker I, De Smedt SC, Demeester J et al (2006) Microbubbles which bind and protect DNA against nucleases. J Control Release 116(2):73–75
119. Willmann JK, Cheng Z, Davis C et al (2008) Targeted microbubbles for imaging tumor angiogenesis: assessment of whole-body biodistribution with dynamic micro-PET in mice. Radiology 249(1):212–219
120. Hernot S, Klibanov AL (2008) Microbubbles in ultrasound-triggered drug and gene delivery. Adv Drug Deliv Rev 60(10):1153–1166
121. Unger EC, McCreery TP, Sweitzer RH et al (1998) Acoustically active lipospheres containing paclitaxel: a new therapeutic ultrasound contrast agent. Invest Radiol 33(12):886–892
122. Tartis MS, McCallan J, Lum AF et al (2006) Therapeutic effects of paclitaxel-containing ultrasound contrast agents. Ultrasound Med Biol 32(11):1771–1780
123. Wang DS, Panje C, Pysz MA et al (2012) Cationic versus neutral microbubbles for ultrasound-mediated gene delivery in cancer. Radiology 264(3):721–732
124. Frenkel PA, Chen S, Thai T et al (2002) DNA-loaded albumin microbubbles enhance ultrasound-mediated transfection in vitro. Ultrasound Med Biol 28(6):817–822
125. Rapoport N (2012) Phase-shift, stimuli-responsive perfluorocarbon nanodroplets for drug delivery to cancer. WIREs Nanomed Nanobi 4(5):492–510
126. Myhr G (2007) Multimodal ultrasound mediated drug release model in local cancer therapy. Med Hypotheses 69(6):1325–1333
127. Caskey CF, Hu X, Ferrara KW (2011) Leveraging the power of ultrasound for therapeutic design and optimization. J Control Release 156(3):297–306
128. Tinkov S, Winter G, Coester C (2010) New doxorubicin-loaded phospholipid microbubbles for targeted tumor therapy: part I – formulation development and in-vitro characterization. J Control Release 143(1):143–150
129. May DJ, Allen JS, Ferrara KW (2002) Dynamics and fragmentation of thick-shelled microbubbles. IEEE Trans Ultrason Ferroelectr Freq Control 49(10):1400–1410
130. Iyer AK, Khaled G, Fang J et al (2006) Exploiting the enhanced permeability and retention effect for tumor targeting. Drug Discov Today 11(17–18):812–818
131. Lovell JF, Huynh E, MacDonald TD et al (2011) Bursting the bubble: microbubble-nanoparticle composites for ultrasound-mediated drug delivery. Nanomedicine (Lond) 6(7):1156–1157
132. Tinkov S, Coester C, Serba S et al (2010) New doxorubicin-loaded phospholipid microbubbles for targeted tumor therapy: in-vivo characterization. J Control Release 148(3):368–372
133. Staples BJ, Pitt WG, Roeder BL et al (2010) Distribution of doxorubicin in rats undergoing ultrasonic drug delivery. J Pharm Sci 99(7):3122–3131
134. Fokong S, Theek B, Wu Z et al (2012) Image-guided, targeted and triggered drug delivery to tumors using polymer-based microbubbles. J Control Release 163(1):75–81
135. Geers B, Lentacker I, Sanders NN et al (2011) Self-assembled liposome-loaded microbubbles: the missing link for safe and efficient ultrasound triggered drug-delivery. J Control Release 152(2):249–256
136. Cochran MC, Eisenbrey J, Ouma RO et al (2011) Doxorubicin and paclitaxel loaded microbubbles for ultrasound triggered drug delivery. Int J Pharm 414(1–2):161–170
137. Rapoport N, Nam KH, Gupta R et al (2011) Ultrasound-mediated tumor imaging and nanotherapy using drug loaded, block copolymer stabilized perfluorocarbon nanoemulsions. J Control Release 153(1):4–15

138. Chen S, Ding JH, Bekeredjian R et al (2006) Efficient gene delivery to pancreatic islets with ultrasonic microbubble destruction technology. Proc Natl Acad Sci U S A 103(22):8469–8474
139. Li P, Zheng Y, Ran H et al (2012) Ultrasound triggered drug release from 10-hydroxycamptothecin-loaded phospholipid microbubbles for targeted tumor therapy in mice. J Control Release 162(2):349–354
140. Korpanty G, Chen S, Shohet RV et al (2005) Targeting of VEGF-mediated angiogenesis to rat myocardium using ultrasonic destruction of microbubbles. Gene Ther 12(17):1305–1312
141. Wang HB, Yang L, Wu J et al (2014) Reduced ischemic injury after stroke in mice by angiogenic gene delivery via ultrasound-targeted microbubble destruction. J Neuropathol Exp Neurol 73(6):548–558
142. Hu YZ, Zhu JA, Jiang YG et al (2009) Ultrasound microbubble contrast agents: application to therapy for peripheral vascular disease. Adv Ther 26(4):425–434
143. Fujii H, Sun Z, Li SH et al (2009) Ultrasound-targeted gene delivery induces angiogenesis after a myocardial infarction in mice. JACC Cardiovasc Imaging 2(7):869–879
144. Zhang Q, Wang Z, Ran H et al (2006) Enhanced gene delivery into skeletal muscles with ultrasound and microbubble techniques. Acad Radiol 13(3):363–367
145. Wang ZG, Ling ZY, Ran HT et al (2004) Ultrasound-mediated microbubble destruction enhances VEGF gene delivery to the infarcted myocardium in rats. Clin Imaging 28(6):395–398
146. Lackey L, Peterson C, Barr RG (2012) Contrast-enhanced ultrasound-guided radiofrequency ablation of renal tumors. Ultrasound Q 28(4):269–274
147. Vlaisavljevich E, Durmaz YY, Maxwell A et al (2013) Nanodroplet-mediated histotripsy for image-guided targeted ultrasound cell ablation. Theranostics 3(11):851–864
148. Xu RX, Povoski SP, Martin EW et al (2010) Targeted delivery of microbubbles and nanobubbles for image-guided thermal ablation therapy of tumors. Expert Rev Med Devices 7(3):303–306
149. Meairs S, Kern R, Alonso A (2012) Why and how do microbubbles enhance the effectiveness of diagnostic and therapeutic interventions in cerebrovascular disease? Curr Pharm Des 18(15):2223–2235
150. Meairs S, Culp W (2009) Microbubbles for thrombolysis of acute ischemic stroke. Cerebrovasc Dis 27(Suppl 2):55–65
151. Kaul S (2009) Sonothrombolysis: a universally applicable and better way to treat acute myocardial infarction and stroke? Who is going to fund the research? Circulation 119(10):1358–1360
152. Wu J, Xie F, Kumar T et al (2014) Improved sonothrombolysis from a modified diagnostic transducer delivering impulses containing a longer pulse duration. Ultrasound Med Biol 40(7):1545–1553
153. de Saint Victor M, Crake C, Coussios CC et al (2014) Properties, characteristics and applications of microbubbles for sonothrombolysis. Expert Opin Drug Deliv 11(2):187–209
154. Liu HL, Fan CH, Ting CY et al (2014) Combining microbubbles and ultrasound for drug delivery to brain tumors: current progress and overview. Theranostics 4(4):432–444
155. Zhang B, Luo Z, Liu J et al (2014) Cytochrome c end-capped mesoporous silica nanoparticles as redox-responsive drug delivery vehicles for liver tumor-targeted triplex therapy in vitro and in vivo. J Control Release 192:192–201
156. Nance E, Timbie K, Miller GW et al (2014) Non-invasive delivery of stealth, brain-penetrating nanoparticles across the blood–brain barrier using MRI-guided focused ultrasound. J Control Release 189:123–132
157. Burgess A, Hynynen K (2014) Drug delivery across the blood–brain barrier using focused ultrasound. Expert Opin Drug Deliv 11(5):711–721

Chapter 6
Multifunctional Hollow Mesoporous Silica Nanoparticles for MR/US Imaging-Guided Tumor Therapy

Yu Chen, Ming Ma, Hangrong Chen, and Jianlin Shi

6.1 Introduction

With the fast development of nanotechnology, nanomedicine, as one of the most important branches of nanotechnology, steps into the ever-increasing development to benefit the human health [1, 2]. Nanomedicine is a multidisciplinary research frontier related to chemistry, material science, biology, and biomedicine [2]. The research of nanomedicine in oncology includes drug delivery, molecular imaging, synergistic therapy, theranostics (concurrent diagnostic imaging and therapy), etc. For instance, the delivery of anticancer drugs via nanocarriers can substantially improve the bioavailability of drugs, enhance therapeutic index, and mitigate the side effects [3–6]. In addition, the introduction of nanoprobes as the contrast agents (CAs) can cause the contrast-enhanced diagnostic imaging performance, which can even realize the molecular imaging of cancer cells [7–9]. On this ground, nanomedicine shows very promising prospects to provide an alternative but highly effective strategy to combat the cancer.

Largely due to the high prospects of nanomedicine in cancer treatment, abundant biocompatible nanosystems with varied chemical compositions and nanostructures have been developed, which can be mainly classified into three types, including organic materials, inorganic materials and organic/inorganic hybrid nanosystems. Organic nanomaterials possess the chemical composition that is very similar to the composition of the human body; thus, they show high biocompatibility and biodegradability [10–13]. Comparatively, biocompatible inorganic nanosystems exhibit high chemical/thermal stability and high drug-lading capacity and multifunctionality [5, 6]. Various inorganic nanoparticles have been developed in nanomedicine,

Y. Chen • M. Ma • H. Chen (✉) • J. Shi
Shanghai Institute of Ceramics, Chinese Academy of Sciences,
1295, Dingxi Road, Shanghai 200050, China
e-mail: hrchen@mail.sic.ac.cn

Z. Dai (ed.), *Advances in Nanotheranostics II*, Springer Series
in Biomaterials Science and Engineering 7, DOI 10.1007/978-981-10-0063-8_6

such as silica [14, 15], magnetic Fe_3O_4, quantum dots, MnO_2 [16], graphene [17–20], MoS_2 [21, 22], mesoporous carbon [23], etc. Among all these inorganic nanosystems, mesoporous silica nanoparticles (designated as MSNs) with well-defined mesopores have attracted even more attentions in nanomedicine. On one hand, the elements silica and oxygen are both the necessary elements for the human body, i.e., they possess high biocompatibility. On the other hand, the mesoporous nanostructure of MSNs endows them with large surface area, high pore volume, and tunable pore sizes, facilitating the encapsulation of guest molecules with high loading capacity and sustained releasing performance. In addition, abundant surface chemistry of MSNs (e.g., Si-OH) makes the surface engineering possible, such as PEGylation, targeting, responsive modification, etc. Based on these merits, MSNs have found the broad applications in anticancer drug delivery, antibacterial, antimetastasis of cancer cells, various diagnostic imagings, biosensing, and even tissue engineering [24–28]. Further systematic biosafety evaluations (e.g., biodistribution, biodegradation, hemocompatibility, histocompatibility, excretion) reveal that MSNs are highly biocompatible at the desirable doses, indicating their high potential for clinical translations [5, 29].

MSNs with unique hollow nanostructure (hollow MSNs, designated HMSNs) are a new subfamily of MSNs combining the merits of both MSNs and hollow nanostructure [30–36]. The introduction of hollow nanostructure into MSNs can endow them with high cargo-loading capacity and reduce the dose frequency [37–39]. Importantly, HMSNs can further reduce the deposition of foreign matters in the body; thus, they have even higher biocompatibility compared to MSNs. The fabrication of HMSNs has become the ever-hot research topic in nanomedicine [40–43]. Figure 6.1a shows the typical design strategy to engineering HMSNs for biomedical applications, including loading drugs, targeting modification, PEGylation,

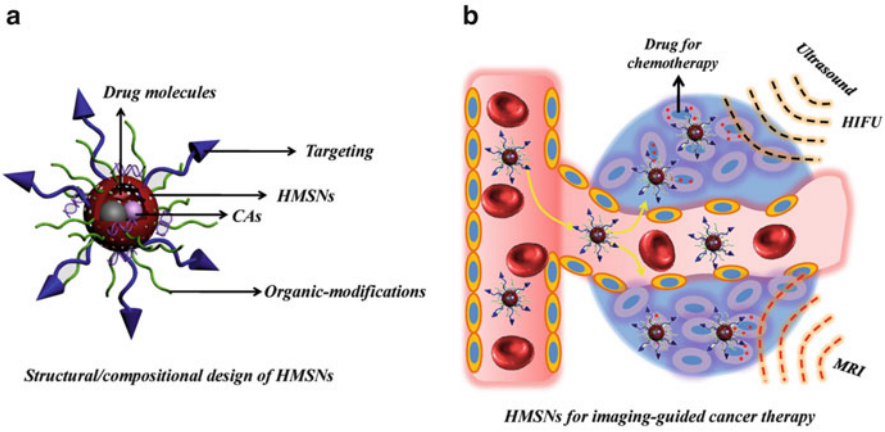

Fig. 6.1 Schematic illustration of the structural/compositional design of HMSNs for biomedical applications (**a**) and HMSNs in blood stream and tumor tissues for MRI imaging-guided HIFU cancer therapy (**b**)

multifunctionalization of CAs, etc. For example, their high drug-loading capacity has been demonstrated, and the corresponding high biocompatibility has been evaluated [44–47]. Especially, these HMSN-based hollow nanoparticles show the high performance in diagnostic imaging, especially in imaging-guided cancer therapy [37, 48]. In addition, the large hollow interior and thin mesoporous silica shell can respond to the ultrasound irradiation for contrast-enhanced ultrasonography [49–52]. Paramagnetic/superparamagnetic functionalization of HMSNs can further endow them with the roles for T_1-/T_2-weighted magnetic resonance imaging (MRI) [48].

In this chapter, we focus on the biomedical applications of HMSNs for tumor diagnostic imaging and therapy, especially for ultrasonography/MR imaging, and high-intensity focused ultrasound (HIFU) synergistic therapy. Importantly, HMSNs can transport within blood vessels and accumulate into tumor tissues, which can treat the tumor for ultrasound focusing therapy and chemotherapy (Fig. 6.1b) under the imaging guidance. The design, synthetic strategies, and characterizations of HMSN-based nanofamilies will be summarized in detail, especially focusing on a novel "structural difference-based selective etching" strategy for tuning the crucial composition/nanostructure of HMSNs, such as particle size, pore size, organic–inorganic hybridization, multifunctionalization, etc. The unresolved critical issues and further developments of HMSN-based nanosystems for imaging-guided cancer treatment and clinical translation will be briefly discussed in the final section.

6.2 Design, Synthesis and Characterization of HMSNs

6.2.1 Synthetic Approach for HMSNs

Based on the advantages of nanosynthetic chemistry, HMSNs with different morphologies and nanostructures have been successfully synthesized. Typically, HMSNs were fabricated by either soft-templating or hard-templating approach (Fig. 6.2) [53]. In principle, the templates are pre-introduced followed by the self-assembly of hydrolyzed/condensed silica/organosilica precursor and surfactants on the surface of templates to form the core/shell structure. After removing the templates and pore-making agents (surfactants), HMSNs with well-defined mesoporous shells and large hollow interiors can be fabricated. In this regard, the introduced templates and self-assembly process substantially influence the crucial/structural parameters of HMSNs, i.e., these parameters can be precisely controlled by choosing adequate templates and adopting desirable synthetic processes.

The hard-templating method has been extensively adopted for the construction of hollow nanoparticles, especially for the synthesis of HMSNs [53]. As early as 1998, Frank Caruso et al. successfully realized the fabrication of hollow silica spheres with particulate sizes between 720 and 1000 nm by using colloidal polystyrene (PS) latex particles as the hard templates [54]. Without using the pore-making

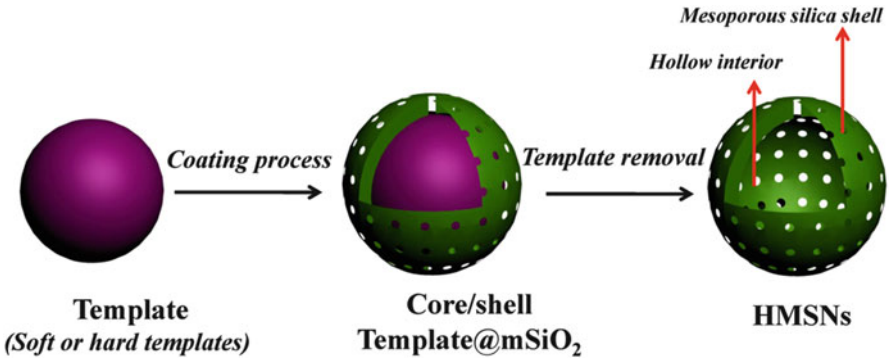

Fig. 6.2 Schematic illustration of templating synthesis for HMSNs

agents such as surfactants, these hollow silica nanoparticles presented no mesoporous structure within the shell. Thus, they had very limited applications because the large hollow interior was inaccessible to guest molecules outside of the particles. Fortunately, Giannelis et al. made the significant progress of fabricating HMSNs with well-defined mesopores in the shell by introducing hexadecyltrimethylammonium bromide (CTAB) as the structural-directing and pore-making agent during the synthesis [55]. Especially, monodispersed spherical HMSNs were successfully prepared by this facile and scalable approach using PS as the hard template. Importantly, the as-synthesized HMSNs showed the well-defined mesopores with high surface area (>1000 m^2/g). The particle size and shell thickness were controlled by either choosing the PS with varied sizes or changing the amounts of adopted silica precursors. In addition, the PS-based hard templates were also adopted by Koumoto et al. to synthesize HMSNs for the sustained release of loaded dye molecules [56].

The hard-templating approach also facilitates the fabrication of HMSNs with different morphologies simply by changing the shapes of hard templates. Shi et al. realized the fabrication of ellipsoidal HMSNs by using ellipsoidal hematite particles as the hard templates [57]. The surface of ellipsoidal hematite could be uniformly coated with a mesoporous silica shell by using tetraethoxysilane (TEOS) and n-octadecyltrimethoxysilane (CTMS) as the co-silica precursor. After the dissolving of hematite core under acidic condition, ellipsoidal HMSNs with the sizes of around 100–200 nm could be synthesized, which exhibited the high drug-storage capability of as high as 726 mg/g (ibuprofen).

Compared to hard-templating approach, the soft-templating method is another efficient methodology to fabricate HMSNs, especially for HMSNs with highly ordered mesoporous structure in the shell. In 2003, Shi et al. successfully prepared HMSNs with 3D-ordered mesopore network by using an oil (TEOS)-in-water emulsion as the soft template, which exhibited the improved hydrothermal stability [58]. The particles synthesized by this approach, however, showed the severe aggregation, limiting their extensive applications. To partially solve this problem, they further used (−)-N-dodecyl-N-methylephedrinium bromide (DMEB) micellar aggregates in water as the soft templates to fabricate highly

dispersed HMSNs with well-defined mesopores in the shell [59]. Lu et al. self-assembled [$C_3F_7O(CFCF_3CF_2O)_2CFCF_3CONH(CH_2)_3N^+(C_2H_5)_2CH_3I^-$] (FC4) and organosilica (1,2-bis(trimethoxysilyl)ethane, BTEB) to form vesicle as the soft templates for the fabrication of organic–inorganic hybrid HMSNs with highly ordered mesopores within the shell. However, the morphology was not very well-defined, restricting their further biomedical applications [60]. Tang et al. reported a fast silicification process in dilute silicate solution to fabricate HMSNs using a vesicle template of cetyltrimethylammonium bromide–sodium dodecyl sulfate–Pluronic P123 (C_{16}TAB-SDS-$EO_{20}PO_{70}EO_{20}$) at a SDS/C_{16}TMAB ratio of 0.6–0.8 [61]. Interestingly, Mokaya et al. used supercritical CO_2-in-water emulsion as the soft template to synthesize HMSNs [62]. Although various soft-templating processes can produce HMSNs with ordered mesopores in the shell, most of HMSNs synthesized by this method are not well defined in morphology and severely aggregated. In addition, the particle size, morphology, and mesopore size are difficult to be controlled using this method because of the intrinsic drawbacks of soft-templating method, i.e., this method is very sensitive to the synthetic processes, which is difficult to be controlled. Therefore, HMSNs fabricated by the soft-templating route are seldom to be used for biomedical applications, especially for in vivo evaluations where HMSNs with high dispersity and uniform particle size/morphology are strongly required.

6.2.2 Structural Difference-Based Selective Etching Strategy

The typical hard-templating approach was based on the different physiochemical properties between the core and shell to remove the core part and leave the shell intact [53]. The chemical compositions between the core and shell are typically different, which can cause the specific physiochemical property differences to realize the creation of the hollow interior. Very recently, a unique "structural difference-based selective etching" strategy has been developed to tune the key structural parameters of HMSNs by building the structural differences between the core and shell while keeping the chemical composition almost the same [30, 63].

It is well known that the Si-O-Si bond of silica framework can be broken under either alkaline condition or HF etching (Fig. 6.3). This principle has been extensively used in industry for the treatment of glasses or ceramics. This chemical essence can be defined as "silica-etching chemistry." Shi's group elaborately used this etching principle to construct HMSNs by building a SiO_2@mSiO_2 core/shell nanostructure where solid silica was used as the inner core followed by coating a mesoporous silica shell onto the surface of initially introduced SiO_2 core [30]. By using FTIR and ^{29}Si MAS NMR characterizations, they found that the mesoporous silica shell exhibited significantly higher silica condensation degree than that of the solid silica shell, i.e., the shell possessed relatively higher stability than the core. After the treatment of SiO_2@mSiO_2 nanoparticles under mild alkaline condition, the solid silica core could be completely removed while the mesoporous silica shell

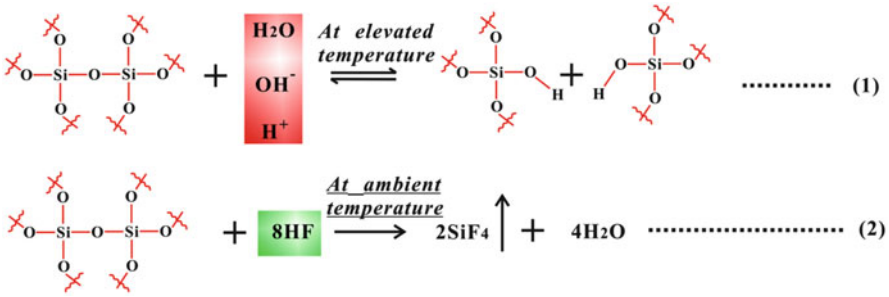

Fig. 6.3 Chemical reactions involved in silica-etching chemistry: (1) reversible alkaline etching and (2) irreversible HF etching

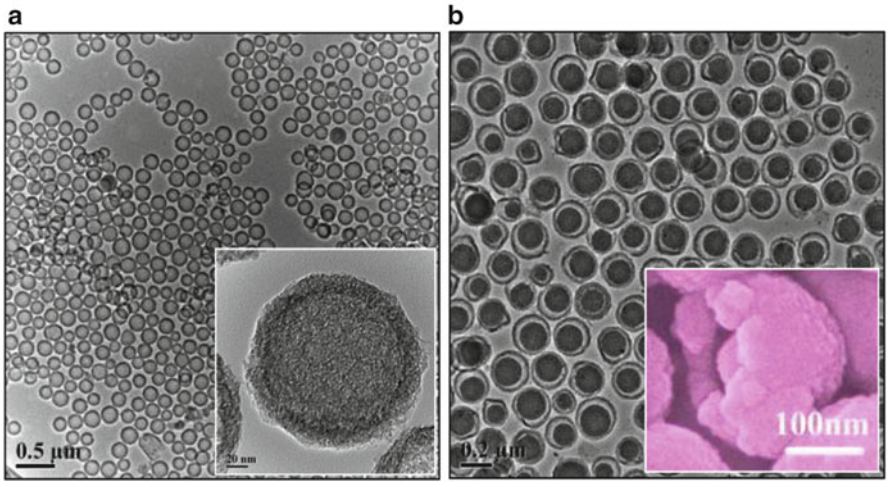

Fig. 6.4 TEM images of HMSNs (**a**, inset, single HMSN with high magnification) and rattle-type HMSNs (**b**, inset, selected SEM image of broken rattle-type HMSN to show the hollow structure) (Reprinted with permission from Ref. [30]. Copyright 2010, American Chemical Society)

kept intact based on this stability difference between the core and shell. Based on this artificially introduced structural difference, highly dispersed HMSNs with well-defined mesoporous and hollow nanostructure could be obtained (Fig. 6.4a), which exhibited high loading capacity for anticancer drug molecules (doxorubicin) [30]. Interestingly, the interface between the core and shell of $sSiO_2@mSiO_2$ could be etched away to produce rattle-type HMSNs simply by changing the etchant concentrations.

It is important to note that this "structural difference-based selectively etching" strategy can be facilely used to control the chemical composition and nanostructure of HMSNs. Firstly, the mature synthetic chemistry for SiO_2 nanoparticles as the core guarantees the easy adjusting of the particle sizes of HMSNs. By choosing SiO_2 core with different sizes, HMSNs could be synthesized from dozens of nanometers to

several hundred nanometers [30]. Secondly, the pore sizes of HMSNs could be tuned simply by controlling the etching process [64]. When the core of SiO_2@mSiO_2 nanoparticles was etched away, the shell was also under the mild etching. Thus, the initial mesopores created by surfactant micelles could be enlarged by the chemical etching process. Based on this mechanism, the mesopore sizes of HMSNs could be controlled from 3.2 nm to larger than 10 nm, which provides the possibility of using HMSNs as the nanocarriers to encapsulate and delivery of large biomacromolecules, such as proteins, enzymes, and genes. Thirdly, the chemical composition of HMSNs also determines their practical applications and related biological behaviors. By a specific chemical homology principle, Shi's group further coated a periodic mesoporous organosilicas (PMOs) onto the surface of solid silica nanoparticles to produce a specific SiO_2@PMOs core/shell nanoparticles (Fig. 6.5a). By further etching the solid silica core away, molecularly organic–inorganic hybrid hollow PMOs (designated as HPMOs) with phenylene-bridged organosilica framework could be fabricated (Fig. 6.5b, c), which were featured with the incorporated organic groups within

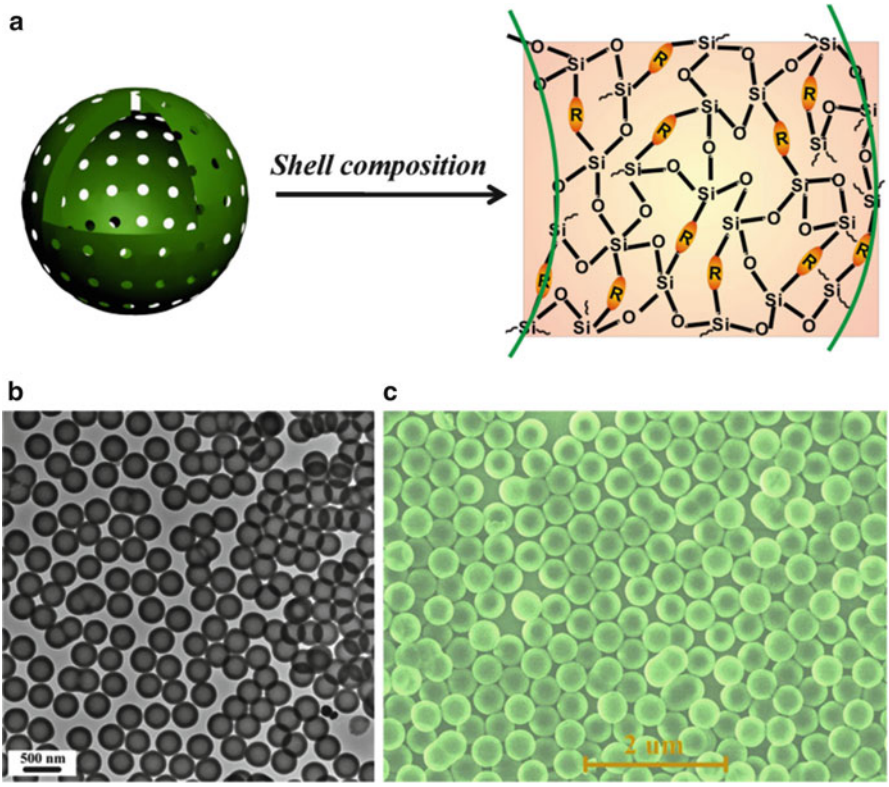

Fig. 6.5 (**a**) Schematic illustration of molecularly organic–inorganic hybrid framework of HPMOs; TEM (**b**) and SEM (**c**) images of hybrid HPMOs (Reprinted with permission from Ref. [65]. Copyright 2013, John Wiley & Sons)

the Si-O-Si framework [65]. These specific organic–inorganic hybrid nanomaterials showed unique biological effects, such as significantly lowered hemolytic effects against red blood cells. They also exhibited the enhanced delivery performance for antimetastasis drugs (silibinin) to inhibit the migration and invasion of cancer cells. Importantly, these obtained hybrid HMSNs could be used for the fabrication of other functional nanoparticles, such as hollow mesoporous carbon nanoparticles (HMCNs) [23]. In addition, the multi-shell nanostructure of HMSNs was reported to be tuned by the successive coating process of mesoporous silica shell by employing different structural-directing agents [42].

The alkaline etching process is a reversible chemical reaction, which means that the presence of reverse reaction may bring with the by-products (Fig. 6.3). Comparatively, the chemical etching by HF is a very fast irreversible reaction, which indicates that this etching principle could avoid the production of by-products. Based on HF etching, the constructed hollow/rattle-type HMSNs have been reported for the delivery or co-delivery of hydrophobic anticancer drugs to circumvent the multidrug resistance of cancer cells [66]. A similar HF-based etching process to prepare rattle-type HMSNs was developed by Tang et al. for the delivery of docetaxel in efficient cancer chemotherapy [46, 67]. The main drawback of HF is the high toxic effect of the etchant (HF), which should be carried out under strict environment to avoid the influences to the human body and environment.

6.2.3 Design and Fabrication of HMSN-Based Multifunctional Composite Nanocapsules

There are typically three routes to functionalize HMSNs for imaging-guided therapy, i.e., putting functional nanocrystals into the hollow interior of HMSNs [37, 48], dispersing nanoparticles into the mesopores [68, 69], and anchoring nanocrystals onto the surface of HMSNs [70, 71]. The "structural difference-based selective etching" strategy could be further extended for the fabrication of mesoporous silica-based composite nanoparticles with functional nanocrystals within the hollow interior. It has been well demonstrated that various functional inorganic nanocrystals M (M = Fe_3O_4, Au, Ag, quantum dots, etc.) could be coated by a uniform silica layer to form the M@SiO_2 core/shell nanostructure [72, 73]. By further coating another mesoporous silica layer onto the surface of M@SiO_2 to form M@SiO_2@mSiO_2 nanoparticles, the middle solid silica layer could be selectively etched away to form rattle-type nanoparticles M@Void@mSiO_2. This specific hollow composite nanostructure shows the following unique structural property relationships. On one hand, the functional M nanocrystals could be used for various catalytic or bioimaging applications. On the other hand, the large hollow interior could endow the carrier with high cargo-loading capacity, especially for drug molecules. In addition, the well-defined mesoporous silica shell provides the diffusion pathways for guest molecules to access the functional M core and large hollow interior. Therefore, this specific M@Void@mSiO_2 nanostructure shows the great potential for various applications, especially in catalysis and biomedicine [63].

The well-defined mesopores also provide the room for the functional nanoparticles. Various nanoparticles, such as MnO_x [68], Fe_3O_4 [74], Au [75], etc., have been dispersed into the mesopores of mesoporous materials. In addition, magnetic Fe_3O_4 nanoparticles were successfully coated onto the surface of MSNs for concurrent MR imaging and chemotherapy [71].

6.2.4 Developments of the Crucial Structural/Compositional Parameters of HMSNs

For biomedical applications, the crucial structural/compositional parameters play the determining roles in biological behaviors and therapeutic/diagnostic performances of HMSNs. The different particle sizes of HMSNs have the varied biodistributions. In addition, HMSNs with tunable pore sizes can realize the delivery of drugs with different molecular sizes. The inert Si-O-Si framework has the low biodegradable rate, which severely restricts their further clinical translation. The introduction of physiologically active organic groups provides an alternative way to tune the biological effects of HMSNs for clinical translations.

Additionally, there is still no standard synthetic method for the fabrication of HMSNs, which would cause the biological evaluation results of HMSNs incomparable with the reported results. Therefore, it is still urgent to develop an easy, environment-friendly, low-cost, and scalable approach to synthesize HMSNs with strictly desirable key compositional/structural parameters to meet the requirements of clinical translation.

6.3 HMSNs as the Contrast Agents (CAs) for MR Imaging

HMSNs are featured with large surface area, high pore volume, tunable pore size, and abundant surface chemistry. The high therapeutic performance of HMSNs for drug delivery shows great potential for clinical translation. Functionalization of MSNs toward HMSN-based hybrid composites could endow them with unique theranostic functions, i.e., concurrent diagnostic imaging and therapy. In this part, the main progresses of HMSN-based composite materials for magnetic resonance imaging (MRI) are introduced, including T_1- and T_2-weighted MR imaging for cancer theranostics.

6.3.1 HMSNs for T_1-Weighted MR Imaging

The large mesopores of mesoporous silica provide the anchoring points for paramagnetic centers, which can be used for T_1-weighted MR imaging. In this regard, the paramagnetic center can get the enhanced accessibility to water molecules to enhance the T_1-weighted MRI performance. For instance, Lin et al. grafted Gd

chelates into the mesopores of mesoporous silica nanoparticles for contrast-enhanced T_1-weighted MR imaging [76]. The relaxivity r_1 could reach as high as 28.8 mM/s at 3 T and 10.2 mM/s at 9.4 T. The well-defined mesopores facilitated the high performance of Gd-based T_1-weighted MRI CAs, which were further demonstrated by several similar researches [77–81]. Shi's group also modified the mesoporous surface of rattle-type Au@Void@$mSiO_2$ with Gd-Si-DTPA for concurrent dark-field light-scattering cell imaging and T_1-weighted MR imaging [48]. The fabricated Au@$mSiO_2$ showed strong surface plasma-enhanced absorption, and the relaxivity r_1 could reach as high as 7.43 mM/s. Thus, this mesoporous composite nanocapsule could be used for dual-modality diagnostic imaging and concurrent anticancer drug delivery.

Manganese (Mn)-based T_1-weighted MRI contrast agents could also be integrated with mesoporous silica for MRI-based theranostic applications. Hyeon et al. coated a mesoporous silica shell onto the surface of MnO nanoparticles, followed by acid etching to form a hollow MnO core (designated as HMnO@$mSiO_2$, Fig. 6.6a, b) [82]. The designed HMnO@$mSiO_2$ exhibited relatively low relaxivity ($r_1 = 0.99$ mM/s), but they could be used for long-term labeling and MRI tracking (Fig. 6.6c, d) of adipose-derived mesenchymal stem cells (MSCs). Chou et al. further encapsulated Ir(III) complex phosphorescence dye into HMnO@$mSiO_2$ to

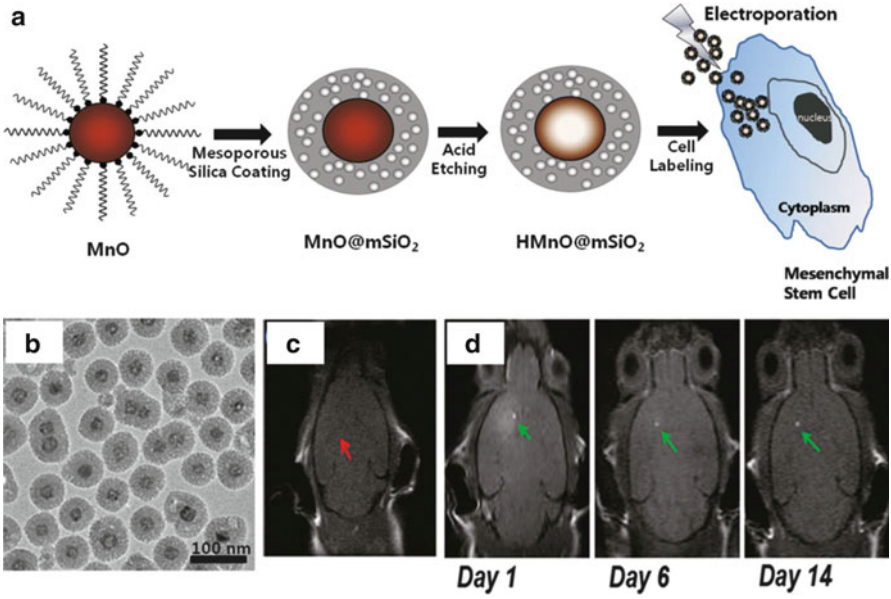

Fig. 6.6 (**a**) Schematic illustration of the synthetic procedure of HMnO@$mSiO_2$ core/shell hollow nanoparticles for labeling MSCs; (**b**) TEM image of HMnO@$mSiO_2$ nanoparticles; in vivo MR imaging of transplanted MSCs; (**c**) no hyperintense signal in mouse transplanted with unlabelled MSCs; and (**d**) hyperintense signal present in mouse transplanted with HMnO@mSO_2-labeled MSCs (Reprinted with permission from Ref. [82]. Copyright 2011, American Chemical Society)

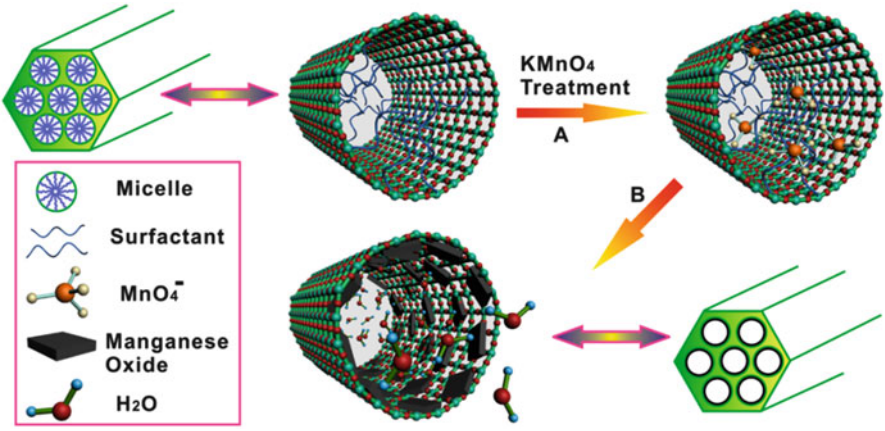

Fig. 6.7 Schematic illustration of the formation and loading of MnO_x nanoparticles into the mesopores of HMSNs (Reprinted with permission from Ref. [68]. Copyright 2012, Elsevier)

endow them with concurrent T_1-weighted MR imaging and photodynamic-therapy functions [83].

To further improve the T_1-weighted MR imaging capability of MnO_x-functionalized MSNs, MnO_x nanoparticles were dispersed into the mesopores of MSNs [68]. The large surface area of well-defined mesopores could guarantee the high dispersity of Mn-based paramagnetic centers to interact with water molecules, causing the high MRI performance. MnO_x nanoparticles were in situ formed within the mesopores by the direct redox reaction between $KMnO_4$ and surfactants (Fig. 6.7). Based on this strategy, the relaxivity r_1 could reach 2.28 mM/s. The same strategy was recently also developed for disperse paramagnetic Fe centers into the mesopores for T_1-weighted MR imaging [74]. Importantly, MnO_x-loaded HMSNs exhibited the pH-responsive T_1-weighted MR imaging performance due to the unique breakup nature of encapsulated MnO_x nanoparticles within the mesopores [69]. The released Mn^{II} reached the maximum chances to intact with water molecules, causing the improved MR imaging performance. The relaxivity r_1 in mild acidic environment could reach as high as 8.81 mM/s (pH = 5.0, Fig. 6.8a, b). In vivo evaluations directly demonstrated that the tumors could be clearly and continuously distinguished with the assistance of MnO_x-functionalized HMSNs (Fig. 6.8c–g). The slow lighting up of the tumor tissues in T_1-weighted MR imaging was due to the gradual release of Mn^{II} under the mild acidic environment of tumors.

6.3.2 HMSNs for T_2-Weighted MR Imaging

Functionalization of HMSNs with magnetic property can endow them with the function of contrast-enhanced T_2-weighted MRI performance (designated as MRI-T_2). The early magnetic mesoporous composite material was based on the coating

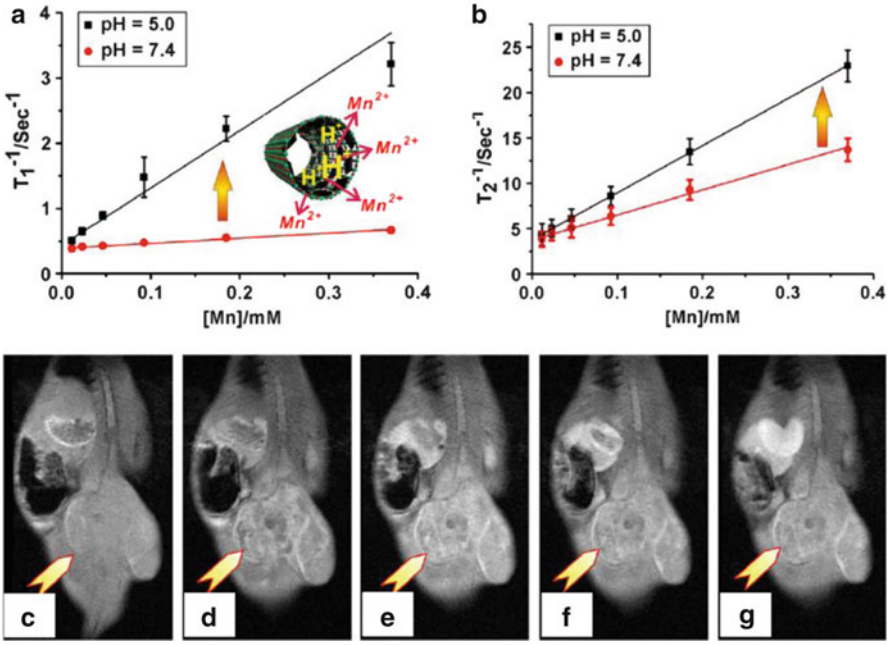

Fig. 6.8 (**a**) T_1 and (**b**) T_2 relaxivity of HMSNs at different pH values (7.4 and 5.0); in vivo T_1-weighted MR imaging of tumors (**c**) before and after intravenous administration of HMSNs for (**d**) 5 min, (**e**) 15 min, (**f**) 30 min, and (**g**) 30 min (Reprinted with permission from Ref. [68]. Copyright 2012, Elsevier)

process to form a mesoporous silica shell onto the surface of magnetic Fe_3O_4 nanoparticles (core/shell structured Fe_3O_4@$mSiO_2$). For example, the synthesized magnetic Fe_3O_4@$mSiO_2$ nanoparticles were found to have the sustained drug-releasing performance for loaded drug molecules [84, 85]. Further coating a fluorescent quantum dot layer onto the surface of magnetic mesoporous composites can endow the carrier with the specific functions of fluorescent/MR dual-modality imaging and chemotherapeutic performances [86]. Hyeon et al. fabricated small Fe_3O_4@$mSiO_2$ nanoparticles by phase-transferring process for in vivo T_2-weighted MR imaging of tumors [87]. They also coated ultrasmall Fe_3O_4 nanoparticles onto the surface of mesoporous silica nanoparticles for in vivo T_2-weighted MR imaging [71].

The elaborate creation of the large hollow interiors within the core/shell Fe_3O_4@$mSiO_2$ nanoparticles to produce Fe_3O_4@Void@$mSiO_2$ can significantly enhance their loading capacity for drug molecules. In this regard, Fe_3O_4@Void@$mSiO_2$ nanoparticles can function as the unique theranostic agent for concurrent cancer diagnostic imaging and chemotherapy. By the thermal treatment of Fe_2O_3@$mSiO_2$ at high temperature under reducing atmosphere, Shi's group created the hollow interior between the Fe_2O_3 core and mesoporous silica shell and transformation of Fe_2O_3 into Fe_3O_4 simultaneously [85]. Based on structural difference-based selective etch-

ing strategy, the middle solid silica part of $Fe_3O_4@SiO_2@mSiO_2$ nanoparticles could be easily removed for enhanced doxorubicin-loading capacity and chemotherapy efficiency [48]. The T_2-weighted MR imaging of tumor-bearing mice showed contrast-enhanced negative imaging performance. Further researches concerning clinical translation of $Fe_3O_4@Void@mSiO_2$ should be focused on the biosafety evaluations and targeting modifications to improve the MRI-T_2 performance of $Fe_3O_4@Void@mSiO_2$.

Other types of hollow mesoporous composite nanocapsules could be synthesized based on the mature nanosynthetic chemistry. For instance, Wu et al. recently developed an in situ decomposition/reduction approach to fabricate a unique hollow nanostructure with magnetic Fe_3O_4 and mesoporous silica double shells (Fig. 6.9a, designated as HMMNS) [88]. The initial β-FeOOH core could be transformed into hollow porous Fe_3O_4 upon thermal treatment. Further folic acid and fluorescent RBITC grafting could endow HMMNS with targeting and fluorescent property, respectively (designated as HMMNS-R/P). The high T_2-weighted MRI performance of HMMNS-R/P was demonstrated by the imaging of the liver and spleen of mice (Fig. 6.9b–d). After delivery of anticancer drug docetaxel and camptothecin into cancer cells, HMMNS-R/P showed enhanced anticancer effect due to the improved bioavailability of hydrophobic anticancer drugs.

6.4 HMSNs as the Contrast Agents (CAs) for Ultrasound Imaging

Ultrasound imaging is one of the most widely used imaging techniques in recent years owing to their advantages in low-cost, noninvasive, and portable real-time imaging. However, compared with other techniques, such as MRI, CT, and PET, the ultrasound imaging often suffers from low resolution. To solve this problem, the ultrasound contrast agents (UCAs) are widely used in medical diagnosis, which can increase the returning ultrasound signal and offer the enhanced borders or tissue resolution owing to the high echogenicity difference. Based on the material composition, the UCAs can be classified as two main types, containing organic- and inorganic-based materials. Currently, the most frequently used UCAs are the gas-filled microbubbles with their shells composed by albumin, galactose, lipid, or polymers [89]. The organic-based UCAs often possess much higher compressibility with about ten orders of magnitude more than any solid and liquid in tissues owing to their soft and elastic shells, thus making UCAs highly echogenic. However, the early clinically applied UCAs, such as the Echovist and Albunex microbubbles, are subjected to instability after intravenous injection with only a few seconds in in vivo blood half-life. To increase the imaging stability and in vivo circulation time, a series of perfluorochemical-based CAs were launched in recent years, several of which, such as SonoVue, Optison, and Imagent, have been FDA approved and applied for the clinical therapy. However, the structure stability and particle size of

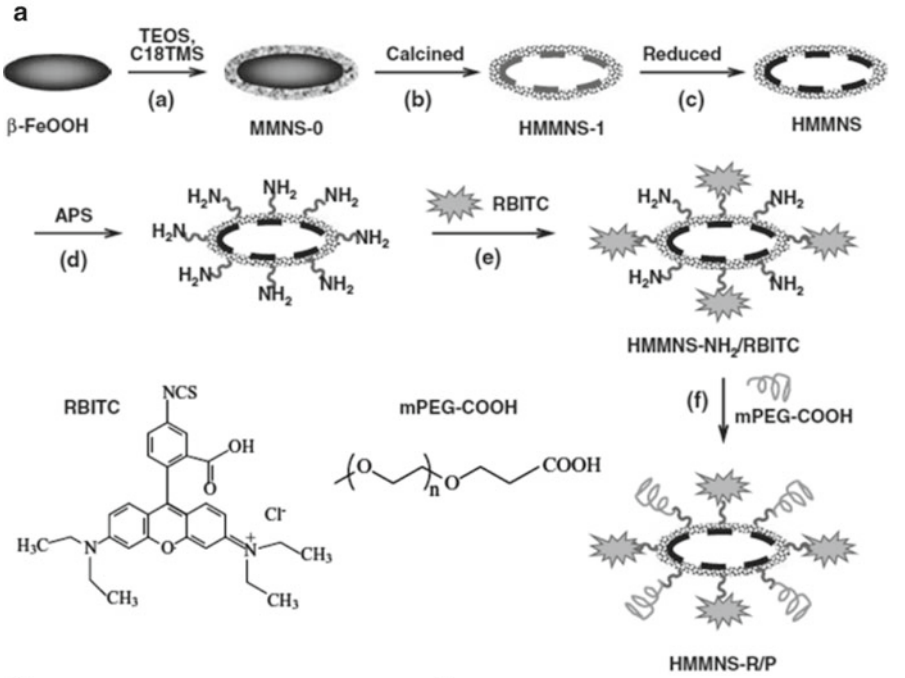
a
TEOS, C18TMS
(a)
β-FeOOH
MMNS-0
Calcined
(b)
HMMNS-1
Reduced
(c)
HMMNS
APS
(d)
RBITC
(e)
HMMNS-NH2/RBITC
RBITC
mPEG-COOH
(f)
mPEG-COOH
HMMNS-R/P

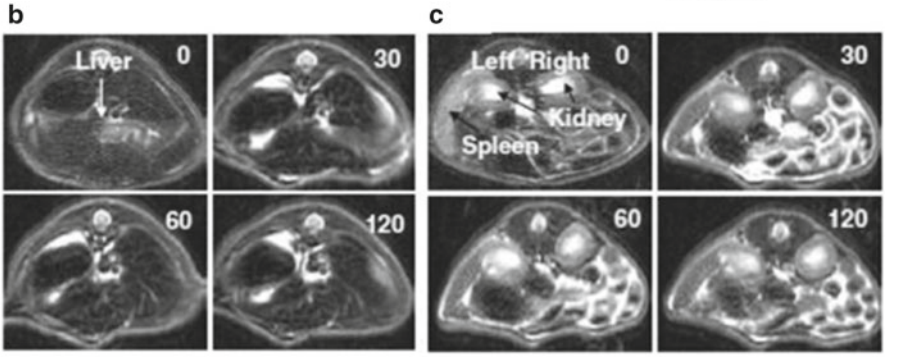
b
Liver
0
30
60
120
c
Left
Right
0
Kidney
Spleen
30
60
120

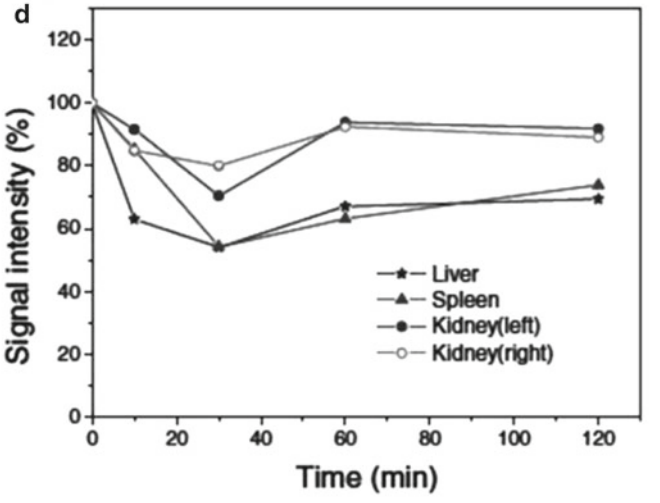
d
Signal intensity (%)
Time (min)
Liver
Spleen
Kidney(left)
Kidney(right)

organic-based UC agents still cannot satisfy the accurate imaging of the tumor region. Furthermore, they generally suffer from dramatic structure collapse in a short time after intravenous injection, along with uncontrolled leakage of perfluorochemical before reaching the targeting region. For example, the mean terminal half-life of SonoVue and Optison were measured to be only 12 and 1.3 min, respectively. To address above problems, a number of reports about inorganic silica-based UCAs have been presented for US imaging in recent decade [50]. The advantages of silica-based UCAs mainly consist of the following aspects: (1) excellent biocompatibility and biodegradability; (2) controllable nanoparticle size and homogeneous size distribution; (3) good stability and the rigid shell that could endure pressure and ultrasound radiation; and (4) easy for further functional modification. Herein, the recent progresses of the silica-based UCAs are summarized as follows.

6.4.1 Imaging Mechanism of HMSN-Based UCAs

The structural instability of organic-based UCAs generally fails to satisfy the requirements of clinical diagnosis application, including long-term storage in liquid state before administration and the continuous ultrasound imaging in biological body. Thus, great efforts have been paid to their stability improvement during past decades. Therein, the medium of the inner core has been progressively upgraded from free gas bubbles (e.g., O_2, N_2) to the liquid droplets (e.g., fluorocarbon liquid); meanwhile, the composition of the outer shell has been gradually developed from micelles to liposomes and proteins. Recently, silica-based hollow materials have been widely researched for the US contrast imaging, mainly based on their significantly enhanced stability compared to organic substances. Additionally, the positive experimental results of the biosafety and biocompatibility of silica nanoparticles further accelerate the development of silica-based hollow materials toward the clinical research.

It is considered that the effectiveness of UCAs is dependent on their dynamic response to the applied ultrasonic field. Unfortunately, the rigid silica shell undergoes the weak volumetric oscillation and thus exhibits much lower energy ultrasonic scattering than organic microbubbles. Therefore, for ultrasound imaging purpose, an optimal particle structure is needed to further increase the intensity of ultrasonic scattering signals. One strategy is to decrease the shell thickness of UCAs. In this strategy, the shell thickness must be accurately controlled as thin as possible, which is sufficient to maintain the particle stability and not to impede the

Fig. 6.9 (**a**) Schematic illustration of the synthetic process for HMMNS-R/P; (**b**) in vivo T_2-weighted MRI of the (**b**) liver and (**c**) kidney/spleen before and after intravenous injection of HMMNS-R/P (dose, 2.5 mg Fe/kg); (**d**) the changes of T_2-weighted MRI signal intensity corresponding to **b** and **c** (Reprinted with permission from Ref. [88]. Copyright 2011, John Wiley and Sons)

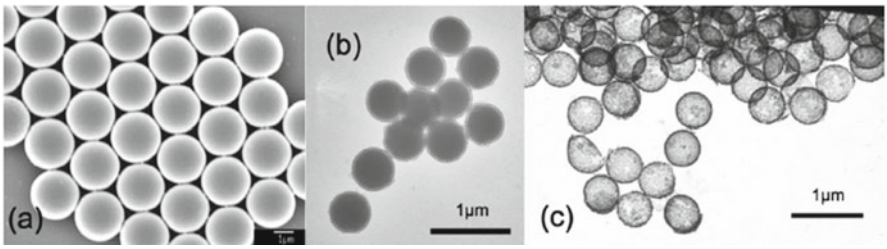

Fig. 6.10 (**a**) SEM images of polystyrene particles with a diameter of 2089 ± 150 nm; (**b**) TEM image shows polystyrene–silica core/shell particles revealing thin silica lamination (silica shell 50 nm, particle diameter 550 nm); (**c**) the etched hollow particles under TEM (Reprinted with permission from Ref. [51]. Copyright 2009, John Wiley and Sons)

volumetric oscillation. Hu et al. have proved that the hollow silica particle, with both micrometer particle size and thin particle wall, could exhibit the same ultrasound imaging efficiency as the commercial applied SonoVue CAs at the initial time [50]. Importantly, the imaging of hollow silica particles can last for more than 20 min, which was much longer than the commercial SonoVue (only for about 16 s). The results also demonstrated that the silica particle with the solid sphere structure exhibited no obvious imaging and was acoustically inactive, while the thin shell of hollow particles played important effect on the ultrasound imaging. Lin et al. fabricated the hollow silica capsules with thin shells (below 30 nm) through the Stöber reaction of tetraethyl orthosilicate (TEOS) and organosilanes on the hard template of polystyrene (PS) spheres, demonstrated as Fig. 6.10 [51]. The diameter of the capsules could be varied from 160 nm to 2520 nm based on the size of PS core. Meanwhile, they elaborately introduced several special organosilanes, such as octyltriethoxysilane (OTES) and bis[3-(trimethoxysilyl)-propyl]amine (TSPA), into the silica condensation to increase the elasticity of silica shell. The ultrasound images obtained using a Siemens Acuson Sequoia 512 scanner demonstrated that the hollow particles composed by TEOS, OTES, and TSPA requires a minimum imaging mechanic index (MI) around 0.5 for the sufficient acoustic-pressure amplitude. Meanwhile, the silica shell can tolerate up to the maximum MI of 1.5, above which the destruction will occur. Importantly, in comparison with the lipid-based system (the maximum MI is 1.0), the silica shell is more stable to be handled in a wide MI range. In current status, scientists mainly focused on the characterization of the sensitivity of silica capsules to ultrasound frequency, as well as optimizing the materials properties in terms of insonation and biocompatibility.

Another strategy is to create multilayers in single UCA. It was theoretically supposed that the multilayer structure possesses the larger ultrasound scattering than single-layer bubbles, owing to the virtue of multiple scattering/reflection interfaces. That is, the ultrasound waves can be scattered and reflected by every interface containing the outer surface and inside interface, resulting in an accumulative ultrasound signal. However, almost all of shell materials (such as phospholipid, PLGA, and protein) tend to form one-layer structure after the self-assembly process for the lowest interface energy. Thus, the fabrication of the multilayer microbubbles based

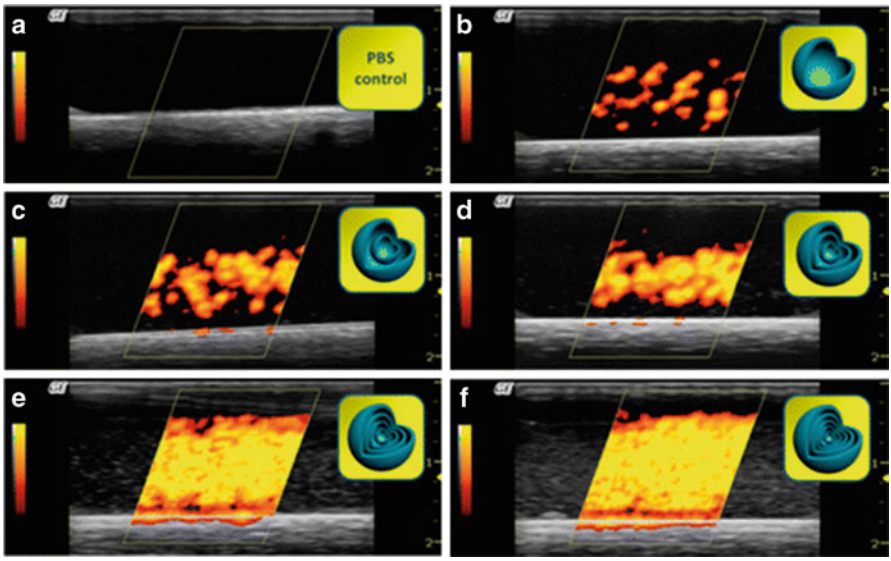

Fig. 6.11 In vitro ultrasound imaging enhanced by MLBs with varied layer numbers in power Doppler mode: (**a**) PBS as the control, (**b**) single layer, (**c**) double layers, (**d**) triple layers, (**e**) quadruple layers, and (**f**) quintuple layers (Reprinted with permission from Ref. [90]. Copyright 2014, American Chemical Society)

on organic substance remains a great challenge to date. In contrast, SiO_2 material exhibits rigid framework and can be structurally stable in various solvents. Two typical methods in silica chemistry, including hydrolytic condensation of silicon precursors and chemical etching of Si-O-Si bonds, could be alternatively and flexibly applied in the preparation of SiO_2-based US agents with different structures. To realize the enhanced US contrast imaging, Wang et al. developed a multilayer microbubbles (MLBs) with overall size below 1 um (Fig. 6.11) [90]. It is found that the contrast enhancement of MLBs is layer dependent and the backscatter signals linearly enhance with the layer numbers. The gray value of five-layer microbubbles exhibited obviously higher gray values (237 dB) in power Doppler mode compared to the one-layer samples (80 dB). Very recently, we systematically investigated the advantages of rattle-type silica particles (with two convex interfaces as shown in Fig. 6.12) on ultrasound imaging compared with the solid and hollow structure particles (with one convex interface) [91]. Especially, the effects of interface numbers on ultrasonic scattering and reflection were quantitatively measured by the simulation calculations. The results demonstrated that the reflection contribution percentage (IRC) of rattle-type silica particles showed about 39 % increase compared to that of both solid and hollow-shaped particles. Meanwhile, for linear scattering contribution (ISC), the value of rattle-type silica particle increased about 44 % and 47 % compared to that of solid and hollow particles, respectively. The further acoustic measurements of three types of silica particles are well consistent with the above theoretic results. Thus, we considered that the multilayer particles with ultrathin-

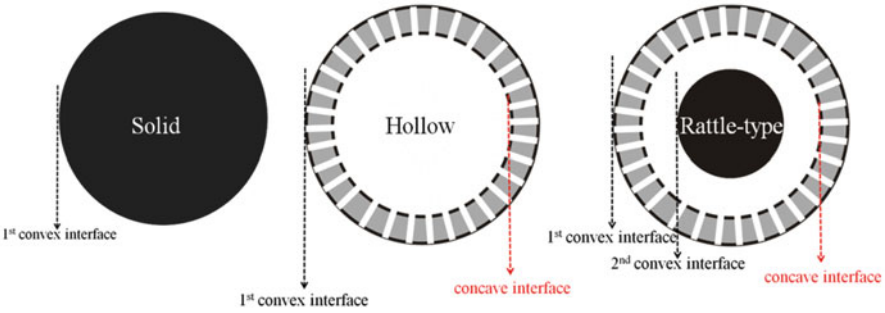

Fig. 6.12 Schematic illustration of the interface difference in solid, hollow, and rattle-type silica nanoparticles. Herein, the number of concave interfaces is mainly responsible for overall scattering/reflection for each particle (Reprinted with permission from Ref. [91]. Copyright 2015, Nature Publishing Group)

walled thickness are promising as the next generation of UCAs for their specific structural advantages toward excellent US imaging.

6.4.2 Phase-Change Material (PCM)-Encapsulated HMSN-Based UCAs

HIFU as a noninvasive and fast therapeutic technique could allow the deposition of ultrasound energy inside the human body. The energy level carried in HIFU radiation is several orders of magnitude greater than that of a general diagnostic ultrasound beam, which is enough to induce cell death through the coagulation necrosis route. Recent studies found that the temperature-sensitive fluorocarbon compounds, including perfluoropentane (PFP), perfluorohexane (PFH), perfluorooctyl bromide (PFOB), etc., could exhibit a "liquid to gas" biphase transition by HIFU irradiation, which can generate acoustic-imaging difference for the in situ detection of the HIFU therapy process. However, these fluorocarbon compounds are super-hydrophobic and poorly soluble in the physiological media, which is limited by the intravenous use. To improve the solubility of fluorocarbon, a series of temperature-sensitive fluorocarbon liquid-encapsulated HMSNs (FC-HMSNs) were designed by Shi's group to improve the solubility of fluorocarbon liquid, thus lowering the HIFU energy threshold and enlarging the lesion site [92, 93].

Considering about the rigid silica shell and nanometer-sized particle, the FC-HMSNs are not ideal in contrast imaging at physiological temperature under standard diagnosis US, which exhibits very limited contribution to the improvement of the contrast ultrasound imaging owing to substantial reduction of the nonlinear backscattering. In contrast, the tissue environment can exhibit significant heat generation under the HIFU irradiation, by which the "liquid to gas" biphase transformation of some fluorocarbon can be generated. Such vaporization process has been considered to enable the nanometer-sized FC-HMSNs to generate large amounts of

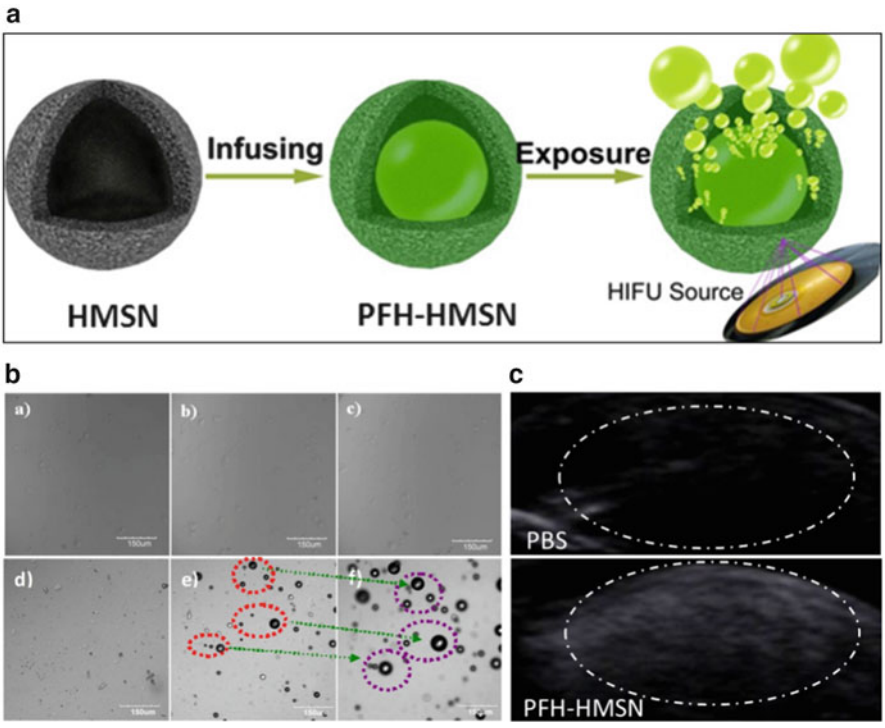

Fig. 6.13 (**a**) Schematic illustration of the fabrication process of PFH-HMSNs. (**b**) Confocal laser scanning microscopy (CLSM) images of empty HMSNs (*a–c*) and PFH-HMSNs (*d–f*) at room temperature (*a*, *d*), heated at 70 °C for 5 s (*b*, *e*) and at 70 °C for 10 s (*c*, *f*) (**c**) The ultrasound imagings of the PBS solution and PFH-HMSNs after heat treatment. (Reprinted with permission from Ref. [92]. Copyright 2012, John Wiley and Sons)

micrometer-sized bubbles by a fusion process of encapsulated fluorocarbon nanobubbles, which can be used for maximally scattering fundamental ultrasound signals thus substantially improving the capabilities of ultrasound imaging, as demonstrated in Fig. 6.13a [94]. The related fusion mechanism and imaging effect have been proved based on a facile heat treatment experiment tracked by microscopy. As demonstrated by Fig. 6.13b, a sequential swelling and merging process of fluorocarbon nanobubbles can be observed after heating perfluorohexane (PFH)-encapsulated HMSNs (PFH-HMSNs) up to a temperature higher than the boiling point of PFH, and comparatively, the blank control (HMSNs without PFH) can hardly generate any microbubbles. Furthermore, the stable imaging effect was found in the presence of PFH-HMSNs after heat treatment compared to that of PBS control (Fig. 6.13c). Thus, the PFH-HMSNs are expected to be efficiently uptaken by the tumor tissues while realizing the highly effective HIFU imaging by the bubble fusion process.

Besides the fluorocarbon liquid, a natural and high biocompatible "solid–liquid–gas" (SLG) triphase transition medium L-menthol (LM) was also introduced as inner core medium [95]. It is noted that LM is a high-volatile solid at room temperature, which can continuously generate the volatile gas in a relatively mild manner. Thus,

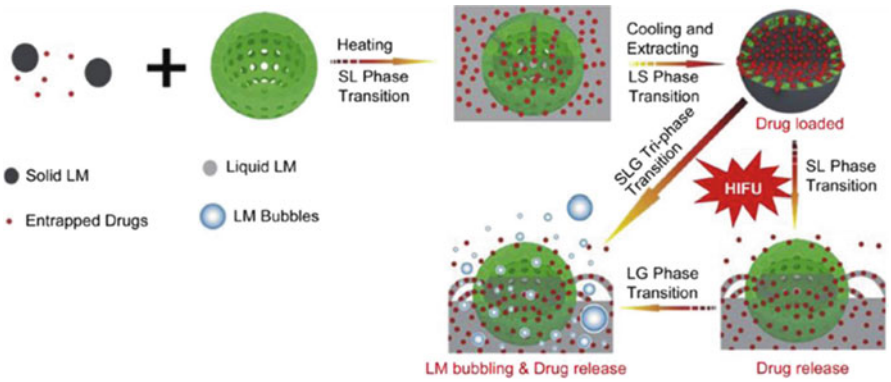

Fig. 6.14 Schematic illustration of the synthesis route of HMSN-LM and the bubble generation process under HIFU irradiation (Reprinted with permission from Ref. [95]. Copyright 2014, Elsevier)

compared to the FC-HMSNs with abrupt and violent biphase transition, this LM-HMSN exhibits the controllable, mild, and continuous phase transition process under HIFU irradiation, as indicated in Fig. 6.14. Such a variance in transition process could generate obvious difference in the US imaging when increasing the environment temperature of US imaging contrast. For FC-HMSNs, both the contrast and average gray values under B fundamental modality and CPSI modality exhibited an abrupt process, with rapid increase in the first 30 s and drop drastically after 30 s. On the contrary, for LM-HMSNs, they could reach maxima in 2 min and maintain at this value for more than 30 min. Meanwhile, a comparative experiment of US imaging at 50 °C environment confirmed the LM-HMSNs could generate the highest imaging quality compared to PBS control and empty HMSNs, especially under tissue harmonic and contrast pulse sequence modalities. This bubbling-generated US imaging enhancement by LM-HMSNs under HIFU irradiation was further confirmed in the in vivo investigation using VX-2 rabbit model [95]. The mechanism of US imaging enhancement of LM-HMSNs is attributed to the emergence of high echogenic bubble due to the evaporation of liquid LM, which is similar as in FC-HMSNs. More importantly, compared to FC-HMSNs, LM-HMSNs exhibit more continuous enhancement of real-time US imaging under HIFU irradiation originating from relatively slow "solid–liquid–gas" (SLG) triphase transition process, which could significantly decrease the synergistic agent dose and enhance the therapeutic duration time.

6.4.3 Intelligent Design of HMSN-Based UCAs

The intelligent biomedical nanosystems have been widely studied in recent years mainly based on the virtues of tumor microenvironment in pH value, reducing condition and enzyme activity. Generally, the organic- or inorganic-based intelligent drug delivery systems often require a polymer coating, nano-cap or nano-valve switches, on the surface to realize the rapid drug release when reaching the tumor

region. Comparatively, the study on the intelligent UCA is still in infancy mainly owing to the fatigue of efficient structure design that could realize the clear echogenic change under different microenvironments. Especially, the traditional microbubbles will suffer from the structure collapse under the specific microenvironment in the tumor region, which cannot offer the efficient tumor imaging with environmental responsiveness. Very recently, a novel kind of intelligent UCAs based on HMSN polymer nanocomposite with both good structure stability and sensitivity to microenvironment change has been proposed, since such nanocomposite could dramatically increase their particles size once the redox stimulus in the tumor region is received [96]. The copolymer of polyethylene glycol-disulfide (S-S)-hyaluronic acid (PEGHA-SS) coated onto the outer surface of nanoparticles can generate the dramatic structure transition from the cross-linking to retrocross-linking state by the redox stimulus in tumor, accompanied by a significantly increased diameter from about 300 nm to 850 nm. This diameter increase could lead to remarkable enhancement in mean gray scales for the retrocross-linking state (with the values of 62, 72, 102) compared to the cross-linking state (with the values of 80, 88, 135) under B-mode, contrast mode, and harmonic mode, respectively.

As we know, hydrogen peroxide (H_2O_2), as the typical component of reactive oxygen species (ROS), was often involved in numerous ailments, such as cancer, inflammatory diseases, and diabetes mellitus. Recently, Gu et al. applied the PBNPs to react with H_2O_2 to produce oxygen bubbles with the sizes from 5 μm to 30 μm in the inflammatory regions, as demonstrated in Fig. 6.15 [97], where the acoustic

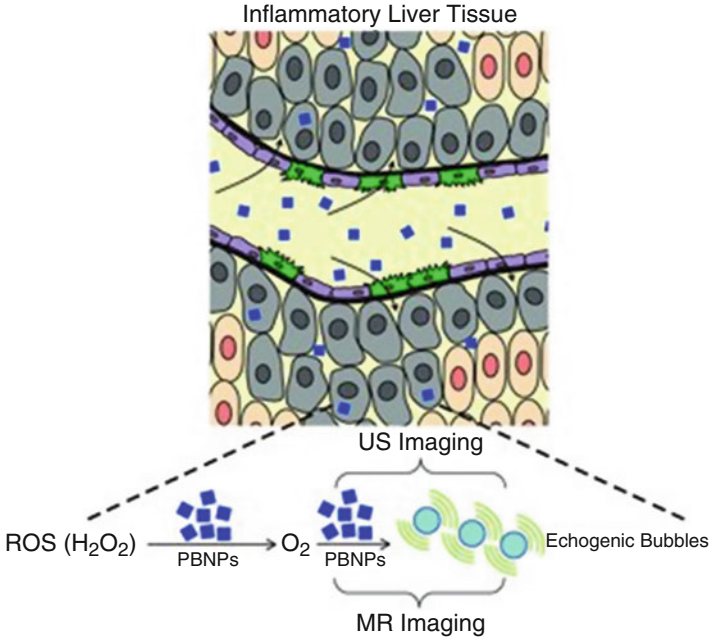

Fig. 6.15 The schematic illustration of the O_2 bubble generation process by PBNPs [97] (Reprinted with permission from Ref. [97]. Copyright 2012, John Wiley and Sons)

change of tissue experiencing oxidative stress could make the tissues detectable by US imaging. The in vivo study results demonstrated that the mean gray scale of the US images remains at baseline intensity levels in the liver of mice without inflammatory disease. In contrast, the mean gray scale of US images in the liver with inflammatory treatment was increased by about 80 % after 15 min of PBNPs injections, which could be utilized as the easy approach for the H_2O_2 quantification. Such PBNPs nanosystem exhibits significantly high imaging capability as proved by the in vitro imaging results, demonstrating that the exploration of new biocompatible compounds with both the nanometer particle size and the stimuli-responsive bubble generation function is a promising strategy for the future intelligent US imaging.

Silica nanoparticles exhibit a wide range of potential in the US contrast imaging application. They have become one of the most rapidly developing subjects in the field of biomedical imaging. As illustrated above, the silica nanoparticles with different shell structures (thin-walled, multiple-walled, and environment-responsive polymer) and interior substances (fluorocarbon and L-menthol) have been successfully designed for the US imaging. Although more and more researches are launched in recent years, it must be clearly recognized that the development of silica-based UCA is just at its starting stage. There are still abundant unknown problems deeded for more deep investigations.

Considering the approval in clinical applications, the application of silica-based UCAs needs the successful control of several factors in fabrication process, including the particle shape, size, dispersal, surface coating, and interior substance. Moreover, though no systematic researches on the harmful effects of hollow silica-based nanoparticles have been obtained, their biodegradability, biocompatibility, and short-and long-term effects in the body will have to be investigated in preclinical research.

From the perspective of clinical application, it was considered that the introduction of a small amount of silica components into the FDA-approved delivery systems, e.g., PLGA, lipid- and protein-based materials, may become the important trend toward highly efficient UCAs. It is anticipated that diversity of silica precursors, such as polysiloxane, silane coupling agents, or silica nanodots, can be efficiently combined with traditional polymeric nanosystems by the chemical or electrostatic interaction, to highly improve the structure stability and in vivo lifetime without losing their imaging efficiency. More importantly, such a strategy of material design based on FDA-approved delivery system could maximally lower the hurdles of clinical application.

6.5 HMSNs for HIFU Tumor Therapy

High-intensity focused ultrasound (HIFU) has been regarded as the most representative noninvasive therapeutic modality for the treatment of diseases [98, 99]. In principle, the ultrasound generated by the transducer outside the body can be

focused onto the lesion part within the body. The high-energy deposition of an ultrasound can generate the transient high temperature to ablate the tumor tissue [100, 101]. In this regard, the lesion tissue can be removed without the need of traditional bleeding surgical process. The high performance and significantly mitigated side effects of HIFU show the great potentials for the therapy of cancer. However, the HIFU-based therapeutic efficiency for the tumor tissue in deep organs is less effective because of the low-energy deposition within tumor tissue caused by the energy loss during long-range transportation. The sole increase of the ultrasound power outside the body may cause the damage of the skin and tissue in the ultrasound-propagation path. Therefore, it is highly desirable to develop new technologies to solve this critical efficiency and safety issues for HIFU-based cancer therapy.

6.5.1 HMSN-Based Composite Nanocapsules for Imaging-Guided HIFU Cancer Surgery

Nano-biotechnology provides an alternative but highly efficient strategy to synergistically improve the HIFU-based therapeutic efficiency against cancer [102]. Especially, the introduction of nanomaterials into tumor can significantly change the acoustic microenvironment of tumor tissues to improve the energy deposition of the ultrasound. Although traditional microbubbles showed the synergistic effect for enhancing the HIFU efficiency [93, 94, 103], the large particle size and low stability severely restrict their further clinical translations.

Recently, Wang et al. encapsulated perfluorohexane (PFH) with low boiling point (~65 °C) into HMSNs (mesoporous silica nanocapsules, also designated as MSNCs) for substantially enhanced HIFU cancer surgery [92]. As the first paradigm, the unique nanostructures of MSNCs could play three roles. Firstly, the SiO_2 shell with well-defined mesopores provides the diffusion path for PFH to access the hollow interiors. Secondly, the hollow interior of MSNCs could store large amounts of PFH to improve the bioavailability of hydrophobic PFH. Thirdly, the well-defined morphology and nanoparticulate sizes guarantee the efficient in vivo transportation to accumulate into tumor tissue. The hydrophobic PFH within the hollow interior of MSNCs exhibited unique temperature-responsive phase-transformation behavior. Upon HIFU irradiation, PFH could diffuse through the mesopores to form the microbubbles as demonstrated both in vitro and in vivo. The high in vivo synergistic effect against liver tumor of rabbits by HIFU irradiation was observed by in situ B-mode ultrasound imaging. Pathological examinations (hematoxylin and eosin, H&E) revealed that highly compact and denatured cancer cells remained at the HIFU power of 400 W for 2 s without the assistance of MSNC-PFH. Comparatively, the introduction of MSNC-PFH could cause the significant cell apoptosis/necrosis, demonstrating the high synergistic effect of MSNC-PFH composite.

For HIFU-based cancer surgery, the accurate predetermination of tumor position is of great significance for efficient and safe ablation of tumor tissues [104]. Ultrasound imaging and MR imaging are the two clinically used imaging modalities

for HIFU guidance [99]. To further improve the imaging performance of MRI, the MnO_x nanoparticles were homogeneously dispersed into the mesopores of HMSNs to fabricate unique mesoporous composite nanocapsules (MCNCs) [105]. The MnO_x nanoparticles within the mesopores can act as the CAs for T_1-weighted MR imaging. In addition, the large hollow interiors and well-defined mesopores could realize the loading and delivery of PFH for HIFU-based synergistic therapy. In this regard, the designed MCNCs could be used for T_1-weighted MRI-guided HIFU cancer surgery. Ex vivo evaluation against degassed bovine liver (Fig. 6.16a) showed that the coagulated liver tissue treated by PFH-MCNCs/PBS (150 W/cm^2, 5 s 86.5 mm^3; 250 W/cm^2, 5 s 153.1 mm^3) was considerably larger than the groups receiving PBS (150 W/cm^2, 5 s 31.7 mm^3; 250 W/cm^2, 5 s 66.6 mm^3) and MCNCs/PBS (150 W/cm^2, 5 s 43.7 mm^3; 250 W, 5 s 109.3 mm^3), demonstrating the high

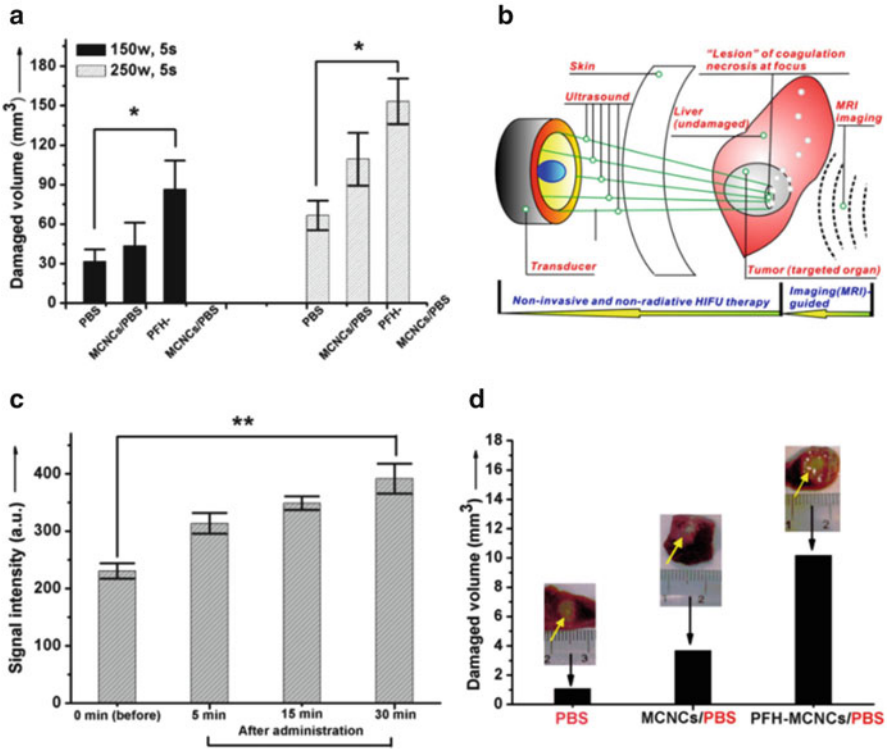

Fig. 6.16 (**a**) Ex vivo evaluation of synergistic antitumor effect of PFH-MCNCs/PBS by calculating the coagulated-tissue volumes of a degassed bovine liver under the HIFU irradiation condition of 150 W/cm^2, 5 s, and 250 W/cm^2, 5 s; (**b**) schematic illustration of MRI-guided HIFU cancer surgery of hepatic neoplasm in rabbits; (**c**) the intensities of T_1-weighted MR imaging of liver tumor before and after intravenous administrations of PFH-HMCNs/PBS; (**d**) in vivo coagulated necrotic-tumor volumes after the HIFU irradiation (150 W/cm^2, 5 s; inset, digital photo of tumor tissues after HIFU irradiation) [105] (Reprinted with permission from Ref. [105]. Copyright 2011, John Wiley and Sons)

synergistic effect caused by PFH-MCNCs. After intravenously administration of PFH-MCNCs into rabbit, they could accumulate into tumor tissue to guide the HIFU irradiation by MRI (Fig. 6.16b). In vivo T_1-weighted MR imaging showed that the boundaries between tumor and normal tissues became clearer by the contrast-enhanced MRI effect of CAs. The T_1-weighted MRI signal of tumor also gave the significant increase (Fig. 6.16c), verifying that PFH-MCNCs entered the tumor tissue. The in vivo synergistic effect of PFH-HMCNs for tumor ablation was further demonstrated by nearly 8.8 and 1.8 times increases in coagulated tumor volume compared to PBS and MCNCs/PBS (Fig. 6.16d).

Ultrasound-guided HIFU cancer surgery has been extensively used in clinic since both the imaging and therapy are based on ultrasound, which means that the imaging and therapeutic apparatus can be easily integrated with each other. Because of the excellent contrast-enhanced ultrasound imaging performance, HMSNs could be potentially used for ultrasound-guided HIFU cancer surgery (Fig. 6.17a). Wang et al. developed a unique organic–inorganic hybrid HMSN-based composite nanocapsules for targeting, redox-responsive ultrasound imaging, and ultrasound imaging-guided HIFU therapy [96]. The surface of HMSNs was grafted with a redox-responsive copolymer of polyethylene glycol-disulfide (S-S) hyaluronic acid (designated as MCNC-PEG-HA_{SS}, abbr. as MPH_{SS}) for targeting (HA) and redox responsiveness (disulfide bond). The introduction of MPHSS-PFH could substantially enhance the ultrasound imaging (Fig. 6.17b) and HIFU ablation efficiency, as demonstrated by the gray changes in the ultrasound imaging (Fig. 6.17c, d). This intelligent HMSN-based hybrid nanocapsule shows the great potential for ultrasound-guided HIFU ablation of tumor because of their high imaging performance of ultrasonography and synergistic effect for HIFU ablation.

6.5.2 HMSN-Based Composite Nanocapsules for Combining Drug Delivery and HIFU Cancer Surgery

Traditional fluorocarbon PFH shows the fast and explosive vaporization behavior upon HIFU irradiation, which cannot exert the role of sustained HIFU-based synergistic therapy. To overcome this drawback, Zhang et al. recently substituted PFH with the biocompatible L-menthol (LM) to be encapsulated into HMSNs [95]. The loaded LM could enhance the HIFU therapeutic efficiency continuously. In addition, the loading of liquid LM into HMSNs could realize the concurrent loading of hydrophilic and/or hydrophobic anticancer drugs. After the phase change into solid state, the drug molecules could be stably encapsulated into the hollow interior. Upon external HIFU irradiation, the SLG triphase change could also trigger the release of drugs. Thus, this intelligent HMSN-based nanosystem could concurrently act as the excellent HIFU-responsive drug-releasing carrier and satisfactory HIFU-based synergistic agent.

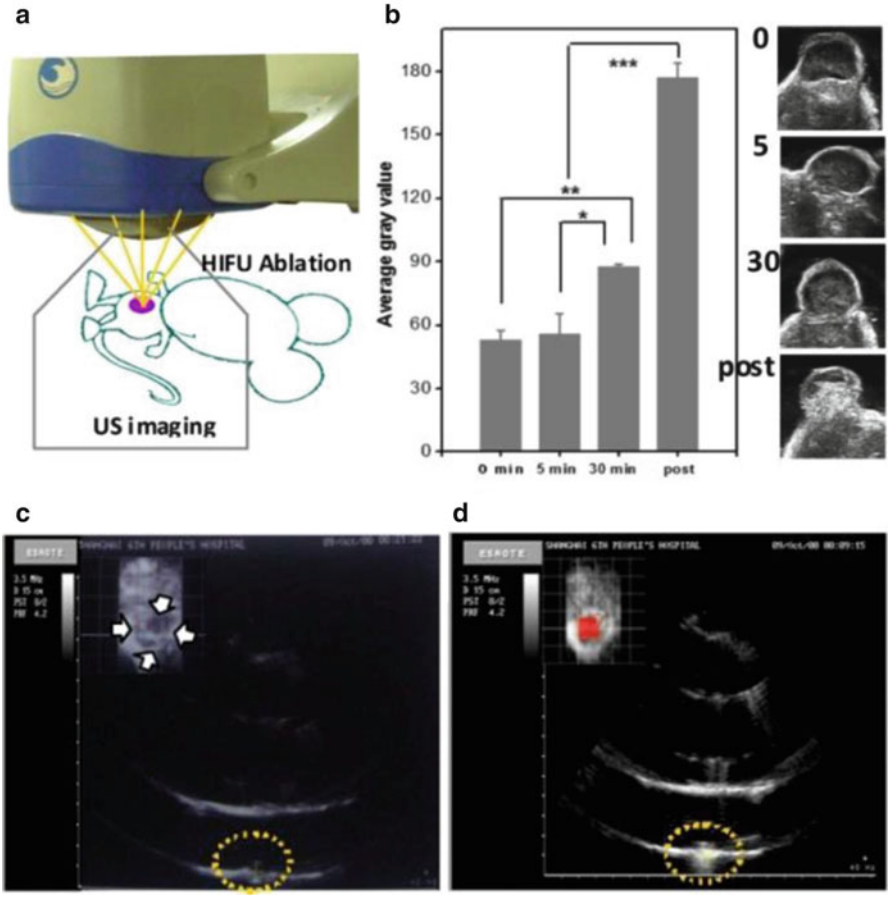

Fig. 6.17 (**a**) Schematic illustration of ultrasound-guided HIFU cancer surgery; (**b**) in vivo ultrasound images of tumor before and after the administration of MPH_{SS}-PFH and then post-HIFU irradiation; ultrasound images of (**c**) pre- and (**d**) post-HIFU treatment of tumors after the injection of MPH_{SS}-PFH for 30 min [96] (Reprinted with permission from Ref. [96]. Copyright 2013, John Wiley and Sons)

To further improve the HIFU-based therapeutic outcome, Ma et al. recently designed a new type of composite nanocapsules, i.e., camptothecin (CPT)/perfluorooctyl bromide (PFOB) as the core and poly(lactic-co-glycolic acid) (PLGA)/thin silica as the shell (Fig. 6.18) [106]. The composite nanocapsules showed high drug-loading capacity for CPT (up to 19 %) and the PLGA/thin silica shell was very sensitive for focused ultrasound. Importantly, the PFOB inner core was very ultrasound sensitive to synergistically improve the HIFU-ablation efficiency. Meanwhile, it was found that this nanocapsule displays a very slow release of CPT drug in the

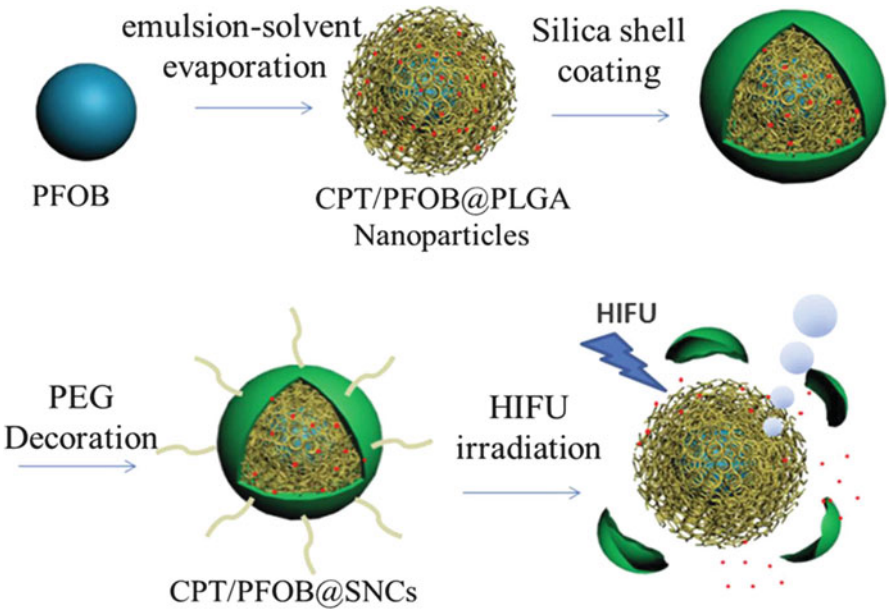

Fig. 6.18 Schematic illustration of the synthetic procedure for CPT/PFOB@SNCs [106] (Reprinted with permission from Ref. [106]. Copyright 2014, John Wiley and Sons)

blood stream but a nearly complete release after exposure to 140 W of HIFU for 5 min. More importantly, the in vivo therapeutic experiment results demonstrated that controlled release of CPT/PFOB@SNCs could efficiently kill the remaining cancer cells after HIFU therapy and thus effectively inhibited tumor recurrence. Thus, it was considered that the designed composite nanocapsules could be simultaneously used as the synergistic agent for HIFU surgery and the controlled drug delivery for chemotherapy, which exhibits significant potential for the clinical application in noninvasive therapy.

The introduction of nanoparticles as the synergistic agents to enhance the HIFU-ablation efficiency occurred very recently. Thus, the actually clinical safety and efficiency of nanoparticle-based synergistic agents should be further clarified in detail based on more research data to support it. The synergistic mechanism also requires further evaluations, testing, and modeling. HMSN-based drug delivery has been almost fully demonstrated; thus, their chemotherapeutic performance to assist HIFU cancer surgery is very promising. However, the accurate synergistic effect of HMSN-based chemotherapy and HIFU ablation is still unclear, which needs further determinations. In addition, other suitable phase-changing materials, besides PFH, PFOB, and LM, with desirable boiling points, should be further developed to perfect the HMSN-based nanosystems for HIFU-based cancer therapy.

6.6 Conclusions and Outlook

In summary, this chapter presents and discusses the specific topic on the US/MRI-guided tumor treatments based on elaborately designed and synthesized HMSNs. The current development of the soft-/hard-templating strategies for HMSNs is firstly discussed in detail. The control of the crucial structural/compositional parameters and multifunctionalization of HMSNs are then also discussed. The approaches of functionalizing HMSNs for ultrasonography and MR imaging are afterward revealed to introduce HMSN-based composite nanocapsules for diagnostic imaging. Finally, the very recent developments of HMSN-based composite nanosystems for HIFU-based cancer surgery are introduced, including HMSNs as the synergistic agent for enhancing the HIFU-ablation efficiency, functionalized HMSNs as the MRI and ultrasonography CAs for diagnostic imaging-guided HIFU therapy, and HMSN-based nanosystems for concurrent HIFU-triggered chemotherapy and HIFU ablation of tumor.

The systematic research work has demonstrated the high performance of HMSNs in diagnostic imaging (ultrasonography and MRI) and HIFU-based cancer synergistic therapy. However, the further clinical translations of these HMSN-based composites still encounter several critical issues to be solved, listed as follows:

(i) The biological effects and biosafety of HMSNs have not been fully revealed and determined, which will substantially hinder their further clinical translations. The inert Si-O-Si framework of HMSNs, though not highly complete structurally, leads to low biodegradable rate, which should be substantially improved by developing several strategies, such as ion doping or organic–inorganic hybridization. The multifunctionalization of HMSNs would cause the complexity of the nanosystems, making the biological evaluations more complicated and difficult. Thus, more in vivo animal experiments should be conducted for biosafety evaluations until all the biosafety issues are fully addressed.

(ii) The performances of HMSNs for diagnostic imaging and therapeutic application should be further improved for cancer treatments. The active targeting of HMSNs should be further constructed to guarantee the efficient accumulation of HMSNs within tumor tissue. In addition, the particle size, pore size, morphology, and dispersity should also be further optimized to satisfy the requirements of different biomedical applications. Especially, the shell elasticity and thickness of HMSNs should be controlled to improve their ultrasonography performances.

(iii) The current researches of HMSN-based nanosystems have mainly concentrated on some fundamental and scientific aspects. To realize the clinical translation, the collaborations among fundamental researches and R&D departments of companies/industries are of great importance to fast promote the practical applications. Much more efforts should be devoted to these collaborations, in order to exhibit a clear and standard route for the commercialization of these promising nanosystems.

Although there are still some unsolved issues to be addressed, the high performance and fast development of HMSNs in biomedicine show great prospect for imaging-guided cancer treatment, especially in ultrasound-based cancer imaging and therapy. Based on the advances of nanosynthetic chemistry, abundant new HMSN-based nanosystems are promising to meet the strict requirements of biomedicine. On this ground, HMSNs will find the practical applications to benefit the human health in personalized cancer treatment in near future.

References

1. LaVan DA, McGuire T, Langer R (2003) Small-scale systems for in vivo drug delivery. Nat Biotechnol 21:1184–1191
2. Wagner V, Dullaart A, Bock AK, Zweck A (2006) The emerging nanomedicine landscape. Nat Biotechnol 24:1211–1217
3. Medarova Z, Pham W, Farrar C, Petkova V, Moore A (2007) In vivo imaging of siRNA delivery and silencing in tumors. Nat Med 13:372–377
4. Ashley CE, Carnes EC, Phillips GK, Padilla D, Durfee PN, Brown PA et al (2011) The targeted delivery of multicomponent cargos to cancer cells by nanoporous particle-supported lipid bilayers. Nat Mater 10:389–397
5. Chen Y, Chen H, Shi J (2013) In vivo bio-safety evaluations and diagnostic/therapeutic applications of chemically designed mesoporous silica nanoparticles. Adv Mater 25:3144–3176
6. Chen Y, Chen H, Shi J (2014) Inorganic nanoparticle-based drug codelivery nanosystems to overcome the multidrug resistance of cancer cells. Mol Pharm 11:2495–2510
7. Rabin O, Perez JM, Grimm J, Wojtkiewicz G, Weissleder R (2006) An X-ray computed tomography imaging agent based on long-circulating bismuth sulphide nanoparticles. Nat Mater 5:118–122
8. Ananta JS, Godin B, Sethi R, Moriggi L, Liu XW, Serda RE et al (2010) Geometrical confinement of gadolinium-based contrast agents in nanoporous particles enhances T-1 contrast. Nat Nanotechnol 5:815–821
9. Chen Y, Chen H, Shi J (2014) Drug delivery/imaging multifunctionality of mesoporous silica-based composite nanostructures. Expert Opin Drug Deliv 11:917–930
10. Constantinides PP, Lambert KJ, Tustian AK, Schneider B, Lalji S, Ma WW et al (2000) Formulation development and antitumor activity of a filter-sterilizable emulsion of paclitaxel. Pharm Res 17:175–182
11. Ganta S, Amiji M (2009) Coadministration of paclitaxel and curcumin in nanoemulsion formulations to overcome multidrug resistance in tumor cells. Mol Pharm 6:928–939
12. Nakano M (2000) Places of emulsions in drug delivery. Adv Drug Deliv Rev 45:1–4
13. Allen TM, Cullis PR (2004) Drug delivery systems: entering the mainstream. Science 303:1818–1822
14. Ambrogio MW, Thomas CR, Zhao YL, Zink JI, Stoddartt JF (2011) Mechanized silica nanoparticles: a new frontier in theranostic nanomedicine. Acc Chem Res 44:903–913
15. Li ZX, Barnes JC, Bosoy A, Stoddart JF, Zink JI (2012) Mesoporous silica nanoparticles in biomedical applications. Chem Soc Rev 41:2590–2605
16. Chen Y, Ye D, Wu M, Chen H, Zhang L, Shi J, Wang L (2014) Breaking up of two-dimensional MnO2 nanosheets promotes ultrasensitive PH-triggered theranostics of cancer. Adv Mater 26(41):7019–7026
17. Chen Y, Xu P, Shu Z, Wu M, Wang L, Zhang S et al (2014) Multifunctional graphene oxide-based triple stimuli-responsive nanotheranostics. Adv Funct Mater 24:4386–4396

18. Feng LY, Wu L, Qu XG (2013) New horizons for diagnostics and therapeutic applications of graphene and graphene oxide. Adv Mater 25:168–186
19. Mao HY, Laurent S, Chen W, Akhavan O, Imani M, Ashkarran AA et al (2013) Graphene: promises, facts, opportunities, and challenges in nanomedicine. Chem Rev 113:3407–3424
20. Yang K, Feng LZ, Shi XZ, Liu Z (2013) Nano-graphene in biomedicine: theranostic applications. Chem Soc Rev 42:530–547
21. Chou SS, Kaehr B, Kim J, Foley BM, De M, Hopkins PE et al (2013) Chemically exfoliated MoS_2 as near-infrared photothermal agents. Angew Chem Int Ed 52:4160–4164
22. Liu T, Wang C, Gu X, Gong H, Cheng L, Shi X et al (2014) Drug delivery with PEGylated MoS_2 nano-sheets for combined photothermal and chemotherapy of cancer. Adv Mater 26:3433–3440
23. Chen Y, Xu P, Wu M, Meng Q, Chen H, Shu Z et al (2014) Colloidal RBC-shaped, hydrophilic, and hollow mesoporous carbon nanocapsules for highly efficient biomedical engineering. Adv Mater 26:4294–4301
24. Wu SH, Hung Y, Mou CY (2011) Mesoporous silica nanoparticles as nanocarriers. Chem Commun 47:9972–9985
25. Rosenholm JM, Mamaeva V, Sahlgren C, Linden M (2012) Nanoparticles in targeted cancer therapy: mesoporous silica nanoparticles entering preclinical development stage. Nanomedicine 7:111–120
26. Vallet-Regi M (2006) Ordered mesoporous materials in the context of drug delivery systems and bone tissue engineering. Chem Eur J 12:5934–5943
27. Lin YS, Hurley KR, Haynes CL (2012) Critical considerations in the biomedical use of mesoporous silica nanoparticles. J Phys Chem Lett 3:364–374
28. Lee JE, Lee N, Kim T, Kim J, Hyeon T (2011) Multifunctional mesoporous silica nanocomposite nanoparticles for theranostic applications. Acc Chem Res 44:893–902
29. Asefa T, Tao Z (2012) Biocompatibility of mesoporous silica nanoparticles. Chem Res Toxicol
30. Chen Y, Chen HR, Guo LM, He QJ, Chen F, Zhou J et al (2010) Hollow/rattle-type mesoporous nanostructures by a structural difference-based selective etching strategy. ACS Nano 4:529–539
31. Fang WJ, Tang SH, Liu PX, Fang XL, Gong JW, Zheng NF (2012) Pd nanosheet-covered hollow mesoporous silica nanoparticles as a platform for the chemo-photothermal treatment of cancer cells. Small 8:3816–3822
32. Gao Y, Chen Y, Ji XF, He XY, Yin Q, Zhang ZW et al (2011) Controlled intracellular release of doxorubicin in multidrug-resistant cancer cells by tuning the shell-pore sizes of mesoporous silica nanoparticles. ACS Nano 5:9788–9798
33. Liu YY, Miyoshi H, Nakamura M (2007) Novel drug delivery system of hollow mesoporous silica nanocapsules with thin shells: preparation and fluorescein isothiocyanate (FITC) release kinetics. Colloids Surf B Biointerfaces 58:180–187
34. Zhang K, Chen HR, Zheng YY, Chen Y, Ma M, Wang X et al (2012) A facile in situ hydrophobic layer protected selective etching strategy for the synchronous synthesis/modification of hollow or rattle-type silica nanoconstructs. J Mater Chem 22:12553–12561
35. Zhu YF, Shi JL, Shen WH, Chen HR, Dong XP, Ruan ML (2005) Preparation of novel hollow mesoporous silica spheres and their sustained-release property. Nanotechnology 16:2633–2638
36. Zhu YF, Shi JL, Shen WH, Dong XP, Feng JW, Ruan ML et al (2005) Stimuli-responsive controlled drug release from a hollow mesoporous silica sphere/polyelectrolyte multilayer core-shell structure. Angew Chem Int Ed 44:5083–5087
37. Zhu YF, Kockrick E, Ikoma T, Hanagata N, Kaskel S (2009) An efficient route to rattle-type Fe_3O_4@SiO_2 hollow mesoporous spheres using colloidal carbon spheres templates. Chem Mater 21:2547–2553
38. Zhu YF, Shi JL, Chen HR, Shen WH, Dong XP (2005) A facile method to synthesize novel hollow mesoporous silica spheres and advanced storage property. Microporous Mesoporous Mater 84:218–222

39. Zhu YF, Shi JL, Li YS, Chen HR, Shen WH, Dong XP (2005) Storage and release of ibuprofen drug molecules in hollow mesoporous silica spheres with modified pore surface. Microporous Mesoporous Mater 85:75–81
40. Chen Y, Chen H-R, Shi J-L (2013) Construction of homogenous/heterogeneous hollow mesoporous silica nanostructures by silica-etching chemistry: principles, synthesis, and applications. Acc Chem Res 47:125–137
41. Chen Y, Chen HR, Guo LM, Shi JL (2011) Magnetic hollow mesoporous silica nanospheres: facile fabrication and ultrafast immobilization of enzymes. J Nanosci Nanotechnol 11:10844–10848
42. Chen Y, Chen HR, Ma M, Chen F, Guo LM, Zhang LX et al (2011) Double mesoporous silica shelled spherical/ellipsoidal nanostructures: synthesis and hydrophilic/hydrophobic anticancer drug delivery. J Mater Chem 21:5290–5298
43. Cheng K, Sun S (2010) Recent advances in syntheses and therapeutic applications of multifunctional porous hollow nanoparticles. Nano Today 5:183–196
44. Liu TL, Li LL, Fu CH, Liu HY, Chen D, Tang FQ (2012) Pathological mechanisms of liver injury caused by continuous intraperitoneal injection of silica nanoparticles. Biomaterials 33:2399–2407
45. Liu HY, Liu TL, Wu XL, Li LL, Tan LF, Chen D et al (2012) Targeting gold nanoshells on silica nanorattles: a drug cocktail to fight breast tumors via a single irradiation with near-infrared laser light. Adv Mater 24:755–761
46. Li LL, Tang FQ, Liu HY, Liu TL, Hao NJ, Chen D et al (2010) In vivo delivery of silica nanorattle encapsulated docetaxel for liver cancer therapy with low toxicity and high efficacy. ACS Nano 4:6874–6882
47. Li LL, Guan YQ, Liu HY, Hao NJ, Liu TL, Meng XW et al (2011) Silica nanorattle-doxorubicin-anchored mesenchymal stem cells for tumor-tropic therapy. ACS Nano 5:7462–7470
48. Chen Y, Chen HR, Zeng DP, Tian YB, Chen F, Feng JW et al (2010) Core/shell structured hollow mesoporous nanocapsules: a potential platform for simultaneous cell imaging and anticancer drug delivery. ACS Nano 4:6001–6013
49. An L, Hu H, Du J, Wei J, Wang L, Yang H et al (2014) Paramagnetic hollow silica nanospheres for in vivo targeted ultrasound and magnetic resonance imaging. Biomaterials 35:5381–5392
50. Hu H, Zhou H, Du J, Wang ZQ, An L, Yang H et al (2011) Biocompatiable hollow silica microspheres as novel ultrasound contrast agents for in vivo imaging. J Mater Chem 21:6576–6583
51. Lin PL, Eckersley RJ, Hall EAH (2009) Ultrabubble: a laminated ultrasound contrast agent with narrow size range. Adv Mater 21:3949–3952
52. Martinez HP, Kono Y, Blair SL, Sandoval S, Wang-Rodriguez J, Mattrey RF et al (2010) Hard shell gas-filled contrast enhancement particles for colour doppler ultrasound imaging of tumors. Medchemcomm 1:266–270
53. Lou XW, Archer LA, Yang ZC (2008) Hollow micro-/nanostructures: synthesis and applications. Adv Mater 20:3987–4019
54. Caruso F, Caruso RA, Mohwald H (1998) Nanoengineering of inorganic and hybrid hollow spheres by colloidal templating. Science 282:1111–1114
55. Qi G, Wang Y, Estevez L, Switzer AK, Duan X, Yang X et al (2010) Facile and scalable synthesis of monodispersed spherical capsules with a mesoporous shell. Chem Mater 22:2693–2695
56. Kato N, Ishii T, Koumoto S (2010) Synthesis of monodisperse mesoporous silica hollow microcapsules and their release of loaded materials. Langmuir 26:14334–14344
57. Zhao WR, Lang MD, Li YS, Li L, Shi JL (2009) Fabrication of uniform hollow mesoporous silica spheres and ellipsoids of tunable size through a facile hard-templating route. J Mater Chem 19:2778–2783

58. Li YS, Shi JL, Hua ZL, Chen HR, Ruan ML, Yan DS (2003) Hollow spheres of mesoporous aluminosilicate with a three-dimensional pore network and extraordinarily high hydrothermal stability. Nano Lett 3:609–612
59. Feng ZG, Li YS, Niu DC, Li L, Zhao WR, Chen HR et al (2008) A facile route to hollow nanospheres of mesoporous silica with tunable size. Chem Commun 23:2629–2631
60. Djojoputro H, Zhou XF, Qiao SZ, Wang LZ, Yu CZ, Lu GQ (2006) Periodic mesoporous organosilica hollow spheres with tunable wall thickness. J Am Chem Soc 128:6320–6321
61. Yeh YQ, Chen BC, Lin HP, Tang CY (2006) Synthesis of hollow silica spheres with mesostructured shell using cationic-anionic-neutral block copolymer ternary surfactants. Langmuir 22:6–9
62. Wang JW, Xia YD, Wang WX, Poliakoff M, Mokaya R (2006) Synthesis of mesoporous silica hollow spheres in supercritical CO2/water systems. J Mater Chem 16:1751–1756
63. Chen Y, Chen HR, Shi JL (2014) Construction of homogenous/heterogeneous hollow mesoporous silica nanostructures by silica-etching chemistry: principles, synthesis, and applications. Acc Chem Res 47:125–137
64. Chen Y, Chu C, Zhou YC, Ru YF, Chen HR, Chen F et al (2011) Reversible pore-structure evolution in hollow silica nanocapsules: large pores for siRNA delivery and nanoparticle collecting. Small 7:2935–2944
65. Chen Y, Xu PF, Chen HR, Li YS, Bu WB, Shu Z et al (2013) Colloidal HPMO nanoparticles: silica-etching chemistry tailoring, topological transformation, and nano-biomedical applications. Adv Mater 25:3100–3105
66. Chen Y, Gao Y, Chen HR, Zeng DP, Li YP, Zheng YY et al (2012) Engineering inorganic nanoemulsions/nanoliposomes by fluoride-silica chemistry for efficient delivery/co-delivery of hydrophobic agents. Adv Funct Mater 22:1586–1597
67. Chen D, Li LL, Tang FQ, Qi SO (2009) Facile and scalable synthesis of tailored silica "nanorattle" structures. Adv Mater 21:3804–3807
68. Chen Y, Chen HR, Zhang SJ, Chen F, Sun SK, He QJ et al (2012) Structure–property relationships in manganese oxide – mesoporous silica nanoparticles used for T-1-weighted MRI and simultaneous anti-cancer drug delivery. Biomaterials 33:2388–2398
69. Chen Y, Yin Q, Ji XF, Zhang SJ, Chen HR, Zheng YY et al (2012) Manganese oxide-based multifunctionalized mesoporous silica nanoparticles for pH-responsive MRI, ultrasonography and circumvention of MDR in cancer cells. Biomaterials 33:7126–7137
70. Liu HY, Chen D, Li LL, Liu TL, Tan LF, Wu XL et al (2011) Multifunctional gold nanoshells on silica nanorattles: a platform for the combination of photothermal therapy and chemotherapy with low systemic toxicity. Angew Chem Int Ed 123:921–925
71. Lee JE, Lee N, Kim H, Kim J, Choi SH, Kim JH et al (2010) Uniform mesoporous dye-doped silica nanoparticles decorated with multiple magnetite nanocrystals for simultaneous enhanced magnetic resonance imaging, fluorescence imaging, and drug delivery. J Am Chem Soc 132:552–557
72. Giersig M, Ung T, LizMarzan LM, Mulvaney P (1997) Direct observation of chemical reactions in silica-coated gold and silver nanoparticles. Adv Mater 9:570–575
73. Lee J, Park JC, Song H (2008) A nanoreactor framework of a Au@SiO_2 yolk/shell structure for catalytic reduction of p-nitrophenol. Adv Mater 20:1523–1528
74. Wu M, Meng Q, Chen Y, Xu P, Zhang S, Li Y et al (2014) Ultrasmall confined iron oxide nanoparticle MSNs as a pH-responsive theranostic platform. Adv Funct Mater 24:4273–4283
75. Liu Z, Che R, Elzatahry AA, Zhao D (2014) Direct imaging Au nanoparticle migration inside mesoporous silica channels. ACS Nano 8(10):10455–10460
76. Taylor KML, Kim JS, Rieter WJ, An H, Lin WL, Lin WB (2008) Mesoporous silica nanospheres as highly efficient MRI contrast agents. J Am Chem Soc 130:2154–2155
77. Li SA, Liu HA, Li L, Luo NQ, Cao RH, Chen DH et al (2011) Mesoporous silica nanoparticles encapsulating Gd_2O_3 as a highly efficient magnetic resonance imaging contrast agent. Appl Phys Lett 98

78. Huang CC, Tsai CY, Sheu HS, Chuang KY, Su CH, Jeng US et al (2011) Enhancing transversal relaxation for magnetite nanoparticles in MR imaging using Gd3 + −chelated mesoporous silica shells. ACS Nano 5:3905–3916
79. Shao YZ, Tian XM, Hu WY, Zhang YY, Liu H, He HQ et al (2012) The properties of Gd_2O_3-assembled silica nanocomposite targeted nanoprobes and their application in MRI. Biomaterials 33:6438–6446
80. Huang XL, Zhang F, Lee S, Swierczewska M, Kiesewetter DO, Lang LX et al (2012) Long-term multimodal imaging of tumor draining sentinel lymph nodes using mesoporous silica-based nanoprobes. Biomaterials 33:4370–4378
81. Liu HM, Wu SH, Lu CW, Yao M, Hsiao JK, Hung Y et al (2008) Mesoporous silica nanoparticles improve magnetic labeling efficiency in human stem cells. Small 4:619–626
82. Kim T, Momin E, Choi J, Yuan K, Zaidi H, Kim J et al (2011) Mesoporous silica-coated hollow manganese oxide nanoparticles as positive T(1) contrast agents for labeling and MRI tracking of adipose-derived mesenchyrnal stem cells. J Am Chem Soc 133:2955–2961. doi:10.1021/ja1084095
83. Peng YK, Lai CW, Liu CL, Chen HC, Hsiao YH, Liu WL et al (2011) A New and facile method to prepare uniform hollow MnO/functionalized mSiO(2) core/shell nanocomposites. ACS Nano 5:4177–4187
84. Zhao WR, Gu JL, Zhang LX, Chen HR, Shi JL (2005) Fabrication of uniform magnetic nanocomposite spheres with a magnetic core/mesoporous silica shell structure. J Am Chem Soc 127:8916–8917
85. Zhao WR, Chen HR, Li YS, Li L, Lang MD, Shi JL (2008) Uniform rattle-type hollow magnetic mesoporous spheres as drug delivery carriers and their sustained-release property. Adv Funct Mater 18:2780–2788
86. Chen Y, Chen HR, Zhang SJ, Chen F, Zhang LX, Zhang JM et al (2011) Multifunctional mesoporous nanoellipsoids for biological bimodal imaging and magnetically targeted delivery of anticancer drugs. Adv Funct Mater 21:270–278
87. Kim J, Kim HS, Lee N, Kim T, Kim H, Yu T et al (2008) Multifunctional uniform nanoparticles composed of a magnetite nanocrystal core and a mesoporous silica shell for magnetic resonance and fluorescence imaging and for drug delivery. Angew Chem Int Ed 47:8438–8441
88. Wu HX, Zhang SJ, Zhang JM, Liu G, Shi JL, Zhang LX et al (2011) A hollow-core, magnetic, and mesoporous double-shell nanostructure: in situ decomposition/reduction synthesis, bioimaging, and drug-delivery properties. Adv Funct Mater 21:1850–1862
89. Xing ZW, Wang JR, Ke HT, Zhao B, Yue XL, Dai ZF et al (2010) The fabrication of novel nanobubble ultrasound contrast agent for potential tumor imaging. Nanotechnology 21
90. Yang P, Zhao F, Ding J, Guo J, Shi W, Wang C et al (2014) Bubble-in-bubble strategy for high-quality ultrasound imaging with a structure coupling effect. Chem Mater 26:2121–2127
91. Zhang K, Chen HR, Guo XS, Zhang D, Zheng YY, Zheng HR et al (2015) Double-scattering/reflection in a single nanoparticle for intensified ultrasound imaging. Sci Rep UK 5
92. Wang X, Chen HR, Chen Y, Ma M, Zhang K, Li FQ et al (2012) Perfluorohexane-encapsulated mesoporous silica nanocapsules as enhancement agents for highly efficient High Intensity Focused Ultrasound (HIFU). Adv Mater 24:785–791
93. Niu DC, Wang X, Li YS, Zheng YY, Li FQ, Chen HR et al (2013) Facile synthesis of magnetite/perfluorocarbon co-loaded organic/inorganic hybrid vesicles for dual-modality ultrasound/magnetic resonance imaging and imaging-guided high-intensity focused ultrasound ablation. Adv Mater 25:2686–2692
94. Zhou Y, Wang Z, Chen Y, Shen H, Luo Z, Li A et al (2013) Microbubbles from gas-generating perfluorohexane nanoemulsions for targeted temperature-sensitive ultrasonography and synergistic HIFU ablation of tumors. Adv Mater 25:4123–4130
95. Zhang K, Chen H, Li F, Wang Q, Zheng S, Xu H et al (2014) A continuous tri-phase transition effect for HIFU-mediated intravenous drug delivery. Biomaterials 35:5875–5885

96. Wang X, Chen H, Zhang K, Ma M, Li F, Zeng D et al (2014) An intelligent nanotheranostic agent for targeting, redox-responsive ultrasound imaging, and imaging guided high- intensity focused ultrasound synergistic therapy. Small 10:1403–1411
97. Yang F, Hu SL, Zhang Y, Cai XW, Huang Y, Wang F et al (2012) A hydrogen peroxide-responsive O_2 nanogenerator for ultrasound and magnetic-resonance dual modality imaging. Adv Mater 24:5205–5211
98. Al-Bataineh O, Jenne J, Huber P (2012) Clinical and future applications of high intensity focused ultrasound in cancer. Cancer Treat Rev 38:346–353
99. Kennedy JE (2005) High-intensity focused ultrasound in the treatment of solid tumours. Nat Rev Cancer 5:321–327
100. Dubinsky TJ, Cuevas C, Dighe MK, Kolokythas O, Hwang JH (2008) High-intensity focused ultrasound: current potential and oncologic applications. Am J Roentgenol 190:191–199
101. Hill CR, terHaar GR (1995) Review article: high intensity focused ultrasound-potential for cancer treatment. Br J Radiol 68:1296–1303
102. Chen Y, Chen H, Shi J (2014) Nanobiotechnology promotes noninvasive high-intensity focused ultrasound cancer surgery. Adv Healthcare Mater 4:158–165
103. Sun Y, Zheng YY, Ran HT, Zhou Y, Shen HX, Chen Y et al (2012) Superparamagnetic PLGA-iron oxide microcapsules for dual-modality US/MR imaging and high intensity focused US breast cancer ablation. Biomaterials 33:5854–5864
104. Napoli A, Anzidei M, Ciolina F, Marotta E, Marincola BC, Brachetti G et al (2013) MR-guided high-intensity focused ultrasound: current status of an emerging technology. Cardiovasc Intervent Radiol 36:1190–1203
105. Chen Y, Chen HR, Sun Y, Zheng YY, Zeng DP, Li FQ et al (2011) Multifunctional mesoporous composite nanocapsules for highly efficient MRI-guided high-intensity focused ultrasound cancer surgery. Angew Chem Int Ed 50:12505–12509
106. Ma M, Xu H, Chen H, Jia X, Zhang K, Wang Q et al (2014) A drug–perfluorocarbon nanoemulsion with an ultrathin silica coating for the synergistic effect of chemotherapy and ablation by high-intensity focused ultrasound. Adv Mater 26:7378–7385

Part III
Nanoparticles for Cancer Theranostics

Chapter 7
Multifunctional Nanoprobes for Multimodality Targeted Imaging and Therapy of Gastric Cancer

Daxiang Cui

7.1 Introduction

Gastric cancer (GC) is the fourth commonest cancer and the second leading cause of cancer-related mortality worldwide [1]. Gastric cancer is the second most common cancer, and the third leading cause of cancer-related death in China [2]. Although gastroscopy has been broadly used for screening early gastric cancer patients, gastric cancer remains very difficult to cure effectively, primarily because most patients present advanced stages of the diseases. Therefore, how to identify early gastric cancer has become a great challenge.

In 1999, we first proposed the project of developing gastric cancer prewarning and early diagnosis system [3]. Since 1999, we try to realize gastric cancer prewarning and early diagnosis by screening early gastric cancer biomarkers, developing new detection method of gastric cancer biomarkers, and establishing gastric cancer prewarning database including molecular imaging database, biomarker database, and information treatment platform [4, 5]. Especially under the support from Chinese Nano Key Fundamental Project (no.2010CB933900), we have achieved great advances in this field.

Great advance has been made in molecular imaging, which has been actively explored potential applications such as tumor early diagnosis, in vivo genotyping, targeted imaging and simultaneously therapy, and surgery navigation [6]. These advances highly depend on the development of multifunctional nanoprobes and also highly depend on the development of nanomaterials and nanotechnology.

D. Cui (✉)
Institute of Nano Biomedicine and Engineering, Department of Instrument Science and Engineering, National Center for Translational Medicine, Collaborative Innovational Center for System Biology, Shanghai Jiao Tong University, Shanghai 200240, People's Republic of China
e-mail: dxcui@sjtu.edu.cn

Z. Dai (ed.), *Advances in Nanotheranostics II*, Springer Series in Biomaterials Science and Engineering 7, DOI 10.1007/978-981-10-0063-8_7

Nanotechnology makes an important contribution toward cancer prevention, diagnosis, imaging, and treatment [7]. It not only provides unprecedented capability for carrying multiple diagnostic and therapeutic payloads in the same package but also facilitates targeting delivery into specific sites across complex biological barriers [8]. The multifunctional integrated system combines different properties such as tumor targeting, imaging, and selective therapy in an all-in-one system, which will provide more useful multimodal approaches in the battle against cancer.

To date, gastric cancer therapeutic methods mainly include surgery, radiation, and chemotherapies, which are generally very effective for early and in situ gastric cancers, but advanced and metastatic cases do not respond to chemotherapy or radiation therapies [9]. Resistance to chemotherapy-induced apoptosis is a major cause for the failure of conventional therapies. The current prognosis of gastric cancer is very poor with 5-year survivals of less than 24 % [10]. Therefore, how to recognize, track, or kill early gastric cancer cells is a great challenge for patients with early gastric cancer.

Current studies show that gastric cancer is not particularly sensitive to traditional therapies, especially to chemotherapy agents, which seems to be closely related to numerous intrinsic or acquired properties of gastric cancer stem cells (CSCs) [11]. Despite the hypothesis of CSCs being challenged, growing evidence has been provided to support the existence of CSCs. The notion that CSCs give rise to GC and may be responsible for invasion, metastasis, and resistance to conventional treatment has profound implications for anticancer targeted therapies [9]. Therefore, GCSC-based targeted therapy is destined to be one of the most effective anticancer strategies.

Immunological studies highly suggest that the reasons for metastasis and recurrence of GC can be summarized as follows [6]:

1. The intrinsic antigenicity weakness of tumor cells and immunological surveillance of the host cannot identify and eliminate the malignant cells that are distributed out of the resection field and the peripheral lymphoid organs.
2. Immunological surveillance defect or dysfunction of the host. After the traditional therapy was done, the residual tumor cells escaped from immunosurveillance revived again.
3. The substantial toxicities of most traditional curative intents, which is often compromised by the extreme feeble immunity of the patient.

Therefore, it is very necessary to develop new therapeutic strategies that could enhance the host immunosurveillance and/or improve immunogenicity of the tumor cell.

Since Obama, the President of the USA, proposed precision medicine project in January of 2015, how to realize precision medicine has become a hotspot. Genomics, big data, and molecular imaging have become key tools to realize precision medicine. Herein we review the main advances of multifunctional nanoprobes for targeted imaging and therapy of gastric cancer in our team over the past several years, explore the clinical translational prospects, and discuss the concepts, issues, approaches, and challenges, with the aim of improving the clinical application of

multifunctional nanoprobes for targeted imaging and therapy of gastric cancer in the near future.

7.2 Multifunctional Fluorescent Magnetic Nanoprobes for Targeted Imaging and Therapy of Gastric Cancer

In 2007, we controllably prepared silica-coated CdTe quantum dots and superparamagnetic nanoparticle composites (FMNPs) with strong fluorescent signals and excellent magnetic properties [12]. We also observed that as-prepared nanoparticles own good biocompatibility and stability [5].

7.2.1 BRCAA1 Antibody-Conjugated FMNPs for Targeted Imaging

In 1999, we screened out and cloned BRCAA1 gene (breast cancer-associated antigen 1 gene) from breast cancer cell line MCF-7 cells [AF208045, also called ARID4B (AT-rich interactive domain-containing protein 4B)] and identified its antigen epitope peptide SSKKQKRSHK [13]. We also prepared BRCAA1 polyclonal antibody and observed that the BRCAA1 protein exhibited overexpression in almost 65 % clinical specimens of gastric cancer tissues [14]. We also observed that BRCAA1 antigen is overexpressed in gastric cancer cell lines such as MKN-1, MKN-74, SGC-7901, KATO-III, and MGC803 cells [15]. Therefore, we predict that BRCAA1 protein may be one potential targeting molecule for in vivo gastric cancer cells.

Based on our previous work, we fully took the advantages of FMNPs and BRCAA1 antigen, prepared monoclonal antibody against BRCAA1 protein, prepared BRCAA1 monoclonal antibody-conjugated fluorescent magnetic nanoprobes (BRCAA1-FMNPs), employed nude mice model loaded with gastric cancer of 5 mm in diameter and IVIS imaging system and magnetic resonance imaging system, and investigated the feasibility of as-prepared nanoprobes for in vivo targeted dual-modality imaging of gastric cancer.

As shown in Table 7.1, we successfully obtained two BRCAA1 monoclonal antibody cell lines with high specificity. As shown in Table 7.2, BRCAA1 monoclonal antibody-conjugated FMNP nanoprobes were successfully prepared with coupling ratio of more than 80 %.

By monitoring real-time fluorescence intensity in the whole body, the tumor targeting character of the anti-BRCAA1-FMNP probe was easily determined in the nude mice loaded with gastric cancer MGC803 cells. As shown in Fig. 7.1a, the whole animals produced fluorescent signals within 30 min of postinjection of nanoprobes, and the subcutaneous tumor tissues could be clearly delineated from the

Table 7.1 Titers of BRCAA1 monoclonal antibodies in ascites fluid induced by hybridoma clone cells by ELISA

Clone	Antibody titer[a]			
	BRCAA1 (C)-OVA[b]	BRCAA1 (C)-BSA[b]	BSA[b]	OVA[b]
S-200-5	1,024,000	1,024,000	<1000	<1000
S-335-5	128,000	512,000	<1000	<1000

[a]The reciprocal of ascites fluid dilution, the first dilution of ascites fluid was 1:1000
[b]The antigens were coated on ELISA plate

Table 7.2 Coupling rate measurement of FMNP-BRCAA1 antibody

	Total concentration of the anti-BRCAA1 antibody (ng/μL)	The concentration of BRCAA1 antibody in residual reaction mixture (ng/μL)	Coupling rate (%)
1	1000.0	197.3	80.27
2	1000.0	191.2	80.88
3	1000.0	203.0	79.70

surrounding background tissue between 1 and 12 h postinjection, with maximum contrast occurring at 6 h postinjection. Strong fluorescence signal was still detected in the tumor site at 6 h postinjection, which indicated that the anti-BRCAA1-FMNP nanoprobes were preferentially accumulated in the tumor tissues. Indeed based on the results in Fig. 7.1b, the higher tumor to background ratio (TBR) value highly suggested that as-prepared nanoprobes preferentially accumulated in tumor tissues compared to normal control tissues. This was confirmed by fluorescence images, which showed that the fluorescence signal of as-prepared nanoprobes in the tumor site was strongest among all mice organs as shown in Fig. 7.1c. In addition, after 12 h postinjection of anti-BRCAA1-FMNP nanoprobes, fluorescence intensity in tumor was still observed clearly, while the uptake of prepared nanoprobes in normal organs was not obvious. These data highly suggest that the prepared nanoprobes can target highly efficient tumor tissues inside nude mice loaded with gastric cancer. We also observed that those nanoprobes in the whole mouse body almost completely disappeared at 12 h postinjection, we also detected the partial nanoprobes exited out from the cholecyst system, and the time-dependent cholecyst clearance of nanoprobes highly suggests that as-prepared nanoprobes cannot stay inside nude mice for longer time; thus, as-prepared nanoprobes own good biosafety [16].

In vivo MR imaging was performed on nude mice loaded with subcutaneous gastric cancer at 12 h post_injection. Representative images of T2 maps were shown in Fig. 7.2; after injecting the nanoprobes, a significant change in signal intensity was observed in some regions of tumors, indicating that there existed accumulation of the nanoprobes in tumor site as shown in Fig. 7.2b, as the arrow showed. As a control, after the mice model with gastric cancer was injected with FMNPs for 12 h, MR imaging was performed in mice, which did not show intensive signal in tumor area (Fig. 7.2a).

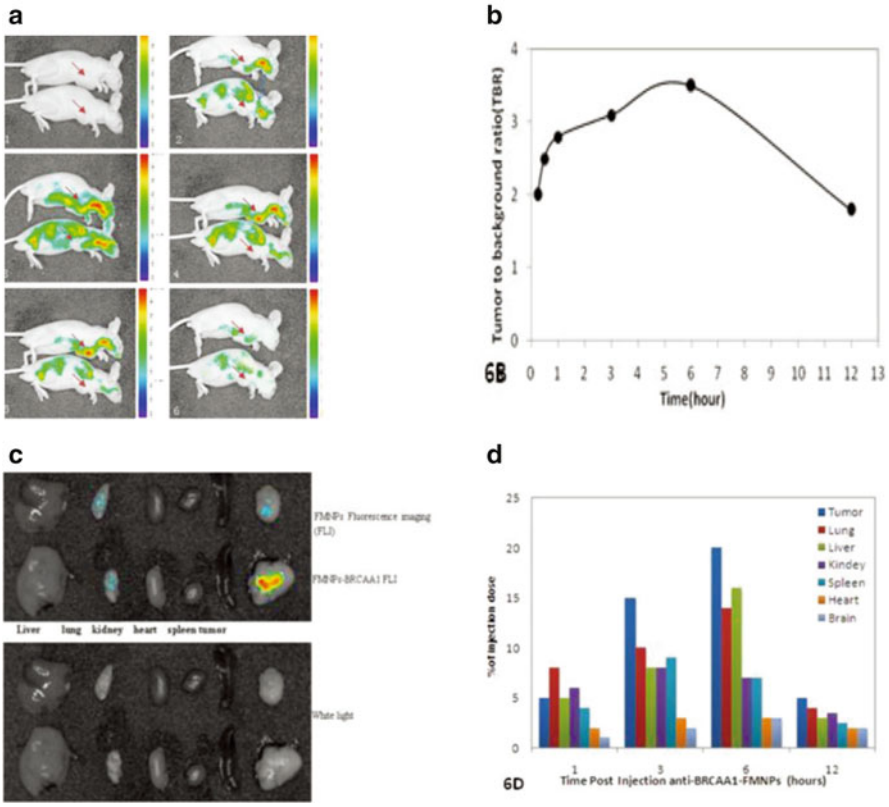

Fig. 7.1 In vivo fluorescence images of tumor accumulation and tissue distribution for anti-BRCAA1-FMNP nanoprobes in MGC803 human gastric tumor-bearing athymic nude mice. (**a**) In vivo fluorescence images of athymic nude mice bearing MGC803 human gastric tumor were obtained after injection of anti-BRCAA1-FMNP nanoprobes at different time points. The tumor location is specified with an *arrow*: A-1, 0 h; A-2, 0.5 h; A-3, 1 h; A-4, 3 h; A-5, 6 h; A-6, 12 h. (**b**) TBR [tissue to background (muscle) ratio] value. The TBR value was determined as follows: TBR = (tumor signal-background signal)/(background signal). (**c**) Ex vivo fluorescence images of dissected organs and tumor of mice bearing MGC803 human gastric tumor sacrificed at 12 h after injection of anti-BRCAA1-FMNP nanoprobes. The fluorescence images of dissected organs and tumor were obtained using a fluorescence imaging system with a 630 nm emission filter. (**d**) Biodistribution of anti-BRCAA1-FMNPs in mice after intravenous injection. Several time points after injection, iron amounts in tissue samples were evaluated by ICP mass spectrometry ($n = 3$) (Reproduced from Ref. [17] by permission of Springer Science + Business Media)

In vitro evaluation of excised major tissues including the liver, lung, spleen, kidney, and heart, as well as the tumor, indicated that the anti-BRCAA1-FMNP probes were mainly uptaken by the tumor tissues, which exhibited strong fluorescence signals, as shown in Fig. 7.1d, whereas other tissues including the liver, lung, spleen, and heart uptook anti-BRCAA1-FMNP nanoprobes very less, which furtherly indicates that as-prepared anti-BRCAA1-FMNP nanoprobes can target gastric cancer

Fig. 7.2 In vivo MR imaging of anti-BRCAA1-FMNP nanoprobes. (**a**) MR imaging of the mice model with gastric cancer injected with FMNPs for 12 h and (**b**) MR imaging of the mice model with gastric cancer injected with anti-BRCAA1-FMNPs for 12 h (Reproduced from Ref. [17] by permission of Springer Science + Business Media)

tissues. We also used H&E staining to check all organs, and no obvious damages were observed in important organs.

Therefore, we successfully prepared a novel anti-BRCAA1-FMNP nanoprobes, which can be used for in vivo two-modal imaging such as fluorescent imaging and magnetic resonance imaging, own an obviously specific targeting ability toward a gastric cancer tissues with 5 mm in diameter during 0.5 and 12 h of postinjection, and own good biocompatibility. The as-prepared multifunctional nanoprobes also can be used for hyperthermia therapy of gastric cancer under in vitro alternating magnetic field irradiation and have great potential in applications such as simultaneous imaging and targeting therapy of clinical gastric cancer in the near future [17].

7.2.2 HAI-178 Antibody-Conjugated FMNPs for Targeted Imaging and Therapy

We also prepared another important nanoprobe, that is, HAI-178 antibody-conjugated fluorescent magnetic nanoprobe, which was successfully used for targeted imaging and hyperthermia therapy of gastric cancer. Dr. Jian Ni group prepared specific monoclonal antibody against α-subunit of ATP synthase, named as HAI-178 antibody, and provided HAI-178 antibody to my group. Our primary studies showed that α-subunit of ATP synthase also exhibited overexpression in

gastric cancer cells and 94.7 % clinical gastric cancer tissues, with no or very low expression in normal gastric mucous tissues, and it should be a potential biomarker with diagnosis value.

We prepared HAI-178 antibody-conjugated fluorescent magnetic nanoparticles (HAI-178-FMNPs) and co-incubated with gastric cancer MGC803 cells and gastric mucous GES-1 cells. Gastric cancer-bearing nude mice models were established and were injected with prepared HAI-178-FMNPs via tail vein and were imaged by magnetic resonance imaging (MRI) and small animal fluorescent imaging system. Results showed that α-subunit of ATP synthase exhibited high expression in 94.7 % gastric cancer tissues. Prepared HAI-178-FMNPs could target actively MGC803 cells, realized fluorescent imaging and magnetic resonance imaging of in vivo gastric cancer, and actively inhibited growth of gastric cancer cells. HAI-178 antibody-conjugated fluorescent magnetic nanoparticles own great potential in applications such as targeted imaging and simultaneous therapy of in vivo early gastric cancer cells in the near future [18].

7.2.3 FMNP-Labeled MSCs for Targeted Imaging and Hyperthermia Therapy

We also prepared FMNP-labeled human MSCs and realized targeted imaging and hyperthermia therapy of gastric cancer. We firstly proposed the concept of stem cell nanotechnology, which is an emerging interdisciplinary field, which refers to the application of nanotechnology in stem cell research and development. Although great advances in the field of stem cells have been and being made, several obstacles must be overcome before their therapeutic application can be realized. These include the development of advanced techniques to understand and control functions of microenvironmental signals and novel methods to track and guide transplanted stem cells. The application of nanomaterials and nanotechnology in stem cell research and development exhibits attracting technological prospects, which provide a new chance to solve current problems that stem cell research and development meets [19, 20].

Mesenchymal stem cells (MSCs) are multipotent stem cells that can differentiate into a variety of cell types, including: osteoblasts (bone cells), chondrocytes (cartilage cells), and adipocytes (fat cells). MSCs possess immunosuppressive or immunomodulatory properties and have the characteristics of home to the sites of active tumorigenesis. Thus, MSCs can be considered as a candidate cell type for cell-based tissue engineering, cancer therapeutics, and regenerative medicine applications. However, the distribution and final fate of MSC cells inside human body are still not clarified well, which urgently need the novel labeling and in vivo tracking technology.

As shown in Fig. 7.3, MSCs were characterized. The silica-coated fluorescent superparamagnetic nanoparticles (FMNPs) were prepared, were evaluated in their

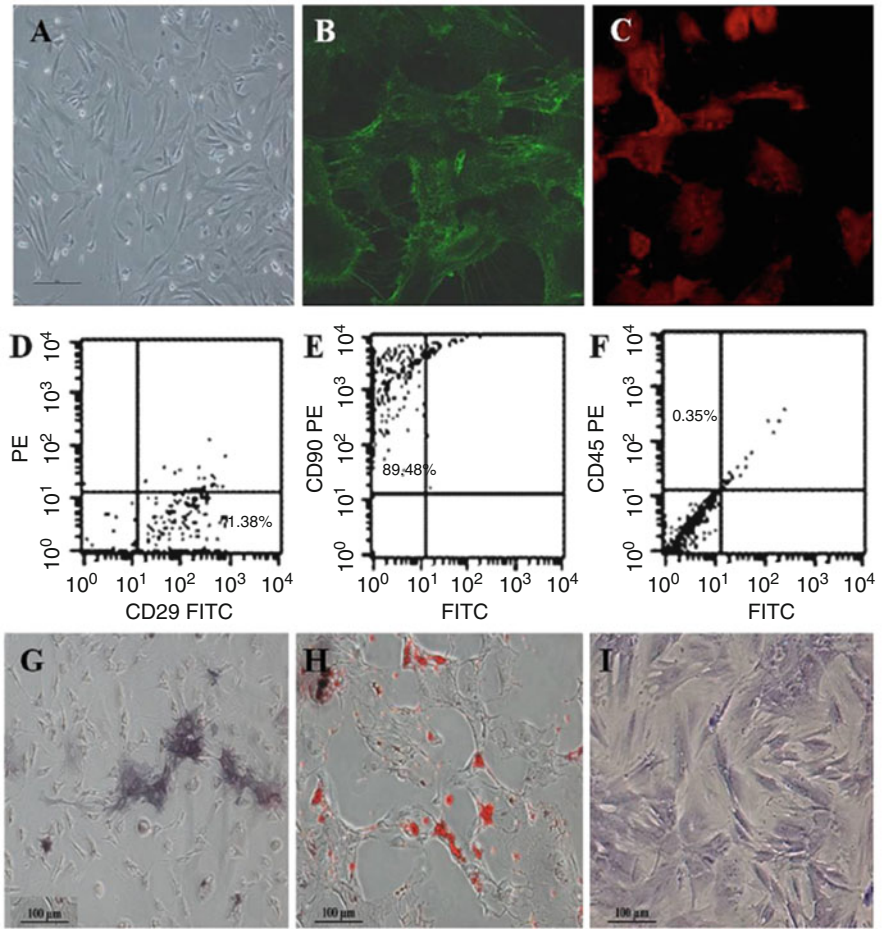

Fig. 7.3 Morphology and immunophenotypic characterization of MSCs. (**A**) The fibroblastic morphology of passage 3 MSCs (magnification = ×100); (**B**) MSCs stained with FITC-conjugated CD29 antibody (×200); (**C**) MSCs stained with PE-conjugated CD90 antibody (×200); (**D**), (**E**), and (**F**) MSCs analyzed by FACS for the positive expression of CD29 (**D**) and CD90 (**E**) and negative expression of CD45 (**F**); (**G**) differentiated osteoblasts tested with alkaline phosphatase staining (×100); (**H**) differentiated adipocytes characterized by oil *red O staining* (×100); (**I**) differentiated chondrocytes verified by toluidine *blue staining* (×100) (Reproduced from Ref. [21] by permission of Springer Science + Business Media)

effects on mesenchymal stem cells (MSCs), and were used to label MSCs and then observed the distribution and final sites of the labeled MSCs in vivo in nude models loaded with gastric cancer. Some chemoattractant cytokines were analyzed by ELISA and Western blotting. As shown in Fig. 7.4, MSCs were labeled with FMNPs efficiently and kept stable fluorescent signal and magnetic properties within 14 days, FMNP-labeled MSCs could target and image in vivo gastric cancer cells after being intravenously injected for 14 days, FMNP-labeled MSCs could significantly

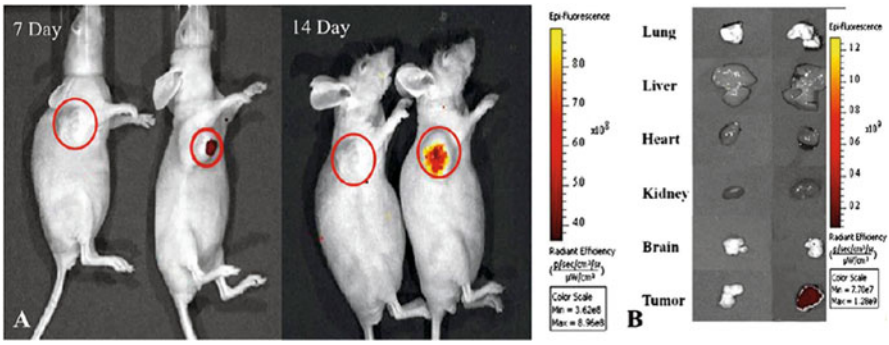

Fig. 7.4 Fluorescent imaging of FMNP-labeled MSCs targeting gastric cancer cells in vivo. (**A**) The in vivo fluorescent images show that tumor sites of the mice in the test group had fluorescent signals after postinjection of FMNP-labeled MSCs at 7 and 14 days (*right*) and tumor sites of the mice in the control group had no fluorescent signal after postinjection of FMNPs at 7 and 14 days (*left*). (**B**) The fluorescent imaging of major organs show that no signal was detected in the tumor and organs of the control group (*left*) and obviously fluorescent signals were detected in the tumor tissues of the test group (*right*) (Reproduced from Ref. [21] by permission of Springer Science + Business Media)

inhibit the growth of in vivo gastric cancer because of hyperthermia effects, and CCL19/CCR7 and CXCL12/CXCR4 axis loops may play key roles in the targeting of MSCs to in vivo gastric cancer. This FMNP-based labeling and tracking technology has great potential in applications such as labeling and tracking implanted cells, evaluating cell therapeutic effects, and recognizing and mapping early gastric cancer cells [21].

7.3 Multifunctional QD Probes for Fluorescent Imaging, Genotyping, and Therapy of Gastric Cancer

7.3.1 RGD-Conjugated RNase A-Associated dRQDs for Targeted Imaging and Therapy

Colloidal semiconductor nanocrystals (NCs), also known as quantum dots (QDs), have gained immense attention due to their unique optical properties, including a broad absorption with narrow photoluminescence spectra, high quantum yields, low photobleaching, and size-dependent emission-wavelength tunability [22]. These fascinating properties make QDs a promising candidate for biological imaging and labeling probes, with significant advantages over conventional fluorescent dyes. However, the toxicity associated with cadmium-containing QDs turned out to be a chief hurdle for in vitro and in vivo biomedical diagnostics [23]. For this reason, a variety of attempts have been made to reduce the toxicity of QDs and improve their biocompatibility, which has become a rapidly growing area of nanoscience research.

Although the surface modification strategy proves to be prosperous, to select an appropriate surface coating material is not easy. More recently, due to the excellent biocompatibility and bioabsorbility, some proteins have been immobilized on the surface of QDs to produce low-toxicity protein–QD hybrid nanomaterials. Additionally, protein molecules have also been adopted to serve as the biomolecular templating agent to regulate the formation of inorganic nanostructures [24]. We reported the first application of bovine pancreatic ribonuclease A (RNase A) as a biomolecular templating agent for preparing CdTe QD clusters in aqueous phase via a chemical reduction approach. We have chosen RNase A due to its unique features. RNase A is a low-molecular-weight protein (124 residues, 13.7 kDa, pI 9.4) with a globular configuration (2.2, 2.8, 3.2 nm). The outstanding thermal stability of the protein is well known, thereby being able to endure the high temperature in our synthesis process. Recently, other groups have reported that RNase A was able to inhibit the development of cancerous cells depending on its enzymatic activity of degrading cellular RNA and has been used as a chemotherapeutic agent in clinical trials. It was found that RNase A inevitably lost its native conformation to form denatured RNase A (dRNase A)-capping CdTe QD clusters (dRQDs). Moreover, dRNase A not only effectively reduced the cytotoxicity of CdTe QDs but also unexpectedly induced a temporal evolution of the luminescence during a 50-day storage period under ambient conditions, as shown in Fig. 7.5. As shown in Fig. 7.6, prepared RNase A-QDs composed of QD clusters, the potential synthesis mechanism is shown in Fig. 7.7. Inspired by these fascinating properties, dRQDs was associated with native RNase A by the physical absorption, which was then coupled with cyclic arginine–glycine–aspartic acid (RGD) peptide c(RGDfK) that served as the targeting biomolecule. A novel multifunctional nanosystem RGD-conjugated RNase A-associated dRQDs (RGD-R-dRQDs) was built up for synchronous targeted cellular imaging and therapeutic applications [25].

7.3.2 Her2 Antibody-Conjugated RQDs for Targeted Imaging and Therapy of In Situ Gastric Cancer

One kind of multifunctional HER2 monoclonal antibody-conjugated RNase A-associated CdTe quantum dot cluster (HER2-RQD) nanoprobes was prepared, and its cytotoxicity was evaluated. Subcutaneous gastric cancer nude mouse models and in situ gastric cancer SCID mouse models were established and were intravenously injected with HER2-RQD nanoprobes, and the biodistribution and therapeutic effects of HER2-RQDs in vivo were evaluated. Results showed that HER2-RQD nanoprobes could selectively kill gastric cancer MGC803 cells, as shown in Fig. 7.8, could target imaging subcutaneous gastric cancer cells at 3 h postinjection and in situ gastric cancer cells at 6 h postinjection, and could inhibit the growth of gastric cancer tissues and extended survival time of gastric cancer-bearing mouse models, which is closely associated with destroying functional RNAs in cytoplasm by

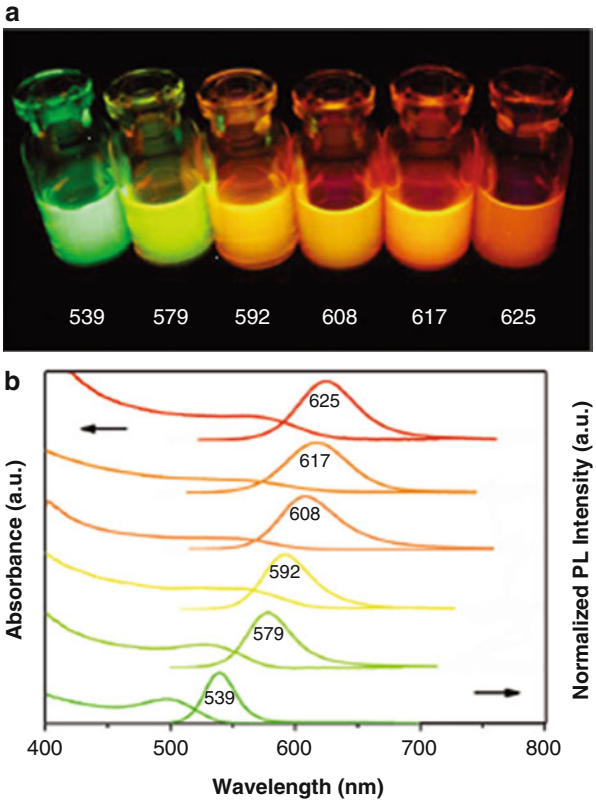

Fig. 7.5 (**a**) Photograph of freshly prepared CdTe QD suspension with different emitting colors in the presence of RNase A as a biomolecular templating agent under a handheld UV lamp. (**b**) Corresponding UV–vis absorption and normalized photoluminescence (PL) spectra (Reproduced from Ref. [25] by permission of John Wiley & Sons Ltd)

RNase A released from HER2-RQD nanoprobes, preventing protein synthesis, and inducing cell apoptosis, as shown in Fig. 7.9. High-performance HER2-RQD nanoprobes exhibit great potential in applications such as in situ gastric cancer targeted imaging and selective therapy in the near future [26].

7.3.3 BRCAA1 and Her2 Monoclonal Antibody-Conjugated PQDs for Targeted Imaging and Therapy

In order to observe multi-target molecule imaging of gastric cancer, we chose the CdSe/ZnS (core/shell) quantum dots (QDs) as prototypical materials, synthesized one kind of new amphiphilic polymer including dentate-like alkyl chains and multiple carboxyl groups, and then used prepared amphiphilic polymer to modify QDs,

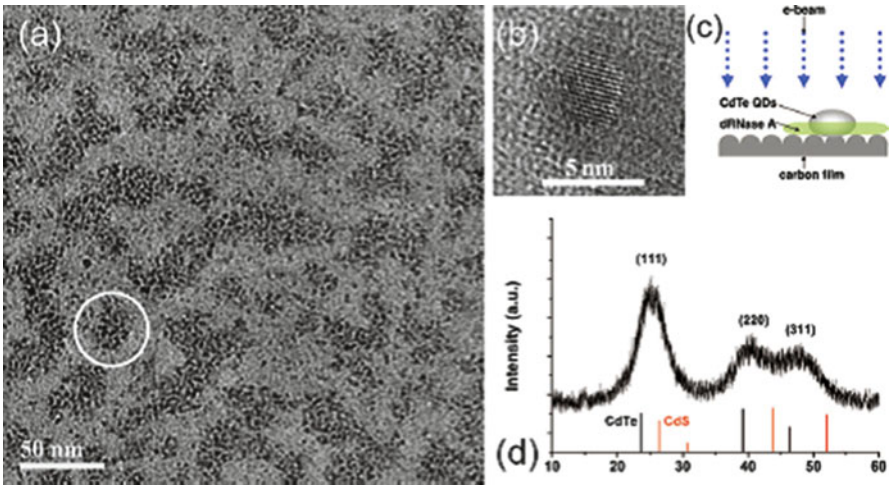

Fig. 7.6 (**a**) TEM image of as-prepared dRQD539. A typical cluster is labeled with a *white circle*. (**b**) High-resolution TEM image (HR-TEM) of an individual CdTe QD. (**c**) Schematic diagram to explain the difference in image contrast in the HR-TEM image during imaging in the vertical section. (**d**) Powder X-ray diffraction (XRD) pattern of dRQD539. Standard diffraction lines of cubic CdTe and cubic CdS are shown for comparison (Reproduced from Ref. [25] by permission of John Wiley & Sons Ltd)

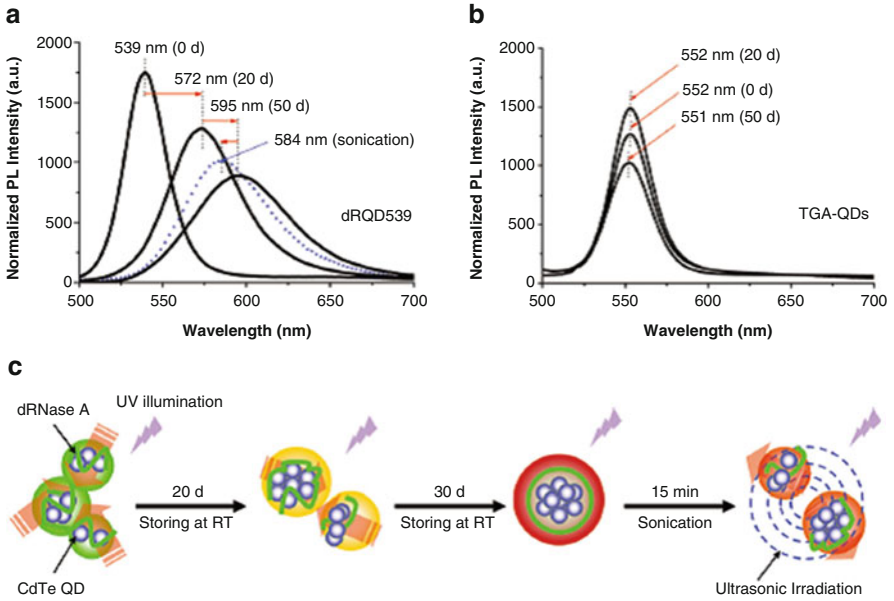

Fig. 7.7 (**a**) Normalized photoluminescence (PL) spectra of dRQD539 (excitation wavelength $\lambda ex = 400$ nm). The three solid lines are the corresponding PL spectra of the same sample stored for 0 day (0 d), 20 days (20 d), and 50 days (50 d), respectively. The *blue dotted line* is the PL spectrum of the 50-day-stored dRQD539 after sonicating for ~15 min in an ultrasonic cell crusher. (**b**) Normalized PL spectra of TGA-capping CdTe QDs stored for 0, 20, and 50 days, respectively. (**c**) Schematic illustration of the potential mechanism for the redshift of emission peaks of dRQD539 during the storage period under ambient conditions (Reproduced from Ref. [25] by permission of John Wiley & Sons Ltd)

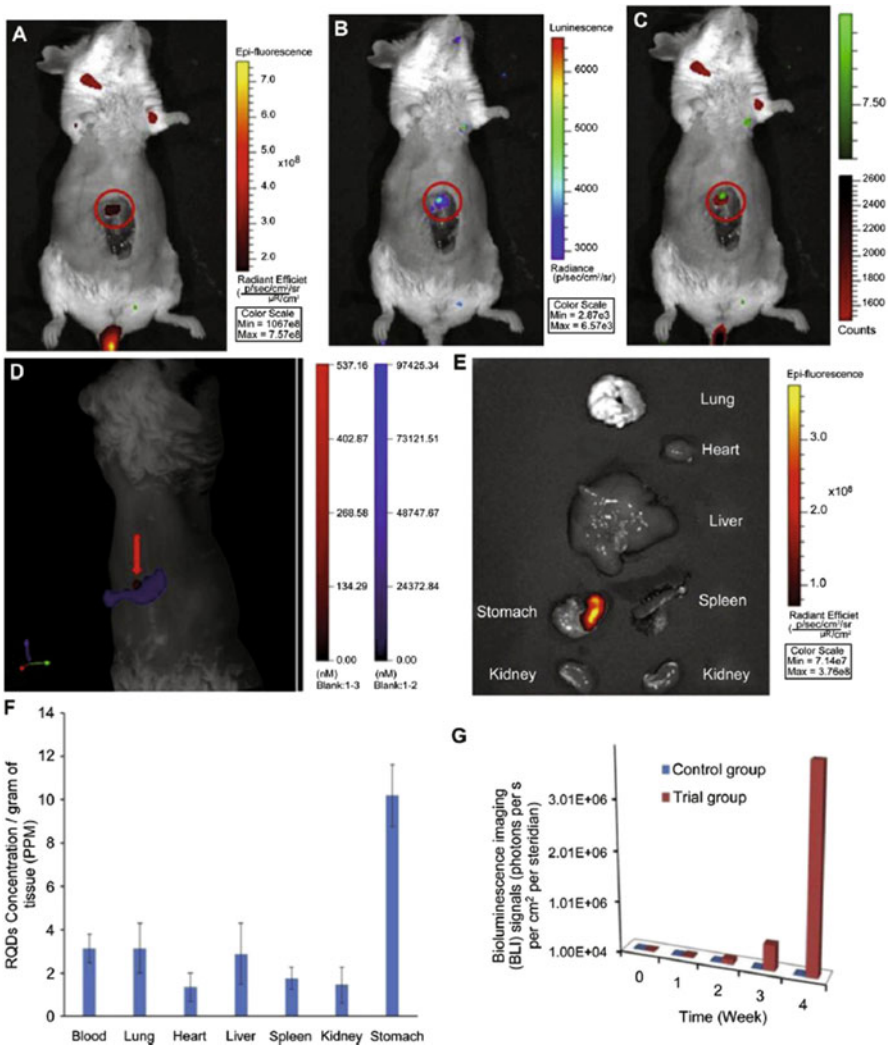

Fig. 7.8 Optical images of HER2-RQD nanoprobe in in situ gastric cancer mice. (**A**) Fluorescence image of HER2-RQD nanoprobe targeted in situ gastric cancer tissue. (**B**) Bioluminescence image of in situ gastric cancer tissue. (**C**) Overlay image of fluorescence and bioluminescence imaging. (**D**) 3D image of HER2-RQD nanoprobe targeted gastric cancer tissue. (**E**) Ex vivo fluorescence image of the dissected organs of the mice sacrificed at 24 h postinjection of HER2-RQD nanoprobes. (**F**) Biodistribution of HER2-RQDs in mice after intravenous injection. The amounts of RQDs in tissue samples were evaluated by ICP mass spectrometry (n ¼ 3). (**G**) Bioluminescence imaging signals of gastric tumor tissues in in situ gastric cancer mice after treated with HER2-RQDs for 4 weeks (Reproduced from Ref. [26] by permission of Elsevier)

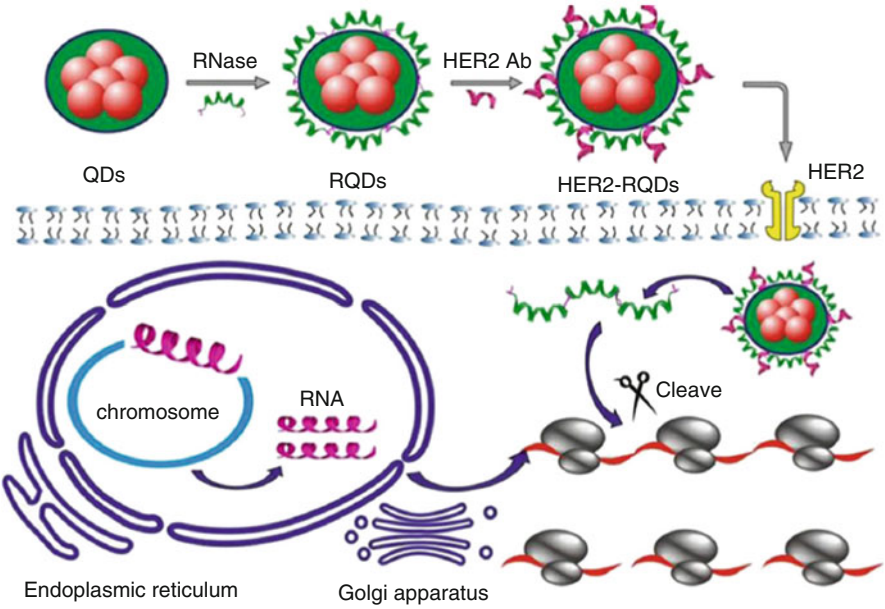

Fig. 7.9 Therapeutic mechanism of as-prepared nanoprobes: HER2-RQD nanoprobes could specifically enter into gastric cancer cells, and RNase A was released from the HER2-RQD nanoprobes under the acid environment, which degraded total RNAs inside gastric cancer cells, inhibiting RNA translation and protein synthesis, and finally induced tumor cells' apoptosis (Reproduced from Ref. [26] by permission of Elsevier)

resultant amphiphilic polymer engineered QDs (PQDs) were conjugated with BRCAA1 and Her2 monoclonal antibody, and prepared BRCAA1-antibody- and Her2-antibody-conjugated QDs were used for in vitro MGC803 cell labeling and in vivo targeted imaging of gastric cancer cells. Results showed that the PQDs exhibited good water solubility, strong photoluminescence (PL) intensity, and good biocompatibility. BRCAA1-antibody- and Her2-antibody-conjugated QD nanoprobes successfully realized targeted imaging of in vivo gastric cancer MGC803 cells. BRCAA1-antibody- and Her2-antibody-conjugated PQDs own great potential in applications such as single-cell labeling and in vivo tracking and targeted imaging and therapeutic effects' evaluation of in vivo early gastric cancer cells in the near future [27].

7.4 Multifunctional Upper Conversion Nanoprobes for Targeted Imaging and Therapy of Gastric Cancer

Upconversion nanoparticles (UCNPs), especially lanthanide-doped nanocrystals, have stolen the limelight due to their seductive optical and chemical features such as low toxicity, large Stokes shifts, high resistance to photobleaching, and

photochemical degradation [28, 29]. Moreover, near-infrared (NIR) excitation contributes to the autofluorescence minimization, a larger penetrating depth, and less harmfulness to cells compared with traditional ultraviolet (UV) excitation. On the other hand, the composites of UCNPs with other materials exert superior performance in a sense broadening the range of biological applications from multimodality imaging, targeted therapy, to biodetections and bioassays. My group firstly reported the OA/ionic liquid two-phase system combining the merits of thermal decomposition method, the ionic liquid (IL)-based strategy, and the two-phase approach is introduced to synthesize high-quality lanthanide-doped NaGdF 4 upconversion nanocrystals with different crystal phases in OA phase and IL phase through a one-step controllable reaction. As shown in Fig. 7.10, oil-dispersible cubic-phase NaGdF 4:Yb, Er (Ho, Tm) nanocrystals with ultrasmall size (∼5 nm) and monodispersity are obtained in the OA phase of the two-phase system via an IL-based reaction. More importantly, water-soluble hexagonal-phase NaGdF 4:Yb, Er nanocrystals are obtained in the same system simply by adopting an extremely facile method to complete the dual-phase transition (crystal-phase transition and OA-phase to IL-phase transition) simultaneously. The synthesized lanthanide-doped NaGdF4 upconversion nanocrystals are effective for dual-mode UCL imaging and CT imaging in vivo [30]. Based on this basis, we also improved the synthesis condition and developed phase- and size-controllable synthesis of hexagonal upconversion rare-earth fluoride nanocrystals through an oleic acid/ionic liquid two-phase system [31], and prepared nanoparticles were successfully used as magnetic nanorattle materials for magnetism-directed targeting imaging and chemical therapy [32].

7.4.1 Lanthanide-Doped NaGdF4 Upconversion Nanocrystals for Dual-Mode UCL Imaging and CT Imaging and Targeted Chemical Therapy

Nanoparticle-based drug system has become a hotspot. How to realize chemical drugs targeted delivery has become a key scientific problem. Nanoengineered drug delivery systems could improve the clinical performance of traditional chemotherapeutic agents and reduce overall toxicity by enhancing the specificity of the drug's delivery through tumor targeting and making elevated local dosages possible. Lanthanide-doped NaGdF4 upconversion nanocrystals own obvious advantages such as near-infrared (NIR) to vis upconversion (UC) excitation. As shown in Fig. 7.11, a nanostructure with both UC and magnetic properties was prepared, named as nanorattle, which contains a hollow volume that can accommodate a drug payload. Prepared nanorattle hollow spheres are composed of rare-earth-doped NaYF4 shells with a Si O2-coated Fe3O4 inner particle, fabricated through an ion-exchange process. The SiO2 shell consists of many holes, which can be used for encapsulating drugs into inner part. As shown in Fig. 7.12, prepared nanorattles can target

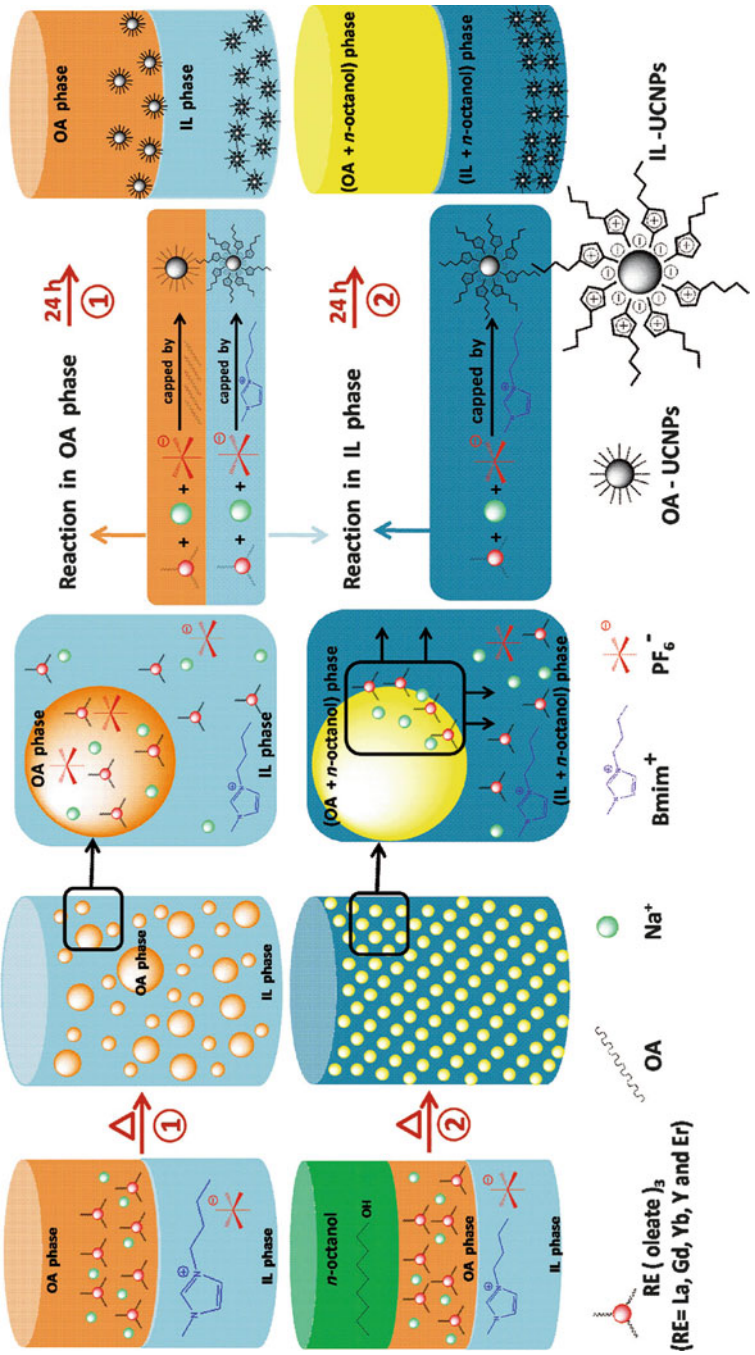

Fig. 7.10 Schematic diagram showing the formation of RE fluoride nanocrystals in the OA/IL and n-octanol-induced two-phase systems (Reproduced from Ref. [30] by permission of John Wiley & Sons Ltd)

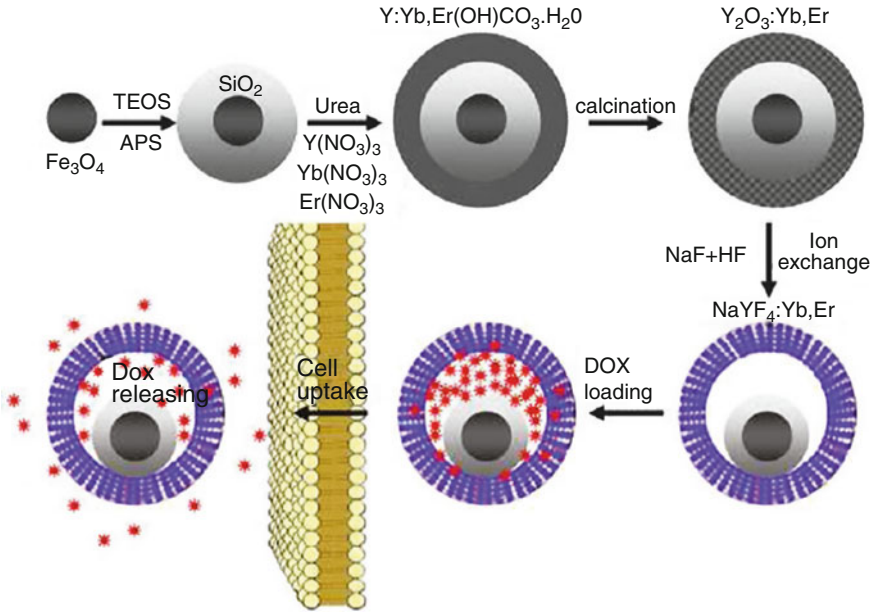

Fig. 7.11 Synthetic procedure for the drug-loaded Fe3O4@SiO2@α-NaYF/Yb, Er nanorattles (DOX-MUC-F-NR) (Reproduced from Ref. [31] by permission of American Chemical Society)

tumor tissues under given external magnetic field and also can realize MRI imaging and NIR fluorescent imaging, as well as release filled drugs in tumor site, markedly inhibiting growth of in vivo tumor tissues. Prepared nanorattles also are confirmed to be good biocompatibility; therefore, prepared nanorattles own great potential in applications such as tumor targeting and imaging and simultaneously treating in the near future [31].

7.4.2 Folic Acid-Conjugated Silica-Modified Upconversion Nanoprobes for Targeted UCL and CT Imaging

Folic acid-conjugated silica-modified LaF_3:Yb,Tm upconversion nanoparticles (UCNPs@SiO_2-FA) with high La content in single particle were strategically designed and prepared for simultaneous targeting dual-modality imaging of upconversion luminescence (UCL) and X-ray computed tomography (CT) [33]. LaF_3 UCNPs were synthesized by a novel oleic acid (OA)/ionic liquid (IL) two-phase system. Afterward, folic acid molecule was covalently anchored on the surface of UCNPs with silane coupling agent. The UCNPs@SiO_2-FA exhibits good stability, water dispersibility and solubility, noncytotoxicity, good biocompatibility, highly selective targeting, excellent X-ray attenuation, and UCL emission under excitation at 980 nm. In vivo UCL and CT images of mice show the UCNPs@SiO_2-FA can be

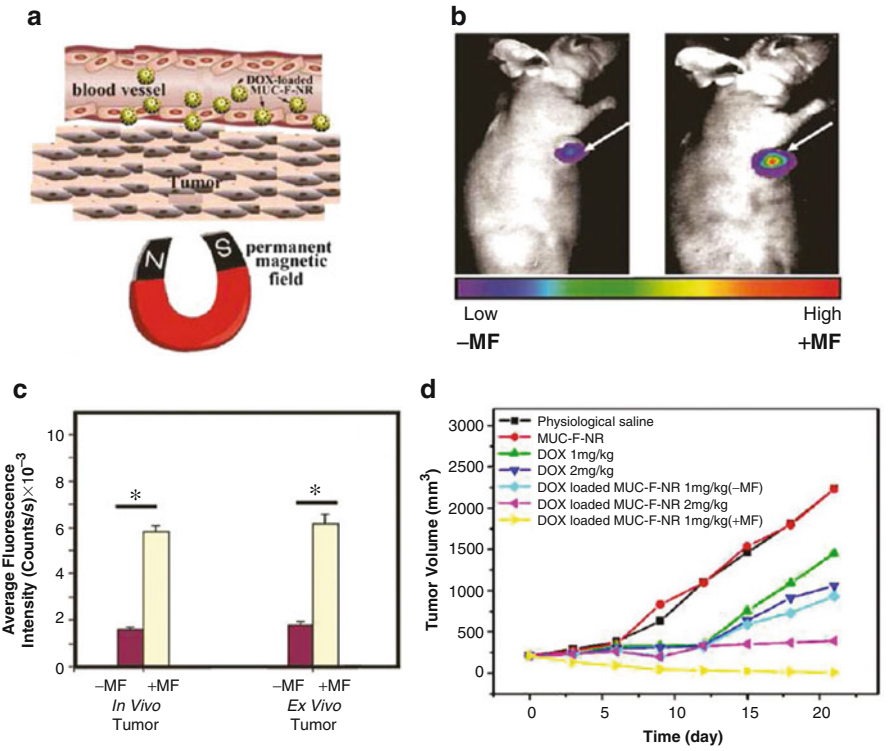

Fig. 7.12 (**a**) Schematic illustration of targeting of DOX-loaded multifunctional drug carrier to tumor cells assisted by an externally applied magnetic field (MF). (**b**) Tumor location as defined by MUC-F-NR intensity increases with 1 h magnetic field treatment. Mice bearing H22 xenograft tumor were injected with DOX-loaded MUC-F-NR (1 mg/kg) and subjected (+MF) or not subjected (MF) to the magnetic field for 1 h. At 24 h postinjection, mice were imaged in vivo. (**c**) The luminescence signal was measured from the whole tumor in vivo and ex vivo (Excitation was provided by the CW infrared laser at 980 nm and upconversion luminescence signals were collected at 650nm ± 10nm. (Fluence rates for 980 nm excitation light were 80 mW/cm^2). (**d**) Tumor volume changes of saline-treated mice compared to mice treated with MUC-F-NR, DOX, and DOX-loaded MUC-F-NR over 21 d in the absence and presence of magnetic field. Data show mean ± SD (n = 5,*p e 0.05) (Reproduced from Ref. [31] by permission of American Chemical Society)

used in targeting dual-modality imaging. These results suggest that the as-prepared nanoprobe is a good candidate with excellent imaging and targeting ability for targeting dual-modality imaging of UCL and CT.

Multimodal contrast agent-based folic acid-conjugated silica-modified LaF_3:Yb,Tmup conversion nanoparticles (UCNPs@SiO_2-FA) with high La content in single particle were strategically designed and developed. We have demonstrated that UCNPs@SiO_2-FA is a good candidate with excellent imaging and targeting ability for UCL imaging and CT imaging in vivo. The prepared UCNPs@SiO_2-FA exhibits good stability, water dispersibility and solubility, noncytotoxicity, good

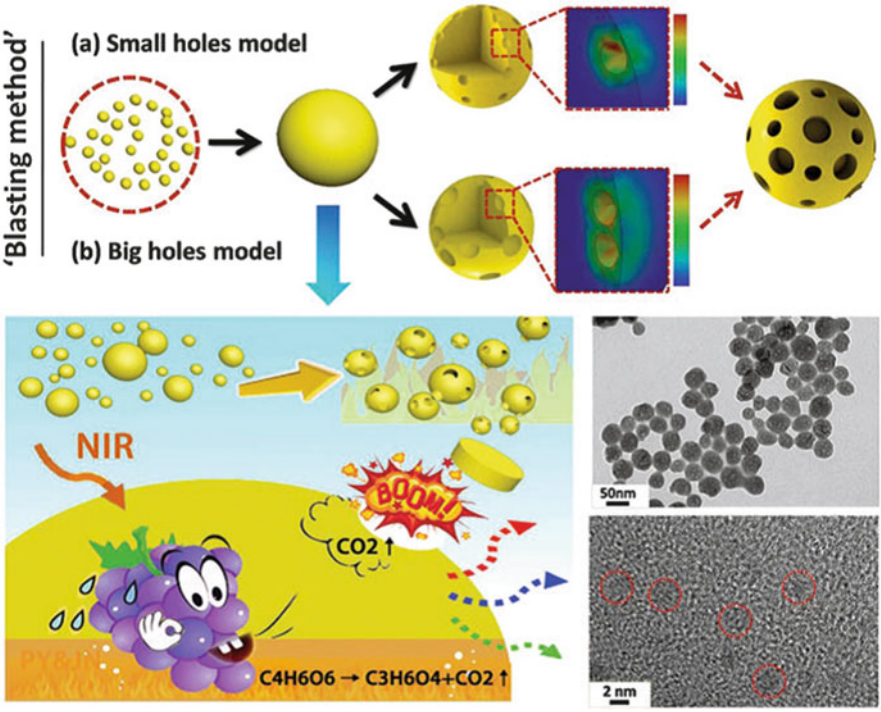

Fig. 7.13 Illustration of the "blasting" method for fabricating porous UNs (Reproduced from Ref. [36] by permission of The Royal Society of Chemistry)

biocompatibility, highly selective targeting, excellent X-ray attenuation, and UCL emission under excitation at 980 nm. Our results indicated that the synthesized UCNPs@SiO_2-FA is effective for simultaneous targeting dual-modality imaging of UCL and CT [34, 35]. It could bring novel opportunities to the next generation of theranostic nanoprobes for simultaneous diagnosis and treatment in vivo.

The phase transition of upconversion nanocrystals (UNs) from cubic to hexagonal structure is of fundamental importance in improving the luminescence intensity by about one or two orders of magnitudes, but the mechanism is still not well understood, and efforts to completely transfer the phase from cubic to hexagonal structure remain a difficult and challenging task. We also developed a novel synthesis method of UCPs, hydrothermal system in which an anion induces the phase transition process to give simultaneous control over the size, morphology, phase, and emission properties. As shown in Fig. 7.13, it shows the mechanism of the "blasting" method for fabricating porous UCPs. We confirm for the first time that the crystal cell oriented rotation driven by an anion in a hydrothermal system promoted the phase transition, and the energy zone figure of the phase transition from cubic to hexagonal structure has been figured out, as shown in Fig. 7.14; we have successfully applied the structural mechanic finite element calculations to validate the reaction process. We have also demonstrated that porous UNs can be rationally

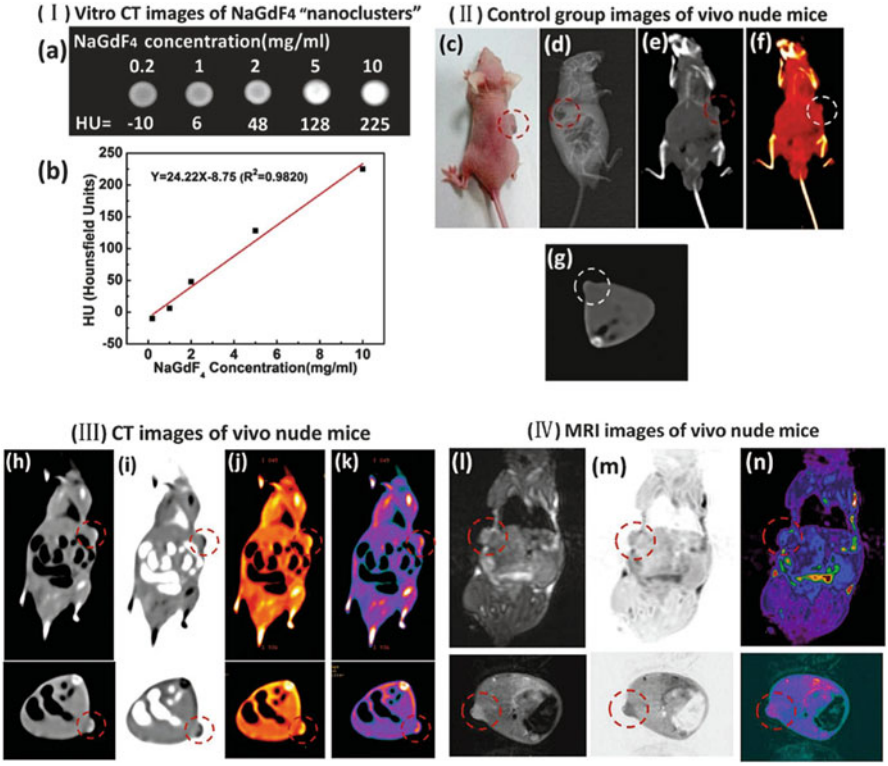

Fig. 7.14 (**I**) In vitro CT images (*a*) of lanthanide-doped NaGdF4 upconversion "nanoclusters" (sub-5 nm) suspended in aqueous solution. CT attenuation (HU) plot (*b*) of NaGdF4 changes along with the concentration of each sample from 0.2 to 10 mg ml^{-1} to further investigate the CT contrast effect. (**II**) Images of control group before injection: (*c*) photograph of the nude mouse model loaded with gastric cancer MGC-803 cells, (*d*) X-ray image, and (*e–g*) CT images of nude mouse as the control group. (**III**) CT images (*h–k*) and (**IV**) MRI images (*l–n*) with NaGdF4 upconversion "nanoclusters" through intravenous injection under the function of passive targeting (Reproduced from Ref. [36] by permission of The Royal Society of Chemistry)

tuned in size (down to 15 nanometers), phase (cubic or hexagonal), and emission properties at precisely defined conditions and were effective for in vitro and in vivo CT imaging [36].

7.5 Multifunctional Gold Nanoprobes for Targeted Imaging and Therapy

GNPs are within the same size domain as many biomaterials, including enzymes, antibodies, and protein receptors. Combined with the unique properties of materials in the nanoscale range, gold nanoparticles provide scope for making measurements

more efficiently than existing molecular materials. Since light absorption from biologic tissue components is minimized at NIR wavelengths, most NPs for in vivo imaging have been designed in order to strongly absorb in the NIR region so as to be used as effective contrast agents [37].

Optical coherence tomography (OCT) is an imaging modality that provides cross-sectional subsurface imaging of biological tissues at micrometer-scale resolution. Briefly, the OCT system can generate a signal based on refractive index mismatches and scattering events. The extra scattering is achieved by using AuNPs, which possess both absorption and scattering properties in the NIR region and provide optical contrast for improved diagnostic imaging at higher light intensities. This property has been used in order to increase the contrast of tumors in mice. Au nanoshells accumulate preferentially in the tumor and so increase the contrast more than in other tissues [38]. In situ OCT based on spherical AuNPs in ophthalmology and dental imaging has also been reported [39]. Moreover, an extension of OCT – photothermal OCT – can fill the spatial niche for in vivo imaging of NP delivery [40].

X-ray, computed tomography (CT), and micro-CT techniques can offer excellent improvements in terms of medical diagnosis. The basic process of these techniques is to detect the X-rays that pass through a sample by exposing a charge-coupled device detector. Due to their high atomic number and electrodensity (e.g., 79 and 19.32 g/cm^3, respectively, vs. the typical X-ray contrast agent, iodine, with values of 53 and 4.9 g/cm^3, respectively), AuNPs have higher attenuation coefficients and are proposed to be used as better contrast agents for X-ray imaging, CT, and micro-CT [39]. AuNPs have demonstrated greater contrast than the iodine-based agents that are currently used in the clinic, as well as reduced toxicity and prolonged circulation times. Moreover, imaging Au at 80–100 keV reduces the signal interference derived from bone absorption and therefore would allow for dose reduction. In addition, fluorescent bioimaging is also achieved with luminescent AuNCs, which can be used for multimodal fluorescence/CT imaging without the need for having two different elements. Via glutathione capping and folic acid conjugation, the as-prepared nanoprobe could target a xenotransplanted tumor model in nude mice, as evaluated by fluorescence/CT dual-mode imaging. Although it is not very common, X-ray fluorescent imaging of AuNPs represents a bioimaging technique with great potential. This method could be of great interest once there are imaging systems in place that have sufficient sensitivity to NP concentrations and, at the same time, are capable of distribution measurements at appropriate tissue depths for in vivo and in vitro studies. Consequently, Ricketts et al. reported that a high detecting sensitivity of AuNPs can be achieved using X-ray fluorescence, enabling a greater depth imaging in comparison with optical modalities [41, 42].

Photoacoustic imaging (PAI) is a hybrid imaging technique; however, it has only become an efficient method of biomedical imaging in recent decades. The development for PAI accounts for the improvement in the machining process and innovative technology relating to the contrast agent. Briefly, after excitation by a laser, a photoabsorber (e.g., an internal photoabsorber, such as hemoglobin, or an external photoabsorber, such as photoacoustic contrast agents) is heated, leading to thermoelastic

expansion. Such expansion can cause acoustic pressure elevations and therefore produce ultrasound waves (usually a rise of 1 mK can cause an 800 Pa pressure rise), which are then detected by a sound transducer before finally being reconstructed as photoacoustic images. NPs, especially AuNPs with NIR absorbance due to their intrinsic LSPR, are very promising for use as photoacoustic signal amplifiers. Two important commercialized, small animal PAI systems are MSOT (iThera Medical GmbH©, Munich, Germany) and Nexus 128 (Endra Life Sciences©, MI, USA). The iThera system is based on multispectral optoacoustic tomography and Nexus 128 is based on hemispherical PAI. Despite the adoption of different strategies for 3D imaging, they are both excellent examples of focusing on a crucial problem in bioimaging and thus obtaining images with high resolution and even in-depth functional information. Unlike OCT, PAI is speckle-free. For example, PEG-coated Au nanoshells have been used as contrast agents in order to image their circulating distribution in the vasculature in the rat brain using PAI. The images of the distribution of nanoshells circulating in the vasculature of a rat brain achieved by deep-penetrating NIR light presented a gradual enhancement of the optical absorption in the brain vessels. Au nanorods and Au nanoprisms have also been extensively used in bioimaging due to their ability to have their maximum plasmon resonance tuned further into the NIR region. Although PAI is promising for applications in biomedical imaging, drug delivery, and PTT, there are some challenges for PAI based on the AuNP platform. First, although its application in cancer imaging has been abundant over the last 5 years, most of the results are obtained from subcutaneous cancer models and are confined within angiography. However, the advantage of PAI is its deep penetration at a high resolution and the potential for in situ cancer diagnostics. The reason for this is the limitation of the laser energy. According to the American National Standards Institute (ANSI), the energy for skin exposure is advised to be lower than 20 mJ/cm^2, but deep penetration is difficult to achieve in this range, so the detection limit needs to be improved by enhancing the NIR absorption of AuNPs. Au nanorods, nano-cages, nanoprisms, or nanostars are particularly useful as PAI contrast agents. Second, the scan speed needs to be improved for PAI. Although this mainly needs the improvement of the mechanical drive, AuNPs at the range of 100 nm, which can prolong the circulation time, may solve this problem via another method. Diagnostics usually require the combination of anatomic imaging as well as functional imaging at the same time. The former can provide the precise location of organs, and the latter is for imaging the anatomical structures of the area of interest. This goal is achieved by either multimodal bioimaging or bioimaging techniques that can achieve the both [43–46].

Theranostics refers to the combination of diagnostics and therapeutics. Due to their LSPR, the strong NIR light absorption of AuNPs makes them a great potential application in PTT, which possesses efficacy and noninvasiveness. There are numerous PTTs based on AuNPs (e.g., antibody- or small-molecule-conjugated AuNPs in tumor therapy). Combined with the aforementioned PAI, AuNPs have great potential to be used as theranostic platforms.

7.5.1 *Folic Acid-Conjugated Gold Nanorods for Targeted Imaging and Therapy*

Multifunctional nanoprobes are designed to own various functions such as tumor targeting, imaging, and selective therapy, which offer great promise for the future of cancer prevention, diagnosis, imaging, and treatment. As shown in Fig. 7.15, silica was applied to replace cetyltrimethylammonium bromide (CTAB) molecules on the surface of gold nanorods (GNRs) by the classic Stöber method, thus eliminating their cytotoxicity and improving their biocompatibility. Folic acid molecule was covalently anchored on the surface of GNRs with silane coupling agent. The resultant folic acid-conjugated silica-modified GNRs show highly selective targeting, as shown in Fig. 7.16, and prepared GNR probes could target and combine tumor cells, exhibiting golden color, enter into tumor cytoplasm by endocytosis pathway as shown in Fig. 7.17, enhance radiation therapy (RT) and photothermal therapy (PTT) effects on MGC803 gastric cancer cells as shown in Fig. 7.18 and Fig. 7.19, and also

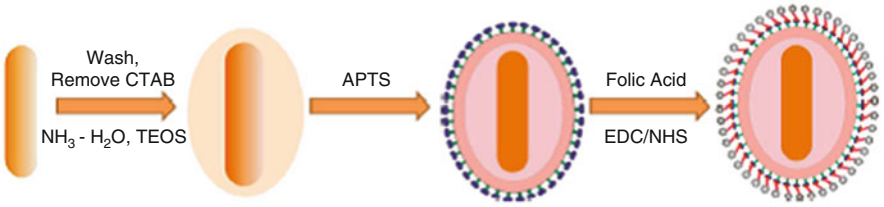

Fig. 7.15 Synthetic procedure of GNR-SiO2-FA (Reproduced from Ref. [47] by permission of Elsevier)

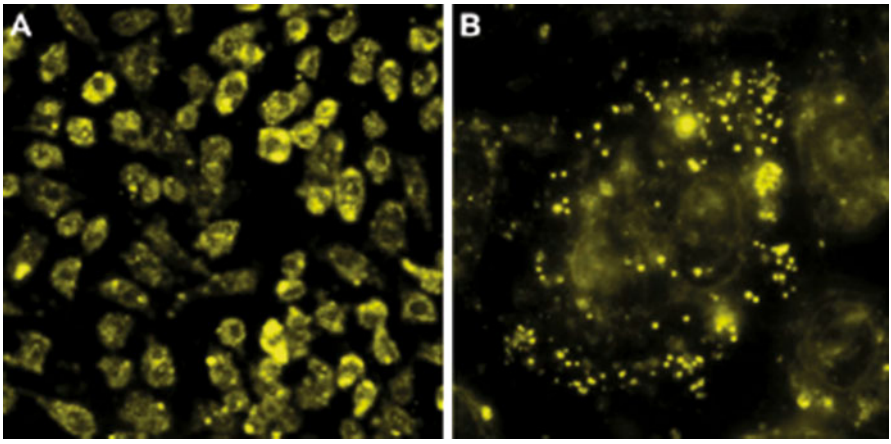

Fig. 7.16 Dark-field scattering images. (**A**) Low magnification image of targeted MGC803 cells incubated with 50 mM GNR-SiO2-FA for 2 h and (**B**) high magnification image of targeted MGC803 cells incubated with 50 mM GNR-SiO2-FA for 30 min, monitored by dark-field microscopy (Reproduced from Ref. [47] by permission of Elsevier)

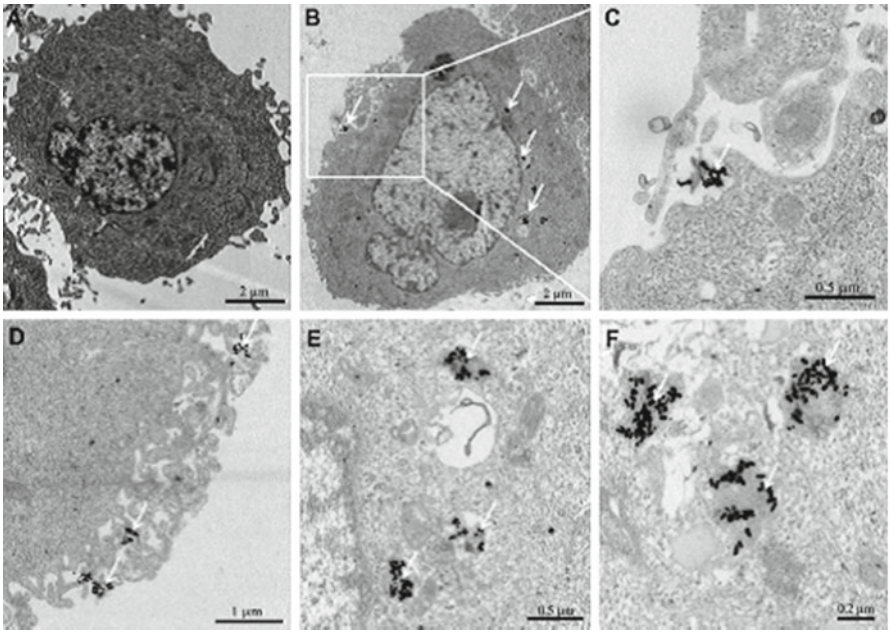

Fig. 7.17 The thin-section TEM images of MGC803 cells incubated with 50 mM of GNR-SiO2-FA for 2 h. (**a**) Control MGC803 cells and (**b–f**) representative ultrastructures of MGC803 cells incubated with GNR-SiO2-FA. *Arrows* denote the GNR-SiO2-FA or their aggregates (Reproduced from Ref. [47] by permission of Elsevier)

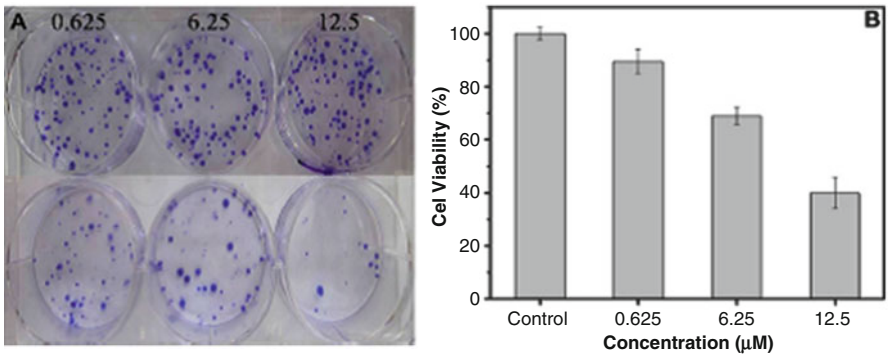

Fig. 7.18 The proliferation photographs (**A**) and cell viability (**B**) of MGC803 cells incubated with 100 mL of varying concentration of GNR-SiO2-FA for 24 h upon 6 Gy of X-ray irradiation. In the photographs (**A**), the *top* column of the cells is without irradiation, and the *bottom* column of the cells is with irradiation (Reproduced from Ref. [47] by permission of Elsevier)

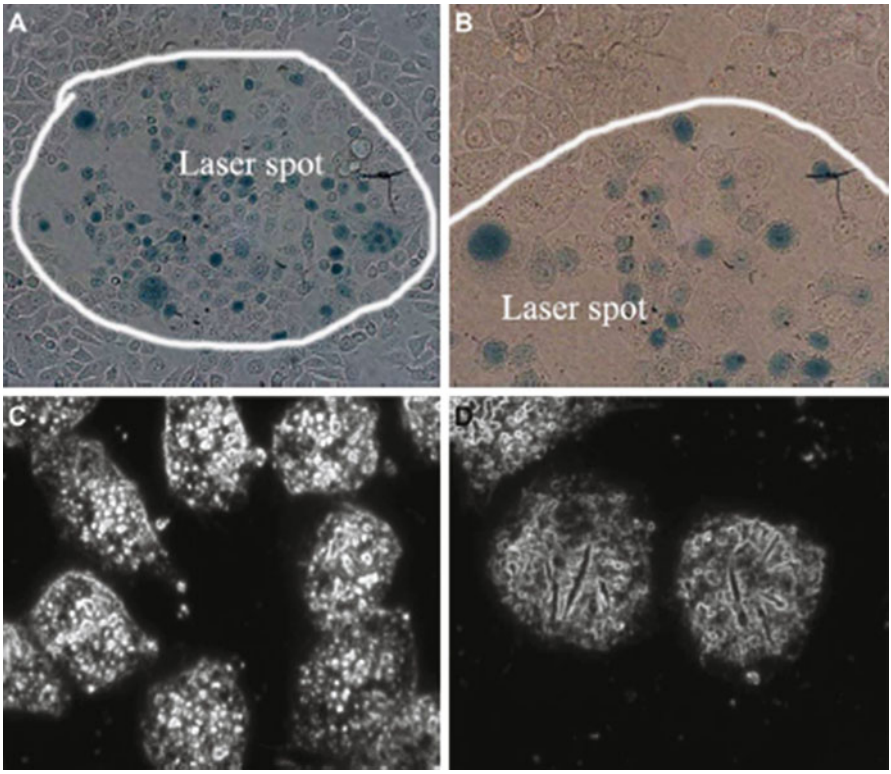

Fig. 7.19 Photothermal therapy effects on MGC803 cells incubated with 12.5 mM of GNR-SiO2-FA for 24 h at 37 °C in the dark prior to irradiation for 3 min with 808 nm laser. (**A**) MGC803 cells on the laser spot, (**B**) MGC803 cells on the boundary of laser spot, and (**C**, **D**) dark-field images of MGC803 cells after irradiation (Reproduced from Ref. [47] by permission of Elsevier)

exhibit strong X-ray attenuation for in vivo X-ray and computed tomography (CT) imaging. In conclusion, the as-prepared nanoprobe is a good candidate with excellent imaging and targeting ability for X-ray/CT imaging-guided targeting dual-mode enhanced RT and PTT [47].

7.5.2 Cetuximab-Conjugated Gold Nanoparticles for SERS Imaging and Therapy

Inspired by the ability of SERS nanoantennas to provide an integrated platform to enhance disease targeting in vivo, we developed a highly sensitive probe for in vivo tumor recognition with the capacity to target specific cancer biomarkers such as epidermal growth factor receptors (EGFR) on human cancer cells and xenograft tumor models. As shown in Fig. 7.20, we used ~90 nm gold nanoparticles capped by a Raman reporter, encapsulated and entrapped by larger polymers and an FDA

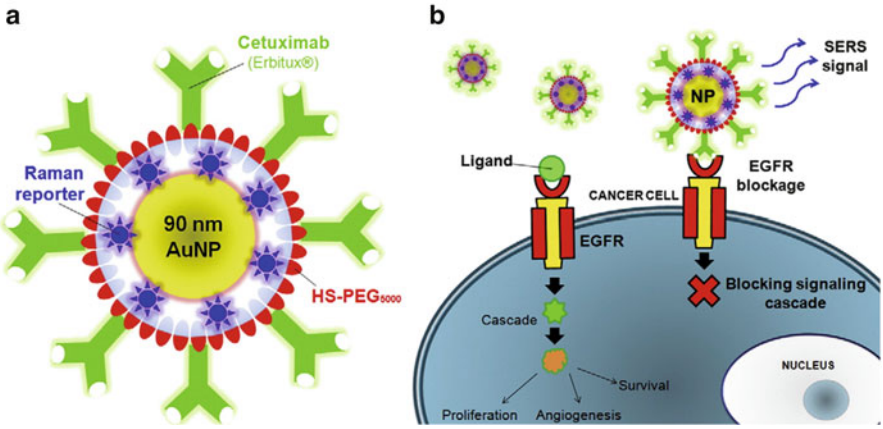

Fig. 7.20 (**A**) Antibody–drug gold SERS nanoantennas – 90 nm AuNPs surrounded by a Raman reporter, encapsulated and entrapped by a larger polyethylene glycol (PEG) polymer and covered with a FDA approved antibody-drug conjugate, the Cetuximab. (**B**) The drug-Raman NPs can easily bind to EGF receptors(EGFR), blocking the EGF protein from reaching the cancer cells and inhibit the signalling cascade. The activation of this cascade will consequently stop proliferation and survival of targeted cells. (Reproduced from Ref. [48] by permission of Elsevier)

antibody–drug conjugate – cetuximab (Erbitux®) – that specifically targets EGFR and turns off a main signaling cascade for cancer cells to proliferate and survive. These drug/SERS gold nanoantennas present a high Raman signal both in cancer cells and in mice bearing xenograft tumors. Moreover, the Raman detection signal is accomplished simultaneously by extensive tumor growth inhibition in mice, making these gold nanoantennas ideal for cancer nanotheranostics, i.e., tumor detection and tumor cell inhibition at the same time [48].

7.5.3 BRCAA1 Antibody-Conjugated Gold Nanoprisms for Targeted Photoacoustic Imaging and Photothermal Therapy

The development of high-resolution nanosized photoacoustic contrast agents is an exciting technological advance as well as a challenge. Herein, two functionalized gold nanoprisms (AuNprs), PEG/RGD-AuNprs and PEG/Brcaa1-AuNprs, were synthesized and used as a combinatorial methodology for in situ photoacoustic imaging, angiography, and local hyperthermia using orthotopic and subcutaneous murine gastric carcinoma models. PEG/RGD-AuNprs are available for tumor angiography, and PEG/Brcaa1-AuNprs are used to target and for in situ imaging of gastric carcinoma orthotopic tumor models. In situ photoacoustic imaging allowed for anatomical and functional imaging at the tumor site. In vivo tumor angiography imaging showed enhancement of the photoacoustic signal in a time-dependent way. Furthermore, photoacoustic imaging showed that tumor vessels were clearly

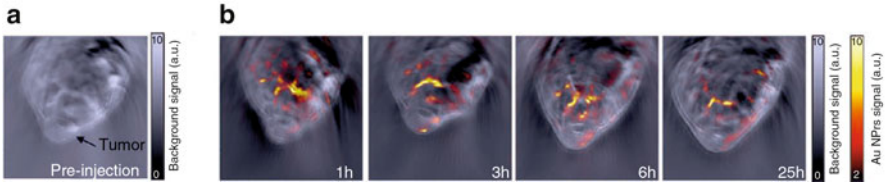

Fig. 7.21 Optoacoustic signals in vivo; (**a**) anatomical (preinjection of the contrast agent) optoacoustic image, taken a wavelength of 710 nm, of a CD-1 mouse xenografted subcutaneously with a HT-29 tumor cell line in the lower back region. The tumor is visible at the *bottom* of the image. Blood vessels are also visible around the middle of the image and correspond to the iliac veins and arteries in the vicinity of the intestines; (**b**) multispectral optoacoustic images of a CD-1 nude mouse bearing a subcutaneous HT-29 tumor cell line and injected with AuNPrs. Anatomical background images acquired at a wavelength of 710 nm and autoscaled per image (*black* and *white*). AuNPr distribution is shown on a *red* to *yellow* scale with a low signal threshold chosen at 20 % of maximum signal (Reproduced from Ref. [49] by permission of John Wiley & Sons Ltd)

damaged after local hyperthermia. This is the first proof of concept using two gold nanoprism probes as high sensitive contrasts and therapeutic agents for in situ tumor detection and inhibition. These smart antibody/peptide AuNprs can be used as an efficient nanotheranostic platform for in vivo tumor detection with high sensitivity as well as for tumor targeting therapy, which results in tumor size reduction and increase mice survival after local hyperthermia with a single-dose injection. As shown in Fig. 7.21, we prepared PEG-modified AuNprs, which were successfully used for in vivo photoacoustic imaging of gastrointestinal tract [49].

7.5.4 CD44v6 Antibody-Conjugated Gold Nanostars for Photoacoustic Imaging and Photothermal Therapy of Gastric Cancer Stem Cells

Developing safe and effective nanoprobes for targeted imaging and selective therapy of gastric cancer stem cells (GCSCs) has become one of the most promising anticancer strategies [50–57]. As shown in Fig. 7.22, gold nanostar-based PEGylated multifunctional nanoprobes were prepared with conjugated CD44v6 monoclonal antibodies (CD44v6-GNS) as the targeting ligands. It was observed that the prepared nanoprobes had high affinity toward GCSC spheroid colonies and destroyed them completely with a low power density upon near-infrared (NIR) laser treatment (790 nm, 1.5 W/cm^2, 5 min) in vitro experiment. Orthotopic and subcutaneous xenografted nude mice models of human gastric cancer were established. As shown in Fig. 7.23, biodistribution and photothermal therapeutic effects after being intravenously injected with the prepared nanoprobes were assessed. Photoacoustic imaging revealed that CD44v6-GNS nanoprobes could target the gastric cancer vascular system actively at 4 h postinjection, while the probes inhibited tumor growth remarkably upon NIR laser irradiation and even extended survivability of the gastric cancer-bearing mice. The CD44v6-GNS nanoprobes exhibited great potential for applications of gastric cancer targeted imaging and photothermal therapy in the near future [58–68].

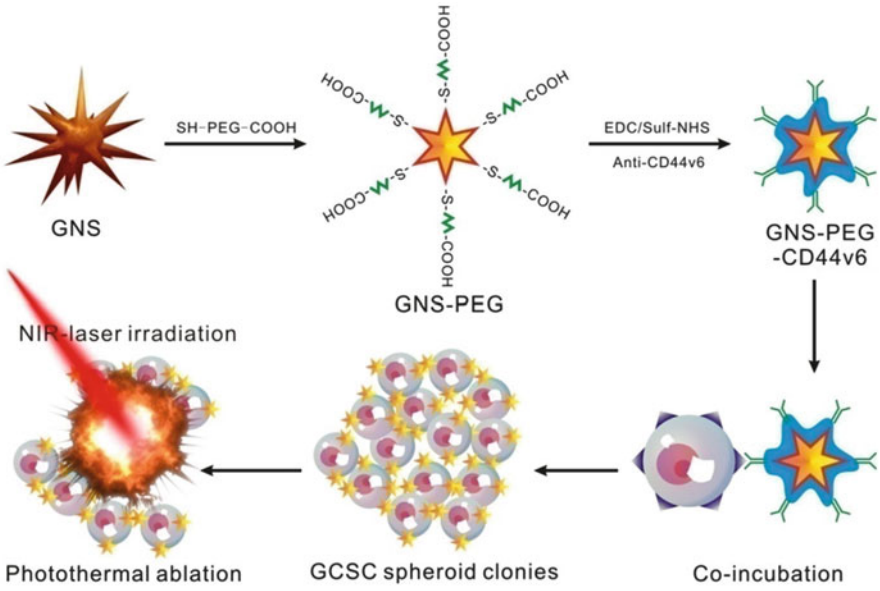

Fig. 7.22 Schematic illustration of the GNS-PEG-CD44v6 nanocomplex synthesis process and the mechanism of GCSC targeted PTT (Reproduced from Ref. [68] by permission of IVY Press)

7.5.5 Folic Acid/ce6-Conjugated Gold Nanoclusters for NIR Fluorescent Imaging and Photodynamic Therapy

Gold nanoclusters (GNCs) attract increasing attention due to their potential applications in sensing, catalysis, optoelectronics, and biomedicine. As shown in Fig. 7.24, the formation of highly fluorescent glutathione (GSH)-capped GNCs is achieved through the delicate control of the reduction kinetics and thermodynamic selection of the Au(I)–SG complexes. Furthermore, the GNC-based nanoprobes are developed by the covalent coupling of folic acid (FA) and PEG (polyethylene glycol) on the surface of GNCs directly, followed by trapping photosensitizer (chlorin e6, Ce6) within PEG networks and attaching to the GNC surface. The fabricated nanoprobes (Ce6@GNCs-PEG 2 K-FA) possess a uniform particle size (hydrodynamic diameter $\approx 6.1 \pm 1.2$ nm), without affecting the yield of singlet oxygen of the trapped Ce6. In vitro studies show the enhanced cellular uptake and satisfactory photodynamic therapy (PDT) effectiveness toward MGC-803 cells when compared with free Ce6. As shown in Fig. 7.25, the biodistribution and excretion pathway studies of the nanoprobes in MGC-803 tumor-bearing nude mice reveal their superior penetration and retention behavior in tumors, while the preserved features of renal clearance and stealthy to reticuloendothelial system are mainly attributed to the small hydrodynamic diameters and the FA-capped PEGylated ligands. The enhanced PDT efficacy and the nontoxicity to mice provide an exciting new nano-platform with promising clinical translational potential [69–76].

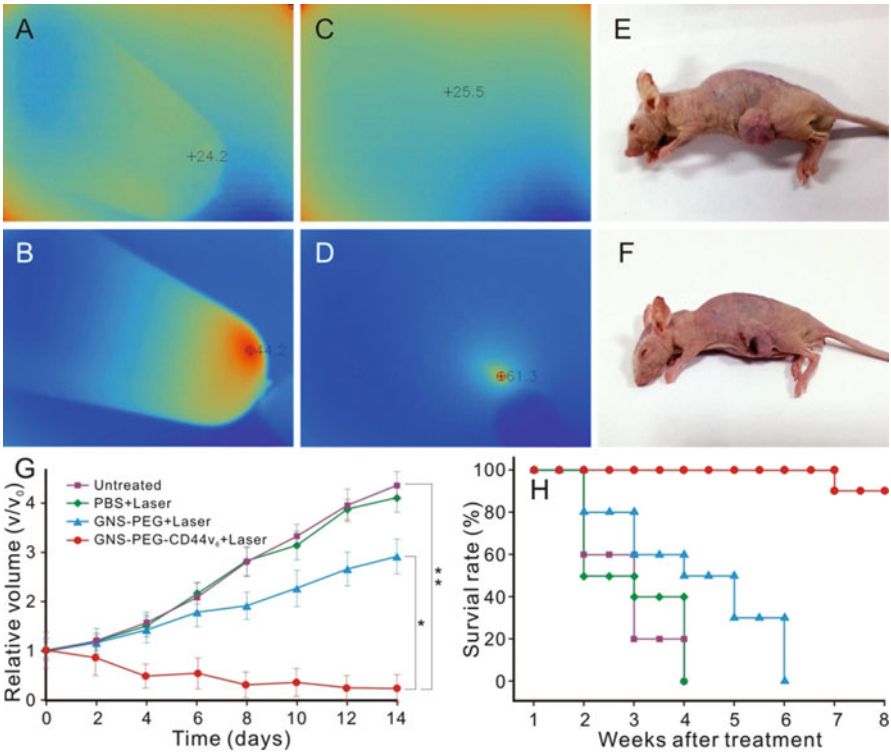

Fig. 7.23 Infrared microscopic imaging: deionized water (**A**) and GNS (**B**) in a tube upon NIR laser irradiation (790 nm, 0.3 W/cm^2, 3 min); subcutaneous tumor of GC without (**C**) and with (**D**) injection of GNS-PEG-CD44v6 upon NIR laser irradiation (790 nm, 1.5 W/cm^2, 3 min). The nude mouse of GC subcutaneous xenograft, injected with nanoparticles before (**E**) and after (**F**) laser irradiation treatment (790 nm, 1.5 W/cm^2, 3 min); (**G**) tumor growth curves of four groups after treatment with GNS-PEG-CD44v6, GNS-PEG, and PBS, respectively, upon NIR laser irradiation (790 nm, 0.8 W/cm^2, 5 min); and the untreated control group. Error bars represent standard deviation ($n = 10$/group). *$p < 0.05$, **$p < 0.01$ (student's t test); (**H**) survival rate of GC tumor-bearing mice within 8 weeks after treatment (Reproduced from Ref. [68] by permission of IVY Press)

7.5.6 *Gold Nanoparticles as a High Efficient siRNA Delivery System*

Gold glyconanoparticles (GlycoNPs) are full of promise in areas like biomedicine, biotechnology, and materials science due to their amazing physical, chemical, and biological properties. Here, siRNA GlycoNPs (AuNP@PEG@Glucose@siRNA) in comparison with PEGylated GlycoNPs (AuNP@PEG@Glucose) were applied in vitro to a luciferase-CMT/167 adenocarcinoma cancer cell line and in vivo via intratracheal instillation directly into the lungs of B6 albino mice grafted with luciferase-CMT/167 adenocarcinoma cells. As shown in Fig. 7.26, siRNA GlycoNPs but not PEGylated GlycoNPs induced the expression of proapoptotic proteins such

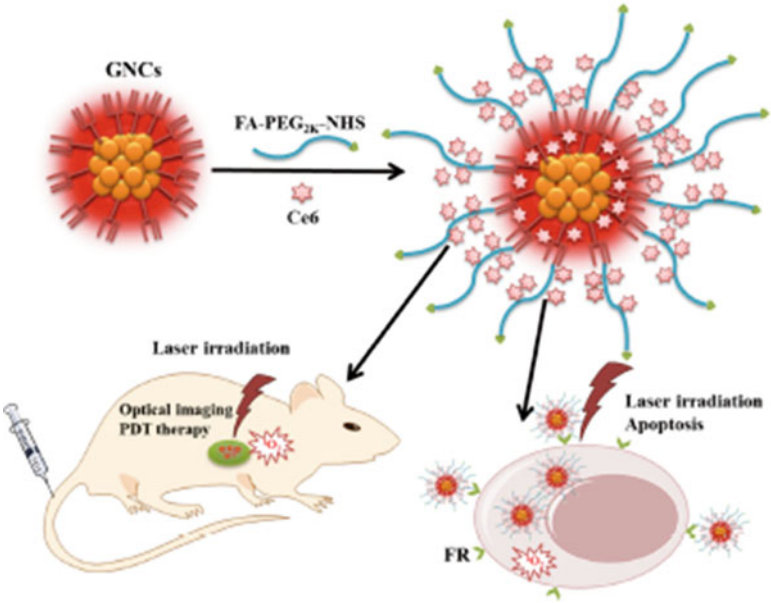

Fig. 7.24 Schematic illustration of the preparation of the GNC-based nanoprobes and their applications in vitro and in vivo (Reproduced from Ref. [76] by permission of John Wiley & Sons Ltd)

as Fas/CD95 and caspases 3 and 9 in CMT/167 adenocarcinoma cells in a dose-dependent manner, independent of the inflammatory response, evaluated by bronchoalveolar lavage cell counting. Moreover, in vivo pulmonary delivered siRNA GlycoNPs were capable of targeting c-Myc gene expression (a crucial regulator of cell proliferation and apoptosis) via in vivo RNAi in tumor tissue, leading to an ~80% reduction in tumor size without associated inflammation [15, 42, 69, 77–84].

Up to now, functionalized gold nanoparticles have been optimized as an effective intracellular in vitro delivery vehicle for siRNAs to interfere with the expression of specific genes by selective targeting and provide protection against nucleases. However, few examples of suchlike in vivo applications have been described so far. We report the use of siRNA/RGD gold nanoparticles capable of targeting tumor cells in a lung cancer syngeneic orthotopic murine model. Therapeutic RGD-nanoparticle treatment resulted in successful targeting evident from significant c-myc oncogene downregulation followed by tumor growth inhibition and prolonged survival of lung tumor-bearing mice, possibly via αvβ3 integrin interaction. Our results suggest that RGD gold nanoparticle-mediated delivery of siRNA by intratracheal instillation in mice leads to successful suppression of tumor cell proliferation and respective tumor size reduction. These results reiterate the capability of functionalized gold nanoparticles for targeted delivery of siRNA to cancer cells toward effective silencing of the specific target oncogene. What is more, we demonstrate that the gold nanoconjugates trigger a complex inflammatory and immune response that might promote the therapeutic effect of the RNAi to reduce tumor size with low doses of siRNA [82, 85].

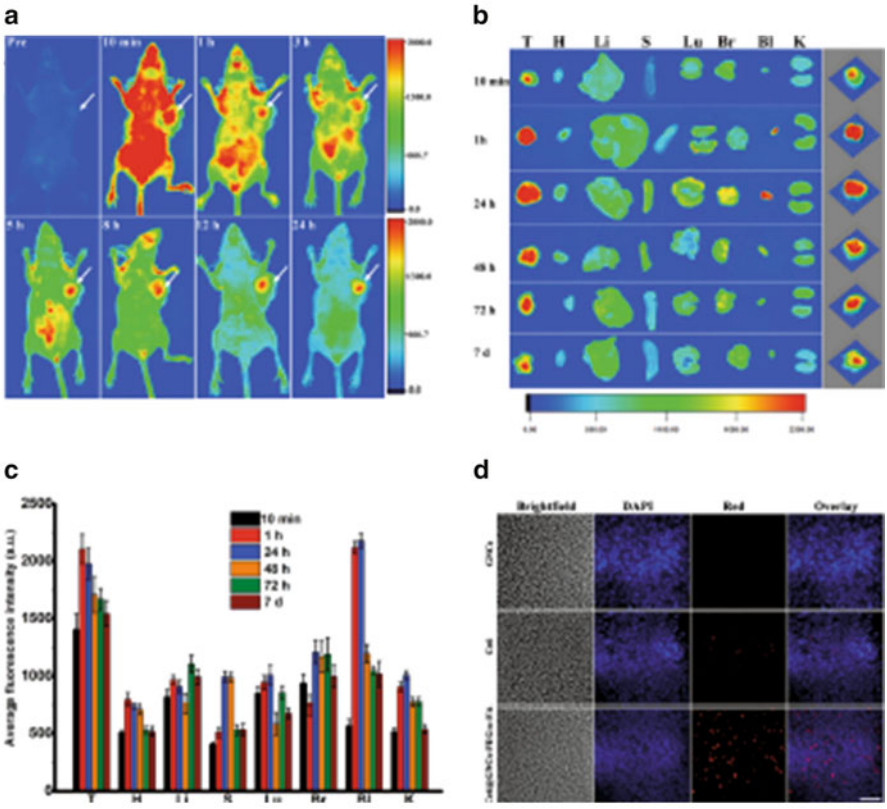

Fig. 7.25 (**a**) In vivo fluorescence imaging of MGC-803 tumor-bearing mouse after intravenous injection of Ce6@GNCs-PEG 2K-FA over a period of 24 h. (**b**) Representative ex vivo fluorescence images of major organs and tumors of mice after different postinjection times. T (tumor), H (heart), Li (liver), S (spleen), Lu (lung), Br (brain), Bl (bladder), K (kidney). The *right* columns were the corresponding 3D surface plot images of pixel intensities obtained from the tumor regions using NIH ImageJ software. (**c**) Quantitative biodistribution of Ce6@GNCs-PEG 2K-FA in different organs and tumors based on ROI analysis of the average fluorescence intensity from tumors and normal tissues (three mice per group). (**d**) Representative fluorescence images of tumor cryosections (10 μm). Images presented are bright-field, *blue fluorescence* (DAPI), *red fluorescence* (>590 nm), and merged (overlap) images. Scale bar, 100 μm (Reproduced from Ref. [76] by permission of John Wiley & Sons Ltd)

7.6 RNA Nanoparticles for Targeted Imaging and siRNA Therapy of Gastric Cancer

In recent years, there have been several new nano-delivery systems with different materials and physicochemical properties to be developed [86–89].However, effective strategies to block tumor progression and prevent metastasis are still very few, and there exist several challenges including specific cancer targeting, tissue penetration, intracellular delivery, toxicities, and side effects due to organ accumulation,

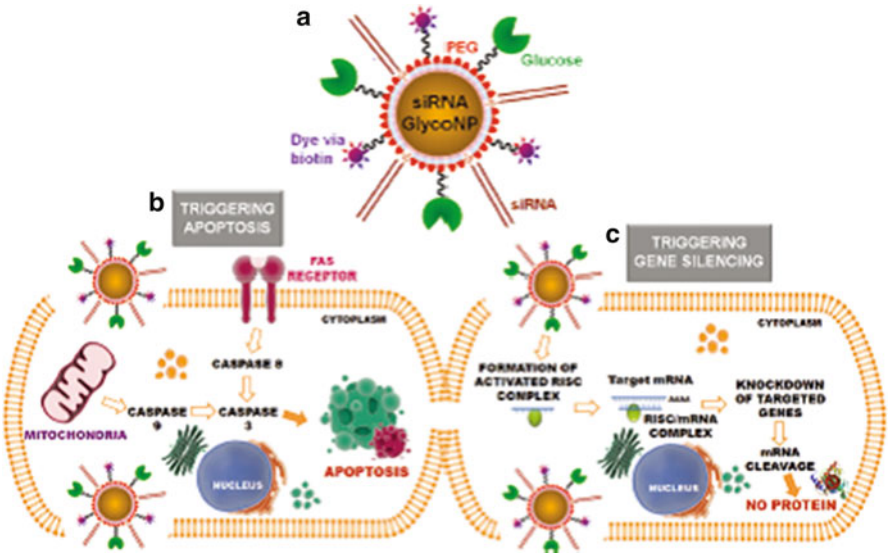

Fig. 7.26 (**a**) Multifunctional siRNA glyconanoparticles (siRNA GlycoNPs) trigger apoptotic pathways (**b**) with the expression of cell death receptors (Fas) and caspases. The death domain-containing receptor Fas can sense an external signal and activate the apoptosis pathway through the Fas-related death domain. This pathway is mediated by the activation of caspase 8, followed by direct cleavage of downstream effect or caspases. The apoptosis pathway can also be initiated in the cytoplasm through activation of intracellular changes resulting in the release of proapoptotic factors from the mitochondria. The release of these factors leads to the activation of caspase 9 and ultimately results in the activation of effector caspases (e.g., caspase 3) and consequently to cell death by apoptosis. (**c**) The siRNA GlycoNPs also have the capacity to trigger gene silencing via activation of the RNA interference pathway, by double-stranded RNA (i.e., siRNA), promoting nucleolytic degradation of the target mRNA and/or translational suppression (Reproduced from Ref. [84] by permission of The Royal Society of Chemistry)

nonspecific cell entry, particle heterogeneity, aggregation, dissociation due to dilution after systemic injection, and unfavorable pharmacological profiles. In recent years, RNA nanotechnology, as an emerging nano-platform, has shown great prospect in clinical theranostic applications [90]. RNA nanoparticles can be fabricated with precise control of shape, size, and stoichiometry, as demonstrated by the packaging RNA (pRNA) of the bacteriophage phi29DNA packaging motor, which forms dimers, trimers, and hexamers, via hand-in-hand interactions of the interlocking loops [45, 46]. The pRNA contains an ultra-stable three-way junction (3WJ) motif, which can be assembled from three short fragments with extremely high affinity. Recently, Prof. Peixuan Guo group has obtained the crystal structure of the pRNA-3WJ motif and a variety of therapeutic RNA nanoparticles using the pRNA-3WJ and pRNA-X motifs as scaffolds have been constructed. The pRNA-3WJ nanoparticles display thermodynamically stable properties, including high melting temperature with low free energy, resistance to denaturation in 8 M urea, and resistance to dissociation at very low concentrations in the blood. Boiling-resistant RNA

nanoparticles with controllable shapes and defined stoichiometry have recently been reported. Various functional groups, such as imaging agents; targeting ligands, such as receptor-binding aptamers; and therapeutic modules, such as siRNA, miRNA, or ribozymes, can be integrated into the 3WJ scaffold without affecting the folding and functionality of the core motif and incorporated functional moieties. Upon 2'-fluoro (2'-F) modifications of uracil (U) and cytosine (C) nucleotides, the RNA nanoparticles become resistant to RNase degradation with enhanced in vivo half-life while retaining authentic functions of the incorporated modules. Furthermore, the pRNA nanoparticles are nontoxic, are non-immunogenic, and display favorable biodistribution and pharmacokinetic profiles in mice. These favorable findings prompted the use of this novel platform for the treatment of stomach cancer, which is one of the challenging tasks in clinical oncology [91–100].

Such targeted delivery systems need a ligand–receptor pair that specifically existed in cancer cells. Many, but not all, cancer cells, including stomach, ovary, lung, breast, kidney, endometrium, colon, and hematopoietic cells, overexpressed folate receptors (FRs) than normal cells for high uptake of folate, since folate is an essential component during DNA replication and methylation in highly proliferating cells. Folic acid (FA), a synthetic oxidized form of folate, has been widely used as a ligand conjugate in various cancer targeting materials. *BRCAA1* (*breast cancer-associated antigen 1, AF208045*) has been confirmed to exhibit overexpression in breast cancer and gastric cancer and no or lower expression in normal gastric mucosa and normal breast tissues. Our previous studies have demonstrated that gastric cancer MGC803 cells were transfected with constructed plasmids of shRNA-BRCAA1, the cell growth was greatly inhibited, and the rate of cell apoptosis was significantly higher than those of untransfected group and mock plasmid transfected group. We also screened out a new antigen epitope SSKKQKRSHK and also screened out matched two monoclonal antibody cell lines and successfully prepared monoclonal antibody-conjugated fluorescent magnetic nanoparticles and realized the targeted imaging and hyperthermal therapy of in vivo gastric cancer. Therefore, the *BRCAA1* gene is a potential therapeutic target for gastric cancer.

My group cooperated with Prof. Peixuan Guo group, adopted an innovative RNA nanotechnology approach to overcome some of the aforementioned challenges, and reported for the first time a new strategy to target and deliver therapeutic BRCAA1 siRNA to in vivo stomach cancer tissues using FA-conjugated pRNA-3WJ nanoparticles, as shown in Fig. 7.27, and prepared RNA nanoparticles displayed 5 nm in diameter, tree fork shaped, using folate as target molecule. Our objective is to construct multifunctional, thermodynamically, and chemically stable RNA nanoparticles harboring sequences that allow specific binding to stomach cancer-specific cell surface antigens or receptors resulting in the internalization of RNA nanoparticles into target cells and delivery of the siRNA, miRNA, and drugs for attaining synergistic effects for the treatment of stomach cancer, as shown in Fig. 7.28, and prepared RNA nanoprobes could actively target in vivo gastric cancer cells, less aggregation in other organs, which show that prepared RNA nanoparticles own good targeting ability. We also investigated the effects of prepared RNA nanoparticles on the regression of gastric cancer tissues in vivo, as shown in Fig. 7.29,

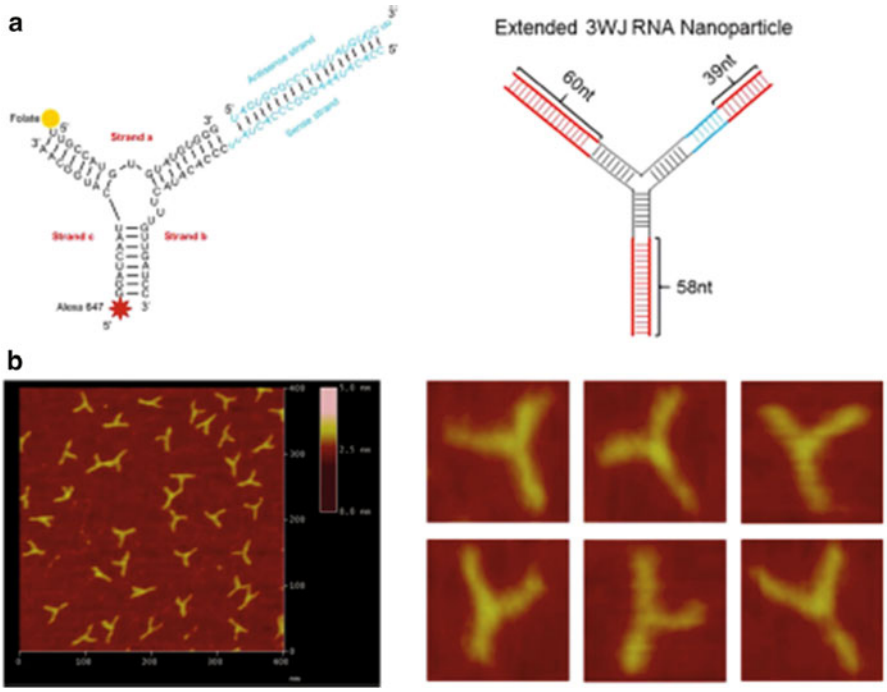

Fig. 7.27 Global structure of the therapeutic RNA nanoparticles with BRCAA1 siRNA. (**a**) Design of the RNA nanoparticles. *Left* is the one used in animal trial. *Right* is the extended one to prepare the AFM images. (**b**) AFM image of extended 3WJ RNA nanoparticles. The RNA complex in *left* of a is estimated to be around 10 nm. Due to convolution of the tip size (~10 nm in diameter) in AFM images, features smaller than the size of the tip cannot be resolved. To characterize the structure of the RNA constructs, the 3WJ nanoparticles were extended by 39–60 base pairs (in *red color*), which is within the persistence length of dsRNA and will not affect the 3WJ folding as described before 31, to generate the AFM image as shown (Reproduced from Ref. [101] by permission of Macmillan Publishers Ltd)

prepared RNA nanoparticles can inhibit the growth of in vivo gastric cancer cells, and the tumor grew slower and slower. We also investigate the potential molecular mechanism by Western blotting, which may be associated with Rb upregulation and Bcl-2 downregulation as well inducing cell apoptosis, and our results fully confirm that prepared RNA nanoparticles own potential clinical applications such as tumor theranostics in the near future.

RNA interference via the use of small interfering RNA (siRNA) is a powerful and useful tool to block gene function through sequence-specific posttranscriptional gene silencing, playing an important role in the downregulation of gene expression. siRNAs can be transfected into mammalian cells by a variety of methods that influence the strength and duration of the silencing response, which in turn is affected by the amount of siRNA effectively delivered and by the potential of each siRNA to suppress its target. Nevertheless, naked siRNAs show extremely short half-lives due to RNases activity, poor chemical stability, and dissociation from the vector. In fact,

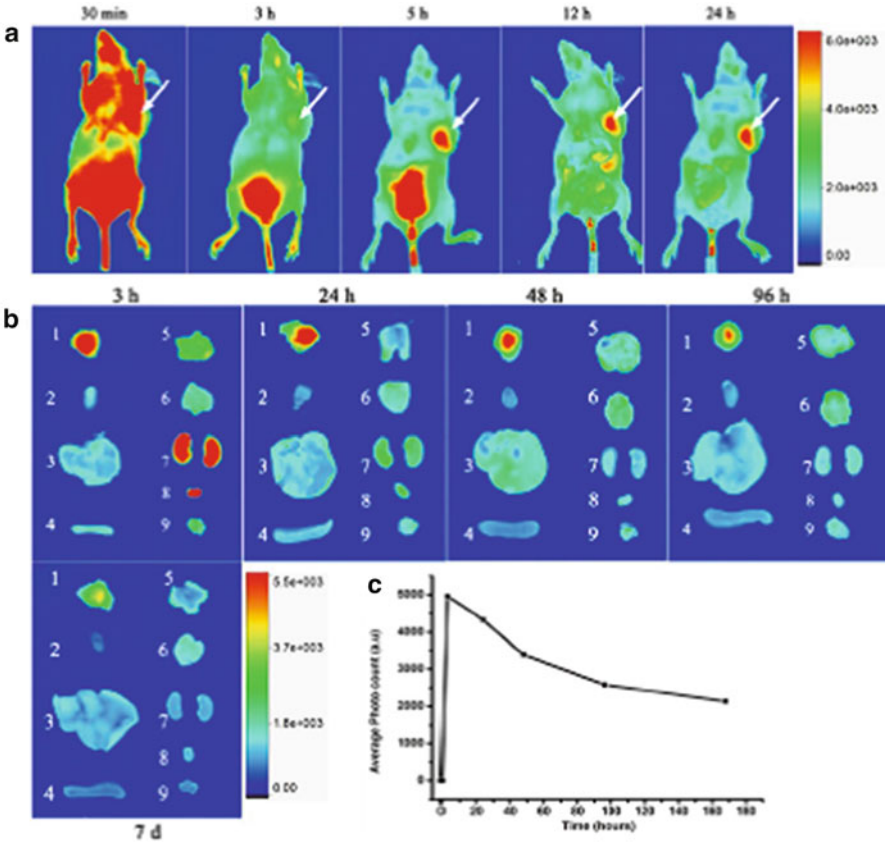

Fig. 7.28 (**a**) Representative in vivo fluorescence images of MGC803-tumor-bearing mouse after iv injection with FA-AlexaFluor647-labeled pRNA nanoparticle. The tumor areas are indicated with *arrows*. (**b**) Representative ex vivo images of tumors and organs. Labels: 1, tumor; 2, heart; 3, liver; 4, spleen; 5, lung; 6, stomach; 7, kidneys; 8, bladder; 9, muscle. (**c**) The average fluorescence intensities from the tumor areas of postinjection (Reproduced from Ref. [101] by permission of Macmillan Publishers Ltd)

the major obstacle to clinical application is the uncertainty about how to deliver siRNA with maximal therapeutic impact [101].

7.7 Carbon Dot-Based Nanoprobes for Targeted Imaging and Photodynamic Therapy

Carbon dots (C-dots), a very recent rising star, as a class of zero-dimensional carbon nanomaterials, possess some of the same major advantageous characteristics of quantum dots (QDs), such as high photostability, tunable emission, and large

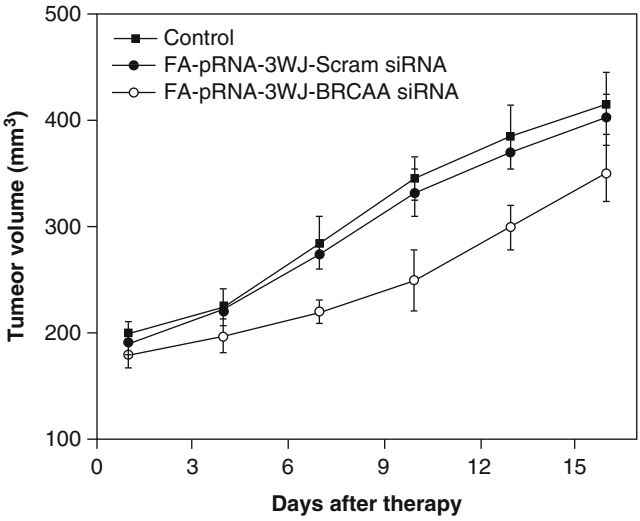

Fig. 7.29 Tumor size curve as the posttreatment time increases (Reproduced from Ref. [101] by permission of Macmillan Publishers Ltd)

two-photon excitation cross sections. Moreover, C-dots exhibit nonblinking fluorescence and excellent water solubility and are cheaply produced. Particularly, C-dots without heavy metal content are more environmentally friendly and can be much safer for biological applications. As shown in Fig. 7.30, we strategically designed and prepared novel multifunctional chlorin e6-conjugated C-dots (C-dots-Ce6) as the light-triggered theranostics for simultaneous enhanced near-infrared fluorescent imaging and photodynamic therapy (PDT) by FRET mechanism [102–108].

Carbon dots exhibit great potential in applications such as molecular imaging and in vivo molecular tracking. However, how to enhance fluorescence intensity of carbon dots has become a great challenge. We report for the first time a new strategy to synthesize fluorescent carbon dots (C-dots) with high quantum yields by using ribonuclease A (RNase A) as a biomolecular templating agent under microwave irradiation. The synthesized RNase A-conjugated carbon dots (RNase A@C-dots) exhibited quantum yields of 24.20 %. The fluorescent color of the RNase A@C--dots can easily be adjusted by varying the microwave reaction time and microwave power. Moreover, the emission wavelength and intensity of RNase A@C-dots displayed a marked excitation wavelength-dependent character. As the excitation wavelength alters from 300 to 500 nm, the photoluminescence (PL) peak exhibits gradually redshifts from 450 to 550 nm, and the intensity reaches its maximum at an excitation wavelength of 380 nm. Its Stokes shift is about 80 nm. Notably, the PL intensity is gradually decreasing as the pH increases, almost linearly dependent, and it reaches the maximum at a pH = 2 condition; the emission peaks also show clearly a redshift, which may be caused by the high activity and perfective dispersion of RNase A in a lower pH solution. In high pH solution, RNase A tends to form RNase A warped carbon dot nanoclusters. Cell imaging confirmed that the RNase A@C--

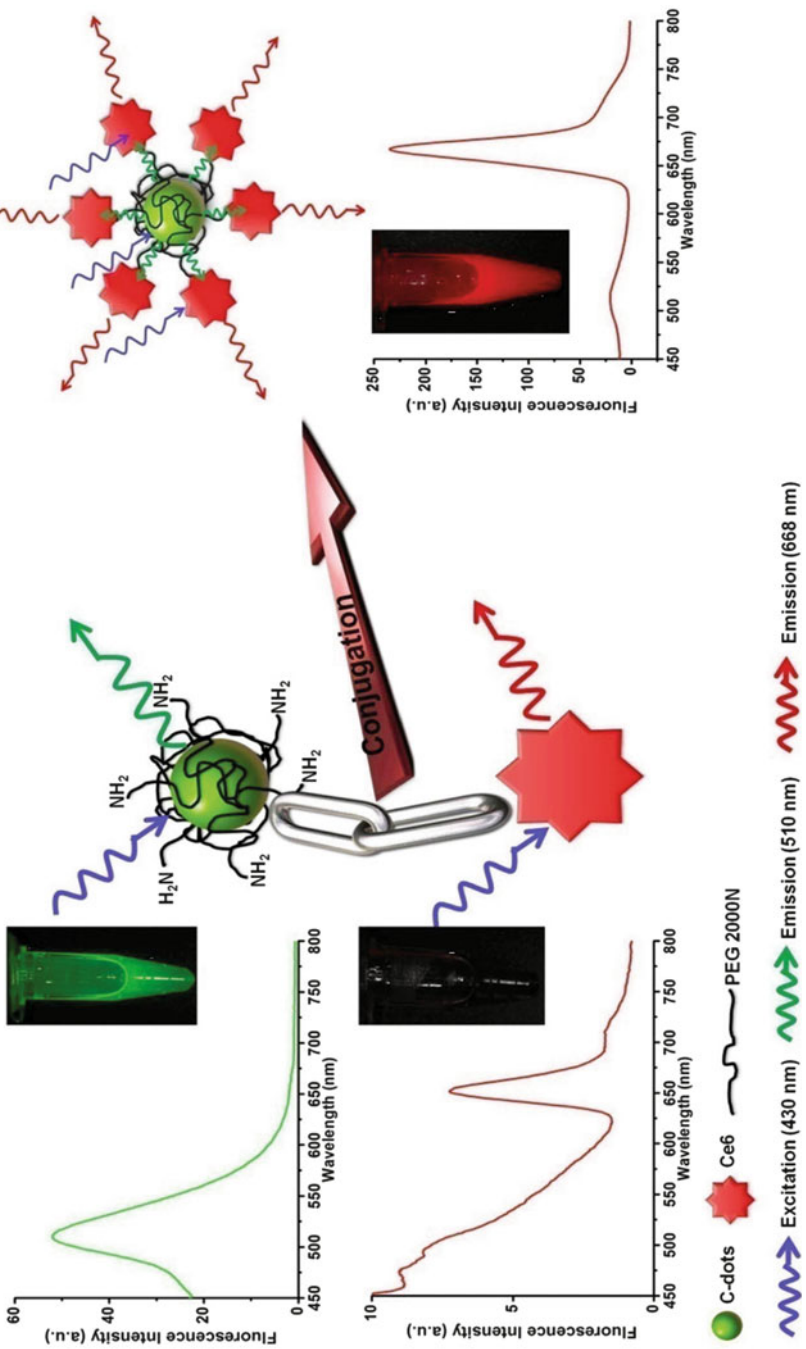

Fig. 7.30 Förster (fluorescence) resonance energy transfer (FRET) process between C-dots and Ce6 (Reproduced from Ref. [108] by permission of John Wiley & Sons Ltd)

dots could enter into the cytoplasm through cell endocytosis. 3D confocal imaging and transmission electron microscopy observation confirmed partial RNase A@C--dots located inside the nucleus. MTT and real-time cell electronic sensing (RT-CES) analysis showed that the RNase A@C-dots could effectively inhibit the growth of MGC-803 cells. Intra-tumor injection test of RNase A@C-dots showed that RNase A@C-dots could be used for imaging in vivo gastric cancer cells. The as-prepared RNase A@C-dots are suitable for simultaneous therapy and in vivo fluorescence imaging of nude mice loaded with gastric cancer or other tumors. We have developed a microwave-assisted one-step synthesis of C-dots with citric acid as carbon source and tryptophan (Trp) as both nitrogen source and passivation agent. The C-dots with uniform size show superior water solubility, excellent biocompatibility, and high quantum yield. Afterward, the PEI (polyethylenimine)-adsorbed C-dot nanoparticles (PEI@C-dot) were applied to deliver survivin siRNA into human gastric cancer cell line MGC-803. The results have confirmed the nanocarrier exhibited excellent biocompatibility and a significant increase in cellular delivery of siRNA, inducing efficient knockdown for survivin protein to 6.1 %. In addition, PEI@Cdots complexes mediated survivin silencing, the arrested cell cycle progression in G1 phase, and cell apoptosis was observed [109]. Carbon dots may be one kind of good contrast agent and drug delivery system.

7.8 Dendritic Cell and Tumor Cell Fused Vaccine for Targeted Imaging and Enhanced Immunotherapy of Gastric Cancer

Dendritic cells (DCs) have been broadly used for clinical therapy of tumor patients and achieved good therapeutic efficacy, displaying the great promising potential in clinical cancer immunotherapy. How to enhance DC immunotherapeutic effect in cancer targeted immunotherapy and prevention is still a great challenge. My group is for the first time to prepare the allogenic DCs and gastric cancer cell fused vaccine combined with cytokine-induced killer cells (CIKs), which realized targeted imaging and enhanced immunotherapy of gastric cancer (GC). The fused vaccine was prepared by PEG-mediated fusion between the mature DCs and inactive gastric cancer MGC803 cells. The immunotherapeutic and prophylactic potential of the fused cells (FCs) was evaluated in tumor-bearing, post-surgery, and tumor-free mice models. The migration and homing process of near-infrared region quantum dots (NIR-QDs) labeled FCs were investigated by real-time animal imaging system. Results showed that the FCs and FC + CIKs could trigger the tumor-specific CTLs (cell toxic lymph cells) against GC cells, target the tumor tissue initiatively and enhance the prophylactic effects, suppress the tumor growth remarkably in vivo, make several tumor tissues in nude model disappeared. This is only very initiative

result, further clinical study will continue to carry out. The allogenic DCs and tumor cell fused vaccine can be used for targeted imaging and enhanced immunotherapy of GC, and the FC + CIKs strategy owns great potential in clinical applications such as early therapy and prevention of tumor-metastasis and relapse in near future [110–113].

7.9 Oral Microcapsule Endoscopy Combined with Nanoprobes for Gastrointestinal Imaging

One kind of oral microcapsule endoscopy was successfully developed by Prof. Guozheng Yan in Shanghai Jiao Tong University as shown in Fig. A, which is composed of several sensors and power system; realizes real-time ultrasensitive detection of five parameters such as temperature, pH value, pressure, hemoglobin, and imaging in gastrointestinal tract; obtained registration certificate of medical devices in China in 2003; and has been used in almost 100 hospitals [114]. Based on the oral capsule endoscopy system, Prof. Yan designed one kind of new type of oral fluorescent nanoprobes and obtained clear fluorescent imaging of gastrointestinal lesions. As shown in Fig. 7.31c, the control image without fluorescent signal was shown in Fig. 7.31b, and the prepared oral endoscopy is with the size of less than 2 cm, as shown in Fig. 7.31a. Furtherly integrated with oral RGD/BRCAA1 antibody-conjugated gold nanoprism probes, the oral capsule endoscopy system can obtain clearer molecular imaging of gastric intestinal tumors and simultaneously realize photothermal therapy in vivo, which provide a new pathway for quick theranostics of clinical gastrointestinal tumor or patients with precancerous lesions.

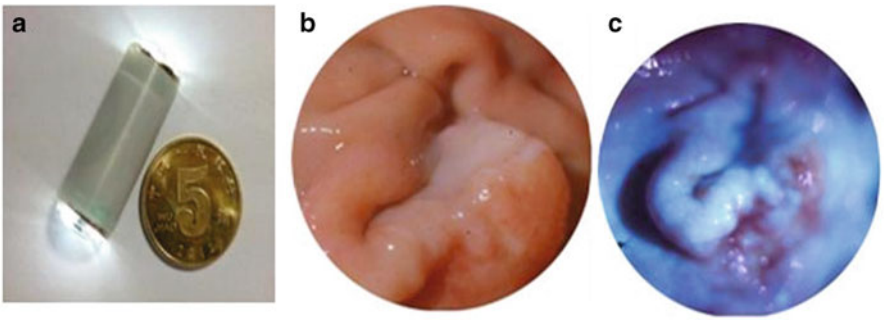

Fig. 7.31 Microcapsule endoscopy combined with fluorescent probes for in situ gastric lesion imaging. (**a**) Oral microcapsule endoscopy; (**b**) normal image of human gastric lesion; (**c**) fluorescent image of human gastric lesion incubated with nanoprobes (Unpublished data, Prof. Guozhen Yan provided)

7.10 Clinical Translational Prospects of Multifunctional Nanoprobes

There have been more than several ten thousand publications regarding nanoprobes in the last decade, and very few of the assessed nanoprobes progressed from bench into bedside. According to Drolet and Lorenzi's "continuum" theory, when a new basic science discovery transfers into proposed human application, proven clinical application, and clinical practice and finally raises public health impact, there are three "translation chasm" gaps that must be bridged. These gaps are human (T1), clinical trials (T2), and translation to practice (T3). Although there have been very promising applications of nanoprobes in many areas, they are still at an early stage of development on the way to reaching the bedside; in other words, they are mostly in the T1 stage, although they may come into clinical trials.

To date, there are several nanoprobes to enter into clinical trials or obtain FDA permission. For example, in 2011, a clinical trial of insulin-coated AuNPs was approved by Midatech Ltd (UK). In addition, AuroShell® (Au@silica nanoshells) from Nanospectra (Nanospectra Biosciences, TX, USA), which is used for thermotherapy, was approved by the FDA in 2012. This has been proven to be effective at an earlier stage in a murine glioma model and in the ablation of prostate cancer in a canine model. Another example is from McNeil's laboratory; after their reports of the biodistribution, immune response, and interactions of AuNPs with human blood, they used AuNPs as a drug delivery system in order to impair the toxicity of TNF-α. It is confirmed to be safe to inject up to three times the amount that had been lethal with previous versions. The modified drug Aurimune™ (CYT-6091) from Cytlmmune Sciences (MD, USA) is a TNF-α-bound, PEGylated colloidal AuNP. Aurimune has passed through a phase I clinical trial and is entering a phase II trial. It is reported that the systemic TNF toxicity of Aurimune was decreased dramatically compared with TNF alone (e.g., the fever side effect was managed) and the target effect was realized. Another product, AuriTol™ (CYT-21001), also from Cytlmmune Sciences, has reached the preclinical stage [37, 114].

An example of a fast, in vitro, Au-based biomedical application is the FDA-approved Verigene® detector device (Nanosphere, IL, USA), which utilizes oligonucleotide-coated AuNPs in order to capture DNA. The Verigene system enables clinicians to rapidly identify and treat the bacteria and viruses that are responsible for some of the most complicated, costly, and fatal infectious diseases [37, 115].

My group established the new method of RNase A-assisted carbon dot synthesis and finished biosafety evaluation of carbon dots in national drug safety evaluation center, confirming to be very safe under the dosage of 100 mg/kg body weight, and we also prepared hyaluronic acid/RGD-conjugated carbon dots and realized targeted imaging and operation boundary identification of in situ gastric cancer and finished 40 specimens of clinical trials, showing the prepared nanoprobes can image the metastasis lymph nodes and display the surgery boundary of gastric cancer.

Although some nanoprobes get through the clinical trials and obtained FDA permission to enter into clinical application, inorganic nanoparticle-based multifunc-

tional nanoprobes exist to be greatly disputed for clinical application, and the reasons are summarized as being unable to be degraded in vivo and long-term left-over in the body, and the further toxicological mechanism is not clarified well. Development of targeting, safe, high-efficient nanoprobes has become a great challenge. Only to solve the biosafety of nanoprobes, multifunctional nanoprobes can be possible to enter into clinical application in the near future [115–117].

7.11 Conclusion Remark

In summary, gastric cancer is one kind of common tumor worldwide, and how to realize theranostics of gastric cancer is a great challenge. Current advances show that gastric cancer therapeutic strategies should focus on early diagnosis and operation therapy, enhanced immunotherapy, and killing gastric cancer stem cells to overcome multidrug resistance (MDR). Facing these strategies, we designed and prepared series of multifunctional nanoprobes for targeted imaging and therapy of gastric cancer, including series of fluorescent magnetic nanoprobes, series of quantum dot nanoprobes and carbon dots, series of gold nanoprobes, series of upconversion nanoprobes, RNA nanoprobes, and nanoprobes for killing gastric cancer stem cells and enhanced immunotherapeutic efficacy. To date, carbon dot-based nanoprobes were evaluated to confirm their safety and were used for identifying the boundary of gastric cancer and tracking metastasis lymph nodes, exhibiting clinical application prospect. In the future, the main challenges to the translational research of these nanoprobes will focus on the better understanding of the interactions between nanoparticles and biomacromolecules and the immune system, the homogeneity of the material preparations, the paucity of the knowledge regarding pertinent biomarkers, and concern regarding biocompatibility. Green synthesis of nanoparticles, multimodality bioimaging (especially PAI), SERS analysis, and theranostics are particular fields of interest. However, designers must possess a systematic view from the beginning as they approach the goal of nanoprobes for translational medical research.

Acknowledgment This work was supported by the Chinese Key Basic Research Program (973 Project) (No. 2010CB933901 and 2015CB931802), the National Natural Scientific Foundation of China (Grant No. 81225010, 81327002, and 31170961), and 863 project of China (no. 2012AA022703 and 2014AA020700), Shanghai Science and Technology Fund (No. 13NM1401500).

References

1. Ferlay J, Shin HR, Bray F, Forman D, Mathers C, Parkin DM (2008) Estimates of worldwide burden of cancer in 2008: GLOBOCAN 2008. Int J Cancer 2010(127):2893–2917
2. Jemal A, Bray F, Center MM, Ferlay J, Ward E, Forman D (2011) Global cancer statistics. CA Cancer J Clin 61:69–90

3. Takahashi T, Saikawa Y, Kitagawa Y (2013) Gastric cancer: current status of diagnosis and treatment. Cancers (Basel) 5:48–63
4. Dicken BJ, Bigam DL, Cass C, Mackey JR, Joy AA, Hamilton SM (2005) Gastric adenocarcinoma: review and considerations for future directions. Ann Surg 241:27–39
5. Uemura N, Okamoto S, Yamamoto S, Matsumura N, Yamaguchi S, Yamakido M et al (2001) Helicobacter pylori infection and the development of gastric cancer. N Engl J Med 345:784–789
6. Comis RL, Carter SK (1974) A review of chemotherapy in gastric cancer. Cancer 34:1576–1586
7. Kuo CY, Chao Y, Li CP (2014) Update on treatment of gastric cancer. J Chin Med Assoc 77(7):345–353
8. Proserpio I, Rausei S, Barzaghi S, Frattini F, Galli F, Iovino D et al (2014) Multimodal treatment of gastric cancer. World J Gastrointest Surg 6:55–58
9. Zhang D, Fan D (2010) New insights into the mechanisms of gastric cancer multidrug resistance and future perspectives. Future Oncol 6:527–537
10. Cui DX, Zhang L, Yan XJ, Zhang LX, Xu JR, Guo YH et al (2005) A microarray-based gastric carcinoma prewarning system. World J Gastroenterol 11:1273–1282
11. Zhang YX, Gao G, Liu HJ, Fu HL, Fan J, Wang K, Chen Y, Li BJ, Zhang CL, Zhi X, He L, Cui DX (2014) Identification of volatile biomarkers of gastric cancer cells and ultrasensitive electrochemical detection based on sensing interface of Au-Ag alloy coated MWCNTs. Theranostics 4:154–62
12. Sykes EA, Chen J, Zheng G, Chan WC (2014) Investigating the impact of nanoparticle size on active and passive tumor targeting efficiency. ACS Nano 8:5696–5706
13. Cui DX, Jin GQ, Gao TW, Sun TB, Tian FR, Estrada GG, Gao HJ, Sarai A (2004) Characterization of BRCAA1 and its novel antigen epitope identification. Cancer Epidemiol Biomarkers Prev 13:1136–1145
14. Yang H, Cui D, Li Q, Huang T, Gao F, He R, Pan BF, Shao J, You XG, Liu FT (2006) Effect of blocking BRCAA1 gene with siRNA on proliferation ofMCF-7 cells and expression of Rb gene. Chin J Cancer Biother 13:181–184
15. Li Z, Huang P, He R, Lin J, Yang S, Zhang X, Ren QS, Cui D (2010) Aptmer-conjugated dendrimer-modified quantum dots for cancer cell targeting and imaging. Mater Lett 64:375–378
16. Ruan J, Wang K, Song H, Xu X, Ji JJ, Cui DX (2011) Biocompatibility of hydrophilic silica-coated CdTe quantum dots and magnetic nanoparticles. Nanoscale Res Lett 6:299
17. Wang K, Ruan J, Qian Q, Song H, Bao CC, Kong YF, Zhang CL, Hu GH, Ni J, Cui DX (2011) BRCAA1 monoclonal antibody conjugated fluorescent magnetic nanoparticles for in vivo targeted magnetofluorescent imaging of gastric cancer. J Nanobiotechnol 9:23
18. Wang C, Bao CC, Liang SJ, Zhang LX, Fu HL, Wang YT, Wang K, Li C, Deng M, Liao QD, Ni J, Cui D (2014) HAI-178 antibody-conjugated fluorescent magnetic nanoparticles for targeted imaging and simultaneous therapy of gastric cancer. Nanoscale Res Lett 9:274
19. Wang Z, Ruan J, Cui DX (2009) Advances and prospect of nanotechnology in stem cells. Nanoscale Res Lett 4:593–605
20. Oswald J, Boxberger S, Jorgensen B, Feldmann S, Ehninger G, Bornhauser M, Werner C (2004) Mesenchymal stem cells can be differentiated into endothelial cells in vitro. Stem Cells 22:377–384
21. Ruan J, Ji JJ, Song H, Qian QR, Wang K, Wang C, Cui D (2012) Fluorescent magnetic nanoparticle-labeled mesenchymal stem cells for targeted imaging and hyperthermia therapy of in vivo gastric cancer. Nanoscale Res Lett 7:309
22. Yu X, Pishko MV (2011) Nanoparticle-based biocompatible and targeted drug delivery: characterization and in vitro studies. Biomacromolecules 12:3205–3212
23. He R, You X, Shao J, Gao F, Pan B, Cui D (2007) Core/shell fluorescent magnetic silica-coated composite nanoparticles for bioconjugation. Nanotechnology 18:3135601

24. Li Q, He R, Gao F, Cui D (2008) The effects of mercaptoacetic acid modified CdTe quantum dots on specificity of polymerase chain reaction. J Shanghai Jiao Tong Univ 5:693–696
25. Kong YF, Chen J, Gao F, Li WT, Xu X, Pandoli O, Yang H, Ji JJ, Cui D (2010) A multifunctional ribonuclease – A-conjugated CdTe quantum dot cluster nanosystem for synchronous cancer imaging and therapy. Small 21:2367–2373
26. Ruan J, Song H, Qian QR, Li C, Wang K, Bao CC, Cui DX (2012) HER2 monoclonal antibody conjugated RNase-A-associated CdTe quantum dots for targeted imaging and therapy of gastric cancer. Biomaterials 33:7093–7102
27. Li C, Yang J, Wang C, Liang S, Zhang C, Chen F, Fu HL, Wang K, Cui D (2014) BRCAA1 antibody – and Her2 antibody-conjugated amphiphilic polymer engineered CdSe/ZnS quantum dots for targeted imaging of gastric cancer. Nanoscale Res Lett 9:244
28. Ma JB, Huang P, He M, Pan LY, Zhou ZJ, Feng LL, Gao G, Cui DX (2012) Folic acid-conjugated LaF3:Yb, Tm@SiO2 nanoprobes for targeting dual-modality imaging of upconversion luminescence and X-ray computed tomography. J Phys Chem B 116:14062–14070
29. Qiu PY, Zhou N, Chen HY, Zhang CL, Gao G, Cui D (2013) Recent advances in lanthanide-doped upconversion nanomaterials: synthesis, nanostructures and surface modification. Nanoscale 5:11522–11525
30. He M, Huang P, Zhang CL, Hu HY, Bao CC, Gao G, Chen F, Wang C, Ma JB, He R, Cui DX (2011) Dual phase-controlled synthesis of uniform lanthanide-doped NaGdF4 upconversion nanocrystals via an OA/ionic liquid two-phase system for in vivo dual-modality imaging. Adv Funct Mater 21:4470–4477
31. Zhang F, Braun GB, Pallaoro A, Zhang YC, Shi YF, Cui D, Moskovits M, Zhao DY, Stucky GD (2012) Mesoporous multifunctional upconversion luminescent and magnetic "nanorattle" materials for targeted chemotherapy. Nano Lett 12:61–67
32. Gao G, Zhang CL, Zhou ZJ, Zhang X, Ma JB, Li C, Jin WL, Cui DX (2012) One-pot hydrothermal synthesis of lanthanide ions doped one-dimensional upconversion submicrocrystals and their potential application in vivo CT imaging. Nanoscale 5:351–362
33. Pan LY, He M, Ma JB, Tang W, Gao G, He R, Su HC, Cui D (2013) Phase and size controllable synthesis of NaYbF4 nanocrystals in oleic acid/ionic liquid two-phase system for targeted fluorescent imaging of gastric cancer. Theranostics 3:210–222
34. Wang K, Ma JB, He M, Gao G, Xu H, Sang J, Wang YX, Zhao BQ, Cui D (2013) Toxicity assessments of near-infrared upconversion luminescent LaF3:Yb, Er in early development of zebrafish embryos. Theranostcis 5:258–266
35. Qiu PY, Zhou N, Wang YN, Zhang CL, Wang Q, Sun RJ, Gao G, Cui D (2014) Tuning lanthanide ion-doped upconversion nanocrystals with different shapes via a one-pot cationic surfactant-assisted hydrothermal strategy. CrystEngComm 16:1859–1863
36. Qiu PY, Sun RJ, Gao G, Yin T, Shen YL, Chen B, Wang K, Zhang CL, Qian XQ, Cui DX (2015) Crystal cell oriented-rotation triggered phase transition of porous upconversion nanocrystals synthesis in hydrothermal system. J Mater Chem B 3:3948–3958
37. Bao C, Conde J, Polo E, Pino P, Moros M, Baptista PV, Grazu V, Cui D, Fuente M (2014) A promising road with challenges: where are gold nanoparticles in translational research? Nanomedicine 9:2353–2370
38. Nguyen DT, Kim D-J, Kim K-S (2011) Controlled synthesis and biomolecular probe application of gold nanoparticles. Micron 42(3):207–227
39. Frens G (1973) Controlled nucleation for the regulation of the particle size in monodisperse gold suspensions. Nature 241(105):20–22
40. Nikoobakht B, El-Sayed MA (2003) Preparation and growth mechanism of gold nanorods (NRs) using seed-mediated growth method. Chem Mater 15(10):1957–1962
41. Conde J, Rosa J, Lima JC, Baptista PV (2012) Nanophotonics for molecular diagnostics and therapy applications. Int J Photoenergy 2012(619530)
42. Li ZM, Huang P, Zhang XJ, Lin J, Yang S, Liu B, Gao F, Xi P, Ren QS, Cui DX (2010) RGD-conjugated dendrimer-modified gold nanorods for in vivo tumor targeting and photothermal therapy. Mol Pharm 7:94–104

43. Zhou ZJ, Zhang CL, Qian QR, Ma JB, He M, Pan LY, Gao G, Fu HL, Wang K, Cui DX (2013) Folic acid-conjugated silica capped gold nanoclusters for targeted fluorescence/X-ray computed tomography imaging. J Nanobiotechnol 11:17
44. Zhang CL, Zhou ZJ, Qian QR, Gao G, Li C, Feng LL, Wang Q, Cui DX (2013) Glutathione-capped fluorescent gold nanoclusters for dual-modal fluorescence/X-ray computed tomography imaging. J Mater Chem B 1:5045–5053
45. Choi J, Yang J, Bang D, Park J, Suh JS, Huh YM et al (2012) Targetable gold nanorods for epithelial cancer therapy guided by near-ir absorption imaging. Small 8:746–753
46. Yuan H, Khoury CG, Wilson CM, Grant GA, Bennett AJ, Vo-Dinh T (2012) In vivo particle tracking and photothermal ablation using plasmon-resonant gold nanostars. Nanomedicine 8:1355–1363
47. Peng H, Bao L, Chunlei Z, Lin J, Luo T, Yang D, He M, Zhiming L, Gao G, Gao Bing F, Shen CD (2011) Folic acid-conjugated Silica-modified gold nanorods for X-ray/CT imaging-guided dual-mode radiation and photo-thermal therapy. Biomaterials 32:9796–9809
48. Conde J˜a, Bao C, Cui D, Baptista PV, Tian F (2014) Antibody-drug gold nanoantennas with Raman spectroscopic fingerprints for in vivo tumour theranostics. J Control Release 183:87–93
49. Bao C, Beziere N, del Pino P, Pelaz B, Estrada G, Tian F, Ntziachristos V, de la Fuente JM, Cui D (2013) Gold nanoprisms as optoacoustic signal nanoamplifiers for in vivo bioimaging of gastrointestinal cancers. Small 9:68–74
50. Vinogradov S, Wei X (2012) Cancer stem cells and drug resistance: the potential of nanomedicine. Nanomedicine (Lond) 7:597–615
51. Clarke MF, Dick JE, Dirks PB, Eaves CJ, Jamieson CH, Jones DL et al (2006) Cancer stem cells-perspectives on current status and future directions: AACR workshop on cancer stem cells. Cancer Res 66:9339–9344
52. Gilbertson RJ, Graham TA (2012) Cancer: resolving the stem-cell debate. Nature 488:462–463
53. Takaishi S, Okumura T, Tu S, Wang SS, Shibata W, Vigneshwaran R et al (2009) Identification of gastric cancer stem cells using the cell surface marker cd44. Stem Cells 27:1006–1020
54. Liu J, Ma L, Xu J, Liu C, Zhang J, Liu J et al (2013) Spheroid body-forming cells in the human gastric cancer cell line mkn-45 possess cancer stem cell properties. Int J Oncol 42:453–459
55. Li R, Wu X, Wei H, Tian S (2013) Characterization of side population cells isolated from the gastric cancer cell line sgc-7901. Oncol Lett 5:877–883
56. Xue Z, Yan H, Li J, Liang S, Cai X, Chen X et al (2012) Identification of cancer stem cells in vincristine preconditioned sgc7901 gastric cancer cell line. J Cell Biochem 113:302–312
57. Brabletz T, Jung A, Spaderna S, Hlubek F, Kirchner T (2005) Opinion: migrating cancer stem cells – an integrated concept of malignant tumour progression. Nat Rev Cancer 5:744–749
58. Duan JJ, Qiu W, Xu SL, Wang B, Ye XZ, Ping YF et al (2013) Strategies for isolating and enriching cancer stem cells: well begun is half done. Stem Cells Dev 22:2221–2239
59. Marhaba R, Klingbeil P, Nuebel T, Nazarenko I, Buechler MW, Zoeller M (2008) Cd44 and epcam: cancer-initiating cell markers. Curr Mol Med 8:784–804
60. Prud'Homme GJ (2012) Cancer stem cells and novel targets for antitumor strategies. Curr Pharm Des 18:2838–2849
61. Chen T, Yang K, Yu J, Meng W, Yuan D, Bi F et al (2012) Identification and expansion of cancer stem cells in tumor tissues and peripheral blood derived from gastric adenocarcinoma patients. Cell Res 22:248–258
62. Zhang C, Li C, He F, Cai Y, Yang H (2011) Identification of cd44 + cd24+ gastric cancer stem cells. J Cancer Res Clin Oncol 137:1679–1686
63. Chen W, Zhang X, Chu C, Cheung WL, Ng L, Lam S et al (2013) Identification of cd44+ cancer stem cells in human gastric cancer. Hepatogastroenterology 60:949–954

64. Misra S, Heldin P, Hascall VC, Karamanos NK, Skandalis SS, Markwald RR et al (2011) Hyaluronan-cd44 interactions as potential targets for cancer therapy. FEBS J 278:1429–1443
65. Jang BI, Li Y, Graham DY, Cen P (2011) The role of cd44 in the pathogenesis, diagnosis, and therapy of gastric cancer. Gut Liver 5:397–405
66. Heider KH, Kuthan H, Stehle G, Munzert G (2004) Cd44v6: a target for antibody-based cancer therapy. Cancer Immunol Immunother 53:567–579
67. Chen Y, Huang K, Li X, Lin X, Zhu Z, Wu Y (2010) Generation of a stable anti-human cd44v6 scfv analysis of its cancer-targeting ability in vitro. Cancer Immunol Immunother 59:933–942
68. Liang SJ, Li C, Zhao CL, Chen YS, Xu L, Bao CC, Wang XY, Liu G, Zhang FC, Cui DX (2015) CD44v6 monoclonal antibody-conjugated gold nanostars for targeted photoacoustic imaging and plasmonic photothermal therapy of gastric cancer stem-like cells. Theranostics 5:879–881
69. Huang P, Xu C, Lin J, Wang C, Wang X, Zhang C, Zhou X, Guo S, Cui DX (2011) Folic acid-conjugated graphene oxide loaded with photosensitizers for targeting photodynamic therapy. Theranostics 1:240–250
70. Chen F, Huang P, Zhu Y, Wu J, Zhang C, Cui DX (2011) The photoluminescence, drug delivery and imaging properties of multifunctional Eu3t/Gd3t dual-doped hydroxyapatite nanorods. Biomaterials 32:9031–9039
71. Kim C, Song HM, Cai X, Yao J, Wei A, Wang LV (2011) In vivo photoacoustic mapping of lymphatic systems with plasmon-resonant nanostars. J Mater Chem 21:2841–2844
72. Wang S, Huang P, Nie L, Xing R, Liu D, Wang Z et al (2013) Single continuous wave laser induced photodynamic/plasmonic photothermal therapy using photosensitizer-functionalized gold nanostars. Adv Mater 25:3055–3061
73. Chen R, Wang X, Yao X, Zheng X, Wang J, Jiang X (2013) Near-ir-triggered photothermal/photodynamic dual-modality therapy system via chitosan hybrid nanospheres. Biomaterials 34:8314–8322
74. Yuan H, Khoury CG, Hwang H, Wilson CM, Grant GA, Vo-Dinh T (2012) Gold nanostars: surfactant-free synthesis, 3d modelling, and two-photon photoluminescence imaging. Nanotechnology 23:075102
75. Park J, Ku M, Kim E, Park Y, Hong Y, Haam S et al (2013) Cd44-specific supramolecular hydrogels for fluorescence molecular imaging of stem-like gastric cancer cells. Integr Biol (Camb) 5:669–672
76. Zhang CL et al (2015) Gold nanoclusters-based nanoprobes for simultaneous fluorescence imaging and targeted photodynamic therapy with superior penetration and retention behavior in tumors. Adv Fun Mater 28:1314–1325
77. Shi J, Zhang H, Wang L, Li L, Wang H, Wang Z et al (2013) PEI-derivatized fullerene drug delivery using folate as a homing device targeting to tumor. Biomaterials 34:251–261
78. Song H, He R, Wang K, Ruan J, Bao CC, Li N, Ji JJ, Cui DX (2010) Anti-HIF-1 alpha antibody-conjugated pluronic triblock copolymers encapsulated with Paclitaxel for tumor targeting therapy. Biomaterials 31:2302–2312
79. Qi L, Wu L, Zheng S, Wang Y, Fu H, Cui DX (2012) Cell-penetrating magnetic nanoparticles for highly efficient delivery and intracellular imaging of siRNA. Biomacromolecules 13:2723–2730
80. Zhou J, Shum KT, Burnett JC, Rossi JJ (2013) Nanoparticle-based delivery of RNAi therapeutics: progress and challenges. Pharmaceuticals (Basel, Switzerland) 6:85–107
81. Weissleder R (2001) A clearer vision for in vivo imaging. Nat Biotechnol 19:316–317
82. Pan B, Cui D, Xu P, Ozkan C, Feng G, Ozkan M et al (2009) Synthesis and characterization of polyamidoamine dendrimer-coated multi-walled carbon nanotubes and their application in gene delivery systems. Nanotechnology 20:125101
83. Nie L, Chen X (2014) Structural and functional photoacoustic molecular tomography aided by emerging contrast agents. Chem Soc Rev 43:7132–7170

84. Code J, Tian FR, Hemandez Y, Bao CC, Baptisa P, Cui D, Stoeger T et al (2015) RNAi-based glyconanoparticles trigger apoptotic pathways for in vitro and in vivo enhanced cancer-cell killing. Nanoscale 7:9083–9091
85. Shen M, Huang Y, Han L, Qin J, Fang X, Wang J et al (2012) Multifunctional drug delivery system for targeting tumor and its acidic microenvironment. J Control Release 161:884–892
86. Murphy EA, Majeti BK, Mukthavaram R, Acevedo LM, Barnes LA, Cheresh DA (2011) Targeted nanogels: a versatile platform for drug delivery to tumors. Mol Cancer Ther 10:972–982
87. Guo P (2010) The emerging field of RNA nanotechnology. Nat Nanotechnol 5:833–842
88. Guo P, Haque F, Hallahan B, Reif R, Li H (2012) Uniqueness, advantages, challenges, solutions, and perspectives in therapeutics applying RNA nanotechnology. Nucleic Acid Ther 22:226–245
89. Guo P, Zhang C, Chen C, Garver K, Trottier M (1998) Inter-RNA interaction of phage phi29 pRNA to form a hexameric complex for viral DNA transportation. Mol Cell 2:149–155
90. Shu D, Moll WD, Deng Z, Mao C, Guo P (2004) Bottom-up assembly of RNA arrays and superstructures as potential parts in nanotechnology. Nano Lett 4:1717–1723
91. Shu Y, Haque F, Shu D, Li W, Zhu Z, Kotb M et al (2013) Fabrication of 14 different RNA nanoparticles for specific tumor targeting without accumulation in normal organs. RNA (New York) 19:767–777
92. Shu D, Shu Y, Haque F, Abdelmawla S, Guo P (2011) Thermodynamically stable RNA three-way junction for constructing multifunctional nanoparticles for delivery of therapeutics. Nat Nanotechnol 6:658–667
93. Abdelmawla S, Guo S, Zhang L, Pulukuri SM, Patankar P, Conley P et al (2011) Pharmacological characterization of chemically synthesized monomeric phi29 pRNA nanoparticles for systemic delivery. Mol Ther 19:1312–1322
94. Zhang H, Endrizzi JA, Shu Y, Haque F, Sauter C, Shlyakhtenko LS et al (2013) Crystal structure of 3WJ core revealing divalent ion-promoted thermostability and assembly of the Phi29 hexameric motor pRNA. RNA (New York) 19:1226–1237
95. Shu Y, Shu D, Haque F, Guo P (2013) Fabrication of pRNA nanoparticles to deliver therapeutic RNAs and bioactive compounds into tumor cells. Nat Protoc 8:1635–1659
96. Haque F, Shu D, Shu Y, Shlyakhtenko LS, Rychahou PG, Evers BM et al (2012) Ultrastable synergistic tetravalent RNA nanoparticles for targeting to cancers. Nano Today 7:245–257
97. Kalli KR, Oberg AL, Keeney GL, Christianson TJ, Low PS, Knutson KL et al (2008) Folate receptor alpha as a tumor target in epithelial ovarian cancer. Gynecol Oncol 108:619–626
98. Teng L, Xie J, Teng L, Lee RJ (2012) Clinical translation of folate receptor-targeted therapeutics. Expert Opin Drug Deliv 9:901–908
99. Ly A, Hoyt L, Crowell J, Kim YI (2012) Folate and DNA methylation. Antioxid Redox Signal 17:302–326
100. Gao W, Xiang B, Meng TT, Liu F, Qi XR (2013) Chemotherapeutic drug delivery to cancer cells using a combination of folate targeting and tumor microenvironment-sensitive polypeptides. Biomaterials 34:4137–4149
101. Cui D, Zhang CL, Liu B, Shu Y, Du T, Li C, Pan F, Yang Y, Ni J, Li H, Brand-Saberi B, Guo PX (2015) Regression of gastric cancer by systemic injection of RNA nanoparticles carrying both ligand and siRNA. Sci Rep 5:10732
102. Chen L, Zheng J, Zhang Y, Yang L, Wang J, Ni J, Cui D, Yu C, Cai ZL (2011) Tumor-specific expression of MicroRNA-26a suppresses human hepatocellular carcinoma growth via cyclin-dependent and -independent pathways. Mol Ther 19:1521–1528
103. Fu HL, Ma Y, Lu LG, Hou P, Li BJ, Jin WL, Cui DX (2014) TET1 exerts its tumor suppressor function by interacting with p53-EZH2 pathway in gastric cancer. J Biomed Nanotechnol 10:1217–1230
104. Khisamutdinov EF, Jasinski DL, Guo P (2014) RNA as a boiling-resistant anionic polymer material to build robust structures with defined shape and stoichiometry. ACS Nano 8:4771–4781

105. Wang X, Yang L, Chen ZG, Shin DM (2008) Application of nanotechnology in cancer therapy and imaging. CA Cancer J Clin 58:97–110
106. Wang Q, Zhang CL, Shen GX, Liu HY, Fu HL, Cui D (2014) Fluorescent carbon dots as an efficient siRNA nanocarrier for its interference therapy in gastric cancer cells. J Nanobiotechnol 12:58
107. Wang K, Gao ZC, Gao G, Wo Y, Wang YX, Shen GX, Cui D (2013) Systematic safety evaluation on photoluminescent carbon dots. Nanoscale Res Lett 8:122
108. Liu HY, Wang Q, Shen GX, Zhang CL, Li C, Ji WH, Wang Cui DX (2014) A multifunctional ribonuclease A-conjugated carbon dot cluster nanosystem for synchronous cancer imaging and therapy. Nanoscale Res Lett 9:397
109. Huang P, Lin J, Wang XS, Wang Z, Zhang CL, He M, Wang K, Chen F, Li ZM, Shen GX, Cui DX, Chen XY (2012) Light-triggered theranostics based on photosensitizer-conjugated carbon dots for simultaneous enhanced-fluorescence imaging and photodynamic therapy. Adv Mater 24:5104–5110
110. Li C, Liang SJ, Zhang CL, Liu YL, Yang M, Zhang JP, Zhi X, Pan F (2015) Cui D.DC integrated inactive gastric cancer cell fused vaccine for targeted imaging and enhanced immunotherapeutic efficacy of gastric cancer. Biomaterials 35:177–187
111. Van de Broek B, Devoogdt N, D'Hollander A, Gijs HL, Jans K, Lagae L et al (2011) Specific cell targeting with nanobody conjugated branched gold nanoparticles for photothermal therapy. ACS Nano 5:4319–4328
112. Park J, Ku M, Kim E, Park Y, Hong Y, Haam S et al (2013) Cd44-specific supramolecular hydrogels for fluorescence molecular imaging of stem-like gastric cancer cells. Integr Biol 5:669–672
113. Burke AR, Singh RN, Carroll DL, Wood JC, D'Agostino RB Jr, Ajayan PM et al (2012) The resistance of breast cancer stem cells to conventional hyperthermia and their sensitivity to nanoparticle-mediated photothermal therapy. Biomaterials 33:2961–2970
114. Lu L, Yan GZ, Zhao K, Xu F (2015) An implantable telemetry platform system with ASIC for in vivo monitoring of gastrointestinal physiological information. IEEE Sensors J 12:3524–3534
115. Chen YS, Frey W, Aglyamov S, Emelianov S (2012) Environment-dependent generation of photoacoustic waves from plasmonic nanoparticles. Small 8:47–52
116. Li W, Sun X, Wang Y, Niu G, Chen X, Qian Z et al (2014) In vivo quantitative photoacoustic microscopy of gold nanostar kinetics in mouse organs. Biomed Opt Express 5:2679–2685
117. Nie L, Huang P, Li W, Yan X, Jin A, Wang Z et al (2014) Early-stage imaging of nanocarrier-enhanced chemotherapy response in living subjects by scalable photoacoustic microscopy. ACS Nano 8:12141–12150

Chapter 8
Functional Nanoparticles for Molecular Imaging-Guided Gene Delivery and Therapy

Tianxin Miao, Yu Zhang, Yun Zeng, Rui Tian, and Gang Liu

8.1 Introduction

Gene therapy has been tremendously applied in treatment of various diseases and disorders. Over 1800 gene therapy clinical trials have been completed, ongoing, or already gained approval worldwide until the year 2012, providing an effective and global recognized effect treatment for cancer, cardiovascular, and other severe diseases [1]. However, the inefficient delivery of genes to target tissues and the inability to monitor delivery of genes and therapeutic responses at both cellular and tissue

The original version of this chapter was revised: The name and affiliation of the author Yu Zhang was corrected. The erratum to this chapter is available at: http://dx.doi.org/10.1007/978-981-10-0063-8_11

T. Miao
Bioengineering Program, College of Engineering and Mathematical Sciences, College of Medicine, University of Vermont, Burlington, VT 05405, USA

Y. Zhang
Electrical Engineering Program, College of Engineering and Mathematical Sciences, University of Vermont, Burlington, VT 05405, USA

Y. Zeng
State Key Laboratory of Molecular Vaccinology and Molecular Diagnostics and Center for Molecular Imaging and Translational Medicine, School of Public Health, Xiamen University, Xiamen, 361102, China

Department of Pharmacology, West China School of Preclinical and Forensic Medicine, Sichuan University, Chengdu, 610041, China

R. Tian • G. Liu (✉)
State Key Laboratory of Molecular Vaccinology and Molecular Diagnostics and Center for Molecular Imaging and Translational Medicine, School of Public Health, Xiamen University, Xiamen, 361102, China
e-mail: gangliu.cmitm@xmu.edu.cn

Z. Dai (ed.), *Advances in Nanotheranostics II*, Springer Series in Biomaterials Science and Engineering 7, DOI 10.1007/978-981-10-0063-8_8

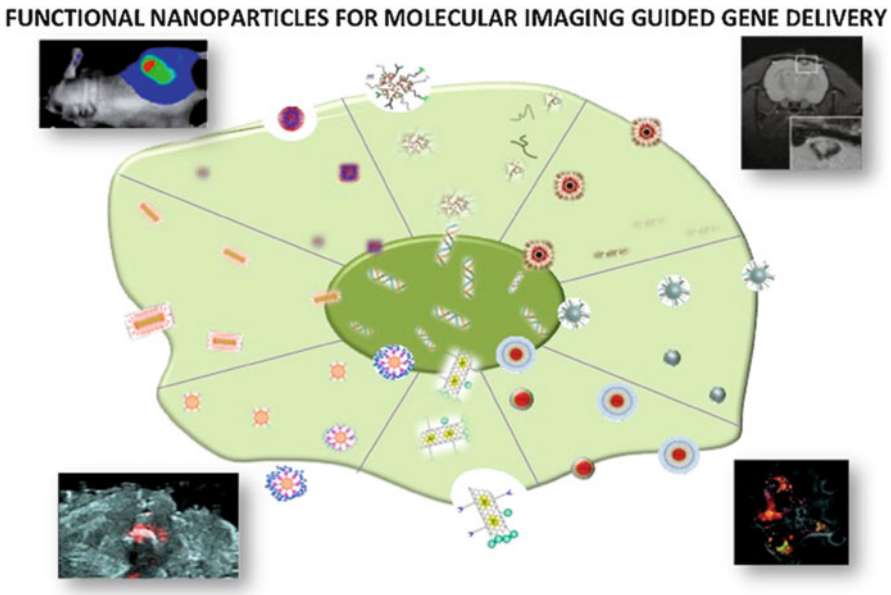

Fig. 8.1 Schematic representation of multifunctional nanoparticles for molecular imaging-guided gene delivery (Reprinted from Ref. [2], Copyright 2010, with permission from Elsevier)

level hinder the success of gene therapy. Fortunately, molecular imaging strategy provides a vital role in assisting gene therapy in a noninvasive and spatiotemporal manner. To better optimize the effectiveness of gene therapy, numerous functional nanoparticles have been developed to achieve this goal while visualizing the delivery process (Fig. 8.1) [2]. This chapter will provide an overview of various functionalized nanoparticles with unique physiochemical properties for molecular imaging-guided gene therapy. In addition, the concept of functionality and cell response will be explored. These multifunctional systems will promote diagnostic evaluation and gene therapy development and predict clinical outcomes, achieving the promise of personalized and advanced medicine.

Gene therapy has great potential to treat various diseases ranging from cystic fibrosis, macular degeneration, Parkinson's disease, and different types of cancers [3–6]. The definition of gene therapy is transferring therapeutic genes into a cell to replace or silence defective ones associated with human disease [2]. Usually, when we replace a gene, we use DNA, and when we try to silence a gene, we use siRNA. Since the discovery of RNAi, there has been an increased interest in developing small interfering RNA (siRNA)-based therapies to complete the sequence-specific posttranscription silencing of aberrant genes in diseases such as cancer [7]. The intrinsic mechanism of RNAi pathway is to silence genes posttranscriptionally. The whole process can be triggered by microRNA (miRNA), short hairpin RNA (shRNA), and synthetic siRNA [8]. The reason why siRNA attracts more application is that it can be introduced into cell directly with processing by enzyme but requires to be delivered into cytoplasm [7]. Generally, four types of barriers prevent its successfully systemic delivery. First, naked siRNA exhibits poor stability in vivo

due to the quick degradation of RNase. Furthermore, rapid clearance by the kidney also shortens its half-life time [9]. Second, the chemical (hydrophilic) and electrostatic (negative) properties hinder its passing through the plasma membrane [10]. Third, off-target effects can be generated due to silencing of genes that have partial homology with the siRNA and engagement of the immune system components to cause immune stimulation [11]. Last, the competence from miRNAs will also inhibit siRNA application since they share the same endogenous pathway [12]. Therefore, the design of safe, efficient, and targetable siRNA delivery vectors remains a major challenge for the success of gene therapy [13].

Fundamentally, there are two types of gene delivery vectors, viral and nonviral vectors. Viral vectors such as adenoviruses and retroviruses have been widely applied in gene therapy for their high transfection efficiency. Nevertheless, immunological problems, insertional mutagenesis, and restrictions in the size of the transfected gene limit its further application in human clinical trials. Therefore, nonviral vector has acquired more and more attention in the past few years as they can overcome the immune and toxicity issues. Nonviral particles are capable of delivery genetic materials, i.e., DNA or RNA, through cellular barriers [14]. Extensively, studies have been worked on improving the transfection efficacy from nonviral nanoparticles [15]. Researchers are searching for nonviral vectors that have high-loading genes, go through cellular barriers without causing immune response, and release genes into targeted cell nucleus. To better localize the gene delivery inside the cellular membrane, visualizing the entire intra-nucleus process without degrading the genetic materials becomes important in designing the nonviral vectors. Hence, it's crucial to design noninvasive while sensitive methods that could not only carry genes across cellular membrane barriers but exploit unique optical or magnetic properties for spatiotemporal molecular imaging of gene delivery [2].

The success of gene therapy mainly depends on the development of gene delivery vector while improved by the molecular imaging as to monitor delivery process. Molecular imaging greatly improves the way researchers and clinicians visualize and investigate complex biochemical phenomena. The definition of molecular imaging is noninvasive, real-time visualization of biochemical events at the cellular and molecular level within living cells, tissues, and/or intact subjects. In general, molecular imaging involves specialized instrumentation used alone or combines with targeted imaging agents, to visualize tissue characteristics and/or biochemical markers. The result gained from molecular imaging will not only help understand biological phenomena and identify regions of pathology but also provide insight on the mechanisms of disease [16].

Nanoparticles are available for multiple chemical modifications. They can be modified through reactions with metal alkoxides, epoxides, such as propylene oxide, and alkyl or aryl isocyanates. In addition, grafting synthetic polymers to the substrate surface is another strategy to improve the chemical functionality and alters the surface topology of the native inorganic and organic materials [17]. All these surface modification could expand nanoparticles' application in guiding medicine toward more informed treatment and management, named "theranostics" [18, 19]. In assisting gene therapy, the probes will provide direct or indirect evaluation of gene delivery or even gene expression, guiding therapeutic gene delivery and monitoring therapeutic response [20].

8.2 Major Non-radiation Medical Imaging Techniques

We have generally discussed the role of medical imaging in disease detection, prognosis, and treatment planning in specific for gene therapy. Major medical imaging techniques include X-ray CT, magnetic resonance imaging (MRI), ultrasound imaging, positron emission tomography (PET), single-photon emission CT (SPECT), optical imaging, and photo acoustic imaging. The inherent quantum characteristics of inorganic nanoparticles make them excellent contrast agents of various imaging techniques. Contrast agent is a medical medium with application to improve the contrast of structures of fluids compared to non-interested area within the body in medical imaging. The term "contrast" refers to the signal difference between adjacent regions, which could be "tissue and bone," "tissue and vessel," or "tissue to tissue (i.e., tumor to normal tissue)." In this session, we will provide a general introduction of major non-radiation imaging techniques – MRI and optical imaging.

8.2.1 Magnetic Resonance Imaging (MRI)

MRI is currently one of the most powerful diagnosis tools in medical science [21]. It is a nonionizing imaging technique, which would produce extraordinary signal contrast for the soft tissue by detecting the nuclear spin of hydrogen atoms inside human bodies [22]. The principle of MRI is based on nuclear magnetic resonance along with the relaxation of proton spins – that is, when the excited nuclei would return to its initial state after removing the radio-frequency (RF) pulse generated by the machine. By measuring the longitudinal relaxation (T1) and the induced magnetization on the perpendicular plane disappearing according to the dephasing of the spins (T2), the MRI is able to generate graphs inside human body. Based on the two different obtained signals, MRI contrast agents are categorized into T1 and T2 binary type. Commercially available T1 contrast agents are usually paramagnetic complexes, such as Gd-related compounds, whereas T2 contrast agents are usually nanoparticles, such as superparamagnetic iron oxide (SPIO) [23]. It needs to be noted that while T1 contrast agents brighten the final signal images of interested part, T2-weighted contrast agents actually reduce signal intensity compared to the normal tissue.

As stated above, T1 relaxation is the process of recovering equilibrium after imposing RF pulse. Human bodies are comprised with different types of molecules with various T1 relaxation time. However, the addition of paramagnetic ions (i.e., Gd^{3+} and Mn^{2+}) will elevate the relaxation potential and thus reduce T1 relaxation time. This is the mechanism of T1-weighted contrast agents to improve the capability of producing brighter signal in images between interested cells or tissues and adjacent area. Actually, gadolinium (Gd^{3+}) has been widely applied in clinician and is shown to be one of the most powerful T1 contrast agents [24]. Approximately, 10 million MRI studies are performed worldwide using Gd^{3+}-based contrast agent each

year [25]. Gd chelates (i.e., Gd-N,N',N",N"'-tetracarboxymethyl-1,4,7,10-tetraazacyclododecane (Gd-DOTA) and Gd-diethylenetriaminepentaacetic acid (Gd-DTPA)) are commonly used Gd compounds for MRI contrast agent. However, they exhibit poor sensitivity and rapid renal clearance, which strictly limit their in vivo application. Therefore, researchers have tried to incorporate Gd chelates on or inside the nanoparticle system, which will not only reduce the toxicity of Gd^{3+} but increase targeted cellular uptake and thus selectively enhance the signal. In addition to Gd chelates, manganese (Mn^{2+})-related compounds also extensively discovered to shorten T1 relaxation time [26]. Nevertheless, the free form of manganese^{+} is toxic and thus needs to be "shelled" before administration. The current only available FDA-approved manganese contrast agent would be Mangafodipir trisodium (Mn-DPDP, Teslascan™). More complex studies are warranted to extend the clinical application of manganese contrast agent. T2-weighted contrast agent would mostly rely on iron nanoparticles, which would be discussed in detail in the following session. Note that researchers have tried to design both T1- and T2-weighted contrast agents to obtain multifunctional magnetic resonance imaging probes at the same time [27].

8.2.2 Optical Imaging

Optical imaging shows advantages in spatial resolution and detection sensitivity in cellular imaging against other medical imaging modalities. However, the autofluorescence of the tissue as well as the light attenuation limits its further application in vivo. Due to its limit penetration ability, optical imaging except near-infrared spectroscopy is mostly applied to examine superficial objects and shallow lesions, such as the subcutaneous or surgically exposed organs, tumors, sentinel lymph nodes, and lymphatic vessels, as well as retinal and choroidal vasculatures [28]. Nanoparticles in assisting optical imaging consist of quantum dots (QDs), gold nanoparticle, and nanoparticles containing organic dyes. There are also fluorophores conjugated silica matrix, which exhibit more than twofold increase in quantum efficiency [29]. Detail information about QD and gold nanoparticles will be discussed in the following session.

It should be noted that due to the limitations in cost, imaging time, resolution, specificity, and detection sensitivity, single-imaging techniques might not be useful for examining one particular aspect of disease or are limited to one stage of therapeutic intervention. Therefore, integrating several imaging techniques into one unifying platform would be a better choice in some extent. Researchers have tried to design nanoparticles for multimodality imaging. For instance, labeling cy5.5 onto iron nanoparticle would obtain a dual-imaging agent for both MRI and NIR imaging [30]. People also conjugate ^{64}Cu chelates onto SPIO to achieve PET/MRI dual-modality nanoparticles [31].

Currently, imaging-guided gene therapy is predominantly applied in cancer therapy. This is because therapeutic genes are often needed to be delivered into

tumor tissue site while slip off for the healthy tissue to eliminate the side effects. However, after administrating into the circulation system, the therapeutics tends to distribute to the whole body bloodstream via osmosis force. Furthermore, they can be hydrolyzed, enzymatically degraded, and excreted through urinary system quickly. To resolve these issues, targeted delivery of gene therapeutics with nanoparticles has been developed to enhance biodistribution, increase circulation half-life, and protect them from microenvironments and thus increasing efficacy and reducing side effects. Therefore, one of the most important parts for imaging-guided gene therapy is to monitor the biodistribution, blood circulation, and tumor accumulation of drug molecules [22]. For example, SPIO and MnSO4 have been extensively applied in assisting MRI [32, 33]. Molecular imaging also offers valuable insight on tumor response for treatment such as angiogenesis inhibition [34]. Aside from monitoring drug distribution, controlling drug distribution in vivo can also be achieved by the magnetic drug targeting, which could be viewed as an extensive application of imaging-guided gene/drug therapy. The intrinsic mechanism of this application depends on the magnetic moment of the externally applied magnetic field. With appropriate external applied magnetic field, therapeutic agents conjugated to magnetic nanoparticles can be attracted to local tissue region under magnetic guidance [35].

8.3 Functionality of Nanoparticles for Imaging-Guided Gene Delivery

As stated above, multiple obstacles, either extra- or intracellular, have impeded the efficacy of gene therapy. Such problems involve the low stability of genetic materials in the blood, poor cellular uptake and inefficient endosomal escape, and disassembly of the nanoparticles in the cytoplasm. Consequently, researchers have been working on tackling these problems in achieving efficient, targeted, and safe nonviral gene delivery utilizing DNA or RNA contained materials that are intended to respond to various extra- or intracellular stimuli (Fig. 8.2) [36]. Figure 8.3 summarizes all the possible multifunctional strategy for molecular imaging-guided gene delivery.

8.3.1 Stabilization of Nucleic Acid Complexion

The incorporation of delivery vector into gene therapy is to protect the native nucleic acids from degradation in the bloodstream. To generate an electrostatically stable environment, cationic polymers, such as polyethylenimine (PEI), poly-L-lysine (PLL), and polyamidoamine (PAMAM), have been used to form nanocarriers for gene delivery [37–39]. Furthermore, decreasing the size and net surface charge will

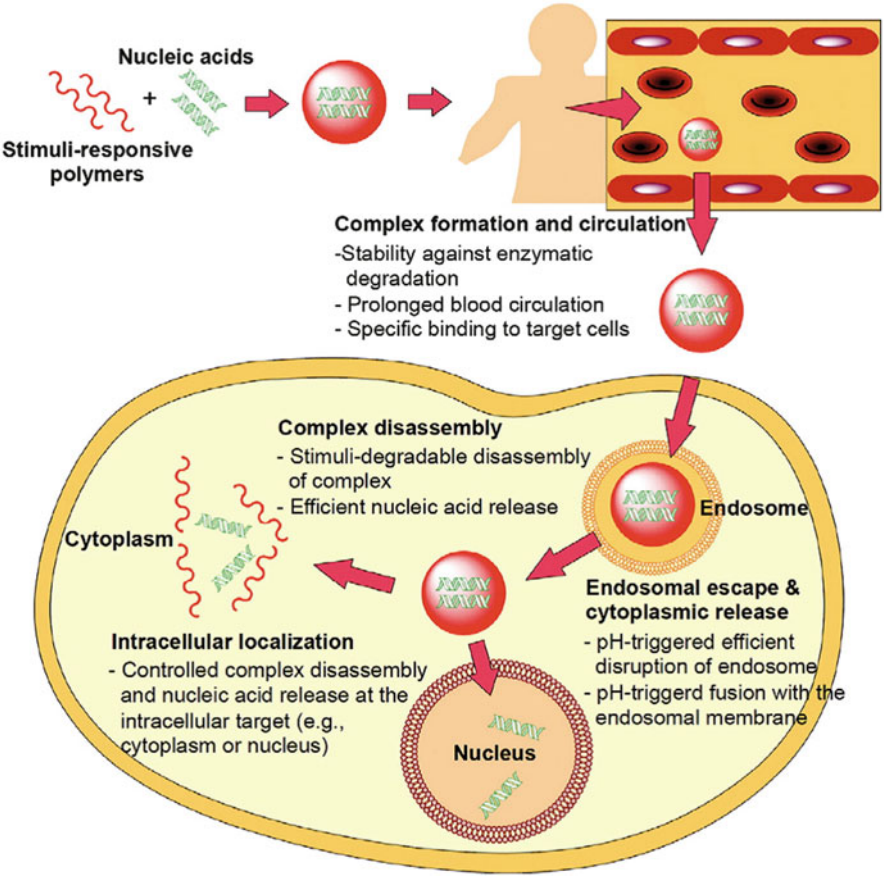

Fig. 8.2 Schematic illustration of multiple stimuli-responsive approaches to overcoming multidimensional (extra- or intracellular) barriers for nonviral gene vector (Reprinted from Ref. [36], Copyright 2012, with permission from Elsevier)

also promote cellular uptake. Nevertheless, they also interact with anionic blood proteins, forming aggregates and thus leading to rapid clearance by reticuloendothelial system (RES). The high ionic environment in the human bloodstream will also debilitate the electrostatic interaction between the cationic carriers and the anionic nucleic acids, resulting an ahead release of genetic materials rather than in the targeted tissue [36]. Stimuli-reducible linkages (i.e., glutathione-cleavable disulfides) have been cross-linking nucleic acid and polymer complex to increase the stability of nucleic acid complexion [40]. However, it should be noted that the cross-linking effects shall be accurately controlled and reversible inside the targeted cell, avoiding over-stabilization. To address this issue, the choice of appropriate stimuli-responsive polymers that not only provide desired stability in circulation system but disassemble intracellularly causing burst release of delivered genetic materials is crucial for achieving efficient gene therapy [36].

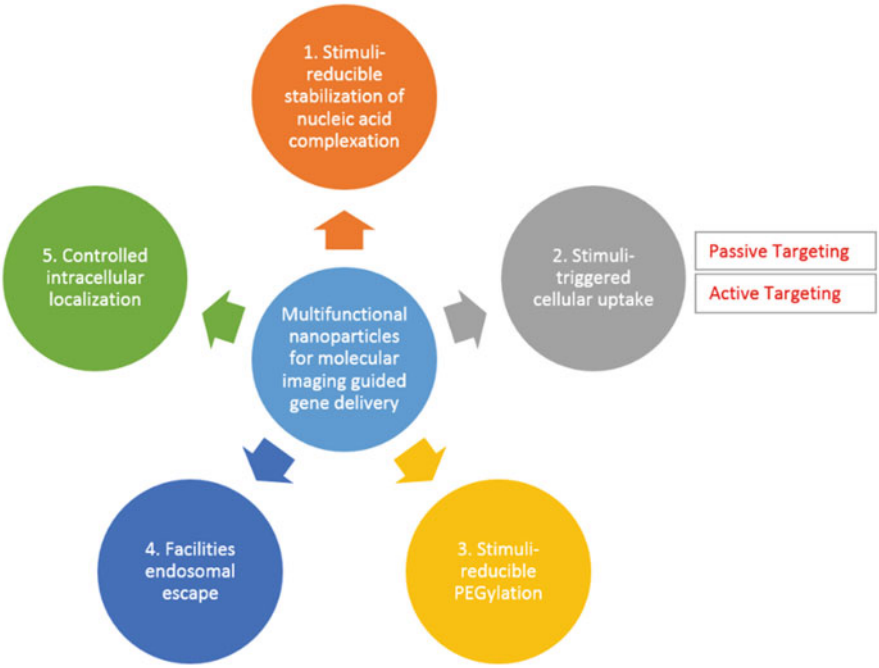

Fig. 8.3 Schematic representation of multifunctional strategy for molecular imaging-guided gene delivery

8.3.2 Stimuli-Triggered Cellular Uptake: Passive and Active Targeting Effect

It is well recognized that targeted gene delivery is a significant approach for accumulation of therapeutic genes in target tissues/cells while reducing side effects [41]. Incorporation active targeting moieties, such as peptides, folic acid, antibodies, and aptamers, have been commonly applied in designing nanoparticles for imaging-guided gene therapy [42–45]. Generally, two strategies, i.e., "passive targeting" and "active targeting," are applied in cancer-targeted gene delivery (Fig. 8.4) [13].

The mechanism of passive targeting comes from the principle of enhanced permeation and retention (EPR) effect of delivery systems, proposed by Matsumura and Maeda in the year 1986 [46]. The rapid invading tumors have tremendous number of endothelial pores in tumor vessels with size ranging from 10 to 1000 nm, allowing nanoparticles to accumulate in the same location. This is also the reason why researchers aim to design nanomaterial for cancer therapy. Thus, the size of nanoparticles is a significant factor for nanocarriers retaining in the tumor location [47].

In contrast to "passive targeting," which takes advantages of the pathological characteristics of the tumor tissue dissimilar to the normal tissue, "active targeting"

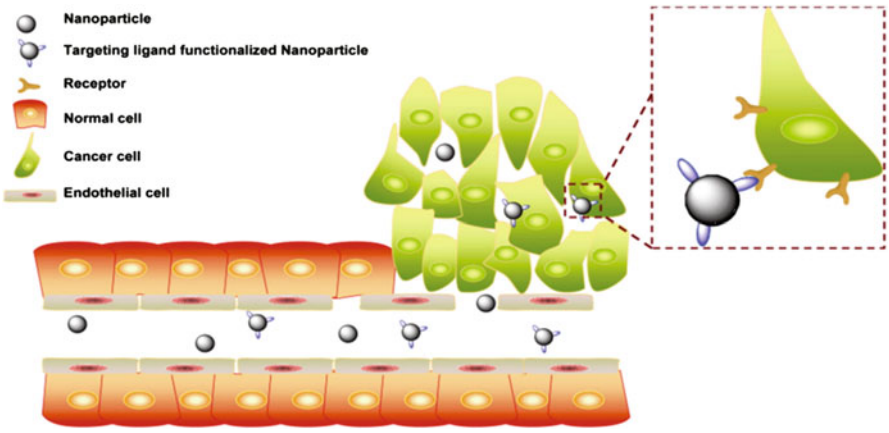

Fig. 8.4 Schematic illustration of the mechanism of EPR effect and "active targeting process." Blood flow is the crucial driving force for imaged-guided gene delivery. The cancer tissue tends to accumulate nanoparticles much more than the normal tissue due to the poorly aligned defective endothelial cells with wide fenestrations, lacking a smooth muscle layer, or innervation with a wider lumen, and impaired functional receptors for angiotensin II. By conjugating target moieties onto nanoparticles, we are able to elevate the delivery efficacy to cancer cells due to the specific high numbers of receptors located on the cancer cell membrane (Reprinted from Ref. [13], Copyright 2014, with permission from Elsevier)

utilizes specific ligand-receptor-mediated interactions between nanoparticles and cancer cells. The well-known ligand-receptor pairs are listed but not limited to folate with folate receptor [48], arginine-glycine-aspartic (RGD)-generated sequence with integrin [49], anti-epidermal growth factor receptor (anti-EGFR) [50], necitumumab (member of epidermal growth factor (EGF) protein), and GE11 peptide [51] with epidermal growth factor receptor (EGFR). The interactions between these ligand-receptor pairs will increase the binding affinity of nanoparticles to cancer cells and thus elevate the cellular uptake via endocytosis, which will be verified by quantitative pharmacokinetic and biodistribution analysis [52].

8.3.3 Stimuli-Reducible PEGylation

Polyethylene glycol (PEG) is the most well-known synthetic polymer in the emerging field of biomaterials for drug delivery. Recently, natural material has been modified with PEG for the fabrication of microcapsule coatings [53, 54], mucoadhesive polymers [55, 56], self-assembling nanospheres [57, 58], and hybrid microspheres [59, 60]. The ability of PEG to influence the pharmacokinetic properties of drugs and drug carriers has been used to modify many different pharmaceutical compounds and components [61]. Biocompatibility and stealth behavior make PEG an ideal material to avoid opsonization and subsequent elimination by the reticuloendothelial system [62]. In addition, PEG-modified products are less immunogenic

and antigenic; hemolysis and aggregation of erythrocytes may also decrease, as can the risk of embolism. However, PEGylation also affects endosomal escape, due to steric impedance. Hence, reversible PEGylation, such as "extracellular enzyme-triggered dePEGylation," has been developed to overcome the poor adhesion and internalization of nanoparticles to cells [63, 64].

8.3.4 Facilitated Endosomal Escape

Endocytosis is one of the major cellular uptake mechanisms, specifically for large biological agents such as DNA, siRNA, and proteins. However, these agents are often trapped in endosomes and degraded by enzymes in the lysosome. Therefore, facilitating endosomal escape is essential in completing gene therapy either with or without the guidance of molecular imaging (Fig. 8.5) [65].

Generally, four types of mechanisms have been used to design nanocarriers to facilitate endosomal escape: (1) *pore formation inside the endosomal membrane*,

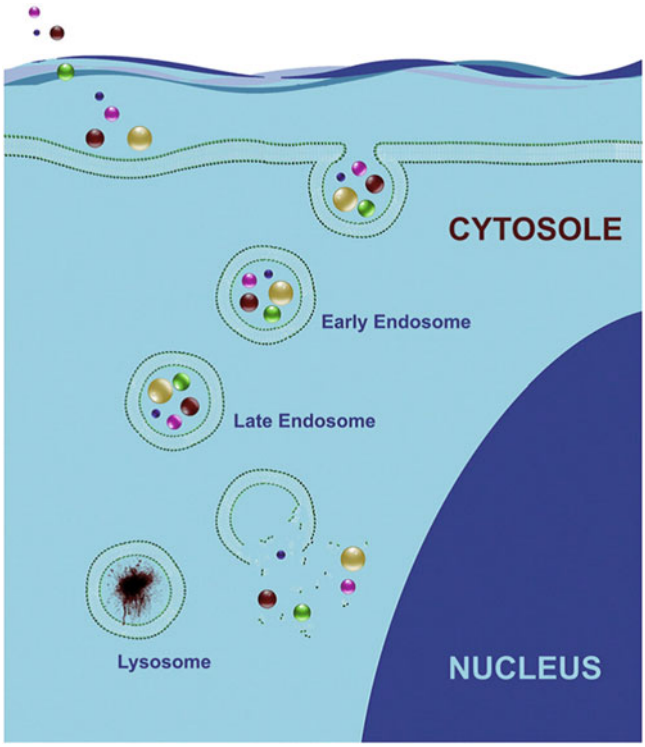

Fig. 8.5 Schematic illustration of the process of cell internalizing therapeutics via endocytosis and subsequent endosomal escape (Reprinted from Ref. [65], Copyright 2011, with permission from Elsevier)

which generates on the interplay between a line tension that closes the pore and a membrane tension that enlarges the pore size [66]; (2) *proton sponge effect*, which triggers an extensive inflow of ions and water into the endosomes, initiating rupture of the endosomal membrane and release of the entrapped components [67]; (3) *external fusion into the endosomal membrane*, which destabilizes the membrane structure via fusogenic peptides in a number of fusion systems [68]; (4) *photochemical disruption*, which generates singlet oxygen with short lifetime, destroying the endosomal membrane, whereas the contents of the organelles remain intact and are delivered to the cytosol [69].

8.3.5 Controlled Intracellular Localization

After cellular internalization and endosomal escape, the biological agents are capable of delivering inside cells. However, different types of delivered nucleic acids have different effective location. That's why we need to control intracellular localization of therapeutic genes. Plasmid DNA should be transfected inside the nucleus, whereas RNA interference usually happens in the cytoplasm [70]. To go through the nucleus barrier for plasmid DNA, the smaller size (<40 kDa) is usually required [71]. It could also be boosted by the nuclear localization signals (NLS), which are similar mechanisms for active targeting via ligand-receptor pair [72].

The functionalities discussed above have successfully enhanced diagnostic evaluation, gene therapy efficacy, and clinical outcome prediction, satisfying the promise of advanced and personalized medicine. The combination of the above strategies with different targeting ligands, imaging labels, genetically engineered genes, and many other agents will serve for effective and controlled imaging-guided gene therapy. In the second part of this chapter, various types of functional nanoparticles and systems for molecular imaging-guided gene delivery will be discussed in detail, and some of the most advanced examples will be highlighted.

8.4 Various Functional Nanoparticles and Systems for Molecular Imaging-Guided Gene Therapy

8.4.1 Polymer-Based Nanoparticles

Negatively charged DNAs can be protected by cationic polymers, forming complex nanoparticles through electrostatic interactions. It is the most widely applied nonviral gene delivery vectors. They provide several advantages, such as (a) the ability to encapsulate wide ranges of DNA or siRNA and prolong the release in vitro and in vivo, (b) large surface area available for targeting ligands, and (c) performing good stability [22]. Several factors account for the high gene transfection efficiency,

including molecular weight, surface charge, amphiphilicity, as well as the structure and shape of nanoparticles. Commonly widely applied polymers include polyethylenimine (PEI) [73], chitosan [74, 75], poly-L-lysine (PLL) [76], poly(amidoamines) [77], and their derivatives [78, 79]. Copolymer of hydrophobic polymers and hydrophilic polymers is used to synthesize self-assembled therapeutic carriers. Multifunctional responsive polymer, which is designed to respond to external stimulus (i.e., pH or electromagnetic radiation), is also actively explored in drug delivery [22]. As stated in the previous chapter, PEGylation has been widely used to coat polymeric nanoparticles to further extend the circulation time and try to avoid clearance by the mononuclear phagocytic system [80]. Another modification strategy to achieve similar goal would be utilizing polaxamers and polaxamer copolymers [81].

The traditional methods to prepare polymeric nanoparticles include spontaneous emulsification, salting out/emulsification-diffusion, solvent evaporation, solvent diffusion, and use of supercritical CO_2 among others. Via these methods, the size for obtained polymeric nanoparticles could range from a few nanometers to hundreds of nanometers. The particle diameter has significantly influenced its circulation life in vivo. Researchers have found out that the nanoparticles with less than 200 nm will possess longer life compare to large particles [82, 83]. Another critical issue related to the therapeutic effect is the mechanical properties of nanoparticles. Beningo et al. have found out that rigid particles are easier to be engulfed by macrophages compared to soft particles. These are important implications in immune clearance of nanoparticles [84]. In addition, the shape also has its intriguing effect on the various functionalities of nanoparticles. These features will serve good application of gene delivery. The incorporation of imaging techniques allows researchers and clinicians to visualize the whole process of gene delivery and therefore is able to identify important issues involved.

8.4.2 Dendrimer-Based Nanoparticles

Dendrimers are innovative cubic dimensional, hyperbranched globular nanopolymeric architectures with nanoscopic size, narrow polydispersity index, excellent controlled molecular structure, and multiple available functionalities at the periphery and cavities. Thus, it becomes one of the most commonly applied nonviral vectors for gene delivery [85]. Dendrimers usually are multivalent macromolecules based on a well-defined cascade motif with three distinct components: a central core, repeated braches, and terminal functional group. The perfectly and defect-free monodisperse characteristics and controllable spherical shapes make it a very useful type of cargo system for drug/gene delivery. Researchers also extent its application for protect catalytic agents, immunodiagnostics, and contrast agents [86–88].

Among all the multifunctional polymers, the amino-terminated poly(amidoamines) (PAMAMs) are the most frequently used dendrimers for gene transfection. The positively charged PAMAM dendrimers and the negatively charged anionic phosphate groups on the DNA backbone form electrostatic bonds and result in the

formation of nanoscale complexes that could prevent DNA degradation. The selection of potential generation and peripheral structure of dendrimers is crucial for successful gene delivery. Low generation is required to biocompatibility issue. However, the weak electrostatic interactions result in a lower transfection. High generation would solve the transfection efficiency issue but may be toxic to cells due to the large number of cationic amino groups introduced into the system. Consequently, it is significant to balance. Recently, several types of dendrimer-based nanoparticles have been developed for both gene delivery and monitoring.

8.4.3 Lipid-Based Nanoparticles

Lipid-based nanoparticles, such as liposomes and micelles, have acquired much attention in the past few decades [89, 90]. The formation of lipid-based nanoparticles utilizes the electrostatic interactions between the negatively charged nucleic acids and positively charged polymers. Therefore, the number of positive charges on the cationic lipid has significantly influenced the transfection efficiency. In addition, the linkage between the hydrophobic and cationic portion of the molecules and the structure of the hydrophobic moieties are also important considerations for designing lipid-based nanoparticles.

Lipid coatings seal the drug or gene perfectly, providing enhanced biocompatibility of the nanoparticles with good pharmacokinetics. The incorporation of imaging techniques into the gene cargo lipid-based systems is new but promising (Fig. 8.6) [91, 92]. Various types of imaging agents, such as quantum dots, iron oxide nanoparticles [93], and gold nanoparticles [94], have been utilized to functionalize lipid-based nanoparticles. Drug or imaging agents loading into liposomes can be achieved via the (1) liposome formation in an aqueous solution saturated with soluble drug, (2) use of organic solvents and solvent exchange mechanism, (3) utilization of lipophilic drugs, and (4) use of pH gradient methods [95].

The administration of lipid-based nanoparticles is via extravasation into the interstitial space from the bloodstream. Since the size of liposomes is of nanosize, they are easily removed by mononuclear phagocyte system (MPS). Therefore, reducing opsonization of liposomes *via* PEGylation is very important to increase their circulation time in the bloodstream [96]. Additionally, these cargo systems can also be surface modified with targeting peptides to increase the binding affinity [97].

Many lipid-based drug delivery cargo systems are going to clinical trial [98]. The first FDA approval nanodrug actually is lipid based, named Doxil®. Doxil® is a liposomal formulation of doxorubicin for cancer therapy in AIDS-related Kaposi sarcoma and multiple myeloma [99]. Speaking of cancer therapy, one of the most attracted applications in this field is the potential of liposomes to fight against multidrug resistance acquired by cancer. Ogawara et al. have shown that PEG liposomal doxorubicin (Doxil®) has antitumor effects on both doxorubicin-resistant and

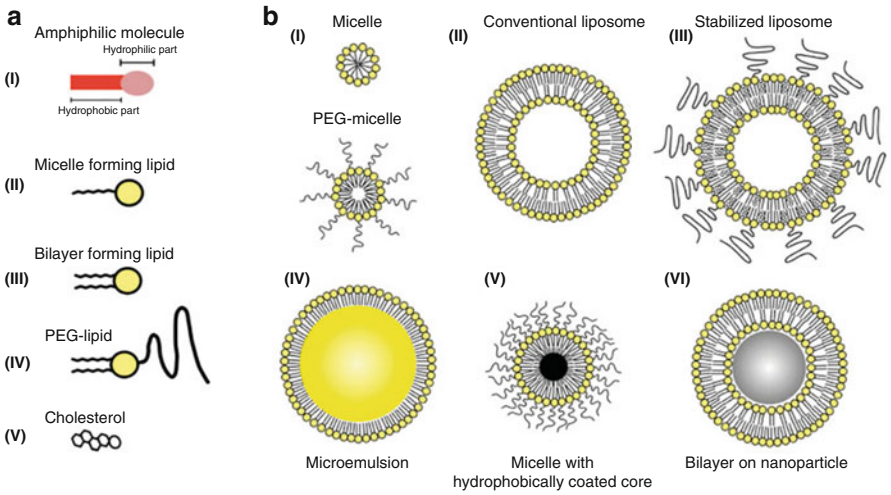

Fig. 8.6 (**a**) Schematic chart for amphiphilic lipids. (*I*) Amphiphiles are consisted of a hydrophilic head with a hydrophobic tail. (*II*) Lipids aim to form micelles usually have a larger hydrophilic head than its hydrophobic tail. (*III*) Two hydrophobic tails would be needed to form bilayer-forming lipids. (*IV*) PEGylation is utilized to enhance pharmacokinetic properties. (*V*) The utilization of cholesterol will stabilize liposomes from degradation. (**b**) List of available lipid aggregates for in vivo use. (*I*) Micelles can be generated either from the micelle-forming lipids or from PEG lipids. (*II*) The convention structure of liposome is phospholipid bilayer. (*III*) Conjugating PEG lipids and cholesterol will stabilize liposomes as stated before. (*IV*) Microemulsions consist of a surfactant (amphiphile) monolayer covering oil. (*V*) Hydrophobic nanoparticles can be incorporated inside micelles. (*VI*) The bilayer structure of lipids could be used to cover nanoparticles, such as silica, mica, glass, or iron oxide (Reproduced from Ref. [91] by permission of John Wiley & Sons Ltd)

non-doxorubicin-resistant C26 cells [100]. However, there's still no evidence of liposomes on promoting gene delivery for resistant cells. More studies would be needed to provide better understanding of lipid nanoparticles in gene therapy.

8.4.4 Iron Oxide Nanoparticles

Iron oxides comprised the main part of magnetic nanoparticles (i.e., magnetite and maghemite) and are the most commonly applied T2-weighted MRI contrast agent. When the size of magnetic nanoparticles within the size limit, which is the flipping rate of coupled magnetic moments, increases rapidly until no net magnetization can be observed, this type of magnetic particles is called superparamagnetic nanoparticles [101]. The superparamagnetic limit of iron oxide nanoparticle is between 20 and 25 nm at room temperature. They often possess colloidal stability, which allows nanoparticles free of interactions without external magnetic field. However, they will align with the field and reach saturation after applying magnetic field [102].

SPIOs have been widely applied in biomedical research, including MRI contrast agent, hyperthermia, and cell separation/labeling [103–106].The popularity of SPIOs accounts for four reasons: (1) SPIOs provide T2-weighted images based on MRI system; (2) magnetic properties can be manipulated and therefore gain various contrast agent with different enhancement; (3) the degradation product could be metabolized and integrated into serum Fe pool to form hemoglobin or other metabolic process; therefore, it's biocompatible; and (4) SPIOs have a large surface area for drug and gene carrying. All these good features have extended its application for in vivo molecular imaging and gene delivery [2].

The traditional synthesis method of the magnetic nanocrystals is the coprecipitation of ferric and ferrous ions in aqueous solutions. The method is facile and green, utilizing non-harmful substrates. However, the product exhibits wide size distribution and defects in the crystal structure [108]. Sun et al. have prepared high-quality iron oxide nanoparticle with thermal decomposition in organic phase [109]. The naked nanoparticles are unstable due to the high surface energy. Nevertheless, surface modification of nanocrystal techniques has made it possible to be stable for biological applications. Without optimized surface modification, the gene may not strongly bind to IONPs, resulting in the instant release of the therapeutic gene during the delivery process. A common strategy to overcome this issue is to use cationic polymers, such as PEI (Fig. 8.7), PLL, chitosan, or dextran as discussed above in the polymeric session. For example, dextran-coated SPIOs can gather in the liver

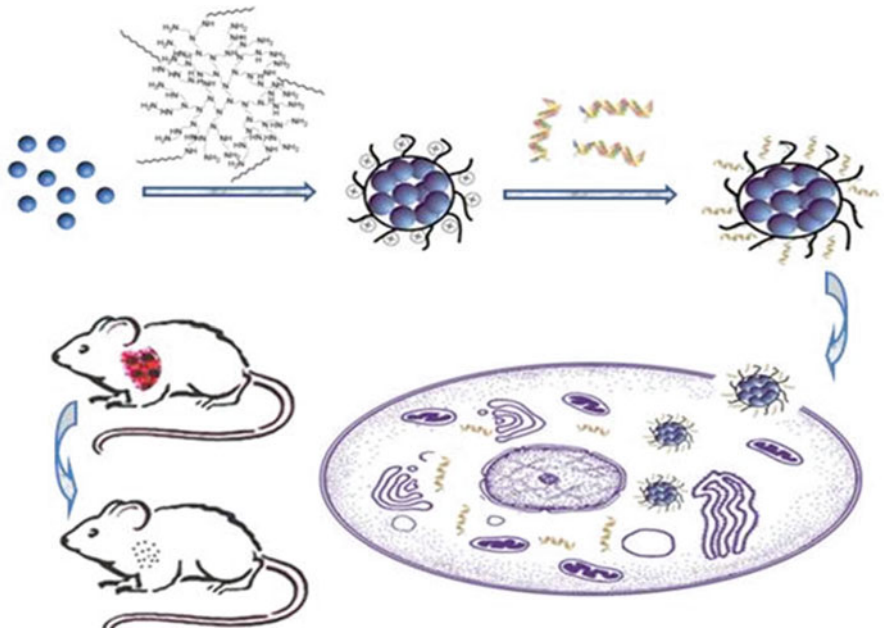

Fig. 8.7 Schematic representation of the preparation and intracellular uptake of Alkyl-PEI2k-IOs/siRNA complexes (Reproduced from Ref. [107] by permission of John Wiley & Sons Ltd)

due to phagocytosis by the reticuloendothelial system (RES) and therefore are able to detect liver tumor since it lacks phagocytic activity [110]. A novel type of GdIO nanoparticles was prepared by thermal decomposition of the mixture of iron oleate and gadolinium oleate precursors. Increased signals in T1-weighted MR images and reduced signals in T2-weighted MR images with the increased metal concentrations of GdIO nanoparticles demonstrated that GdIOs can act as both negative and positive contrast agents.

As stated in the previous session, the principle of magnetic guidance has been applied for selective delivery of therapeutic agents to target sites with external permanent magnetic fields. This is extensively applied with IONPs. For instance, IONPs with lipid coating will exhibit excellent stability under fluidic condition and are capable of accumulating at desired places with a gradient magnetic field and thus enhancing siRNA silencing efficiency with the magnetic force-assisted transfection [111]. In another study, dual-modality contrast agent was designed for siRNA delivery and green fluorescent protein (GFP) to NIH 3 T3 cells with PEI coating. Driven by the external magnetic force, the transfection depth could reach 2.1–3.3 mm in 3D cell culture [112]. The magnetic-assisting gene therapy has been more and more popular. However, it is still unknown whether the magnetic-targeted delivery is better than EPR effect mediated by either passive or active targeting ligands [13].

8.4.5 Quantum Dots

Quantum dots (QDs) are colloidal nanosized semiconductor particles, exhibiting special electronic and optical properties that are tunable with different sizes and shapes [113]. QDs could be excited over a wide range of wavelengths and emit narrow symmetric bands with limited photobleaching that can be fine-tuned during the synthesis techniques [114, 115]. Despite the emergence of other materials, the most popular material choices remain CdSe [116] and CdTe [117]. In order to improve the luminescence properties, T=the typical structure of QDs is core-shell construction with an inorganic capping layer of ZnS surrounding the nanocrystal core (e.g., CdSe/ZnS) [118]. Due to the large surface area-to-volume ratios of QDs, the surface modification would be a significant consideration for developing all types of assays, bioprobes, and biosensors based on QDs. In addition to retain the favorable optical properties of QDs, the surface modification strategy should also allow bioconjugation, impart aqueous solubility, and not impede the efficient use of FRET. The synthesis of QD bioconjugates is essential for designing multifunctional bioprobes and biosensors. Figure 8.9 provides several general modification strategies. Enzymes [119], small molecular-binding proteins [120], antibodies [121], and oligonucleotides [122] are lists of biorecognition agents that have been conjugated onto QDs. The development of simple and effective conjugating chemistry, which is orthogonal to common biological functions, will be prestigious strategies for preparation of QD conjugates. With such chemistry, we are able to facilitate QDs with a variety of unique biomolecules and thus enable to extend application for bioanalyses [123] (Fig. 8.8).

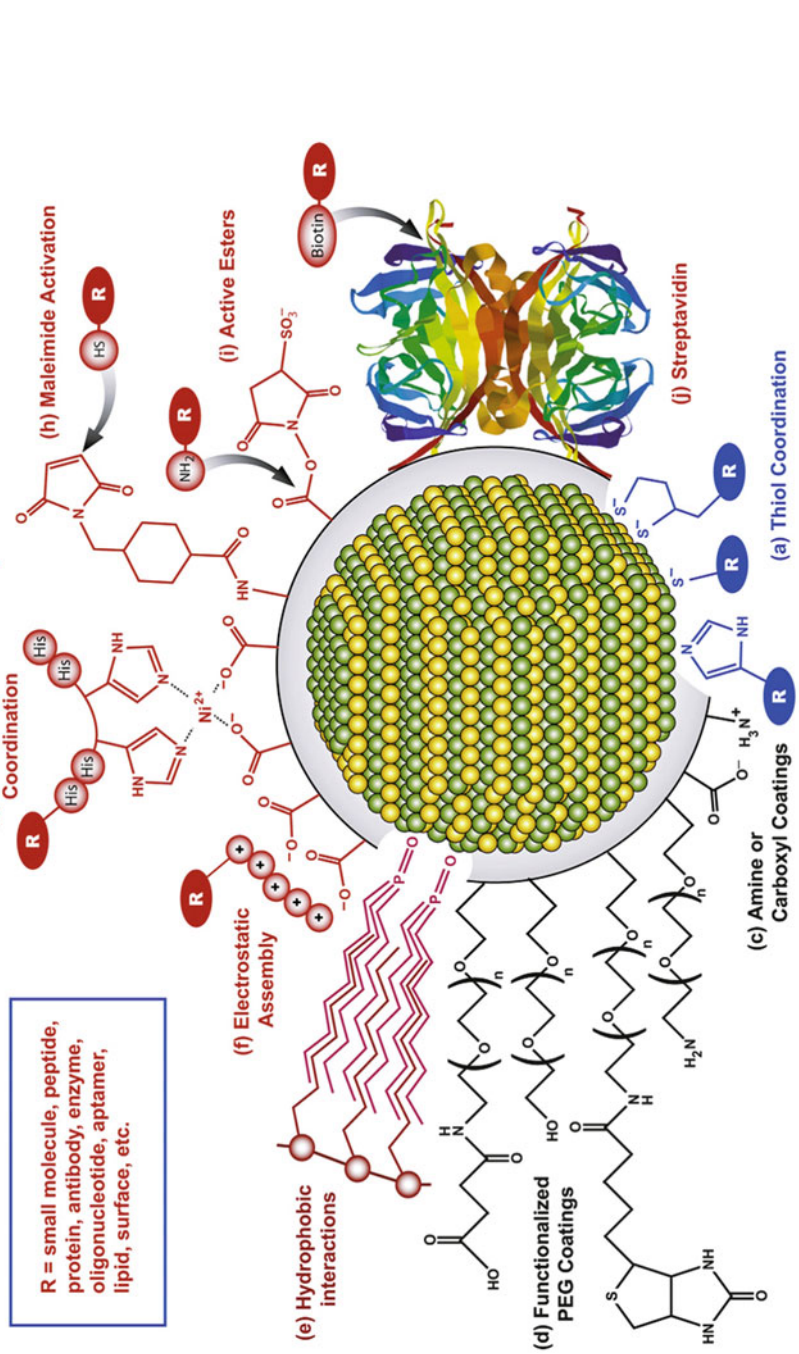

Fig. 8.8 Schematic illustration of selected surface modification strategies for QDs. The *gray periphery* around QD represents a general coating, which could be associated with the surface of the QD via various types of reactions with the listed functional groups from (Reprinted from Ref. [123], Copyright 2010, with permission from Elsevier)

8.4.6 Other Organic and Inorganic Nanoparticles

8.4.6.1 Carbon Nanotubes

Carbon nanotubes are hollow cylindrical molecules formed in a series of hexagonal lattice structure through carbon atoms with π bonding. It has been explored for many biomedical applications since it first came out in the year 1991 [124]. Based on the formation structure, carbon nanotubes are categorized with two dominant forms: single-walled carbon nanotubes (SWCNTs) and multi-walled carbon nanotubes (MWCNTs). Both SWCNTs and MWCNTs can be functionalized with a pyrrolidine ring, and then a wide variety of biomolecules, imaging agents, and drugs can be conjugated [125]. Carbon nanotubes have a wide variety of structures, with diameter ranging from 0.4 to 100 nm. Lengths typically range from hundreds of nanometers up to tens of micrometers [2]. Pantarotto et al. first utilized carbon nanotubes as gene vector [126]. Since then, researchers have been utilized it to design multifunctional biomaterials for gene therapy due to carbon nanotubes' appealing features, such as unparalleled optical/electrical properties and needle-like shape. The process of penetrating the cell membrane through a nanoneedle model can be visualized via transmission electron microscopy (TEM) [126]. Generally, nucleic acids can either be covalently functionalized by oxidation of the carbon nanotubes in acidic condition by 1,3-dipolar cycloaddition or stacking with carbon nanotubes using nonpolar ring via hydrophobic or $\pi - \pi$ interaction. Electrostatic interactions will also be useful to bind plasmid DNA; however, ammonium functionalization is pre-request [2].

Two advantages about carbon nanotubes as nonviral gene delivery system include the unique length-to-diameter ratio and surface modification. Although there is little knowledge about the effect of length-to-diameter ratio, it is still an important parameter to control the complexion of nucleic acids with carbon nanotubes [127]. It should be pointed out that both SWCNTs and MWCNTs have been used as nucleic acid delivery vector. However, more researchers would be needed to discuss the relationship between spatial/morphology properties and gene transfection efficacy (Fig. 8.9) [128].

The other advantage would be its larger surface area available for chemical modification. The goal of surface medication of carbon nanotubes for gene therapy is to increase the complexed nucleic acids and thus enhance the gene transfection efficiency. However, over conjugating nucleic acid may hinder the carbon nanotubes from translation into cells due to the high electrostatic surface charges. Therefore, it is crucial to balance the amount of loading nucleic acids while maintaining the neutral electrostatics [128]. To increase the quantity of complexed nucleic acid, cationic groups have been conjugated onto the surface of either SWCNTs or MWCNTs. For instance, PEI, which is rich in amines, was functionalized onto MWNTs to deliver plasmid DNA to a panel of different mammalian cells, such as COS7, HepG2, and 293 cells [129]. Other amine-conjugated carbon nanotubes are also reported to

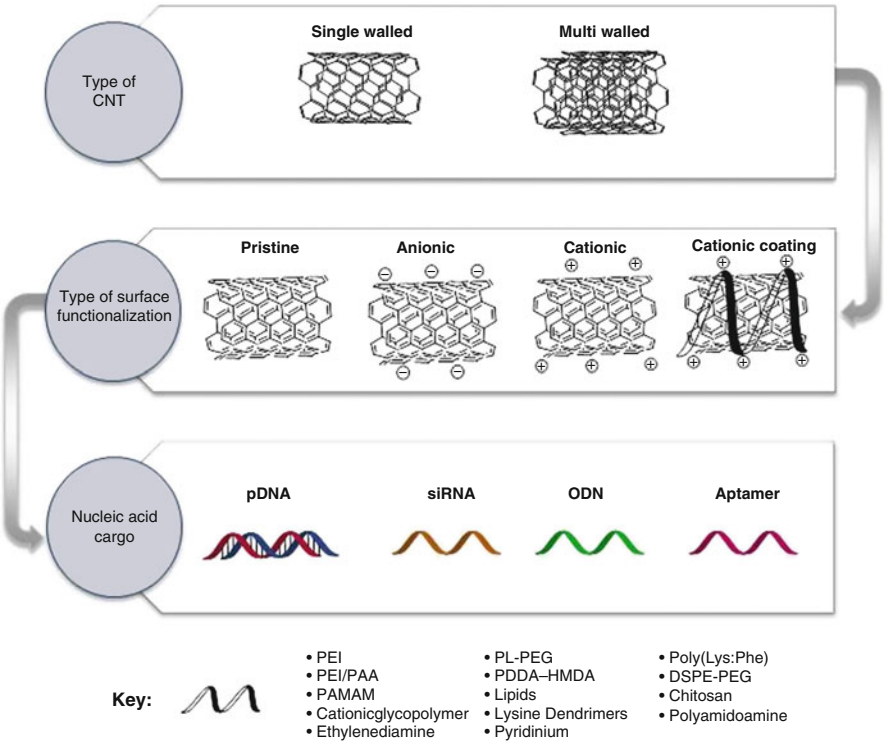

Fig. 8.9 List of two types of carbon nanotubes and various types of surface modification strategy with possible nucleic acid cargo for gene delivery using carbon nanotubes. Single-walled or multi-walled carbon nanotubes can serve as structural backbone available for numerous surface modifications to achieve sufficient gene delivery. Plasmid DNA (double-stranded *red* and *blue structure*), siRNA (single-stranded *orange structure*), ODNs (single-stranded *green structure*), and aptamers (single-stranded *pink structure*) have been incorporated into carbon nanotube system. Taking advantage of different cationic coatings that adsorbed onto the surface of CNTs will extend their application in gene therapy (Reprinted from Ref. [128], Copyright 2013, with permission from Elsevier)

explore the transfection abilities of carbon nanotubes via gene delivery both in vitro and in vivo [130–132].

We have discussed the multiple requirements for gene therapy vectors. These also need to fit into the demanding criteria for carbon nanotubes. In addition, the correlation between vector characteristics and the choice of genetic cargo to be delivered into target cells should also be considered as a major factor. Carbon nanotubes have shown to successfully deliver plasmid DNA [133], siRNA [134], shRNA [128], miRNA [135], oligonucleotides (ODNs) [136], and aptamers DNA/RNA [137]. The geno-pharmacology of carbon nanotube-mediated gene therapeutic can

be divided into three categories. First, the ex vivo gene transfection of isolated cells returns the modified cells back to the host. There's little evidence showing the effectiveness of using carbon nanotubes here. Only splenic B cells and cortical neurons have been shown to be effective [138]. A more widely used application would utilize carbon nanotube for gene therapy via direct presentation of the genetic cargo to the targeted tissue. The application includes intratumorally for cancer therapy or intracranially for various neurological applications [128]. Various types of siRNA have been incorporated in the carbon nanotube system. siRNA targeting HIf-1α would significantly reduce the gene activity though the tumor size was not shown to be shrank [139]. However, in another study, peri-lesion stereotactic administration of carbon nanotube, siCaspase-3 constructs, will not only diminish neurodegeneration but also elevate functional preservation of motor capabilities in diseased animals [132]. The last category falls into the in vivo delivery via the bloodstream for gene therapy. By conjugating NGF and Asn-Gly-Arg peptide motif, Wang et al. were able to design RNAi/near-infrared (NIR) photothermal-combined therapy with excellent antitumor activity [140]. Researchers also invented carbon nanotube-loaded electrodes or biosensors. With the support of hydrogel system, plasmid DNA (encoded with vascular endothelial growth factor (VEGF) and Ang(1)) has been encapsulated into carbon nanotubes non-covalently to create implantable bioactive stents for prevention therapy of stenosis and vascular damage following surgery and angioplasty [141]. It should be noted that recently researchers have tried to design dual-delivery vector using carbon material. By using Alkyl-PEI2k for surface passivation, photonic Cdots could be simply developed into a simple and versatile nanoparticulate siRNA and delivery vehicle [142].

The idea of utilizing carbon nanotubes as gene delivery vehicle is promising with various attractive characteristics. However, there's still gaps where research may fit in, such as the formulation of genetic cargo and finding the most efficacious route of delivery in vivo. Upon these engineering issues, modulating inherent reactions from the host's immune system, inflammatory potential, and cytotoxicity are still great needs to make carbon nanotubes as great candidate for gene therapy [128].

8.4.6.2 Silica Nanoparticles

As the major component of sand and glass, silica is a versatile material, which is available for chemical and physical modification and therefore gains wide application in nanobiotechnology as gene carrier or fluorescent nano-probes [143]. The following distinctive properties of silica nanoparticles have made it an applicable material for controlled release delivery application. (1) The particle size can range from 50 to 300 nm, providing a capable agent for endocytosis by living animal and plant cells without causing significant cytotoxicity. (2) The size distribution is narrowed down between 2 and 6 nm, and therefore, it can have a more precise release file compared to the uneven nanoparticles. (3) Silica nanoparticles are stable under heating, high pH, mechanical loading, and hydrolysis environment, becoming a more reliable and foreseeable agent for gene therapy. (4) The large unique porous

structure will not only load huge amount of drugs or genes but also avoid drug leaking since there is no interconnectivity between individual channels. (5) The large surface area makes it available for various chemical and physical modification. It should be noted that silica nanoparticles have both internal and external surface, allowing double functionality design to be achieved in single particle with different moieties [144]. The goal is "to achieve effective cellular delivery". Then both anchoring group and charging transfer group will be modified onto the surface of to allow for electrostatic interaction with DNA [145]. PLL is also bound to silica nanoparticles for enhancing intracellular delivery of oligonucleotides. The incorporation of fluorescein isothiocyanate (FITC) helps to visualize and monitor the entire process. PLL also shortens the endosome/lysosome entrapped time since it could destabilize the lipid membrane, which therefore protects DNAs from staying in the acidic environment too long. Ring opening N-carboxyanhydride (NCA) polymerization and click chemistry will be used to engraft PLL onto silica nanoparticles with density of one chain per 1 nm^2, which will be an effective modification strategy for developing functionalized silica nanoparticles [146].

Researchers have tested the biocompatibility of silica particles by different methods. Common microscopic method shows cell morphology remains the same after coculturing with silica nanoparticles. 3-(4,5-dimethylthiazol-2-yl)-2,5-diphenyltetrazolium bromide (MTT) test confirmed there's no significant difference for mitochondrial activity before or after exposing to silica nanoparticles [147, 148]. To really visualize and confirm the intracellular uptake of silica nanoparticles, people have utilized flow cytometry [149], transmission electron microscopy [144], and confocal fluorescent microscopy [150] along with various types of fluorescents. The future research focus on silica nanoparticles will be to utilize functionalized silica nanoparticles to perform specific tasks inside cells, such as altering cellular processes by sequestration or immobilization of metabolites or other functional biomolecules [150].

8.4.6.3 Gold Nanoparticles

Gold nanoparticles (AuNPs) have been widely applied over the past decades in photothermal therapy, DNA mismatch detection, biosensing, molecular imaging, and gene therapy. The unique optical properties presented by AuNPs come from the strong and tunable surface plasmon resonance (SPR) in the near-infrared (NIR) spectroscopy range, which can trigger photothermal effect with hereby a variety of biological activities. In addition to the SPR property, AuNPs can be easily tailored to a desirable shape and size [13]. They can be prepared in a wide range of monodisperse sizes, from 2 to 250 nm, and can be synthesized into a variety of shapes, which will affect their properties. Possible shapes include gold nanorod, nanoplates, branch nanostructures, and nanoparticles [151]. Actually, it is the size and shape that affect SPR. This is because the plasmon is confined to the surface, and as the diameter gets smaller, the energy required to collectively excite motion of the surface plasmon electrons increases [152]. Therefore, AuNPs with diameter close to

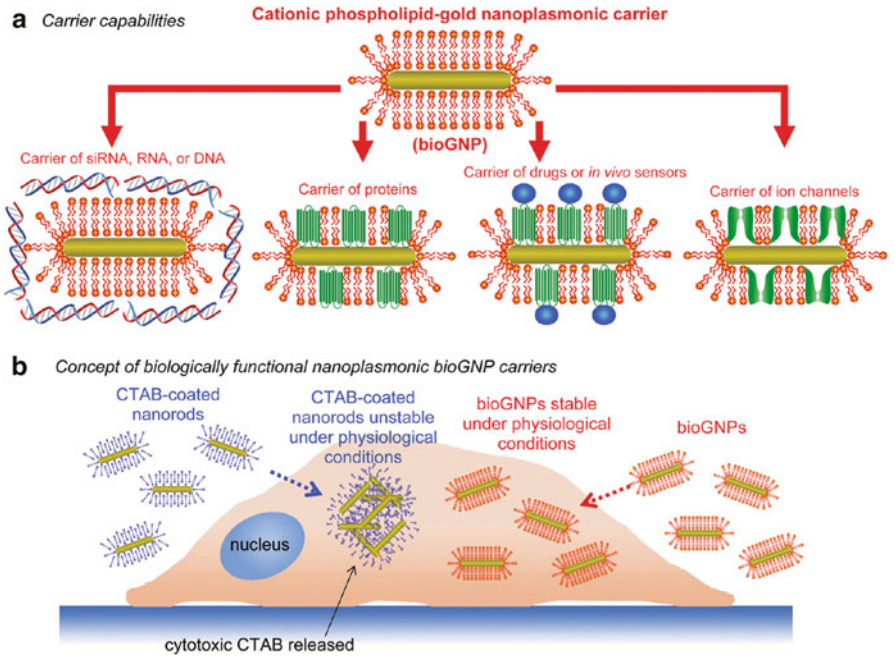

Fig. 8.10 Schematic representation of the idea of biologically functional cationic phospholipid-gold nanoplasmonic carriers. (**a**) The cationic phospholipid bilayer member surrounded gold nanoplasmonic carriers are able to deliver various types of biomolecules such as RNA oligonucleotides, DNA oligonucleotides, siRNA, proteins, and drugs by binding to the positively charged surface or by incorporation into the membrane. (**b**) While cetrimonium bromide (CTAB) dissociated from the nanorods' surface will affect the performance of gold nanorods, the nontoxic bioGNPs are highly stable and able to obtain unique optical properties for plasmonic-based applications (Reprinted with the permission from Ref. [154]. Copyright 2009 American Chemical Society)

5 nm would have a maximum absorbance at 520 nm. However, the maximum absorbance could shift to more than 1000 nm if we have tuned the particle size larger than 5 nm. This maximum absorbance also refers to the colors of the nanoparticles [153]. In addition, AuNPs have the capability to form covalent bonds for surface modification, especially with thiol group. Thiolation of AuNPs using cysteamine would demonstrate enabled biofunctionalization, improve colloidal stability, and maintain plamonic properties and good biocompatibility under physiological conditions (Fig. 8.10) [154].

Due to the versatile properties, AuNPs attract wider application than SPIOs and fall into three major categories: (1) AuNPs for labeling and visualizing, (2) AuNPs for gene delivery vehicle, and (3) AuNPs as heat source [155].

AuNPs as Labeling and Visualizing One of the AuNPs' traditional applications would be immunostaining. The goal of immunostaining is to label specific molecules by antibody so that they can be visualized owing to the contrast with other structures or molecules of the cell. The protocol of immunostaining with AuNPs

requires the fixation of cells and addition of antibody-conjugated AuNPs afterward. The antibody will direct AuNPs to bind specific interested region, while the AuNPs will provide extraordinary contrast for TEM imaging with high lateral resolution and larger structures can also be imaged with optical microscopes [155]. The antibody-conjugated AuNPs can also be specific to the organ of interest in animal, which allow them to be contrast agents for X-rays. However, the colloidal nanoparticles only possess short circulation time, and therefore, it can be cleared from the bloodstream by the liver and kidneys fast. Nevertheless, gold nanoparticles can be imaged with signal-to-noise ratio with X-ray computer tomography, and therefore, short exposure time would be enough for imaging, reducing radiation at the same time [156, 157]. Conjugating Gd supramolecular complexes or IONPs makes AuNPs as good MRI contrast agent. To synthesize Gd-conjugated AuNPs, surface modification with a supramolecular ligand which could ultimately complex the Gd ion will be performed after synthesizing AuNPs [158]. The idea of combining IONP and AuNP is to design a triple probe for MRI/CT imaging contrast agent and optical imaging. There are two ways to associate them – iron oxide core with gold surface or gold core with iron surface. These dual MRI/optical agents are also of practical interest due to the advanced catalytic properties [159].

AuNPs for Gene Delivery Vehicle AuNPs can be loaded with massive DNA as nanobullets for gene therapy inside cells. DNA will be absorbed onto the surface of AuNPs and shot into the cells along with AuNPs [160]. Depending on the size of loaded gold particles, it will require different types of guns with various gas pressure or electric discharges [161]. Three major reasons account AuNPs' wide application. First, they can be synthesized in a measurable fashion with low size distribution [162]. Second, multiple functional moieties, not only nucleic acids but also targeting agents, can be surface modified onto AuNPs [163]. Finally, the cytotoxicity, biodistribution, and in vivo excretion properties can be precisely controlled via the particle size, shape, and surface functionality [164, 165].

AuNPs as Theranostics When gold particles absorb light, the instinct free electrons in the free electrons are excited, which then cause the collective oscillation of the free electrons. Via interaction between the crystal lattice and the electrons, the electrons relax and the thermal energy is transferred to the lattice. Then the heat would dissipate into the surrounding tissues in vivo [166]. This provides an effective treatment for cancer called "hyperthermia." The idea of hyperthermia is to utilize the sensitivity of body temperature. It is known that the human temperatures above 37 °C lead to fever and temperatures above 42 °C are lethal. Therefore, we can direct colloidal AuNPs to cancer area by conjugating the particle surface with ligands that are specific to receptors overexpressed in cancer cells. If we could stimuli particles to heat, then the temperature of cells close to the particles is raised, and therefore, these cells can be killed [167]. The AuNPs' heating property can be stimulated by absorption of light. Therefore, with appropriate surface chemical modification, we will be able to design AuNPs targeting to tumor area and killing cancer cells. Since the size and quantity can be controlled in vivo, AuNPs are able to kill cancerous tissues without exposing the entire organism to increase the temperatures

[168]. The heating property also could dissociate double-stranded DNA into two single strands. Therefore, researchers have conjugated DNA onto AuNPs to locally deliver DNA into cells. Similar concepts have also been used to disassemble protein aggregates by local heating [169].

8.5 Conclusions

Fifteen years ago, Dr. Verna said that "there are only three problems in gene therapy-delivery, delivery and delivery." Until now, "delivery" is still the main issue for achieving successful gene therapy. Multifunctional nanoparticle-based gene delivery systems have shown great success due to the following: (1) nanoparticles are usually biologically degradable with minimal cytotoxicity, (2) nanoparticles have wide surface area available for chemical modification to improve the physiochemical characteristics with simple purification method, and (3) nanoparticles have unique optical and magnetic properties, making it possible to visualize the delivery process both in vitro and in vivo [13]. However, such novel nanoparticles are now still in lab research period, among which very few types of them have gone to clinical trial. The aggregation or disintegration of nanoparticles and the toxic effects associated with exposure to inorganic nanoparticles hinder their application in clinical application. More translational research would be needed to expand and testify the nanoparticles' role in gene therapy. Collaborations from multidisciplinary subjects, including engineering, chemistry, biology, and medicine, would be of great need to design multifunctional nanoparticles for imaging-guided gene delivery and to provide versatile treatment strategies for various diseases including cancer.

Acknowledgments This work was supported by the College of Engineering and Mathematical Sciences at the University of Vermont, the Major State Basic Research Development Program of China (973 Program) (Grant Nos. 2014CB744503 and 2013CB733802), the National Natural Science Foundation of China (NSFC) (Grant Nos. 81422023, 81101101, 81371596, and 51273165), the Key Project of Chinese Ministry of Education (Grant No. 212149), the Fundamental Research Funds for the Central Universities, China (Grant No. 2013121039), and the Program for New Century Excellent Talents in University (NCET-13-0502).

References

1. Ginn SL, Alexander IE, Edelstein ML, Abedi MR, Wixon J (2013) Gene therapy clinical trials worldwide to 2012 – an update. J Gene Med 15(2):65–77. doi:10.1002/jgm.2698
2. Liu G, Swierczewska M, Lee S, Chen X (2010) Functional nanoparticles for molecular imaging guided gene delivery. Nano Today 5(6):524–539. doi:10.1016/j.nantod.2010.10.005
3. Castellani S, Conese M (2010) Lentiviral vectors and cystic fibrosis gene therapy. Viruses 2(2):395–412
4. Acland GM, Aguirre GD, Ray J, Zhang Q, Aleman TS, Cideciyan AV, Pearce-Kelling SE, Anand V, Zeng Y, Maguire AM (2001) Gene therapy restores vision in a canine model of childhood blindness. Nat Genet 28(1):92–95

5. Allen PJ, Feigin A (2014) Gene-based therapies in Parkinson's disease. Neurotherapeutics 11(1):60–67
6. Cross D, Burmester JK (2006) Gene therapy for cancer treatment: past, present and future. Clin Med Res 4(3):218–227
7. Whitehead KA, Langer R, Anderson DG (2009) Knocking down barriers: advances in siRNA delivery. Nat Rev Drug Discov 8(2):129–138
8. Wang J, Lu Z, Wientjes MG, Au JL (2010) Delivery of siRNA therapeutics: barriers and carriers. AAPS J 12(4):492–503. doi:10.1208/s12248-010-9210-4
9. Liu X-Q, Sun C-Y, Yang X-Z, Wang J (2013) Polymeric-micelle-based nanomedicine for siRNA delivery. Part Part Syst Char 30(3):211–228. doi:10.1002/ppsc.201200061
10. Oh Y-K, Park TG (2009) siRNA delivery systems for cancer treatment. Adv Drug Deliv Rev 61(10):850–862
11. Bumcrot D, Manoharan M, Koteliansky V, Sah DW (2006) RNAi therapeutics: a potential new class of pharmaceutical drugs. Nat Chem Biol 2(12):711–719
12. Kanasty R, Dorkin JR, Vegas A, Anderson D (2013) Delivery materials for siRNA therapeutics. Nat Mater 12(11):967–977
13. Wang Z, Liu G, Zheng H, Chen X (2014) Rigid nanoparticle-based delivery of anti-cancer siRNA: challenges and opportunities. Biotechnol Adv 32(4):831–843. doi:10.1016/j.biotechadv.2013.08.020
14. Zaidi SK, Young DW, Javed A, Pratap J, Montecino M, van Wijnen A, Lian JB, Stein JL, Stein GS (2007) Nuclear microenvironments in biological control and cancer. Nat Rev Cancer 7(6):454–463
15. Jones CH, Chen C-K, Ravikrishnan A, Rane S, Pfeifer BA (2013) Overcoming nonviral gene delivery barriers: perspective and future. Mol Pharm 10(11):4082–4098. doi:10.1021/mp400467x
16. James ML, Gambhir SS (2012) A molecular imaging primer: modalities, imaging agents, and applications. Physiol Rev 92(2):897–965. doi:10.1152/physrev.00049.2010
17. Kango S, Kalia S, Celli A, Njuguna J, Habibi Y, Kumar R (2013) Surface modification of inorganic nanoparticles for development of organic–inorganic nanocomposites – a review. Prog Polym Sci 38(8):1232–1261. doi:10.1016/j.progpolymsci.2013.02.003
18. Kaittanis C, Shaffer TM, Thorek DL, Grimm J (2014) Dawn of advanced molecular medicine: nanotechnological advancements in cancer imaging and therapy. Crit Rev Oncog 19(3–4):143–176
19. Hu TY (2014) Multidisciplinary efforts driving translational theranostics. Theranostics 4(12):1209–1210
20. Niu G, Chen X (2009) Noninvasive visualization of microRNA by bioluminescence imaging. Mol Imaging Biol 11(2):61–63. doi:10.1007/s11307-008-0190-z
21. Na HB, Song IC, Hyeon T (2009) Inorganic nanoparticles for MRI contrast agents. Adv Mater 21(21):2133–2148. doi:10.1002/adma.200802366
22. Bao G, Mitragotri S, Tong S (2013) Multifunctional nanoparticles for drug delivery and molecular imaging. Annu Rev Biomed Eng 15:253–282. doi:10.1146/annurev-bioeng-071812-152409
23. Strijkers GJ, Mulder WJ, van Tilborg GA, Nicolay K (2007) MRI contrast agents: current status and future perspectives. Anticancer Agents Med Chem 7(3):291–305
24. Zhu D, Liu F, Ma L, Liu D, Wang Z (2013) Nanoparticle-based systems for t1-weighted magnetic resonance imaging contrast agents. Int J Mol Sci 14(5):10591–10607. doi:10.3390/ijms140510591
25. Ratzinger G, Agrawal P, Korner W, Lonkai J, Sanders HM, Terreno E, Wirth M, Strijkers GJ, Nicolay K, Gabor F (2010) Surface modification of PLGA nanospheres with Gd-DTPA and Gd-DOTA for high-relaxivity MRI contrast agents. Biomaterials 31(33):8716–8723. doi:10.1016/j.biomaterials.2010.07.095
26. Su H, Wu C, Zhu J, Miao T, Wang D, Xia C, Zhao X, Gong Q, Song B, Ai H (2012) Rigid Mn(ii) chelate as efficient MRI contrast agent for vascular imaging. Dalton Trans 41(48):14480–14483. doi:10.1039/C2DT31696J

27. Luo K, Tian J, Liu G, Sun J, Xia C, Tang H, Lin L, Miao T, Zhao X, Gao F, Gong Q, Song B, Shuai X, Ai H, Gu Z (2010) Self-assembly of SiO2/Gd-DTPA-polyethylenimine nanocomposites as magnetic resonance imaging probes. J Nanosci Nanotechnol 10(1):540–548
28. Sevick-Muraca EM (2012) Translation of near-infrared fluorescence imaging technologies: emerging clinical applications. Annu Rev Med 63:217–231. doi:10.1146/annurev-med-070910-083323
29. Larson DR, Ow H, Vishwasrao HD, Heikal AA, Wiesner U, Webb WW (2008) Silica nanoparticle architecture determines radiative properties of encapsulated fluorophores. Chem Mater 20(8):2677–2684. doi:10.1021/cm7026866
30. Kircher MF, Mahmood U, King RS, Weissleder R, Josephson L (2003) A multimodal nanoparticle for preoperative magnetic resonance imaging and intraoperative optical brain tumor delineation. Cancer Res 63(23):8122–8125
31. Lee HY, Li Z, Chen K, Hsu AR, Xu C, Xie J, Sun S, Chen X (2008) PET/MRI dual-modality tumor imaging using arginine-glycine-aspartic (RGD)-conjugated radiolabeled iron oxide nanoparticles. J Nucl Med 49(8):1371–1379. doi:10.2967/jnumed.108.051243
32. Mahmoudi M, Sant S, Wang B, Laurent S, Sen T (2011) Superparamagnetic iron oxide nanoparticles (SPIONs): development, surface modification and applications in chemotherapy. Adv Drug Deliv Rev 63(1–2):24–46. doi:10.1016/j.addr.2010.05.006
33. Viglianti BL, Abraham SA, Michelich CR, Yarmolenko PS, MacFall JR, Bally MB, Dewhirst MW (2004) In vivo monitoring of tissue pharmacokinetics of liposome/drug using MRI: illustration of targeted delivery. Magn Reson Med 51(6):1153–1162. doi:10.1002/mrm.20074
34. Turetschek K, Preda A, Floyd E, Shames D, Novikov V, Roberts T, Wood J, Fu Y, Carter W, Brasch R (2003) MRI monitoring of tumor response following angiogenesis inhibition in an experimental human breast cancer model. Eur J Nucl Med 30(3):448–455. doi:10.1007/s00259-002-1000-5
35. Shapiro B (2009) Towards dynamic control of magnetic fields to focus magnetic carriers to targets deep inside the body. J Magn Magn Mater 321(10):1594. doi:10.1016/j.jmmm.2009.02.094
36. Shim MS, Kwon YJ (2012) Stimuli-responsive polymers and nanomaterials for gene delivery and imaging applications. Adv Drug Deliv Rev 64(11):1046–1059. doi:10.1016/j.addr.2012.01.018
37. Lemkine GF, Demeneix BA (2001) Polyethylenimines for in vivo gene delivery. Curr Opin Mol Ther 3(2):178–182
38. Zhang X, Oulad-Abdelghani M, Zelkin AN, Wang Y, Haikel Y, Mainard D, Voegel JC, Caruso F, Benkirane-Jessel N (2010) Poly(L-lysine) nanostructured particles for gene delivery and hormone stimulation. Biomaterials 31(7):1699–1706. doi:10.1016/j.biomaterials.2009.11.032
39. Zhou J, Wu J, Hafdi N, Behr J-P, Erbacher P, Peng L (2006) PAMAM dendrimers for efficient siRNA delivery and potent gene silencing. Chem Commun 22:2362–2364. doi:10.1039/B601381C
40. McKenzie DL, Kwok KY, Rice KG (2000) A potent new class of reductively activated peptide gene delivery agents. J Biol Chem 275(14):9970–9977
41. Dachs GU, Dougherty GJ, Stratford IJ, Chaplin DJ (1997) Targeting gene therapy to cancer: a review. Oncol Res 9(6–7):313–325
42. Schiffelers RM, Ansari A, Xu J, Zhou Q, Tang Q, Storm G, Molema G, Lu PY, Scaria PV, Woodle MC (2004) Cancer siRNA therapy by tumor selective delivery with ligand-targeted sterically stabilized nanoparticle. Nucleic Acids Res 32(19), e149, http://www.ncbi.nlm.nih.gov/pubmed/15520458
43. Low PS, Henne WA, Doorneweerd DD (2007) Discovery and development of folic-acid-based receptor targeting for imaging and therapy of cancer and inflammatory diseases. Acc Chem Res 41(1):120–129
44. Brannon-Peppas L, Blanchette JO (2012) Nanoparticle and targeted systems for cancer therapy. Adv Drug Deliv Rev 64:206–212

45. Bagalkot V, Zhang L, Levy-Nissenbaum E, Jon S, Kantoff PW, Langer R, Farokhzad OC (2007) Quantum dot-aptamer conjugates for synchronous cancer imaging, therapy, and sensing of drug delivery based on bi-fluorescence resonance energy transfer. Nano Lett 7(10):3065–3070
46. Matsumura Y, Maeda H (1986) A new concept for macromolecular therapeutics in cancer chemotherapy: mechanism of tumoritropic accumulation of proteins and the antitumor agent smancs. Cancer Res 46(12 Pt 1):6387–6392
47. Fang J, Nakamura H, Maeda H (2011) The EPR effect: unique features of tumor blood vessels for drug delivery, factors involved, and limitations and augmentation of the effect. Adv Drug Deliv Rev 63(3):136–151. doi:10.1016/j.addr.2010.04.009
48. Kularatne SA, Low PS (2010) Targeting of nanoparticles: folate receptor. Methods Mol Biol (Clifton, NJ) 624:249–265. doi:10.1007/978-1-60761-609-2_17
49. Danhier F, Breton AL, Préat V (2012) RGD-based strategies to target alpha(v) beta(3) integrin in cancer therapy and diagnosis. Mol Pharm 9(11):2961–2973. doi:10.1021/mp3002733
50. Vecchione L, Jacobs B, Normanno N, Ciardiello F, Tejpar S (2011) EGFR-targeted therapy. Exp Cell Res 317(19):2765–2771. doi:10.1016/j.yexcr.2011.08.021
51. Li Z, Zhao R, Wu X, Sun Y, Yao M, Li J, Xu Y, Gu J (2005) Identification and characterization of a novel peptide ligand of epidermal growth factor receptor for targeted delivery of therapeutics. FASEB J 19(14):1978–1985. doi:10.1096/fj.05-4058com
52. Huang X, Peng X, Wang Y, Wang Y, Shin DM, El-Sayed MA, Nie S (2010) A reexamination of active and passive tumor targeting by using rod-shaped gold nanocrystals and covalently conjugated peptide ligands. ACS Nano 4(10):5887–5896. doi:10.1021/nn102055s
53. Chang SJ, Lee CH, Hsu CY, Wang YJ (2002) Biocompatible microcapsules with enhanced mechanical strength. J Biomed Mater Res 59:118–126
54. Miao T, Rao KS, Spees JL, Oldinski RA (2014) Osteogenic differentiation of human mesenchymal stem cells through alginate-graft-poly(ethylene glycol) microsphere-mediated intracellular growth factor delivery. J Control Release 192(0):57–66. doi:10.1016/j.jconrel.2014.06.029
55. Davidovich-Pinhas M, Bianco-Peled H (2011) Alginate-PEGAc: a new mucoadhesive polymer. Acta Biomater 7:625–633
56. Davidovich-Pinhas M, Bianco-Peled H (2011) Physical and structural characteristics of acrylated poly(ethylene glycol)-alginate conjugates. Acta Biomater 7:2817–2825
57. Meng X-W, Qin J, Liu Y, Fan M-M, Li B-J, Zhang S, Yu X-Q (2010) Degradable hollow spheres based on self-assembly inclusion. Chem Commun 46:643–645
58. Meng X-W, Ha W, Cheng C, Dong Z-Q, Ding L-S, Li B-J, Zhang S (2011) Hollow nanospheres based on the self-assembly of alginate-graft-poly(ethylene glycol) and α-cyclodextrin. Langmuir 27:14401–14407
59. Mahou R, Wandrey C (2010) Alginate-poly(ethylene glycol) hybrid microspheres with adjustable physical properties. Macromolecules (Washington, DC, US) 43(3):1371–1378. doi:10.1021/ma902469f
60. Mahou R, Tran NM, Dufresne M, Legallais C, Wandrey C (2012) Encapsulation of Huh-7 cells within alginate-poly(ethylene glycol) hybrid microspheres. J Mater Sci-Mater M 23(1):171–179. doi:10.1007/s10856-011-4512-3
61. Knop K, Hoogenboom R, Fischer D, Schubert US (2010) Poly(ethylene glycol) in drug delivery: pros and cons as well as potential alternatives. Angew Chem Int Ed 49(36):6288–6308. doi:10.1002/anie.200902672
62. Bassyouni F, ElHalwany N, Abdel Rehim M, Neyfeh M (2013) Advances and new technologies applied in controlled drug delivery system. Res Chem Intermed:1–36. doi:10.1007/s11164-013-1338-2
63. Andresen TL, Thompson DH, Kaasgaard T (2010) Enzyme-triggered nanomedicine: drug release strategies in cancer therapy. Mol Membr Biol 27(7):353–363. doi:10.3109/09687688.2010.515950

64. Walker GF, Fella C, Pelisek J, Fahrmeir J, Boeckle S, Ogris M, Wagner E (2005) Toward synthetic viruses: endosomal pH-triggered deshielding of targeted polyplexes greatly enhances gene transfer in vitro and in vivo. Mol Ther 11(3):418–425. doi:10.1016/j.ymthe.2004.11.006
65. Varkouhi AK, Scholte M, Storm G, Haisma HJ (2011) Endosomal escape pathways for delivery of biologicals. J Control Release 151(3):220–228. doi:10.1016/j.jconrel.2010.11.004
66. Huang HW, Chen F-Y, Lee M-T (2004) Molecular mechanism of peptide-induced pores in membranes. Phys Rev Lett 92(19):198304
67. Miller DK, Griffiths E, Lenard J, Firestone RA (1983) Cell killing by lysosomotropic detergents. J Cell Biol 97(6):1841–1851
68. Epand RM (2003) Fusion peptides and the mechanism of viral fusion. Biochim Biophys Acta 1614(1):116–121
69. Lou PJ, Lai PS, Shieh MJ, Macrobert AJ, Berg K, Bown SG (2006) Reversal of doxorubicin resistance in breast cancer cells by photochemical internalization. Int J Cancer 119(11):2692–2698. doi:10.1002/ijc.22098
70. Zeng Y, Cullen BR (2002) RNA interference in human cells is restricted to the cytoplasm. RNA 8(7):855–860
71. van der Aa MA, Mastrobattista E, Oosting RS, Hennink WE, Koning GA, Crommelin DJ (2006) The nuclear pore complex: the gateway to successful nonviral gene delivery. Pharm Res 23(3):447–459. doi:10.1007/s11095-005-9445-4
72. Zanta MA, Belguise-Valladier P, Behr JP (1999) Gene delivery: a single nuclear localization signal peptide is sufficient to carry DNA to the cell nucleus. Proc Natl Acad Sci U S A 96(1):91–96
73. Alexis F, Zeng J, Shu W (2006) PEI nanoparticles for targeted gene delivery. Cold Spring Harb Protoc 2006(1):pdb. prot4451
74. Koping-Hoggard M, Tubulekas I, Guan H, Edwards K, Nilsson M, Varum KM, Artursson P (2001) Chitosan as a nonviral gene delivery system. Structure–property relationships and characteristics compared with polyethylenimine in vitro and after lung administration in vivo. Gene Ther 8(14):1108–1121. doi:10.1038/sj.gt.3301492
75. Saranya N, Moorthi A, Saravanan S, Devi MP, Selvamurugan N (2011) Chitosan and its derivatives for gene delivery. Int J Biol Macromol 48(2):234–238. doi:10.1016/j.ijbiomac.2010.11.013
76. Toncheva V, Wolfert MA, Dash PR, Oupicky D, Ulbrich K, Seymour LW, Schacht EH (1998) Novel vectors for gene delivery formed by self-assembly of DNA with poly (L-lysine) grafted with hydrophilic polymers. Biochim Biophys Acta 1380(3):354–368
77. Shcharbin D, Shakhbazau A, Bryszewska M (2013) Poly(amidoamine) dendrimer complexes as a platform for gene delivery. Expert Opin Drug Deliv 10(12):1687–1698. doi:10.1517/17425247.2013.853661
78. Benns JM, Choi JS, Mahato RI, Park JS, Kim SW (2000) pH-sensitive cationic polymer gene delivery vehicle: N-Ac-poly(L-histidine)-graft-poly(L-lysine) comb shaped polymer. Bioconjug Chem 11(5):637–645
79. Choi YH, Liu F, Kim J-S, Choi YK, Jong Sang P, Kim SW (1998) Polyethylene glycol-grafted poly-l-lysine as polymeric gene carrier. J Control Release 54(1):39–48. doi:10.1016/S0168-3659(97)00174-0
80. Moghimi SM, Hunter AC, Murray JC (2001) Long-circulating and target-specific nanoparticles: theory to practice. Pharmacol Rev 53(2):283–318
81. Jeong B, Gutowska A (2002) Lessons from nature: stimuli-responsive polymers and their biomedical applications. Trends Biotechnol 20(7):305–311
82. Juliano RL, Stamp D (1975) The effect of particle size and charge on the clearance rates of liposomes and liposome encapsulated drugs. Biochem Biophys Res Commun 63(3):651–658
83. Stolnik S, Illum L, Davis SS (2012) Long circulating microparticulate drug carriers. Adv Drug Deliv Rev 64(Suppl (0)):290–301. doi:10.1016/j.addr.2012.09.029

84. Beningo KA, Wang YL (2002) Fc-receptor-mediated phagocytosis is regulated by mechanical properties of the target. J Cell Sci 115(Pt 4):849–856
85. Kesharwani P, Jain K, Jain NK (2014) Dendrimer as nanocarrier for drug delivery. Prog Polym Sci 39(2):268–307. doi:10.1016/j.progpolymsci.2013.07.005
86. Svenson S, Tomalia DA (2005) Dendrimers in biomedical applications – reflections on the field. Adv Drug Deliv Rev 57(15):2106–2129. doi:10.1016/j.addr.2005.09.018
87. Lee CC, MacKay JA, Frechet JMJ, Szoka FC (2005) Designing dendrimers for biological applications. Nat Biotechnol 23(12):1517–1526. http://www.nature.com/nbt/journal/v23/n12/suppinfo/nbt1171_S1.html
88. Amirkhanov NV, Zhang K, Aruva MR, Thakur ML, Wickstrom E (2010) Imaging human pancreatic cancer xenografts by targeting mutant KRAS2 mRNA with [111In]DOTAn-Poly(diamidopropanoyl)m-KRAS2 PNA-d(Cys-Ser-Lys-Cys) nanoparticles. Bioconjug Chem 21(4):731–740. doi:10.1021/bc900523c
89. Lin Q, Chen J, Zhang Z, Zheng G (2014) Lipid-based nanoparticles in the systemic delivery of siRNA. Nanomedicine (Lond) 9(1):105–120. doi:10.2217/nnm.13.192
90. Miller AD (2013) Lipid-based nanoparticles in cancer diagnosis and therapy. J Drug Delivery 2013:9. doi:10.1155/2013/165981
91. Mulder WJ, Strijkers GJ, van Tilborg GA, Griffioen AW, Nicolay K (2006) Lipid-based nanoparticles for contrast-enhanced MRI and molecular imaging. NMR Biomed 19(1):142–164. doi:10.1002/nbm.1011
92. Gilleron J, Querbes W, Zeigerer A, Borodovsky A, Marsico G, Schubert U, Manygoats K, Seifert S, Andree C, Stoter M, Epstein-Barash H, Zhang L, Koteliansky V, Fitzgerald K, Fava E, Bickle M, Kalaidzidis Y, Akinc A, Maier M, Zerial M (2013) Image-based analysis of lipid nanoparticle-mediated siRNA delivery, intracellular trafficking and endosomal escape. Nat Biotechnol 31(7):638–646. doi:10.1038/nbt.2612, http://www.nature.com/nbt/journal/v31/n7/abs/nbt.2612.html#supplementary-information
93. Jiang S, Eltoukhy AA, Love KT, Langer R, Anderson DG (2013) Lipidoid-coated iron oxide nanoparticles for efficient DNA and siRNA delivery. Nano Lett 13(3):1059–1064. doi:10.1021/nl304287a
94. Tatur S, Maccarini M, Barker R, Nelson A, Fragneto G (2013) Effect of functionalized gold nanoparticles on floating lipid bilayers. Langmuir 29(22):6606–6614. doi:10.1021/la401074y
95. Qiu L, Jing N, Jin Y (2008) Preparation and in vitro evaluation of liposomal chloroquine diphosphate loaded by a transmembrane pH-gradient method. Int J Pharm 361(1–2):56–63. doi:10.1016/j.ijpharm.2008.05.010
96. Malam Y, Loizidou M, Seifalian AM (2009) Liposomes and nanoparticles: nanosized vehicles for drug delivery in cancer. Trends Pharmacol Sci 30(11):592–599. doi:10.1016/j.tips.2009.08.004
97. Pearce TR, Shroff K, Kokkoli E (2012) Peptide targeted lipid nanoparticles for anticancer drug delivery. Adv Mater (Deerfield Beach, Fla) 24(28):3803–3822, 3710. doi:10.1002/adma.201200832
98. Puri A, Loomis K, Smith B, Lee JH, Yavlovich A, Heldman E, Blumenthal R (2009) Lipid-based nanoparticles as pharmaceutical drug carriers: from concepts to clinic. Crit Rev Ther Drug Carrier Syst 26(6):523–580
99. Barenholz Y (2012) Doxil® – the first FDA-approved nano-drug: lessons learned. J Control Release 160(2):117–134. doi:10.1016/j.jconrel.2012.03.020
100. Ogawara K, Un K, Tanaka K, Higaki K, Kimura T (2009) In vivo anti-tumor effect of PEG liposomal doxorubicin (DOX) in DOX-resistant tumor-bearing mice: involvement of cytotoxic effect on vascular endothelial cells. J Control Release 133(1):4–10. doi:10.1016/j.jconrel.2008.09.008
101. Krishnan K, Pakhomov A, Bao Y, Blomqvist P, Chun Y, Gonzales M, Griffin K, Ji X, Roberts B (2006) Nanomagnetism and spin electronics: materials, microstructure and novel properties. J Mater Sci 41(3):793–815

102. Lee J-H, Huh Y-M, Y-w J, J-w S, J-t J, Song H-T, Kim S, Cho E-J, Yoon H-G, Suh J-S (2006) Artificially engineered magnetic nanoparticles for ultra-sensitive molecular imaging. Nat Med 13(1):95–99
103. Lin C, Cai S, Feng J (2012) Positive contrast imaging of SPIO nanoparticles. J Nanomater 2012:9. doi:10.1155/2012/734842
104. Sadhukha T, Wiedmann TS, Panyam J (2013) Inhalable magnetic nanoparticles for targeted hyperthermia in lung cancer therapy. Biomaterials 34(21):5163–5171. doi:10.1016/j.biomaterials.2013.03.061
105. Baraki H, Zinne N, Wedekind D, Meier M, Bleich A, Glage S, Hedrich HJ, Kutschka I, Haverich A (2012) Magnetic resonance imaging of soft tissue infection with iron oxide labeled granulocytes in a rat model. PLoS One 7(12), e51770. doi:10.1371/journal.pone.0051770
106. Patel D, Kell A, Simard B, Deng J, Xiang B, Lin H-Y, Gruwel M, Tian G (2010) Cu^{2+}–labeled, SPION loaded porous silica nanoparticles for cell labeling and multifunctional imaging probes. Biomaterials 31(10):2866–2873
107. Liu G, Xie J, Zhang F, Wang Z, Luo K, Zhu L, Quan Q, Niu G, Lee S, Ai H, Chen X (2011) N-Alkyl-PEI-functionalized iron oxide nanoclusters for efficient siRNA delivery. Small 7(19):2742–2749. doi:10.1002/smll.201100825
108. Ai H, Flask C, Weinberg B, Shuai XT, Pagel MD, Farrell D, Duerk J, Gao J (2005) Magnetite-loaded polymeric micelles as ultrasensitive magnetic-resonance probes. Adv Mater 17(16):1949–1952. doi:10.1002/adma.200401904
109. Sun S, Zeng H, Robinson DB, Raoux S, Rice PM, Wang SX, Li G (2003) Monodisperse MFe2O4 (M=Fe, Co, Mn) nanoparticles. J Am Chem Soc 126(1):273–279. doi:10.1021/ja0380852
110. Clement O, Siauve N, Cuenod CA, Frija G (1998) Liver imaging with ferumoxides (Feridex): fundamentals, controversies, and practical aspects. Top Magn Reson Imaging 9(3):167–182
111. del Pino P, Munoz-Javier A, Vlaskou D, Rivera Gil P, Plank C, Parak WJ (2010) Gene silencing mediated by magnetic lipospheres tagged with small interfering RNA. Nano Lett 10(10):3914–3921. doi:10.1021/nl102485v
112. Zhang C, Gao S, Jiang W, Lin S, Du F, Li Z, Huang W (2010) Targeted minicircle DNA delivery using folate–poly(ethylene glycol)–polyethylenimine as non-viral carrier. Biomaterials 31(23):6075–6086. doi:10.1016/j.biomaterials.2010.04.042
113. Alivisatos AP (1996) Semiconductor clusters, nanocrystals, and quantum dots. Science 271(5251):933–937. doi:10.1126/science.271.5251.933
114. Gao J, Chen K, Xie R, Xie J, Yan Y, Cheng Z, Peng X, Chen X (2010) In vivo tumor-targeted fluorescence imaging using near-infrared non-cadmium quantum dots. Bioconjug Chem 21(4):604–609. doi:10.1021/bc900323v
115. Cai W, Chen K, Li ZB, Gambhir SS, Chen X (2007) Dual-function probe for PET and near-infrared fluorescence imaging of tumor vasculature. J Nucl Med 48(11):1862–1870. doi:10.2967/jnumed.107.043216
116. Chen O, Zhao J, Chauhan VP, Cui J, Wong C, Harris DK, Wei H, Han H-S, Fukumura D, Jain RK, Bawendi MG (2013) Compact high-quality CdSe–CdS core–shell nanocrystals with narrow emission linewidths and suppressed blinking. Nat Mater 12(5):445–451. doi:10.1038/nmat3539, http://www.nature.com/nmat/journal/v12/n5/abs/nmat3539.html#supplementary-information
117. Amelia M, Lincheneau C, Silvi S, Credi A (2012) Electrochemical properties of CdSe and CdTe quantum dots. Chem Soc Rev 41(17):5728–5743. doi:10.1039/C2CS35117J
118. Dabbousi BO, Rodriguez-Viejo J, Mikulec FV, Heine JR, Mattoussi H, Ober R, Jensen KF, Bawendi MG (1997) (CdSe)ZnS Core−shell quantum dots: synthesis and characterization of a size series of highly luminescent nanocrystallites. J Phys Chem B 101(46):9463–9475. doi:10.1021/jp971091y
119. Yuan J, Wen D, Gaponik N, Eychmüller A (2013) Enzyme-encapsulating quantum dot hydrogels and xerogels as biosensors: multifunctional platforms for both biocatalysis and fluorescent probing. Angew Chem Int Ed 52(3):976–979. doi:10.1002/anie.201205791

120. Wang J, Xia J (2011) Preferential binding of a novel polyhistidine peptide dendrimer ligand on quantum dots probed by capillary electrophoresis. Anal Chem 83(16):6323–6329. doi:10.1021/ac2011922
121. East DA, Mulvihill DP, Todd M, Bruce IJ (2011) QD-antibody conjugates via carbodiimide-mediated coupling: a detailed study of the variables involved and a possible new mechanism for the coupling reaction under basic aqueous conditions. Langmuir 27(22):13888–13896. doi:10.1021/la203273p
122. Algar WR, Krull UJ (2006) Adsorption and hybridization of oligonucleotides on mercaptoacetic acid-capped CdSe/ZnS quantum dots and quantum dot-oligonucleotide conjugates. Langmuir 22(26):11346–11352. doi:10.1021/la062217y
123. Algar WR, Tavares AJ, Krull UJ (2010) Beyond labels: a review of the application of quantum dots as integrated components of assays, bioprobes, and biosensors utilizing optical transduction. Anal Chim Acta 673(1):1–25. doi:10.1016/j.aca.2010.05.026
124. Belin T, Epron F (2005) Characterization methods of carbon nanotubes: a review. Mater Sci Eng: B 119(2):105–118. doi:10.1016/j.mseb.2005.02.046
125. Cheung W, Pontoriero F, Taratula O, Chen AM, He H (2010) DNA and carbon nanotubes as medicine. Adv Drug Deliv Rev 62(6):633–649. doi:10.1016/j.addr.2010.03.007
126. Pantarotto D, Singh R, McCarthy D, Erhardt M, Briand J-P, Prato M, Kostarelos K, Bianco A (2004) Functionalized carbon nanotubes for plasmid DNA gene delivery. Angew Chem Int Ed 43(39):5242–5246. doi:10.1002/anie.200460437
127. Singh R, Pantarotto D, McCarthy D, Chaloin O, Hoebeke J, Partidos CD, Briand JP, Prato M, Bianco A, Kostarelos K (2005) Binding and condensation of plasmid DNA onto functionalized carbon nanotubes: toward the construction of nanotube-based gene delivery vectors. J Am Chem Soc 127(12):4388–4396. doi:10.1021/ja0441561
128. Bates K, Kostarelos K (2013) Carbon nanotubes as vectors for gene therapy: past achievements, present challenges and future goals. Adv Drug Deliv Rev 65(15):2023–2033. doi:10.1016/j.addr.2013.10.003
129. Boussif O, Lezoualc'h F, Zanta MA, Mergny MD, Scherman D, Demeneix B, Behr JP (1995) A versatile vector for gene and oligonucleotide transfer into cells in culture and in vivo: polyethylenimine. Proc Natl Acad Sci U S A 92(16):7297–7301
130. Wang X, Ren J, Qu X (2008) Targeted RNA interference of cyclin A2 mediated by functionalized single-walled carbon nanotubes induces proliferation arrest and apoptosis in chronic myelogenous leukemia K562 cells. ChemMedChem 3(6):940–945. doi:10.1002/cmdc.200700329
131. Podesta JE, Al-Jamal KT, Herrero MA, Tian B, Ali-Boucetta H, Hegde V, Bianco A, Prato M, Kostarelos K (2009) Antitumor activity and prolonged survival by carbon-nanotube-mediated therapeutic siRNA silencing in a human lung xenograft model. Small 5(10):1176–1185
132. Al-Jamal KT, Gherardini L, Bardi G, Nunes A, Guo C, Bussy C, Herrero MA, Bianco A, Prato M, Kostarelos K, Pizzorusso T (2011) Functional motor recovery from brain ischemic insult by carbon nanotube-mediated siRNA silencing. Proc Natl Acad Sci 108(27):10952–10957. doi:10.1073/pnas.1100930108
133. Zheng M, Jagota A, Strano MS, Santos AP, Barone P, Chou SG, Diner BA, Dresselhaus MS, Mclean RS, Onoa GB (2003) Structure-based carbon nanotube sorting by sequence-dependent DNA assembly. Science 302(5650):1545–1548
134. Liu Z, Winters M, Holodniy M, Dai H (2007) siRNA delivery into human T cells and primary cells with carbon-nanotube transporters. Angew Chem Int Ed 46(12):2023–2027
135. Dong H, Ding L, Yan F, Ji H, Ju H (2011) The use of polyethylenimine-grafted graphene nanoribbon for cellular delivery of locked nucleic acid modified molecular beacon for recognition of microRNA. Biomaterials 32(15):3875–3882
136. Gao H, Kong Y, Cui D, Ozkan CS (2003) Spontaneous insertion of DNA oligonucleotides into carbon nanotubes. Nano Lett 3(4):471–473
137. Lu Y, Liu J (2006) Functional DNA nanotechnology: emerging applications of DNAzymes and aptamers. Curr Opin Biotechnol 17(6):580–588

138. Cai D, Mataraza JM, Qin ZH, Huang Z, Huang J, Chiles TC, Carnahan D, Kempa K, Ren Z (2005) Highly efficient molecular delivery into mammalian cells using carbon nanotube spearing. Nat Methods 2(6):449–454. doi:10.1038/nmeth761
139. Bartholomeusz G, Cherukuri P, Kingston J, Cognet L, Lemos R, Leeuw TK, Gumbiner-Russo L, Weisman RB, Powis G (2009) In vivo therapeutic silencing of hypoxia-inducible factor 1 alpha (HIF-1alpha) using single-walled carbon nanotubes noncovalently coated with siRNA. Nano Res 2(4):279–291. doi:10.1007/s12274-009-9026-7
140. Wang L, Shi J, Zhang H, Li H, Gao Y, Wang Z, Wang H, Li L, Zhang C, Chen C, Zhang Z, Zhang Y (2013) Synergistic anticancer effect of RNAi and photothermal therapy mediated by functionalized single-walled carbon nanotubes. Biomaterials 34(1):262–274. doi:10.1016/j.biomaterials.2012.09.037
141. Wang X, Wang X, Wang X, Chen F, Zhu K, Xu Q, Tang M (2013) Novel electrochemical biosensor based on functional composite nanofibers for sensitive detection of p53 tumor suppressor gene. Anal Chim Acta 765(0):63–69. doi:10.1016/j.aca.2012.12.037
142. Wang L, Wang X, Bhirde A, Cao J, Zeng Y, Huang X, Sun Y, Liu G, Chen X (2014) Carbon-dot-based two-photon visible nanocarriers for safe and highly efficient delivery of siRNA and DNA. Adv Healthcare Mater 3(8):1203–1209. doi:10.1002/adhm.201300611
143. Liu Y, Lou C, Yang H, Shi M, Miyoshi H (2011) Silica nanoparticles as promising drug/gene delivery carriers and fluorescent nano-probes: recent advances. Curr Cancer Drug Targets 11(2):156–163
144. Slowing II, Vivero-Escoto JL, Wu C-W, Lin VSY (2008) Mesoporous silica nanoparticles as controlled release drug delivery and gene transfection carriers. Adv Drug Deliv Rev 60(11):1278–1288. doi:10.1016/j.addr.2008.03.012
145. Zhu S-G, Xiang J-J, Li X-L, Shen S-R, Lu H-b, Zhou J, Xiong W, Zhang B-C, Nie X-M, Zhou M, Tang K, Li G-Y (2004) Poly(l-lysine)-modified silica nanoparticles for the delivery of antisense oligonucleotides. Biotechnol Appl Biochem 39(2):179–187. doi:10.1042/BA20030077
146. Kar M, Vijayakumar PS, Prasad BLV, Gupta SS (2010) Synthesis and characterization of poly-l-lysine-grafted silica nanoparticles synthesized via NCA polymerization and click chemistry. Langmuir 26(8):5772–5781. doi:10.1021/la903595x
147. Chung TH, Wu SH, Yao M, Lu CW, Lin YS, Hung Y, Mou CY, Chen YC, Huang DM (2007) The effect of surface charge on the uptake and biological function of mesoporous silica nanoparticles in 3T3-L1 cells and human mesenchymal stem cells. Biomaterials 28(19):2959–2966. doi:10.1016/j.biomaterials.2007.03.006
148. Kim JS, Yoon TJ, Yu KN, Noh MS, Woo M, Kim BG, Lee KH, Sohn BH, Park SB, Lee JK, Cho MH (2006) Cellular uptake of magnetic nanoparticle is mediated through energy-dependent endocytosis in A549 cells. J Vet Sci 7(4):321–326
149. He X, Li Y, He D, Wang K, Shangguan J, Shi H (2014) Aptamer-fluorescent silica nanoparticles bioconjugates based dual-color flow cytometry for specific detection of Staphylococcus aureus. J Biomed Nanotechnol 10(7):1359–1368
150. Park HS, Kim CW, Lee HJ, Choi JH, Lee SG, Yun YP, Kwon IC, Lee SJ, Jeong SY, Lee SC (2010) A mesoporous silica nanoparticle with charge-convertible pore walls for efficient intracellular protein delivery. Nanotechnology 21(22):225101. doi:10.1088/0957-4484/21/22/225101
151. Herranz F, Almarza E, Rodriguez I, Salinas B, Rosell Y, Desco M, Bulte JW, Ruiz-Cabello J (2011) The application of nanoparticles in gene therapy and magnetic resonance imaging. Microsc Res Tech 74(7):577–591. doi:10.1002/jemt.20992
152. Jung LS, Campbell CT, Chinowsky TM, Mar MN, Yee SS (1998) Quantitative interpretation of the response of surface plasmon resonance sensors to adsorbed films. Langmuir 14(19):5636–5648. doi:10.1021/la971228b
153. Kurihara K, Suzuki K (2002) Theoretical understanding of an absorption-based surface plasmon resonance sensor based on Kretchmann's theory. Anal Chem 74(3):696–701

154. Lee SE, Sasaki DY, Perroud TD, Yoo D, Patel KD, Lee LP (2009) Biologically functional cationic phospholipid–gold nanoplasmonic carriers of RNA. J Am Chem Soc 131(39):14066–14074. doi:10.1021/ja904326j
155. Sperling RA, Rivera Gil P, Zhang F, Zanella M, Parak WJ (2008) Biological applications of gold nanoparticles. Chem Soc Rev 37(9):1896–1908. doi:10.1039/B712170A
156. Hainfeld JF, Slatkin DN, Focella TM, Smilowitz HM (2006) Gold nanoparticles: a new X-ray contrast agent. Br J Radiol 79(939):248–253. doi:10.1259/bjr/13169882
157. Gosselin RE (1956) The uptake of radiocolloids by macrophages in vitro; a kinetic analysis with radioactive colloidal gold. J Gen Physiol 39(5):625–649
158. Warsi MF, Adams RW, Duckett SB, Chechik V (2010) Gd-functionalised Au nanoparticles as targeted contrast agents in MRI: relaxivity enhancement by polyelectrolyte coating. Chem Commun (Camb) 46(3):451–453. doi:10.1039/b915223g
159. Shevchenko EV, Bodnarchuk MI, Kovalenko MV, Talapin DV, Smith RK, Aloni S, Heiss W, Alivisatos AP (2008) Gold/iron oxide core/hollow-shell nanoparticles. Adv Mater 20(22):4323–4329. doi:10.1002/adma.200702994
160. Chen D-R, Wendt C, Pui DH (2000) A novel approach for introducing bio-materials into cells. J Nanopart Res 2(2):133–139. doi:10.1023/A:1010084032006
161. Yang NS, Burkholder J, Roberts B, Martinell B, McCabe D (1990) In vivo and in vitro gene transfer to mammalian somatic cells by particle bombardment. Proc Natl Acad Sci 87(24):9568–9572
162. Daniel M-C, Astruc D (2004) Gold nanoparticles: assembly, supramolecular chemistry, quantum-size-related properties, and applications toward biology, catalysis, and nanotechnology. Chem Rev 104(1):293–346
163. Bowman M-C, Ballard TE, Ackerson CJ, Feldheim DL, Margolis DM, Melander C (2008) Inhibition of HIV fusion with multivalent gold nanoparticles. J Am Chem Soc 130(22):6896–6897. doi:10.1021/ja710321g
164. Wang B, He X, Zhang Z, Zhao Y, Feng W (2012) Metabolism of nanomaterials in vivo: blood circulation and organ clearance. Acc Chem Res 46(3):761–769. doi:10.1021/ar2003336
165. Ghosh P, Han G, De M, Kim CK, Rotello VM (2008) Gold nanoparticles in delivery applications. Adv Drug Deliv Rev 60(11):1307–1315
166. Govorov A, Zhang W, Skeini T, Richardson H, Lee J, Kotov N (2006) Gold nanoparticle ensembles as heaters and actuators: melting and collective plasmon resonances. Nanoscale Res Lett 1(1):84–90
167. Choi M-R, Stanton-Maxey KJ, Stanley JK, Levin CS, Bardhan R, Akin D, Badve S, Sturgis J, Robinson JP, Bashir R, Halas NJ, Clare SE (2007) A cellular Trojan Horse for delivery of therapeutic nanoparticles into tumors. Nano Lett 7(12):3759–3765. doi:10.1021/nl072209h
168. Huff TB, Tong L, Zhao Y, Hansen MN, Cheng J-X, Wei A (2007) Hyperthermic effects of gold nanorods on tumor cells. Nanomedicine 2(1):125–132
169. Hamad-Schifferli K, Schwartz JJ, Santos AT, Zhang S, Jacobson JM (2002) Remote electronic control of DNA hybridization through inductive coupling to an attached metal nanocrystal antenna. Nature 415(6868):152–155. http://www.nature.com/nature/journal/v415/n6868/suppinfo/415152a_S1.html

Chapter 9
Multifunctional Mesoporous/Hollow Silica for Cancer Nanotheranostics

Huiyu Liu, Linlin Li, Shunhao Wang, and Qi Yang

9.1 Introduction

Cancers now figure among the leading causes of morbidity and mortality worldwide. According to the world cancer reports of WHO, there were 14 million new cases and 8.2 million cancer-related deaths in 2012. The number of new cases is expected to rise by about 70 % over the next two decades [1]. Most likely because of a late stage at diagnosis and limited access to timely and standard treatment, cancer survivals tend to be poorer in developing countries. These, no doubt, will largely increase the global burden of cancer [2, 3].

To ease the growing burden, the progresses in the areas of nanoscience and nanotechnology allow us to do more with less. Using extremely miniaturized technologies, nanotechnology is now possible to carry out more innovative and effective approaches in cancer research, including prevention, diagnosis, monitoring, and therapy [4–9]. Now, this concept has been defined as "nanomedicine" for the application of nanotechnology to the prevention and treatment of various kinds of disease in human beings. By 2008, 20 nanomedicines have been approved by the FDA [10]. For now, over 200 of nanomedicines have been approved or in various stages of clinical study, like Doxil®, DaunoXome, and Abraxane [11]. The basic

H. Liu (✉) • S. Wang
College of Life Science and Technology, Beijing University of Chemical Technology, Beijing 100029, People's Republic of China
e-mail: liuhy@mail.ipc.ac.cn

L. Li
Beijing Institute of Nanoenergy and Nanosystems, Chinese Academy of Sciences, Beijing 100083, People's Republic of China

Q. Yang
Xuanwu Hospital, Capital Medical University, No.45 Changchun Street, Xicheng District, Beijing 100053, China

Z. Dai (ed.), *Advances in Nanotheranostics II*, Springer Series in Biomaterials Science and Engineering 7, DOI 10.1007/978-981-10-0063-8_9

points of the dramatically increasing nanomedicine are based on three rules: (a) efficient loading of the drugs, (b) successful delivering the given drugs to the targeted region, and (c) successful releasing the drug [12, 13].

Nanomedicines can be simply divided into organic nanomedicines and inorganic ones. Organic drug delivery systems include liposomes, dendrimers, polymeric micelles, and drug–polymer conjugates [14–17]. Inorganic ones mainly have silica NPs, gold NPs, iron oxide NPs, carbon materials, and other hollow or porous inorganic NPs [18–26]. Among these NPs, mesoporous silica NPs have attracted significant interest because of their good biocompatibility and high drug loading for in vivo applications (Scheme 9.1) [18, 27]. The origin study of silica-based mesoporous materials has been almost simultaneously started by Mobil Corporation in the USA [28] and Kuroda research team in Japan in the 1990s [28]. After almost 20 years, the performance of exceptionally high surface, uniformly sized, hydrophilic surface favoring long circulation, excellent biocompatibility, versatile silane chemistry for surface functionalization, ease of large-scale synthesis, and low cost of NP production has led to various applications of MSNPs as "nanocarriers" for the drug cargos. In 2011, Cornell dots (C dots), a kind of fluorescent silica nanoparticle with ~6 nm size, have been designed for lighting up cancer cells and helping cancer therapy which has been approved by the FDA for its first-in-human clinical trial [18, 29]. This no doubt highlights the great potential in clinical translation of MSN delivery platform.

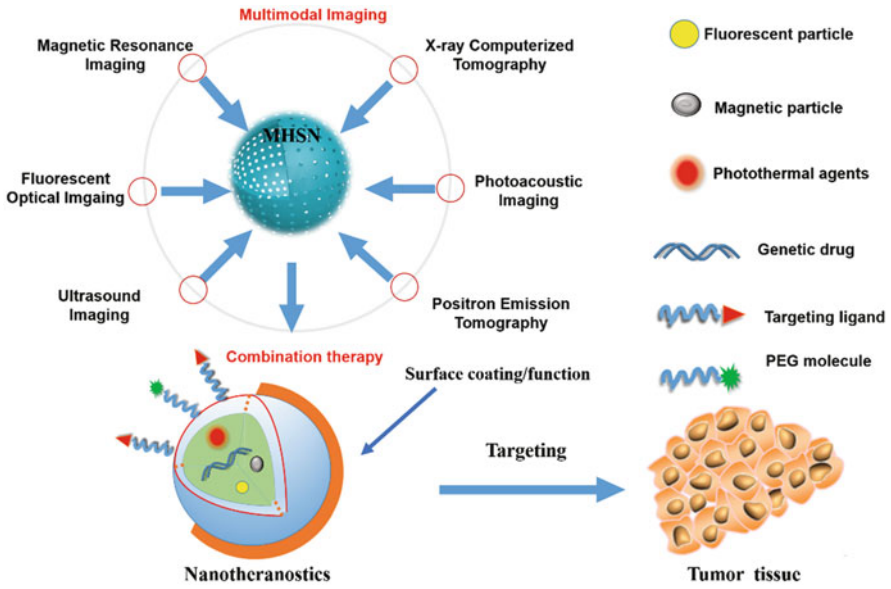

Scheme 9.1 Various mesoporous/hollow silica (MHSN)-based nanocomposites for multimodality imaging and combination therapy

Promised by their fascinating drug delivery properties, mesoporous/hollow silica nanoparticles (MHSN) are recently reviewed for their theranostic applications [30]. The new concept of "nanotheranostics" is raised for the integrating of diagnostic imaging and therapy, which brings new vision for personalized cancer therapy [31]. The potential merits of the imaging-guided nanotheranostics compared with single diagnosis and/or therapy are obvious: (*A*) It could integrate several different imaging probes into one particle, providing comprehensive and accurate diagnosis than one. (*B*) It shows the potential in combination or synergetic effect for a more effective therapy. (*C*) It helps to predict the therapeutic responses with simultaneous monitoring of the efficacy of therapeutic interventions. (*D*) It may be used to monitor and quantify the drug releasing during therapy. *This chapter* aims to introduce some state-of-the-art examples in MHSN for their multimodal imaging and nanotheranostics for cancer therapy, to highlight the reasons why silica has been considered as an excellent candidate as versatile multifunctional platform, and to conclude with our personal perspectives on the future directions in which this field might be focusing.

9.2 MHSN-Based Fluorescent Optical Imaging (FOI) and Medical Imaging

9.2.1 MHSN-Based FOI

Developing noninvasive, quantitative, real-time visual observation requires various noninvasive imaging techniques. In vivo fluorescence imaging technique has been widely used in biomedical research because of its advantages of sensitive detection, quick imaging, simple operation, and no radioactive harm. Aiming for these properties, the key point is the design of the imaging probe with high sensitivity. In recent years, with the development of nanotechnology, a variety of functional fluorescent nanomaterials have been developed and applied for in vivo imaging-guided therapy, especially those who have high signal-to-background ratio, good biocompatibility, and excellent optical properties. Some typical fluorescence optical imaging (FOI) probes include organic fluorescent dyes [32, 33], quantum dots (QD) [34, 35], carbon nanotubes [36, 37], graphene [38], upconversion nanoparticles [39–42], carbon dots [43, 44], and the like. This part will focus on in vivo FOI probes using fluorescent silica nanoparticles. In most cases, silica has been used as a coating protection layer for the above functional fluorescent probes.

Organic fluorescent dye-containing MHSN can be prepared by conjugating or loading fluorescent dyes into the MHSN matrix. This is an efficient method to protect the organic dyes from quenching or degrading [45]. Besides, dye-doped MHSN can also enhance their circulation half-life via enhance permeation (EPR) effect in targeting tumor, which will help getting detailed information during therapy. For example, a fluorescein isothiocyanate (FITC)-conjugated mesoporous silica

nanoparticle (MSN) has been developed to deliver antisense PNA and silence B-cell lymphoma 2 (Bcl-2) protein expression in cancer cells [33]. It is a simple way to overcome the problems of poor cell permeability of antisense peptide nucleic acid (PNA). Mou et al. have synthesized a series of MSNs with a good control in size, polydispersity, and morphology. They have functionalized them with a fluorescent dye and Herceptin to target breast cancer for combined therapy and imaging [46]. FOI usually suffers a problem of photon propagation in targeting tissues. To overcome this problem, near-infrared (NIR) dye-based nanoprobes are popularly used in many studies [47–50]. Lo's group has developed an NIR MSN by entrapping indocyanine green (ICG) into MSN via electrostatic interactions. ICG is an FDA-approved NIR dye in clinical use with an emission in the NIR window [47]. Using this nanoprobe, Lo et al. also have studied the influence of the surface charge on the biodistribution of ICG-MSN. The results have suggested that it has the possibility to control the biodistribution and excretion by tuning the surface charge of MSN [51].

Recently, fluorescent MHSN particles with a diameter <10 nm gained much attention. Among them, Cornell dots are attractive as the first inorganic diagnostic bio-probe in clinical trial. They have been synthesized in Wiesner's group [24, 52]. After that, a kind of ultrasmall (<10 nm) multicolor dot has been developed in the same group using a catalyst of ammonium hydroxide. The particle is ~9.3 nm with unique single pore. Green (TMR) and blue (DEAC) dyes have been conjugated to this ultrasmall single-pore fluorescent silica nanoparticle (Fig. 9.1b) [52], while for NIR fluorescence, silane-conjugated Cy5.5 is added into the reaction along with tetramethoxysilane (TMOS), and the quantum enhancement of the Cy5.5 was around 1.3-fold. Biodistribution demonstrated that these Cornell dots have an increase in renal excretion and a decrease liver uptake compared to the pristine particles without modification (Fig. 9.1a) [24].

In addition to organic fluorescent dyes, some fluorescent carbon dots (CDs), graphene quantum dots [53], gold clusters [54, 55], and semiconductor quantum dots, such as CdSe [56, 57], CdTe [58], and CuSe/ZnS [34, 59], have been incorporated into MHSN particles or coated with solid silica layer. Although this structure can increase the hydrophilic size of these dots, it is still attractive for the stability, water solubility, and low toxicity brought by the silica framework.

Carbon nanomaterials, such as carbon nanotubes, nanofibers, and graphenes, are becoming increasingly important in many applications. The conventional carbon materials are a typical kind of narrow bandgap material and generally do not have fluorescent properties. However, recent studies show that carbon nanotubes can emit fluorescence under certain conditions [36, 37]. The surface of carbon nanoparticles by polymer modification also can produce strong fluorescence. With the nontoxic, cheap, good stability, and other advantages, fluorescent carbon materials show a promise in the in vivo imaging. Graphene quantum dots (GQDs) have been first reported by Wang et al. to be embedded into MHSN spheres as a biolabel through a solvothermal route. Graphite oxide is the carbon source and 3-(2-aminoethylamino)-propyltrimethoxysilane is a surface modifier. Attractively,

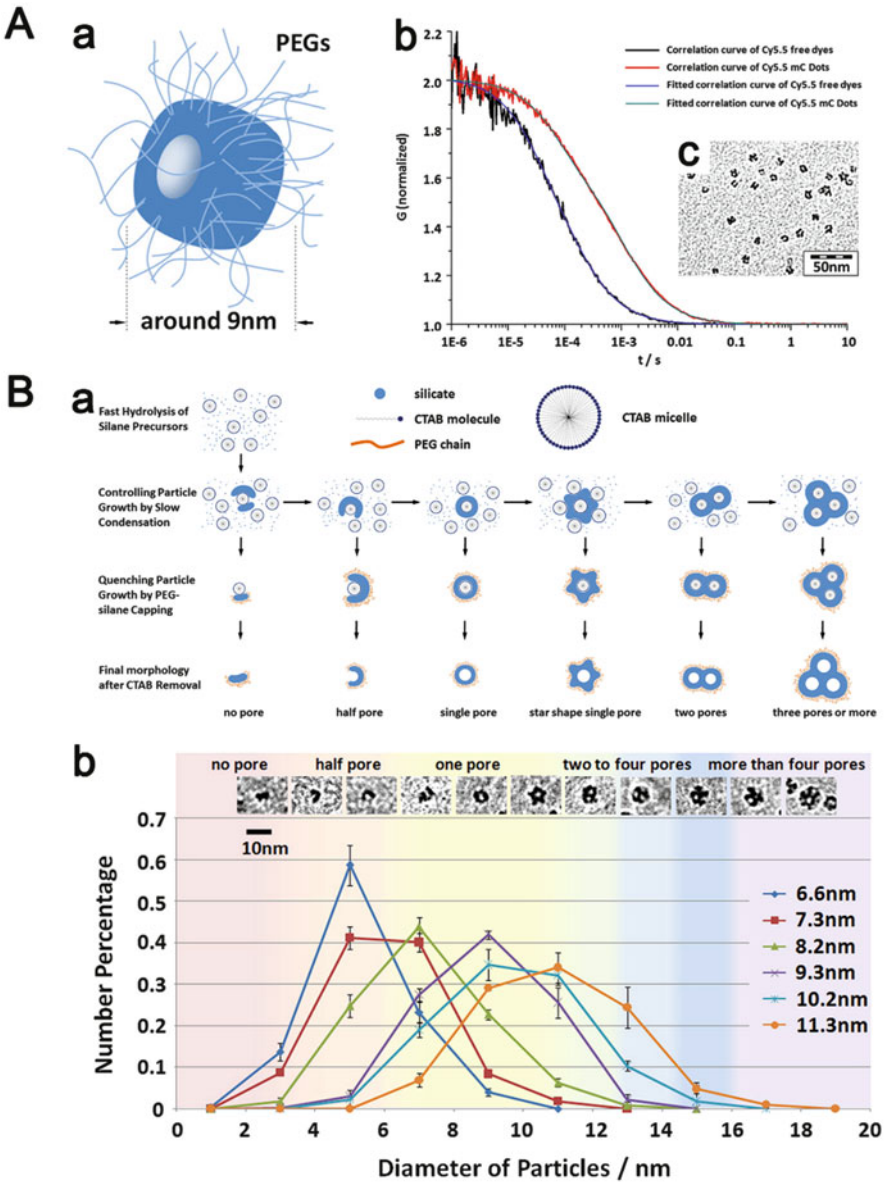

Fig. 9.1 (**A**) (*a*) Schematic of a single-pore PEGylated MSN, (*b*) normalized fluorescent correlation spectroscopy curves for Cy5.5 dye with/without mC dots, and (*c*) TEM image of the Cy5.5 mC dots (Reprinted with permission from Ref. [24]. Copyright 2012 American Chemical Society) (**B**) (*a*) Schematic illustration of the synthesis of ultrasmall mesoporous silica nanoparticles with different particle size and morphology and (*b*) particle size distributions as determined by TEM image correlate particle morphology with size (Reprinted with permission from Ref. [52]. Copyright 2013 American Chemical Society)

the GQDs not only can be served as fluorescent chromophores but also can affect the formation of MHSN's bilayer architecture [53].

Noble metal nanoclusters have obtained great attention in this decade [60, 61]. Different from plasmonic gold or silver nanoparticles, gold or silver nanoclusters only have a few numbers of atoms (<150). The main reason for their high fluorescence has been speculated to be the interband transition of Au $5d^{10}$ to 6sp with or without the ligand metal charge transfer between the metal and the ligands. Mark's group has synthesized a library of silica (100 nm)–gold cluster (2 nm) shell–core nanoparticles, with high Stokes shift and good monodispersity. Attractively, their fluorescence shows good stability in 5 months, indicating the perfect protective role of silica shell [54].

Semiconductor nanocrystals, also known as QDs, are composed of II–VI and III–V elements. The particle size is generally between 1 and 10 nm [62, 63]. Compared with the traditional fluorescent dyes, QDs exhibit excellent optical and mechanical properties. Firstly, they have broad excitation spectrum, narrow emission spectrum, and high quantum yield. By adjusting the particle size, one can obtain a series of QDs with different emitting lights from the UV to the NIR. Also, QDs with different emission fluorescence can be excited by the same excitation source, realizing a multichannel biological detection. In addition, QDs have a larger Stokes shift which can effectively avoid the excitation interference on the signal and improve the imaging sensitivity. Again, QDs have a strong resistance to photobleaching, showing good and large molar extinction coefficient. Based on these excellent characteristics, QDs have been widely applied to various fluorescent optical imaging techniques [34]. Silica coating is considered as an effective way to reduce the long-term toxicity caused by the elements (e.g., cadmium, selenium, and tellurium) commonly used in the synthesis of QDs. For instance, Gong et al. have synthesized PEGylated liposome CdSe/ZnS (QDs)/MHSN core–shell nanoparticles by layer-by-layer coating for cell imaging. The novel system significantly enhanced biocompatibility by liposome and MHSN coating. And MHSN can also reduce the toxicity of QDs through inhibiting the oxidation process on the surface of QDs [64]. In another study, Xia and his coworkers have proposed a multifunctional nanocomposites by incorporating gold nanorods (Au NRs) and CdSe/ZnS QDs into folic acid (FA)-conjugated silica matrix to achieve computed tomography (CT) and fluorescence imaging and active targeting photothermal therapy by FA targeting ligand (Fig. 9.2) [65].

Upconversion fluorescence nanoparticle (UCNP) is a kind of rare earth luminescent material. It can emit a short wavelength fluorescence under the excitation of a long wavelength. Generally, the short wavelength is 400–850 nm under an excitation by 980 nm light. Compared to other fluorescence imaging probes (fluorescent dyes and semiconductor quantum dots), UCNP has the advantages of low toxicity, good chemical stability, high fluorescence signals, and large Stokes shift [42]. In addition, the excitation light of UCNPs is normally infrared light which can effectively avoid the absorption and scattering of the fluorescence of biological tissues, avoid the interference of organisms' autofluorescence, and enhance the

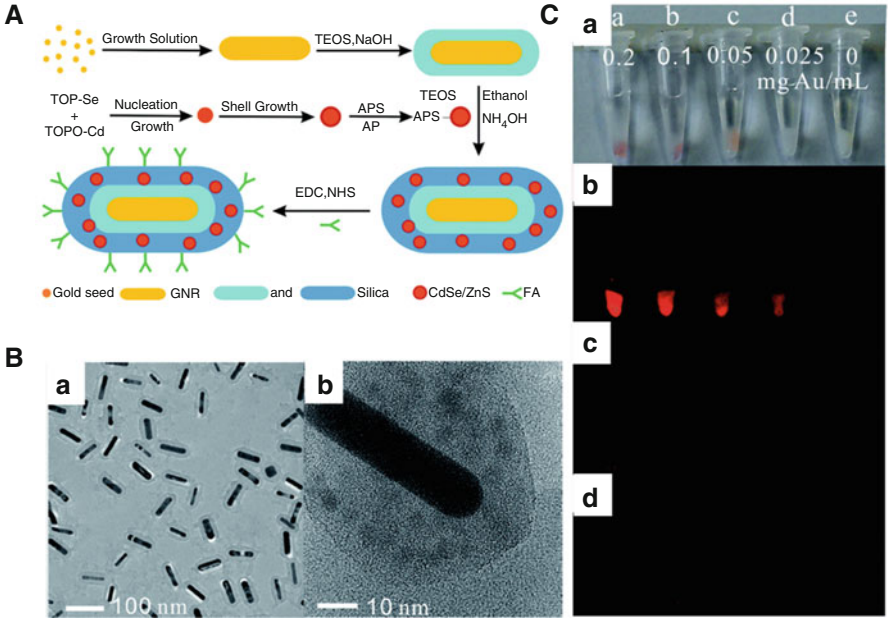

Fig. 9.2 (**a**) Schematic illustration of the synthetic procedure of Au NR@SiO_2@QD-FA. (**b**) TEM images of (*a*) Au NR@SiO_2 and (*b*) enlarged TEM image of a single Au NR@SiO_2@QD. (**c**) In vitro targeted fluorescence imaging of HeLa cells and A549 cells. (*a*) Digital photographs of NP-treated cells under bright light, (*b*) HeLa cells treated with Au NR@SiO_2@QD-FA, (*c*) HeLa cells treated with Au NR@SiO_2@QD, and (*d*) A549 cells treated with Au NR@SiO_2@QD-FA illuminated by 365 nm UV light (Reproduced from Ref. [65] by permission of The Royal Society of Chemistry)

signal-to-noise ratio. An inert silica shell on UCNPs is favorable to convert the hydrophobic nanocrystals (NCs) to water, increase emission intensity, and decrease the toxicity. Shi's group has synthesized size-controllable and monodisperse MHSN-coated UCNP ($NaYF_4$:Tm/Yb/Gd) for near-infrared fluorescence and magnetic resonance imaging (MRI). It's worth noting that MHSN shell not only reduces fluorescence quenching and toxicity of UCNPs but also improves imaging contrast for T_1-weighted MRI by facilitating interaction between water molecules with gadolinium-based core [66]. In addition, new NIR dye-doped core–shell-structured nanocomposites ($NaYF_4$:Er^{3+},Yb^{3+}@SiO_2) with both diagnostic and therapeutic features have been synthesized in single nanoparticles by Shan et al. In this structure, $NaYF_4$:Er^{3+},Yb^{3+} nanoparticles are used as optical agents in bioimaging for diagnosis. And the therapy has been achieved by NIR dye-doped core–shell-structured $NaYF_4$:Er^{3+},Yb^{3+}@SiO_2 nanocomposites [41]. Recently, Niu et al. have loaded Gd_2O_3:Yb/Er and anticancer drugs into mesoporous silica with 2D MCM-41 and 3D MCM-48 network by one-step process, which is modified by 5 nm gold nanoparticles. Interestingly, the photothermal effect of gold nanoparticles was excited and

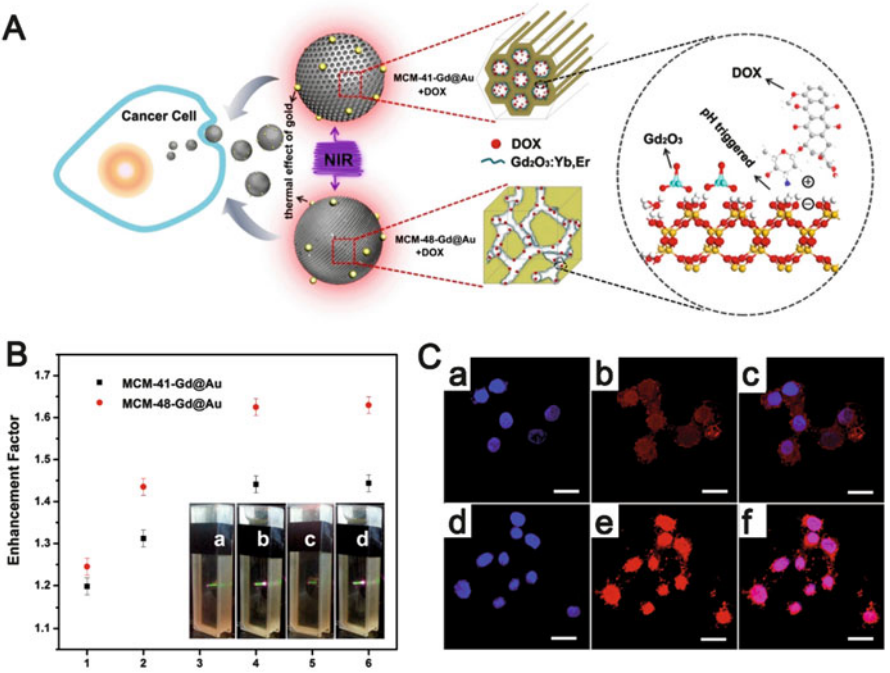

Fig. 9.3 (**a**) Schematic structure diagram of DOX-loaded MCM-41-Gd@Au and MCM-48-Gd@Au. (**b**) Curve of plotting the upconversion luminescence enhancement factor with different MCM-41(48)-Gd/Au molar ratios (insets are the luminescent photographs for (*a*) MCM-41-Gd, (*b*) MCM-41-Gd@Au, (*c*) MCM-48-Gd, and (*d*) MCM-48-Gd@Au with MCM-41(48)-Gd/Au of 4). (**c**) CLSM images of human SKOV3 ovarian cancer cells incubated with MCM-41-Gd@Au + DOX at 37 °C (30 min (*a–c*), 3 h (*d–f*)) (Reprinted with permission from Ref. [40]. Copyright 2014 American Chemical Society)

anticancer drugs were released at the same time under 980 nm NIR irradiation. And the luminescence intensity of UCNPs is also enhanced by gold nanoparticles due to the surface plasmon resonance (SPR) effect (Fig. 9.3) [40].

9.2.2 Medical Imaging

Medical imaging refers to the use of several different technologies to obtain the internal body image in order to diagnose, monitor, or treat medical conditions and diseases. From the 1950s of the last century, medical imaging has entered into a rapid development period. Today, almost all of the physical methods have been more or less penetrated into the field of medical imaging. They provide more and more precise and accurate structure of the human body, playing a critical role in improving the effectiveness of clinical diagnosis and treatment. Modern medical

imaging technology mainly includes ultrasound imaging, X-ray computed tomography (CT), magnetic resonance imaging (MRI), positron emission tomography (PET), etc. They are similar in terms of basic principles: acquiring the internal images with the help of certain kind of physical energy (such as X-ray, ultrasound, and so on) by interacting with the human tissue, the detector receives the returned energy from the human tissue, which carries the morphology, structure of internal body tissues or organs, and physiological function of information. These information are extracted, calculated, and simulated and finally shown in the form of images. In this part, we will discuss some imaging modalities integrated into silica nanocomposites for medical imaging.

9.2.2.1 Ultrasound

Ultrasound imaging (sonography) uses high-frequency acoustic wave to obtain the images of soft tissues, such as muscles and internal organs. The advantages of ultrasound imaging are noninvasive, nondestructive, low cost, and easy portability [67, 68]. The most important point is that it can provide real-time dynamic image of human body section. However, it still has some limitations in clinical practice [69]. Because the human body gas and bones will hinder the ultrasonic beam, ultrasound imaging is not suitable for organs rich in bubbles, such as the lung, gastrointestinal organs, and the bone. Because of its physical properties and ultrasonic constraints, the quality of the acquired image is usually poor, and the edge of the image is fuzzy. So, the accuracy of ultrasonic imaging diagnosis highly relies on the operator's experience.

Ultrasound contrast agents (UCAs) provide the possibility to overcome the above problems [70]. The common ultrasound contrast agents include phospholipid-coated microbubbles [71–73], fluorocarbon gases, nonionic surfactant-encapsulated microbubbles [74], biodegradable microencapsulate [75], and liquid fluorocarbon nanocapsule [76]. Recently, several groups have reported using silica-based nanomaterials as the ultrasound contrast agents [77–81]. Lin et al. have used polystyrene template core coated with thin silica lamination as a UCA. The designed sizes are below 4 μm for a safe passage through the pulmonary capillary bed (Fig. 9.4) [82]. Martinez et al. have used polystyrene spheres as templates coated with ~10 nm porous silica shell to make a mesoporous hollow silica. Then, the particles are filled with perfluorocarbon gas as an efficient ultrasound contrast agents. This structure is attractive for its uniform size control, strong adsorption to tissue and cells immobilizing particles at the tissue injection site, a long imaging lifetime, and a silica surface that can be easily modified with targeting ligands or small molecules to adjust the surface charge and polarity [83].

Different from these strategies, Zhang et al. have designed a brand-new structure using double-scattering/reflection layers in a single silica particle, compared to those UCAs with the same composition but different structures. This twofold or more scattering to incident ultrasound may have a higher utilization efficiency in incident ultrasound energy than that of a single layer nanoparticle [84].

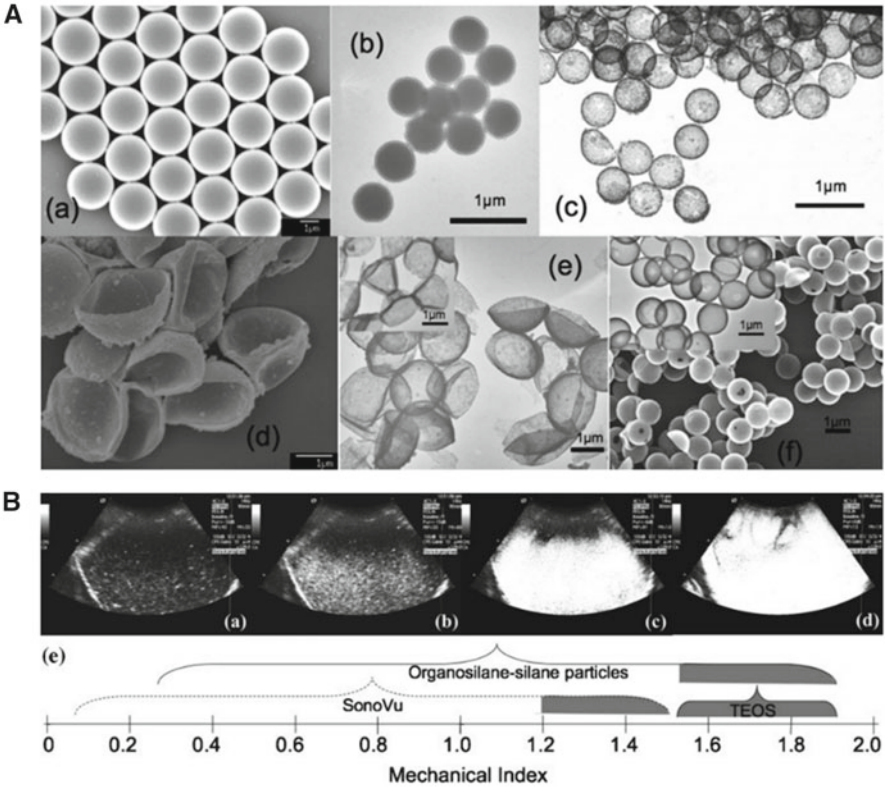

Fig. 9.4 (**a**) (*a–c*) SEM and TEM images of the growth of hollow silica-based shell (~550 nm, *c*) including negatively charged polystyrene particles (2089 ± 150) nm (*a*) and polystyrene-silica core–shell particles (silica shell 50 nm, ~550 nm) (*b*). (*d–e*) SEM and TEM images of octyl-triethoxysilane (OTES)-bis[3-(trimethoxysilyl)-propyl]amine (TSPA)-tetraethyl orthosilicate (TEOS) composite hollow particles, respectively (both shells <30 nm), which collapses within high-vacuum electron microscopy (2580 nm), and (*f*) SEM (*left*) and TEM (*right*) images of composite laminate of TSPA-TEOS particles that also have shells <30 nm, retaining a stiff spherical shape (2150 nm), with few particles collapsed. (**b**) In vitro ultrasound images. For CPS scanning mode, the gain was kept at 10 dB with varying MI, MI = (*a*) 0.53, (*b*) 0.73, (*c*) 0.9, and (*d*) 1.5. (*e*) Image uses a mechanical index (MI) scale to illustrate the insonation pressure amplitude range for contrast enhancement (Reproduced from Ref. [82] by permission of John Wiley & Sons Ltd)

9.2.2.2 CT

A computed tomography (CT) scan is an imaging method that uses X-rays to create the pictures of the body. It shows a faster scan rate and high-resolution cross-sectional scanning. Especially, because of the good skeletal penetration of X-ray, CT could get a high accuracy in the diagnosis of intracranial tumors. But CT imaging also has its limitations. The first problem is that X-ray radiation may cause human body's injury. Even with the most advanced instrument having a very low

level of radiation dose, the damage is still inevitable [85, 86]. At the same time, because the density difference of the human body soft tissue is not obvious, the resolution of CT for soft tissue is low, so it is difficult to get a clear image of the soft tissue without contrast agent.

The most contrast agent of CT used in clinic is iodine compound [87–89]. But the small-molecule iodine contrast agent can be rapidly excreted from the kidney, resulting in a very short imaging time and limiting their application. More important, a considerable number of patients are allergic to iodinated contrast agents, thus delaying the disease diagnosis. Recent studies found that the inorganic nanoparticles as CT contrast agents hold a promise in CT imaging [90, 91]. In addition to the contrast enhancement, it has long blood circulation and easy functionalities.

Xue et al. have fabricated a multimodal imaging probe by loading iodinated oil into fluorescent mesoporous silica-coated SPIONs (i-fmSiO_4@SPIONs). SPIONs have been prepared by a coprecipitation of ferric and ferrous salts. The mesoporous silica shells are subsequently coated with a silica sol–gel reaction. This probe has an advantage of imaging soft tissue via MRI, seeing electron-dense materials through CT, and observing fluorescence by FOI [92]. Because of a higher X-ray absorption coefficient than iodine agents, gold is now attractive for CT imaging. Zhou et al. have fabricated a promising CT imaging contrast agent for in vivo gastric cancer. They have synthesized gold clusters coated with silica shells, then conjugated folate as a multimodal probe (AuNCs@SiO_2-FA). The attenuation value (HU) of the probe is to evaluate the CT contrast effects of the probe by a micro-CT equipment. HU is found to exhibit a well-correlated linear relationship ($R^2 = 0.9917$) as a function of the probe's concentration, and the after-to-before signal ratios are, respectively, 3.83 and 4.26, presenting distinguished CT signals [93].

Similar to Au atom, Bi has the largest atomic number (Au, 79; Bi, 83) and X-ray attenuation coefficient (Bi, 5.74 $cm^2\ g^{-1}$ at 100 keV), implying that Bi might be the most promising contrast agent of CT. In a communication, Chen et al. have developed a dual-modal probe composed of Bi_2S_3 nanoparticles and QDs for CT/FOI. Because of the use of a reverse microemulsion method, Bi_2S_3 NPs are uniform and monodispersed. Then they are wrapped with QDs in SiO_2. The results have proved Bi_2S_3–QD@SiO_2–PEG is excellent in the CT and fluorescence imaging both in vitro and in vivo (Fig. 9.5) [94].

9.2.2.3 MRI

Magnetic resonance imaging (MRI) is a clinically used medical imaging technique to investigate the anatomy and physiology of the body in both health and disease. It is a powerful noninvasive imaging technique that provides contrast between different soft tissues of the body, which makes it especially useful in imaging the brain, muscles, heart, and cancers compared with other medical imaging techniques. Compared with CT imaging, MRI doesn't use any ionizing radiation, so it is a safer imaging modality. In MRI, a T_1-weighted image generally shows the normal soft

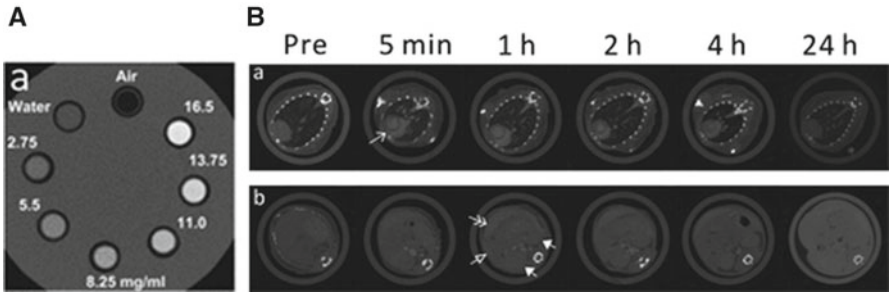

Fig. 9.5 (**a**) X-ray CT imaging of Bi_2S_3–QD@SiO_2–PEG nanoparticles as a function of the concentration. (**b**) In vivo X-ray CT imaging (heart (*a*, *open arrow*), liver (*double arrow*), spleen (*hollow arrow*), and kidneys (*b*, *solid arrow*)) of a mouse at different time points after injecting Bi_2S_3–QD@SiO_2–PEG nanoparticles (0.6 mg Bi per g body weight) by the tail vein (Reproduced from Ref. [94] by permission of The Royal Society of Chemistry)

tissue anatomy such as fat, whereas a T_2-weighted image reveals pathological phenomena such as tumors and inflammation.

MRI contrast agents can change the relaxation times of atoms within the body tissue and modify the contrast in the image. The most commonly used intravenous MRI contrast agents are based on chelates of gadolinium that is used for a kind of T_1-weighted imaging in clinic. However, with high nephrotoxicity, neurotoxicity, and rapid metabolism from the body, gadolinium(III)-containing MRI contrast agents have been incorporated into silica nanoparticles to decrease the Gd^{3+} leakage and increase biocompatibility, blood circulation time, and tumor-targeting ability after intravenous administration. Early in 2004, Mou and coworkers have loaded gadolinium into mesoporous silica using cationic long-chain surfactant as a template and gadolinium hydroxide and tetraethoxysilane (TEOS) as precursors. The covalent bonding between metal and the silica network makes it less susceptible to leach in contrast to ion-exchanged metal species [95].

Prof. Wenbin Lin at University of North Carolina has done lots of works in this scope [96, 97]. They put forward that grafting of Gd chelates onto MSN can increase the efficiency of MR contrast agents, because of MSN could carry a large payload of Gd centers and enhance water accessibility of the Gd chelates [98, 99]. They have loaded Gd-DTTA into MSN with a high loading mount of 15.7–20.1 wt%. On a per millimolar Gd basis, the particles have an r_1 of 28.8 mM^{-1} s^{-1} at 3 T MRI scanner and 10.2 mM^{-1} s^{-1} at 9.4 T. The r_2 relaxivities are 65.5 mM^{-1} s^{-1} at 3 T and 110.8 mM^{-1} s^{-1} at 9.4 T, respectively. The r_1 and r_2 values on a per millimolar particle basis are 7.0×10^5 mM^{-1} s^{-1} (3 T)/2.48×10^5 mM^{-1} s^{-1} (9.4 T) and 1.6×10^6 mM^{-1} s^{-1} (3 T)/2.7×10^6 (9.4 T), respectively. The relaxivity values are larger than their synthesized solid silica nanoparticles that are coated with multilayers of Gd-DTPA derivative [96]. The effectiveness of MSN-Gd is evaluated in vivo. After tail vein injection of a low dosage of 2.1 μmol kg^{-1} MSN-Gd, a significant T_1-weighted enhancement is visible in the aorta of a DBA/1 J mouse 15 min postinjection. They also have grafted Gd-DTPA chelates onto the surface of MSNs [100]. With a low dosage of

2.1 μmol kg^{-1} by intravenous injection, the MSN-Gd nanocomposites have a significant T_1-weighted enhancement. And at a higher concentration of 31 μmol kg^{-1}, it can be an efficient T_2-weighted contrast agents. Kleitz and coworkers have synthesized 3D pore network hybrid $GdSi_xO_y$ MSN with cubic *Ia3d* mesopore structure to facilitate mass transport processes. It provides a significant increase in ^1H longitudinal relaxivity (18.5 s^{-1} mM^{-1}; 4.6 times higher than Gd-DTPA) and low r_2/r_1 ratios (1.56) [101]. Lee and coworkers have synthesized Mn^{2+}-doped silica nanoparticles for hepatocyte-targeted T_1-weighted MRI [102]. The nanoparticles have unique MR contrast-enhancing characteristics that activated T_1-weighted MR imaging only under low pH conditions by liberating Mn^{2+} irons from the nanoparticles. Thus, it results in a differentiation of enhancement periods between tumor and normal tissues. Shi and coworkers have found that Mn^{2+}-doped MSN could be used simultaneously for T_1- and T_2-weighted MR imaging with high r_1 and r_2 values. They have deduced that it may be attributed to the T_2 relaxivity time shortening by ultrasmall manganese oxide nanoclusters (<2 nm), while higher surface-to-volume ratio exhibited a larger proportion of nanocompensated surface spins on the antiferromagnetic core and higher magnetization values, which may cause shorter T_2 relaxation time and thereafter higher r_2 value (Fig. 9.6) [103].

In addition to paramagnetic molecular complexes of gadolinium (Gd^{3+}) and manganese (Mn^{2+}) chelates, nanoparticles with the paramagnetic ion such as Gd_2O_3 [104] and MnO [105] nanoparticles also can accelerate longitudinal (T_1) relaxation under low concentrations as T_1-weighted MR contrast agents. For increasing the biocompatibility and improving biodistribution, silica is coated onto these kinds of nanoparticles. Lin and coworkers have coated MgO nanorods with a silica layer for T_1-weighted image [106]. Hyeon, Gilad, and coworkers have synthesized hollow manganese oxide (HMnO)-encapsulated mesoporous silica with core–shell structure (HMnO@$mSiO_2$) by acidic etching MnO-encapsulated mesoporous silica [107]. The paramagnetic HMnO@$mSiO_2$ nanoparticles show significantly higher molar T_1 relaxivity than previously reported MnO composite nanoparticles. It is explained the improvement of HMnO@$mSiO_2$ over MnO@$mSiO_2$ without hollow structure might be contributed from that the increased surface area-to-volume ratio further increased the exchange of the water with Mn^{2+} ions. Chou and coworkers have synthesized 2–3 nm antiferromagnetic α-iron oxide–hydroxide (α-FeOOH) nanocolloids within the pore of MSNs as T_1-weighted contrast agents (Fig. 9.7) [108]. The nanocomposites show low magnetization (M_z) of 0.0006 at H = 2 T at 300 K, which is four orders of magnitude smaller than any current ultrasmall iron oxide NPs (>5 emu g^{-1}) reported to date, hence ensuring the low r_2 ($\propto M_z$) (7.64 mM^{-1} s^{-1}) and r_2/r_1 ratio (2.03) at 4.7 T.

Superparamagnetic nanoparticles (SPIO) and ultrasmall superparamagnetic iron oxide (USPIO) as T_2 imaging contrast agents including Feridex, Combidex, Resovist, Lumirem, and Clariscan have been approved to use in clinic [109]. However, it appears that all these agents have not been widely used for different kinds of reasons. Now in preclinical studies, silica is used as a coating material to encapsulate superparamagnetic nanoparticles to form a core–shell nanocomposite. It can improve the dispersal ability and increase chemical stability and biocompatibility,

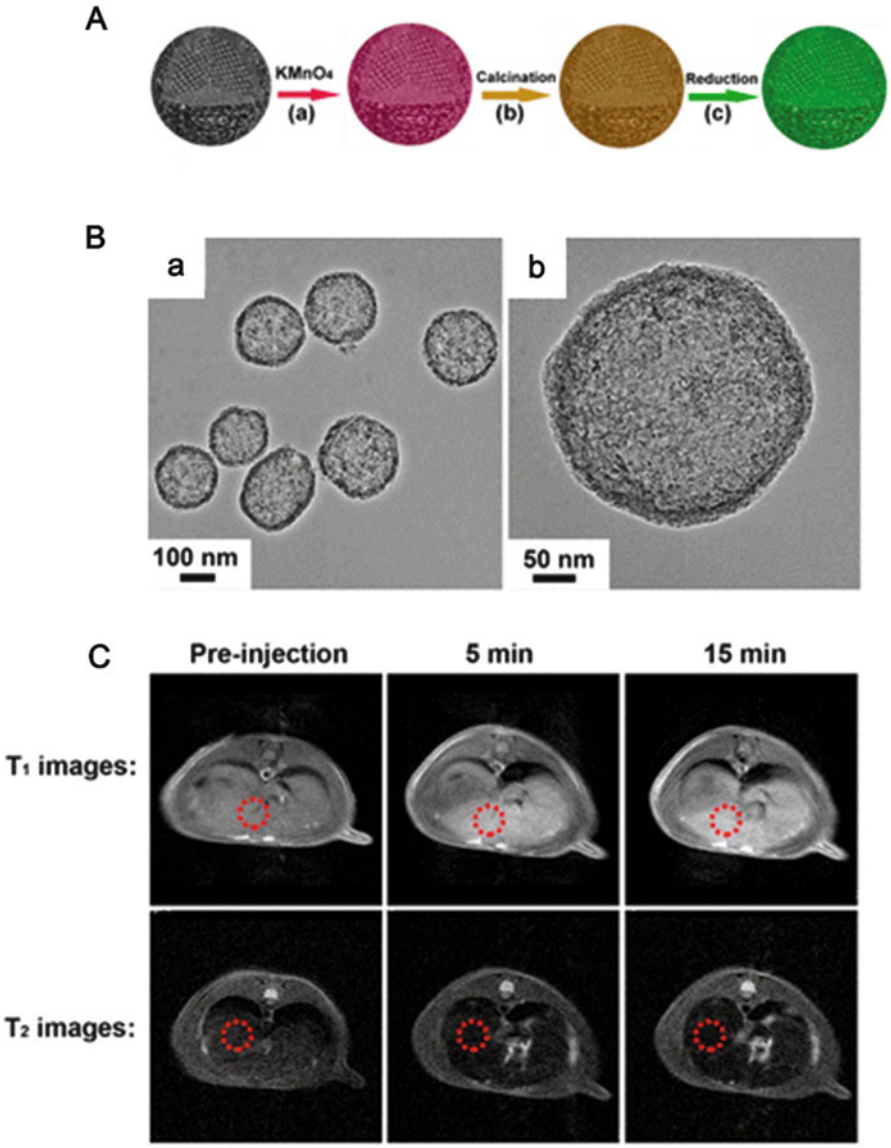

Fig. 9.6 (**a**) Schematic formation process of manganese-loaded dual-mesoporous silica spheres (Mn-DMSSs). (**b**) TEM images of Mn-DMSSs (*a*, *b*). (**c**) In vivo T_1- and T_2-weighted MR images of SD rat liver before and after intravenous injection of Mn-DMSS nanoparticles with a dose of 0.5 mg Mn kg^{-1} at different time points (5 and 15 min) on a 3.0 T MRI scanner (Reprinted with permission from Ref. [103]. Copyright 2013 American Chemical Society)

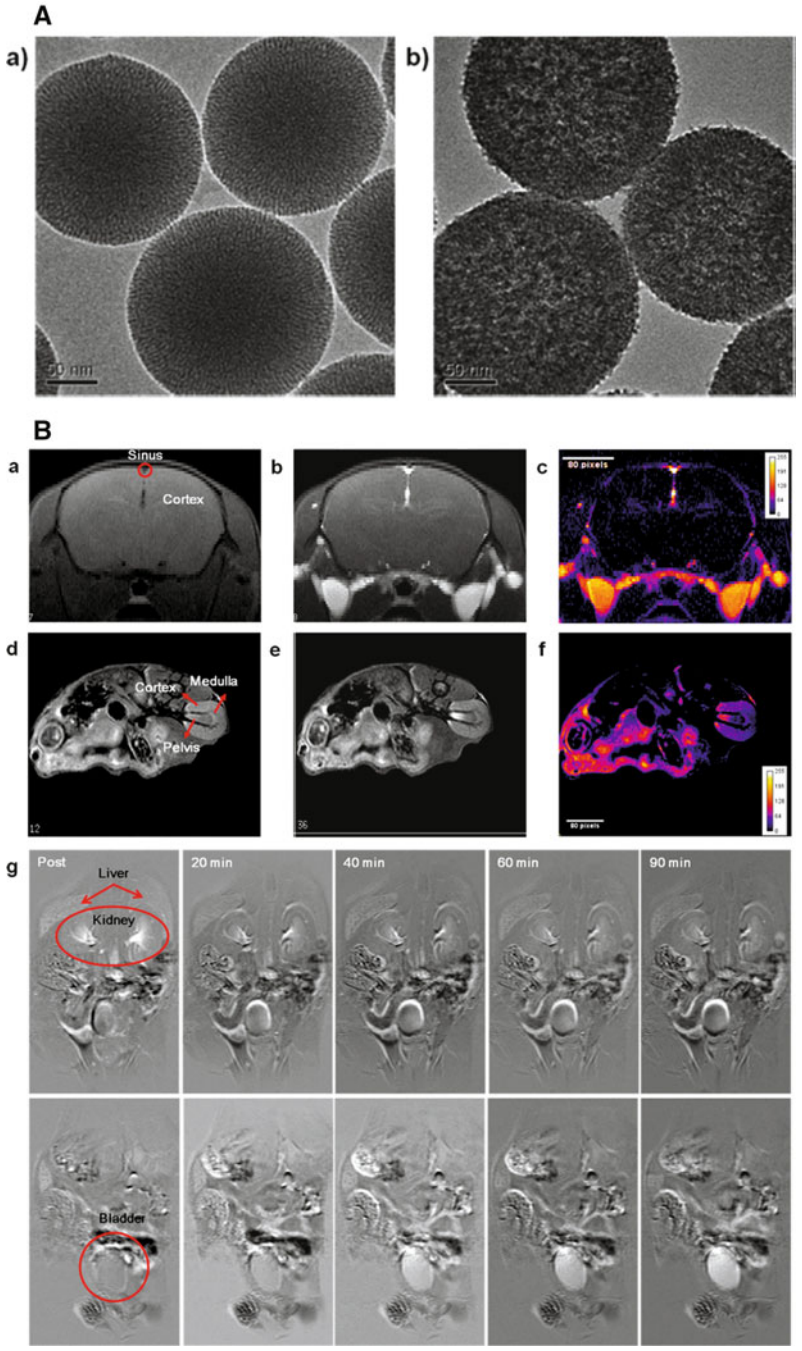

Fig. 9.7 (**a**) TEM images of (*a*) wormlike mesoporous silica (WMSN) (CTAB) and (*b*) FeOOH/WMSN. (**b**) In vivo T_1-weighted image of mouse brain and kidney (*a*, *d*) 0 and (*b*, *e*) 10 min, and (*c*, *f*) subtraction image of these two time frames, (*g*) subtraction T_1-weighted images of a mouse liver and kidney (*first row*) and bladder (*second row*) 10, 20, 40, 60, and 90 min after intravenous injection of FeOOH/WMSN-PEG. Sequential enhancement of the renal pelvis followed by the urinary bladder is noted (Reprinted with permission from Ref. [108]. Copyright 2013 American Chemical Society)

which may open many new clinical applications of the magnetic nanoparticles. In 2004, Kopelman and coworkers have reported synthesizing silica-embedded iron oxide nanoparticles for T_2-weighted images and chemically modified the particle surface to reduce nonspecific protein binding [110]. Sanchez and coworkers have incorporated nanomaghemite into mesoporous silica particles, and the synthesized hybrid nanomaterials are used for hyperthermia and an effective T_2-weighted MRI [111]. Lee and coworkers have synthesized superparamagnetic iron oxide nanoparticles (SPIONs) directly in the pores of silica nanotubes (SNTs). The nuclear magnetic resonance (NMR) relaxivities of 500 nm particles in length and of 60 nm in diameter were $r_1 = 1.6\ mM^{-1}\ s^{-1}$ and $r_2 = 264\ mM^{-1}\ s^{-1}$, and for the particles of 2 μm in length and 70 nm in diameter, the r_1 and r_2 were 3.0 and 358 $mM^{-1}\ s^{-1}$, respectively [112]. Shi and coworkers have synthesized thiol-functionalized superparamagnetic silica composite nanoparticles for T_2-weighted MR imaging [113]. Briefly, 5 nm magnetite nanoparticles and polystyrene$_{100}$-block-poly(acrylic acid)$_{16}$(PS_{100}-*b*-PAA_{16}) in oil phase are self-assembled into micelle-like aggregates. The nanocomposites are further coated with silica layer by hydrolysis and condensation of 3-mercaptopropyltrimethoxysilane (MPTMS). The as-prepared composites have a size smaller than 100 nm, and the size and magnetic nanoparticles in each nanocomposite could be tailored. Delville and coworkers have reported the fine-tuning of the relaxometry of $\gamma Fe_2O_3@SiO_2$ core–shell nanoparticles by adjusting the thickness of the coated silica layer [114]. They have found that the silica thickness had a significant impact on the r_1 at low B_0 field, r_2, and $r_2^{\#}$ relaxivities at medium and high B_0 field, as a result of decreased outer-sphere relaxation effects. This result provides clues for the design of magnetic nanoparticle-based contrast agents and their optimization for specific applications in medical diagnosis.

In providing complementary diagnosis information, nanocomposite with dual-contrast T_1- and T_2-weighted magnetic resonance imaging is also developed [115, 116]. Recently, it is found that ultrasmall magnetic Fe_3O_4 nanoparticles (<6 nm) can be used as T_1 or $T_1 + T_2$ dual MR CAs [117]. Besides that incorporating one chemical or nanoparticle that simultaneously possesses T_1- and T_2-weighted imaging ability, silica as matrix can perfectly integrate two or more kinds of entities into one nanoparticle.

Yang and coworkers have synthesized gadolinium-labeled superparamagnetic iron oxide and coated it with silica for targeted dual-contrast T_1- and T_2-weighted MRI of tumor [115]. They also have developed multifunctional arginine–glycine–aspartic acid (RGD) peptide-conjugated nanoscale coordination polymers (NCPs) with a diameter of about 80 nm using 1,1'-dicarboxyl ferrocene as building blocks and Gd^{III} ions as metallic node and coated it with silica to form nanocomposites [118]. After intravenous injection into mice with tumor overexpressing high-affinity $\alpha_v\beta_3$ integrin, it shows that the signal of T_1-weighted MR imaging is positively enhanced 47 ± 5 % and negatively decreased 33 ± 5 % from T_2-weighted MR imaging. This kind of T_1-weighted positive and T_2-weighted negative enhancement in the dual-mode MR imaging can significantly improve the diagnosis accuracy.

9.2.2.4 PET

Positron emission tomography (PET) is a functional imaging technique with a nuclear medicine that produces three-dimensional image of the body [119]. It has the advantages of selective imaging for a particular organ or tissue, tracing the abnormal changes on the function, metabolism, and genes of human organs with accurate quantitative analysis. Because the radioactive isotope has a certain half-life, PET imaging can realize the dynamic observation with "selective angiography ability" and "dynamic function determination ability." However, because PET system is expensive and complicated to operate, radioactive isotope is still an unsafe factor, and PET is not used widely. Thus, it is urgent to develop contrast agents for PET to increase imaging contrast and decrease radical dose.

Now, the most widely applied PET-active isotope in clinic is ^{18}F, typically in the form of ^{18}F-labeled fluorodeoxyglucose in order to target the tracer to high-glucose-using cells. However, the half-life of ^{18}F is very short (109.8 min). Radioisotopes of other elements under research have similar shortcomings. Silica can be used as coating materials to decrease the toxicity, increase the bloodstream circulation, and improve the targeting ability of these isotopes. Kim and coworkers have tethered ^{18}F onto MSN with particle size of 100–150 nm. After *i.v.* injection into mice bearing a subcutaneous U87 MG tumor, the ^{18}F-MSN shows a persistently strong tumor signal in PET-CT imaging, whereas the mice given free ^{18}F have considerably less tumor uptake with a renal clearance of ^{18}F activity [120]. Lindén and coworkers have immobilized $^{89}Zr^{4+}$ through covalent attachment of the complexing agent p-isothiocyanatobenzyldesferrioxamine (DFO-NCS) to large-pore MSNs. The ^{89}Zr-DFO-MSNs with dose of 0.5 mg kg^{-1} into mice show an order of magnitude lower than previously reported PET-MSN for PET imaging [121].

Cai and coworkers have conjugated copper-64 (^{64}Cu, $t_{1/2} = 12.7$ h) and 800 CW (a near-infrared fluorescence dye) onto MSN for PET and NIR fluorescence multimodal imaging. The nanoparticles are also tethered with a human/murine chimeric monoclonal antibody TRC105 to target tumor vasculature for tumor-specific imaging (Fig. 9.8a, b) [122]. They also have developed ^{64}Cu-tethered MSN for actively targeted PET imaging and drug delivery (Fig. 9.8c) [123]. The first-in-human clinical trial of ultrasmall inorganic hybrid nanoparticles, "C dots," has been tethered with ^{124}I for PET imaging, together with NIR fluorescence dye of Cy5 for fluorescent imaging [124]. Kang and coworkers have developed a silica nanoparticle incorporating ^{68}Ga, NIR dye, and magnetic particles for multimodal PET/MRI/NIRF imaging [125].

9.2.2.5 Photoacoustic Imaging (PAI)

PAI is an emerging noninvasive and nonionizing imaging technique developed in the twenty-first century [126, 127]. During PAI process, nonionizing laser pulses penetrate into biological tissues. The biological tissues absorb the laser energy based on the characteristics of their composition. The delivered energy will be

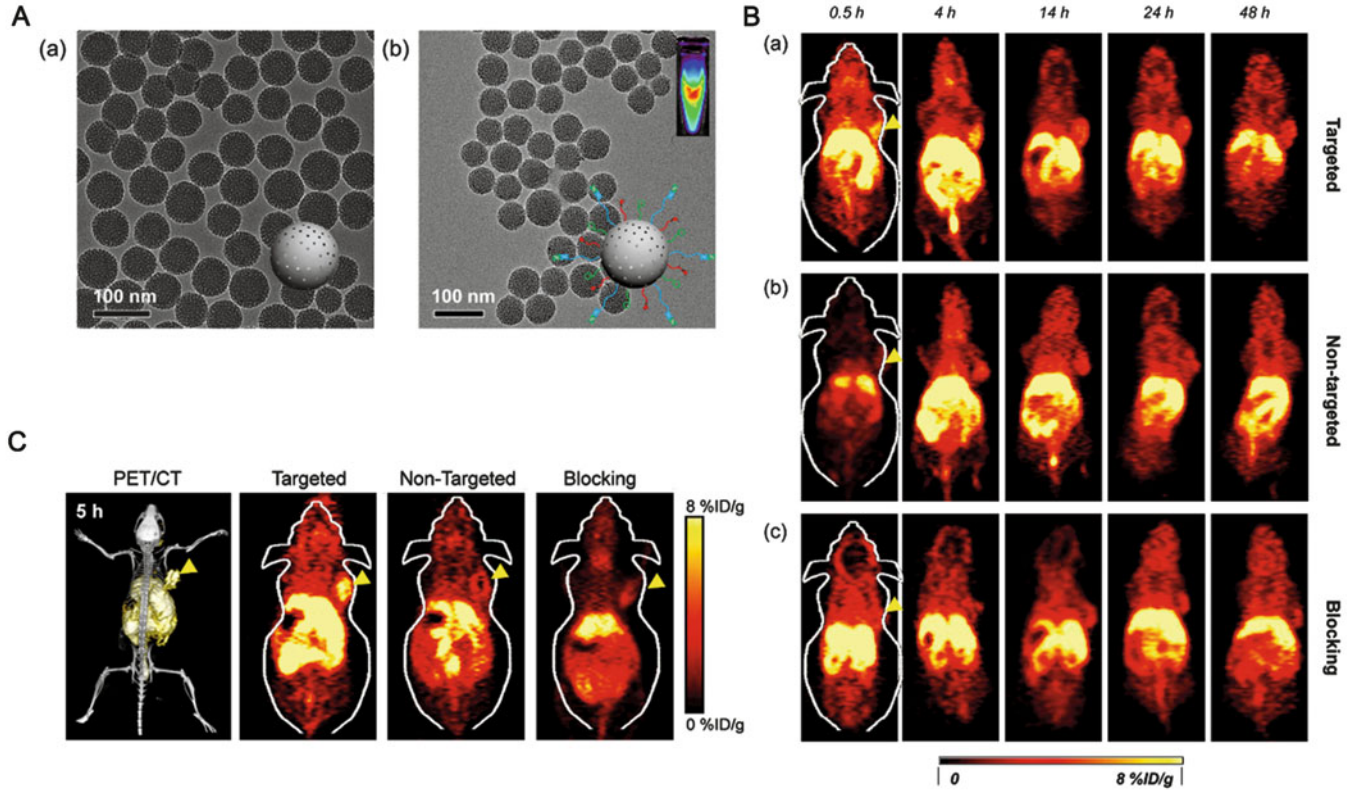

Fig. 9.8 (**a**) TEM images of (*a*) pure MSN and (*b*) MSN-800CW-TRC105 (Fab). Insets in (*a*) and (*b*) show the schemes of MSN and MSN-800CW-TRC105 (Fab). An optical image of MSN-800CW-TRC105 (Fab) acquired from IVIS spectrum in vivo imaging system (Ex = 745 nm, Em = 800 nm) is also shown in the *upper right* portion of (*b*). (**b**) Serial coronal PET images of 4 T1 tumor-bearing mice at different time points postinjection of (*a*) ^{64}Cu-MSN-800CW-TRC105 (Fab), (*b*) ^{64}Cu-MSN-800CW, and (*c*) ^{64}Cu-MSN-800CW-TRC105 (Fab) with a blocking dose of TRC105 (1 mg/mouse). Tumors are indicated by *yellow arrowheads* (Reprinted with permission from Ref. [122]. Copyright 2014 American Chemical Society). (**c**) Representative PET-CT and PET images of mice in the three groups at 5 h postinjection (Reprinted with permission from Ref. [123]. Copyright 2013 American Chemical Society)

absorbed and converted into heat by a transient increase in temperature (~10 mK), then contraction stress changes and leads to subsequent thermoelastic expansion of the absorbent, generating an ultrasonic acoustic signal which can be detected by wideband transducers surrounding the object. Because of the advantageous integration of both optical imaging and acoustic imaging, PAI can realize a propagation of the photons in the diffuse region with a relatively lower scattering coefficients (~2–3 orders) of absorbents compared with other optical imaging method. This is favorable to overcome the main challenge caused by the hemoglobin absorption and tissue scatter in optical imaging [128], which enables PAI up to ~50 mm deep with a resolution of <1 mm [129].

Gold-based NPs are one of the most outstanding materials being explored for PAT, such as gold nanorods [130, 131], NPs [132], nanocages [133], agglomerates [134], hollow nanoshells [135], and composite materials [136, 137]. Interestingly, silica coating has an enhancement in the gold-based PAI. Chen et al. have reported that silica shell as a dielectric shell has a great impact on the photoacoustic signal of gold nanorods. About threefold higher photoacoustic signals are generated by silica-coated gold nanorods than that of nanorods without silica coating. The authors speculate the main reason is the difference in the optical absorption between the gold nanorod with and without silica coating. After silica coating, the absorption of gold nanorods increases due to the dielectric constant change of the environment, resulting in a strong increase in the photoacoustic signal [138].

Jokerst et al. also have used silica-coated gold nanorod as a contrast agent for photoacoustic imaging of mesenchymal stem cells in rodent muscle tissue. Different from Chen's report, they think the silica coating favors the cellular uptake more than fivefold than non-coating one. At the same time, no obvious toxicity or proliferation changes are observed in cells in the contrast agent group. They think this low background technique allows imaging of down to 100,000 cells in vivo (Fig. 9.9) [139].

Compared to gold-based NPs, the absorption coefficients of carbon nanomaterials are relatively low. But this doesn't hinder their applications as various bioimaging contrast agents [140], including PAI and thermoacoustic imaging [141]. For example, Pramanik et al. used a single-walled carbon nanotube (SWNT) as a noninvasive approach to detect the sentinel lymph node. SWNTs are fabricated using the carbon vapor deposition (CVD) method with Fe as the metal catalyst and show promise in significant signal enhancement in PAI [142]. SWNTs also can be offered as an MRI contrast agent. Liu et al. coated SWNT with mesoporous silica for imaging-guided combination therapy of cancer. The main role of mesoporous silica shell is for loading therapeutic molecules combined with PAI and MRI [143].

In the above parts, we describe various modern medical imaging technologies. But each imaging method has its own shortcomings. For example, the optical imaging has a limited penetration depth and low space resolution; MRI's sensitivity is low but has a high cost, and its imaging needs longer time; PET imaging has a high cost, and the patient has potential radiation threat. Recently, multimodal imaging probes can combine optical imaging and molecular imaging to realize high sensitivity and high-resolution image. As introduced above, silica is the most widely used

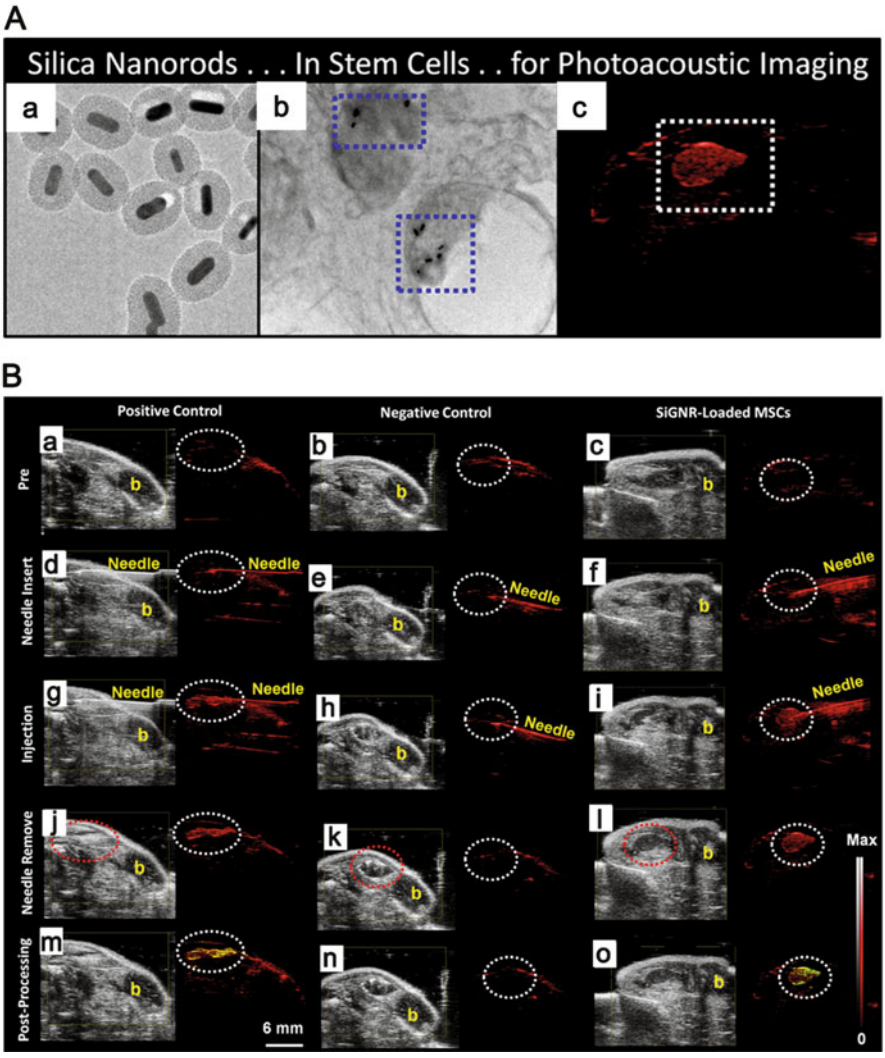

Fig. 9.9 (**a**) TEM images of silica-coated gold nanorods (SiGNRs) (*a*), confirmation of SiGNRs inside mesenchymal stem cells (MSCs) (*b*), and in vivo PA images after injecting SiGNR-labeled MSCs (*c*). (**b**) In vivo B-mode (*gray scale*) and PA (*red*) images of a positive control (0.7 nM SiGNRs; *left*), negative control (0 nM SiGNRs (no cells); *middle*), and 800 000 SiGNR-labeled MSCs (*right*) all in 50 % Matrigel/PBS into the hind limb muscle of an athymic mouse by intramuscular injection (Reprinted with permission from Ref. [139]. Copyright 2012 American Chemical Society)

framework for integrating the multiple kinds of imaging agents into one nanoparticle for multimodal imaging with easiness of synthesis, uniform size, tunable structure, and good biocompatibility.

9.3 MHSN-Guided Imaging and Therapy for Nanotheranostics

"Theranostics" is coined to define the efforts to develop more specific, individualized therapies for various diseases into one single agent [144]. With the deeper understanding of tumor biology, people more and more realize that the microenvironment, inner regulation, and dynamic changes of tumor could cause great differences between individual tumor patients. This arose from the fact that most diseases, including cancer, are immensely heterogeneous. All existing therapies are only effective for limited patients at a selective stage of disease. Therefore, it is very necessary to closely monitor the efficacy of treatment during cancer therapy, allowing for a more accurate diagnosis and specific treatment plan.

The emergence of nanotechnology offers the possibility of combining diagnosis and therapy together. Though nanoparticle-based theranostics are still in very early stages of development, the individual part of imaging and therapy is struggling into clinical trials. Personalized medicine will no doubt make NP-based theranostics one of the research hotspots. In the above section, we discuss the research development of silica-based FOI and medical imaging. Besides, silica MHSN is a good drug carrier for hydrophobic [145] and hydrophilic drugs [146, 147], genes [148], and other therapeutic modalities [149–151]. In addition, silica also has the potential to help overcome the severe toxic side effect of chemodrugs to normal tissues due to the lack of tumor selectivity, reversing the multidrug resistance (MDR) to free chemotherapeutic drugs and the deadly metastases of cancer cells [152]. Therefore, in this part, we will focus on the buildup and application of silica-based imaging-guided therapies, as well as on the understanding of the association of functional modalities which may affect the transport, delivery, and release of the silica-loading cargos.

9.3.1 Silica-Guided Imaging and Chemotherapy

9.3.1.1 Silica-Guided FOI and Chemotherapy

Dr. Brinker's group has done a lot of work in a new structure "protocell" [153–157]. It is constructed by the liposome fusion on an MHSN simultaneously loading the imaging and therapy cargos, creating a "protocell" for the delivery across the cell membrane [155]. This structure has a very interesting property. The lipid membrane on silica core could retain a fluidity and stability in the biological environment compared with liposomes with the same membrane but without silica-supported core.

When the targeting ligand anchored on the liposome membrane, protocell structure can achieve avid binding for targeting cells with relatively low densities of targeting ligands. They report a very impressive 10,000-fold greater affinity of protocells modified with a targeting peptide binding to human hepatocellular cancer cells than that of hepatocytes, endothelial cells, or immune cells (Fig. 9.10) [157]. They also proved protocells have a 10- to 100-fold greater capacity for siRNA loading in physiological conditions [158]. By synergistically combining properties of MSNs and liposomes, protocells can load a mixture of therapeutic (toxins, drugs, and siRNA) and diagnostic agents (QDs, dyes). The results prove that this structure was favorable in promoting positive targeting and endosomal escaping.

Huan et al. also have done much work in silica-based theranostics. They attempt to conjugate the FOI organic molecular dyes (FITC, ICG, and the like) on the mesoporous silica cores along with loading the chemotherapeutic agents to human tumors in nude mice [159–162]. These attempts include coating PEI/PEG layer on MSNP for the stromal targeting of the PDAC tumors. This design enables delivering the TGF receptor kinase inhibitor which could interfere the pericyte-mediated stromal vascular obstruction and then promoting efficacy of the second-wave therapeutic agents. Recently, they have developed a custom-designed procedure in coating lipid biofilm on MSNPs. A high-loading gemcitabine (GEM) is rapidly encapsulated in the silica core. This biofilm procedure also allows the co-delivery of the hydrophobic PTX in the liposome shell in a ratiometric-controlled fashion. Compared to the therapy effects on tumor growth of the negative control (saline), paclitaxel (PTX)/GEM co-delivering liposome-MSNP shows a significantly higher rate of tumor shrinkage than that of other groups. The group of GEM/PTX-loaded particles needs 12 times Abraxane to get the comparable tumor shrinkage of the PTX/GEM co-delivering liposome-MSNP group. This is promising in a treatment plan for the sequential therapy by two chemodrugs.

Our group has paid much attention to the rattle-type mesoporous silica theranostics [163–175]. In our studies, FOI agent (FITC) is conjugated to the PEGylated silica nanorattle for loading docetaxel. The loading efficiency was as high as 32 %. About 80 % of drugs are released within 5 days. The study also has proved that the doxorubicin (DOX) showed pH sensitivity from the silica nanorattle, showing a high drug release rate at pH 4 than at pH 7.4. This behavior benefits drug releasing in the cytoplasm of cancer cells after their endocytosis (Fig. 9.12c) [167]. By conjugating NIR dye of ICG onto the particles, the silica nanorattles can realize real-time NIR FOI during drug delivery in vivo. We also have proved this fluorescent silica nanorattle could be efficiently anchored to the mesenchymal stem cells by conjugating the specific antibody (CD73, CD90, and the like). The intracellular retention time for silica nanorattles is over 48 h, which is enough for the cell-guiding tumor-tropic delivery [166]. He et al. have synthesized oxygen-deficient luminescent mesoporous silica nanoparticles for synchronous drug delivery and imaging. In their typical synthesis, triethoxysilane (TES) is selected instead of the common used TEOS as silicon source to fabricate MSN. Oxygen vacancies are produced by

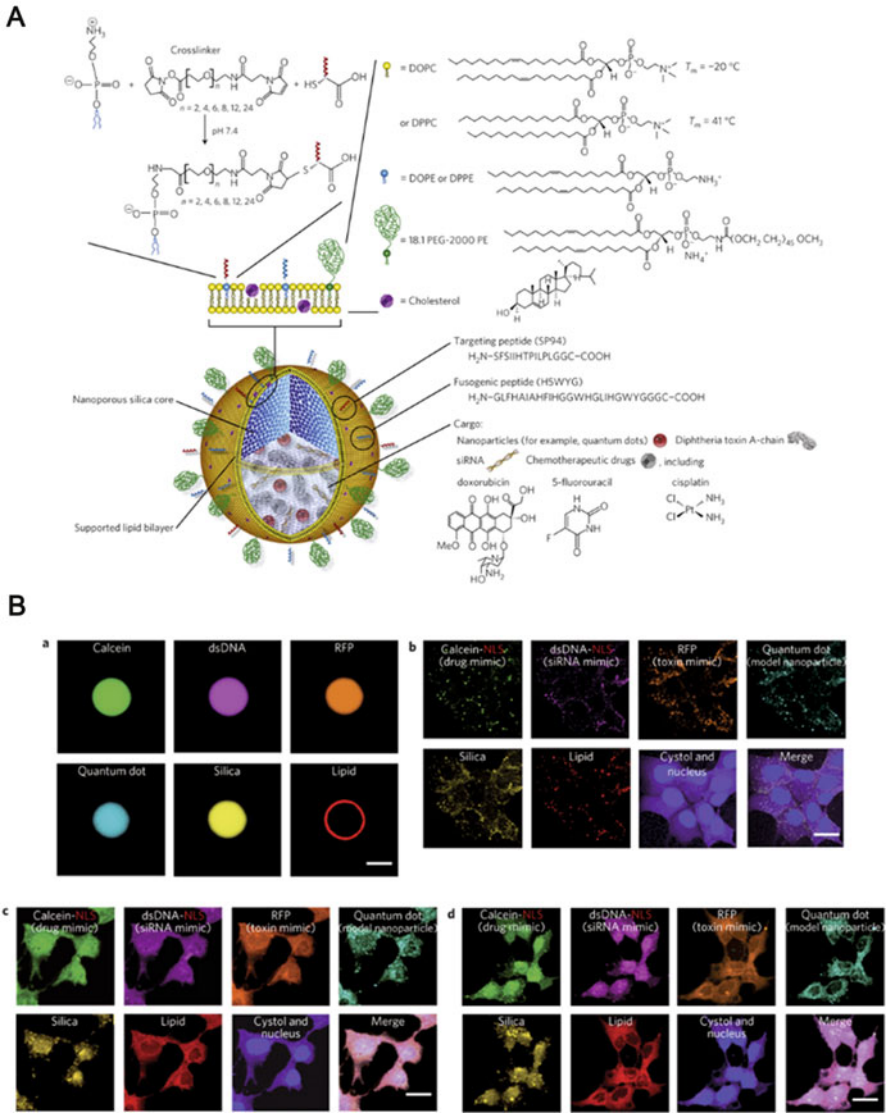

Fig. 9.10 (**a**) Schematic illustration of the nanoporous particle-supported lipid bilayer, depicting the disparate types of therapeutic and diagnostic agent that can be loaded within the nanoporous silica core, as well as the ligands that can be displayed on the surface of the supported lipid bilayer (SLB). (**b**) Targeted delivery of multicomponent cargos (calcein (*green*), an Alexa Fluor 647-labeled dsDNA oligonucleotide (*magenta*), RFP (*orange*), and CdSe/ZnS quantum dots (*teal*)) to the cytosol and nuclei of HCC cells (Reprinted with permission from Macmillan Publishers Ltd: Ref. [157], copyright 2011)

dehydrogenation between O_3Si-H terminal groups during post-calcination at 600 °C. This consequently induces the defect-related luminescence of MSN endowing the particle as the potential theranostic candidate [176].

9.3.1.2 Silica-Guided Medical Imaging and Chemotherapy

Hyeon et al. have focused a lot on the iron oxide nanocrystal coated with a silica shell [177]. Then the monodisperse particles are functionalized with FITC and rhodamine B. The FOI is used to measure the particle internalization in cancer cells. Moreover, the r_1 and r_2 relaxivity values of particles are 3.40 and 245 mM^{-1} s^{-1}, respectively. DOX is also loaded to evaluate its therapeutic efficacy in the SK-BR-3 cell line [178].

Additionally, they further report the synthesis of dye-doped iron oxide-coating MSNs for multimodal imaging. In this approach, FITC or tetramethylrhodamine (TRITC) is conjugated in the channels, and the iron oxide is chemically assembled to the exterior surface of MSNs. DOX is also loaded into the particles, and effective antitumor efficacy was realized in the B16-F10 cell line [179].

Chen et al. have synthesized a kind of ellipsoidal rattle-type mesoporous silica with magnetic Fe_3O_4 core using a selective etching strategy [180]. Fe_3O_4 core, as the T_2 contrast agent, plays a monitoring role on the therapeutic efficiency. DOX is loaded into the particles for a higher drug loading and sustained release [181]. They also designed a structure of mesoporous silica-coating Bi_2S_3 nanoparticles (BMSN) by surfactant-induced condensation method. The most advantage of this particle is the high X-ray enhancement and high DOX-loading efficiency (45 %). The comparable study shows that the BMSN group in the X-ray therapy has only a 2.10-fold increase in tumor volume through 24 days, while in the X-ray beam treatment alone group, the tumor volume increases to 4.40-fold. Thus, it is expected that the BMSNs can be applied as a highly efficient multifunctional nanosystem to realize the enhanced chemo- and radiotherapy in the further clinical applications (Fig. 9.11) [182].

Besides silica-based MRI-/FOI-guided theranostics, Chen et al. have fabricated functional mesoporous SiO_2 nanoparticles with the ability of positively targeting positron emission tomography (PET) imaging and drug delivery in 4 T1 tumor-bearing mice. About 80 nm silica nanoparticles are conjugated with thiol groups, PEGylation, TRC105 antibody (specific for CD105/endoglin), and ^{64}Cu labels, holding great potential for future image-guided drug delivery and targeted cancer therapy [123].

9.3.2 Silica-Guided Imaging and Phototherapies

Light therapy or phototherapy consists of exposure under daylight or specific wavelengths of light using lasers, light-emitting diodes, fluorescent lamps, and the like. In most cases, phototherapy is associated with the treatment of skin disorders.

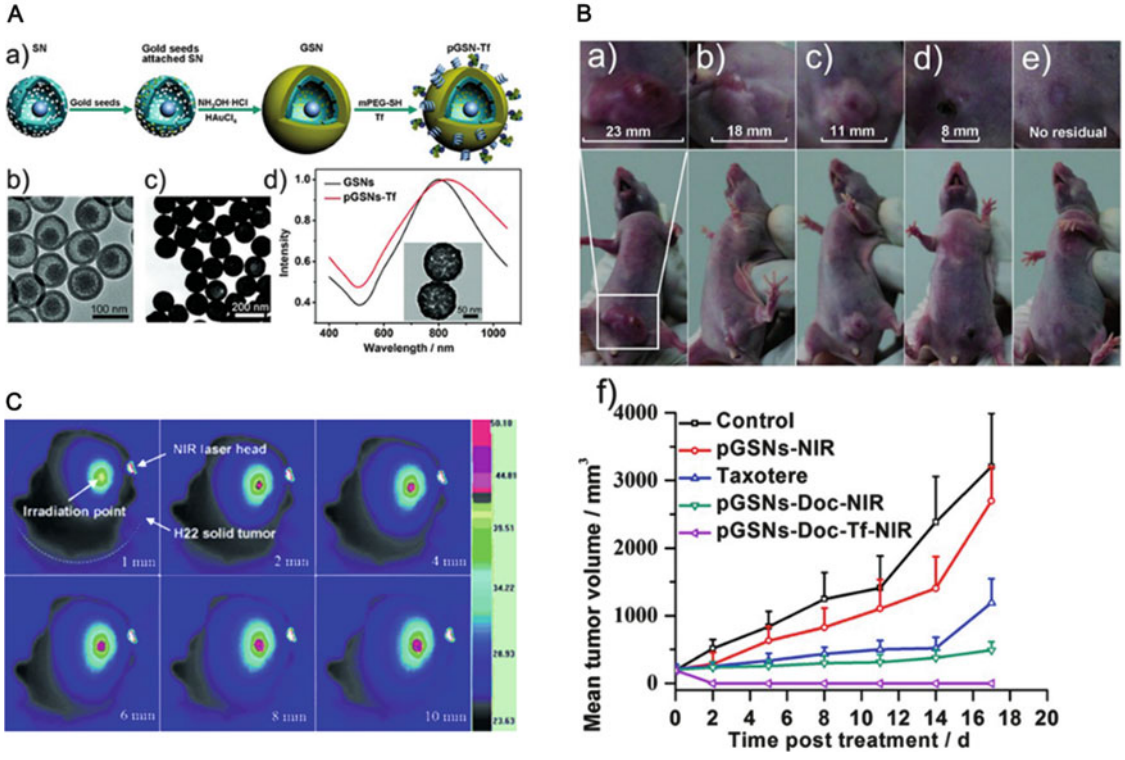

Fig. 9.11 (**a**) (*a*)Schematic diagram of gold nanoshells on silica nanorattles (GSNs) synthesis and bioconjugation, (*b*–*c*) TEM image SNs and GSNs, and (*d*) extinction spectra of PEG-functionalized gold nanoshells on silica nanorattles (pGSNs) and Tf-functionalized gold nanoshells on silica nanorattles (pGSNs-Tf); the inset is the TEM image of pGSNs-Tf. (**b**) (*a*–*e*) Photographs at day 17 of representative mice from groups of (*a*) control, (*b*) pGSNs-NIR, (*c*) Taxotere, (*d*) pGSNs-Doc-NIR, (*e*) pGSNs-Doc-Tf-NIR, and (*f*) in vivo antitumor activities of control group, pGSNs-NIR, Taxotere, pGSNs-Doc-NIR, and pGSNs-Doc-Tf-NIR group on MCF-7 bearing nude BALB/c mice (Reproduced from Ref. [171] by permission of John Wiley & Sons Ltd). (**c**) Infrared thermal images of an excised pGSNs-injected H22 solid tumor sample at different time points under NIR laser irradiation (Reproduced from Ref. [167] by permission of John Wiley & Sons Ltd)

Recently, researches pay much attention to the application of phototherapy into cancer cell killing. In this approach, cancer cells are exposed under the light, preferably NIR light (which has a high tissue penetration ability in this light window), involving a phototherapy agent to convert light energy into heat or generating reactive oxygen species (ROS), further killing cancer cells without causing serious damage to the normal tissues. In this part, we will focus on the silica-guided imaging and phototherapies.

9.3.2.1 Silica-Guided Imaging and Photothermal Therapy

Various photothermal agents have been used as a versatile, multimodal platform for both cancer diagnosis and therapies. Organic photothermal agents include indocyanine green (ICG, a clinically approved agent) [183, 184], heptamethine indocyanine dye [185], polypyrrole NPs [186, 187], and the like. Typical inorganic photothermal agents include various gold-based nanomaterials (nanorods [188], nanoshells [157, 171, 189], and nanocages) [190, 191], carbon-based nanomaterials (nanotubes [192], graphene [193], spheres [194]), CuS nanoparticles [195–200], transition metal dichalcogenides [201, 202], and the like.

Gold nanorods have a long surface plasmon resonance (LSPR) which can be adjusted between 650 and 950 nm. But this nanomaterial bears some disadvantages: low specific surface area limiting the drug loading, prone to aggregate resulting in a blueshifting spectrum, and a relative higher toxicity due to the surface cetyltrimethylammonium bromide (CTAB) bilayers. Zhang et al. have developed gold nanorods coated with mesoporous spheres as a cancer theranostic platform. The silica shell is ~30 nm with a large specific surface area for high loading of DOX. Without conjugating other imaging probes, two-photon imaging (TPI) contrast properties of gold nanorod are employed in this study to observe the intracellular behaviors of the particles. Under NIR light irradiation, DOX has a triggered release, thus providing two therapeutic modes alone with TPI [203]. However, this design also has a problem. Because the interactions between chemotherapeutic molecules and the inner cavities of silica are weak, there is a rising concern of the drug premature release during blood circulation. To overcome it, Liu et al. introduce 1-tetradecanol (TD) as a gatekeeper to regulate the drug release. TD is a phase-changing material with a melting temperature of 39 °C. Their designed DOX-loaded GNR@MSNPs-FA nanoparticles can realize a synergistic therapy for local heating, chemotherapy, and gate-controlled drug release. Given the photoacoustic imaging performance of GNR, this nanoparticle can also be used in diagnosis [204].

Our group has developed a structure of a thin gold nanoshell on a mesoporous silica nanorattle core. The positively charged surface of nanorattle simplifies the gold nanoshell coating process. This structure has a compact and thin gold shell, uniform size, tunable NIR light absorption, and high payload of drug properties. We conjugate ICG for the FOI. Our cellular and in vivo research results show that the synergistic effects of gold nanoshells on silica nanorattles are better than the

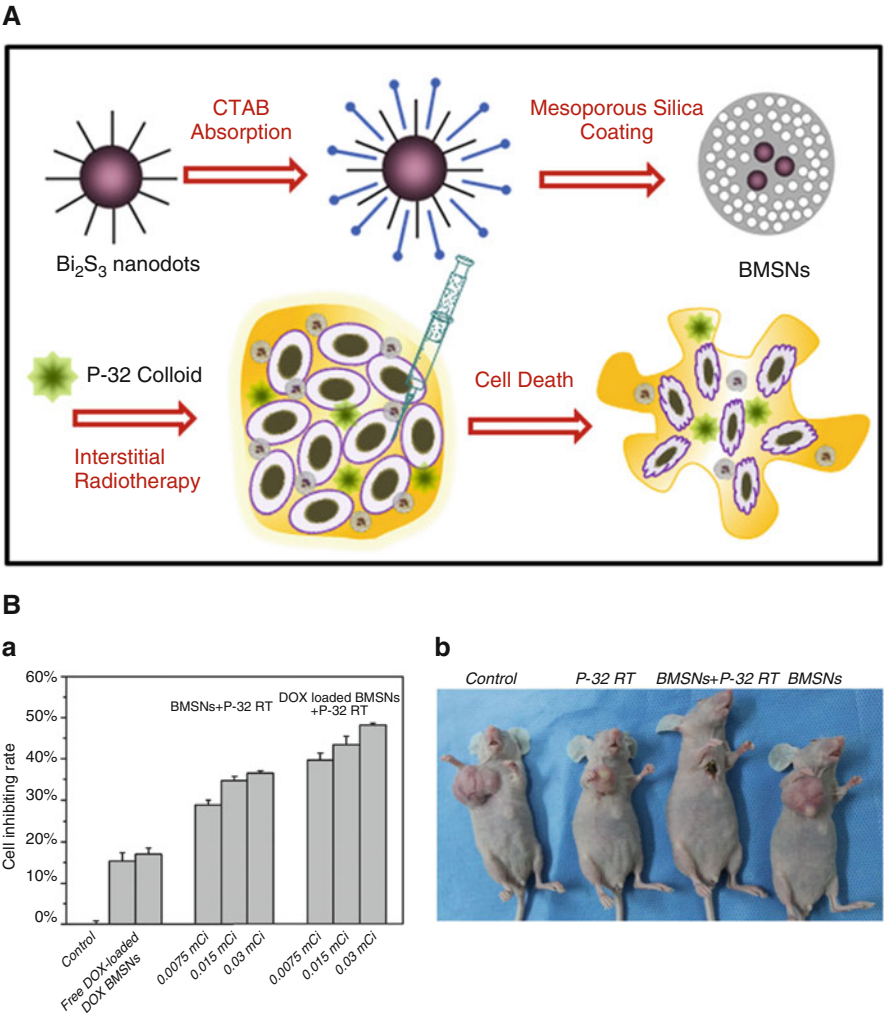

Fig. 9.12 (**a**) Schematic illustration of the synthetic process of Bi2S3 nanoparticles with a coating of mesoporous silica (BMSNs) and its application in interstitial therapy. (**b**) (*a*) Cytotoxicity profiles of PC3 cells after 24 h of treatment with free DOX, DOX-loaded BMSNs, BMSNs + P-32 RT, and DOX-loaded BMSNs + P-32 RT. The concentration of DOX drug and BMSNs was fixed at 5.0 and 100.0 μg/mL, respectively. For P-32 RT treatment, the cells were cultured with P-32 at different irradiation doses (0.0075, 0.015, and 0.03 mCi). (*b*) The tumor volume at 24th day after each treatment (saline, BMSNs, P-32 RT, and BMSNs + P-32 RT) was demonstrated by the photograph (Reprinted from Ref.[182], Copyright 2015, with permission from Elsevier)

chemotherapy or photothermal therapy alone [157]. In a following study, we conjugate a positive targeting molecular transferrin on the surface of gold shells. FITC is loaded for FOI of the particles. The results demonstrate that a single NIR light irradiation could completely regress the tumor growth (Fig. 9.12a, b) [171].

In other studies, magnetic NCs are encapsulated in the silica nanoparticles, then coated with gold nanoshell, for photothermal therapy and MR imaging [205–208]. But this design often causes a low content of Fe_3O_4 in the final nanocomposites, inducing weak MRI [209, 210]. Sharma et al. have developed sub-50 nm gold-speckled silica nanoparticles, combining fluorescent and photothermal properties. The green fluorescence is doped into the particles for a cellular visualization [209]. Liu et al. have used single-walled carbon nanotubes (SWNTs) coated with mesoporous silica-loading DOX. Upon the NIR light irradiation, the drug triggered a release resulting in a synergistic cell killing. SWNTs can be used as both PA and MR imaging agent due to their strong NIR absorbance and metal NP decoration [143].

9.3.2.2 Silica-Guided Imaging and Photodynamic Therapy

Photodynamic therapy (PDT) is also called photochemotherapy using photosensitizers selectively sensitive to the light. Under a specific light irradiation, photosensitizers generate ROS, such as singlet oxygen ($^1O_2$) and free radicals, and become toxic to kill cancer cells. PDT has been applied in the clinic for some medical conditions like wet age-related macular degeneration and malignant cancers [211]. However, because most photosensitizer molecules have disadvantages of hydrophobility, like prone to aggregate, low quantum yield, low extinction coefficients, and absorption at relatively short wavelengths, nanoparticles have been widely explored as photosensitizers, such as polymeric nanoparticles, liposomes, ceramic nanoparticles, proteins, gold nanoparticles, carbon nanomaterials, quantum dots (QDs), upconversion nanoparticles (UCNPs), and so on [212–221].

For silica-guided imaging and photodynamic therapy, Huang et al. have constructed photo-theranostics of silica-coated gold nanoclusters conjugated with Ce6 for fluorescence imaging-guided PDT. Mesoporous silica-coating shell enables a high Ce6 photosensitizer loading and decreases the undesired release of Ce6 during its blood circulation. Both fluorescence of Ce6 and luminescence of gold clusters are responsible for the FOI of the particles' subcellular behaviors (Fig. 9.13) [222]. Lv et al. have used upconversion luminescent GdOF:Ln as core and mesoporous silica as shell for cancer therapy. Due to the codoped Yb/Er/Mn in GdOF, the red emission from the GdOF:Ln is greatly enhanced and can transfer energy to ZnPc, the photodynamic agent, and then produce the singlet oxygen. At the same time, carbon dots outside the shell are a photothermal agent to generate heat under 980 nm NIR light irradiation. Simultaneously, heat will accelerate the DOX release, resulting in a synergistic therapy. Also, rare earth ions have doped in the particles and endow them with excellent UCL imaging, magnetic resonance imaging (MRI), and computed tomography (CT) imaging (Fig. 9.14a) [223]. Zhao et al. have presented a core–shell-structured Fe_3O_4@mSiO_2. Fe_3O_4 nanoparticles are synthesized by a common coprecipitation method, then mesoporous silica is coated, and methylene blue (MB), a hydrophilic phenothiazinium photosensitizer, is encapsulated. Their $^1O_2$ generation capability is assessed by DPBF, a $^1O_2$ probe in acetonitrile which reacts with $^1O_2$ causing a decrease in the DPBF absorption at 400 nm. The studies

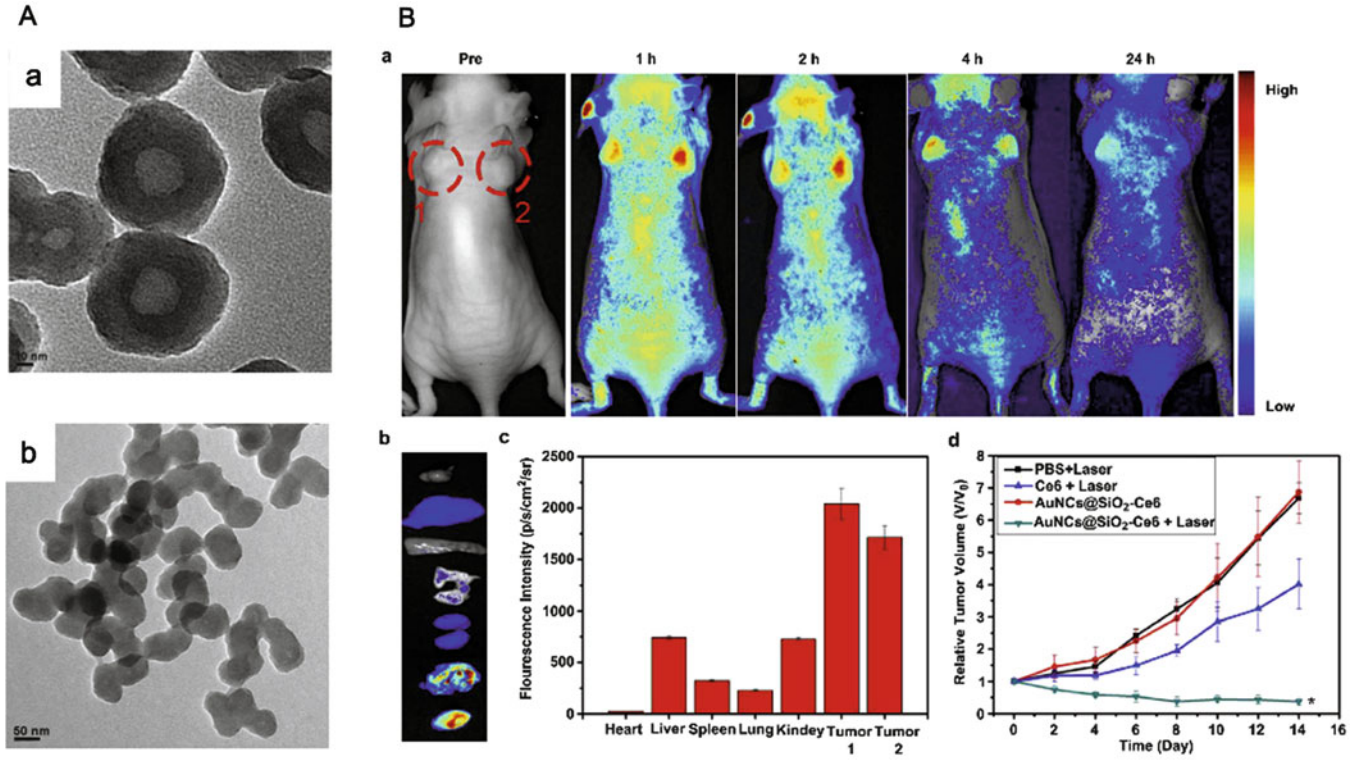

Fig. 9.13 (**a**) TEM images of AuNCs@SiO_2 (*a*) and AuNCs@SiO_2-Ce6 (*b*). (**b**) (*a*) Real-time in vivo NIR fluorescence images after intravenous injection of AuNCs@SiO_2-Ce6 in nude mice at different time points. Red circles indicate the location of tumors. (*b*) Ex vivo images of mouse tissues (from *top* to *bottom*: the heart, liver, spleen, lung, kidneys, tumor 1, tumor 2). (*c*) The fluorescence intensity of organs harvested at 24 h time point from postinjection mice. (*d*) Tumor growth curves of different groups of tumor-bearing mice after treatment (Reprinted from Ref. [222], Copyright 2013, with permission from Elsevier)

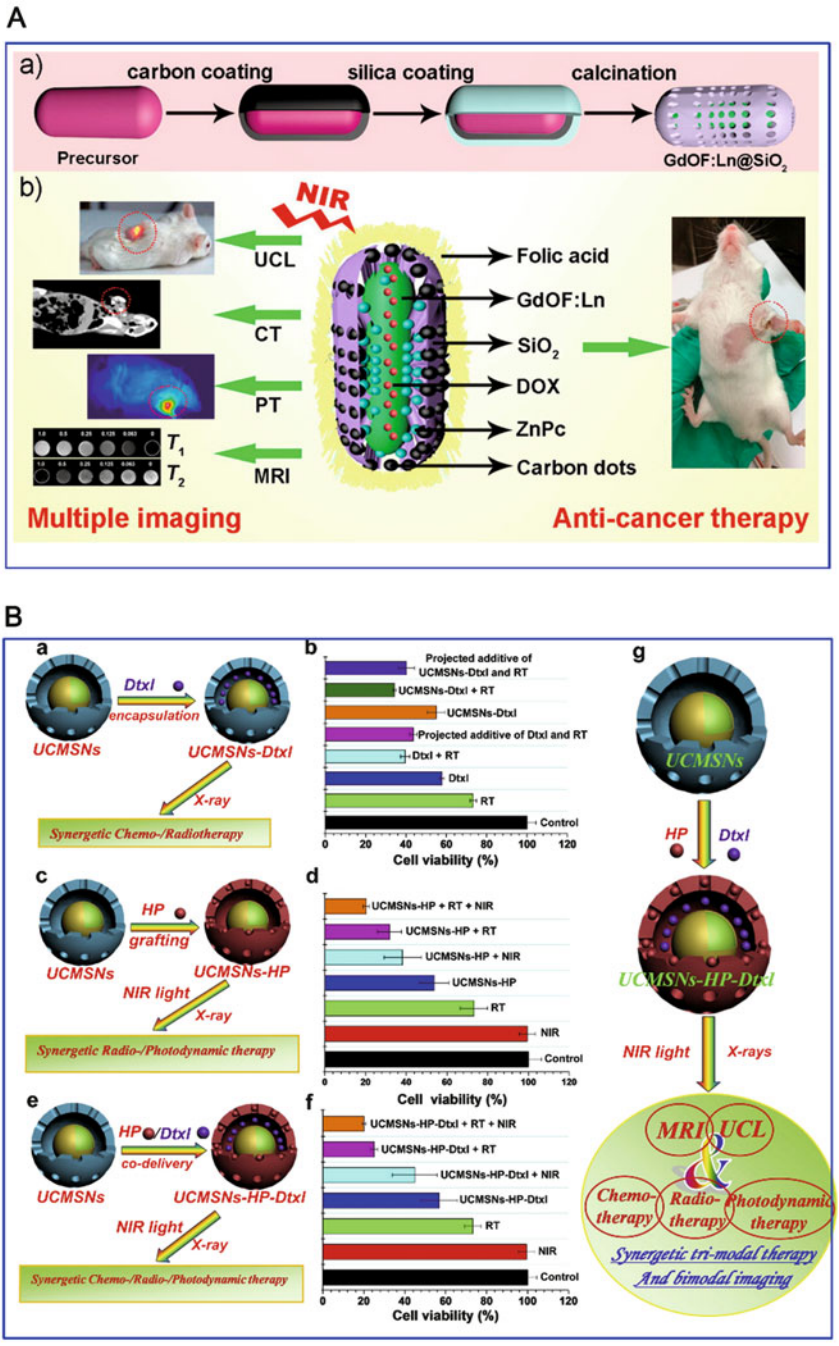

Fig. 9.14 (**a**) Schematic illustration for the synthesis of GdOF:Ln@SiO_2 ZnPc-CDs microcapsule and bio-application for multiple imaging and antitumor therapy (Reprinted with permission from Ref. [223]. Copyright 2015 American Chemical Society). (**b**) (*a*) Schematic diagram and (*b*) in vitro evaluation of synergetic chemo-/radiotherapy effects on HeLa cells after co-incubated with

show this particle could serve as both an FOI and PDT probe in the cancer therapy [224].

Different from the above studies, Zhao et al. have used mesoporous silica shells as a spacer to adjust the enhancement factors of one- and two-photon excitation fluorescence of the gold nanorods for a porphyrin molecule, T790. They have found when the separation distance between gold nanorods and T790 was varied from 34 to 20 nm, the enhancement factors are 2.1 and 11.8, respectively. This particle is attractive for two-photon cell imaging and two-photon photodynamic therapy with improved efficiency [225].

9.3.3 Integration of Multimodal Imaging and Combination Therapy

As expounded in the above section, multimodal imaging may increase the accuracy of diagnosis by integrating the advantages of multiple modalities for complementary functional imaging. Meanwhile, integration of several kinds of therapeutic methods into one combination therapy may increase the therapeutic efficacy and decrease cancer recurrence and metastasis. With the versatile silica as matrix, multiple kinds of imaging modalities include MRI, FOI, CT, and others, as well as therapeutic agents such as chemotherapeutic drugs, photosensitizer, and photothermal converting agents. The ability for multimodal imaging cannot only increase the accuracy of diagnosis but monitor the therapeutic outcome of the combination therapy and track the biodistribution of nanoparticles [226]. Song and coworkers have coated mesoporous silica layers onto gold nanorod and tether a fluorescent dye of RBITC onto silica for fluorescent imaging. Chemotherapeutic drug of DOX is loaded into mesoporous silica for chemotherapy along with photothermal therapy from gold nanorod [227]. Khlebtsov and coworkers have coated gold/silver nanocage with mesoporous silica that was functionalized with photodynamic sensitizer Yb-2,4-dimethoxyhematoporphyrin (Yb-HP). The nanocomposites can combine the ability of PDT, PTT, and fluorescent imaging into one nanoparticle [228]. Similarly, Wang and coworkers have created a double-walled Au nanocage/silica nanorattle by combining two "hollow-excavated strategies" of galvanic replacement and "surface-protected etching." The hollow nanocomposites integrate the ability of surface-enhanced Raman scattering (SERS), chemotherapy, and photothermal

Fig. 9.14 (continued) 0.5 μg/mL free Dtxl/UCMSNs-Dtxl. (*c*) Schematic diagram and (*d*) in vitro evaluation of synergetic radio-/photodynamic therapy effects on HeLa cells after co-incubated with 150 μg/mL UCMSNs-HP. (*e*) Schematic diagram and (*f*) in vitro evaluation of synergetic chemo-/radio-/photodynamic therapy effects on HeLa cells after co-incubated with 5 μg/mL UCMSNs-HP-Dtxl. (*g*) Schematic diagram of synergetic chemo-/radio-/photodynamic trimodal therapy as well as magnetic/upconversion luminescent (MR/UCL) bimodal imaging with HP/Dtxl co-loaded UCMSNs (UCMSNs-HP-Dtxl) (Reprinted from Ref. [233], Copyright 2014, with permission from Elsevier)

therapy [229]. Stevens and coworkers have integrated gold quantum dots within the mesoporous and hollow silica nanoparticles, alongside larger gold nanoparticles within the shell's central cavity. The "quantum rattle" structure integrates three complementary imaging modalities of near-infrared fluorescence, photoacoustic, and magnetic resonance imaging, as well as the chemotherapy and photothermal therapy [230]. Cui and coworkers have coated mesoporous silica layer onto gold nanorods for concurrent photothermal therapy and enhanced radiation therapy and CT imaging [231]. Lin and coworkers have coated mesoporous silica onto upconversion luminescent (UCL) GdOF:Ln (codoped with Yb/Er/Mn) and conjugated PDT agent (ZnPc) and carbon dots for photothermal therapy. Among the elements, Gd^{3+} ions can play an effective role as the intermediate sublattice in enhancing the doped activator efficiency, and Gd^{3+}/Yb^{3+}-doped particles have been proved to be excellent CT contrast agents due to the high atomic and strong X-ray attenuation. The loaded DOX can be stimuli released with thermal effect. Thus, the nanocomposites have integrated fluorescent imaging, MRI, CT imaging, and combination therapy of PDT, PTT, and chemotherapy [223].

Shi and coworkers have done lots of works focused on multimodal imaging-guided combination therapy. They reported the synthesis of multifunctional MR imaging-guided high-intensity focused ultrasound (HIFU) synergistic agents for cancer surgery based on hollow mesoporous silica [232]. Manganese oxide nanoparticles are synthesized in situ within the mesopore network of hollow mesoporous silica nanocapsules (MCNCs), which act as T_1-weighted MR imaging agent. Perfluorohexane (PFH) is encapsulated into the hollow interior, which can easily gasify and generate bubble when heat is generated by HIFU. The nanocomposites can be delivered to the targeted tumor tissue in the liver of rabbits for focused ultrasound to achieve an enhanced synergistic therapeutic effect in HIFU. They also have synthesized sub-80 nm rattle-structured silica nanocomposites with upconversion luminescent $NaYF_4$:Yb/Er/Tm@$NaGdF_4$ core–shell particle as core and mesoporous silica as shell. The nanocomposites have incorporated a radio-/photosensitizer hematoporphyrin (HP) and radiosensitizer/chemodrug docetaxel (Dtxl). Under NIR excitation and X-ray irradiation, the synergetic chemo-/radio-/photodynamic trimodal therapy could induce a complete tumor elimination with the assistance of simultaneous magnetic/upconversion luminescent bimodal imaging (Fig. 9.14b) [233].

With deeper research and knowledge, many kinds of nanocrystals have been found to have multiple abilities for diagnosis and therapy. For instance, plasmatic gold nanorods, nanoshells, and nanocages not only can be used as a photothermal conversion agent but also can be used as a contrast agent of CT or photoacoustic imaging. Magnetic nanoparticles for MRI also are developed for magnetically targeting and photothermal therapy. Gd-containing upconversion nanocrystals can be used for both T_1-weighted MR imaging and upconversion fluorescence imaging. Thus, in designing multifunctional silica-based nanocomposites for multimodal imaging-guided combination therapy, it is important to rationally design the nanocomposites with minimum kinds of building blocks and simplest synthesis but with maximum kinds of functions.

9.4 Conclusion and Perspective

Multifunctional silica nanocomposites with versatile structure, flexible integrating ability, tunable surface chemistry, and multiple performances have been considered as a rising star for multifunctional cancer diagnosis and therapy. As a multifunctional matrix, silica can act as a coating material or connecting matrix to integrate not only different kinds of imaging including fluorescent optical imaging, ultrasound imaging, computed tomography, magnetic resonance imaging, positron emission tomography, and photoacoustic imaging but also therapeutic modalities for chemotherapy, photothermal therapy, and photodynamic therapy. By coating silica on other functional nanoparticles, the biocompatibility of these nanoparticles could be increased. In addition, the in vivo biodistribution, metabolism, and excretion may be real-time monitored as needed. In general, the integration of multimodal diagnosis and combination of multiple therapeutic modalities into one nanoparticle, formed theranostic nanocomposites, have several advantages. Firstly, the combination of several therapeutic modalities into one nanoparticle realizes synergistic therapeutic effect over one single therapeutic method to induce more efficient therapeutic outcome. In cancer therapy, it has been reported that the combination therapy could help for reversing multidrug resistance and reducing metastasis. Simultaneously, the combined imaging ability enables more accurate imaging diagnosis and provides many useful information for therapy through the full course before, during, and after therapy. Before initiating treatment, it is essential to carry out diagnostic imaging to understand the biologic stage and cellular phenotype of cancer. From the complementary multimodal imaging such as MRI, FOI, CT, US, etc., a general outline of the tumor including the stage, tumor size, phenotype, and metastasis could be given to the doctors and patients. During therapy, rapid real-time imaging especially near-infrared fluorescent imaging can tell the surgeons where the tumor and its boundary is. After therapy, it could real-time monitor the therapy outcome. Meanwhile, integrating into one nanoparticle, the nanocomposites could track the biodistribution and clearance of loaded chemotherapeutic drugs. These useful information could help physicians to decide next-step therapeutic schedule. Now, most of these works are undergoing preclinical research in labs. It was encouraging that a kind of ultrasmall multimodal silica nanoparticles (Cornell dots, C dots) has recently been approved by the FDA for the first-in-human clinical trial for targeted diagnostics of advanced melanoma. Nevertheless, it is still a long way to translate the multifunctional silica nanoparticles into clinical market before accumulating sufficient evidence to prove their safety and efficacy.

Nevertheless, there are still some challenges that need to be solved before successful applications of multifunctional silica nanomaterials. Some improvements in terms of research directions seem to be necessary. Firstly, many theranostic studies are still proof of concept. In clinical diagnosis and treatment, it is a great challenge to simultaneously realize multiple functions of diagnosis and therapy in one nanoparticle. In designing the silica-based nanocomposites, it is important to use simple, reproducible, controllable, and scalable synthesizing method to get multifunctional silica

nanoparticles. In addition, the nanocomposites should not be multifunctionalized at the expense of the biocompatibility and dispersity in physiological condition. Second, in designing the nanoparticles, the researchers should take into account that it had different pharmacokinetic requirements of imaging modalities and therapeutic agents. How to meet the needs of each functional modality including imaging and therapy in vivo is very difficult and maybe differential among patients. Thus, the nanocomposites should be designed elaborately. Third, although silica matrix is used to increase the biocompatibility of imaging or therapeutic agents, the potential toxicity of these agents after exposure or leakage should be paid enough attentions especially their long-term in vivo toxicity.

In conclusion, exciting progresses have been made for silica-based multimodal imaging and theranostics for cancer therapy. With the diversity and multifunctionality of silica-based nanocomposites, it is a promising way to develop cooperative therapies or simultaneous utility of multiple imaging functions to guide the delivery of the nanomedicine. It is anticipated that the silica nanocomposites can induce a more effective personalized cancer therapy in the near future.

References

1. Stewart B, Wild CP (2014) World cancer report 2014. WHO Press, France
2. Jemal A, Bray F, Center MM, Ferlay J, Ward E, Forman D (2011) Global cancer statistics. CA Cancer J Clin 61(2):69–90. doi:10.3322/caac.20107
3. Siegel R, Naishadham D, Jemal A (2013) Cancer statistics, 2013. CA Cancer J Clin 63(1):11–30. doi:10.3322/caac.21166
4. Schroeder A, Heller DA, Winslow MM, Dahlman JE, Pratt GW, Langer R, Jacks T, Anderson DG (2012) Treating metastatic cancer with nanotechnology. Nat Rev Cancer 12(1):39–50. doi:10.1038/nrc3180
5. Petros RA, DeSimone JM (2010) Strategies in the design of nanoparticles for therapeutic applications. Nat Rev Drug Discov 9(8):615–627. doi:10.1038/nrd2591
6. Sanhai WR, Sakamoto JH, Canady R, Ferrari M (2008) Seven challenges for nanomedicine. Nat Nanotechnol 3(5):242–244. doi:10.1038/nnano.2008.114
7. Moghimi SM, Hunter AC, Murray JC (2005) Nanomedicine: current status and future prospects. FASEB J 19(3):311–330. doi:10.1096/fj.04-2747rev
8. Ferrari M (2005) Cancer nanotechnology: opportunities and challenges. Nat Rev Cancer 5(3):161–171. doi:10.1038/nrc1566
9. Jones D (2007) Cancer nanotechnology: small, but heading for the big time. Nat Rev Drug Discov 6(3):174–175. doi:10.1038/nrd2285
10. Davis ME, Chen ZG, Shin DM (2008) Nanoparticle therapeutics: an emerging treatment modality for cancer. Nat Rev Drug Discov 7(9):771–782. doi:10.1038/nrd2614
11. Etheridge ML, Campbell SA, Erdman AG, Haynes CL, Wolf SM, McCullough J (2013) The big picture on nanomedicine: the state of investigational and approved nanomedicine products. Nanomed Nanotechnol 9(1):1–14. doi:10.1016/j.nano.2012.05.013
12. Bae YH, Park K (2011) Targeted drug delivery to tumors: myths, reality and possibility. J Control Release 153(3):198–205. doi:10.1016/j.jconrel.2011.06.001
13. Lammers T, Hennink WE, Storm G (2008) Tumour-targeted nanomedicines: principles and practice. Br J Cancer 99(3):392–397. doi:10.1038/sj.bjc.6604483

14. Al-Jamal WT, Kostarelos K (2011) Liposomes: from a clinically established drug delivery system to a nanoparticle platform for theranostic nanomedicine. Acc Chem Res 44:1094–1104. doi:10.1021/ar200105p
15. Astruc D, Boisselier E, Ornelas C (2010) Dendrimers designed for functions: from physical, photophysical, and supramolecular properties to applications in sensing, catalysis, molecular electronics, photonics, and nanomedicine. Chem Rev 110(4):1857–1959. doi:10.1021/cr900327d
16. Duncan R (2006) Polymer conjugates as anticancer nanomedicines. Nat Rev Cancer 6(9):688–701. doi:10.1038/nrc1958
17. Lammers T, Subr V, Ulbrich K, Hennink WE, Storm G, Kiessling F (2010) Polymeric nanomedicines for image-guided drug delivery and tumor-targeted combination therapy. Nano Today 5(3):197–212. doi:10.1016/j.nantod.2010.05.001
18. Benezra M, Penate-Medina O, Zanzonico PB, Schaer D, Ow H, Burns A, DeStanchina E, Longo V, Herz E, Iyer S, Wolchok J, Larson SM, Wiesner U, Bradbury MS (2011) Multimodal silica nanoparticles are effective cancer-targeted probes in a model of human melanoma. J Clin Invest 121(7):2768–2780. doi:10.1172/JCI45600
19. Cheng K, Peng S, Xu CJ, Sun SH (2009) Porous hollow Fe_3O_4 nanoparticles for targeted delivery and controlled release of cisplatin. J Am Chem Soc 131(30):10637–10644. doi:10.1021/ja903300f
20. Gupta AK, Gupta M (2005) Synthesis and surface engineering of iron oxide nanoparticles for biomedical applications. Biomaterials 26(18):3995–4021. doi:10.1016/j.biomaterials.2004.10.012
21. Liong M, Lu J, Kovochich M, Xia T, Ruehm SG, Nel AE, Tamanoi F, Zink JI (2008) Multifunctional inorganic nanoparticles for imaging, targeting, and drug delivery. ACS Nano 2(5):889–896. doi:10.1021/nn800072t
22. Liu HY, Chen D, Li LL, Liu TL, Tan LF, Wu XL, Tang FQ (2011) Multifunctional gold nanoshells on silica nanorattles: a platform for the combination of photothermal therapy and chemotherapy with low systemic toxicity. Angew Chem Int Ed 50(4):891–895. doi:10.1002/anie.201002820
23. Liu Z, Chen K, Davis C, Sherlock S, Cao Q, Chen X, Dai H (2008) Drug delivery with carbon nanotubes for in vivo cancer treatment. Cancer Res 68(16):6652–6660. doi:10.1158/0008-5472.can-08-1468
24. Ma K, Sai H, Wiesner U (2012) Ultrasmall sub-10 nm near-infrared fluorescent mesoporous silica nanoparticles. J Am Chem Soc 134(32):13180–13183. doi:10.1021/ja3049783
25. Son S, Bai X, Lee S (2007) Inorganic hollow nanoparticles and nanotubes in nanomedicine part 1. Drug/gene delivery applications. Drug Discov Today 12(15–16):650–656. doi:10.1016/j.drudis.2007.06.002
26. Yang XY, Zhang XY, Liu ZF, Ma YF, Huang Y, Chen YS (2008) High-efficiency loading and controlled release of doxorubicin hydrochloride on graphene oxide. J Phys Chem C 112(45):17554–17558. doi:10.1021/jp806751k
27. Barbe C, Bartlett J, Kong LG, Finnie K, Lin HQ, Larkin M, Calleja S, Bush A, Calleja G (2004) Silica particles: a novel drug-delivery system. Adv Mater 16(21):1959–1966. doi:10.1002/adma.200400771
28. Yanagisawa T, Shimizu T, Kuroda K, Kato C (1990) The preparation of alkyltriinethylainonium–kaneinite complexes and their conversion to microporous materials. Bull Chem Soc Jpn 63(4):988–992. doi:10.1246/bcsj.63.988
29. Bradbury MS, Phillips E, Montero PH, Cheal SM, Stambuk H, Durack JC, Sofocleous CT, Meester RJC, Wiesner U, Patel S (2013) Clinically-translated silica nanoparticles as dual-modality cancer-targeted probes for image-guided surgery and interventions. Integr Biol 5(1):74–86. doi:10.1039/C2IB20174G
30. Lee JE, Lee N, Kim T, Kim J, Hyeon T (2011) Multifunctional mesoporous silica nanocomposite nanoparticles for theranostic applications. Acc Chem Res 44(10):893–902. doi:10.1021/ar2000259

31. Bhirde AA, Liu G, Jin A, Iglesias-Bartolome R, Sousa AA, Leapman RD, Gutkind JS, Lee S, Chen XY (2011) Combining portable Raman probes with nanotubes for theranostic applications. Theranostics 1:310–321. doi:10.7150/thno/v01p0310
32. Jiang S, Gnanasammandhan MK, Zhang Y (2010) Optical imaging-guided cancer therapy with fluorescent nanoparticles. J R Soc Interface 7(42):3–18. doi:10.1098/rsif.2009.0243
33. Ma X, Devi G, Qu Q, Toh DF, Chen G, Zhao Y (2014) Intracellular delivery of antisense peptide nucleic acid by fluorescent mesoporous silica nanoparticles. Bioconjug Chem 25(8):1412–1420. doi:10.1021/bc5002714
34. Medintz IL, Uyeda HT, Goldman ER, Mattoussi H (2005) Quantum dot bioconjugates for imaging, labelling and sensing. Nat Mater 4(6):435–446. doi:10.1038/nmat1390
35. Ballou B, Lagerholm BC, Ernst LA, Bruchez MP, AS W (2004) Noninvasive imaging of quantum dots in mice. Bioconjug Chem 15(1):79–86. doi:10.1021/bc034153y
36. Cherukuri P, Bachilo SM, Litovsky SH, RB W (2004) Near-infrared fluorescence microscopy of single-walled carbon nanotubes in phagocytic cells. J Am Chem Soc 126(48):15638–15639. doi:10.1021/ja0466311
37. Robinson JT, Hong G, Liang Y, Zhang B, Yaghi OK, Dai H (2012) In vivo fluorescence imaging in the second near-infrared window with long circulating carbon nanotubes capable of ultrahigh tumor uptake. J Am Chem Soc 134(25):10664–10669. doi:10.1021/ja303737a
38. Yoo JM, Kang JH, Hong BH (2015) Graphene-based nanomaterials for versatile imaging studies. Chem Soc Rev. doi:10.1039/c5cs00072f
39. Chen Q, Wang C, Cheng L, He W, Cheng Z, Liu Z (2014) Protein modified upconversion nanoparticles for imaging-guided combined photothermal and photodynamic therapy. Biomaterials 35(9):2915–2923. doi:10.1016/j.biomaterials.2013.12.046
40. Niu N, He F, Ma P, Gai S, Yang G, Qu F, Wang Y, Xu J, Yang P (2014) Up-conversion nanoparticle assembled mesoporous silica composites: synthesis, plasmon-enhanced luminescence, and near-infrared light triggered drug release. ACS Appl Mater Interfaces 6(5):3250–3262. doi:10.1021/am500325w
41. Shan G, Weissleder R, Hilderbrand SA (2013) Upconverting organic dye doped core-shell nano-composites for dual-modality NIR imaging and photo-thermal therapy. Theranostics 3(4):267–274. doi:10.7150/thno.5226
42. Wang F, Banerjee D, Liu Y, Chen X, Liu X (2010) Upconversion nanoparticles in biological labeling, imaging, and therapy. Analyst 135(8):1839–1854. doi:10.1039/c0an00144a
43. Cao L, Wang X, Meziani MJ, Lu FS, Wang HF, Luo PG, Lin Y, Harruff BA, Veca LM, Murray D, Xie S-Y, Sun Y-P (2007) Carbon dots for multiphoton bioimaging. J Am Chem Soc 129(37):11318–11319. doi:10.1021/ja073527l
44. Yang S-T, Cao L, Luo PG, Lu FS, Wang X, Wang HF, Meziani MJ, Liu YF, Qi G, Sun Y-P (2009) Carbon dots for optical imaging in vivo. J Am Chem Soc 131(32):11308–11309. doi:10.1021/ja904843x
45. Santra S, Dutta D, Walter GA, Moudgil BM (2005) Fluorescent nanoparticle probes for cancer imaging. Technol Cancer Res Treat 4(6):593–602. doi:10.1177/153303460500400603
46. Tsai C-P, Chen C-Y, Hung Y, Chang F-H, Mou C-Y (2009) Monoclonal antibody-functionalized mesoporous silica nanoparticles (MSN) for selective targeting breast cancer cells. J Mater Chem 19(32):5737–5743. doi:10.1039/b905158a
47. Lee C-H, Cheng S-H, Wang Y-J, Chen Y-C, Chen N-T, Souris J, Chen C-T, Mou C-Y, Yang C-S, Lo L-W (2009) Near-infrared mesoporous silica nanoparticles for optical imaging: characterization and in vivo biodistribution. Adv Funct Mater 19(2):215–222. doi:10.1002/adfm.200800753
48. Luo S, Zhang E, Su Y, Cheng T, Shi C (2011) A review of NIR dyes in cancer targeting and imaging. Biomaterials 32(29):7127–7138. doi:10.1016/j.biomaterials.2011.06.024
49. Luo T, Huang P, Gao G, Shen GX, Fu S, Cui DX, Zhou CG, Ren QS (2011) Mesoporous silica-coated gold nanorods with embedded indocyanine green for dual mode X-ray CT and NIR fluorescence imaging. Opt Express 19(18):17030–17039. doi:10.1364/OE.19.017030

50. Palantavida S, Tang R, Sudlow GP, Akers WJ, Achilefu S, Sokolov I (2014) Ultrabright NIR fluorescent mesoporous silica nanoparticles. J Mater Chem B 2(20):3107–3114. doi:10.1039/c4tb00287c
51. Souris JS, Lee CH, Cheng SH, Chen CT, Yang CS, Ho JA, Mou CY, Lo LW (2010) Surface charge-mediated rapid hepatobiliary excretion of mesoporous silica nanoparticles. Biomaterials 31(21):5564–5574. doi:10.1016/j.biomaterials.2010.03.048
52. Ma K, Werner-Zwanziger U, Zwanziger J, Wiesner U (2013) Controlling growth of ultrasmall sub-10 nm fluorescent mesoporous silica nanoparticles. Chem Mater 25(5):677–691. doi:10.1021/cm303242h
53. Wen T, Yang B, Guo Y, Sun J, Zhao C, Zhang S, Zhang M, Wang Y (2014) Organosilane-functionalized graphene quantum dots and their encapsulation into bi-layer hollow silica spheres for bioimaging applications. Phys Chem Chem Phys 16(42):23188–23195. doi:10.1039/c4cp03339f
54. Le Guével X, Hötzer B, Jung G, Schneider M (2011) NIR-emitting fluorescent gold nanoclusters doped in silica nanoparticles. J Mater Chem 21(9):2974–2981. doi:10.1039/c0jm02660c
55. Wu X, Li C, Liao S, Li L, Wang T, Su Z, Wang C, Zhao J, Sui C, Lin J (2014) Silica-encapsulated Gd^{3+}-aggregated gold nanoclusters for in vitro and in vivo multimodal cancer imaging. Chem Eur J 20(29):8876–8882. doi:10.1002/chem.201403202
56. Kim Y, Jeon JB, Chang JY (2012) CdSe quantum dot-encapsulated molecularly imprinted mesoporous silica particles for fluorescent sensing of bisphenol A. J Mater Chem 22(45):24075–24080. doi:10.1039/c2jm34798a
57. Bardi G, Malvindi MA, Gherardini L, Costa M, Pompa PP, Cingolani R, Pizzorusso T (2010) The biocompatibility of amino functionalized CdSe/ZnS quantum-dot-Doped SiO_2 nanoparticles with primary neural cells and their gene carrying performance. Biomaterials 31(25):6555–6566. doi:10.1016/j.biomaterials.2010.04.063
58. Lin Y-S, Wu S-H, Hung Y, Chou Y-H, Chang C, Lin M-L, Tsai C-P, Mou C-Y (2006) Multifunctional composite nanoparticles: magnetic, luminescent, and mesoporous. Chem Mater 18(22):5170–5172. doi:10.1021/cm061976z
59. Durgadas CV, Sreenivasan K, Sharma CP (2012) Bright blue emitting CuSe/ZnS/silica core/shell/shell quantum dots and their biocompatibility. Biomaterials 33(27):6420–6429. doi:10.1016/j.biomaterials.2012.05.051
60. Chen L-Y, Wang C-W, Yuan ZQ, Chang H-T (2015) Fluorescent gold nanoclusters: recent advances in sensing and imaging. Anal Chem 87(1):216–229. doi:10.1021/ac503636j
61. Zhang LB, Wang E (2014) Metal nanoclusters: new fluorescent probes for sensors and bioimaging. Nano Today 9(1):132–157. doi:10.1016/j.nantod.2014.02.010
62. Kim J, Lee JE, Lee J, Yu JH, Kim BC, An K, Hwang Y, Shin C-H, Park J-G, Kim J, Hyeon T (2006) Magnetic fluorescent delivery vehicle using uniform mesoporous silica spheres embedded with monodisperse magnetic and semiconductor nanocrystals. J Am Chem Soc 128(3):688–689. doi:10.1021/ja0565875
63. Sathe TR, Agrawal A, Nie SM (2006) Mesoporous silica beads embedded with semiconductor quantum dots and iron oxide nanocrystals: dual-function microcarriers for optical encoding and magnetic separation. Anal Chem 78(16):5627–5632. doi:10.1021/ac0610309
64. Pan J, Wan D, Gong J (2011) PEGylated liposome coated QDs/mesoporous silica core-shell nanoparticles for molecular imaging. Chem Commun 47(12):3442–3444. doi:10.1039/c0cc05520d
65. Xia H-X, Yang X-Q, Song J-T, Chen J, Zhang M-Z, Yan D-M, Zhang L, Qin M-Y, Bai L-Y, Zhao Y-D, Ma Z-Y (2014) Folic acid-conjugated silica-coated gold nanorods and quantum dots for dual-modality CT and fluorescence imaging and photothermal therapy. J Mater Chem B 2(14):1945–1953. doi:10.1039/c3tb21591a
66. Liu JN, Bu WB, Zhang SJ, Chen F, Xing HY, Pan LM, Zhou LP, Peng WJ, Shi JL (2012) Controlled synthesis of uniform and monodisperse upconversion core/mesoporous silica shell nanocomposites for bimodal imaging. Chem Eur J 18(8):2335–2341. doi:10.1002/chem.201102599

67. Abou-Elkacem L, Bachawal SV, Willmann JK (2015) Ultrasound molecular imaging: moving towards clinical translation. Eur J Radiol. doi:10.1016/j.ejrad.2015.03.016
68. Kiessling F, Fokong S, Bzyl J, Lederle W, Palmowski M, Lammers T (2014) Recent advances in molecular, multimodal and theranostic ultrasound imaging. Adv Drug Deliv Rev 72:15–27. doi:10.1016/j.addr.2013.11.013
69. Gessner R, Dayton PA (2010) Advances in molecular imaging with ultrasound. Mol Imaging 9(3):117–127. doi:10.2310/7290.2010.00022
70. Deshpande N, Needles A, Willmann JK (2010) Molecular ultrasound imaging: current status and future directions. Clin Radiol 65(7):567–581. doi:10.1016/j.crad.2010.02.013
71. Borden MA, Caskey CF, Little E, Gillies RJ, Ferrara KW (2007) DNA and polylysine adsorption and multilayer construction onto cationic lipid-coated microbubbles. Langmuir 23(18):9401–9408. doi:10.1021/la7009034
72. Hasik MJ, Kim DH, Howle LE, Needham D, Prush DP (2002) Evaluation of synthetic phospholipid ultrasound contrast agents. Ultrasonics 40(9):973–982. doi:10.1016/S0041-624X(02)00384-0
73. Takalkar AM, Klibanov AL, Rychak JJ, Lindner JR, Ley K (2004) Binding and detachment dynamics of microbubbles targeted to P-selectin under controlled shear flow. J Control Release 96(3):473–482. doi:10.1016/j.jconrel.2004.03.002
74. Xing ZW, Ke HT, Wang JR, Zhao B, Yue XL, Dai ZF, Liu JB (2010) Novel ultrasound contrast agent based on microbubbles generated from surfactant mixtures of Span 60 and polyoxyethylene 40 stearate. Acta Biomater 6(9):3542–3549. doi:10.1016/j.actbio.2010.03.007
75. Wheatley MA, Forsberg F, Oum K, Ro R, El-Sherif D (2006) Comparison of in vitro and in vivo acoustic response of a novel 50:50 PLGA contrast agent. Ultrasonics 44(4):360–367. doi:10.1016/j.ultras.2006.04.003
76. Pisani E, Tsapis N, Galaz B, Santin M, Berti R, Taulier N, Kurtisovski E, Lucidarme O, Ourevitch M, Doan BT, Beloeil JC, Gillet B, Urbach W, Bridal SL, Fattal E (2008) Perfluorooctyl bromide polymeric capsules as dual contrast agents for ultrasonography and magnetic resonance imaging. Adv Funct Mater 18(19):2963–2971. doi:10.1002/adfm.200800454
77. Chen Y, Chen HR, Sun Y, Zheng YY, Zeng DP, Li FQ, Zhang SJ, Wang X, Zhang K, Ma M, He QJ, Zhang LL, Shi JL (2011) Multifunctional mesoporous composite nanocapsules for highly efficient MRI-guided high-intensity focused ultrasound cancer surgery. Angew Chem 50(52):12505–12509. doi:10.1002/anie.201106180
78. Milgroom A, Intrator M, Madhavan K, Mazzaro L, Shandas R, Liu BL, Park D (2014) Mesoporous silica nanoparticles as a breast-cancer targeting ultrasound contrast agent. Colloid Surface B 116:652–657. doi:10.1016/j.colsurfb.2013.10.038
79. Niu DC, Wang X, Li YS, Zheng YP, Li FQ, Chen HR, Gu JL, Zhao WR, Shi JL (2013) Facile synthesis of magnetite/perfluorocarbon co-loaded organic/inorganic hybrid vesicles for dual-modality ultrasound/magnetic resonance imaging and imaging-guided high-intensity focused ultrasound ablation. Adv Mater 25(19):2686–2692. doi:10.1002/adma.201204316
80. Wang X, Chen H, Zheng Y, Ma M, Chen Y, Zhang K, Zeng D, Shi J (2013) Au-nanoparticle coated mesoporous silica nanocapsule-based multifunctional platform for ultrasound mediated imaging, cytoclasis and tumor ablation. Biomaterials 34(8):2057–2068. doi:10.1016/j.biomaterials.2012.11.044
81. Wang X, Chen HR, Chen Y, Ma M, Zhang K, Li FQ, Zheng YY, Zeng DP, Wang Q, Shi JL (2012) Perfluorohexane-encapsulated mesoporous silica nanocapsules as enhancement agents for highly efficient high intensity focused ultrasound (HIFU). Adv Mater 24(6):785–791. doi:10.1002/adma.201104033
82. Lin P-L, Eckersley RJ, Hall EAH (2009) Ultrabubble: a laminated ultrasound contrast agent with narrow size range. Adv Mater 21(38–39):3949–3952. doi:10.1002/adma.200901096
83. Martinez HP, Kono Y, Blair SL, Sandoval S, Wang-Rodriguez J, Mattrey RF, Kummel AC, Trogler WC (2010) Hard shell gas-filled contrast enhancement particles for colour Doppler ultrasound imaging of tumors. Med Chem Commun 1(4):266–270. doi:10.1039/c0md00139b

84. Zhang K, Chen HR, Guo XS, Zhang D, Zheng YY, Zheng HR, Shi JL (2015) Double-scattering/reflection in a single nanoparticle for intensified ultrasound imaging. Sci Rep 5:8766. doi:10.1038/srep08766
85. Ritman EL (2002) Molecular imaging in small animals-roles for micro-CT. J Cell Biochem Suppl 87(39):116–124. doi:10.1002/jcb.10415
86. Brenner DJ, Elliston CD, Hall EJ, Berdon WE (2001) Estimated risks of radiation-induced fatal cancer from pediatric CT. Am J Roentgenol 176(2):289–296. doi:10.2214/ajr.176.2.1760289
87. Rabin O, Manuel Perez J, Grimm J, Wojtkiewicz G, Weissleder R (2006) An X-ray computed tomography imaging agent based on long-circulating bismuth sulphide nanoparticles. Nat Mater 5(2):118–122. doi:10.1038/nmat1571
88. Kong WH, Lee WJ, Cui ZY, Bae KH, Park TG, Kim JH, Park K, Seo SW (2007) Nanoparticulate carrier containing water-insoluble iodinated oil as a multifunctional contrast agent for computed tomography imaging. Biomaterials 28(36):5555–5561. doi:10.1016/j.biomaterials.2007.08.044
89. Aviv H, Bartling S, Kieslling F, Margel S (2009) Radiopaque iodinated copolymeric nanoparticles for X-ray imaging applications. Biomaterials 30(29):5610–5616. doi:10.1016/j.biomaterials.2009.06.038
90. Jakhmola A, Anton N, Vandamme TF (2012) Inorganic nanoparticles based contrast agents for X-ray computed tomography. Adv Healthcare Mater 1(4):413–431. doi:10.1002/adhm.201200032
91. Cho EC, Glaus C, Chen J, Welch MJ, Xia Y (2010) Inorganic nanoparticle-based contrast agents for molecular imaging. Trends Mol Med 16(12):561–573. doi:10.1016/j.molmed.2010.09.004
92. Xue SH, Wang Y, Wang MX, Zhang L, Du XX, Gu HC, Zhang CF (2014) Iodinated oil-loaded, fluorescent mesoporous silica-coated iron oxide nanoparticles for magnetic resonance imaging/computed tomography/fluorescence trimodal imaging. Int J Nanomedicine 9(1):2527–2538. doi:10.2147/IJN.S59754
93. Zhou ZJ, Zhang CL, Qian QR, Ma JB, Huang P, Zhang X, Pan LY, Gao G, Fu HL, Fu S, Song H, Zhi X, Ni J, Cui DX (2013) Folic acid-conjugated silica capped gold nanoclusters for targeted fluorescence/X-ray computed tomography imaging. J Nanobiotechnol 11(17):1–12. doi:10.1186/1477-3155-11-17
94. Chen J, Yang XQ, Meng YZ, Qin MY, Yan DM, Qian Y, Xu GQ, Yu Y, Ma ZY, Zhao YD (2013) Reverse microemulsion-mediated synthesis of Bi_2S_3-QD@SiO_2-PEG for dual modal CT-fluorescence imaging in vitro and in vivo. Chem Commun 49(100):11800–11802. doi:10.1039/c3cc47710j
95. Lin YS, Hung Y, Su JK, Lee R, Chang C, Lin ML, Mou CY (2004) Gadolinium(III)-incorporated nanosized mesoporous silica as potential magnetic resonance imaging contrast agents. J Phys Chem B 108(40):15608–15611. doi:10.1021/Jp047829a
96. Rieter WJ, Kim JS, Taylor KML, An HY, Lin WL, Tarrant T, Lin WB (2007) Hybrid silica nanoparticles for multimodal imaging. Angew Chem Int Ed 46(20):3680–3682. doi:10.1002/anie.200604738
97. Taylor KML, Kim JS, Rieter WJ, An H, Lin WL, Lin WB (2008) Mesoporous silica nanospheres as highly efficient MRI contrast agents. J Am Chem Soc 130(7):2154–2155. doi:10.1021/Ja710193c
98. Kim JS, Rieter WJ, Taylor KML, An H, Lin WL, Lin WB (2007) Self-assembled hybrid nanoparticles for cancer-specific multimodal imaging. J Am Chem Soc 129(29):8962–8963. doi:10.1021/Ja073062z
99. Davies GL, Kramberger I, Davis JJ (2013) Environmentally responsive MRI contrast agents. Chem Commun 49(84):9704–9721. doi:10.1039/C3cc44268c
100. Vivero-Escoto JL, Taylor-Pashow KML, Huxford RC, Della Rocca J, Okoruwa C, An HY, Lin WL, Lin WB (2011) Multifunctional mesoporous silica nanospheres with cleavable Gd(III) chelates as MRI contrast agents: synthesis, characterization, target-specificity, and renal clearance. Small 7(24):3519–3528. doi:10.1002/smll.201100521

101. Guillet-Nicolas R, Bridot JL, Seo Y, Fortin MA, Kleitz F (2011) Enhanced relaxometric properties of MRI "positive" contrast agents confined in three-dimensional cubic mesoporous silica nanoparticles. Adv Funct Mater 21(24):4653–4662. doi:10.1002/adfm.201101766
102. Kim SM, Im GH, Lee DG, Lee JH, Lee WJ, Lee IS (2013) Mn^{2+}-doped silica nanoparticles for hepatocyte-targeted detection of liver cancer in T_1-weighted MRI. Biomaterials 34(35):8941–8948. doi:10.1016/j.biomaterials.2013.08.009
103. Niu DC, Luo XF, Li YS, Liu XH, Wang X, Shi JL (2013) Manganese-loaded dual-mesoporous silica spheres for efficient T_1- and T_2-weighted dual mode magnetic resonance imaging. ACS Appl Mater Interfaces 5(20):9942–9948. doi:10.1021/Am401856w
104. Bridot JL, Faure AC, Laurent S, Riviere C, Billotey C, Hiba B, Janier M, Josserand V, Coll JL, Vander Elst L, Muller R, Roux S, Perriat P, Tillement O (2007) Hybrid gadolinium oxide nanoparticles: multimodal contrast agents for in vivo imaging. J Am Chem Soc 129(16):5076–5084. doi:10.1021/Ja068356j
105. Na HB, Lee JH, An KJ, Park YI, Park M, Lee IS, Nam DH, Kim ST, Kim SH, Kim SW, Lim KH, Kim KS, Kim SO, Hyeon T (2007) Development of a T_1 contrast agent for magnetic resonance imaging using MnO nanoparticles. Angew Chem Int Ed 46(28):5397–5401. doi:10.1002/anie.200604775
106. Taylor KML, Rieter WJ, Lin WB (2008) Manganese-based nanoscale metal-organic frameworks for magnetic resonance imaging. J Am Chem Soc 130(44):14358–14359. doi:10.1021/Ja803777x
107. Kim T, Momin E, Choi J, Yuan K, Zaidi H, Kim J, Park M, Lee N, McMahon MT, Quinones-Hinojosa A, Bulte JWM, Hyeon T, Gilad AA (2011) Mesoporous silica-coated hollow manganese oxide nanoparticles as positive T_1 contrast agents for labeling and MRI tracking of adipose-derived mesenchymal stem cells. J Am Chem Soc 133(9):2955–2961. doi:10.1021/Ja1084095
108. Peng YK, Liu CL, Chen HC, Chou SW, Tseng WH, Tseng YJ, Kang CC, Hsiao JK, Chou PT (2013) Antiferromagnetic iron nanocolloids: a new generation *in vivo* T_1 MRI contrast agent. J Am Chem Soc 135(49):18621–18628. doi:10.1021/Ja409490q
109. Wang YX (2011) Superparamagnetic iron oxide based MRI contrast agents: current status of clinical application. Quant Imaging Med Surg 1(1):35–40. doi:10.3978/j.issn.2223-4292.2011.08.03
110. Yan F, Xu H, Anker J, Kopelman R, Ross B, Rehemtulla A, Reddy R (2004) Synthesis and characterization of silica-embedded iron oxide nanoparticles for magnetic resonance imaging. J Nanosci Nanotechnol 4(1–2):72–76. doi:10.1166/Jnn.2004.074
111. Julian-Lopez B, Boissiere C, Chaneac C, Grosso D, Vasseur S, Miraux S, Duguet E, Sanchez C (2007) Mesoporous maghemite-organosilica microspheres: a promising route towards multifunctional platforms for smart diagnosis and therapy. J Mater Chem 17(16):1563–1569. doi:10.1039/B615951f
112. Bai X, Son SJ, Zhang SX, Liu W, Jordan EK, Frank JA, Venkatesan T, Lee SB (2008) Synthesis of superparamagnetic nanotubes as MRI contrast agents and for cell labeling. Nanomedicine-UK 3(2):163–174. doi:10.2217/17435889.3.2.163
113. Niu DC, Li YS, Ma Z, Diao H, Gu JL, Chen HR, Zhao WR, Ruan ML, Zhang YL, Shi JL (2010) Preparation of uniform, water-soluble, and multifunctional nanocomposites with tunable sizes. Adv Funct Mater 20(5):773–780. doi:10.1002/adfm.200901493
114. Pinho SLC, Pereira GA, Voisin P, Kassem J, Bouchaud V, Etienne L, Peters JA, Carlos LD, Mornet S, Geraldes CFGC, Rocha J, Delville MH (2010) Fine tuning of the relaxometry of gamma-Fe_2O_3@SiO_2 nanoparticles by tweaking the silica coating thickness. ACS Nano 4(9):5339–5349. doi:10.1021/Nn101129r
115. Yang H, Zhuang YM, Sun Y, Dai AT, Shi XY, Wu DM, Li FY, Hu H, Yang SP (2011) Targeted dual-contrast T_1- and T_2-weighted magnetic resonance imaging of tumors using multifunctional gadolinium-labeled superparamagnetic iron oxide nanoparticles. Biomaterials 32(20):4584–4593. doi:10.1016/j.biomaterials.2011.03.018

116. Li Z, Yi PW, Sun Q, Lei H, Zhao HL, Zhu ZH, Smith SC, Lan MB, Lu GQ (2012) Ultrasmall water-soluble and biocompatible magnetic iron oxide nanoparticles as positive and negative dual contrast agents. Adv Funct Mater 22(11):2387–2393. doi:10.1002/adfm.201103123
117. Tromsdorf UI, Bruns OT, Salmen SC, Beisiegel U, Weller H (2009) A highly effective, non-toxic T_1 MR contrast agent based on ultrasmall PEGylated iron oxide nanoparticles. Nano Lett 9(12):4434–4440. doi:10.1021/Nl902715v
118. Yang H, Qin CY, Yu C, Lu Y, Zhang HW, Xue FF, Wu DM, Zhou ZG, Yang SP (2014) RGD-conjugated nanoscale coordination polymers for targeted T_1 – and T_2 -weighted magnetic resonance imaging of tumors in vivo. Adv Funct Mater 24(12):1738–1747. doi:10.1002/adfm.201302433
119. Bailey DL, Townsend DW, Valk PE, Maisey MN (2005) Positron emission tomography: basic sciences. Springer, London
120. Lee SB, Kim HL, Jeong HJ, Lim ST, Sohn MH, Kim DW (2013) Mesoporous silica nanoparticle pretargeting for PET imaging based on a rapid bioorthogonal reaction in a living body. Angew Chem Int Ed Engl 52(40):10549–10552. doi:10.1002/anie.201304026
121. Miller L, Winter G, Baur B, Witulla B, Solbach C, Reske S, Linden M (2014) Synthesis, characterization, and biodistribution of multiple ^{89}Zr-labeled pore-expanded mesoporous silica nanoparticles for PET. Nanoscale 6(9):4928–4935. doi:10.1039/c3nr06800e
122. Chen F, Nayak TR, Goel S, Valdovinos HF, Hong H, Theuer CP, Barnhart TE, Cai W (2014) In vivo tumor vasculature targeted PET/NIRF imaging with TRC105(Fab)-conjugated, dual-labeled mesoporous silica nanoparticles. Mol Pharm 11(11):4007–4014. doi:10.1021/mp500306k
123. Chen F, Hong H, Zhang Y, Valdovinos HF, Shi SX, Kwon GS, Theuer CP, Barnhart TE, Cai WB (2013) In vivo tumor targeting and image-guided drug delivery with antibody-conjugated, radio labeled mesoporous silica nanoparticles. ACS Nano 7(10):9027–9039. doi:10.1021/Nn403617j
124. Phillips E, Penate-Medina O, Zanzonico PB, Carvajal RD, Mohan P, Ye Y, Humm J, Gonen M, Kalaigian H, Schoder H, Strauss HW, Larson SM, Wiesner U, Bradbury MS (2014) Clinical translation of an ultrasmall inorganic optical-PET imaging nanoparticle probe. Sci Transl Med 6(260):260ra149. doi:10.1126/scitranslmed.3009524
125. Kim JS, Kim YH, Kim JH, Kang KW, Tae EL, Youn H, Kim D, Kim SK, Kwon JT, Cho MH, Lee YS, Jeong JM, Chung JK, Lee DS (2012) Development and in vivo imaging of a PET/MRI nanoprobe with enhanced NIR fluorescence by dye encapsulation. Nanomedicine-UK 7(2):219–229. doi:10.2217/nnm.11.94
126. Wang LHV (2009) Multiscale photoacoustic microscopy and computed tomography. Nat Photonics 3(9):503–509. doi:10.1038/nphoton.2009.157
127. MH X, LHV W (2006) Photoacoustic imaging in biomedicine. Rev Sci Instrum 77(4):041101. doi:10.1063/1.2195024
128. Wang LHV, Wu H (2007) Biomedical optics: principles and imaging. Wiley, Hoboken
129. Ermilov SA, Khamapirad T, Conjusteau A, Leonard MH, Lacewell R, Mehta K, Miller T, Oraevsky AA (2009) Laser optoacoustic imaging system for detection of breast cancer. J Biomed Opt 14(2):024007. doi:10.1117/1.3086616
130. Chen Y-S, Frey W, Kim S, Homan K, Kruizinga P, Sokolov K, Emelianov S (2010) Enhanced thermal stability of silica-coated gold nanorods for photoacoustic imaging and image-guided therapy. Opt Express 18(9):8867–8878. doi:10.1364/OE.18.008867
131. Agarwal A, Huang SW, O'Donnell M, Day KC, Day M, Kotov N, Ashkenazi S (2007) Targeted gold nanorod contrast agent for prostate cancer detection by photoacoustic imaging. J Appl Phys 102(6):064701. doi:10.1063/1.2777127
132. Zhang Q, Iwakuma N, Sharma P, Moudgil BM, Wu C, McNeill J, Jiang H, Grobmyer SR (2009) Gold nanoparticles as a contrast agent for in vivo tumor imaging with photoacoustic tomography. Nanotechnology 20(39):395102. doi:10.1088/0957-4484/20/39/395102

133. Song KH, Kim C, Cobley CM, Xia YN, Wang LHV (2009) Near-infrared gold nanocages as a new class of tracers for photoacoustic sentinel lymph node mapping on a rat model. Nano Lett 9(1):183–188. doi:10.1021/nl802746w
134. Mallidi S, Larson T, Tam J, Joshi PP, Karpiouk A, Sokolov K, Emelianov S (2009) Multiwavelength photoacoustic imaging and plasmon resonance coupling of gold nanoparticles for selective detection of cancer. Nano Lett 9(8):2825–2831. doi:10.1021/nl802929u
135. Lu W, Huang Q, Ku G, Wen XX, Zhou M, Guzatov D, Brecht P, Su R, Oraevsky A, Wang LHV, Li C (2010) Photoacoustic imaging of living mouse brain vasculature using hollow gold nanospheres. Biomaterials 31(9):2617–2626. doi:10.1016/j.biomaterials.2009.12.007
136. Wang YW, Xie XY, Wang XD, Ku G, Gill KL, O'Neal DP, Stoica G, Wang LHV (2004) Photoacoustic tomography of a nanoshell contrast agent in the in vivo rat brain. Nano Lett 4(9):1689–1692. doi:10.1021/nl049126a
137. Li M-L, Wang JC, Schwartz JA, Gill-Sharp KL, Stoica G, Wang LHV (2009) In-vivo photoacoustic microscopy of nanoshell extravasation from solid tumor vasculature. J Biomed Opt 14(1):010507. doi:10.1117/1.3081556
138. Chen YS, Frey W, Kim S, Kruizinga P, Homan K, Emelianov S (2011) Silica-coated gold nanorods as photoacoustic signal nanoamplifiers. Nano Lett 11(2):348–354. doi:10.1021/nl1042006
139. Jokerst JV, Thangaraj M, Kempen PJ, Sinclair R, Gambhir SS (2012) Photoacoustic imaging of mesenchymal stem cells in living mice via silica-coated gold nanorods. ACS Nano 6(7):5920–5930. doi:10.1021/nn302042y
140. Hong H, Gao T, Cai WB (2009) Molecular imaging with single-walled carbon nanotubes. Nano Today 4(3):252–261. doi:10.1016/j.nantod.2009.04.002
141. Pramanik M, Wang LHV (2009) Thermoacoustic and photoacoustic sensing of temperature. J Biomed Opt 14(5):054024. doi:10.1117/1.3247155
142. Pramanik M, Song KH, Swierczewska M, Green D, Sitharaman B, Wang LHV (2009) In vivo carbon nanotube-enhanced non-invasive photoacoustic mapping of the sentinel lymph node. Phys Med Biol 54(11):3291–3301. doi:10.1088/0031-9155/54/11/001
143. Liu JJ, Wang C, Wang XJ, Wang XD, Cheng L, Li YG, Liu Z (2015) Mesoporous silica coated single-walled carbon nanotubes as a multifunctional light-responsive platform for cancer combination therapy. Adv Funct Mater 25(3):384–392. doi:10.1002/adfm.201403079
144. Rp F (1992) There's plenty of room at the bottom. In: Crandall BC, Lewis J (eds) Nanotechnology: research and perspectives. MIT Press, Boston, pp 347–363
145. Lu J, Liong M, Zink JI, Tamanoi F (2007) Mesoporous silica nanoparticles as a delivery system for hydrophobic anticancer drugs. Small 3(8):1341–1346. doi:10.1002/smll.200700005
146. Liu Q, Zhang JX, Sun W, Xie QR, Xia WL, Gu HC (2012) Delivering hydrophilic and hydrophobic chemotherapeutics simultaneously by magnetic mesoporous silica nanoparticles to inhibit cancer cells. Int J Nanomed 7:999–1013. doi:10.2147/IJN.S28088
147. Fan JQ, Fang G, Wang XD, Zeng F, Xiang YF, Wu SZ (2011) Targeted anticancer prodrug with mesoporous silica nanoparticles as vehicles. Nanotechnology 22(45):455102. doi:10.1088/0957-4484/22/45/455102
148. Slowing II, Vivero-Escoto JL, Wu CW, Lin VS (2008) Mesoporous silica nanoparticles as controlled release drug delivery and gene transfection carriers. Adv Drug Deliv Rev 60(11):1278–1288. doi:10.1016/j.addr.2008.03.012
149. Tarn D, Ashley CE, Xue M, Carnes EC, Zink JI, Brinker CJ (2013) Mesoporous silica nanoparticle nanocarriers: biofunctionality and biocompatibility. Acc Chem Res 46(3):792–801. doi:10.1021/ar3000986
150. Luo GF, Chen WH, Liu Y, Lei Q, Zhuo RX, Zhang XZ (2014) Multifunctional enveloped mesoporous silica nanoparticles for subcellular co-delivery of drug and therapeutic peptide. Sci Rep 4:6064. doi:10.1038/srep06064

151. Kwon S, Singh RK, Perez RA, Abou Neel EA, Kim HW, Chrzanowski W (2013) Silica-based mesoporous nanoparticles for controlled drug delivery. J Tissue Eng 4:2041731413503357. doi:10.1177/2041731413503357
152. He QJ, Shi JL (2014) MSN anti-cancer nanomedicines: chemotherapy enhancement, overcoming of drug resistance, and metastasis inhibition. Adv Mater 26(3):391–411. doi:10.1002/adma.201303123
153. Dengler EC, Liu JW, Kerwin A, Torres S, Olcott CM, Bowman BN, Armijo L, Gentry K, Wilkerson J, Wallace J, Jiang XM, Carnes EC, Brinker CJ, Milligan ED (2013) Mesoporous silica-supported lipid bilayers (protocells) for DNA cargo delivery to the spinal cord. J Control Release 168(2):209–224. doi:10.1016/j.jconrel.2013.03.009
154. Sun J, Jakobsson E, Wang Y, Brinker C (2015) Nanoporous silica-based protocells at multiple scales for designs of life and nanomedicine. Life 5(1):214–229. doi:10.3390/life5010214
155. Liu JW, Stace-Naughton A, Jiang XM, Brinker CJ (2009) Porous nanoparticle supported lipid bilayers (protocells) as delivery vehicles. J Am Chem Soc 131(4):1354–1355. doi:10.1021/ja808018y
156. Porotto M, Yi F, Moscona A, LaVan DA (2011) Synthetic protocells interact with viral nanomachinery and inactivate pathogenic human virus. PLoS One 6(3), e16874. doi:10.1371/journal.pone.0016874
157. Ashley CE, Carnes EC, Phillips GK, Padilla D, Durfee PN, Brown PA, Hanna TN, Liu J, Phillips B, Carter MB, Carroll NJ, Jiang X, Dunphy DR, Willman CL, Petsev DN, Evans DG, Parikh AN, Chackerian B, Wharton W, Peabody DS, Brinker CJ (2011) The targeted delivery of multicomponent cargos to cancer cells by nanoporous particle-supported lipid bilayers. Nat Mater 10(5):389–397. doi:10.1038/nmat2992
158. Ashley CE, Carnes EC, Epler KE, Padilla DP, Phillips GK, Castillo RE, Wilkinson DC, Wilkinson BS, Burgard CA, Kalinich RM, Townson JL, Chackerian B, Willman CL, Peabody DS, Wharton W, Brinker CJ (2012) Delivery of small interfering RNA by peptide-targeted mesoporous silica nanoparticle-supported lipid bilayers. ACS Nano 6(3):2174–2188. doi:10.1021/nn204102q
159. Meng H, Mai WX, Zhang HY, Xue M, Xia T, Lin SJ, Wang X, Zhao Y, Ji ZX, Zink JI, Nel AE (2013) Codelivery of an optimal drug/siRNA combination using mesoporous silica nanoparticles to overcome drug resistance in breast cancer in vitro and in vivo. ACS Nano 7(2):994–1005. doi:10.1021/nn3044066
160. Mai WX, Meng H (2013) Mesoporous silica nanoparticles: a multifunctional nano therapeutic system. Integr Biol 5(1):19–28. doi:10.1039/c2ib20137b
161. Meng H, Zhao Y, Dong JY, Xue M, Lin Y-S, Ji ZX, Mai WX, Zhang HY, Chang CH, Brinker CJ, Zink JI, Nel AE (2013) Two-wave nanotherapy to target the stroma and optimize gemcitabine delivery to a human pancreatic cancer model in mice. ACS Nano 7(11):10048–10065. doi:10.1021/nn404083m
162. Meng H, Xue M, Xia T, Ji ZX, Tarn DY, Zink JI, Nel AE (2011) Use of size and a copolymer design feature to improve the biodistribution and the enhanced permeability and retention effect of doxorubicin-loaded mesoporous silica nanoparticles. ACS Nano 5(5):4131–4144. doi:10.1021/nn200809t
163. Li LL, Tang FQ, Liu HY, Liu TL, Hao NJ, Chen D, Teng X, He JQ (2010) In vivo delivery of silica nanorattle encapsulated docetaxel for liver cancer therapy with low toxicity and high efficacy. ACS Nano 4(11):6874–6882. doi:10.1021/nn100918a
164. Tan LF, Chen D, Liu HY, Tang FQ (2010) A silica nanorattle with a mesoporous shell: an ideal nanoreactor for the preparation of tunable gold cores. Adv Mater 22(43):4885–4889. doi:10.1002/adma.201002277
165. Huang LX, Li LL, Liu TL, Hao NJ, Liu HY, Chen D, Tang FQ (2011) The shape effect of mesoporous silica nanoparticles on biodistribution, clearance, and biocompatibility in vivo. ACS Nano 5(7):5390–5399. doi:10.1021/nn200365a

166. Li LL, Guan YQ, Liu HY, Hao NJ, Liu TL, Meng XW, Fu CH, Li YZ, Qu QL, Zhang YG, Ji SY, Chen L, Chen D, Tang FQ (2011) Silica nanorattle-doxorubicin-anchored mesenchymal stem cells for tumor-tropic therapy. ACS Nano 5(9):7462–7470. doi:10.1021/nn202399w
167. Liu HY, Chen D, Li LL, Liu TL, Tan LF, Wu XL, Tang FQ (2011) Multifunctional gold nanoshells on silica nanorattles: a platform for the combination of photothermal therapy and chemotherapy with low systemic toxicity. Angew Chem 50(4):891–895. doi:10.1002/anie.201002820
168. Liu TL, Li LL, Teng X, Huang XL, Liu HY, Chen D, Ren J, He JQ, Tang FQ (2011) Single and repeated dose toxicity of mesoporous hollow silica nanoparticles in intravenously exposed mice. Biomaterials 32(6):1657–1668. doi:10.1016/j.biomaterials.2010.10.035
169. Gao FP, Li LL, Liu TL, Hao NJ, Liu HY, Tan LF, Li HB, Huang XL, Peng B, Yan CM, Yang LQ, Wu XL, Chen D, Tang FQ (2012) Doxorubicin loaded silica nanorattles actively seek tumors with improved anti-tumor effects. Nanoscale 4(11):3365–3372. doi:10.1039/c2nr12094a
170. Liu HY, Liu TL, Li LL, Hao NJ, Tan LF, Meng XW, Ren J, Chen D, Tang FQ (2012) Size dependent cellular uptake, in vivo fate and light-heat conversion efficiency of gold nanoshells on silica nanorattles. Nanoscale 4(11):3523–3529. doi:10.1039/c2nr30396e
171. Liu HY, Liu TL, Wu XL, Li LL, Tan LF, Chen D, Tang FQ (2012) Targeting gold nanoshells on silica nanorattles: a drug cocktail to fight breast tumors via a single irradiation with near-infrared laser light. Adv Mater 24(6):755–761. doi:10.1002/adma.201103343
172. Fu CH, Liu TL, Li LL, Liu HY, Chen D, Tang FQ (2013) The absorption, distribution, excretion and toxicity of mesoporous silica nanoparticles in mice following different exposure routes. Biomaterials 34(10):2565–2575. doi:10.1016/j.biomaterials.2012.12.043
173. Liu HY, Liu TL, Wang H, Li LL, Tan LF, Fu CH, Nie GJ, Chen D, Tang FQ (2013) Impact of PEGylation on the biological effects and light heat conversion efficiency of gold nanoshells on silica nanorattles. Biomaterials 34(28):6967–6975. doi:10.1016/j.biomaterials.2013.05.059
174. Liu TL, Liu HY, Fu CH, Li LL, Chen D, Zhang YQ, Tang FQ (2013) Smaller silica nanorattles reabsorbed by intestinal aggravate multiple organs damage. J Nanosci Nanotechnol 13(10):6506–6516. doi:10.1166/jnn.2013.7545
175. Liu TL, Liu HY, Fu CH, Li LL, Chen D, Zhang YQ, Tang FQ (2013) Silica nanorattle with enhanced protein loading: a potential vaccine adjuvant. J Colloid Interfaces Sci 400:168–174. doi:10.1016/j.jcis.2013.03.005
176. He QJ, Shi JL, Cui XZ, Wei CY, Zhang LX, Wu W, Bu WB, Chen HR, Wu HX (2011) Synthesis of oxygen-deficient luminescent mesoporous silica nanoparticles for synchronous drug delivery and imaging. Chem Commun 47(28):7947–7949. doi:10.1039/c1cc11479d
177. Kim J, Kim HS, Lee N, Kim T, Kim H, Yu T, Song IC, Moon WK, Hyeon T (2008) Multifunctional uniform nanoparticles composed of a magnetite nanocrystal core and a mesoporous silica shell for magnetic resonance and fluorescence imaging and for drug delivery. Angew Chem 47(44):8438–8441. doi:10.1002/anie.200802469
178. Vivero-Escoto JL, Huxford-Phillips RC, Lin W (2012) Silica-based nanoprobes for biomedical imaging and theranostic applications. Chem Soc Rev 41(7):2673–2685. doi:10.1039/c2cs15229k
179. Lee JE, Lee N, Kim H, Kim J, Choi SH, Kim JH, Kim T, Song IC, Park SP, Moon WK, Hyeon T (2010) Uniform mesoporous dye-doped silica nanoparticles decorated with multiple magnetite nanocrystals for simultaneous enhanced magnetic resonance imaging, fluorescence imaging, and drug delivery. J Am Chem Soc 132(2):552–557. doi:10.1021/ja905793q
180. Chen Yu, Chen HR, Zeng DP, Tian YB, Chen F, Feng JW, Shi JL (2010) Core/shell structured hollow mesoporous nanocapsules: a potential platform for simultaneous cell imaging and anticancer drug delivery. ACS Nano 4(10):6001–6013. doi:10.1021/nn1015117
181. Wu HX, Zhang SJ, Zhang JM, Liu G, Shi JL, Zhang LX, Cui XZ, Ruan ML, He QJ, Bu WB (2011) A hollow-core, magnetic, and mesoporous double-shell nanostructure: in situ decomposition/reduction synthesis, bioimaging, and drug-delivery properties. Adv Funct Mater 21(10):1850–1862. doi:10.1002/adfm.201002337

182. Ma M, Huang Y, Chen H, Jia X, Wang S, Wang Z, Shi J (2015) Bi_2S_3-embedded mesoporous silica nanoparticles for efficient drug delivery and interstitial radiotherapy sensitization. Biomaterials 37:447–455. doi:10.1016/j.biomaterials.2014.10.001
183. Yu J, Javier D, Yaseen MA, Nitin N, Richards-Kortum R, Anvari B, Wong MS (2010) Self-assembly synthesis, tumor cell targeting, and photothermal capabilities of antibody-coated indocyanine green nanocapsules. J Am Chem Soc 132(6):1929–1938. doi:10.1021/ja908139y
184. Zheng XH, Zhou FF, Wu BY, Chen WR, Xing D (2012) Enhanced tumor treatment using biofunctional indocyanine green-containing nanostructure by intratumoral or intravenous injection. Mol Pharm 9(3):514–522. doi:10.1021/mp200526m
185. Cheng L, He W, Gong H, Wang C, Chen Q, Cheng Z, Liu Z (2013) PEGylated micelle nanoparticles encapsulating a non-fluorescent near-infrared organic dye as a safe and highly-effective photothermal agent for in vivo cancer therapy. Adv Funct Mater 23(47):5893–5902. doi:10.1002/adfm.201301045
186. Yang K, Xu H, Cheng L, Sun CY, Wang J, Liu Z (2012) In vitro and in vivo near-infrared photothermal therapy of cancer using polypyrrole organic nanoparticles. Adv Mater 24(41):5586–5592. doi:10.1002/adma.201202625
187. Zha ZB, Yue XL, Ren QS, Dai ZF (2013) Uniform polypyrrole nanoparticles with high photothermal conversion efficiency for photothermal ablation of cancer cells. Adv Mater 25(5):777–782. doi:10.1002/adma.201202211
188. El-Sayed IH, Huang X, El-Sayed MA (2006) Selective laser photo-thermal therapy of epithelial carcinoma using anti-EGFR antibody conjugated gold nanoparticles. Cancer Lett 239(1):129–135. doi:10.1016/j.canlet.2005.07.035
189. Hirsch LR, Stafford RJ, Bankson JA, Sershen SR, Rivera B, Price RE, Hazle JD, Halas NJ, West JL (2003) Nanoshell-mediated near-infrared thermal therapy of tumors under magnetic resonance guidance. Proc Natl Acad Sci U S A 100(23):13549–13554. doi:10.1073/pnas.2232479100
190. Au L, Zheng DS, Zhou F, Li Z-Y, Li XD, Xia YN (2008) A quantitative study on the photothermal effect of immuno gold nanocages targeted to breast cancer cells. ACS Nano 2(8):1645–1652. doi:10.1021/nn800370j
191. Chen JY, Wang DL, Xi JF, Au L, Siekkinen A, Warsen A, Li Z-Y, Zhang H, Xia YN, Li XD (2007) Immuno gold nanocages with tailored optical properties for targeted photothermal destruction of cancer cells. Nano Lett 7(5):1318–1322. doi:10.1021/nl070345g
192. Liu Z, Davis C, Cai W, He L, Chen XY, Dai HJ (2008) Circulation and long-term fate of functionalized, biocompatible single-walled carbon nanotubes in mice probed by Raman spectroscopy. Proc Natl Acad Sci U S A 105(5):1410–1415. doi:10.1073/pnas.0707654105
193. Li M, Yang XJ, Ren JS, Qu KG, Qu XG (2012) Using graphene oxide high near-infrared absorbance for photothermal treatment of Alzheimer's disease. Adv Mater 24(13):1722–1728. doi:10.1002/adma.201104864
194. Wang L, Sun Q, Wang X, Wen T, Yin J-J, Wang P, Bai R, Zhang X-Q, Zhang L-H, Lu AH, Chen CY (2015) Using hollow carbon nanospheres as a light-induced free radical generator to overcome chemotherapy resistance. J Am Chem Soc 137(5):1947–1955. doi:10.1021/ja511560b
195. Ku G, Zhou M, Song SL, Huang Q, Hazle J, Li C (2012) Copper sulfide nanoparticles as a new class of photoacoustic contrast agent for deep tissue imaging at 1064 nm. ACS Nano 6(8):7489–7496. doi:10.1021/nn302782y
196. Song G, Wang Q, Wang Y, Lv G, Li C, Zou R, Chen Z, Qin Z, Huo K, Hu R, Hu J (2013) A low-toxic multifunctional nanoplatform based on Cu_9S_5@$mSiO_2$ core-shell nanocomposites: combining photothermal- and chemotherapies with infrared thermal imaging for cancer treatment. Adv Funct Mater 23(35):4281–4292. doi:10.1002/adfm.201203317
197. Tian QW, Jiang FR, Zou RJ, Liu Q, Chen ZG, Zhu MF, Yang SP, Wang JL, Wang JH, Hu JQ (2011) Hydrophilic Cu_9S_5 nanocrystals: a photothermal agent with a 25.7 % heat conversion efficiency for photothermal ablation of cancer cells in vivo. ACS Nano 5(12):9761–9771. doi:10.1021/nn203293t

198. Tian QW, Tang MH, Sun YG, Zou RJ, Chen ZG, Zhu MF, Yang SP, Wang JL, Wang JH, Hu JQ (2011) Hydrophilic flower-like CuS superstructures as an efficient 980 nm laser-driven photothermal agent for ablation of cancer cells. Adv Mater 23(31):3542–3547. doi:10.1002/adma.201101295
199. Wang SH, Riedinger A, Li HB, Fu CH, Liu HY, Li LL, Liu TL, Tan LF, Barthel MJ, Pugliese G, De Donato F, D'Abbusco MS, Meng XW, Manna L, Meng H, Pellegrino T (2015) Plasmonic copper sulfide nanocrystals exhibiting near-infrared photothermal and photodynamic therapeutic effect. ACS Nano 9(2):1788–1800. doi:10.1021/nn506687t
200. Zhou M, Zhang R, Huang M, Lu W, Song SL, Melancon MP, Tian M, Liang D, Li C (2010) A chelator-free multifunctional [^{64}Cu]CuS nanoparticle platform for simultaneous micro-PET/CT imaging and photothermal ablation therapy. J Am Chem Soc 132(43):15351–15358. doi:10.1021/ja106855m
201. Chou SS, Kaehr B, Kim J, Foley BM, De M, Hopkins PE, Huang J, Brinker CJ, Dravid VP (2013) Chemically exfoliated MoS_2 as near-infrared photothermal agents. Angew Chem 52(15):4160–4164. doi:10.1002/anie.201209229
202. Li J, Jiang F, Yang B, Song XR, Liu Y, Yang HH, Cao DR, Shi WR, Chen GN (2013) Topological insulator bismuth selenide as a theranostic platform for simultaneous cancer imaging and therapy. Sci Rep 3:1998. doi:10.1038/srep01998
203. Zhang ZJ, Wang LM, Wang J, Jiang XM, Li XH, Hu ZJ, Ji YL, Wu XC, Chen CY (2012) Mesoporous silica-coated gold nanorods as a light-mediated multifunctional theranostic platform for cancer treatment. Adv Mater 24(11):1418–1423. doi:10.1002/adma.201104714
204. Liu J, Detrembleur C, De Pauw-Gillet MC, Mornet S, Jerome C, Duguet E (2015) Gold nanorods coated with mesoporous silica shell as drug delivery system for remote near infrared light-activated release and potential phototherapy. Small. doi:10.1002/smll.201402145
205. Dong W, Li Y, Niu D, Ma Z, Gu J, Chen Y, Zhao W, Liu X, Liu C, Shi J (2011) Facile synthesis of monodisperse superparamagnetic Fe_3O_4 Core@hybrid@Au shell nanocomposite for bimodal imaging and photothermal therapy. Adv Mater 23(45):5392–5397. doi:10.1002/adma.201103521
206. Ji XJ, Shao RP, Elliott AM, Stafford RJ, Esparza-Coss E, Bankson JA, Liang G, Luo Z-P, Park K, Markert JT, Li C (2007) Bifunctional gold nanoshells with a superparamagnetic iron oxide-silica core suitable for both MR imaging and photothermal therapy. J Phys Chem C 111(17):6245–6251. doi:10.1021/jp0702245
207. Kim J, Park S, Lee JE, Jin SM, Lee JH, Lee IS, Yang I, Kim J-S, Kim SK, Cho M-H, Hyeon T (2006) Designed fabrication of multifunctional magnetic gold nanoshells and their application to magnetic resonance imaging and photothermal therapy. Angew Chem 118(46):7918–7922. doi:10.1002/ange.200602471
208. Lee J, Yang J, Ko H, Oh S, Kang J, Son J, Lee K, Lee SW, Yoon HG, Suh JS, Huh YM, Haam S (2008) Multifunctional magnetic gold nanocomposites: human epithelial cancer detection via magnetic resonance imaging and localized synchronous therapy. Adv Funct Mater 18(2):258–264. doi:10.1002/adfm.200700482
209. Lai BH, Chen DH (2013) LaB_6 nanoparticles with carbon-doped silica coating for fluorescence imaging and near-IR photothermal therapy of cancer cells. Acta Biomater 9(7):7556–7563. doi:10.1016/j.actbio.2013.03.034
210. Sharma P, Brown SC, Singh A, Iwakuma N, Pyrgiotakis G, Krishna V, Knapik JA, Barr K, Moudgil BM, Grobmyer SR (2010) Near-infrared absorbing and luminescent gold speckled silica nanoparticles for photothermal therapy. J Mater Chem 20(25):5182. doi:10.1039/c0jm00354a
211. Chen J, Keltner L, Christophersen J, Zheng F, Krouse M, Singhal A, Wang S-S (2002) New technology for deep light distribution in tissue for phototherapy. Cancer J 8(2):154–163. doi:10.1038/sj.bjc.6603241
212. Li B, Moriyama EH, Li F, Jarvi MT, Allen C, Wilson BC (2007) Diblock copolymer micelles deliver hydrophobic protoporphyrin IX for photodynamic therapy. Photochem Photobiol 83(6):1505–1512. doi:10.1111/j.1751-1097.2007.00194.x

213. Huang P, Xu C, Lin J, Wang C, Wang XS, Zhang CL, Zhou XJ, Guo SW, Cui DX (2011) Folic acid-conjugated graphene oxide loaded with photosensitizers for targeting photodynamic therapy. Theranostics 1:240–250. doi:10.7150/thno/v01p0240
214. Xiao Y, Hong H, Matson VZ, Javadi A, Xu W, Yang Y, Zhang Y, Engle JW, Nickles RJ, Cai W, Steeber DA, Gong S (2012) Gold nanorods conjugated with doxorubicin and cRGD for combined anticancer drug delivery and PET imaging. Theranostics 2(8):757–768. doi:10.7150/thno.4756
215. Wang S, Gao R, Zhou F, Selke M (2004) Nanomaterials and singlet oxygen photosensitizers: potential applications in photodynamic therapy. J Mater Chem 14(4):487. doi:10.1039/b311429e
216. Bechet D, Couleaud P, Frochot C, Viriot ML, Guillemin F, Barberi-Heyob M (2008) Nanoparticles as vehicles for delivery of photodynamic therapy agents. Trends Biotechnol 26(11):612–621. doi:10.1016/j.tibtech.2008.07.007
217. Chatterjee DK, Fong LS, Zhang Y (2008) Nanoparticles in photodynamic therapy: an emerging paradigm. Adv Drug Deliv Rev 60(15):1627–1637. doi:10.1016/j.addr.2008.08.003
218. Wang C, Tao H, Cheng L, Liu Z (2011) Near-infrared light induced in vivo photodynamic therapy of cancer based on upconversion nanoparticles. Biomaterials 32(26):6145–6154. doi:10.1016/j.biomaterials.2011.05.007
219. Huang P, Lin J, Yang DP, Zhang CL, Li ZM, Cui DX (2011) Photosensitizer-loaded dendrimer-modified multi-walled carbon nanotubes for photodynamic therapy. J Control Release 152(1):e33–e34. doi:10.1016/j.jconrel.2011.08.105
220. Juzenas P, Chen W, Sun YP, Coelho MA, Generalov R, Generalova N, Christensen IL (2008) Quantum dots and nanoparticles for photodynamic and radiation therapies of cancer. Adv Drug Deliv Rev 60(15):1600–1614. doi:10.1016/j.addr.2008.08.004
221. Samia ACS, Chen XB, Burda C (2003) Semiconductor quantum dots for photodynamic therapy. J Am Chem Soc 125(51):15736–15737. doi:10.1021/ja0386905
222. Huang P, Lin J, Wang S, Zhou Z, Li Z, Wang Z, Zhang C, Yue X, Niu G, Yang M, Cui D, Chen X (2013) Photosensitizer-conjugated silica-coated gold nanoclusters for fluorescence imaging-guided photodynamic therapy. Biomaterials 34(19):4643–4654. doi:10.1016/j.biomaterials.2013.02.063
223. Lv RC, Yang PP, He F, Gai SL, Li CX, Dai YL, Yang GX, Lin J (2015) A yolk-like multifunctional platform for multimodal imaging and synergistic therapy triggered by a single near-infrared light. ACS Nano 9(2):1630–1647. doi:10.1021/nn5063613
224. Zhao XL, Chen ZY, Zhao HL, Zhang DH, Tao L, Lan MB (2014) Multifunctional magnetic nanoparticles for simultaneous cancer near-infrared imaging and targeting photodynamic therapy. RSC Adv 4(107):62153–62159. doi:10.1039/C4RA10801A
225. Zhao T, Yu K, Li L, Zhang T, Guan Z, Gao N, Yuan P, Li S, Yao SQ, Xu QH, Xu GQ (2014) Gold nanorod enhanced two-photon excitation fluorescence of photosensitizers for two-photon imaging and photodynamic therapy. ACS Appl Mater Interfaces 6(4):2700–2708. doi:10.1021/am405214w
226. Wang TT, Chai F, Wang CG, Li L, Liu HY, Zhang LY, Su ZM, Liao Y (2011) Fluorescent hollow/rattle-type mesoporous Au@SiO_2 nanocapsules for drug delivery and fluorescence imaging of cancer cells. J Colloid Interfaces Sci 358(1):109–115. doi:10.1016/j.jcis.2011.02.023
227. Jiang ZL, Dong B, Chen BT, Wang J, Xu L, Zhang S, Song HW (2013) Multifunctional Au@$mSiO_2$/rhodamine B isothiocyanate nanocomposites: cell imaging, photocontrolled drug release, and photothermal therapy for cancer cells. Small 9(4):604–612. doi:10.1002/smll.201201558
228. Khlebtsov B, Panfilova E, Khanadeev V, Bibikova O, Terentyuk G, Ivanov A, Rumyantseva V, Shilov I, Ryabova A, Loshchenov V, Khlebtsov NG (2011) Nanocomposites containing silica-coated gold-silver nanocages and Yb-2,4-dimethoxyhematoporphyrin: multifunctional capability of IR-luminescence detection, photosensitization, and photothermolysis. ACS Nano 5(9):7077–7089. doi:10.1021/Nn2017974

229. Hu F, Zhang Y, Chen G, Li C, Wang Q (2015) Double-walled Au nanocage/SiO_2 nanorattles: integrating SERS imaging, drug delivery and photothermal therapy. Small 11(8):985–993. doi:10.1002/smll.201401360
230. Hembury M, Chiappini C, Bertazzo S, Kalber TL, Drisko GL, Ogunlade O, Walker-Samuel S, Krishna KS, Jumeaux C, Beard P, Kumar CS, Porter AE, Lythgoe MF, Boissiere C, Sanchez C, Stevens MM (2015) Gold-silica quantum rattles for multimodal imaging and therapy. Proc Natl Acad Sci U S A 112(7):1959–1964. doi:10.1073/pnas.1419622112
231. Huang P, Bao L, Zhang CL, Lin J, Luo T, Yang DP, He M, Li ZM, Gao G, Gao B, Fu S, Cui DX (2011) Folic acid-conjugated silica-modified gold nanorods for X-ray/CT imaging-guided dual-mode radiation and photo-thermal therapy. Biomaterials 32(36):9796–9809. doi:10.1016/j.biomaterials.2011.08.086
232. Chen Y, Chen HR, Sun Y, Zheng YY, Zeng DP, Li FQ, Zhang SJ, Wang X, Zhang K, Ma M, He QJ, Zhang LL, Shi JL (2011) Multifunctional mesoporous composite nanocapsules for highly efficient MRI-guided high-intensity focused ultrasound cancer surgery. Angew Chem Int Ed 50(52):12505–12509. doi:10.1002/anie.201106180
233. Fan WP, Shen B, Bu WB, Chen F, He QJ, Zhao KL, Zhang SJ, Zhou LP, Peng WJ, Xiao QF, Ni DL, Liu JN, Shi JL (2014) A smart upconversion-based mesoporous silica nanotheranostic system for synergetic chemo-/radio-/photodynamic therapy and simultaneous MR/UCL imaging. Biomaterials 35(32):8992–9002. doi:10.1016/j.biomaterials.2014.07.024

Chapter 10
Multimodal Micelles for Theranostic Nanomedicine

Hengte Ke and Huabing Chen

10.1 Introduction

Nanomedicine is an interdisciplinary field involving medicine, pharmaceutics, biology, chemistry, and material science [1], in which the nanocarriers including polymeric micelles, polymeric vesicles, liposomes, dendrimers, and inorganic nanoparticles play a key role for the application of nanomedicine in cancer therapy [2–6]. Recently, theranostic nanomedicine has been extensively explored by integrating imaging and therapeutic agents within the nanocarriers for cancer theranostics [7–12]. To date, polymeric micelles as a promising nanocarrier have received great attention for cancer therapy during the past two decades. The micelles have the core-shell structure with the size range of 10 ~ 100 nm, which are generally assembled from amphiphilic polymers in aqueous solutions. The micelles exhibit excellent biocompatibility, high drug-loading capacity, good cellular uptakes, preferable pharmacokinetics, as well as enhanced tumor accumulation and intracellular delivery. Moreover, the micelles can generate some intriguing features including smart drug release and active targeting through versatile polymer design and facile functionalization for smart cancer-targeted drug delivery. In particular, the further integration of imaging and therapeutic agents into the micelles may provide imaging-guided cancer therapy and therapeutic monitoring. In addition, the multimodal theranostic micelles can also provide synergistic anticancer efficacy or complementary imaging features for precise imaging and enhanced cancer therapy. The theranostic multifunctional micelles are highly potential to achieve personalized cancer theranostics. In this chapter, we focus on the recent progress of multimodal

H. Ke • H. Chen (✉)
Jiangsu Key Laboratory of Translational Research and Therapy for Neuro-Psycho-Diseases, and College of Pharmaceutical Sciences, Soochow University, Suzhou 215123, China
e-mail: chenhb@suda.edu.cn

Z. Dai (ed.), *Advances in Nanotheranostics II*, Springer Series in Biomaterials Science and Engineering 7, DOI 10.1007/978-981-10-0063-8_10

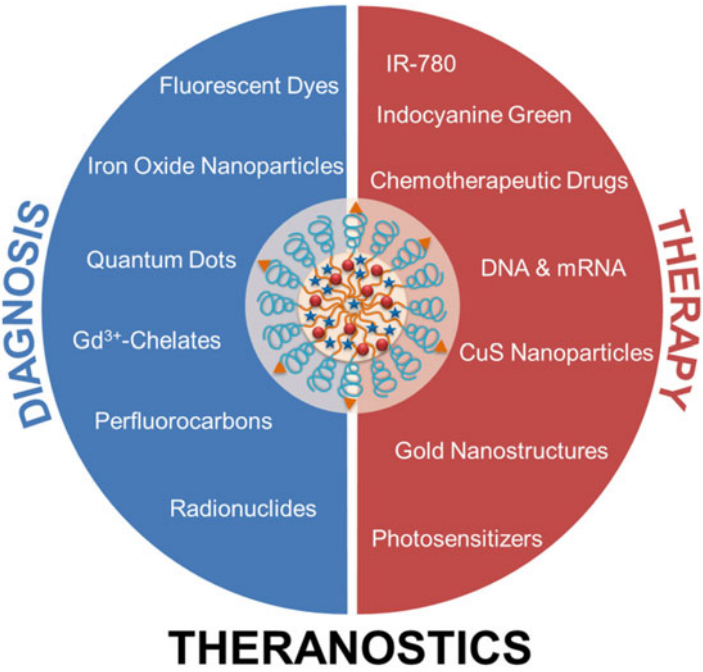

Fig. 10.1 Schematic illustration of multimodal micelles for theranostic nanomedicine

micelles as theranostic nanocarriers for cancer imaging and therapeutic applications (Fig. 10.1), and their perspectives on the existing challenges and future opportunities are also discussed.

10.2 Theranostic Micelles for Imaging and Chemotherapy

Chemotherapeutic compounds are extensively used in the field of cancer therapy. However, small molecular compounds often have limited capabilities for cancer therapy owing to their poor pharmacokinetics, undesirable biodistribution, insufficient intracellular delivery, and severe adverse side effects. Polymeric micelles as efficient nanocarriers may address these drawbacks by affording high payloads of anticancer drugs, prolonged circulation, enhanced cancer-targeting capacity, and efficient cellular uptake. The diagnostic imaging can be integrated with chemotherapeutic drugs for generating multimodal theranostic micelles, which may provide effective detection of tumor and therapeutic monitoring for precise cancer chemotherapy.

10.2.1 Micelles for Fluorescent Imaging and Chemotherapy

Currently, various medical imaging techniques including magnetic resonance imaging (MRI), ultrasound (US) imaging, X-ray computed tomography (CT), and positron emission computed tomography (PET) have been extensively used for cancer imaging. Recently, fluorescent imaging has been explored as a new ultrasensitive imaging modality for cancer imaging. The micelles encapsulating fluorescent dyes and drug have been evaluated for tumor identification and treatment [13, 14]. The fluorescent imaging has poor tissue penetration and limited spatial resolution, so fluorescent dyes with near-infrared (NIR) emission (650 ~ 900 nm) are considered as potential imaging probes for in vivo fluorescent imaging.

The multifunctional micelles were constructed using graft copolymer poly(2-hydroxylethyl methacrylate-histidine)-g-poly-(d,l-lactide) for theranostic nanomedicine. The micellar cores had the pH-sensitive property from histidine group for intracellular drug delivery, and NIR fluorescent dye, Cy5.5, and folate were, respectively, conjugated with micellar shells for achieving imaging and targeting capacity [15]. The micelles had an average diameter of about 200 nm and a significant pH-dependent release of doxorubicin (DOX). The fluorescent imaging indicates that the modification of folate on the micelles resulted in two-fold tumor accumulation and enhanced tumor growth inhibition as compared to the micelles without folate modification. The results indicate that Cy5.5-labeled, folate-modified micelles encapsulating DOX have great potential in fluorescence-guided chemotherapy (Fig. 10.2).

Quantum dots (QDs), or semiconductor nanocrystals, have unique optical properties such as high quantum yield, broad absorption with narrow fluorescent spectra compared to other fluorescent molecules such as organic dyes. Their high sensitivity and persistent fluorescent properties allow QDs to be applied for in vivo diagnosis [16–18]. Wang et al. developed the QD-embedded and paclitaxel (PTX)-loaded micelles for fluorescent imaging and intracellular delivery (Fig. 10.3). The in vivo QD fluorescent imaging indicates that the micelles exhibited the strong fluorescence at tumor site at 3-h post-injection and reveal a promising ability to identify the tumor. Moreover, the polymeric micelles also exhibited the "on-off" drug release feature responding to pH, which can trigger the drug release from the micelles in the acidic lysosomes, resulting in higher chemotherapeutic efficacy [19]. Other micelles encapsulating CdSe QDs were also reported to act as an efficient theranostic nanocarrier for fluorescent imaging-guided chemotherapy [20].

Unlike QDs with toxic concerns [21], ultrabright gold nanoclusters (AuNCs) with size less than 2 nm were also developed for fluorescent imaging, owing to their strong fluorescence and biocompatibility [22]. AuNC as a fluorescent imaging probe was conjugated into the transferrin-modified micelles consisting of D-alpha-tocopheryl polyethylene glycol succinate (TPGS) for targeted delivery of docetaxel (DTX) [23]. Transferrin as a targeting ligand can facilitate the nanocarrier to be internalized into cancer cells [24]. The micelles could provide a good fluorescent identification on the tumor from AuNC and simultaneously exhibit enhanced

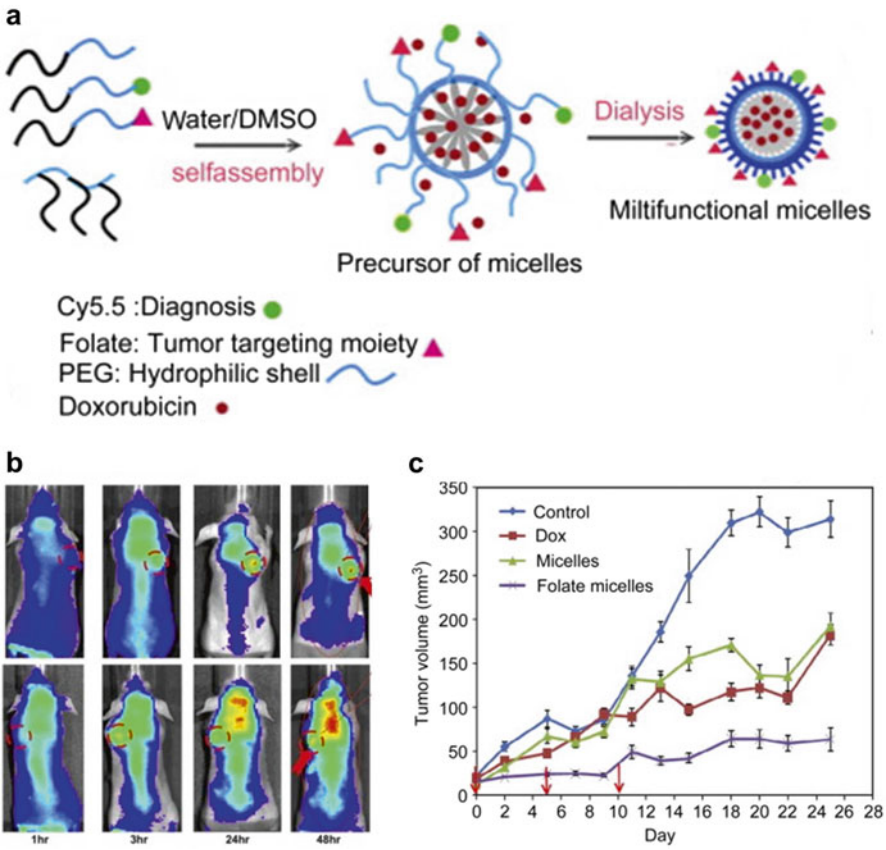

Fig. 10.2 (**a**) Schematic representation of DOX-loaded multifunctional micelles. (**b**) In vivo fluorescent imaging of HeLa tumor-xenografted nude mice injected with micelles (*upper row*) and folate micelles (*bottom row*) (*red circle* specifies the location of tumor). (**c**) Tumor growth inhibition of HeLa xenografts in nude mice ($n=3$) (Reprinted from Ref. [15]. Copyright 2010, with permission from Elsevier)

efficacy, indicating a great advantage for real-time fluorescent imaging and cancer therapy (Fig. 10.4).

10.2.2 Micelles for MRI and Chemotherapy

Magnetic resonance imaging (MRI) as a clinical imaging technique can provide excellent spatial resolution for the diagnosis of diseases [25–27]. The introduction of MRI contrast agents can produce contrast enhancement of brightness or darkness at tumor [28]. For instance, clinically approved Gd-DTPA and (1,2-diaminocyclohexane)

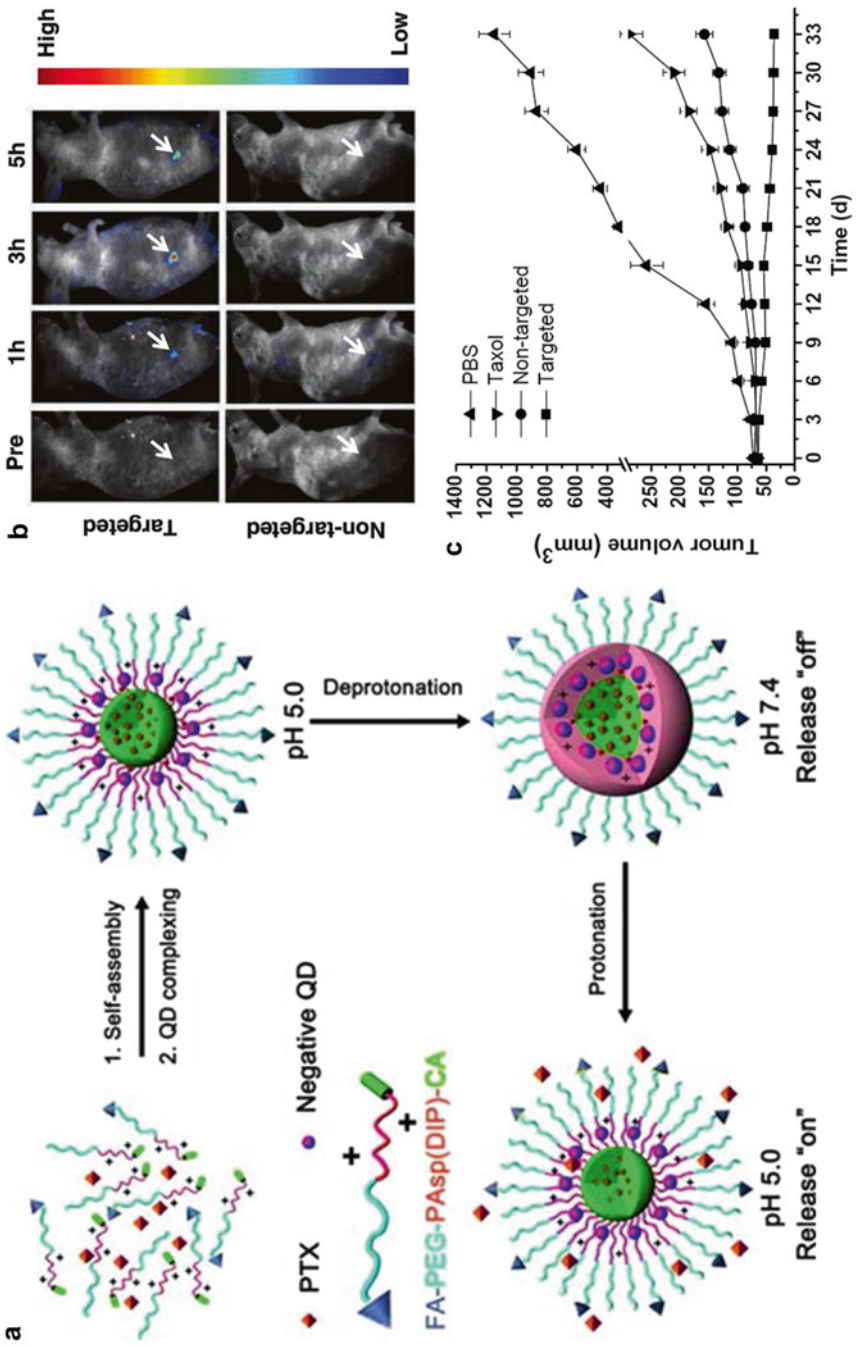

Fig. 10.3 (**a**) Illustrative preparation of PTX-/QD-loaded micelles. (**b**) In vivo QD fluorescent images of the tumor-bearing nude mice injected with QD-loaded targeted micelles via tail vein. (**c**) Tumor growth inhibition on tumor-bearing nude mice injected with different formulations (Reproduced from Ref. [19] by permission of John Wiley & Sons Ltd)

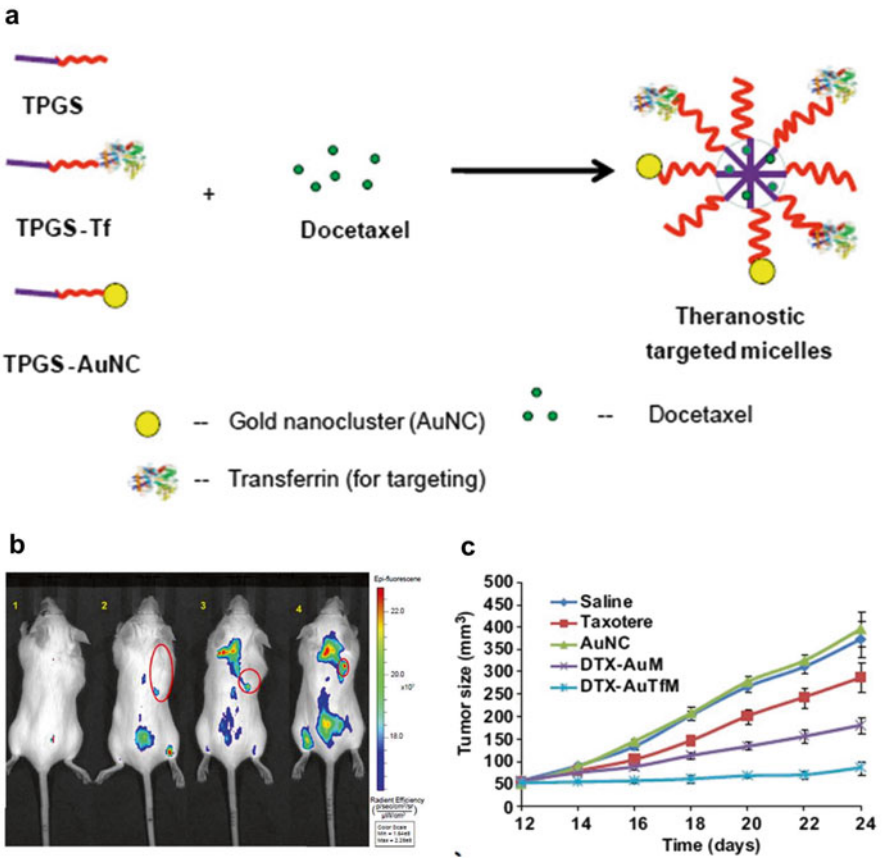

Fig. 10.4 (**a**) Schematic diagram for transferrin receptor-targeted theranostic micelles. (**b**) In vivo fluorescent images of targeted tumor imaging in mice (*1*. saline; *2*. AuNC; *3*. nontargeted theranostic micelles; *4*. theranostic micelles). (**c**) Tumor size changes of the mice treated with different formulations (Reprinted from Ref. [23]. Copyright 2015, with permission from Elsevier)

platinum(II) (DACHPt) were encapsulated into multifunctional polymeric micelles for fabricating a theranostic nanoplatform for simultaneous MRI and chemotherapy [29]. The micelles exhibited an increase of longitudinal relaxivity by about 24 times when compared with free Gd-DTPA, indicating a remarkable contrast enhancement on an orthotopic human pancreatic tumor. With the help of MR imaging, the micelles might provide an ideal optimization for cancer therapy. The micelles not only showed strong anticancer effect but also could achieve real-time monitoring of drug distribution and tumor accumulation, indicating a promising theranostic feature.

Superparamagnetic iron oxide nanoparticles (SPIOs) are widely applied T_2-weighted MRI contrast agents, which can provide a negative contrast enhancement of target lesion in MRI due to their high susceptibility and biocompatibility [30–36]. Nasongkla et al. fabricated DOX-/SPIO-loaded multifunctional polymeric

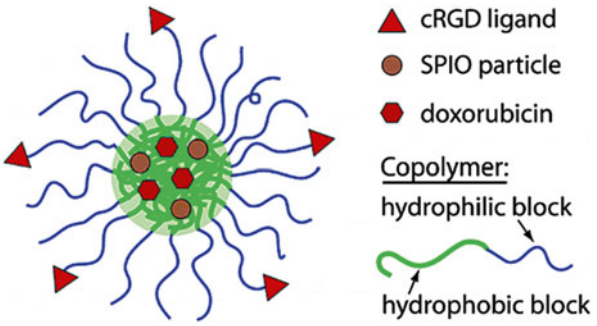

Fig. 10.5 Schematic diagram of SPIO- and DOX-encapsulated multifunctional micelles (Reprinted with the permission from Ref. [37]. Copyright 2006 American Chemical Society)

micelles for MRI imaging and chemotherapy [37]. cRGD on the surface of multifunctional polymeric micelles could selectively bind to $\alpha_v\beta_3$-expressing tumor cells for active cancer targeting, allowing ultrasensitive MRI imaging and delivery of chemotherapeutic drugs (Fig. 10.5). Similar designs of multifunctional micelles with targeting moieties for theranostic nanomedicine were also reported [38–41].

Chen et al. synthesized folic acid-conjugated carboxymethyl lauryl chitosan (FA-CLC), which was used to fabricate theranostic micelles encapsulating SPIO and camptothecin (CPT) [42]. The micelles could accumulate at the tumor sites owing to folate-mediated targeting and magnetism-enhanced EPR effect. Afterward, therapeutic ultrasound irradiation was further employed to enhance the site-specific internalization of the micelles [21–24]. The in vivo T_2-weighted imaging was used to monitor the enhanced accumulation of micelles at the tumor, which thus resulted in enhanced antitumor efficacy of CPT (Fig. 10.6).

10.2.3 Micelles for US Imaging and Chemotherapy

Ultrasound (US) imaging as a clinical imaging modality possesses a unique advantage owing to its real-time manner and low cost [43]. US also acts as an ideal candidate for imaging-guided cancer therapy. The use of ultrasound contrast agents (UCAs) effectively improves the resolution and sensitivity of clinical ultrasound imaging [44–46]. Typical UCAs are composed of an inner gaseous core with a thin shell coating. The shell materials including proteins [47], surfactants [48], polymers [49], and lipids [50] are used to form a protective layer outside the inner gas cores like sulfur hexafluoride (SF_6) and perfluorocarbons (PFCs) [51–53].

Rapoport et al. constructed DOX-/perfluoropentane (PFP)-loaded micelles using the biodegradable block copolymer poly(ethylene glycol)-poly(l-lactide) (PEG-PLLA). PFP nanodroplets could be evaporated under physiologic temperatures because of their low boiling point of 29 °C. The evaporation could result in the formation of microbubbles for enhanced ultrasound imaging and US-triggered chemotherapy [54, 55], indicating the successful theranostics (Fig. 10.7).

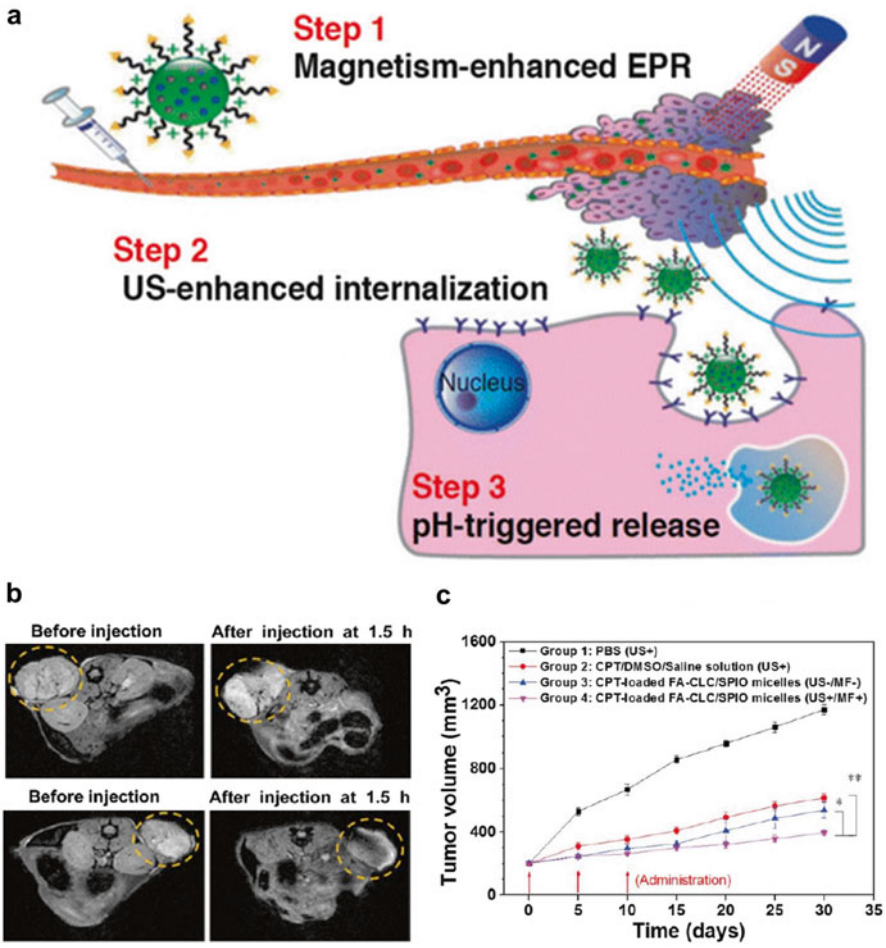

Fig. 10.6 (**a**) Schematic illustration of CPT-loaded FA-CLC/SPIO micelles for sequential stimuli-responsive cancer imaging and chemotherapy. (**b**) T_2-weighted MR images of tumor sites acquired from tumor-bearing nude mice before and after injection of the FA-CLC/SPIO micelles in the absence of magnetic attraction (*upper row*) or coupled with exposure to magnetic attraction (*bottom row*). (**c**) In vivo therapeutic efficacy of CPT-loaded FA-CLC/SPIO micelles in tumor-bearing nude mice with or without sequential administration of magnetic attraction and therapeutic sonication (Reprinted with the permission from Ref. [42]. Copyright 2015 American Chemical Society)

DOX-loaded calcium carbonate ($CaCO_3$) hybrid micelles were also developed through in situ mineralization approach [56]. The multifunctional micelles could trigger carbon dioxide (CO_2) bubbles at acid pH at tumors, generating echogenic signals to produce excellent US contrast enhancement, while there were no adequate CO_2 bubbles in the liver or normal tissues, indicating a selective tumor imaging feature. Meanwhile, the micelles also resulted in effective antitumor efficacy on the tumor-bearing mice, implying that the micelles can act as a potential smart theranostic platform for US imaging and simultaneous cancer chemotherapy (Fig. 10.8).

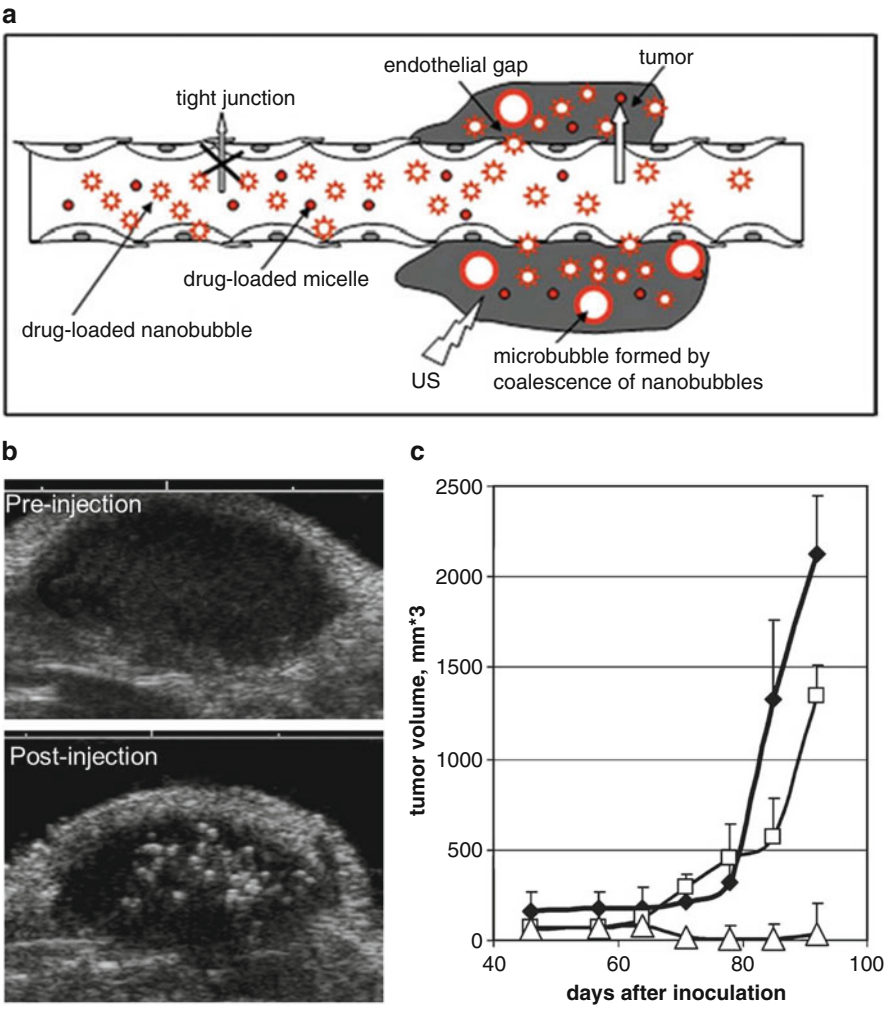

Fig. 10.7 (**a**) Schematic illustration of drug-loaded PFP micelles for ultrasound-triggered tumor therapy. (**b**) US imaging in the tumor after intravenous injection of drug-loaded PFP micelles. (**c**) Ultrasound-triggered therapeutic efficacy (*filled diamonds*, control; *open squares*, injection of drug-loaded PFP micelles without US exposure; *open triangles*, injection of drug-loaded PFP micelles with US exposure) (Reprinted with the permission from Ref. [54]. Copyright 2007 Oxford University Press)

10.2.4 Micelles for PET and Chemotherapy

Positron emission computed tomography (PET) is known as a valuable tool for cancer imaging by providing excellent tissue penetration, ultrasensitivity, and quantitative accuracy [57]. PET can detect the pairs of gamma rays emitted from positron-emitting radionuclide, which may be incorporated into a nanoplatform for theranostic application.

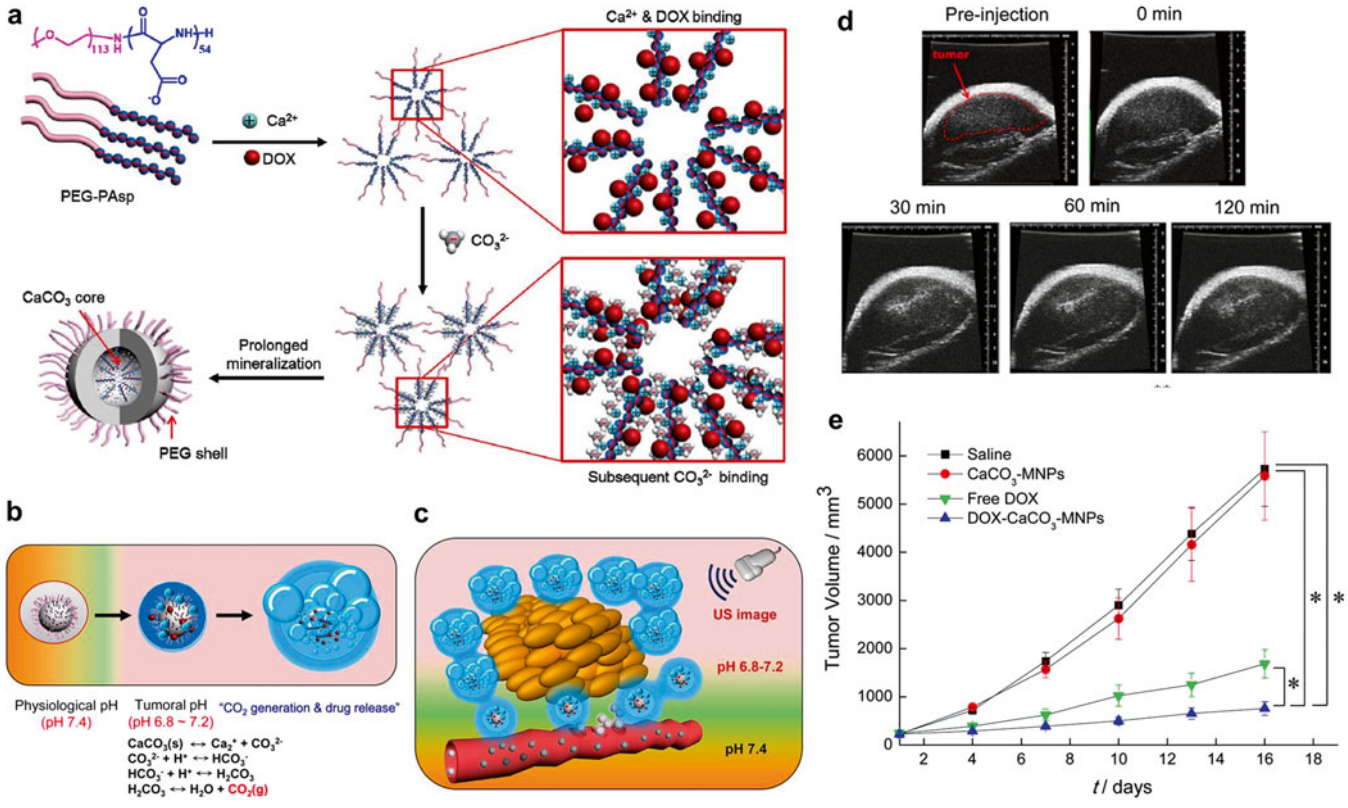

Fig. 10.8 (**a**) Schematic illustration of fabrication process of DOX-loaded $CaCO_3$ hybrid micelles. (**b**) Mechanism of CO_2 generation and drug release from the micelles. (**c**) Bubble generation and drug release after accumulation of DOX-loaded $CaCO_3$ hybrid micelles at tumor tissues. (**d**) In vivo US imaging of the tumors via the intratumoral injection of DOX-loaded $CaCO_3$ hybrid micelles. (**e**) Tumor growth profiles after various treatments (Reprinted with the permission from Ref. [56]. Copyright 2015 American Chemical Society)

A DOX-loaded unimolecular micelle system was developed using dendritic amphiphilic block copolymer poly(amidoamine)-poly(l-lactide)-b-poly(ethylene glycol) conjugated with 1,4,7-triazacyclononane-N, N', N-triacetic acid (NOTA, a macrocyclic chelator for ^{64}Cu) and anti-CD105 monoclonal antibody (TRC105) [58]. The micelles showed a uniform size distribution, pH-sensitive drug release behavior, and CD105-associated cellular uptake. ^{64}Cu-labeled targeted micelles exhibited an enhanced tumor accumulation on 4T1 murine breast tumor-bearing mice, validated by PET imaging. The multifunctional micelles exhibited cancer-targeted, PET-assisted, and pH-sensitive drug delivery for cancer theranostics (Fig. 10.9). Similar micellar nanotheranostics was achieved by using other copoly-

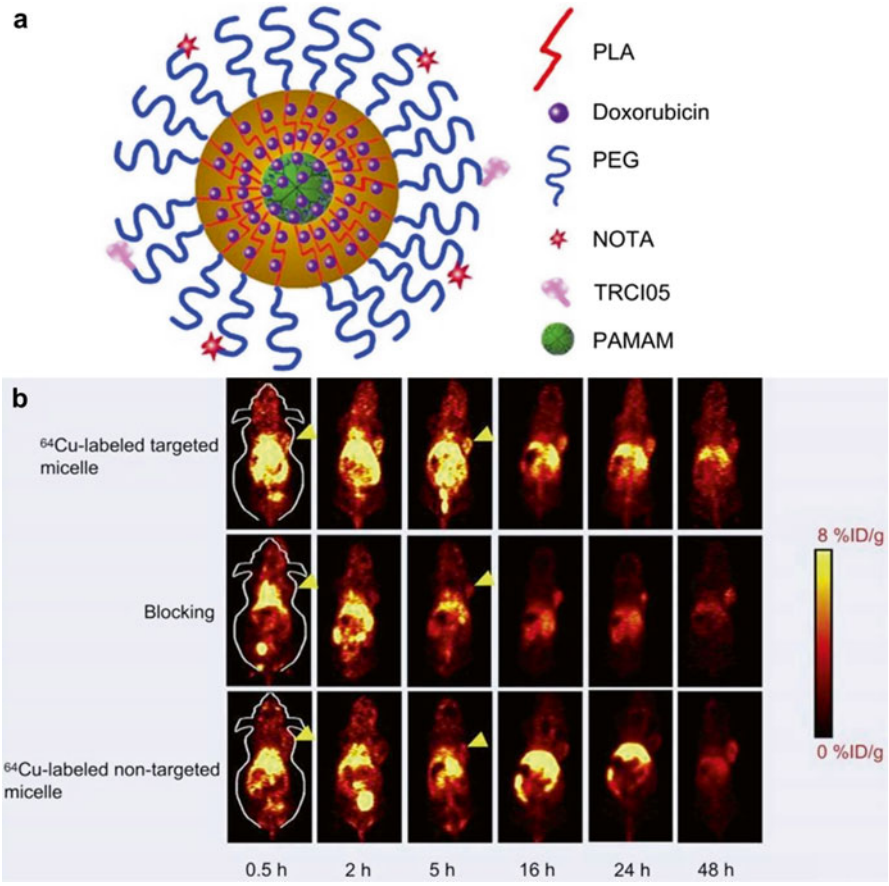

Fig. 10.9 (**a**) Schematic illustration of the multifunctional ^{64}Cu-labeled and drug-loaded unimolecular micelles. (**b**) Serial coronal PET images of 4T1 tumor-bearing mice at different time points post-injection of ^{64}Cu-labeled targeted micelles, nontargeted micelles, or targeted micelles with a blocking dose of TRC105 (Reprinted from Ref. [58]. Copyright 2013, with permission from Elsevier)

mer such as poly(2-hydroxyethyl methacrylate)-poly(l-lactide)-poly(ethylene glycol) (PHEMA-PLLA-PEG) [59].

10.3 Theranostic Micelles for Imaging and Photothermal Therapy

Thermal therapy has been explored as a noninvasive modality to treat cancer through hyperthermia during the past decades owing to its good efficiency and low adverse side effect [60–63]. Photothermal therapy (PTT) is considered as an emerging strategy that can achieve cancer therapy by irradiating exogenous photo-absorbing agents such as organic near-infrared (NIR) cyanine dyes [64, 65], inorganic nanomaterials such as graphene oxide [66, 67], and gold nanomaterials [68–71], which can effectively convert NIR light to hyperthermia for achieving tumor ablation.

Indocyanine green (ICG) is a clinically used NIR fluorescent dye. However, the application of ICG is seriously affected by numerous disadvantages including chemical degradation, low quantum yield, nonspecific binding to blood proteins, and rapid clearance from the body. The encapsulation of ICG within polymeric micellar system is highly potential to overcome these drawbacks [72, 73].

ICG is able to act as light absorber for photothermal therapy, which allows it to act as a bifunctional agent with fluorescent imaging and photothermal therapy capabilities. Phospholipid-polyethylene glycol (PL-PEG) was used to fabricate ICG-loaded micelles modified with folic acid (FA) and integrin $\alpha_v\beta_3$ monoclonal antibody (mAb) for cancer-targeted delivery of ICG [74, 75]. The micelles exhibited more efficiently photothermal effect than free ICG. The targeting micelles could be internalized and retained in targeted cancer cells via ligand-mediated endocytosis pathway for cell imaging and selective photothermal cell destruction under the irradiation of 808-nm laser. The micelles could not only be used as a NIR fluorescent dye but also achieve efficient in vivo photothermal therapy for cancer treatment (Fig. 10.10). Wu et al. employed amphiphilic triblock copolymers of poly(ethylene glycol)-b-poly(l-lysine)-b-poly(l-leucine) to construct ICG-loaded micelles via hydrophobic interaction and hydrophilic electrostatic interaction between ICG and polymers [76]. The micelles could significantly improve the quantum yield and fluorescent stability when compared with free ICG. The in vivo experiments confirmed the excellent passive tumor-targeting ability, which allows the micelles to generate an ideal theranostic effect for near-infrared fluorescent (NIRF) imaging and photothermal therapy. Folate-conjugated poly(2-ethyl-2-oxazoline)-b-poly(ε-caprolactone) micelles were also applied for ICG encapsulation for NIRF imaging and significant photothermal therapy [77]. Chen et al. constructed theranostic ICG-loaded micelle system using monomethoxy poly(ethylene glycol)-poly(l-aspartic acid) for long-term cancer fluorescent imaging with enhanced contrast and superior photothermal therapy [64].

IR-780 iodide, a more stable NIR dye than ICG, is a lipophilic cation heptamethine dye with higher fluorescence intensity [78]. IR-780 exhibits increased photo-

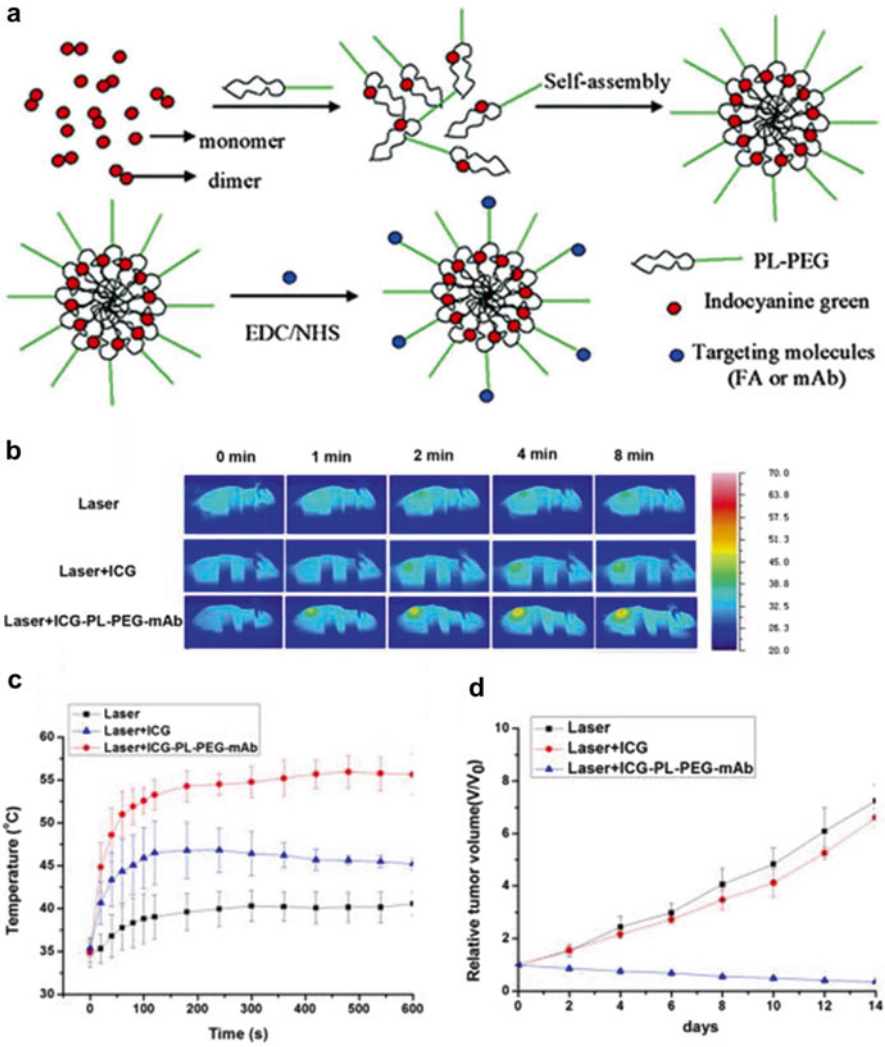

Fig. 10.10 (**a**) Schematic diagram of self-assembly of ICG-PL-PEG micelles and their targeted modification. (**b**) Thermographic images of mice bearing U87-MG tumors under different treatments. (**c**) Maximum surface temperature of the irradiated area as a function of the irradiation time. (**d**) Time-dependent tumor growth curves of U87-MG tumor after various treatments (Reprinted with the permission from Ref. [74, 75]. Copyright 2011, 2012 American Chemical Society)

stability and quantum yield and reduced photobleaching [79]. Yuan et al. developed self-assembled IR-780-loaded micelles [80]. The micelles showed specific targeting to the tumor for NIRF imaging-guided tumor ablation without significant toxicity, indicating a potential theranostic feature (Fig. 10.11).

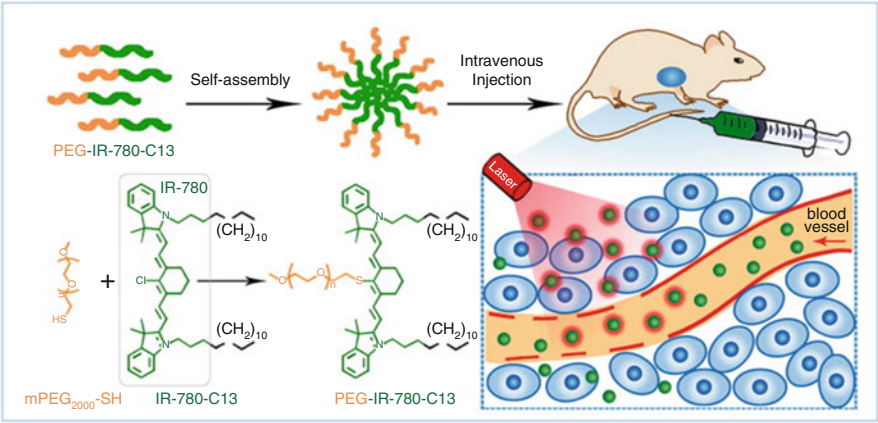

Fig. 10.11 Schematic of IR-780-loaded micelles for NIR fluorescent imaging-guided photothermal therapy (Reprinted from Ref. [80]. Copyright 2015, with permission from Elsevier)

Gold nanomaterials exhibit good biocompatibility as well as magnificent optical and electronic properties, making them possible to be used in biological and medical applications [81, 82]. Due to their strong absorption in NIR region and high photothermal conversion efficiency, various gold nanostructures such as gold nanorods (AuNRs) [83], gold nanoshell (AuNS) [84–86], and gold nanocages [87, 88] could induce significantly photothermal therapeutic efficacy [89]. Gold nanomaterials can also act as an ideal candidate of CT contrast agents, which can provide about 2.7-fold contrast enhancement than iodine [90–93]. Deng et al. developed a smart hybrid building block onto the gold nanoparticles (AuNPs) through an improved thiolation method. The conjugation of AuNPs with amphiphilic polymers resulted in strong interparticle plasmonic coupling to the NIR region for enhanced PTT and high X-ray absorption for CT contrast imaging (Fig. 10.12) [94].

10.4 Theranostic Micelles for Imaging and Photodynamic Therapy

Photodynamic therapy (PDT) is a powerful treatment method for destroying cancer cells selectively through reactive singlet oxygen (ROS) or free radical species generated by photosensitizers (PSs) upon light irradiation at a proper wavelength [95, 96]. PSs as a bifunctional agent could be used in both imaging and therapy due to their strong fluorescence and singlet oxygen generation upon irradiation [97]. However, the clinical utility of PDT is affected by their hydrophobicity and low targeting ability [98]. The polymeric micelles may overcome these drawbacks to achieve specific delivery of PSs [99].

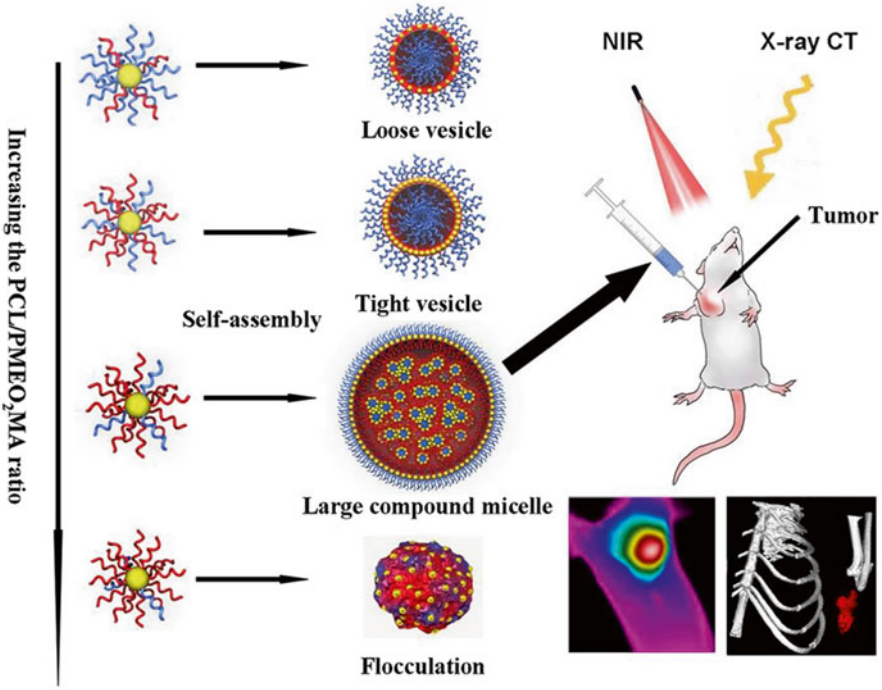

Fig. 10.12 Schematic representation of assemblies composed by PCL-/$PMEO_2MA$-grafted AuNPs and their potential application in CT imaging-guided photothermal therapy (Reprinted with the permission from Ref. [94]. Copyright 2014 Ivyspring International Publisher)

Koo et al. encapsulated protoporphyrin IX (PpIX) into pH-responsive polymeric micelles, which can trigger release of PpIX at the acidic extracellular pH of tumors [100]. The micelles generated a good in vivo fluorescent imaging at the tumor sites owing to the EPR effect. After 633-nm irradiation (3 mW cm^{-2}), the micelles produced cytotoxic singlet oxygen which induced cell damage and subsequent tumor ablation, indicating the micelles could be used for fluorescent imaging and PDT treatment (Fig. 10.13).

10.5 Theranostic Micelles for Imaging and Gene Therapy

Gene therapy utilizes gene vectors to facilitate cellular uptake of DNA with high transfection efficiency, making it a promising approach for treating various diseases [101]. Polymeric micelles can act as an effective vehicle for gene delivery. The coupling of the micelles with imaging features can provide real-time tracking and monitoring of gene therapy.

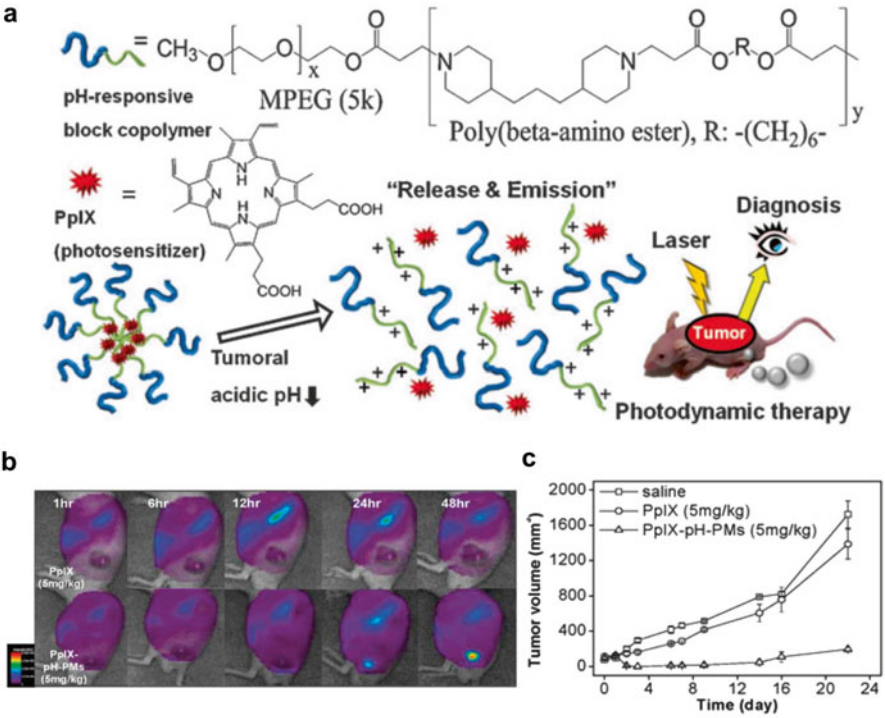

Fig. 10.13 (**a**) The micellization/demicellization transition of PpIX-loaded micelles for in vivo simultaneous tumor fluorescent imaging and photodynamic therapy. (**b**) In vivo noninvasive fluorescent imaging of free PpIX and PpIX-loaded micelles on the tumor-bearing mice. (**c**) Tumor growth of tumor-bearing mice treated with PDT treatment (Reproduced from Ref. [100] by permission of The Royal Society of Chemistry)

Tan et al. report a sensitive and selective approach for combined mRNA detection and gene therapy using molecular beacon micelle flares (MBMFs) [102]. Modification of molecular beacons with a diacyl lipid group resulted in the self-assembly into MBMFs with a DNA sequence composed of a target-recognition loop to quench the fluorescence via bringing the quencher and fluorophore close (off state). After cellular internalization, MBMFs triggered a conformational change opening the loop when hybridization to the target mRNA, and then allowed the generation of fluorescence via physical separation of fluorophore from the quencher (on state). Furthermore, the hybridization of MBMFs to the target mRNA can specifically inhibit gene expression, leading to the suppression of cancer cell growth. It indicates that the micelles act as a versatile nanoplatform for fluorescent detection and gene therapy (Fig. 10.14).

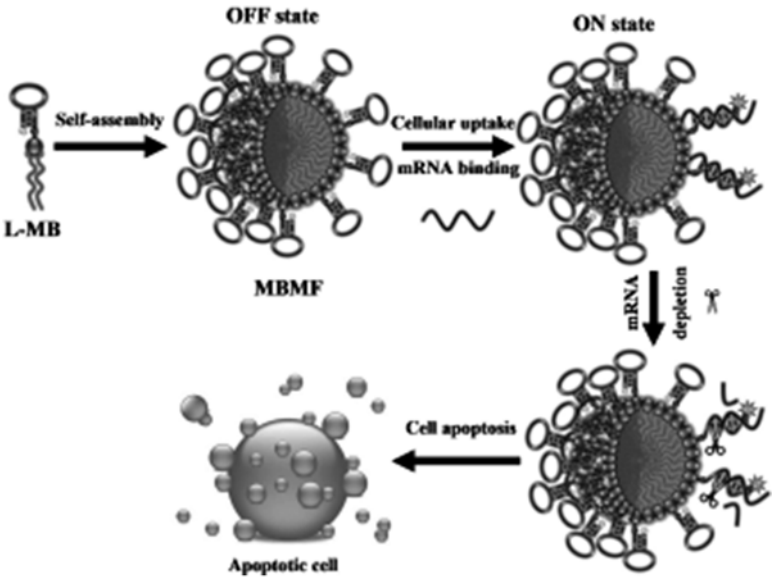

Fig. 10.14 Schematic illustration of molecular beacon micelle flares for intracellular mRNA detection and gene therapy (Reproduced from Ref. [102] by permission of John Wiley & Sons Ltd)

10.6 Theranostic Micelles for Multimodal Imaging and Combination Therapy

Clinically, two or more imaging techniques are usually applied together to reach reliable diagnostic results for precise cancer therapy, since each imaging modality has its unique advantages and limitations. Moreover, the combination of various cancer treatments can also provide more preferable cancer therapeutic efficacy. Thus, in the recent years, the multimodal imaging and combinational therapy have attracted much attention [103].

Radionuclide-labeled micelles have been developed for noninvasive imaging via single photon emission computed tomography (SPECT) [104]. Rhenium-188 (^{188}Re, $t_{1/2} = 16.9$ h) is a promising isotope for cancer imaging, which was incorporated into the IR-780-loaded micelles for fabricating multifunctional micelles with dual-modal SPECT/NIRF imaging and PTT [105]. The ^{188}Re-labeled IR-780 micelles could guide the drug delivery and monitor the tumor accumulation, intratumoral distribution, as well as release kinetics of drug. Moreover, the micelles successfully achieved tumor photothermal ablation. It indicates that the micelles could act as multifunctional platform for multimodal imaging-guided cancer therapy (Fig. 10.15).

Recently, poly(lactic-co-glycolic acid)-lecithin-polyethylene glycol was used to fabricate DOX-/ICG-loaded micelles to achieve fluorescent imaging and thermo-

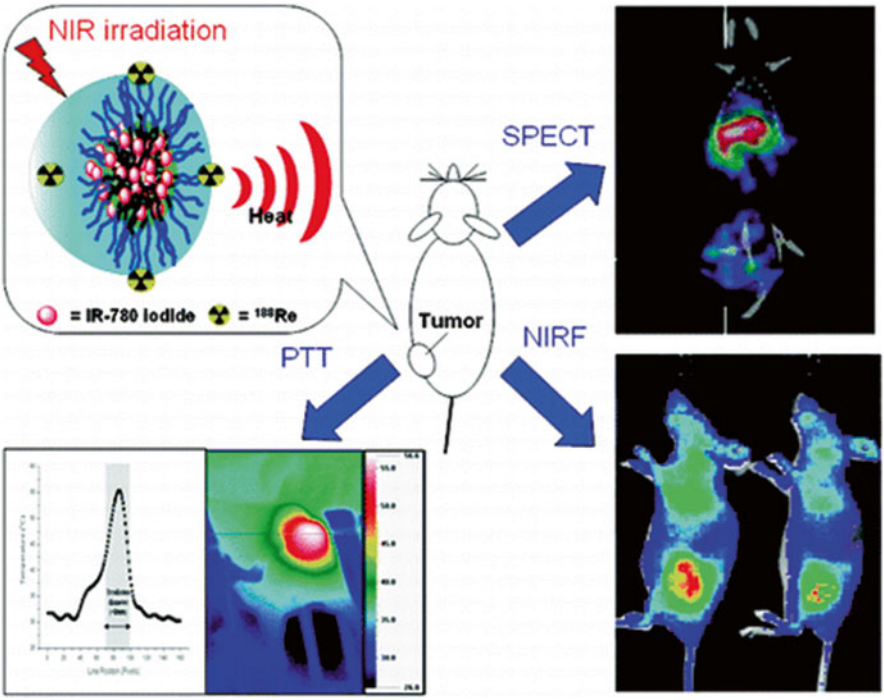

Fig. 10.15 Schematic diagram of ^{188}Re-labeled IR-780 micelles for dual-modal SPECT/NIRF imaging and photothermal therapy of cancer (Reprinted with the permission from Ref. [105]. Copyright 2011 American Chemical Society)

chemotherapy [106]. The micelles exhibited the enhanced release of DOX under NIR irradiation and longer retention at tumor. The fluorescent imaging of the micelles provided the in vivo tumor localization for guiding the cancer treatment. The micelles could induce both the apoptosis and cell necrosis under irradiation and result in synergistic efficacy as compared to the chemotherapy or PTT alone. In addition, monomethoxy poly(ethylene glycol)-b-poly(l-aspartic acid) (mPEG-b-PAsp) micelles were also used to fabricate the DOX-/ICG-loaded theranostic micelles [107]. Upon NIR irradiation, the micelles can induce NIRF imaging, acute PTT efficacy via hyperthermia, and simultaneous synergistic chemotherapy via singlet oxygen-triggered disruption of lysosomal membranes, indicating that the micelles are highly capable of imaging and synergistic tumor ablation (Fig. 10.16). Moreover, the mPEG-b-PAsp micelles were further explored for dual-modal imaging and PTT [108, 109]. The photosensitizer (Ce6) and cyanine dye (cypate) were co-encapsulated into the micelles for fluorescent/photoacoustic (PA) imaging and sequential synergistic PTT/PDT treatments [65]. The NIRF/PA imaging displayed high contrast and spatial resolution at the tumor, providing precise anatomical tumor location and their inner vasculatures for guiding PTT/PDT treatment. Subsequently,

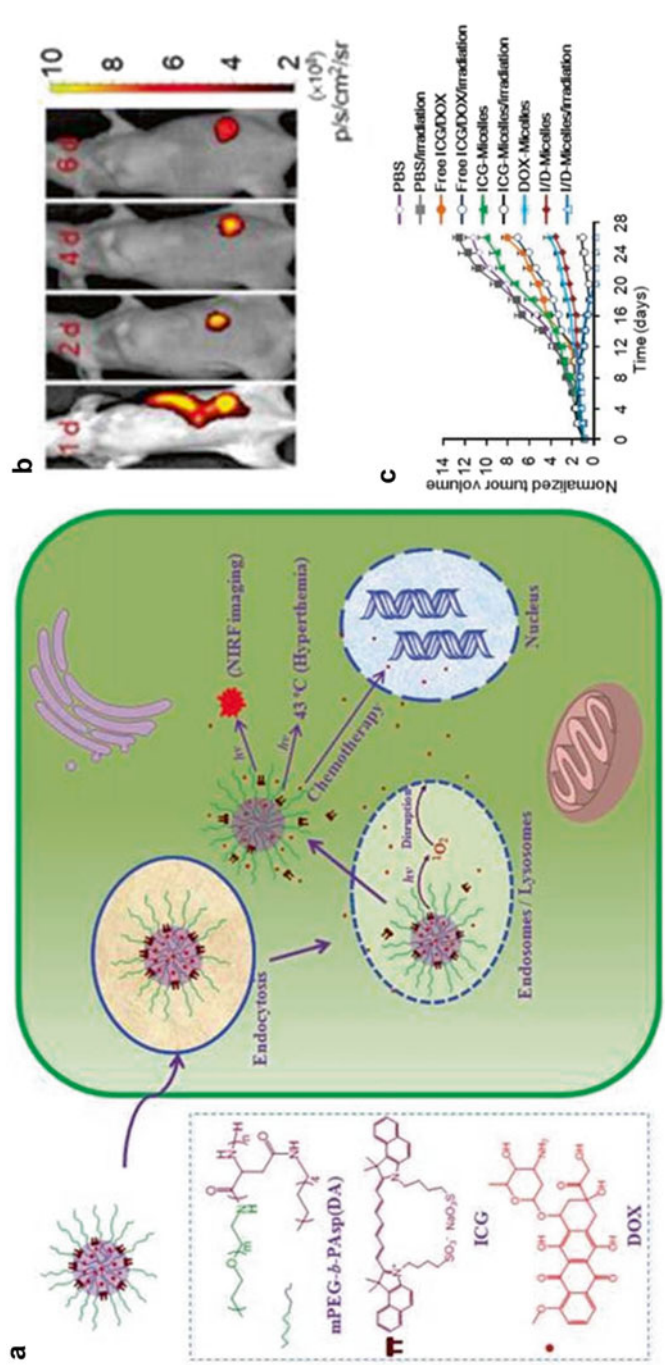

Fig. 10.16 (**a**) Schematic illustration of highly efficient hierarchical cyanine-based micelles for NIRF imaging and synergistic photothermal/chemotherapy for cancer eradication. (**b**) In vivo NIRF imaging of the mice bearing A549 tumor injected with DOX-/ICG-loaded micelles. (**c**) Tumor growth inhibition profiles of the mice bearing A549 tumor treated with various formulations (Reprinted with the permission from Ref. [107]. Copyright 2014 Ivyspring International Publisher)

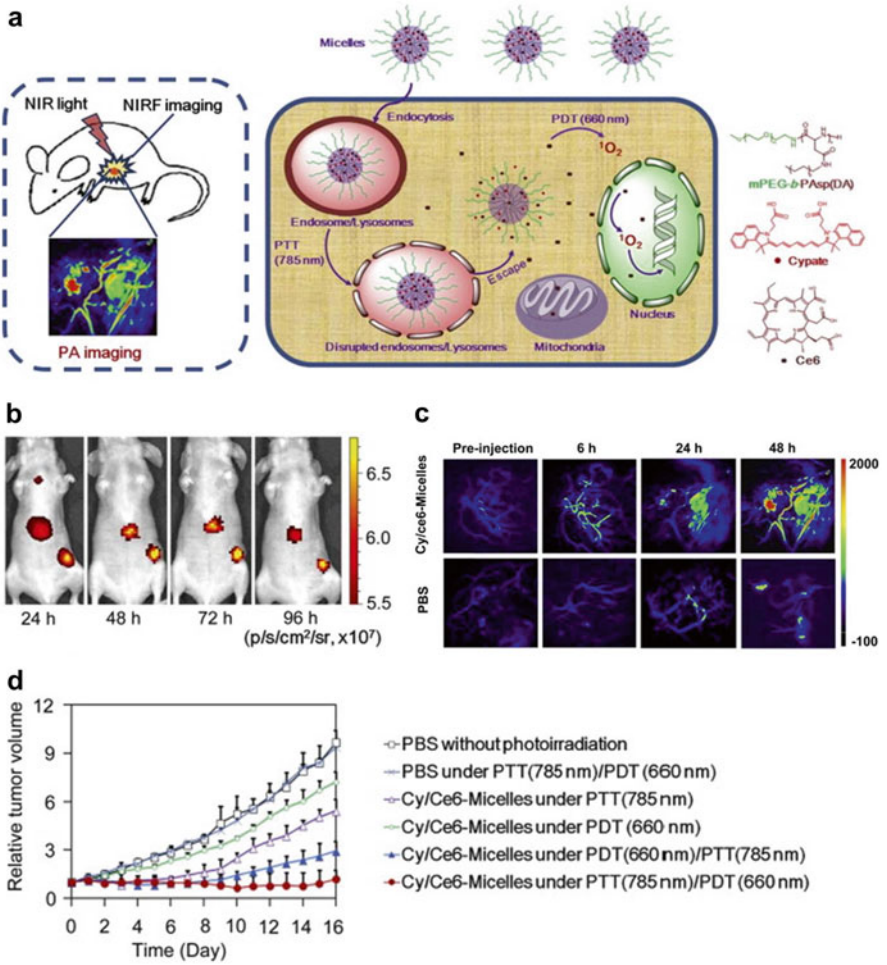

Fig. 10.17 (**a**) Schematic illustration of PS-loaded micelles integrating cyanine dye for dual-modal cancer imaging and synergistic therapy of PTT and PDT via an enhanced cytoplasmic delivery of PS. (**b**) In vivo NIRF imaging and (**c**) PA imaging of the mice bearing 4T1 tumor injected with cypate and Ce6 co-loaded micelles. (**d**) Tumor growth inhibition profiles of the mice bearing 4T1 tumor after various treatments (Reprinted from Ref. [65]. Copyright 2014, with permission from Elsevier)

the micelles further generated severe photothermal damage on cancer cells and destabilization of the lysosomes upon PTT irradiation, which subsequently facilitated synergistic PTT/PDT efficacy. The multimodal micelles as a multifunctional platform show great potentials for multimodal imaging and synergistic cancer therapy (Fig. 10.17).

10.7 Perspectives

The micelles possess promising potentials in both cancer imaging and therapy. In particular, the micelles are highly capable of generating multimodal imaging capacities including spatial resolution and sensitivity and synergistic cancer therapy with enhanced efficacy, since the polymer design and functionalization provide versatile tools for the fabrication of multifunctional theranostic micelles. The multimodal features provide complementary imaging features to generate precise tumor identification for guiding cancer treatment and therapeutic monitoring. Meanwhile, the micelles can generate synergistic anticancer efficacy through certain synergistic effect such as lysosomal disruption-mediated cytoplasmic delivery of anticancer drugs, which is preferable to the combinational treatment or mono-modal treatment. To date, the exploration of theranostic micelles is still undergoing new challenges including injectable polymer development, complex preparation, precise control of nanostructure, limited loading capacity, various intracellular translocation demands of imaging and therapeutic agents, as well as required imaging or therapeutic outcome, which might limit their clinical translation. In addition, there is still the absence of the guidance in the field of theranostic nanocarriers such as theranostic micelles, although there are some regulatory policies for the clinical development of nanocarriers. The development of theranostic micelles needs more precise polymer design with clinical potential and reasonable integration of imaging and therapeutic agents in the future.

References

1. Farokhzad OC, Langer R (2006) Nanomedicine: developing smarter therapeutic and diagnostic modalities. Adv Drug Deliv Rev 58(14):1456–1459
2. Barreto JA, O'Malley W, Kubeil M, Graham B, Stephan H, Spiccia L (2011) Nanomaterials: applications in cancer imaging and therapy. Adv Mater 23(12):H18–H40
3. Lammers T, Aime S, Hennink WE, Storm G, Kiessling F (2011) Theranostic nanomedicine. Acc Chem Res 44(10):1029–1038
4. Weissleder R, Pittet MJ (2008) Imaging in the era of molecular oncology. Nature 452(7187):580–589
5. Willmann JK, van Bruggen N, Dinkelborg LM, Gambhir SS (2008) Molecular imaging in drug development. Nat Rev Drug Discov 7(7):591–607
6. Hrkach J, Von Hoff D, Mukkaram Ali M, Andrianova E, Auer J, Campbell T, De Witt D, Figa M, Figueiredo M, Horhota A, Low S, McDonnell K, Peeke E, Retnarajan B, Sabnis A, Schnipper E, Song JJ, Song YH, Summa J, Tompsett D, Troiano G, Van Geen Hoven T, Wright J, LoRusso P, Kantoff PW, Bander NH, Sweeney C, Farokhzad OC, Langer R, Zale S (2012) Preclinical development and clinical translation of a PSMA-targeted docetaxel nanoparticle with a differentiated pharmacological profile. Sci Transl Med 4(128):128–139
7. Warner S (2004) Diagnostics plus therapy = theranostics. Scientist 18(16):38–39
8. Lammers T, Kiessling F, Hennink WE, Storm G (2010) Nanotheranostics and image-guided drug delivery: current concepts and future directions. Mol Pharm 7(6):1899–1912
9. Sun D (2010) Nanotheranostics: integration of imaging and targeted drug delivery. Mol Pharm 7(6):1879

10. Mura S, Couvreur P (2012) Nanotheranostics for personalized medicine. Adv Drug Deliv Rev 64(13):1394–1416
11. Chen XY, Gambhlr SS, Cheon J (2011) Theranostic nanomedicine. Acc Chem Res 44(10):841
12. Mikhaylov G, Mikac U, Magaeva AA, Itin VI, Naiden EP, Psakhye I, Babes L, Reinheckel T, Peters C, Zeiser R, Bogyo M, Turk V, Psakhye SG, Turk B, Vasiljeva O (2011) Ferri-liposomes as an MRI-visible drug-delivery system for targeting tumours and their microenvironment. Nat Nanotechnol 6(9):594–602
13. Liu Y, Miyoshi H, Nakamura M (2007) Nanomedicine for drug delivery and imaging: a promising avenue for cancer therapy and diagnosis using targeted functional nanoparticles. Int J Cancer 120(12):2527–2537
14. Mundargi RC, Babu VR, Rangaswamy V, Patel P, Aminabhavi TM (2008) Nano/micro technologies for delivering macromolecular therapeutics using poly(d, l-lactide-co-glycolide) and its derivatives. J Control Release 125(3):193–209
15. Tsai HC, Chang WH, Lo CL, Tsai CH, Chang CH, Ou TW, Yen TC, Hsiue GH (2010) Graft and diblock copolymer multifunctional micelles for cancer chemotherapy and imaging. Biomaterials 31(8):2293–2301
16. Smith AM, Gao XH, Nie SM (2004) Quantum dot nanocrystals for in vivo molecular and cellular imaging. Photochem Photobiol 80(3):377–385
17. Medintz IL, Uyeda HT, Goldman ER, Mattoussi H (2005) Quantum dot bioconjugates for imaging, labelling and sensing. Nat Mater 4(6):435–446
18. Mulder WJM, Koole R, Brandwijk RJ, Storm G, Chin PTK, Strijkers GJ, Donega CD, Nicolay K, Griffioen AW (2006) Quantum dots with a paramagnetic coating as a bimodal molecular imaging probe. Nano Lett 6(1):1–6
19. Wang W, Cheng D, Gong F, Miao X, Shuai X (2012) Design of multifunctional micelle for tumor-targeted intracellular drug release and fluorescent imaging. Adv Mater 24(1):115–120
20. Kumar R, Kulkarni A, Nagesha DK, Sridhar S (2012) In vitro evaluation of theranostic polymeric micelles for imaging and drug delivery in cancer. Theranostics 2(7):714–722
21. Santra S (2012) The potential clinical impact of quantum dots. Nanomedicine (Lond) 7(5):623–626
22. Luo Z, Yuan X, Yu Y, Zhang Q, Leong DT, Lee JY, Xie J (2012) From aggregation-induced emission of Au(I)–thiolate complexes to ultrabright Au(0)@Au(I)–thiolate core–shell nanoclusters. J Am Chem Soc 134(40):16662–16670
23. Muthu MS, Kutty RV, Luo Z, Xie J, Feng SS (2015) Theranostic vitamin E TPGS micelles of transferrin conjugation for targeted co-delivery of docetaxel and ultra bright gold nanoclusters. Biomaterials 39:234–248
24. Tavano L, Muzzalupo R, Mauro L, Pellegrino M, Andò S, Picci N (2013) Transferrin-conjugated pluronic niosomes as a new drug delivery system for anticancer therapy. Langmuir 29(41):12638–12646
25. Chou SW, Shau YH, Wu PC, Yang YS, Shieh DB, Chen CC (2010) In vitro and in vivo studies of FePt nanoparticles for dual modal CT/MRI molecular imaging. J Am Chem Soc 132(38):13270–13278
26. Cheng H, Nair G, Walker TA, Kim MK, Pardue MT, Thule PM, Olson DE, Duong TQ (2006) Structural and functional MRI reveals multiple retinal layers. Proc Natl Acad Sci U S A 103(46):17525–17530
27. McEvoy LK, Fennema-Notestine C, Roddey JC, Hagler DJ Jr, Holland D, Karow DS, Pung CJ, Brewer JB, Dale AM (2009) Alzheimer disease: quantitative structural neuroimaging for detection and prediction of clinical and structural changes in mild cognitive impairment. Radiology 251(1):195–205
28. Aime S, Crich SG, Gianolio E, Giovenzana GB, Tei L, Terreno E (2006) High sensitivity lanthanide(III) based probes for MR-medical imaging. Coord Chem Rev 250(11–12):1562–1579

29. Kaida S, Cabral H, Kumagai M, Kishimura A, Terada Y, Sekino M, Aoki I, Nishiyama N, Tani T, Kataoka K (2010) Visible drug delivery by supramolecular nanocarriers directing to single-platformed diagnosis and therapy of pancreatic tumor model. Cancer Res 70(18):7031–7041
30. Tong S, Hou S, Zheng Z, Zhou J, Bao G (2010) Coating optimization of superparamagnetic iron oxide nanoparticles for high T2 relaxivity. Nano Lett 10(11):4607–4613
31. Laurent S, Forge D, Port M, Roch A, Robic C, Vander Elst L, Muller RN (2008) Magnetic iron oxide nanoparticles: synthesis, stabilization, vectorization, physicochemical characterizations, and biological applications. Chem Rev 108(6):2064–2110
32. Yoo D, Lee JH, Shin TH, Cheon J (2011) Theranostic magnetic nanoparticles. Acc Chem Res 44(10):863–874
33. Yu Y, Sun D (2010) Superparamagnetic iron oxide nanoparticle 'theranostics' for multimodality tumor imaging, gene delivery, targeted drug and prodrug delivery. Expert Rev Clin Pharmacol 3(1):117–130
34. Zou P, Yu Y, Wang YA, Zhong Y, Welton A, Galban C, Wang S, Sun D (2010) Superparamagnetic iron oxide nanotheranostics for targeted cancer cell imaging and pH-dependent intracellular drug release. Mol Pharm 7(6):1974–1984
35. Ghosh D, Lee Y, Thomas S, Kohli AG, Yun DS, Belcher AM, Kelly KA (2012) M13-templated magnetic nanoparticles for targeted in vivo imaging of prostate cancer. Nat Nanotechnol 7(10):677–682
36. Lee JH, Huh YM, Jun YW, Seo JW, Jang JT, Song HT, Kim S, Cho EJ, Yoon HG, Suh JS, Cheon J (2007) Artificially engineered magnetic nanoparticles for ultra-sensitive molecular imaging. Nat Med 13(1):95–99
37. Nasongkla N, Bey E, Ren J, Ai H, Khemtong C, Guthi JS, Chin S-F, Sherry AD, Boothman DA, Gao J (2006) Multifunctional polymeric micelles as cancer-targeted, MRI-ultrasensitive drug delivery systems. Nano Lett 6(11):2427–2430
38. Yang X, Chen Y, Yuan R, Chen G, Blanco E, Gao J, Shuai X (2008) Folate-encoded and Fe_3O_4-loaded polymeric micelles for dual targeting of cancer cells. Polymer 49(16):3477–3485
39. Guthi JS, Yang SG, Huang G, Li S, Khemtong C, Kessinger CW, Peyton M, Minna JD, Brown KC, Gao J (2010) MRI-visible micellar nanomedicine for targeted drug delivery to lung cancer cells. Mol Pharm 7(1):32–40
40. Li Y, Ma J, Zhu H, Gao X, Dong H, Shi D (2013) Green synthetic, multifunctional hybrid micelles with shell embedded magnetic nanoparticles for theranostic applications. ACS Appl Mater Interfaces 5(15):7227–7235
41. Ao L, Wang B, Liu P, Huang L, Yue C, Gao D, Wu C, Su W (2014) A folate-integrated magnetic polymer micelle for MRI and dual targeted drug delivery. Nanoscale 6(18):10710–10716
42. Chen H-P, Chen M-H, Tung F-I, Liu T-Y (2015) A novel micelle-forming material used for preparing a theranostic vehicle exhibiting enhanced in vivo therapeutic efficacy. J Med Chem 58(9):3704–3719
43. Liu Z, Kiessling F, Gätjens J (2010) Advanced nanomaterials in multimodal imaging: design, functionalization, and biomedical applications. J Nanomater 2010:894303
44. Cosgrove D (2006) Ultrasound contrast agents: an overview. Eur J Radiol 60(3):324–330
45. Xing ZW, Ke HT, Wang JR, Zhao B, Yue XL, Dai ZF, Liu JB (2010) Novel ultrasound contrast agent based on microbubbles generated from surfactant mixtures of span 60 and polyoxyethylene 40 stearate. Acta Biomater 6(9):3542–3549
46. Xing ZW, Wang JR, Ke HT, Zhao B, Yue XL, Dai ZF, Liu JB (2010) The fabrication of novel nanobubble ultrasound contrast agent for potential tumor imaging. Nanotechnology 21(14):145607
47. Barnhart J, Levene H, Villapando E, Maniquis J, Fernandez J, Rice S, Jablonski E, Gjoen T, Tolleshaug H (1990) Characteristics of Albunex: air-filled albumin microspheres for echocardiography contrast enhancement. Invest Radiol 25(Suppl 1):S162–S164

48. Forsberg F, Basude R, Liu J-B, Alessandro J, Shi WT, Rawool NM, Goldberg BB, Wheatley MA (1999) Effect of filling gases on the backscatter from contrast microbubbles: theory and in vivo measurements. Ultrasound Med Bio 25(8):1203–1211
49. El-Sherif DM, Wheatley MA (2003) Development of a novel method for synthesis of a polymeric ultrasound contrast agent. J Biomed Mater Res A 66A(2):347–355
50. Leong-Poi H, Christiansen J, Heppner P, Lewis CW, Klibanov AL, Kaul S, Lindner JR (2005) Assessment of endogenous and therapeutic arteriogenesis by contrast ultrasound molecular imaging of integrin expression. Circulation 111(24):3248–3254
51. Arthur Kort IK (1982) Microbubble formation: in vitro and in vivo observation. J Clin Ultrasound 10(3):117–120
52. Blomley MJK, Cooke JC, Unger EC, Monaghan MJ, Cosgrove DO (2001) Science, medicine, and the future – microbubble contrast agents: a new era in ultrasound. Br Med J 322(7296):1222–1225
53. Raisinghani A, DeMaria AN (2002) Physical principles of microbubble ultrasound contrast agents. Am J Cardiol 90(10A):3J–7J
54. Rapoport N, Gao Z, Kennedy A (2007) Multifunctional nanoparticles for combining ultrasonic tumor imaging and targeted chemotherapy. J Natl Cancer Inst 99(14):1095–1106
55. Gao Z, Kennedy AM, Christensen DA, Rapoport NY (2008) Drug-loaded nano/microbubbles for combining ultrasonography and targeted chemotherapy. Ultrasonics 48(4):260–270
56. Min KH, Min HS, Lee HJ, Park DJ, Yhee JY, Kim K, Kwon IC, Jeong SY, Silvestre OF, Chen X, Hwang YS, Kim EC, Lee SC (2015) pH-controlled gas-generating mineralized nanoparticles: a theranostic agent for ultrasound imaging and therapy of cancers. ACS Nano 9(1):134–145
57. James ML, Gambhir SS (2012) A molecular imaging primer: modalities, imaging agents, and applications. Physiol Rev 92(2):897–965
58. Guo J, Hong H, Chen G, Shi S, Zheng Q, Zhang Y, Theuer CP, Barnhart TE, Cai W, Gong S (2013) Image-guided and tumor-targeted drug delivery with radiolabeled unimolecular micelles. Biomaterials 34(33):8323–8332
59. Guo J, Hong H, Chen G, Shi S, Nayak TR, Theuer CP, Barnhart TE, Cai W, Gong S (2014) Theranostic unimolecular micelles based on brush-shaped amphiphilic block copolymers for tumor-targeted drug delivery and positron emission tomography imaging. ACS Appl Mater Interfaces 6(24):21769–21779
60. Kim JH, Hahn EW, Tokita N (1978) Combination hyperthermia and radiation therapy for cutaneous malignant melanoma. Cancer 41(6):2143–2148
61. Corry PM, Barlogie B, Tilchen EJ, Armour EP (1982) Ultrasound-induced hyperthermia for the treatment of human superficial tumors. Int J Radiat Oncol Biol Phys 8(7):1225–1229
62. Arcangeli G, Barni E, Cividalli A, Mauro F, Morelli D, Nervi C, Spano M, Tabocchini A (1980) Effectiveness of microwave hyperthermia combined with ionizing radiation: clinical results on neck node metastases. Int J Radiat Oncol Biol Phys 6(2):143–148
63. Brusentsov NA, Nikitin LV, Brusentsova TN, Kuznetsov AA, Bayburtskiy FS, Shumakov LI, Jurchenko NY (2002) Magnetic fluid hyperthermia of the mouse experimental tumor. J Magn Magn Mater 252(1–3):378–380
64. Yang H, Mao H, Wan Z, Zhu A, Guo M, Li Y, Li X, Wan J, Yang X, Shuai X, Chen H (2013) Micelles assembled with carbocyanine dyes for theranostic near-infrared fluorescent cancer imaging and photothermal therapy. Biomaterials 34(36):9124–9133
65. Guo M, Mao H, Li Y, Zhu A, He H, Yang H, Wang Y, Tian X, Ge C, Peng Q, Wang X, Yang X, Chen X, Liu G, Chen H (2014) Dual imaging-guided photothermal/photodynamic therapy using micelles. Biomaterials 35(16):4656–4666
66. Robinson JT, Tabakman SM, Liang Y, Wang H, Casalongue HS, Vinh D, Dai H (2011) Ultrasmall reduced graphene oxide with high near-infrared absorbance for photothermal therapy. J Am Chem Soc 133(17):6825–6831
67. Yang K, Zhang S, Zhang G, Sun X, Lee ST, Liu Z (2010) Graphene in mice: ultrahigh in vivo tumor uptake and efficient photothermal therapy. Nano Lett 10(9):3318–3323

68. O'Neal DP, Hirsch LR, Halas NJ, Payne JD, West JL (2004) Photo-thermal tumor ablation in mice using near infrared-absorbing nanoparticles. Cancer Lett 209(2):171–176
69. Melancon MP, Zhou M, Li C (2011) Cancer theranostics with near-infrared light-activatable multimodal nanoparticles. Acc Chem Res 44(10):947–956
70. Rai P, Mallidi S, Zheng X, Rahmanzadeh R, Mir Y, Elrington S, Khurshid A, Hasan T (2010) Development and applications of photo-triggered theranostic agents. Adv Drug Deliver Rev 62(11):1094–1124
71. Huang X, El-Sayed IH, Qian W, El-Sayed MA (2006) Cancer cell imaging and photothermal therapy in the near-infrared region by using gold nanorods. J Am Chem Soc 128(6):2115–2120
72. Kirchherr A-K, Briel A, Mäder K (2009) Stabilization of indocyanine green by encapsulation within micellar systems. Mol Pharm 6(2):480–491
73. Rodriguez VB, Henry SM, Hoffman AS, Stayton PS, Li X, Pun SH (2008) Encapsulation and stabilization of indocyanine green within poly(styrene-alt-maleic anhydride) block-poly(styrene) micelles for near-infrared imaging. J Biomed Opt 13(1):014025
74. Zheng X, Xing D, Zhou F, Wu B, Chen WR (2011) Indocyanine green-containing nanostructure as near infrared dual-functional targeting probes for optical imaging and photothermal therapy. Mol Pharm 8(2):447–456
75. Zheng X, Zhou F, Wu B, Chen WR, Xing D (2012) Enhanced tumor treatment using biofunctional indocyanine green-containing nanostructure by intratumoral or intravenous injection. Mol Pharm 9(3):514–522
76. Wu L, Fang S, Shi S, Deng J, Liu B, Cai L (2013) Hybrid polypeptide micelles loading indocyanine green for tumor imaging and photothermal effect study. Biomacromolecules 14(9):3027–3033
77. Yan L, Qiu L (2015) Indocyanine green targeted micelles with improved stability for near-infrared image-guided photothermal tumor therapy. Nanomedicine (Lond) 10(3):361–373
78. Yue C, Liu P, Zheng M, Zhao P, Wang Y, Ma Y, Cai L (2013) IR-780 dye loaded tumor targeting theranostic nanoparticles for NIR imaging and photothermal therapy. Biomaterials 34(28):6853–6861
79. Lu C, Das S, Magut PK, Li M, El-Zahab B, Warner IM (2012) Irradiation induced fluorescence enhancement in PEGylated cyanine-based NIR nano- and mesoscale GUMBOS. Langmuir 28(40):14415–14423
80. Yuan A, Qiu X, Tang X, Liu W, Wu J, Hu Y (2015) Self-assembled PEG-IR-780-C13 micelle as a targeting, safe and highly-effective photothermal agent for in vivo imaging and cancer therapy. Biomaterials 51:184–193
81. Lim YT, Park OO, Jung HT (2003) Gold nanolayer-encapsulated silica particles synthesized by surface seeding and shell growing method: near infrared responsive materials. J Colloid Interface Sci 263(2):449–453
82. Kennedy LC, Bickford LR, Lewinski NA, Coughlin AJ, Hu Y, Day ES, West JL, Drezek RA (2011) A new era for cancer treatment: gold-nanoparticle-mediated thermal therapies. Small 7(2):169–183
83. Tong L, Wei QS, Wei A, Cheng JX (2009) Gold nanorods as contrast agents for biological imaging: optical properties, surface conjugation and photothermal effects. Photochem Photobiol 85(1):21–32
84. Hirsch LR, Stafford RJ, Bankson JA, Sershen SR, Rivera B, Price RE, Hazle JD, Halas NJ, West JL (2003) Nanoshell-mediated near-infrared thermal therapy of tumors under magnetic resonance guidance. Proc Natl Acad Sci U S A 100(23):13549–13554
85. Loo C, Lowery A, Halas NJ, West J, Drezek R (2005) Immunotargeted nanoshells for integrated cancer imaging and therapy. Nano Lett 5(4):709–711
86. Gobin AM, Lee MH, Halas NJ, James WD, Drezek RA, West JL (2007) Near-infrared resonant nanoshells for combined optical imaging and photothermal cancer therapy. Nano Lett 7(7):1929–1934

87. Chen J, Wang D, Xi J, Au L, Siekkinen A, Warsen A, Li ZY, Zhang H, Xia Y, Li X (2007) Immuno gold nanocages with tailored optical properties for targeted photothermal destruction of cancer cells. Nano Lett 7(5):1318–1322
88. Chen JY, Glaus C, Laforest R, Zhang Q, Yang MX, Gidding M, Welch MJ, Xia YN (2010) Gold nanocages as photothermal transducers for cancer treatment. Small 6(7):811–817
89. Jain PK, Huang X, El-Sayed IH, El-Sayed MA (2008) Noble metals on the nanoscale: optical and photothermal properties and some applications in imaging, sensing, biology, and medicine. Acc Chem Res 41(12):1578–1586
90. Geso M (2007) Gold nanoparticles: a new X-ray contrast agent. Br J Radiol 80(949):64–65
91. Popovtzer R, Agrawal A, Kotov NA, Popovtzer A, Balter J, Carey TE, Kopelman R (2008) Targeted gold nanoparticles enable molecular CT imaging of cancer. Nano Lett 8(12):4593–4596
92. Kim D, Park S, Lee JH, Jeong YY, Jon S (2007) Antibiofouling polymer-coated gold nanoparticles as a contrast agent for in vivo x-ray computed tomography imaging. J Am Chem Soc 129(24):7661–7665
93. Alric C, Taleb J, Le Duc G, Mandon C, Billotey C, Le Meur-Herland A, Brochard T, Vocanson F, Janier M, Perriat P, Roux S, Tillement O (2008) Gadolinium chelate coated gold nanoparticles as contrast agents for both X-ray computed tomography and magnetic resonance imaging. J Am Chem Soc 130(18):5908–5915
94. Deng H, Zhong Y, Du M, Liu Q, Fan Z, Dai F, Zhang X (2014) Theranostic self-assembly structure of gold nanoparticles for NIR photothermal therapy and X-Ray computed tomography imaging. Theranostics 4(9):904–918
95. Chatterjee DK, Fong LS, Zhang Y (2008) Nanoparticles in photodynamic therapy: an emerging paradigm. Adv Drug Deliv Rev 60(15):1627–1637
96. Yano S, Hirohara S, Obata M, Hagiya Y, Ogura S-i, Ikeda A, Kataoka H, Tanaka M, Joh T (2011) Current states and future views in photodynamic therapy. J Photochem Photobiol C 12(1):46–67
97. Lee SJ, Park K, Oh YK, Kwon SH, Her S, Kim IS, Choi K, Kim H, Lee SG, Kim K, Kwon IC (2009) Tumor specificity and therapeutic efficacy of photosensitizer-encapsulated glycol chitosan-based nanoparticles in tumor-bearing mice. Biomaterials 30(15):2929–2939
98. Konan YN, Gurny R, Allemann E (2002) State of the art in the delivery of photosensitizers for photodynamic therapy. J Photochem Photobiol B 66(2):89–106
99. de Smet M, Langereis S, van den Bosch S, Grull H (2010) Temperature-sensitive liposomes for doxorubicin delivery under MRI guidance. J Control Release 143(1):120–127
100. Koo H, Lee H, Lee S, Min KH, Kim MS, Lee DS, Choi Y, Kwon IC, Kim K, Jeong SY (2010) In vivo tumor diagnosis and photodynamic therapy via tumoral pH-responsive polymeric micelles. Chem Commun 46(31):5668–5670
101. Aw MS, Kurian M, Losic D (2013) Polymeric micelles for multidrug delivery and combination therapy. Chemistry 19(38):12586–12601
102. Chen T, Wu CS, Jimenez E, Zhu Z, Dajac JG, You M, Han D, Zhang X, Tan W (2013) DNA micelle flares for intracellular mRNA imaging and gene therapy. Angew Chem Int Ed 52(7):2012–2016
103. Louie AY (2010) Multimodality imaging probes: design and challenges. Chem Rev 110(5):3146–3195
104. Hoang B, Lee H, Reilly RM, Allen C (2009) Noninvasive monitoring of the fate of 111In-labeled block copolymer micelles by high resolution and high sensitivity MicroSPECT/CT imaging. Mol Pharm 6(2):581–592
105. Peng CL, Shih YH, Lee PC, Hsieh TM, Luo TY, Shieh MJ (2011) Multimodal image-guided photothermal therapy mediated by ^{188}Re-labeled micelles containing a cyanine-type photosensitizer. ACS Nano 5(7):5594–5607
106. Zheng M, Yue C, Ma Y, Gong P, Zhao P, Zheng C, Sheng Z, Zhang P, Wang Z, Cai L (2013) Single-step assembly of DOX/ICG loaded lipid – polymer nanoparticles for highly effective chemo-photothermal combination therapy. ACS Nano 7(3):2056–2067

107. Wan Z, Mao H, Guo M, Li Y, Zhu A, Yang H, He H, Shen J, Zhou L, Jiang Z, Ge C, Chen X, Yang X, Liu G, Chen H (2014) Highly efficient hierarchical micelles integrating photothermal therapy and singlet oxygen-synergized chemotherapy for cancer eradication. Theranostics 4(4):399–411
108. Yu J, Javier D, Yaseen MA, Nitin N, Richards-Kortum R, Anvari B, Wong MS (2010) Self-assembly synthesis, tumor cell targeting, and photothermal capabilities of antibody-coated indocyanine green nanocapsules. J Am Chem Soc 132(6):1929–1938
109. Luo S, Zhang E, Su Y, Cheng T, Shi C (2011) A review of NIR dyes in cancer targeting and imaging. Biomaterials 32(29):7127–7138

ERRATUM

Chapter 8
Functional Nanoparticles for Molecular Imaging-Guided Gene Delivery and Therapy

Tianxin Miao, Yu Zhang, Yun Zeng, Rui Tian, and Gang Liu

Z. Dai (ed.), *Advances in Nanotheranostics II*, Springer Series
in Biomaterials Science and Engineering 7, DOI 10.1007/978-981-10-0063-8

DOI 10.1007/978-981-10-0063-8_11

In Chapter 8 titled "Functional Nanoparticles for Molecular Imaging-Guided Gene Delivery and Therapy", the name and affiliation of the author Yu Zhang was incorrect.

In the List of Contributors in the FM, the name and affiliation of Yu Zhang has been missed.

The author name and correct affiliation should read as follows:

Y. Zhang
Electrical Engineering Program, College of Engineering and Mathematical Sciences, University of Vermont, Burlington, VT 05405, USA

The online version of the original chapter can be found at
http://dx.doi.org/10.1007/978-981-10-0063-8_8